PETROELASTIC APPROXIMATIONS FOR QUANTITATIVE 4D SEISMIC INTERPRETATION

Erick Raciel Alvarez Galvez

A Thesis Submitted for the Degree of Doctor of Philosophy

Institute of Petroleum Engineering

Heriot-Watt University

October 2014

ABSTRACT

4D seismic interpretation generally involves analysing changes in amplitude or travel times between a base-line survey (ideally pre-production) and subsequent monitor surveys. Amplitude analysis is commonly performed by calculating the 4D amplitude difference – given by the subtraction of time-shift corrected monitor - base amplitude volumes. This thesis focuses on the development of theoretical approximations that allow explaining, from a physics perspective, the relation between the 4D amplitude signal and production-related changes in pore pressure and fluid saturation. The main objective of finding such approximations is to aid 4D interpretation, by providing physical insights in a quick and intuitive manner that conventional modelling cannot offer.

The approximations developed here are expressed in terms of constants and variables with clear physical meaning. This helps in identifying the role that each parameter has in the resulting 4D seismic signal, allowing us to identify those terms with the largest impact and uncertainty. The first conclusion obtained from our derivations is that, except for porosity, the parameters involved act as groups of parameters rather than as individual parameters to form the 4D seismic signal. It is also possible to demonstrate how porosity plays a major role in the magnitude of the 4D signal (this is intuitive for saturation but not for pressure). It was found that, for low porosities, pressure is expected to dominate over saturation and vice-versa. Another important observation is that the magnitude of the rock stress sensitivity determines the polarity of 4D amplitude changes in places where pressure and saturation signals cancel each other (like around injectors). The formulations also allow the analysis of the angle dependence (4D AVO). We observe that, regardless of the type of AVO anomaly of the reservoir in the seismic base line, the 4D AVO signatures behave in a similar way and the role of the overlaying shale in the 4D amplitude variation with angle is minimal. Additionally, previous research has shown that the rock stress sensitivity carries the

largest uncertainty and, using the formulations, a methodology was devised to determine a constraint, based on field data observations at injector wells from different fields.

The first approximation developed considers a single interface applicable for non-compacting oil reservoirs with no free gas. Subsequent approximations were developed to define the 4D response of fluid contacts, which are applicable to non-compacting reservoirs, including those where free gas is present. The fluid contact equations for the oil-water system were used to develop a technique to estimate residual oil saturation from 4D seismic amplitudes and the method was tested in two North Sea datasets. Finally, an incidental outcome of the new formulations is their potential to be used for 4D seismic inversion to compute pressure and saturation changes. We provide a basic (map-based) implementation of 4D inversion applicable to oil reservoirs with no free gas. The inversion scheme has a straight-forward implementation and requires a minimal amount of *a priori* information and constraints. It was found that, three angle stacks are required as a minimum to obtain a meaningful inversion result.

I dedicate this work with all my love to my son Edison and my nephews Noé and Ethan.

(Dedico este trabajo con todo mi amor a mi hijo Edison y mis sobrinos Noé e Ethan)

"Our greatest weakness lies in giving up. The most certain way to succeed is always to try just one more time"

Nuestra mayor debilidad es darse por vencido. La forma más certera de tener éxito es siempre intentarlo una vez más

Thomas Alva Edison

American Inventor

ACKNOWLEDGEMENTS

Antes que nada: ¡Gracias a Dios!

I want to thank my dear wife Eva, for all the support, love and understanding. Infinite thanks to my son Edison: you are my inspiration and my greatest pride, thanks for your patience and unconditional love.

Agradezco infinitamente a mis padres por todo su apoyo, su amor incondicional y sobre todo por darme el mejor ejemplo. De igual forma a mis hermanas por todo su apoyo y cariño, así como a mis amados sobrinos Ethan y Noé. Gracias también a mis tías, mi abuelita, mis suegros, cuñados y a todos mis amigos por ser parte de mí. Un agradecimiento especial a mis casi-hermanos Alejandro Mera, Cesar Cornejo y Jaume Hernández que siempre han creído en mí y me han apoyado. Finalmente, a Papito Temo, Mamita Elvia, Abuelito Beto y Noé C. B, los extrañamos mucho.

Special thanks to my dear friend and mentor Jonathan Hall thanks for all your teachings, support, and encouragement during these years. To my supervisor Colin MacBeth, thanks for a great and fruitful collaboration, you are the best geophysicist I know, a real scientist and a great person; I have learnt a lot much from you during these years.

I thank Senergy Ltd. for 3 years of financial support for this research, particularly to David Sherrard and Les Coats. Many thanks to the ETLP sponsors and my colleagues for their insights and suggestions, In particular to Hamed Amini for his help with the sim2seis and his friendship. I also thank Esso Exploration and Production UK Limited as well as my current employer Shell UK Ltd. for permissions to use their data in Chapter 6. In particular, I am grateful to Jonathan Brain, Mariano Floricich and John Wild. Special thanks also to my PhD examiners, Professor Eric Mackay and Professor Yanghua Wang for their valuable insights and feedback on this work.

DECLARATION STATEMENT

ACADEMIC REGISTRY
Research Thesis Submission

Name:	ERICK RACIEL ALVAREZ GALVEZ		
School/PGI:	INSTITUTE OF PETROLEUM ENGINEERING		
Version: *(i.e. First, Resubmission, Final)*	FIRST	Degree Sought (Award **and** Subject area)	PhD, PETROLEUM ENGINEERING

Declaration

In accordance with the appropriate regulations I hereby submit my thesis and I declare that:

1) the thesis embodies the results of my own work and has been composed by myself
2) where appropriate, I have made acknowledgement of the work of others and have made reference to work carried out in collaboration with other persons
3) the thesis is the correct version of the thesis for submission and is the same version as any electronic versions submitted*.
4) my thesis for the award referred to, deposited in the Heriot-Watt University Library, should be made available for loan or photocopying and be available via the Institutional Repository, subject to such conditions as the Librarian may require
5) I understand that as a student of the University I am required to abide by the Regulations of the University and to conform to its discipline.

* *Please note that it is the responsibility of the candidate to ensure that the correct version of the thesis is submitted.*

Signature of Candidate:		Date:	29-10-2014

Submission

Submitted By *(name in capitals)*:	ERICK RACIEL ALVAREZ GALVEZ
Signature of Individual Submitting:	
Date Submitted:	29-10-2014

For Completion in the Student Service Centre (SSC)

Received in the SSC by *(name in capitals)*:			
Method of Submission *(Handed in to SSC; posted through internal/external mail)*:	Handed to SSC		
E-thesis Submitted ***(mandatory for final theses)***			
Signature:		Date:	

Please note this form should bound into the submitted thesis.

Updated February 2008, November 2008, February 2009, January 2011

PUBLICATIONS RELATED TO THIS WORK

Part of the work contained in this thesis has also been presented in the following publications:

Chapters 2 and 3:

Alvarez, E. and MacBeth C. (2014). An insightful parameterisation for the flatlander's interpretation of time-lapsed seismic data: Geophysical prospecting. Vol 62, No 1. 75-96.

Chapter 3:

Alvarez, E. and MacBeth C. (2012). Constraining the Petroelastic Model with a Flatlander's Interpretation of the 4D Signal: 74th EAGE Conference & Exhibition, Copenhagen. Y019

Chapter 5:

Alvarez, E. and MacBeth C. (2014). Quantification of Residual Oil Saturation Using 4D Seismic Data: 76th EAGE Conference & Exhibition, Amsterdam. We G102 15

The publications cited above are attached to this thesis in Appendix 3.

NOMENCLATURE

This section presents a list of the symbols and quantities mentioned or used in this thesis, organised by subject and in order of appearance.

Landrø (1999) equations and modifications (Meadows, 2001; Trani, et al., 2013)

Property	Description	Units
ΔR_o	Time lapse change in the AVO gradient	unit-less
ΔG	Time lapse change in the AVO intercept	unit-less
α	P wave velocity	km/s
β	S wave velocity	km/s
ρ	Density	kg/m^3
$j_\propto, k_\propto$	Empirical fit for P velocity with respect to saturation changes	unit-less
$l_\propto, m_\propto$	Empirical fits for P velocity with respect to pressure changes	MPa^{-1}
l_β, m_β	Empirical fits for S velocity with respect to pressure changes	MPa^{-1}
k_ρ	Empirical fits for density with respect to saturation changes	unit-less
$\Delta\alpha$	Time lapse change in P velocity	km/s
$\Delta\beta$	Time lapse change in S velocity	unit-less
$\Delta\rho$	Time lapse change in density	unit-less
$\frac{\Delta\alpha}{\alpha}$	Time lapse P velocity reflectivity	unit-less
$\frac{\Delta\beta}{\beta}$	Time lapse S velocity reflectivity	unit-less
$\frac{\Delta\rho}{\rho}$	Time lapse density reflectivity	unit-less
ΔP	Time lapse change in reservoir pressure	MPa
ΔS	Time lapse change in fluid saturation	unit-less
ΔIP	Time lapse change in P impedance	kg/sm^2
ΔIS	Time lapse change in S impedance	kg/sm^2
$\frac{\Delta IP}{IP}$	Time lapse P impedance reflectivity	unit-less
$\frac{\Delta IS}{IS}$	Time lapse P impedance reflectivity	unit-less
ΔT_{PP}	Time lapse change in time arrivals (time-shifts)	unit-less
α_0^r	Base line interval velocity	km/s

$\delta\alpha_0^r$	Absolute change in the velocity between baseline and monitor	km/s
D	Reservoir time thickness	ms

MacBeth et al. (2006a) formulation

Property	Description	Units
ΔS	Time lapse change in fluid saturation	unit-less
ΔP	Time lapse change in reservoir pressure	MPa
$\frac{\Delta A}{\overline{A_0}}$	Time lapse change in amplitude of any seismic attribute normalised to the average response of the base	unit-less
$\frac{\Delta S}{\bar{S}}$	Time lapse change in fluid saturation normalised to the average response of the base	unit-less
$\frac{\Delta P}{\bar{P}_i}$	Time lapse change in reservoir pressure normalised to the average response of the base	unit-less
CS	Empirical constant controlling saturation related effects	unit-less
CP	Empirical constant controlling pressure related effects	unit-less

Gassmann equations (1951) and related models

Property	Description	Units
κ_{sat}	Bulk modulus of the saturated rock	GPa
κ_{dry}	Bulk modulus of the matrix (grains + pores)	GPa
κ_m	Bulk modulus of the mineral (grains)	GPa
κ_{fl}	Bulk modulus of the fluid filling the pores	GPa
ϕ	Porosity	fraction
μ_{sat}	Shear modulus of the saturated rock	GPa
μ_{dry}	Shear modulus of the matrix (grains + pores)	GPa
μ_m	Shear modulus of the mineral (grains)	GPa
f_i	Volume fraction of the i-th mineral or fluid	fraction
κ_{fl-i}	Bulk modulus of the i-th fluid	GPa
κ_{m-i}	Bulk modulus of the i-th mineral	GPa
$\Delta\kappa_{sat}$	Change in the bulk modulus as a result of fluid replacement at the porosity ϕ	GPa
$\Delta\kappa_R$	Change in the Reuss average of minerals and fluids evaluated at the reference porosity ϕ_R	GPa

ϕ_R	Reference porosity obtained from the graphical representation of Gassmann equations (Mavko and Mukerji, 1995)	unit-less
$\Delta\kappa_{fl}$	Change in the bulk modulus of the fluid as a result of fluid replacement	GPa

Velocity as a function of effective stress

Property	Description	Units
σ_{eff}	Effective stress	MPa
σ_{ob}	Overburden stress	MPa
α	Stress coefficient	unit-less
P	Reservoir pressure or pore pressure	MPa
$V(\sigma_{eff})$	P velocity as a function of effective stress	km/s
$V(\sigma_{max})$	P velocity at the maximum effective stress measured	km/s
a, b, c	Empirical fits obtained from a velocity versus effective stress plot	unit-less
e	Euler's number e ≈ 2.71828	unit-less
V_0	P velocity at zero effective stress	km/s
V_∞	P velocity at the "infinity" effective stress	

MacBeth (2004) equations

Property	Description	Units
κ_∞	Bulk modulus at the "infinity" effective stress	GPa
E_κ	Defines the slope of the stress sensitivity curve for the bulk modulus before the asymptote	unit-less
P_κ	Defines the effective stress value at which the bulk modulus stress sensitivity curve asymptotes	MPa
μ_∞	Shear modulus at the "infinity" effective stress	GPa
E_μ	Defines the slope of the stress sensitivity curve for the shear modulus before the asymptote	unit-less
P_μ	Defines the effective stress value at which the shear modulus stress sensitivity curve asymptotes	MPa
κ_m	Bulk modulus of the mineral forming the rock	GPa
μ_m	Shear modulus of the mineral forming the rock	GPa

ε'	Stress coefficient, equivalent to the ratio between porosity and the critical porosity	unit-less
ϕ_c	Critical porosity, the maximum porosity a rock allows before falling apart	fraction

Mass balance equation

Property	Description	Units
ρ	Bulk density	kg/m^3
ρ_i	Density of the i-th mineral	kg/m^3
ρ_m	Density of the mineral forming the rock	kg/m^3
S_{wi}	Water saturation at the initial state	fraction
ρ_w	Density of water	kg/m^3
ρ_o	Density of oil	kg/m^3

Derivation of the time lapse AVO equation as a function of elastic parameters

Property	Description	Units
$R(\theta)$	Angle dependent reflection coefficient	unit-less
$\overline{V_P}$	Average compressional velocity across the interface	km/s
$\overline{V_S}$	Average shear velocity across the shale/sand interface	km/s
$\Delta\kappa$	Difference of bulk modulus across the shale/sand interface	GPa
$\bar{\kappa}$	Average bulk modulus across the shale/sand interface	GPa
$\Delta\mu$	Difference of shear modulus across the shale/sand interface	GPa
$\bar{\mu}$	Average shear modulus across the shale/sand interface	GPa
$\Delta\rho$	Difference of density across the shale/sand interface	kg/m^3
$\Gamma_1, \Gamma_2, \Gamma_3$	Angle dependent functions from Gray et al. (1999) equation	unit-less
$\bar{M}$	Average P modulus across the shale/sand interface	GPa
$\bar{\rho}$	Average density across the shale/sand interface	kg/m^3
$\Delta R(\theta)_{TL}$	Time lapse angle dependent reflection coefficient	unit-less
$\Delta\kappa^b$	Bulk modulus difference across the interface at the seismic base	GPa
$\Delta\kappa^m$	Bulk modulus difference across the interface at the monitor	GPa
$\Delta\mu^b$	Shear modulus difference across the interface at the seismic base	GPa
$\Delta\mu^m$	Shear modulus difference across the interface at the monitor	GPa
$\Delta\rho^b$	Difference in density across the interface at the seismic base	kg/m^3

$\Delta\rho^m$	Difference in density across the interface at the seismic monitor	kg/m^3
$\Delta\kappa_{TL}$	Time lapse difference in the bulk modulus (monitor - base)	GPa
$\Delta\mu_{TL}$	Time lapse difference in the shear modulus (monitor - base)	GPa
$\Delta\rho_{TL}$	Time lapse difference in density (monitor - base)	kg/m^3
κ^b	Bulk modulus of the reservoir at the seismic base	GPa
μ^b	Shear modulus of the reservoir at the seismic base	GPa
ρ^b	Density of the reservoir at the seismic base	kg/m^3
$\overline{\kappa^b}$	Average bulk modulus across the interface at the seismic base	GPa
$\overline{\kappa^m}$	Average bulk modulus across the interface at the monitor	GPa
$\overline{\mu^b}$	Average shear modulus across the interface at the seismic base	GPa
$\overline{\mu^m}$	Average shear modulus across the interface at the monitor	GPa
$\overline{\rho^b}$	Average density across the interface at the seismic base	kg/m^3
$\overline{\rho^m}$	Average density across the interface at the monitor	kg/m^3
κ^{sh}	Bulk modulus of the overlaying shale	GPa
μ^{sh}	Shear modulus of the overlaying shale	GPa
ρ^{sh}	Density of the overlaying shale	kg/m^3

Derivation of the time lapse AVO equation as a function of pressure and saturation changes

Property	**Description**	**Units**
ΔS_w	Time lapse change in water saturation	unit-less
ΔP	Time lapse change in reservoir pressure	MPa
S_{wi}	Water saturation at the initial state	v/v
P_i	Initial reservoir pressure	MPa
$\Delta S_w/S_{wi}$	Time lapse pressure saturation change reflectivity	unit-less
$\Delta P/P_i$	Time lapse pressure change reflectivity	unit-less
S_{wc}	Connate water saturation	v/v
S_{or}	Residual oil saturation	v/v
ϕ	Porosity	fraction
NTG	Net to gross	fraction
P^b	Reservoir pressure of the seismic base	MPa
P^m	Reservoir pressure of the seismic monitor	MPa
κ_m	bulk modulus of the sand mineral (generally quartz)	GPa

σ_{ob}	Overburden stress	MPa
$\Delta\kappa_{dry}$	Time lapse difference in the dry bulk modulus (monitor - base)	GPa
ε	Pore stiffness constant, defined as function of porosity and the reference porosity from the linear form of Gassmann ($\varepsilon = \phi/\phi_R$)	unit-less
κ_o^b	Bulk Modulus of oil at the initial state	GPa
κ_w^b	Bulk Modulus of water at the initial state	GPa
ρ_o^b	Density of oil at the initial state	kg/m^3
ρ_w^b	Density of water at the initial state	kg/m^3
O_κ	Local gradient of the fluid pressure sensitivity curve for oil bulk modulus	unit-less
W_κ	Local gradient of the fluid pressure sensitivity curve for water bulk modulus	unit-less
A_κ	Local gradient of the stress sensitivity curve for the bulk modulus evaluated at the initial pressure P_i	MPa^{-1}
B_μ	Local gradient of the stress sensitivity curve for the shear modulus evaluated at the initial pressure P_i	MPa^{-1}
W_ρ	Local density gradient for the fluid pressure sensitivity of water	kg/m^3 MPa^{-1}
O_ρ	Local density gradient for the fluid pressure sensitivity of oil	kg/m^3 MPa^{-1}
$\bar{\Gamma}_1, \bar{\Gamma}_2, \bar{\Gamma}_3$	Average angle dependent functions for a specific angle range	unit-less
ε'	stress coefficient (related to critical porosity ($\varepsilon' \approx \phi/\phi_C$)	unit-less
α	stress coefficient (Hoffman, et al., 2005)	unit-less
$\Delta A(\theta)_{TL}$	Average time lapse amplitude around a given interface	unit-less
C_S	Constant controlling the contribution of water saturation changes to the time lapse amplitude	unit-less
C_P	Constant controlling the contribution of reservoir pressure changes to the time lapse amplitude	unit-less
N_1	Bulk modulus fluid contrast	unit-less
N_2	Density fluid contrast	unit-less
N_3	Bulk modulus rock stress sensitivity	unit-less
N_4	Shear modulus rock stress sensitivity	unit-less
N_5	Bulk modulus fluid pressure sensitivity	unit-less
N_6	Density fluid pressure sensitivity	unit-less

m	Constant introduced to remove the dimensions of the pressure related terms. m = 1 MPa	MPa
$\overline{s(t)}$	Average wavelet scaling	unit-less
${C_P}^{rock}$	Constant controlling the contribution of the rock stress sensitivity to the time lapse amplitude	unit-less
${C_P}^{fluid}$	Constant controlling the contribution of the fluid pressure sensitivity to the time lapse amplitude	unit-less
C_S/C_P	Fluid contrast/stress sensitivity ratio. Controls the dominance of saturation over pressure in the 4D signal or vice versa	unit-less
FC	Fluid contrast (equivalent to C_S)	unit-less
RSS	Rock stress sensitivity (equivalent to ${C_P}^{rock}$)	unit-less
FPS	Fluid pressure sensitivity (equivalent to ${C_P}^{fluid}$)	unit-less

Derivation of the time lapse AVO equations for oil-water contact movements

Property	**Description**	**Units**
$\Delta R(\theta)^b_{oowc}$	Angle dependent reflection coefficient of the original oil-water contact at the seismic base line.	unit-less
$\Delta\kappa^b_{oowc}$	Difference in the bulk modulus across the fluid interface formed by the original oil-water contact at the seismic base line.	GPa
$\Delta\mu^b_{oowc}$	Difference in the shear modulus across the fluid interface formed by the original oil-water contact at the seismic base line.	GPa
$\Delta\rho^b_{oowc}$	Difference in density across the fluid interface formed by the original oil-water contact at the seismic base line.	kg/m^3
$\overline{M^b}$	Average P modulus across the fluid interface formed by the original oil-water contact at the seismic base line	GPa
$\overline{\rho^b}$	Average density across the fluid interface formed by the original oil-water contact at the seismic base line	kg/m^3
κ^b_{Sw}	Bulk modulus of the water saturated rock at the seismic base line pressure	GPa
κ^b_{So}	Bulk modulus of the oil saturated rock at the seismic base line pressure	GPa
ρ^b_{Sw}	Density of the water saturated rock at the seismic base line pressure	kg/m^3

ρ_{So}^{b}	Density of the oil saturated rock at the seismic base line pressure	kg/m^3
M_{Sw}^{b}	P modulus of the water saturated rock at the seismic base line pressure	GPa
M_{So}^{b}	P modulus of the oil saturated rock at the seismic base line pressure	GPa
$\Delta R(\theta)_{oowc}^{m}$	Angle dependent reflection coefficient of the original oil-water contact at the monitor	unit-less
$\Delta\kappa_{oowc}^{m}$	Difference in the bulk modulus across the fluid interface formed by the original oil-water contact at the monitor	GPa
$\Delta\mu_{oowc}^{m}$	Difference in the shear modulus across the fluid interface formed by the original oil-water contact at the monitor	GPa
$\Delta\rho_{oowc}^{m}$	Difference in density across the fluid interface formed by the original oil-water contact at the monitor	kg/m^3
$\overline{M^m}$	Average P modulus across the fluid interface formed by the original oil-water contact at the monitor	GPa
$\overline{\rho^m}$	Average density across the fluid interface formed by the original oil-water contact at the monitor	kg/m^3
κ_{Sw}^{m}	Bulk modulus of the water saturated rock at the monitor pressure	GPa
κ_{sp}^{m}	Bulk modulus of the swept zone (water partially replacing oil) at the monitor pressure	GPa
ρ_{Sw}^{m}	Density of the water saturated rock at the monitor pressure	kg/m^3
ρ_{sp}^{m}	Density of the swept zone (water partially replacing oil) at the monitor pressure	kg/m^3
M_{Sw}^{m}	P modulus of the water saturated rock at the monitor pressure	GPa
M_{sp}^{m}	P modulus of the swept zone (water partially replacing oil) at the monitor pressure	GPa
$\Delta R(\theta)_{oowc}$	Time lapse angle dependent reflection coefficient at the original oil-water contact	unit-less
$\Delta\kappa_{oowc}$	Time lapse difference in the bulk modulus at the original oil-water contact	GPa
$\Delta\rho_{oowc}$	Time lapse difference in density at the original oil-water contact	GPa
$\Delta R(\theta)_{powc}$	Time lapse angle dependent reflection coefficient at the produced oil-water contact	unit-less

$\Delta\kappa_{powc}$	Time lapse difference in the bulk modulus at the produced oil-water contact	GPa
$\Delta\rho_{powc}$	Time lapse difference in density at the produced oil-water contact	GPa
C_S^o	Constant controlling the contribution of fluid saturation changes to the time lapse amplitude in oil-water systems	unit-less
C_P^o	Constant controlling the contribution of reservoir pressure changes to the time lapse amplitude in oil-water systems	unit-less
N_1^o	Bulk modulus fluid contrast for in oil-water systems	unit-less
N_2^o	Density fluid contrast for in oil-water systems	unit-less
N_3^o	Bulk modulus rock stress sensitivity for in oil-water systems	unit-less
N_5^o	Bulk modulus fluid pressure sensitivity for in oil-water systems	unit-less
N_6^o	Density fluid pressure sensitivity for in oil-water systems	unit-less
ζ_{BP}	Defines the polarity of the fluid pressure sensitivity in relation of the bubble point pressure	unit-less
$\Delta R(\theta)_{owc}^{comp}$	Composite time lapse angle dependent reflection coefficient, combines the original and produced oil-water contacts below tuning thickness	unit-less
i	Imaginary number = $\sqrt{-1}$	unit-less
ω	frequency	Hz
Δt_o	Two way time thickness of the swept zone (area between the original and produced oil-water contact)	ms
$\dot{s}(t)$	Time derivative of the wavelet	unit-less

Derivation of the time lapse AVO equations for a combination of fluid contact movements (oil reservoirs with pre-existing or forming gas cap)

Property	Description	Units
S_{org}	Residual oil saturation to gas	v/v
S_{gro}	Residual gas saturation to oil	v/v
S_{grw}	Residual gas saturation to water	v/v
ΔS_g	Time lapse gas saturation change	v/v
$\Delta R(\theta)_{TL}^{comp}$	Composite time lapse angle dependent reflection coefficient, combines the top of the reservoir and internal fluid contact	unit-less

	reflections below tuning thickness	
$\Delta R(\theta)_{top}$	Time lapse angle dependent reflection coefficient at the top of the reservoir (shale/sand interface)	unit-less
$\Delta R(\theta)_{ogoc}$	Time lapse angle dependent reflection coefficient at the original gas-oil contact	unit-less
$\Delta R(\theta)_{pgoc}$	Time lapse angle dependent reflection coefficient at the produced gas-oil contact	unit-less
$\Delta R(\theta)_{base}$	Time lapse angle dependent reflection coefficient at the base of the reservoir (sand/shale interface)	unit-less
$\Delta A(\theta)_{TL}^{comp}$	Composite time lapse amplitude, combines the reservoir and internal fluid contact reflections below tuning thickness	unit-less
Δt_g	Two way time thickness of the gas transition zone (area between the original and produced gas-oil contact)	ms
t_T	Total two way time thickness of the reservoir	ms
${C_S}^m$	Constant controlling the contribution of fluid saturation changes to the time lapse amplitude in gas-oil systems	unit-less
${C_P}^m$	Constant controlling the contribution of reservoir pressure changes to the time lapse amplitude in gas-oil systems	unit-less
N_1^m	Bulk modulus fluid contrast for in gas-oil systems	unit-less
N_2^m	Density fluid contrast for in gas-oil systems	unit-less
N_3^m	Bulk modulus rock stress sensitivity for in gas-oil systems	unit-less
N_5^m	Bulk modulus fluid pressure sensitivity for in gas-oil systems	unit-less
N_6^m	Density fluid pressure sensitivity for in gas-oil systems	unit-less

Derivation of the time lapse AVO equations for gas-water contact movements

Property	**Description**	**Units**
$\Delta R(\theta)_{ogwc}$	Time lapse angle dependent reflection coefficient at the original gas-water contact	unit-less
$\Delta R(\theta)_{pgwc}$	Time lapse angle dependent reflection coefficient at the produced gas-water contact	unit-less
${C_S}^G$	Constant controlling the contribution of fluid saturation changes to the time lapse amplitude in gas-water systems	unit-less
${C_P}^G$	Constant controlling the contribution of reservoir pressure	unit-less

	changes to the time lapse amplitude in gas-water systems	
N_1^G	Bulk modulus fluid contrast for in gas-water systems	unit-less
N_2^G	Density fluid contrast for in gas-water systems	unit-less
N_3^G	Bulk modulus rock stress sensitivity for in gas-water systems	unit-less
N_5^G	Bulk modulus fluid pressure sensitivity for in gas-water systems	unit-less
N_6^G	Density fluid pressure sensitivity for in gas-water systems	unit-less

Derivation equations to estimate remaining oil saturation

Property	Description	Units
S_{orw}^{pore}	Pore scale residual oil saturation to water	v/v
S_{oir}	Irreducible oil saturation	v/v
ROS	Remaining oil saturation (after water sweep)	v/v
$\Delta A(\theta)_{oowc}^{before}$	Pre-production amplitude at the original oil water contact	unit-less
$\Delta A(\theta)_{oowc}^{after}$	Post-production amplitude at the original oil water contact	unit-less
$\Delta A(\theta)_{oowc}$	Time lapse angle dependent amplitude at the original oil-water contact	unit-less
ΔA_{oowc}^{far}	Far angle time lapse amplitude at the original oil-water contact	unit-less
$\Delta A(\theta)_{owc}^{comp}$	Composite time lapse angle dependent amplitude, combines the original and produced oil-water contacts below tuning thickness	unit-less
ΔA_{comp}^{far}	Far angle composite time lapse amplitude, combines the original and produced oil-water contacts below tuning thickness	unit-less

4D Inversion for pressure and saturation

Property	Description	Units
$\mathbf{d}$	Data observation matrix	n/a
$\mathbf{G}$	Data kernel matrix	n/a
$\mathbf{m}$	Estimate parameters matrix	n/a
E	Estimated least square error	n/a
ΔA_{TL}^{obs}	Observed time lapse amplitude	unit-less
ΔA_{TL}^{pred}	Predicted time lapse amplitude	unit-less
$\mathbf{m}^{LS}$	Least square solution to the estimate parameter matrix	n/a
$\mathbf{G}^{T}$	Transpose of the data kernel matrix	n/a
$\mathbf{H}$	Equality constraint data kernel matrix	n/a

$\mathbf{H}^{T}$	Transpose of the equality constraint data kernel matrix	n/a
$\mathbf{h}$	Equality constraint data observation matrix	n/a
λ	Lagrange multipliers	n/a
C_S^{χ}, C_P^{χ}	Saturation and pressure constants at a given angle where the equality constraint is satisfied	n/a
$\lvert A \rvert$	Determinant of the inversion matrix $[\mathbf{GG}^{T}]$	n/a
$\mathbf{N}$	Data resolution matrix, provides a measure of the match between observations and predictions	n/a
$\mathbf{G}^{-g}$	Data kernel matrix that satisfies the inversion solution	n/a
$\mathbf{d}^{obs}$	Observed data matrix	n/a
$\mathbf{d}^{pred}$	Predicted data matrix	n/a
$\mathbf{I}$	Identity matrix	n/a
δ_{ij}	Represents the elements of the identity matrix	n/a
$\mathbf{R}$	Model resolution matrix, provides a measurement of whether the inverted parameters can be uniquely resolved	n/a
$[\mathbf{cov}_{u}\boldsymbol{m}]$	Unit model covariance matrix, provides a way of evaluating the inversion stability and sensitivity to noise	n/a

Conclusions and recommendations

Property	Description	Units
$STOIIP$	Stock tank oil initially in place	stb
GRV	Gross rock volume	km^3
B_{oi}	Formation volume factor	rb/stb
RF	Recovery factor	unit-less
ΔV_{tot}	Total oil production	stb
V_o	Volume of oil	stb
V_g	Volume of gas	stb
V_w	Volume of water	stb
C_{fl}	Fluid compressibility	GPa^{-1}
C_o	Compressibility of oil	GPa^{-1}
C_w	Compressibility of water	GPa^{-1}
C_g	Compressibility of gas	GPa^{-1}

LIST OF TABLES

LIST OF FIGURES

Chapter 1: Introduction

"No estudio para saber más sino para ignorar menos"

I do not study to know more, but to ignore less

Juana de Asbaje (Sor Juana Inés de la Cruz)

Mexican Poet and self-taught scholar

In this chapter I set the scene of the thesis and define my objectives and motivations. Relevant previous research is described here, together with a basic description of theories, equations and concepts that will constitute the foundation of the theoretical and practical developments in this research.

1.1 The Challenge

The analysis of 4D seismic is concerned with the identification and mapping of areas related to the effects of reservoir production. The final goal of such analysis is to monitor reservoir performance, improve production forecast, and hence improve reservoir management. Traditionally, 4D seismic analysis is performed qualitatively, as, in general, it is relatively straightforward to build an understanding of the causal relationship between well production and recovery and time-lapsed seismic signatures (Huang et al. 2011). For instance, it is now relatively well known that pore pressure increases due to injection into an isolated reservoir compartment or that an increase in gas saturation due to a drop below a bubble point may lead to a reservoir softening (impedance reduction) and a corresponding change on the mapped seismic amplitudes (Parr, Marsh and Griffin 2000). A pore pressure decrease, due to primary depletion with limited water influx, or water saturation increase, due to water from an injector (or aquifer), leads to a reservoir hardening (impedance increase).

It is also known that 4D seismic signals of pore pressure change plus saturation change could overlap substantially, making interpretation more challenging (Floricich et al. 2006). The link between the seismic data and the reservoir changes induced by production and recovery is important and is known to strongly depend on an in situ seismic-scale petroelastic model (the group of parameters that relate the rock and fluid physics to 4D seismic changes). It is this connection that is investigated in this work, with the overall objective being to devise simple approximations that can relate seismic, engineering and rock/fluid physics domains for ease of interpretation. This is of benefit, as it provides a way of gaining more physical insight into the controlling components of the 4D seismic signal, offering the potential to separate pore pressure and saturation changes in a way that conventional forward modelling cannot offer.

Let us consider the following example: We are producing a large oil reservoir somewhere in the North Sea where several wells have been drilled, based on 4D seismic. There is a relatively good understanding about reservoir behaviour: for instance, it is known that the reservoir is depleting rapidly (hardening signals are expected) but pressure is already below the bubble point, therefore gas out of solution related signals are expected (softening). The reservoir production has to be maintained through water injection, so water flooding signals (hardening) and pressure build-up (softening) signals are also expected. 4D amplitude differences extracted at the top of the reservoir are displayed in Figure 1.1.

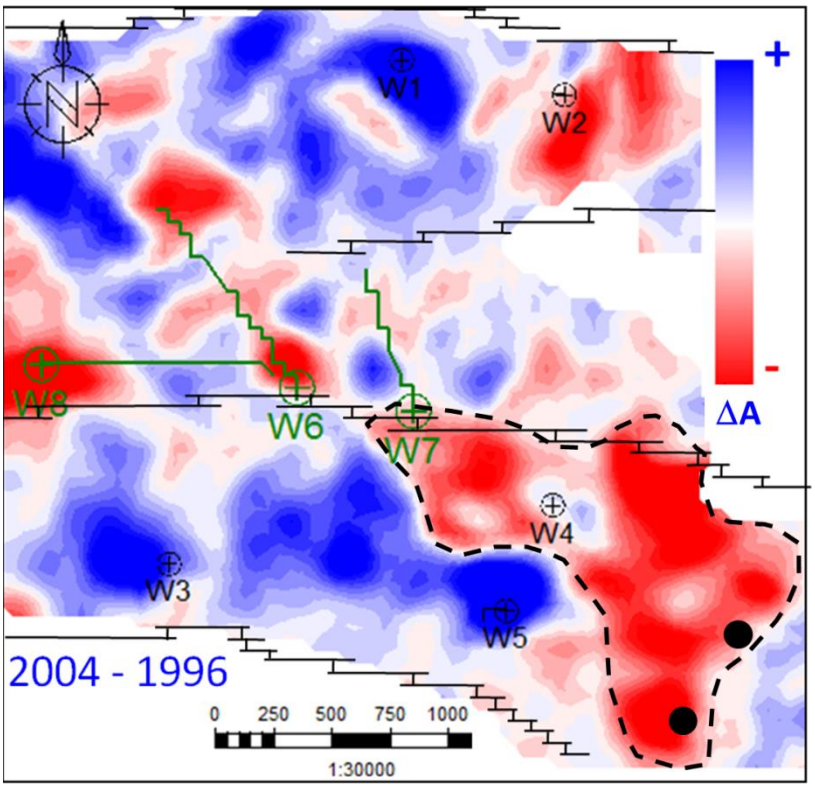

Figure 1.1: 4D amplitude map from a North Sea dataset. Blue signals are a combination of depletion and water flooding due to injection; red signals are a combination of pressure up and gas out of solution. The black dotted line shows what was considered a compartment around injector W4. The black dots are wells which targeted bypassed oil but produced only gas.

An injector well (W4) was drilled to provide pressure support to existing producers in the area (green wells); however no pressure increase was observed in any of the producers. The 4D seismic clearly displays a softening signal around this well (black

dotted line). Based on the amplitude map, two wells were planned targeting bypassed oil inside that area (black dots). Both wells found depleted sands and produced only gas. What happened? A post mortem analysis showed that there is an additional fault separating the injector from the new wells and the softening signal was related to gas ex-solution.

Now let us assume that our objective is to define infill drilling targets for enhanced oil recovery (EOR), we need to distinguish pressure depletion signals from signals related to water flooded areas. Clearly, the 4D difference map cannot be interpreted intuitively, based on rules of thumb. One option is to use simulation-to-seismic modelling to model different plausible scenarios; another option would be to try 4D inversion for pressure and saturation. Both options are time consuming and the decision cannot wait for the inversion modelling results. What if we had a petroelastic approximation that allowed us to quickly assess the expected magnitudes of the depletion, water flooding, gas out of solution and pressure up signals? What if our approximation allowed us to interpret not only the full stack but also the pre-stack data? If so, we could accelerate the interpretation process and make our decision without having to sacrifice our technical assessment. This is the type of scenario where new petroelastic approximations could add value and this is what defines the overall objective of this thesis. To understand the objectives more clearly, an analogy can be made by contrasting the accuracy of forward numerical calculation using full Zoeppritz equations but the reservoir description insight gained by using the Rutherford and Williams (1989) Amplitude versus offset (AVO) classification derived from Shuey (1985) approximations. It is this type of insightful reservoir description that we ultimately seek in our approach.

1.2 Current status of 4D seismic interpretation

There are a number of published petroelastic approximations and interpretation methods that have attempted to solve the issues described above. All these methods

are relevant for our research, as they highlight the importance of the petroelastic model for 4D seismic interpretation and the challenges remaining. A summary of those methods is presented in the next section.

1.2.1 Landrø's relations for 4D interpretation and further modifications

Landrø (1999) provided the first attempt at developing expressions for the 4D AVO behaviour of a single reservoir interface. In this work, each pressure or saturation change term is weighted by a coefficient dependent on the reservoir's elastic constants, which, in turn, must be numerically computed from empirical fluid equations and suitably calibrated laboratory-based measurements. Landrø combined Smith & Gidlow's (1987) and Shuey's (1985) approximations to Zoeppritz's equations to determine the relationship between the gradient and intercept with pressure and saturation changes. This was done by calculating the reflectivities at the pre-production and post-production states and taking the 4D difference approximated to the first order. The general forms of Landrø's equations are expressed as follows:

$$\Delta R_0 \approx \frac{1}{2}\left(k_\alpha \Delta S + k_\rho \Delta S + l_\alpha \Delta P + m_\alpha \Delta P^2\right), \tag{1.1a}$$

$$\Delta G \approx \frac{1}{2}\left(k_\alpha \Delta S + l_\alpha \Delta P + m_\alpha \Delta P^2\right) - \left(\frac{4\beta^2}{\alpha^2}\right)\left(l_\beta \Delta P + m_\beta \Delta P^2\right), \tag{1.1b}$$

where ΔR_0 and ΔG are the time lapse changes in the intercept and gradient respectively, α is the P-wave velocity, β is the S-wave velocity, $k_\alpha, k_\rho, l_\alpha, m_\alpha, l_\beta$ and m_β are empirical polynomial fits, which can be obtained by plotting the changes in P-velocity, S-velocity and density with respect to changes in water saturation and effective stress (Figure 1.2) and are empirically defined as follows:

$$\frac{\Delta\alpha}{\alpha} \approx k_\alpha \Delta S + l_\alpha \Delta P + m_\alpha \Delta P^2, \tag{1.2a}$$

$$\frac{\Delta\beta}{\beta} \approx k_\beta \Delta S + l_\beta \Delta P + m_\beta \Delta P^2 , \qquad (1.2b)$$

$$\frac{\Delta\rho}{\rho} \approx k_\rho \Delta S . \qquad (1.2c)$$

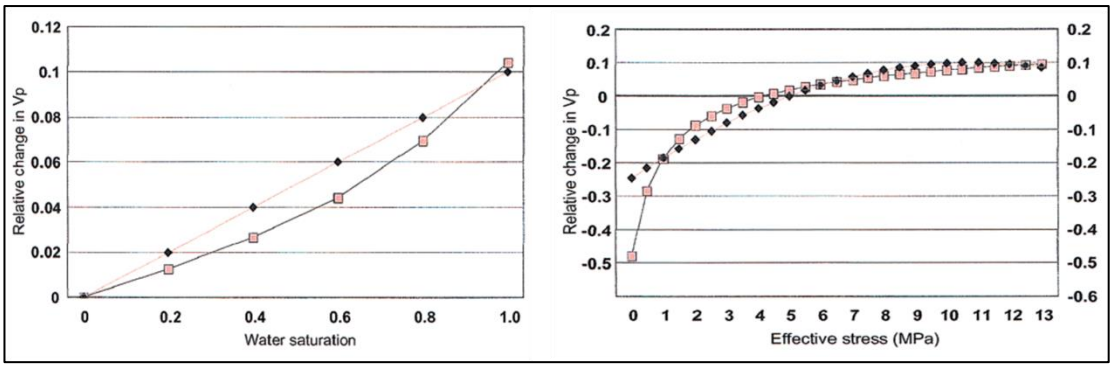

Figure 1.2: Example of time lapse velocity changes plotted against water saturation (left) and effective stress changes (right), from which the empirical constants from Landrø's equations are obtained (Landrø, 2001)

For the Gullfaks field, Landrø found that equations 1.2a and 1.2b are reduced to:

$$\Delta S \approx 8(\Delta R_0 + \Delta G) \qquad (1.3a)$$

and

$$\Delta P \approx 23\Delta R_0 - 35\Delta G. \qquad (1.3b)$$

Using equations 1.3a and 1.3b, Landrø was able to distinguish pressure and saturation changes in the Gullfaks field (**Figure 1.3**). Following this work, Meadows (2001) proposed two modifications to Landrø's method. The first modification is to use Aki and Richard's approximation to solve for P and S impedance reflectivities instead of gradient and intercept which gives similar results to the original method:

$$\frac{\Delta I_P}{I_P} \approx k_\rho \Delta S + k_\alpha \Delta S + l_\alpha \Delta P + m_\alpha \Delta P^2 , \qquad (1.4a)$$

$$\frac{\Delta I_S}{I_S} \approx k_\rho \Delta S + k_\beta \Delta S + l_\beta \Delta P + m_\beta \Delta P^2 . \qquad (1.4b)$$

Where $(\Delta I_P/\mathrm{I_P})$ is the P wave impedance reflectivity and $(\Delta I_S/\mathrm{I_S})$ is the S wave impedance reflectivity respectively. The constants k, l and m are empirical fits obtained by plotting the P wave velocity (α) and S wave velocity (β) versus pressure (ΔP) and saturation (ΔS) changes.

The second modification is to use the original expressions, in terms of gradient and intercept, but incorporating higher order terms to the empirical fits of the velocity versus pressure and velocity versus water saturation plots, leading to:

$$\Delta R_0 \approx \frac{1}{2}\left(k_\rho \Delta S + k_\alpha \Delta S + j_\alpha \Delta S^2 + l_\alpha \Delta P + m_\alpha \Delta P^2\right) \tag{1.5a}$$

and

$$\Delta G \approx \frac{1}{2}\left(k_\alpha \Delta S + j_\alpha \Delta S^2 + l_\alpha \Delta P + m_\alpha \Delta P^2\right) - \left(\frac{4\beta^2}{\alpha^2}\right)\left(l_\beta \Delta P + m_\beta \Delta P^2\right). \tag{1.5b}$$

Meadows' proposed modifications, although in principle representing more accurately the theoretical pressure and saturation curves, in practice, have the downside of increasing the complexity and adding non-uniqueness to the solutions. A further modification to Landrø's method was suggested by Trani et al. (2011). They introduced an equation defining 4D time-shifts as a constraint to Landrø's equation, resulting in the following formulation:

$$\Delta T_{PP} \approx -\frac{2D}{\alpha_0^r + \delta\alpha_0^r}\left(k_\alpha \Delta S + j_\alpha \Delta S^2 + l_\alpha \Delta P + m_\alpha \Delta P^2\right). \tag{1.6}$$

Here, ΔT_{PP} is the 4D time shift, D is the reservoir thickness, α_0^r is the base line interval velocity and $\delta\alpha_0^r$ is the absolute change in the reservoir velocity between baseline and monitor survey, the rest of the parameters are the same as above. This equation is then inverted, in combination with Landrø's equations, using the Gauss-Newton algorithm.

The main disadvantage of Landrø's approach (and subsequent modifications) in terms of 4D interpretation, is that these equations do not provide enough information about

the way the petroelastic model is reflected in the 4D signal. Since a great number of empirical fits are required, it is not possible to develop any general insights about the parameter(s) that control the observed amplitude changes, for example, if these are expected to change vertically or laterally or how to account for such variations. Nevertheless, these developments are a useful starting point and do highlight that, for most reservoirs under production and recovery, linear relations to pore pressure and water saturation may suffice to describe the 4D signal. The modifications to Landrø's method also highlight that introducing non-linearity and more complexity in the equations reduces our ability to develop insights into the rock and fluid physics. Therefore, in petroelastic approximations, a balance must be found between accuracy and interpretability.

Figure 1.3: Inversion results using Landrø's approach for the Gullfaks field. (Left) water saturation changes. (Right) reservoir pressure changes (Landrø, 2001). Yellow colour indicates the largest changes.

1.2.2 4D interpretation using cross-plots and rock physics templates

Tura and Lumley (1998) developed a workflow that allows taking AVO inversion results to interpret pressure and fluid saturations in cross-plots. This is achieved by first, performing a conventional 3D AVO inversion in all vintages, to obtain P and S

impedances. Second, taking the 4D differences by subtracting monitor minus base (in ΔI_P and ΔI_S domains). Third, using well based information and rock and fluid physics equations, such as Gassmann (1951), and some empirical equations to account for pressure changes (such as Mavko, 1998). Finally, interpretation templates are constructed (Figure 1.4) and used to interpret pressure and saturation changes (ΔP and ΔS_w).

Cole et al. (2002) extended this approach to incorporate changes in gas saturation, using a non-linear rock physics model, and tested it in the Schiehallion field (Figure 1.5). In 2009, Andersen et al. developed a similar approach to jointly interpret 3D and 4D AVO inversions. They defined rock physics templates using P-impedance and the V_P/V_S ratio (Figure 1.6), and used a multi-attribute classification scheme to analyse the 3D inverted properties, from which they generated a *lithology cube*, using a static rock physics template; a 4D effect cube is then generated in a similar way but using a dynamic template. Finally they combined both results to generate a joint interpretation template (Figure 1.7), which allowed them to identify targets by highlighting areas where no 4D change was identified and at the same time there was potential sand presence (bypassed oil).

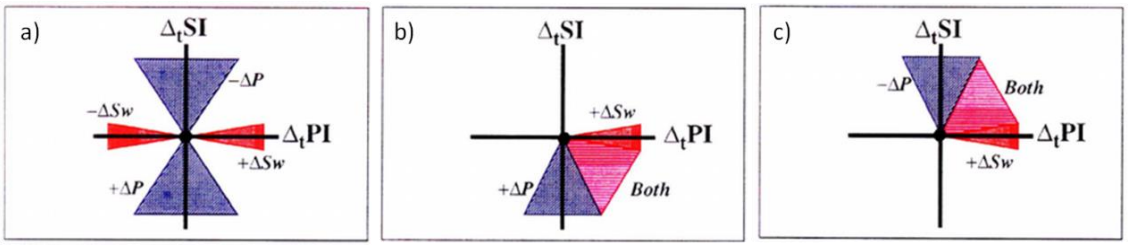

Figure 1.4. Rock physics interpretation templates: (a) Water saturation effects (red) and pressure effects (blue); (b) Expected changes for water injection; (c) Expected changes for primary depletion. (Modified from Tura and Lumley, 1998)

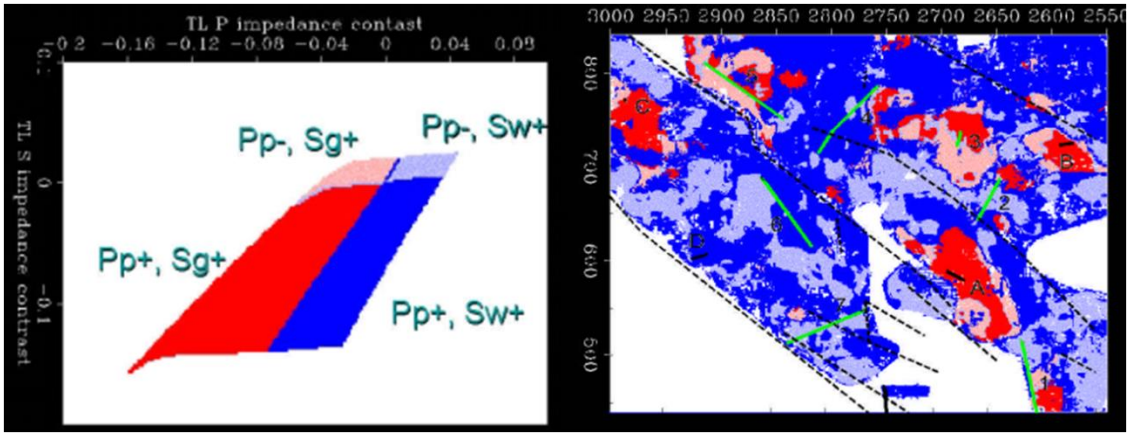

Figure 1.5: Interpretation template showing combined pressure, water and gas saturation changes and semi-quantitative results obtained in the Schiehallion field (Modified from Cole, et al., 2002)

This type of approach implicitly assumes that the same distributions observed or modelled at well locations will be preserved in the inverted seismic volumes. Furthermore, if there is a 4D change that is not included in the interpretation template, it can be incorrectly associated with something else. Additionally, small changes in the parameterisation of the templates or the selection of one particular rock model over another will lead to different interpretations.

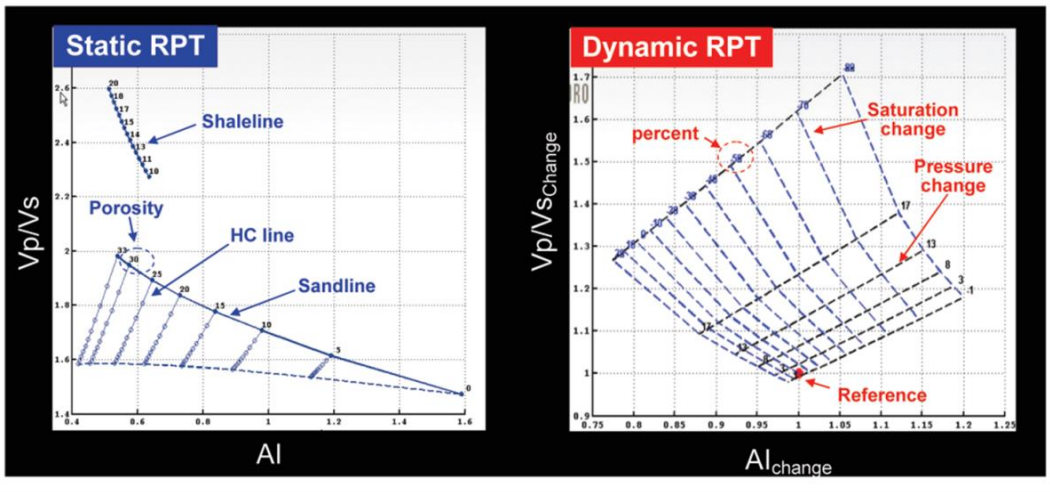

Figure 1.6: Rock physics templates used for static and dynamic interpretations using AVO inverted P-impedance and V_P/V_S ratio. (Andersen, et al., 2009)

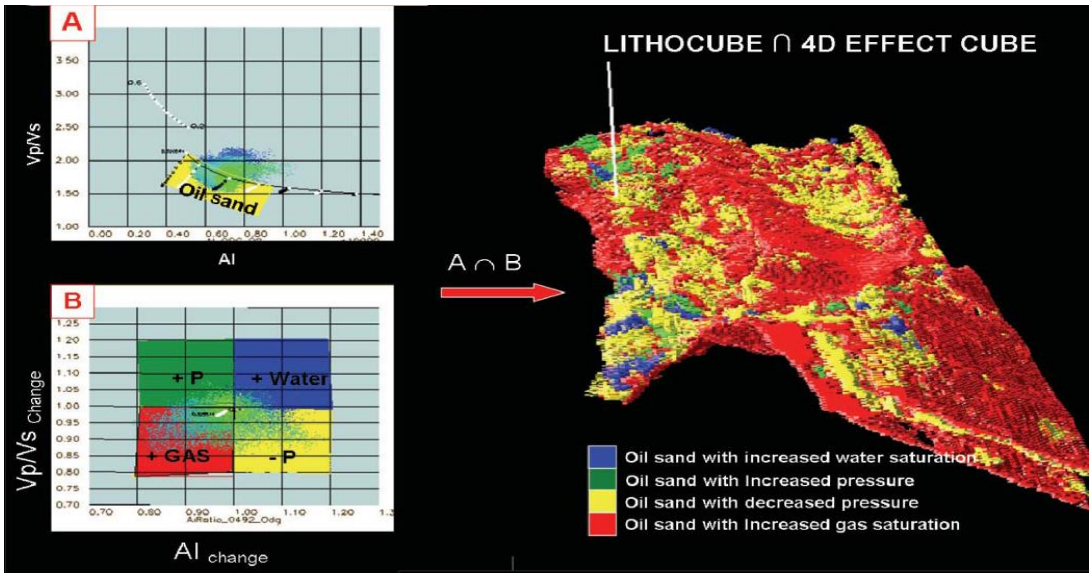

Figure 1.7: Combined static and dynamic rock physics interpretation. (A) Lithology discrimination. (B) 4D reservoir changes. The 3D picture is the combination of both effects (Andersen, et al., 2009).

Another disadvantage is that the interpretation results carry the same uncertainties as 3D AVO inversions (such as non-uniqueness, bias, dependence on the initial model, wavelet uncertainty). Of particular importance is that non-repeatable noise (or minor non-4D related differences between the inversion results in different vintages) will be included in the template and can be interpreted as a genuine reservoir change.

1.2.3 The linear petroelastic model

Another interpretation scheme was proposed by MacBeth, et al. (2006a), through a heuristic equation called the "*Linear Petroelastic Model (LPEM)*", which assumes a linear relation between the normalised pressure and saturation changes and the normalised seismic time lapse signatures. The general equation takes the form:

$$\frac{\Delta A(x,y)}{\overline{A_0}} = CS\frac{\Delta S(x,y)}{\bar{S}} + CP\frac{\Delta P(x,y)}{\overline{P_i}} \quad , \tag{1.7}$$

where the constants C_S and C_P are empirical fits, $\overline{A_0}$, $\bar{S}$ and $\overline{P_l}$ are the average base line seismic saturation and pressure measurements. In practice, these constants are derived by organising equation 1.7 in the form of a matrix, using multiple seismic attributes (including AVO) at well locations where ΔS_o and ΔP are known, and then a least square approach is used to invert for C_S and C_P:

$$\begin{bmatrix} \frac{\Delta A(x,y)_1}{\overline{A_0}} \\ \frac{\Delta A(x,y)_2}{\overline{A_0}} \\ \vdots \\ \frac{\Delta A(x,y)_n}{\overline{A_0}} \end{bmatrix} = \begin{bmatrix} \frac{\Delta S(x,y)_1}{\bar{S}} & \frac{\Delta P(x,y)_1}{\overline{P_l}} \\ \frac{\Delta S(x,y)_2}{\bar{S}} & \frac{\Delta P(x,y)_2}{\overline{P_l}} \\ \vdots & \vdots \\ \frac{\Delta S(x,y)_n}{\bar{S}} & \frac{\Delta P(x,y)_n}{\overline{P_l}} \end{bmatrix} \begin{bmatrix} CS \\ CP \end{bmatrix} . \quad (1.8)$$

Here, $\Delta A_1 \ldots \Delta A_n$ are the normalised amplitude changes at each well location, $\Delta S_1 \ldots \Delta S_n$ and $\Delta P_1 \ldots \Delta P_n$ are the saturation and pressure measurements at the well locations, respectively. Floricich (2006) extended this analysis by adding a multi-attribute classification scheme, where equation 1.8 is applied simultaneously to multiple attribute volumes (including AVO). Principal component analysis (PCA) is performed to determine the most representative C_S and C_P, and a Bayesian classification scheme is used to come up with probabilistic maps of ΔS and ΔP. He used this approach to separate pressure and saturation in the Cormorant field (Figure 1.8).

Although the results obtained through the approaches of MacBeth (2006a) and Floricich (2006) look promising but, in terms of interpretation it is difficult to gain any insights from this approach. Since the constants C_S and C_P are empirical and statistically determined, it is not possible to infer their actual physical meaning or to gain any insights with respect to their lateral variation or their relation to the attributes used for the calculations. Nevertheless, these successful results once more highlight that describing the 4D amplitude difference as a linear weighted function of pressure and saturation changes may not be a bad starting point in our endeavour to define a new petroelastic approximation.

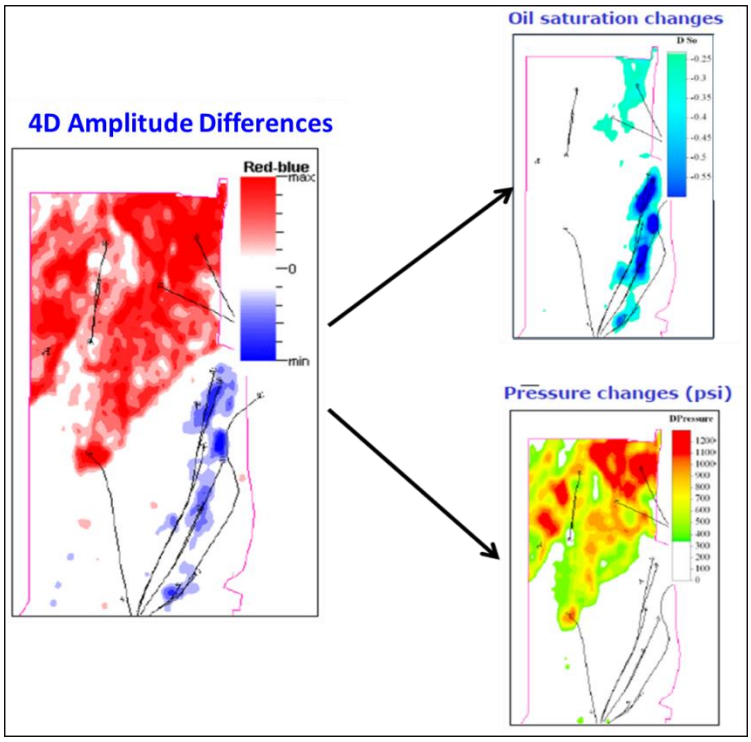

Figure 1.8: Results of 4D inversion using the linear petroelastic model through a multi-attribute analysis and Bayesian classification in the Cormorant field (Floricich, 2006).

1.3 The need for new petroelastic approximations

The methodologies mentioned above highlight some of the important advances made in the problem of separating pressure and saturation effects from 4D seismic data. However, such methods are focused on inversion (computing pressure and saturation changes) rather than on interpretation (developing an understanding of how pressure and saturation affect the 4D seismic amplitudes). For this reason, there are still areas with room for improvement, some of which are:

- There is a high dependence on empirical constants that have no clear physical interpretation; this masks the influence of the petroelastic model in the final results.
- It would be useful to be able to explicitly identify how lateral variations in key reservoir properties such as porosity, fluid contrast, fluid compressibility or

rock frame stress sensitivity affect the pore pressure or saturation change contributions to the 4D seismic signature.

- Current rock physics modelling and 4D inversion techniques are time consuming and the uncertainties are not easy to calculate. It would be useful to have a single equation that can be used to aid 4D seismic interpretations.
- A theoretical petroelastic approximation that includes the 4D AVO could help in extending 4D interpretations to the use of pre-stack data.

It is expected that new theoretical approximations could provide a way of obtaining more physical insights into the controlling components of the 4D seismic signal, and potentially separate pore pressure and saturation changes, providing a quick yet accurate and insightful alternative to conventional 4D modelling workflows.

1.4 Conceptual framework for petroelastic modelling

In order to develop approximations that have some physical meaning, we need to develop an understanding of rock and fluid physics and existing equations that relate seismic changes to changes in rock properties. Many rock physics equations exist that allow modelling diverse rock properties, such as cementation, pore shapes, grain contacts, mineral inclusions, etc. However, we are only interested in the equations which are relevant for 4D seismic interpretation. It is important to mention that this research focuses on non-compacting reservoirs (i.e. where no geomechanical effects are visible in the overburden), therefore only elastic changes are considered.

Conventional rock physics modelling for exploration or field development, generally involves fluid substitutions, for instance to calculate the theoretical AVO response of a sandstone below the oil-water contact from the known AVO response of a reservoir sand. However, in 4D seismic we wish to model, interpret and calculate production related effects; therefore the objectives of rock physics analysis become slightly more complicated. For instance, if we have a few producers and two water injectors in an oil

field, we may wish to calculate the amplitude response of the water-flooding signal, so that we can try to detect it from the observed 4D seismic amplitudes. In this case, the water flooding signal will be affected not only by water saturation changes, but also by reservoir pressure changes. Therefore, it is necessary to find a way of combining pressure and saturation effects in order to model the desired 4D signal in a realistic and engineering-consistent manner. In the following section, I review the relevant equations that will be part of our theoretical development in this research.

1.4.1 Gassmann equations (1951) and their parameterisation

One of the most important developments in rock physics was the Gassmann equations (Gassmann, 1951). These allow computing the change in the bulk modulus associated with a change in the fluid filling the pores. These equations are formulated in this form:

$$\frac{\kappa_{sat}}{\kappa_m - \kappa_{sat}} = \frac{\kappa_{dry}}{\kappa_m - \kappa_{dry}} + \frac{\kappa_{fl}}{\phi\left(\kappa_m - \kappa_{fl}\right)} \tag{1.9a}$$

$$\mu_{sat} = \mu_{dry} \ , \tag{1.9b}$$

where κ_{sat} is the bulk modulus saturated with a given fluid, κ_{dry} is the bulk modulus of the rock frame (minerals and pores), κ_m is the bulk modulus of the mineral forming the rock, κ_{fl} is the bulk modulus of the fluid, μ_{sat} is the shear modulus of the saturated rock, μ_{dry} is the shear modulus of the rock frame and ϕ is porosity.

An important assumption of this equation is that the seismic frequency needs to be low enough to allow the fluid to move and compensate for any pore pressure changes affecting the rock frame. A rule of thumb is that this equation is valid for frequencies of less than 100 Hz; however, the equation has been applied successfully at sonic log frequencies in the order of 100 KHz and starts breaking down at ultra-sonic frequencies (1 MHz) as found by Mavko, et al., (1998). These equations also assume that there is no change in the pore pressure resulting from the fluid change, which implies that κ_{dry}

and μ_{dry} remain constant throughout the fluid substitution process. This is obviously not the case in 4D seismic, since as soon as we start producing, pore pressure changes are induced into the reservoir. For this reason, we need to introduce additional functions into the Gassmann equations to incorporate such changes. A useful starting point is the practical form of the Gassmann equations, shown below, which shows which parameters are expected to change with pressure and fluid saturation:

$$\kappa_{sat}(P, S_w) = \kappa_{dry}(\sigma_{eff}) + \frac{\left[1 - \frac{\kappa_{dry}(\sigma_{eff})}{\kappa_m}\right]^2}{\frac{\phi}{\kappa_{fl}(P, S_w)} + \frac{1-\phi}{\kappa_m} - \frac{\kappa_{dry}(\sigma_{eff})}{{\kappa_m}^2}} \quad , \tag{1.10a}$$

$$\mu_{dry}(\sigma_{eff-1}) \neq \mu_{dry}(\sigma_{eff-2}) \, . \tag{1.10b}$$

From equations 1.10 we can observe that there are three parameters we need to consider that depend on pore pressure changes, the bulk and shear modulus of the rock frame (κ_{dry} and μ_{dry}), which determine the changes in the rock frame resulting from increase or decrease of grain to grain contact as pore pressure changes (rock stress sensitivity), and the bulk modulus of the fluid (κ_{fl}), which controls the pressure effects on the fluids (fluid pressure sensitivity).

The fluid bulk modulus in Gassmann's equations (κ_{fl}) is assumed to be related to a single fluid; however, in practice there is more than one fluid saturating the rock. Hence, it is required to calculate an "effective" bulk modulus. Wood (1955) showed that the effective velocity of a fluid mixture can be computed accurately by the use of the Reuss iso-stress average (1929), when the heterogeneities are small compared to the wavelength, therefore:

$$\frac{1}{\kappa_{fl}} = \sum_{i=1}^{N} \frac{f_i}{\kappa_{fl-i}} \quad , \tag{1.11}$$

where f_i are the volume fractions and κ_{fl-i} the bulk moduli of each fluid. Using these principles, Mavko and Mukerji (1995) derived a simple linear form of Gassmann's equation, but expressed in terms of the bulk modulus change $\Delta\kappa_{sat}$:

$$\Delta\kappa_{sat}(\phi) = \frac{\phi}{\phi_R}\Delta\kappa_R(\phi_R), \tag{1.12}$$

where $\Delta\kappa_R(\phi_R)$ is the change in the Reuss average of the minerals and fluids evaluated at the reference porosity ϕ_R. This equation was derived from the graphical construct shown in **Figure 1.9**. Here, each line represents a Reuss average for a particular fluid, evaluated at different porosities. According to Mavko and Mukerji "*the change in rock bulk modulus between any two pore fluids is proportional to the change in Reuss average for the same two fluids evaluated at the intercept porosity ϕ_R, which is a measure of the pore-space stiffness*". Since the pore-fluid bulk modulus is much smaller than mineral moduli, equation 1.12 can be approximated as follows:

$$\Delta\kappa_{sat}(\phi) \approx \frac{\phi}{{\phi_R}^2}\Delta\kappa_{fl}. \tag{1.13}$$

The mineral bulk modulus (κ_m) in clean sands can be obtained from common ultrasonic measurements of pure minerals (Wang, 2000); However, when other minerals are present in the sands (feldspars, clays, calcite cements, etc.) it may be also necessary to compute the effective mineral bulk modulus. Hill (1952) showed that the effective mineral bulk modulus could be found somewhere between the weighted arithmetic average, also called iso-strain average (Voigt, 1907), and their harmonic average (Reuss average), so he proposed the following equation:

$$\kappa_m \approx \frac{1}{2}\left[\sum_{i=1}^{N} f_i\,\kappa_{m-i} + \left(\sum_{i=1}^{N}\frac{f_i}{\kappa_{m-i}}\right)^{-1}\right]. \tag{1.14}$$

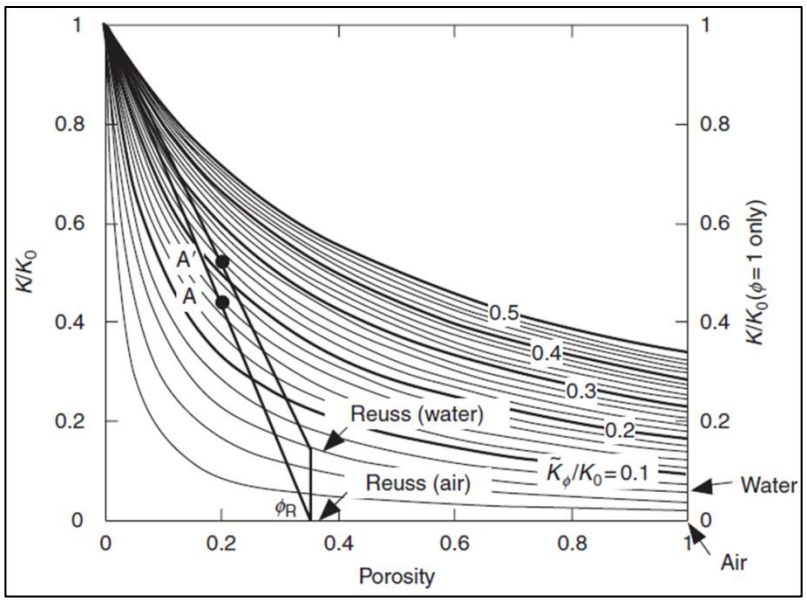

Figure 1.9: Graphical representation of Gassmann equations for fluid combinations (from Mavko and Mukerji, 1995).

1.4.2 Seismic velocities and effective stress

Pore pressure changes are not reflected in the same way at different depths. As depth increases, so does compaction, which increases grain to grain contact and therefore reduces the impact of pore pressure effects. In normal circumstances, a deep reservoir would be less sensitive to pore pressure changes than a shallow reservoir. To account for these variations, it is useful to express changes in pore pressure as a function of effective stress, which is defined as follows:

$$\sigma_{eff} = \sigma_{ob} - \alpha P \quad , \tag{1.15}$$

where, σ_{ob} is the overburden stress, α is the effective stress coefficient and P is the pore pressure. Although it is a subject of many discussions (Hofmann, et al., 2004; Gurevich, 2004), it is generally accepted that for practical geophysical applications $\phi \leq \alpha \leq 1$. The negative sign in equation 1.15 implies that pore pressure effects (affecting the fluids) counteract changes in the overburden stress (affecting the rock matrix). For instance, above the bubble point pressure, a reduction in the pore pressure

will lead to an increase in the grain to grain contact in the matrix, resulting in an impedance increase (hardening), whereas in the fluids, the same reduction in pore pressure will make the fluid density decrease and hence lead to a reduction in the fluid velocity (softening). However, such effects have different magnitudes and normally it is expected that the fluid changes are small in comparison to changes in the rock frame, although this of course depends on the value of α.

It is known in rock physics that P and S velocities increase exponentially with increasing effective stress (Figure 1.10), and several empirical and semi-empirical equations exist to account for those variations. Based on laboratory measurements, Mavko (1998) proposes two empirical exponential relations which are normalised by the velocity at the maximum stress. The equations have the following form:

$$\frac{V(\sigma_{eff})}{V(\sigma_{max})} = a - b\, e^{-\frac{\sigma_{eff}}{c}} \quad , \tag{1.16}$$

where V can be either P or S velocity; $V(\sigma_{max})$ is the velocity measured at the maximum stress and a, b, and c are empirical fits to the data. Eberhart-Phillips et al., (1989) developed a series of empirical formulas to predict pressure effects on velocities of dry or wet rocks. These formulas were generalised by Shapiro (2003) as follows:

$$V(\sigma_{eff}) = V_0 - b(\sigma_{eff} - c\, e^{-d\,\sigma_{eff}}) \,. \tag{1.17}$$

As before, V can be either P or S velocity. V_0, b, c and d are empirical fits to the data. Vernik and Hamman (2009) attempted to provide some physical insight into the empirical fits of equation 1.16, and they found some strong correlations between the parameters. Yan & Han (2009) inferred that equation 1.17 contains more parameters that are required and they proposed the next set of empirical equations:

$$V(\sigma_{eff}) = V_\infty\,(1-c)e^{-\frac{\sigma_{eff}}{b}} \quad , \tag{1.18a}$$

$$c = \frac{V - V_0}{V_\infty} \quad , \tag{1.18b}$$

where V_∞ is the maximum velocity and V_0 the velocity at zero effective stress. All the models mentioned above have the disadvantage of being expressed in terms of velocities rather than elastic moduli. However, the common approach is to use any of the relations above and assuming a linear function of density with porosity, the stress sensitivity of the bulk and shear modulus is introduced into Gasssmann equations.

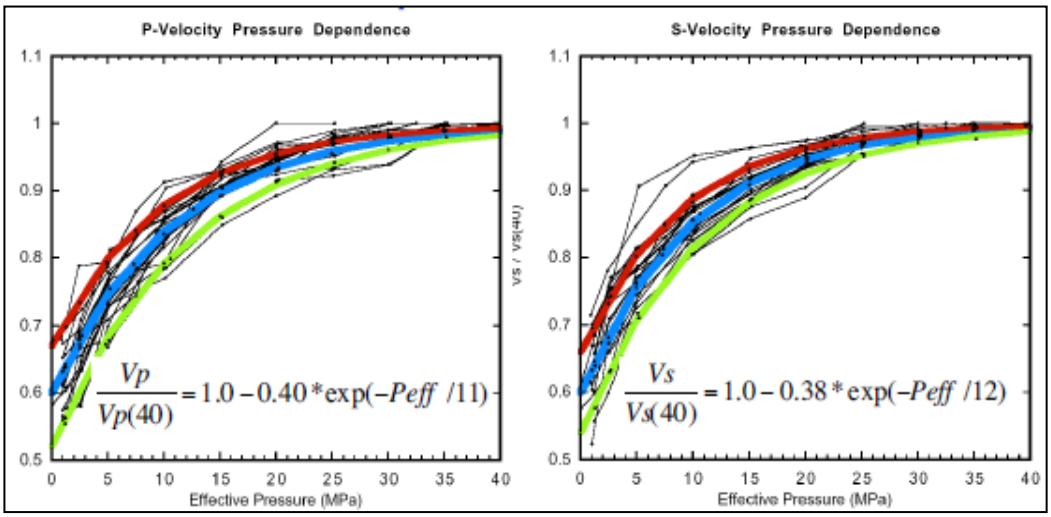

Figure 1.10: Changes in P and S velocities with effective stress, from laboratory measurements, showing the well-known exponential behaviour (Mavko, 1996).

1.4.3 MacBeth (2004) rock stress sensitivity equations

MacBeth (2004) developed equations to describe the pressure dependence on the dry bulk modulus (κ_{dry}) and dry shear modulus (μ_{dry}). Unlike the formulations stated above, these equations have a clearer theoretical foundation. In his equations, he uses the excess compliance to describe all the internal weaknesses in the rock, regardless of their origin. The equations have the following functional form:

$$\kappa_{dry}(\sigma_{eff}) = \frac{\kappa_\infty}{1 + E_\kappa e^{-\frac{\sigma_{eff}}{P_\kappa}}} \quad , \tag{1.19a}$$

$$\mu_{dry}(\sigma_{eff}) = \frac{\mu_\infty}{1 + E_\mu e^{-\frac{\sigma_{eff}}{P_\mu}}} \quad . \tag{1.19b}$$

Each equation contains three controlling parameters: for the bulk modulus, E_κ and P_κ define the rate of change of the compressional stress sensitivity and κ_∞ is the maximum bulk modulus value, to which the curves asymptote. Similarly, for the shear modulus E_μ and P_μ define the rate of change of the shear stress sensitivity and μ_∞ is the maximum shear modulus value, to which the curves asymptote. The constants E_κ and E_μ are unit-less, P_κ, P_μ and σ_{eff} (effective stress) have units of MPa. These equations were tested against 17 different measurements performed in sandstones with different porosities, demonstrating the robustness of the formulations. Based on these observations, MacBeth found a strong dependence on porosity in the terms κ_∞ and μ_∞ (Figure 1.11) and weak dependencies on the rest of the parameters. Although not explicitly defined in his paper, these observations imply that the porosity dependence can be incorporated into the formulations as follows:

$$\kappa_{dry}(\sigma_{eff}) = \frac{\kappa_\mathrm{m}(1 - \varepsilon'\phi)}{1 + E_\kappa e^{-\frac{\sigma_{eff}}{P_\kappa}}} \ , \tag{1.20a}$$

$$\mu_{dry}(\sigma_{eff}) = \frac{\mu_\mathrm{m}(1 - \varepsilon'\phi)}{1 + E_\mu e^{-\frac{\sigma_{eff}}{P_\mu}}} \ , \tag{1.20b}$$

where $\varepsilon' \approx 2.8$ for the rocks studied and κ_m and μ_m are the mineral bulk and shear modulus. An alternative approach is to make $\varepsilon' = \phi/\phi_\mathrm{c}$, where ϕ_c is the critical porosity (Nur et al., 1995). By doing this we can provide a more intuitive physical interpretation of equations 1.20. For instance, as σ_{eff} increases and approaches ∞, porosity (ϕ) will approach zero (all pores and micro-cracks are closing) and therefore both μ_{dry} and κ_{dry} will approach the values of the pure mineral moduli (μ_m and κ_m). On the other hand, as we approach surface conditions ($\sigma_{eff} \to 0$), porosity will approach its critical value ϕ_c (as the rock becomes a suspension) and therefore both

μ_{dry} and κ_{dry} will tend to zero. The combination of the constants E_κ and P_κ determine how sensitive the rock is to changes in the effective stress, and can be considered as summaries of the total rock weaknesses, independently of its origin (MacBeth, 2004). For our purposes, MacBeth's equations represent the following advantages over the empirical equations mentioned above:

- The equations require only two fitting parameters, which have a physical significance, therefore reducing the ambiguity in the parameterisation;
- The porosity dependence is explicitly defined;
- The equations are expressed in terms of the parameters that go into Gassmann equations (κ_{dry}, μ_{dry}, κ_m, μ_m), which make them compatible and easy to incorporate for 4D modelling purposes.

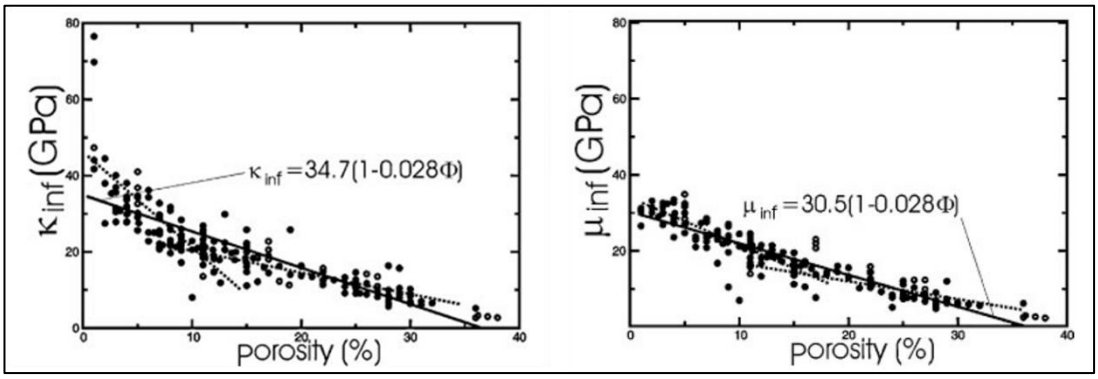

Figure 1.11: Porosity dependence of κ_∞ and μ_∞ (Modified from MacBeth, 2004).

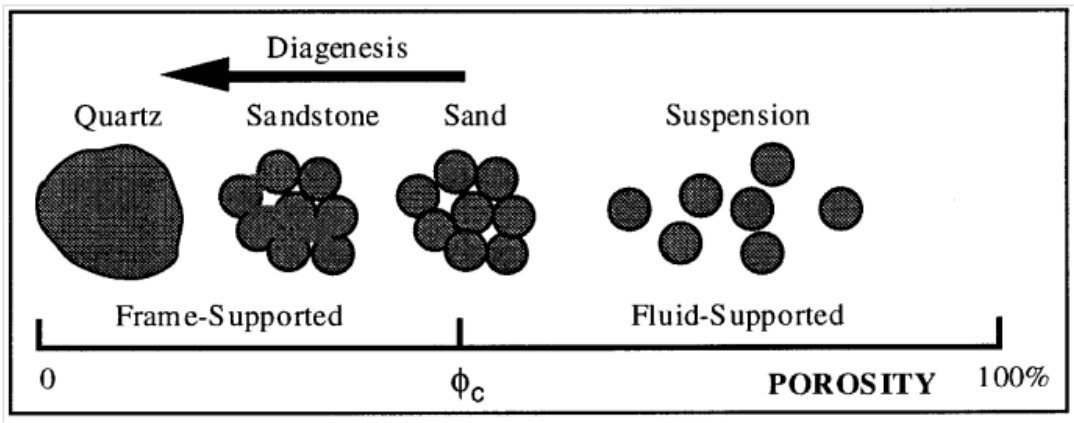

Figure 1.12: Physical interpretation of critical porosity (Mavko, et al., 1998).

1.4.4 Fluid pressure sensitivity

Describing how fluids behave with pressure and temperature changes is important for reservoir engineering purposes. Reservoir oils can behave like liquids or gases, depending on pressure and temperature conditions, so it is crucial to know at which specific pressure and temperature this change of phase occurs: this is commonly called the "Bubble point pressure" (P_B). Depending on the oil composition, which is related to its oil gravity or API gravity (a measure of how heavy or light a petroleum liquid is compared to water) and the reservoir temperature, the value of P_B will change (Batzle et al., 2006) as illustrated in Figure 1.13. Batzle and Wang (1992) provide a series of equations that allow estimating the changes in the bulk modulus to changes in fluid composition, reservoir pressure and temperature. Although the behaviour of oils at the bubble point pressure is complex, Batzle and Wang equations predict that as soon as pressure is above or below this point, the bulk modulus changes with pressure are nearly linear and with similar gradient in magnitude, but with opposite sign (Figure 1.14). This flip in polarity makes sense, since below the bubble point pressure, gas dissolved into the oil comes out of solution, which means that oil loses its lighter components and hence it becomes heavier with decreasing pressure (Falahat, et al. 2013).

These observations are valid within the range of pressures generally observed in 4D surveys, which are in the order of a few MPa (MacBeth, 2006b); beyond 8 MPa of pressure change, the non-linearity of the behaviour becomes important.

Similarly, gases display a near linear behaviour with changes in pressure, as shown in Figure 1.15, and water also shows a linear behaviour and a nearly negligible change in pressure within the ranges of changes we usually expect to see in 4D seismic (Figure 1.16). This implies that the fluid pressure sensitivity for oil, gas and water can be introduced into the 4D rock physics equations as a simple linear function with respect to pressure.

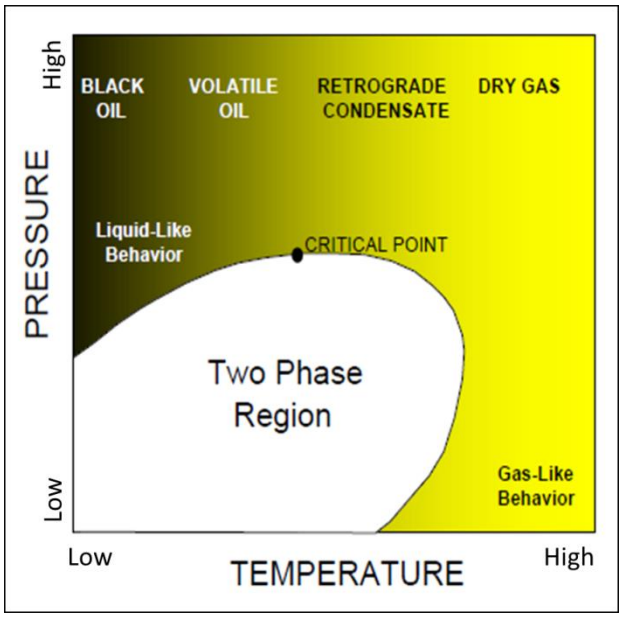

Figure 1.13: Theoretical behaviour of hydrocarbons with reservoir pressure and temperature changes (Batzle et al., 2006).

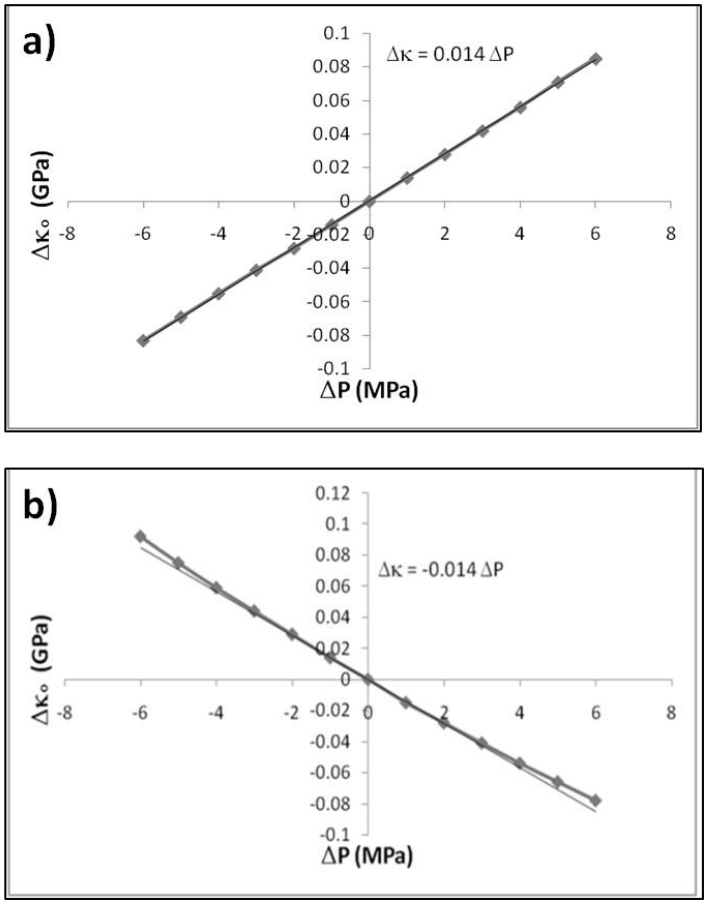

Figure 1.14: Bulk modulus calculated with Batzle & Wang equations (1992) for a North Sea Oil with properties detailed in Table 1.1. (a) above and (b) below the bubble point pressure.

Table 1.1: Reservoir properties used in the Batzle and Wang (1992) calculation in Figure 1.13.

Reservoir Properties					
Pressure initial (MPa)	Temperature (°F)	Salinity (ppm)	Gas gravity	Gas Oil Ratio (Mscf/stb)	Oil Density (API)
20	136	1800	0.58639	0.35	25

The sources of information for the incorporation of fluid pressure effects can be empirical relations (Batzle & Wang, 1992), equations of state (fluid flow simulation), a combination of both (American National Institute of Standards and Testing – NIST software), or most commonly, from pressure volume and temperature measurements (PVT) taken in the field.

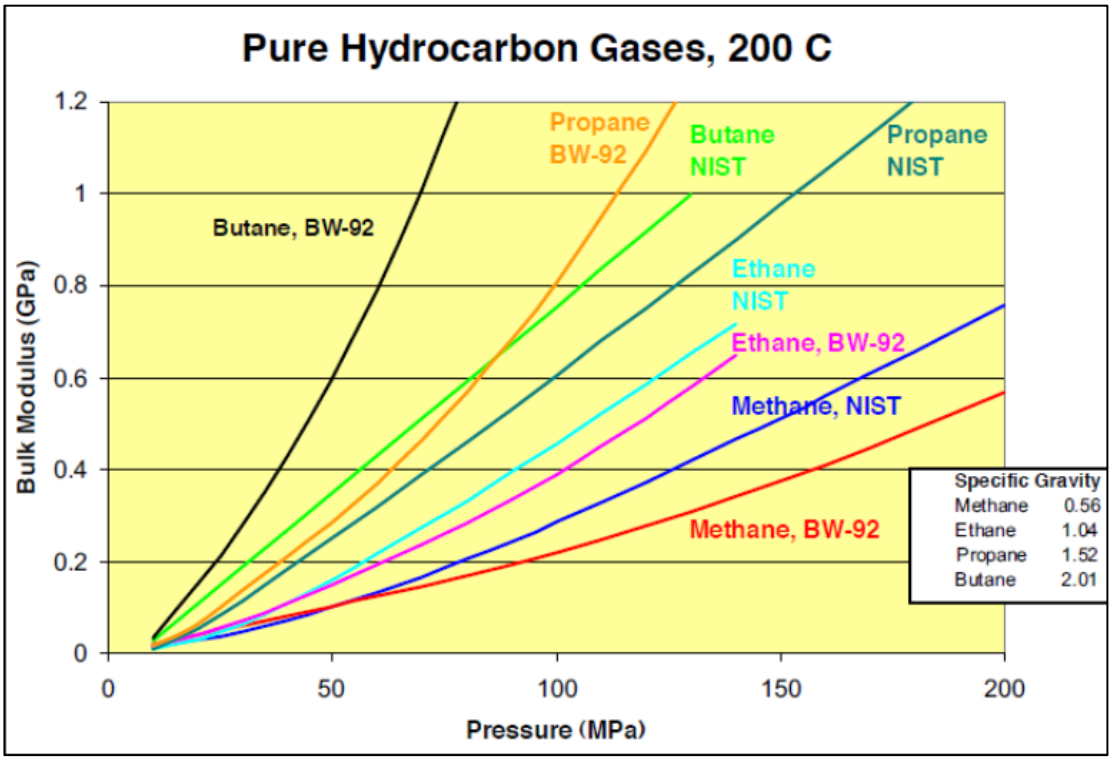

Figure 1.15 Fluid pressure sensitivity curves obtained from Batzle & Wang equations and the NIST software for different types of gases. (Walls & Dvorkin, 2005).

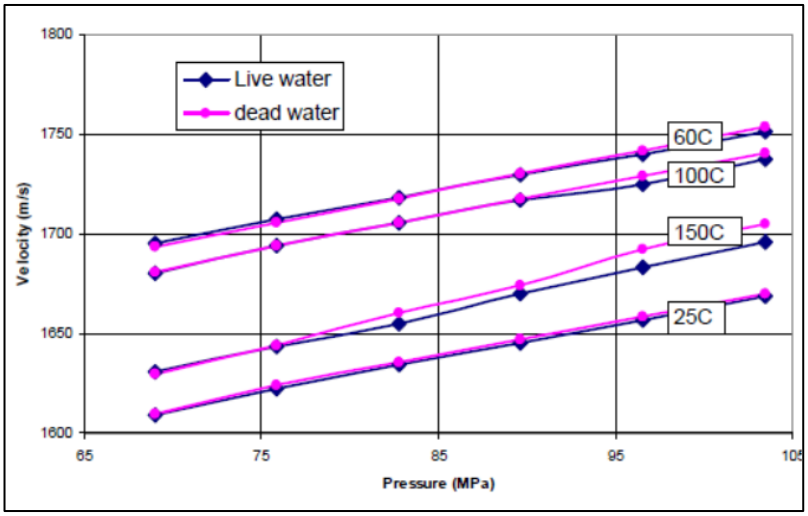

Figure 1.16. Fluid pressure sensitivity of water with and without gas dissolved, displaying very linear trends and small changes with pressure. (Han and Batzle, 2001).

1.4.5 Density modelling, mass balance equation

Another important equation in rock physics is that governing the relation of porosity, mineralogy and fluids with the bulk density. It is widely accepted that density changes linearly with changes in the mineral and fluid composition of the rock; the equation defining these changes is known as the mass balance equation:

$$\rho = \sum_{i=1}^{n} f_i \rho_i \quad . \tag{1.21}$$

Here, ρ is the bulk density, f_i is the volume fraction of the i^{th} mineral and ρ_i its corresponding density. In practical form, equation 1.21 can be expressed as

$$\rho = (1-\phi)\rho_m + \phi S_{wi}\rho_w + \phi(1-S_{wi})\rho_o \quad . \tag{1.22}$$

In terms of 4D changes, density is sensitive to changes in fluid content and, for non-compacting reservoirs, the only changes in density are related to the fluid pressure sensitivity.

1.5 Summary of observations in this chapter

- A number of 4D interpretation techniques are currently available; all of these have been applied with some degree of success. However, there is still a need to gain more physical insights into the controlling parameters that drive the 4D seismic changes related to production.

- The overall objective of the thesis is to develop petroelastic approximations that can help the interpretation of 4D seismic amplitude differences, (including the 4D AVO changes). It is envisaged that such approximations will need to keep the assumptions to the minimum and it will be important that all parameters involved have a clear physical interpretation

- A number of pre-established rock and fluid physics models are already available in the industry: this chapter has summarised those that will form the basis of our theoretical developments.

Chapter 2: Theoretical development for an oil-water system

"The important thing in science is not so much to obtain new facts as to discover new ways of thinking about them"

Lo importante en la ciencia no es tanto obtener nuevos datos como descubrir nuevas formas de analizarlos

Sir William Bragg

English physicist, chemist and mathematician

In this chapter, theoretical approximations are developed to describe the angle-dependent 4D amplitude differences as functions of reservoir pressure (ΔP) and water saturation (ΔSw). The equation is formulated initially for oil reservoirs above the bubble point pressure (where no free gas is present) and it is based on a single interface calculation. The accuracy of the new equation is tested against numerical modelling as well as on a North Sea dataset, by comparing the predictions against the results of a simulation to seismic modelling program (sim2seis).

In the previous chapter, I reviewed the relevant rock and fluid physics models that mathematically describe the changes experienced in the rock properties resulting from reservoir production. In this chapter, I intend to define a seamless integration of such models, so that 4D amplitude changes (observed at any given angle of incidence) can be directly related to changes in pore pressure and fluid saturation. As a starting point, I consider a non-compacting oil reservoir (i.e. geomechanics effects in the overburden are negligible) with a basal aquifer drive and where no free gas is present.

2.1 Definition of the time lapse reflectivity equation as a function of angle

Consider a simple physical model (Figure 2.1), where the reservoir is represented by a single interface, given by the contrast between a producing reservoir and an overlying inert shale (seal). For the purposes of this current work, I assume the reservoir can be represented by its sand properties and that elastic property changes are due to variations in pressure and water saturation only. No variations with net-to-gross or reservoir thickness are treated at this stage.

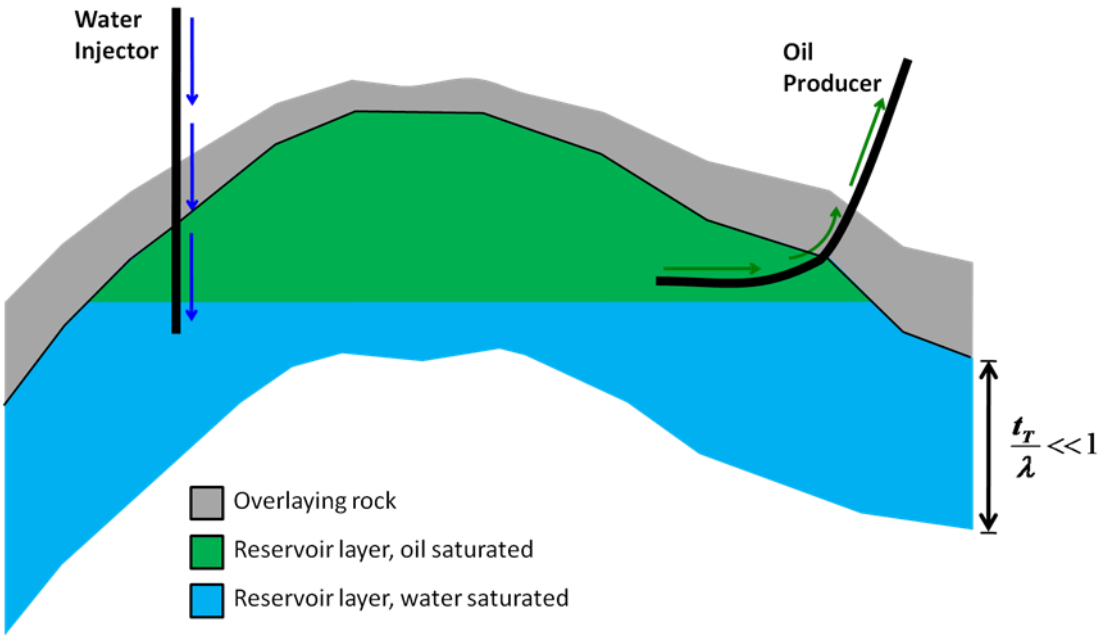

Figure 2.1: Conceptual Reservoir Model

The angle dependent reflectivity for the shale/sand interface (top reservoir) at the initial reservoir state (base line) can be defined using Aki and Richards' approximation expressed in terms of the elastic moduli κ, μ and ρ (Grey et al., 1999):

$$R(\theta) = \left[1 - \frac{4}{3}\left(\frac{\overline{V_S}}{\overline{V_P}}\right)^2\right] \Gamma_1 \frac{\Delta\kappa}{\bar{\kappa}} + \Gamma_2 \frac{\Delta\rho}{\bar{\rho}} + \left(\frac{\overline{V_S}}{\overline{V_P}}\right)^2 \Gamma_3 \frac{\Delta\mu}{\bar{\mu}} \ , \qquad (2.1a)$$

where:

$$\Gamma_1 = \frac{1}{4}\sec^2\theta; \qquad \Gamma_2 = \frac{1}{2} - \frac{1}{4}\sec^2\theta \qquad and \qquad \Gamma_3 = \frac{1}{3}\sec^2\theta - 2\sin^2\theta \ . \qquad (2.1b)$$

Here, the symbols $\Delta\kappa, \Delta\mu$ and $\Delta\rho$ represent the differences of the properties across the reservoir – shale interface, and the properties $\bar{\kappa}, \bar{\mu}, \bar{\rho}, \overline{V_P}$ and $\overline{V_S}$ are averages across the interface. This equation is useful for our purposes because it formulates the reflectivity directly as functions of the elastic moduli, which are known functions of the rock and fluid physics (see Chapter 1). A further simplification can be made to this equation, since $\overline{V_P}^2 = \bar{M}/\bar{\rho}$:

$$R(\theta) = \Gamma_1 \frac{\Delta\kappa}{\bar{M}} + \Gamma_2 \frac{\Delta\rho}{\bar{\rho}} + \Gamma_3 \frac{\Delta\mu}{\bar{M}} \qquad , \qquad (2.2)$$

where $\bar{M}$ is the P–Modulus. Now, let us consider the application to a reservoir that is imaged before, and then during its lifetime of production and recovery. The time-lapsed change in the reflection coefficient $\Delta R(\theta)_{\mathrm{TL}}$ between the monitor and the pre-production (baseline) survey time is calculated as follows:

$$\Delta R(\theta)_{TL} = \Gamma_1 \left(\frac{\Delta\kappa^m}{\overline{M^m}} - \frac{\Delta\kappa^b}{\overline{M^b}}\right) + \Gamma_2 \left(\frac{\Delta\rho^m}{\overline{\rho^m}} - \frac{\Delta\rho^b}{\overline{\rho^b}}\right) + \Gamma_3 \left(\frac{\Delta\mu^m}{\overline{M^m}} - \frac{\Delta\mu^b}{\overline{M^b}}\right), \qquad (2.3)$$

Here, the superscripts "b" and "m" denote that the properties belong to the base line or monitor respectively. We define the time-lapse perturbations ($\Delta\kappa_{\mathrm{TL}}, \Delta\mu_{\mathrm{TL}}$ and $\Delta\rho_{\mathrm{TL}}$) by the following:

$$\Delta\kappa_{\mathrm{m}} = \Delta\kappa_{\mathrm{TL}} + \kappa^b;\ \ \Delta\mu^m = \Delta\mu_{\mathrm{TL}} + \mu^b \ \ \text{and} \ \ \Delta\rho^m = \Delta\rho_{\mathrm{TL}} + \rho^b\ , \tag{2.4a}$$

$$\overline{\kappa^m} = \overline{\kappa^b}\left(1 + \frac{\Delta\kappa_{TL}}{2\overline{\kappa^b}}\right);\ \overline{\mu^m} = \overline{\mu^b}\left(1 + \frac{\Delta\mu_{TL}}{2\overline{\mu^b}}\right) \text{ and } \overline{\rho^m} = \overline{\mu^b}\left(1 + \frac{\Delta\rho_{TL}}{2\overline{\rho^b}}\right). \tag{2.4b}$$

The sub-index "TL" denotes the time lapse difference (monitor - base). Substituting equations 2.4a and 2.4b in 2.3 and approximating to the first order using a Taylor's expansion we obtain:

$$\Delta R(\theta)_{TL} = \ \Gamma_1\left(\frac{\Delta\kappa_{\mathrm{TL}}}{\overline{M^b}} - \frac{\Delta\kappa^b\Delta\mathrm{M}_{TL}}{\overline{M^b}2\overline{M^b}}\right) + \Gamma_2\left(\frac{\Delta\rho_{\mathrm{TL}}}{\overline{\rho^b}} - \frac{\Delta\rho_{\mathrm{TL}}{}^2}{\overline{\rho^b}2\overline{\rho^b}}\right) + \Gamma_3\left(\frac{\Delta\mu_{\mathrm{TL}}}{\overline{M^b}} - \frac{\Delta\mu^b\Delta\mathrm{M}_{TL}}{\overline{M^b}2\overline{M^b}}\right). \tag{2.5}$$

Since $\Delta\mathrm{M}_{TL} = \Delta\kappa_{\mathrm{TL}} + \frac{4}{3}\Delta\mu_{\mathrm{TL}}$, equation 2.5 can be rearranged as

$$\Delta R(\theta)_{TL} \approx \ \left[\Gamma_1\frac{\Delta\kappa_{\mathrm{TL}}}{\overline{M^b}}\right]\alpha_{\mathrm{TL}} + \Gamma_2\frac{\Delta\rho_{\mathrm{TL}}}{\overline{\rho^b}} + \left[\Gamma_3\frac{\Delta\mu_{\mathrm{TL}}}{\overline{M^b}}\right]\beta_{\mathrm{TL}}\ , \tag{2.6a}$$

where

$$\alpha_{\mathrm{TL}} = \left(1 - \frac{\kappa^b - \kappa^{sh}}{2\overline{M^b}} - \frac{\Gamma_3}{\Gamma_1}\frac{\mu^b - \mu^{sh}}{2\overline{M^b}}\right) \tag{2.6b}$$

and

$$\beta_{\mathrm{TL}} = \left(1 - \frac{2}{3}\frac{\mu^b - \mu^{sh}}{\overline{M^b}} - \frac{2}{3}\frac{\Gamma_1}{\Gamma_3}\frac{\kappa^b - \kappa^{sh}}{\overline{M^b}}\right). \tag{2.6c}$$

Equation 2.6 is valid to the first order and is accurate for angles up to the critical angle; the upper-index "sh" refers to the shell properties above the interface (assumed constant with time-lapse), which affect the angle dependence. Figure 2.2 shows the comparison of the approximation of equation 4 with respect to the full Aki and Richards' solution, using typical values for a North Sea reservoir described in Table 2.1; the normalised RMS error is less than 2% below the critical angle.

Table 2.1: Parameters used in the numerical modelling exercise to test equation 2.8.

Shale		
V_P	V_S	ρ_b
2.650	1.323	2140

Base Line				
V_P	V_S	ρ_b	S_{wc}	P_i
3.332	2.020	2180	0.2	20

Monitor – Case 1					Monitor – Case 2				
V_P	V_S	ρ_b	ΔP	ΔS_w	V_P	V_S	ρ_b	ΔP	ΔS_w
3.244	1.946	2179	+ 4 MPa	0.6	3.391	2.071	2181	- 4 MPa	0.6

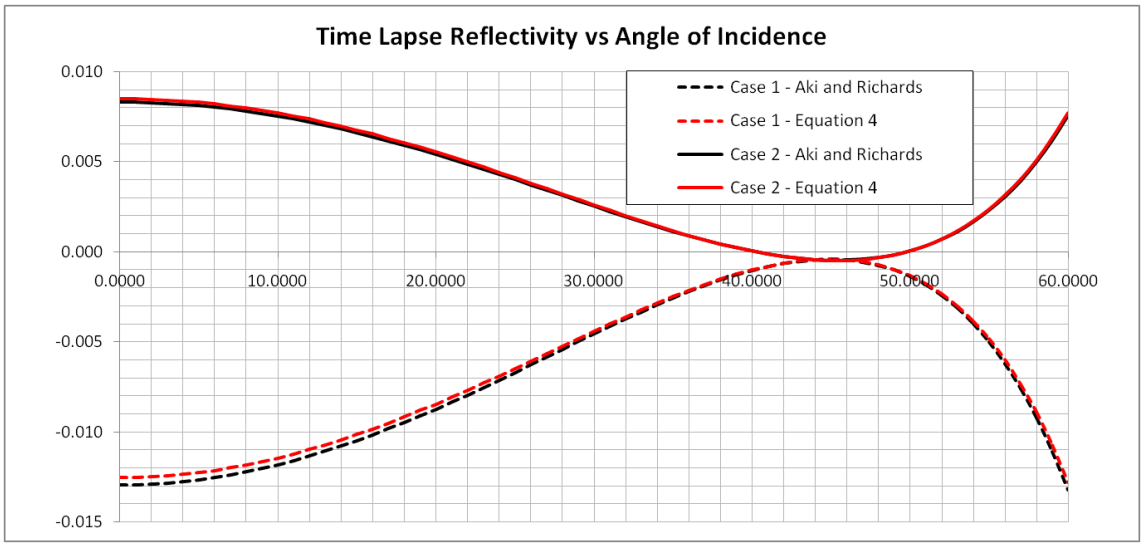

Figure 2.2: Approximation of equation 2.8 compared with the full Aki and Richards' solution, using the parameters shown in table 2-1.

For angles less than 35 degrees, equation 2.6 can be further simplified as

$$\Delta R(\theta)_{TL} \approx \left[\Gamma_1 \frac{\Delta\kappa_{\mathrm{TL}}}{\overline{M^b}}\right] + \Gamma_2 \frac{\Delta\rho_{\mathrm{TL}}}{\overline{\rho^b}} + \left[\Gamma_3 \frac{\Delta\mu_{\mathrm{TL}}}{\overline{M^b}}\right]. \tag{2.7}$$

Now that we have obtained a simple equation to compute the time lapse reflectivity as a function of the angle of incidence, we can focus on determining the relation between $\Delta\kappa_{TL}$, $\Delta\rho_{\mathrm{TL}}$ and $\Delta\mu_{TL}$ and pore pressure (ΔP) and water saturation (ΔS_w) changes by incorporating the rock and fluid physics.

2.2 Changes in the bulk modulus with ΔP and ΔS_w

The starting point for this development is the linear form of Gassmann described in Chapter 1, which can be re-written as

$$\Delta\kappa_{TL}(\Delta P, \Delta S_w) = \Delta\kappa_{dry}(\Delta \mathrm{P}) + \varepsilon\phi\Delta\kappa_{fl}(\Delta P, \Delta S_w)\,. \tag{2.8}$$

This equation is valid for rocks with porosity above 15% (Han and Batzle, 2004). The coefficient is a measure of the pore stiffness, given by ($\varepsilon = \phi/{\phi_R}^2$) and its value can be found normally between 2.5 and 3.

To calculate the change in the fluid bulk modulus ($\Delta\kappa_{fl}$), it is important to remember that, although there is always more than one fluid in the rock (Figure 2.3), not all of them are expected to have a noticeable 4D effect. Of particular importance is the distinction between capillary bound water and oil (which does not change under normal water flooding conditions), and the free fluids (free water and oil, in this case). The presence of these fluids limits the range of variation of the expected change in water (or oil) saturation. For instance, the maximum expected saturation change due to a water flooding yields a working maximum of $(1 - S_{wc} - S_{or})$, where S_{wc} is the connate water and S_{or} is the irreducible oil saturation.

Using the uniform fluid distribution equation described in Chapter 1, we can estimate the time lapse change in the fluid bulk modulus at a constant pressure, as follows:

$$\Delta\kappa_{fl} = \frac{\Delta \mathrm{S_w}\left(\kappa_w^b - \kappa_o^b\right)}{\left[1 - S_{wi}\left(1 - \frac{\kappa_o^b}{\kappa_w^b}\right)\right]^2 - \Delta \mathrm{S_w}\left(1 - \frac{\kappa_o^b}{\kappa_w^b}\right)\left[1 - S_{wi}\left(1 - \frac{\kappa_o^b}{\kappa_w^b}\right)\right]}. \tag{2.9}$$

Expansion as a Taylor's series gives

$$\Delta\kappa_{fl}(0, \Delta S_w) \approx \Delta S_w \left[\frac{\left(\kappa_o^b/\kappa_w^b\right)\left(\kappa_w^b - \kappa_o^b\right)}{(1 - S_{\mathrm{wi}})^2 + \left(\kappa_o^b/\kappa_w^b\right)S_{\mathrm{wi}}}\right]\,. \tag{2.10}$$

Here, κ_o^b and κ_w^b are the bulk modulus of oil and water respectively, measured at the initial reservoir pressure. To add the pressure effects, we assume local linear gradients for the fluid pressure sensitivity:

$$O_\kappa = \frac{\kappa_o^m - \kappa_o^b}{\mathrm{P^m} - \mathrm{P^b}} \tag{2.11a}$$

and

$$W_\kappa = \frac{\kappa_w^m - \kappa_w^b}{\mathrm{P^m} - \mathrm{P^b}} \ . \tag{2.11b}$$

Hence,

$$\kappa_o^m = \kappa_o^b + O_\kappa \Delta P \tag{2.12a}$$

and

$$\kappa_w^m = \kappa_w^b + W_\kappa \Delta P. \tag{2.12b}$$

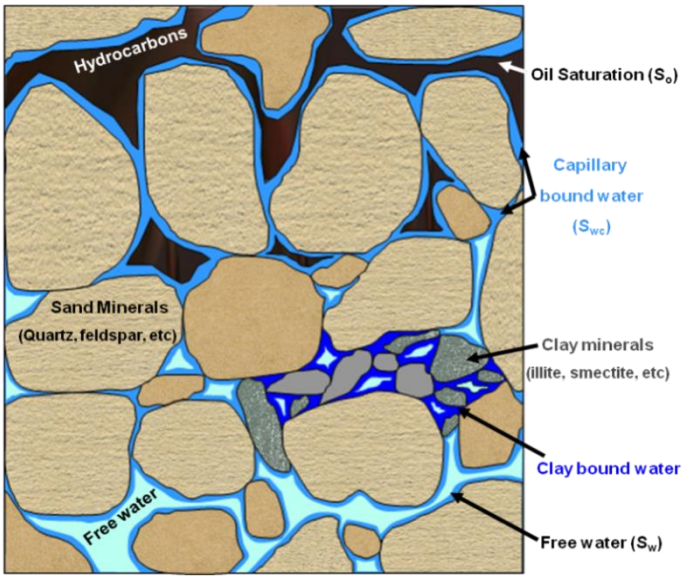

Figure 2.3: Schematic representation of a reservoir rock and the different fluid and solid phases.

Again, using the uniform fluid distribution equation, the fluid pressure contribution calculated at zero water saturation change is:

$$\Delta\kappa_{fl}(\Delta P, 0) = \frac{1}{\frac{S_{wi}}{\kappa_w^b + W_\kappa \Delta P} + \frac{1 - S_{wi}}{\kappa_o^b + O_\kappa \Delta P}} - \frac{1}{\frac{S_{wi}}{\kappa_w^b} + \frac{1 - S_{wi}}{\kappa_o^b}} \quad , \tag{2.13}$$

obtaining:

$$\Delta\kappa_{fl}(\Delta P, 0) = \Delta P \frac{\kappa_w^b (1 - S_{wc}) O_\kappa + \kappa_o^b W_\kappa S_{wc}}{S_{wc} \kappa_o^b + \kappa_w^b (1 - S_{wc})} . \tag{2.14}$$

To incorporate the changes in pore pressure associated with the rock frame (κ_{dry}), we use the MacBeth (2004) equations:

$$\kappa_{dry}(P) = \frac{\kappa_m (1 - \varepsilon' \phi)}{1 + E_\kappa e^{-\frac{\sigma_{eff(P)}}{P_\kappa}}} \quad . \tag{2.15}$$

It is convenient for these calculations to linearise equation 2.15 and express it in terms of pore pressure rather than effective stress changes. To do this, we calculate the local gradient in pore pressure around the initial reservoir pressure, as follows:

$$\kappa_{dry}(P_f) = \kappa_m (1 - \varepsilon' \phi) \left[\frac{1}{1 + E_\kappa e^{-\frac{\sigma_{ob} - \alpha P_i}{P_\kappa}}} + \frac{\partial \mathrm{P}}{\partial \mathrm{P_i}} \left(\frac{1}{1 + E_\kappa e^{-\frac{\sigma_{ob} - \alpha P_i}{P_\kappa}}} \right) \right] \quad . \tag{2.16}$$

Solving the equation and rearranging terms gives

$$\Delta\kappa_{dry}(P) \approx -(1 - \varepsilon' \phi)(\alpha \kappa_m A_\kappa) \Delta P \, , \tag{2.17a}$$

Where

$$A_\kappa = \frac{E_\kappa e^{\frac{\sigma_{ob} - \alpha P_i}{P_\kappa}}}{P_\kappa \left(1 + E_\kappa e^{\frac{\sigma_{ob} - \alpha P_i}{P_\kappa}} \right)^2} \quad . \tag{2.17b}$$

Here, A_κ is the local gradient of the stress sensitivity curve evaluated at the initial reservoir pressure. Substituting equations 2.10, 2.14 and 2.17 into 2.8, we obtain the combined pressure and saturation time-lapse changes in the bulk modulus:

$$\Delta\kappa_{TL}(\Delta P, \Delta S_w) \approx \varepsilon\phi\Delta S_w \left[\frac{\left(\kappa_o^b/\kappa_w^b\right)\left(\kappa_w^b - \kappa_o^b\right)}{(1-S_{\mathrm{wi}})^2 + \left(\kappa_o^b/\kappa_w^b\right)S_{\mathrm{wi}}}\right] - \Delta P\left[(1-\varepsilon'\phi)(\alpha\kappa_m A_\kappa) - \frac{\kappa_w^b(1-S_{wc})O_\kappa + \kappa_o^b W_\kappa S_{wc}}{S_{wc}\kappa_o^b + \kappa_w^b(1-S_{wc})}\right]. \quad (2.18)$$

Equation 2.18 constitutes a "pressure dependent" Gassmann calculation, which includes changes due to fluid displacement, pore pressure effects in the fluids (as pressure drops, fluids get "softer") and changes in the rock frame due to induced changes in effective stress (by dropping pressure, the rock "hardens", due to increased grain to grain contact). It is important to note that, although the equation looks complex, the majority of the parameters are constant and relatively easy to calculate based on field data.

2.3 Changes in the shear modulus with ΔP and ΔS_w

One of the fundamental results from Gassmann's theory is the fact that the shear modulus does not change with fluid saturation changes, hence $\Delta\mu(\Delta S_w) = 0$. Therefore, only changes in rock stress are needed in these derivations. Following an equivalent route as for the bulk modulus, we start with MacBeth (2004):

$$\mu_{dry}(\sigma_{eff}) = \frac{\mu_m(1-\varepsilon'\phi)}{1 + E_\mu e^{-\frac{\sigma_{eff}}{P_\mu}}}\ . \quad (2.19)$$

After linearization, we obtain

$$\Delta\mu_{TL}(P) \approx -(1-\varepsilon'\phi)\left(\alpha\mu_m B_\mu\right)\Delta P\ , \quad (2.20)$$

where

$$B_\mu = \frac{E_\mu e^{\frac{\sigma_{ob}-\alpha P_i}{P_\mu}}}{P_\mu\left(1+E_\mu e^{\frac{\sigma_{ob}-\alpha P_i}{P_\mu}}\right)^2}\ . \tag{2.21}$$

Similarly, B_μ is the local gradient of the stress sensitivity curve, evaluated around the initial reservoir pressure.

2.4 Changes in density with ΔP and ΔSw

For density, assuming a non-compacting reservoir (porosity remains constant with production), pressure related changes in density are only related to the fluids. By introducing local gradients for the fluid pressure sensitivity, we obtain the next expression:

$$\Delta\rho_{TL}(\Delta\mathrm{P},\Delta\mathrm{S_w}) = \Delta\mathrm{S_w}\,\phi\left(\rho_w^b-\rho_o^b\right)+\Delta\mathrm{P}\,\phi\,\left[S_{wi}W_\rho+(1-S_{wi})O_\rho\right]. \tag{2.22}$$

2.5 Angle dependent 4D seismic response as a function of ΔP and ΔS_w

Finally, to bring all the above together, we have obtained relatively simple equations relating changes in the elastic moduli and density to changes in pressure and saturation. Introducing equations 2.18, 2.20 and 2.22 into equation 2.7 we obtain

$$\Delta R_{TL} \approx \frac{\Delta S_w}{S_{\mathrm{wi}}}\,\phi[\bar{\Gamma}_1N_1+\bar{\Gamma}_2N_2]-\frac{\Delta P}{P_i}\left[(1-\varepsilon'\phi)[\bar{\Gamma}_1N_3+\bar{\Gamma}_3N_4]-\phi[\bar{\Gamma}_1N_5+\bar{\Gamma}_2N_6]\right], \tag{2.23a}$$

Where

$$N_1 = \left[\frac{\varepsilon}{\bar{M}}\frac{S_{\mathrm{wi}}\left(\kappa_o^b/\kappa_w^b\right)\left(\kappa_w^b-\kappa_o^b\right)}{(1-S_{\mathrm{wi}})^2+\left(\kappa_o^b/\kappa_w^b\right)S_{\mathrm{wi}}}\right], \tag{2.23b}$$

$$N_2 = \frac{S_{\mathrm{wi}}\left(\rho_w^b - \rho_o^b\right)}{\bar{\rho}} \ , \tag{2.23c}$$

$$N_3 = P_i\left[\frac{\alpha\kappa_m A_\kappa}{\bar{M}}\right] \ , \tag{2.23d}$$

$$N_4 = P_i\left[\frac{\alpha\mu_m B_\mu m}{\bar{M}}\right], \tag{2.23e}$$

$$N_5 = P_i\left[\frac{\varepsilon}{\bar{M}}\frac{\kappa_w^b(1-S_{wc})O_\kappa + \kappa_o^b W_\kappa S_{wc}}{S_{wc}\kappa_o^b + \kappa_w^b(1-S_{wc})}\right], \tag{2.23f}$$

$$N_6 = P_i\left[\frac{S_{wi}W_\rho + (1-S_{wi})O_\rho}{\bar{\rho}}\right] \ . \tag{2.23g}$$

In this new equation, the terms $\bar{\Gamma_1}, \bar{\Gamma_2}$ and $\bar{\Gamma_3}$ are now averages over the functions of the incidence angle. Typical values for the near offset data with a range of incidence from 0 to 10 degrees are $\bar{\Gamma_1} = 0.25,\ \bar{\Gamma_2} = 0.24$ and $\bar{\Gamma_3} = 0.33$. For far offsets, defined between 25 and 35 degrees, for example, the same equation 2.23 a holds, but now $\bar{\Gamma_1} = 0.33,\ \bar{\Gamma_2} = 0.17$ and $\bar{\Gamma_3} = -0.06$. The coefficients N_1 to N_6 are functions of the parameters of the petroelastic model.

Each of these *N*-constants has a direct physical interpretation: N_1relates to the contrast in bulk modulus between water (the displacing fluid) and the mobile oil, N_2 is the corresponding density contrast, $N_3$and N_4define the rock stress sensitivity (both the bulk and shear modulus parts), and finally, N_5 and N_6 represent the impact of pressure changes on the fluid bulk modulus and density. Table 2.2 and Table 2.3 show a list of the required parameters to use these equations, as well as a short description and the input units

Table 2.2: Parameters related to water saturation changes in the time lapse reflectivity.

Property	Description	Units	NS dataset
κ_o^b	Bulk Modulus of oil at the initial state	GPa	1.31
κ_w^b	Bulk Modulus of water at the initial state	GPa	2.59
ρ_o^b	Density of oil at the initial state	kg/m^3	830
ρ_w^b	Density of water at the initial state	kg/m^3	1010
$\bar{M}$	Average P modulus between sand and overlying shale	GPa	17.13
$\bar{\rho}$	Average density between sand and overlying shale	kg/m^3	2440
ε	Stress coefficient (linear form of Gassmann)	unit-less	6.25
S_{wi}	Water saturation at the initial state	v/v	0.15

Table 2.3: Parameters related to pressure changes in the time-lapse reflectivity.

Property	Description	Units	NS dataset
α	stress coefficient (Hoffman, et al., 2005)	unit-less	0.91
κ_m	bulk modulus of the sand mineral (generally quartz)	GPa	36
ε'	stress coefficient (related to critical porosity ($\varepsilon' \approx \phi/\phi_C$)	unit-less	2.8
A_κ	local gradient of the stress sensitivity curve for κ_{dry}, evaluated at the initial pressure	MPa^{-1}	0.003
B_μ	local gradient of the stress sensitivity curve for μ_{dry}, evaluated at the initial pressure	MPa^{-1}	0.008
W_κ	local gradient of the fluid pressure sensitivity curve for water bulk modulus	unit-less	0.006
O_κ	local gradient of the fluid pressure sensitivity curve for oil bulk modulus	unit-less	0.013
W_ρ	local gradient of the fluid pressure sensitivity curve for water density	kg/m^3 MPa^{-1}	0.4
O_ρ	local gradient of the fluid pressure sensitivity curve for oil density	kg/m^3 MPa^{-1}	0.5
σ_{ob}	Overburden stress	MPa	40
P_i	Initial reservoir pressure	MPa	20

2.6 Validation of the new equations and numerical modelling

The accuracy of the approximation in equation 2.23a is tested against full numerical computation using the complete rock and fluid physics equations (Gassmann, 1951, MacBeth, 2004, Batzle & Wang, 1992, Aki & Richards, 1980). Since it is not possible to separate pressure and saturation effects using the full equations (a clear advantage of the new formulation), for comparison purposes, changes in the time-lapse reflectivity are calculated for a fixed water saturation change but varying pressure change, and vice versa. Figure 2.4 shows the calculation for both the near (0 degrees) and far (30 degrees) angle stacks, using a constant ΔSw = 0.62 and varying ΔP between -6 and +6 MPa; Figure 2.5 shows the calculations for a constant ΔP = 4 MPa and varying ΔS_w between 0 and + 62 % ($\Delta S_w = 1 - S_{or} - S_{wc}$). These comparisons are made based on the conditions of a typical North Sea clastic reservoir, using the parameters from Table 2.2 and Table 2.3, producing time-lapse changes in the reflectivity between 0 and 0.22 (mean seismic reflectivity around 0.12). To compute the errors between the full rock and fluid physics models and our first order approximation (equation 2.23a), the normalised root mean square error is then calculated by taking the difference of the approximate and *exact* solutions, dividing by the magnitude of the time-lapse reflectivity change for the *exact* solution, and then multiplying by 100 to convert to a percentage. Figure 2.6 shows the errors associated with the near angle responses in Figure 2.4 and Figure 2.5.

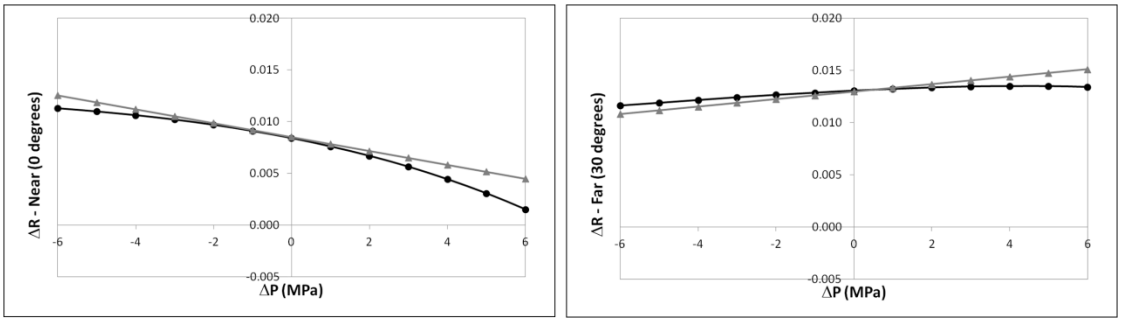

Figure 2.4: Time lapse reflectivity for a constant ΔSw = 0.62 and varying ΔP: in black, the full scale equations; in grey, our first order approximation (equation 2.23a), left: near angles; right: far angles.

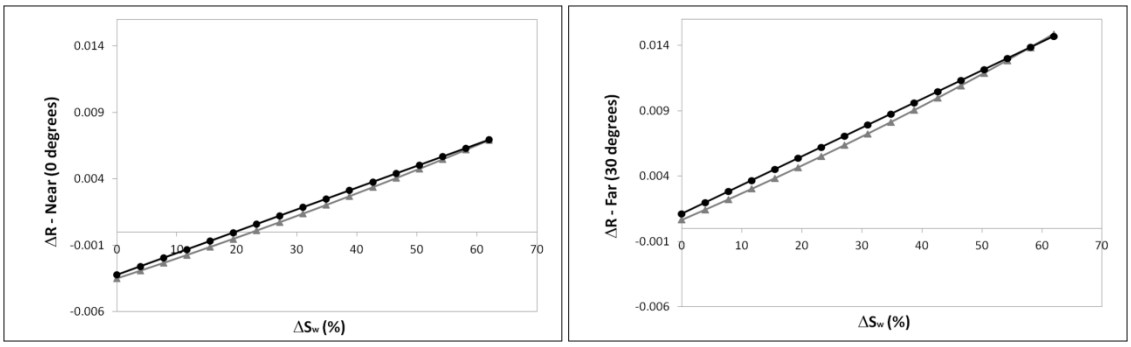

Figure 2.5: Time lapse reflectivity for a constant ΔP = 4 MPa and varying ΔS_w: in black, the full - scale equations; in grey, our first order approximation (equation 2.23a); left: near angles; right: far angles.

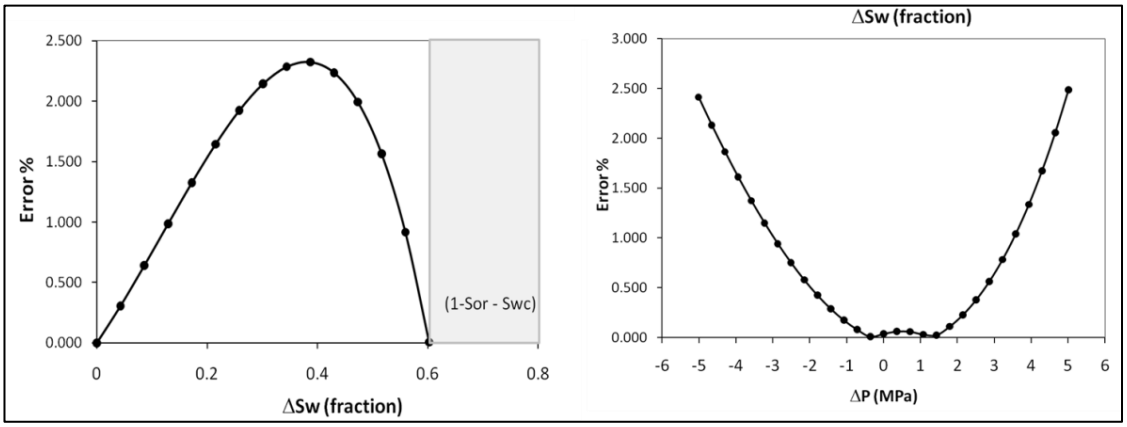

Figure 2.6: Average reflection coefficient computed with full equations compared against our first order approximation (equation 2.23a): left: errors in ΔS_w; right: errors in ΔP.

Another validation performed was to compute the reflectivity for a constant ΔP = 4 MPa, constant $\Delta S_w = 0.62$ and introducing variations in porosity between 0 and 40%. Calculations were performed for the near (Figure 2.7) and far (Figure 2.8) angle stacks. In both cases the errors are small and less than 2% for all porosities smaller than 35%. Next, the equations are validated against changes in the overlying shale properties. For this, the sand properties were kept fixed and several shale properties were introduced into the model using the published values by Castagna and Smith (1994), shown in Table 2.4, obtained from wire line log data and core samples from different parts of the world. The sand property values for the base line are as follows: $V_P = 3.5\ km/s$, $V_S = 2.2\ km/s$ and $\rho = 2.16\ g/cc$.

Table 2.4: Shale properties from Castagna and Smith (1994); highlighted in yellow: the properties of the North Sea Example, from Amini and MacBeth (2011).

V_P (km/s)	V_S (km/s)	ρ (kg/m3)	μ $(GPa\_$	κ (GPa)	M (GPa)
1.94	0.77	2100	1.25	6.24	7.90
2.10	1.03	2100	2.23	6.29	9.26
2.31	0.94	1900	1.68	7.90	10.14
2.31	0.85	2180	1.58	9.53	11.63
2.38	0.94	2270	2.01	10.18	12.86
2.59	1.39	2300	4.44	9.50	15.43
2.74	1.39	2060	3.98	10.16	15.47
2.65	1.32	2140	3.75	10.03	15.03
2.77	1.52	2290	5.29	10.52	17.57
2.77	1.52	2300	5.31	10.56	17.65
2.75	1.26	2430	3.86	13.23	18.38
2.87	1.30	2270	3.84	13.58	18.70
2.77	1.27	2450	3.95	13.53	18.80
2.77	1.45	2670	5.61	13.00	20.49
3.05	1.69	2340	6.68	12.86	21.77
3.27	1.65	2200	5.99	15.54	23.52
3.21	1.60	2390	6.12	16.47	24.63
3.35	1.72	2360	6.98	17.18	26.49
3.51	1.85	2460	8.42	19.08	30.31
3.60	2.26	2400	12.26	14.76	31.1
3.81	1.85	2630	9.00	26.18	38.18
4.06	2.18	2580	12.26	26.18	42.53
4.69	2.61	2490	16.96	32.15	54.77

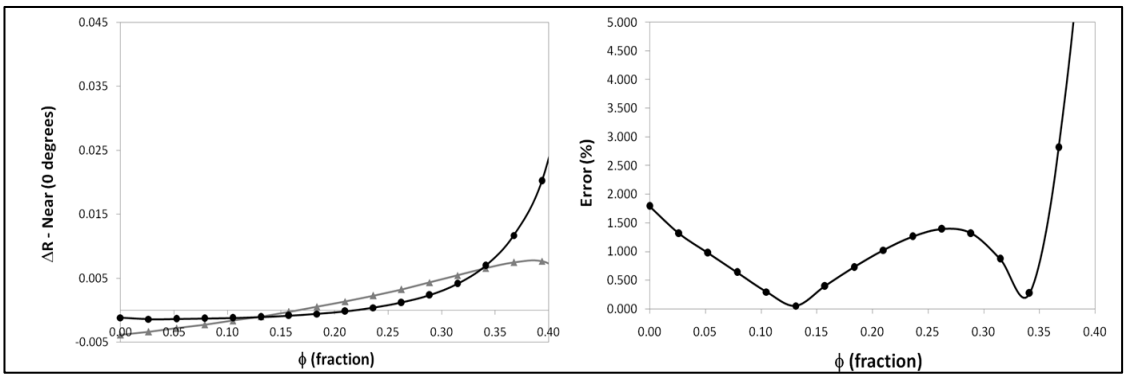

Figure 2.7: Left: Near angle time lapse reflectivity for a constant $\Delta P = 4$ MPa, constant $\Delta S_w = 0.62$ and varying porosity: in black, the full scale equations; in grey, our first order approximation (equation 2.23a). Right: prediction errors.

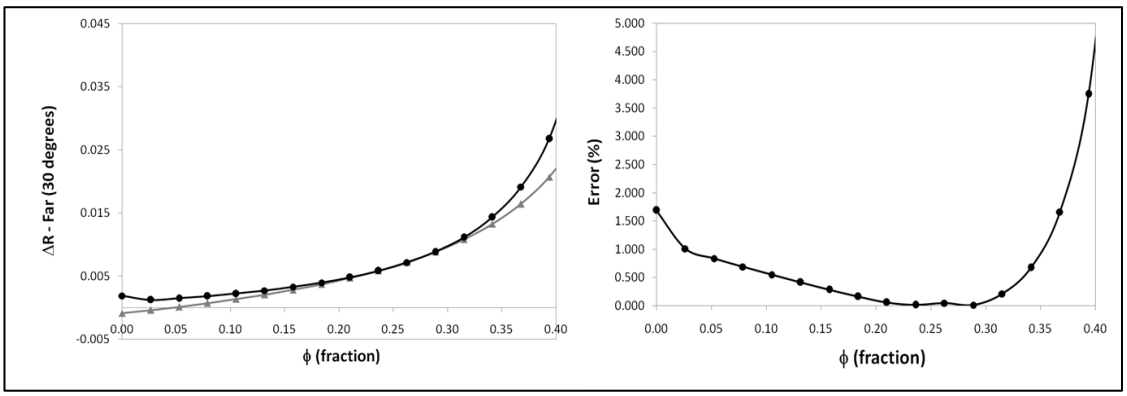

Figure 2.8: Left: Far angle time lapse reflectivity for a constant $\Delta P = 4$ MPa, constant $\Delta S_w = 0.62$ and varying porosity: in black, the full scale equations; in grey, our first order approximation (equation 2.23a). Right: prediction errors.

Figure 2.9 shows the results of this modelling, displaying the near and far angle responses. Interestingly, in terms of AVO, regardless of what the shale properties are, the polarity change between nears and fars seems to be a result of the change in pressure and saturation and only weighted by the change in the shale properties. This makes sense, as the P to S reflectivity contrast ($R_P - R_S$) has been observed to decrease with depth (Gregory, 1977, Castagna and Smith, 1994). The plot also shows the comparison between the full scale modelling and our approximation, demonstrating that the errors remain reasonably small even though the variability of the shale properties is high.

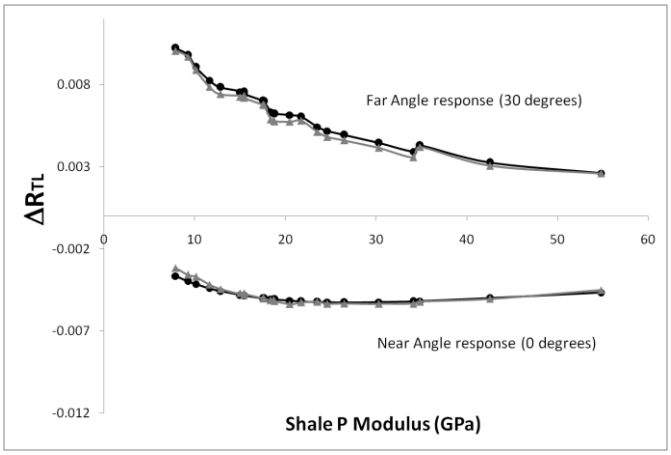

Figure 2.9: Time lapse reflectivity calculated for the North Sea example but using different overlying shale properties in the calculation. In black, the full scale equations; in grey, our first order approximation (equation 2.23a).

Finally, a comparison of equation 2.23a with full convolution-based simulator to seismic modelling (Amini and MacBeth, 2011) and the observed full stack data also further validates the approach, with normalised errors in the maps of less than 5%, despite the possibility of tuning effects and wave interferences (Figure 2.12). For this particular North Sea case, statistics generated from the full-field flow simulation model indicate that pressure changes in this compartmentalised field are typically in the range -6MPa to +6MPa, although they can be as high as 12MPa (Figure 2.10), and water saturation changes in the range +0% to 62% are appropriate for this reservoir (Figure 2.11). It is found that the errors in the analytic approximations remain less than 5% within these practical working limits.

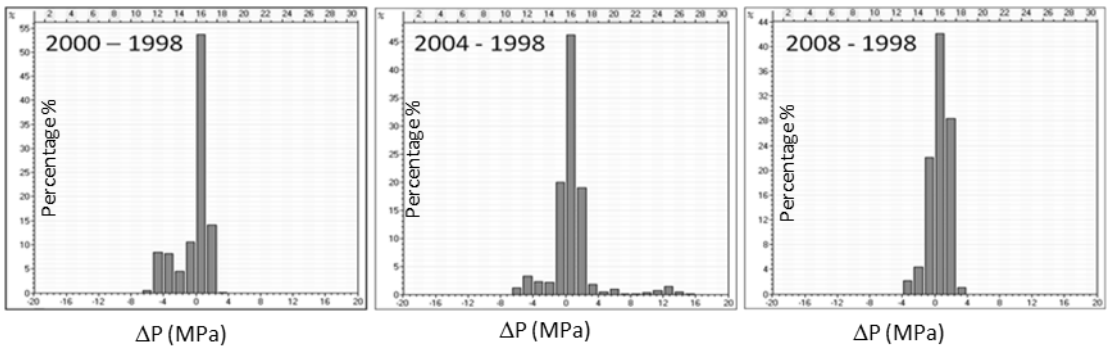

Figure 2.10: Statistics from the flow simulation, showing the change in pressure (ΔP) for different monitors.

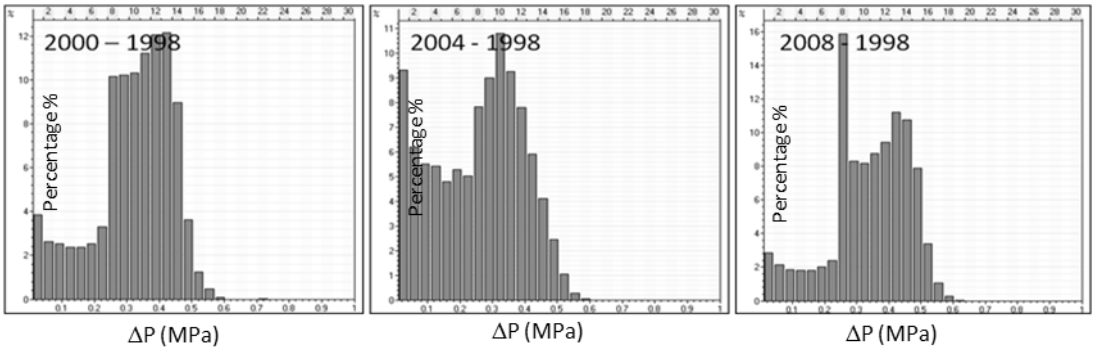

Figure 2.11: Statistics from the flow simulation, showing the change in water saturation (ΔS_w) for different monitors.

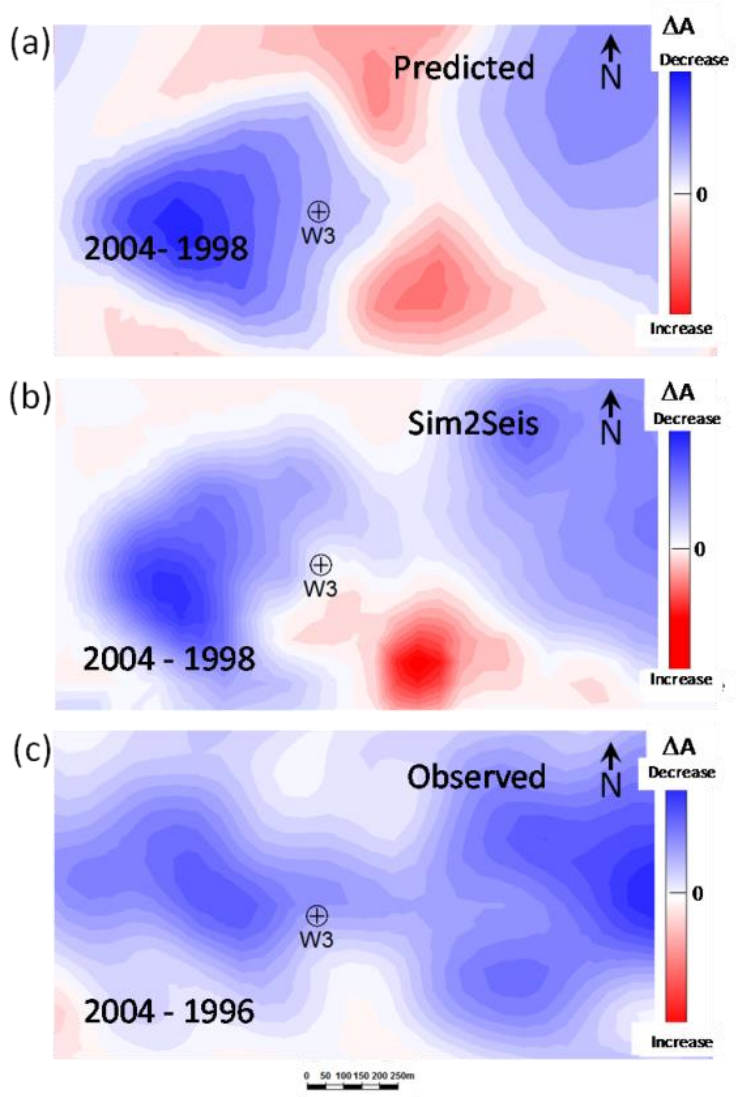

Figure 2.12: Validation of results: (a) predictions based on the approximate equation (2.23a); (b) computation from the sim2seis; (c) Observed 4D seismic response.

2.7 Expressing the new equations in the engineering domain

As discussed in Chapter 1, MacBeth et al. (2006a) suggest an expression that is linear in pressure and saturation change; this model provided a useful way to invert for pressure and saturation changes, using any type of seismic attribute In that equation, the coefficients CP and CS are empirical weights determined from the correlation between the 4D seismic and well production data and each term is normalised by the base line reservoir properties (amplitude, water saturation and pressure, respectively). One of the main sources of uncertainty and ambiguity in this model is the determination of these CS and CP constants. Another issue was that little insight can be obtained about the physical interpretation of these constants and the impact of the petroelastic model in the final result; however, there is an obvious benefit in relating the time lapse amplitude to pressure and saturation changes using a simple model with only two constants.

Since we have managed to separate the pressure and saturation effects in the seismic, we can use the results of equation 2.23a (geophysics domain equation) to generate an even simpler expression, which can still hold the benefits of having only two constants weighting the contributions of pressure and saturation changes:

$$\overline{\Delta A}_{TL}(x,y,\theta) = \left\{ \mathrm{C_S}(x,y,\theta)\frac{\Delta S_w}{S_{wi}} - \mathrm{C_P}(x,y,\theta)\frac{\Delta P}{P_i} \right\} \overline{\mathrm{s}(t)} \quad , \tag{2.24a}$$

where

$$\mathrm{C_S} = \phi[\bar{\Gamma}_1 N_1 + \bar{\Gamma}_2 N_2] \tag{2.24b}$$

and

$$\mathrm{C_P} = \left[(1-\varepsilon'\phi)[\bar{\Gamma}_1 N_3 + \bar{\Gamma}_3 N_4] - \phi[\bar{\Gamma}_1 N_5 + \bar{\Gamma}_2 N_6]\right]. \tag{2.24c}$$

This time, $\mathrm{C_S}$ and $\mathrm{C_P}$ relate directly to the fundamental constants N_1 to N_6, and their relation to porosity gives them a lateral variation in space; these constants also now have an angle dependence, which allows the use of pre-stack data, the constant $\overline{\mathrm{s}(t)}$

represents the wavelet response averaged over the interval if interest, defined as a scalar. The negative sign is preserved so that, regardless of whether the impedance contrast at the event of interest is low to high, or high to low, the coefficients C_S and C_P remain positive. This also makes sense, as an increase in water saturation (hardening of impedance) has an opposing physical effect on the reservoir to an increase in pore pressure (softening of impedance). Finally, the units of C_P are MPa^{-1}, whereas C_S is unit-less. Another important observation is that the pressure term contains explicit expressions for the rock stress sensitivity and fluid pressure sensitivity; therefore for interpretation purposes we can generate the more explicit expression:

$$\overline{\Delta A}_{TL}(x,y) \approx \left\{ C_S(x,y,\theta)\frac{\Delta S_w}{S_{wi}} - \left[C_P^{rock}(x,y,\theta) - C_P^{fluid}(x,y,\theta)\right]\frac{\Delta P}{P_i}\right\} \overline{s(t)}, \qquad (2.25a)$$

$$C_P^{rock} = (1-\varepsilon'\phi)[\bar{\Gamma}_1 N_3 + \bar{\Gamma}_3 N_4] \quad , \qquad (2.25b)$$

$$C_P^{fluid} = \phi[\bar{\Gamma}_1 N_5 + \bar{\Gamma}_2 N_6]\,. \qquad (2.25c)$$

Here, C_S is the same as defined in 2.24. The parameterisation in (2.25a) captures in quantitative form much about the time-lapse seismic signature that is already well understood intuitively, and at a qualitative level, for basic feasibility studies (for example, Lumley et al. 1997). The equation provides a way of identifying how individual reservoir conditions affect the petroelastic model, and, in turn, how this might control and modify the resultant mapped seismic response.

The dependence on porosity is now captured explicitly, and it is possible to observe how the time-lapse seismic signature scales with this parameter. This is intuitive for saturation but not for pressure, but is consistent with the findings of Falahat et al. (2011) and previous empirical observations (MacBeth et al. 2006a). The saturation term is further controlled by a group of parameters which scale directly with the contrast between the water and oil bulk moduli and densities. On the pressure side of equation

(2.25a), there are two competing lumped parameter groups: the first relates to the magnitude of rock frame stress sensitivity and the second to the variation of the bulk modulus and density of the fluids. The equation shows that these last two terms must compete against each other. There are also some unexpected results. The magnitude of the N_1 and N_5 components is observed to depend on the initial saturation state of the reservoir, although only the variation for N_1 is predicted to be significant. This implies that the relative magnitude of these terms might vary over time when interpreting 4D signatures derived from multiple surveys, unless each monitor is deliberately referred back to the baseline survey.

2.8 Summary of observations in this chapter

- An approximation has been developed that relates first-order pore pressure and saturation changes to mapped time-lapsed seismic amplitudes and brings out the explicit role of the petroelastic model parameters.

- The new equations allow the calculation of the time lapse reflectivity at any angle of incidence below the critical angle, with observed errors less than 5% for $\Delta P \leq \pm 6\ MPa$ and $\Delta Sw \leq (1 - S_{or} - S_{wc})$.

- The theoretical models used imply that the equations work at their best for porosities higher than 10% and lower than the critical porosity. It can also be concluded that the equations are valid regardless of the magnitude of the shale/sand contrast and for any AVO class observed.

- The main advantage of the new equations with respect to similar past developments (Landrø, 2000, Meadows, 2004, MacBeth, 2006a) is the ability to separate pressure and saturation signals by direct correlation to the parameters of the petroelastic model, without the need for unphysical empirical fits to the

data, and they are consistent with the rock and fluid physics models generally accepted in the industry.

- The equations are expressed in a consistent notation to the MacBeth et al., (2006a) equations, and provide a physical interpretation to the C_S and C_P constants, which previously were empirically defined.

Chapter 3: Interpretation insights from the new approximation

"As far as the laws of mathematics refer to reality, they are not certain, and as far as they are certain, they do not refer to reality"

Cuando las leyes matemáticas se refieren a la realidad, no son precisas. Cuando estas son precisas, no se refieren a la realidad

Albert Einstein

German physicist

In this chapter, a numerical exercise is performed on the equations developed in Chapter 2, using the parameters of a North Sea field. The objective is to develop physical insights with respect to the parameters that dominate the 4D response, and in particular on the angle dependence (4D AVO).

In Chapter 2 I developed an equation that explicitly relates pressure and saturation changes to the time lapse amplitude. This equation allows analysis of how the different components of the petroelastic model interplay to form the 4D seismic signal. A numerical exercise is performed with the objective of understanding which parameters dominate the seismic response. I am particularly interested in the roles of porosity, the overlying shale properties, fluid properties, the angle dependence and the relative magnitudes of the pressure and saturation signals.

3.1 Importance of porosity

A rather obvious observation on equation 2.25a is that both C_{P} and C_S have a strong dependence on porosity, and, intuitively, it is expected that saturation changes become stronger as porosity gets larger (C_S is proportional to porosity). However, for pressure this is not very obvious, since pressure has two components, C_P^{rock} and C_P^{fluid}, one of them proportional to porosity and the other proportional to the rock volume.

Figure 3.1 shows the results of the modeling exercise for a constant $\Delta P = +4\ MPa$, and $\Delta S_w = 0.62$ (water injection scenario) for a varying porosity ($0 \geq \phi \leq 0.4$), to facilitate the analysis, the denominators S_{wi} and P_i in equation 2.25a are now included as part of C_S and C_P. In order to show each term with its proper magnitude and contribution to the total response, the products $C_S\Delta S_w$ and the absolute value of $|C_S\Delta P|$ are plotted, together with the total reflectivity ($C_S\Delta S_w - C_P\Delta P$). The left plot shows the near angle responses and the right plot shows the far angles. The first observation here is that the pressure term dominates, in the near angles, for all porosities up to 25% (making the total response negative); from this point onwards, the saturation term dominates (making the total response positive). In the far angles, the situation is a bit different, the pressure term dominates only in very small porosities of less than 10%; after this point, the response is dominated by the saturation term. Interestingly, the pressure term shows a very small magnitude compared with the near angle response, whereas the

magnitude of the saturation term is not very different between near and far angles below 30 degrees.

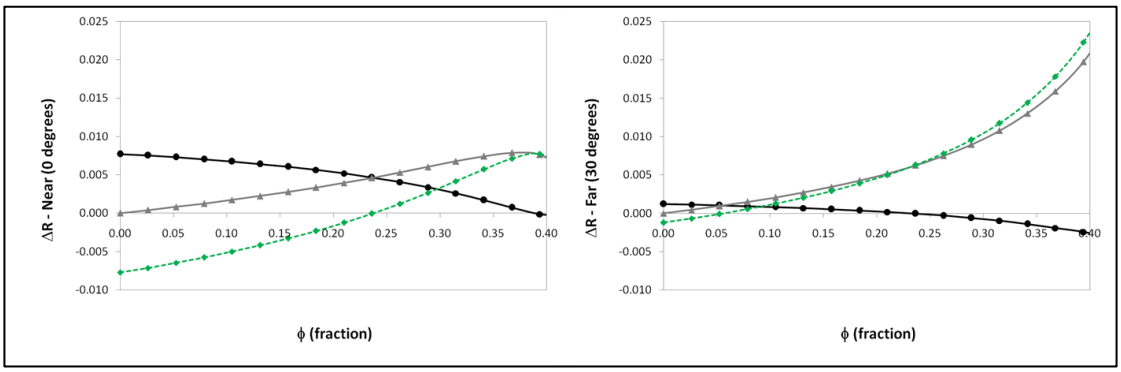

Figure 3.1: Time lapse reflectivity for a constant ΔP = 4 MPa, constant ΔS_w= 0.62 and varying porosity: left: near angle response; right: far angle response. The black curve is $|C_P \Delta P|$, the grey curve is $C_S \Delta S_w$ and the green curve is the total response ($C_S \Delta S_w - C_P \Delta P$).

Figure 3.2 shows a similar modeling exercise, but this time for a negative pressure increase of $\Delta P = -4\,MPa$ and $\Delta S_w = 0.62$ (oil production scenario) for a varying porosity ($0 \geq \phi \leq 0.4$). The curve nomenclatures are the same as in the previous example. Here we can observe that in this case both pressure and saturation terms act in the same direction (they both harden the rock). An interesting observation, however, is that, in the near angles, the saturation term is small and increases with porosity and the pressure term is exactly the opposite; therefore, at low porosity one would expect the pressure effects to dominate, and vice-versa. In the far angles, similarly, as in the previous example, the magnitude of the pressure term is very small compared to that on the near angles, whereas the saturation response does not change significantly with angle of incidence.

From this numerical exercise and from the analytic derivation of the equation we can determine the following:

- For small porosities, the pressure response is expected to dominate;
- For large porosities, the saturation term will dominate;
- The pressure response is expected to be larger in the near angles compared to the fars;

- The saturation response changes little with the angle of incidence compared to the pressure signal.

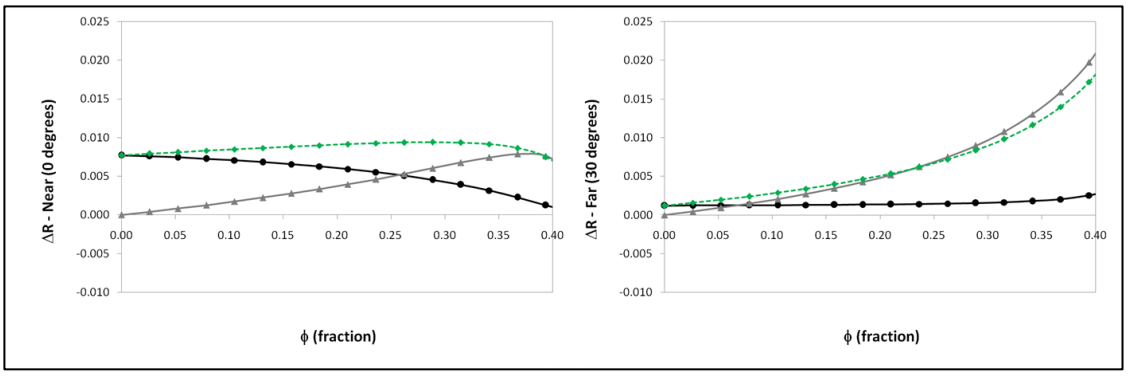

Figure 3.2: Time lapse reflectivity for a constant ΔP = -4 MPa, constant ΔS_w= 0.62 and varying porosity: left: near angle response; right: far angle response. The black curve is $|C_P \Delta P|$, the grey curve is $C_S \Delta S_w$ and the green curve is the total response ($C_S \Delta S_w - C_P \Delta P$).

These observations obtained analytically and numerically are in agreement with empirical observations shown in the literature (Landrø, 2001, Meadows, 2002, Lumley, 1997 and others). Even though these plots were generated using parameters from a North Sea field, from a physics perspective, we consider that these observations can be generalized to other types of reservoirs, although the crossover points at which pressure and saturation intersect depend on the petroelastic model parameters and therefore this crossover point is data dependent.

3.2 Rock Stress sensitivity versus fluid pressure sensitivity

To examine the relative impact of the pressure term on the time-lapsed seismic, C_P is split up into two components and each component plotted for both increasing and decreasing pressure changes, and their variation with oil API is shown in Figure 3.3**.** According to these calculations, when pressure decreases, $C_P^{rock} \Delta P$ is positive and $C_P^{fluid} \Delta P$ is negative and thus, as anticipated, the pressure-related variations of the fluid properties act in the opposite direction to the rock stress sensitivity. The explanation is that, as pressure decreases, the rock frame hardens due to increasing

effective stress but the fluids become more compressible, and hence, their bulk modulus and density decrease. Interestingly, $C_P^{rock} \gg C_P^{fluid}$ in the cases examined, and it appears that the rock stress sensitivity outweighs the fluid effect. Indeed, $\left|C_P^{fluid}\right|$ is estimated to be fairly small in magnitude when compared to the saturation term C_S for a range of oils and it is found that this may be valid as a generality. However, it should be acknowledged that C_P^{rock} carries a high uncertainty (MacBeth, 2004, Eiken and Tøndel, 2005) and correct numerical assignment of this term depends on a range of factors that may enhance or diminish the stress sensitivity relative to the calibration offered by laboratory core plug measurements. Current prevailing opinion is that the laboratory measurements over-predict the rock frame stress sensitivity. If this were true, this would reduce C_P^{rock} such that the overall contribution from the pressure change becomes even smaller. C_P^{fluid}, on the other hand carries less uncertainty, as comparatively more is known about the fluids in situ, particularly their behaviour with pressure (Clark, 1992, Batzle and Wang, 1992).

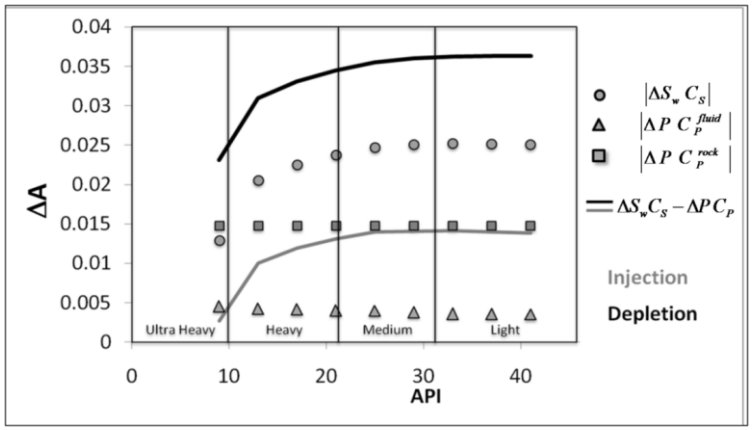

Figure 3.3: Change in seismic amplitude with oil API, showing the magnitude of contributions to saturation and pore pressure: solid lines are the total amplitude change for pore pressure down (black) and pore pressure up (grey).

3.3 AVO dependence of C_P and C_S

The relative weighting of pressure and saturation changes on angle-dependent seismic data carries important information and a way of separating pressure and saturation

effects. This dependence has been discussed to some degree in the literature (for example, in Trani et al., 2011). A direct conclusion can be deduced from the data example of Landrø (2001) for Gullfaks, suggesting that the fars are dominated by saturation whilst the nears show both saturation and pressure changes, which is consistent with the observations made in Figure 3.1 and Figure 3.2. This AVO behaviour can be explained by equation (2.43), and by inspection of the functions of the incidence angle, $\overline{\Gamma_1}, \overline{\Gamma_2}$ and , $\overline{\Gamma_3}$ in Figure 3.4. The function $\overline{\Gamma_2}$ is of particular importance, as it multiplies the shear modulus term (which changes only with pressure). According to my calculations, this quantity reduces with increasing angle and becomes negative after 30° for the North Sea case- this implies that the rock stress sensitivity will decrease with increasing angle, therefore making the far angles less sensitive to pressure and more sensitive to saturation. In other words, it is the pressure term that carries a stronger AVO effect than the saturation term.

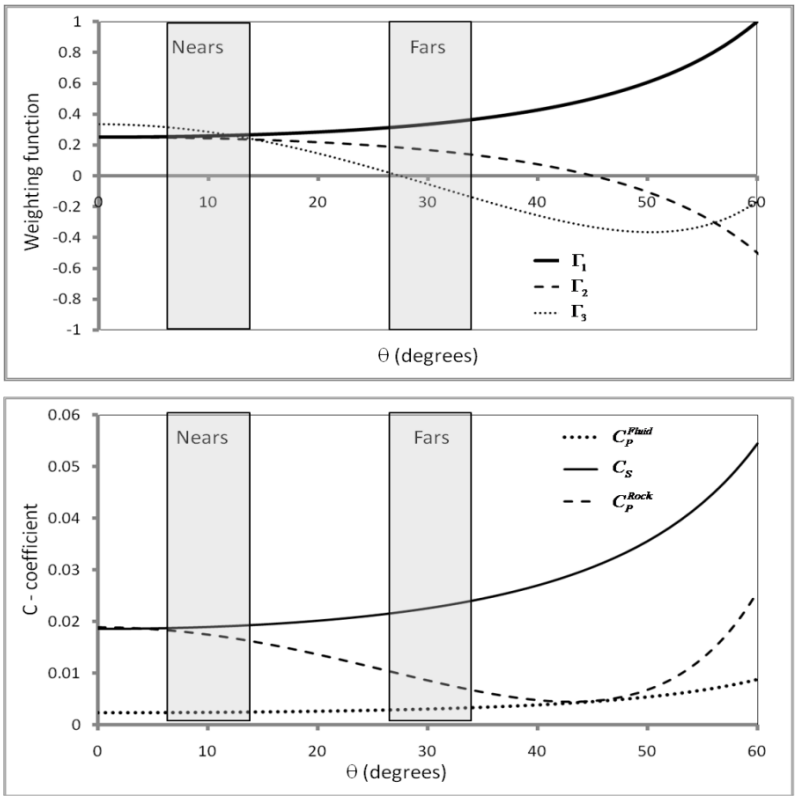

Figure 3.4: Top: trigonometric functions of offset which weight the AVO terms in the North Sea example. Bottom: The individual components of the amplitude response ($C_S\,\Delta S_w$, $\Delta P\,C_P^{rock}$ and $\Delta P\,C_P^{fluid}$), for a saturation change of 0.6 and pore pressure change of 5MPa.

Figure 3.5 and Figure 3.6 show the expected variations of the time lapse amplitude for pressure changes (ΔP) between -7 and +7 MPa, and saturation changes going from zero to $\Delta S_w = (1 - S_{wc} - S_{or})$. The annotations indicate the areas of the plot where saturation or pressure changes dominate, as well as where these interfere constructively. The most important thing to notice in is that the polarity change of the time lapse amplitude depends upon the relative magnitudes of ΔP and ΔS_w.

Figure 3.8 was generated assuming a constant $\Delta S_w = (1 - S_{wc} - S_{or})$ and a varying positive ΔP (representing a water injection). It can be observed that the relative magnitude between pressure and saturation signals depends on the parameters of the petroelastic model, represented in the plot as variations in the C_S/C_P ratio. It can also be observed that porosity plays a crucial role in this pressure/saturation interplay. Clearly, as porosity increases, saturation is expected to dominate, whereas for small porosities pressure will dominate. The plot also shows the variations in the near angle (top) and those for the far angles (bottom), indicating, as expected, that the far angles are almost mostly influenced by saturation changes and the nears show a combination of pressure and saturation signals.

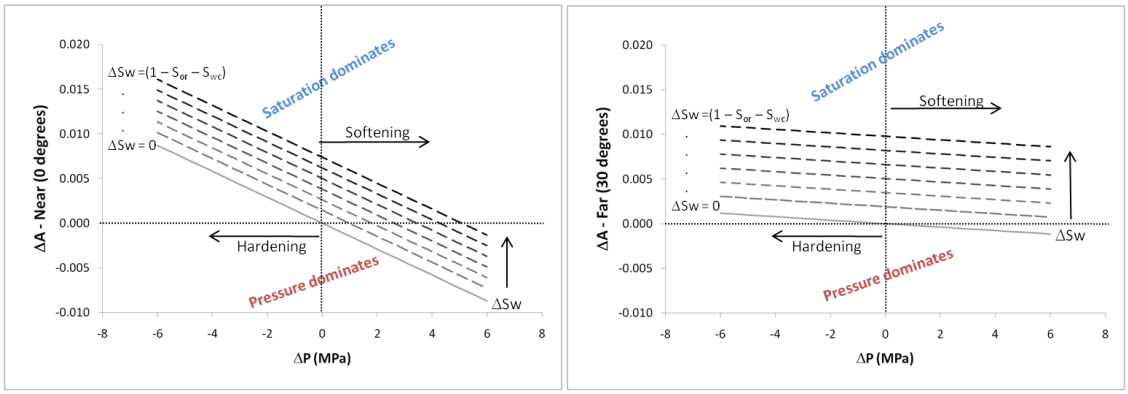

Figure 3.5: ΔP versus ΔA showing constant lines of ΔS_w. Left: near angles; right: far angles. As expected, the far angles are almost completely saturation dominant.

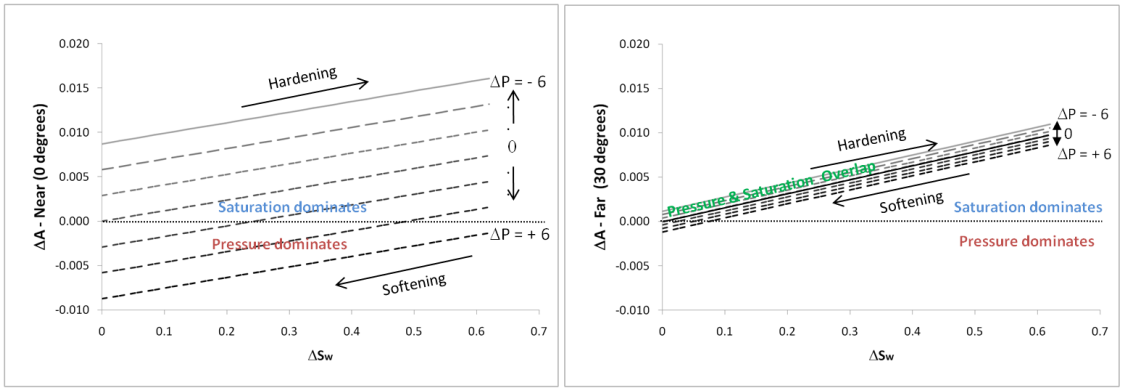

Figure 3.6: Changes in time lapse amplitude (ΔA) relative to ΔP and ΔS_w. Left: near angles; right: far angles. As expected, the far angles are almost completely saturation dominant.

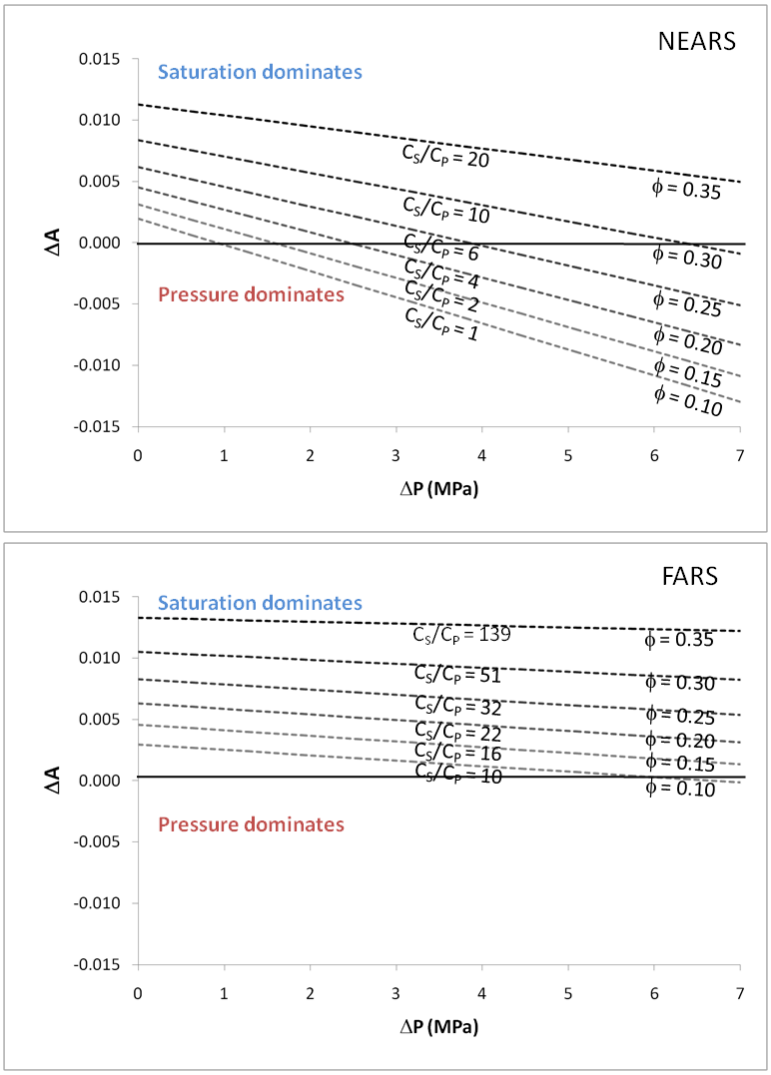

Figure 3.7: Change in 4D seismic signature with pore pressure changes for a range of porosities and a fixed (maximum) water saturation change. Top: Near-offset amplitudes in the angular range 0 to 10 degrees. Bottom: Far-offset amplitudes in the angular range 20 to 30 degrees.

3.4 Time lapse AVO behaviour of oil-water sands

In order to provide a useful way of interpreting AVO changes using the time lapse (angle dependent) reflectivity, a modelling exercise was performed by using the shale properties from the Castagna and Smith (1994) dataset as well as the real shale properties for the field. This data, in combination with the base line sand properties of the North Sea example, allowed modelling the four AVO classes from Rutherford-Williams & Castagna's classification. The selected properties are shown in Table 3.1.

Table 3.1: Values used for the modelling exercise, showing the type of AVO produced in combination with the North Sea sand properties. In yellow, the original field shale properties.

$V_P\ (km/s)$	$V_S\ (km/s)$	ρ (kg/m^3)	$\mu\ (GPa)$	κ (GPa)	M (GPa)	AVO
2.65	1.32	2140	3.75	10.03	15.03	Class I
3.05	1.69	2340	6.68	12.86	21.77	Class II a
3.35	1.72	2460	7.28	17.90	27.61	Class II b
3.80	1.85	2630	9.00	25.98	37.98	Class III
4.69	2.61	2490	16.96	32.15	54.77	Class IV

Figure 3.8 gives the results of the modelling exercise using the rock and fluid physics equations. The reflection coefficient of the base is shown in grey and the monitor in black, for each of the cases modelled. It is clear that, although the sand properties are fixed, just by changing the shale properties it is possible to simulate the four AVO classes, since these depend upon the shale/sand contrast. The actual properties of the North Sea example show a Class I, which agrees with observations in the field and AVO modelling studies (Loizou, et al., 2008). Figure 3.9 shows the time lapse reflection coefficient computed both by taking the difference of base and monitor and from equation 2.43 for a constant $\Delta P = +4MPa$ and $\Delta S_w = 0.6$. As expected from previous observations, the time lapse AVO behaviour is almost independent from the shale properties; in all cases, the time lapse reflectivity starts as a negative, indicating a pressure dominant signal ($C_S \Delta S_w < C_P \Delta P$) and as the angle of incidence increases, $C_P \Delta P$ decreases (see Figure 3.4); therefore, the time lapse reflectivity becomes positive,

indicating a saturation dominant signal ($C_S \Delta S_w > C_P \Delta P$). Interestingly, even though the base line and monitor AVO responses are completely different in each case, the time lapse AVO response is very stable and the only noticeable difference is the angle at which the signal changes sign (pressure and saturation signal crossover). Most importantly, the crossover angle is smaller for Class I (22°), and gradually increases with the rest of the classes, although for Class III and IV it is about the same (27°). The implication of this behaviour is that pressure signals are expected to be slightly stronger in Class I AVO, whereas in Class III and IV, saturation signals could be more dominant.

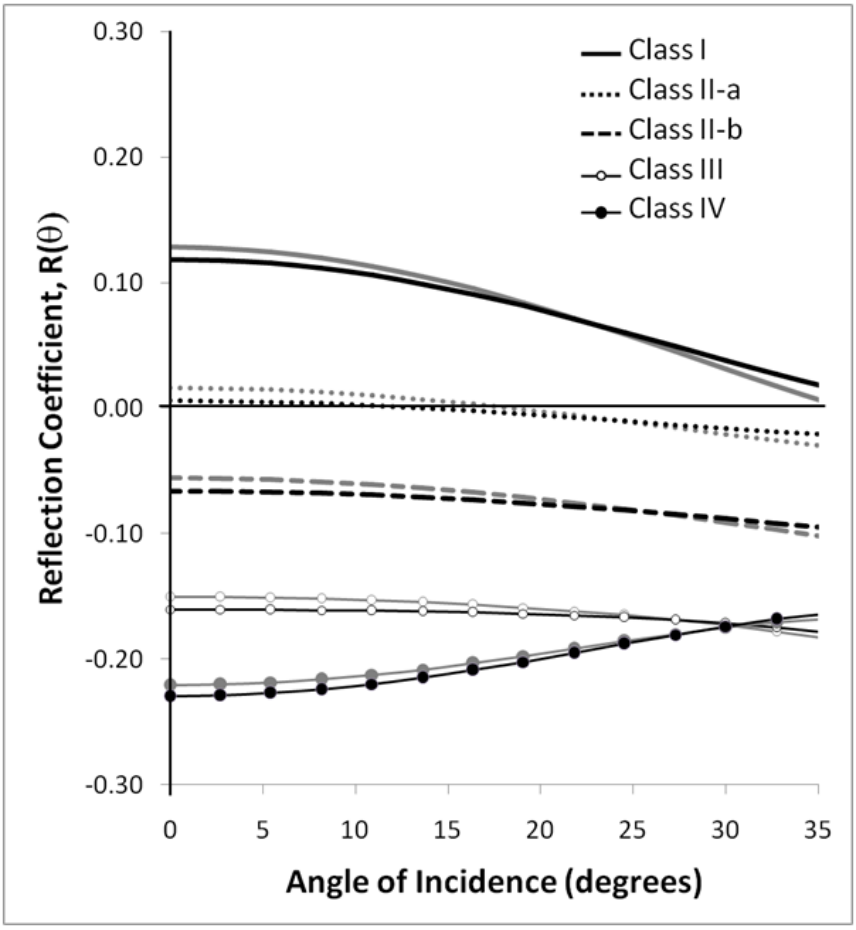

Figure 3.8: Time lapse AVO modelling exercise for water injection using the shale properties of Table 2-6 and using the sand properties from the North Sea example. In grey, the AVO responses of the base line, and in black, the AVO responses of the monitor for each case.

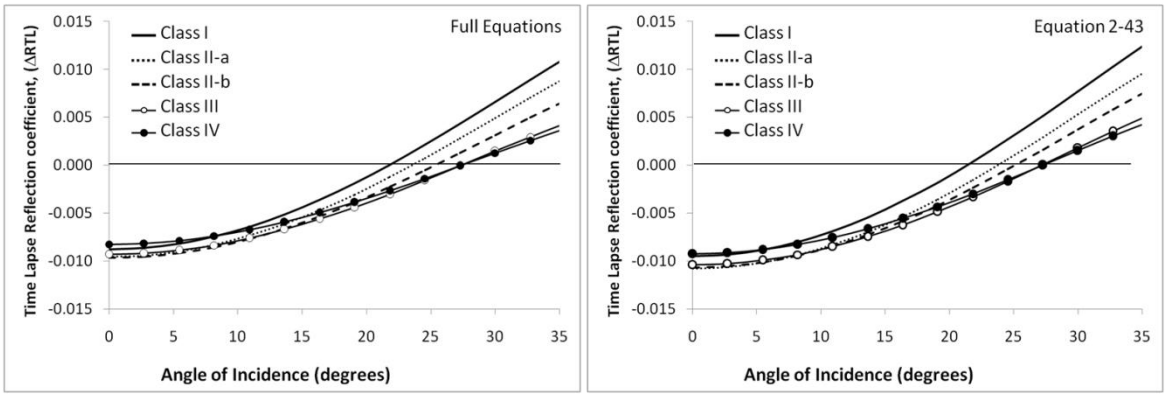

Figure 3.9: Time lapse AVO calculated for each of the AVO classes using a constant $\Delta P = +4MPa$ and $\Delta S_w = 0.62$. Left: full rock and fluid physics equations; Right: predictions of equation 2.43.

A depletion exercise was also performed using a constant $\Delta P = -3\ MPa$ and $\Delta S_w = 0.6$ and the results are shown in Figure 3.10 and Figure 3.11, since in this case both pressure and saturation affect the rocks in the same way (reservoir hardening), the plots do not show a significant variation of amplitude with angle. Similarly to the previous case, the time lapse AVO responses are very similar, regardless of the type of AVO of the base and monitor. One of the main advantages of the newly developed equations is the possibility of separating the pressure and saturation contributions on the time lapse seismic response: this opens up new ways of understanding 4D seismic data from a quantitative perspective, which could be potentially useful during 4D feasibility studies, 4D interpretation projects, simulation to seismic processes and pressure-saturation inversion.

An example of the type of insights that can be gained with this separation of pressure and saturation is shown in Figure 3.12, which is a plot of the time lapse responses of the exercise shown in Figure 3.9 using the actual properties of the North Sea Example and, $\Delta P = \pm 3\ MPa$ and $\Delta S_w = 0.6$, the upper figure is the pressure up modelling and the lower picture shows the depletion case.

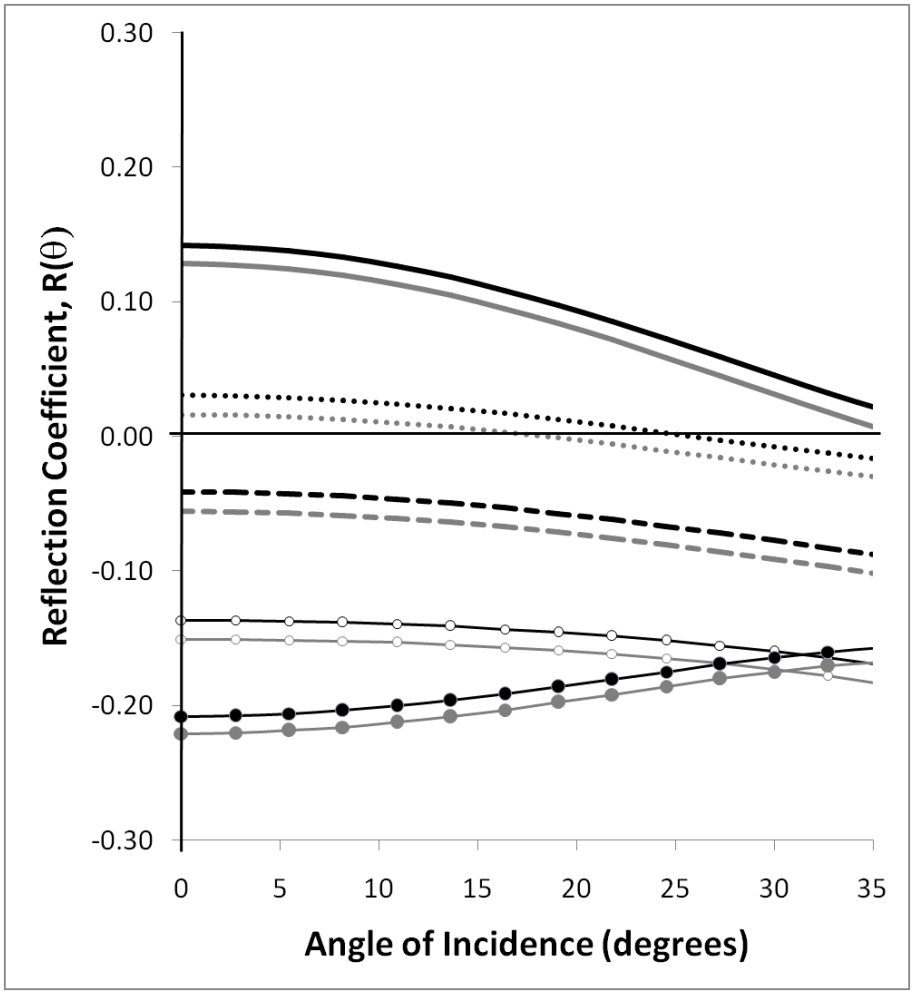

Figure 3.10: AVO depletion modelling exercise using the shale properties of Table 2.4 (Chapter 2), and using the sand properties from the North Sea example. In grey, the AVO responses of the base line and in black, the AVO responses of the monitor, for each case.

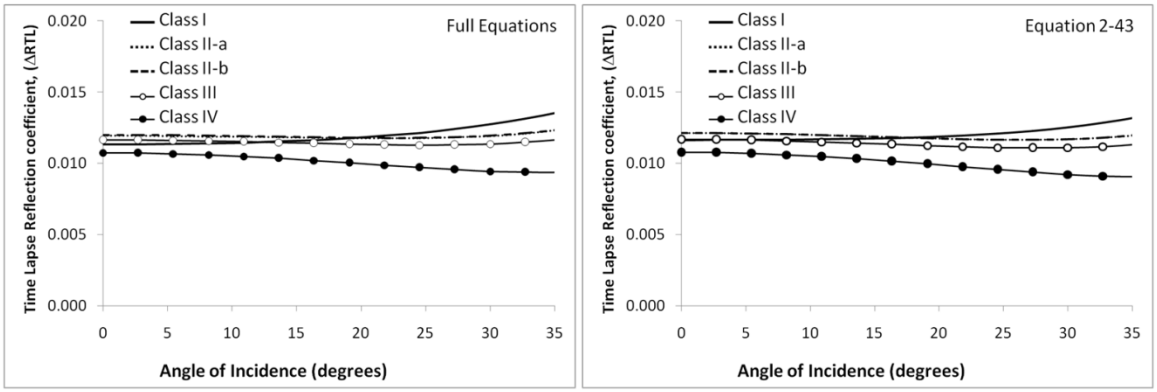

Figure 3.11: Time lapse AVO calculated for each of the AVO classes using a constant $\Delta P = -3MPa$ and $\Delta S_w = 0.62$. Left: full rock and fluid physics equations; Right: predictions of equation 2.23a (Chapter 2).

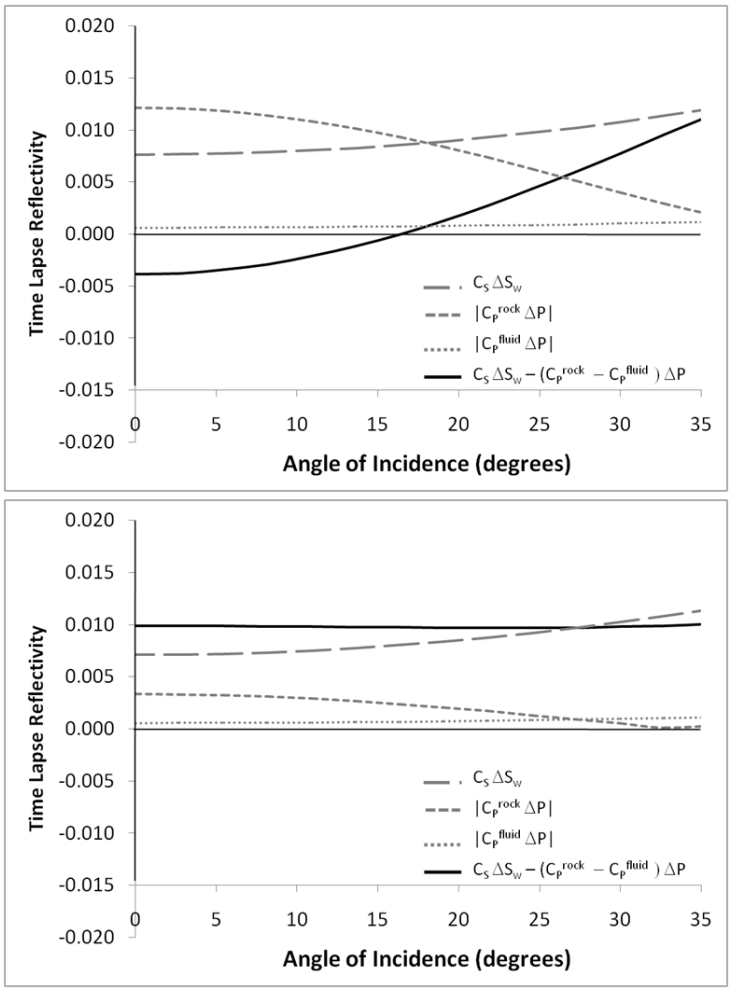

Figure 3.12: Time Lapse AVO modelling, showing the contributions of the pressure and saturation signals into the final response. Top: modelling pressure up; bottom: modelling pressure down.

Let us now look at the pressure up case: the rock stress sensitivity shows a strong response in the near angles and then rapidly decreases with angle to become almost zero at 35 degrees. The saturation signal starts at about half the magnitude of the rock stress sensitivity and slightly increases with angle of incidence. At about 17 degrees, there is a crossover point between pressure and saturation signals, indicating that these cancel each other. After that point, the saturation signal becomes dominant and the pressure keeps decreasing. Another interesting fact is that the fluid pressure sensitivity shows a very small angle variation, and, most importantly, its magnitude remains very small compared to that of the saturation and pressure signals.

In the pressure down exercise the situation is quite different. The AVO response of the total combined 4D AVO response shows almost no variation with the angle of incidence, which is a very interesting feature; and from Figure 3.11 we know that this behaviour is likely to be a general behaviour regardless, of the AVO type of the base and monitor signals. The importance of this lack of variation with angle is that, from the time lapse reflectivity alone, it would be very difficult to determine if the signal is due to pressure or saturation. This explains in a graphical way why the pressure down signal has been documented as less pronounced than the pressure up signal (MacBeth, 2006, Staples, 2006). However, with our equations, it is now possible to plot the contributions of the pressure and saturation signals without the need to model multiple scenarios. This can simplify the interpretation process, for instance if we wish to determine whether a certain location shows pressure down or water flooding (or both) and in what proportion.

An example of the application of this knowledge in practical terms would be, for instance, during a 4D feasibility study. One could design a survey in such a way that there is enough angle range to be able to capture the pressure-saturation crossover in the pressure up signal, or the angle at which the pressure effects disappear in the pressure down signal. This would potentially allow the identification of areas with bypassed oil, that is, places where there is no water saturation change but there is a pressure down signal. Another application would be during the AVO processing, where one would be able to select the appropriate angle bands in order to have a representative 4D AVO response from the resultant angle stacks. Additionally, a very important piece of information that can be obtained from this modelling is to understand the magnitude of the pressure signal that is required to be visible in the seismic. All these observations are not obvious by looking only at the full combined 4D signal, particularly in the case where no pressure up signal can be observed (depletion), as in this case, both pressure and saturation affect the amplitudes in a similar way (impedance increase).

Finally, the same modelling exercise was performed for all AVO class types and the saturation and pressure signals are shown in Figure 3.13. As observed before, the general AVO behaviour of the pressure and saturation signals is very similar (saturation slightly increasing with angle and pressure rapidly decreasing with angle). The only noticeable differences are the crossover angle of the pressure and saturation signal and the angle at which the pressure signal is expected to reach zero.

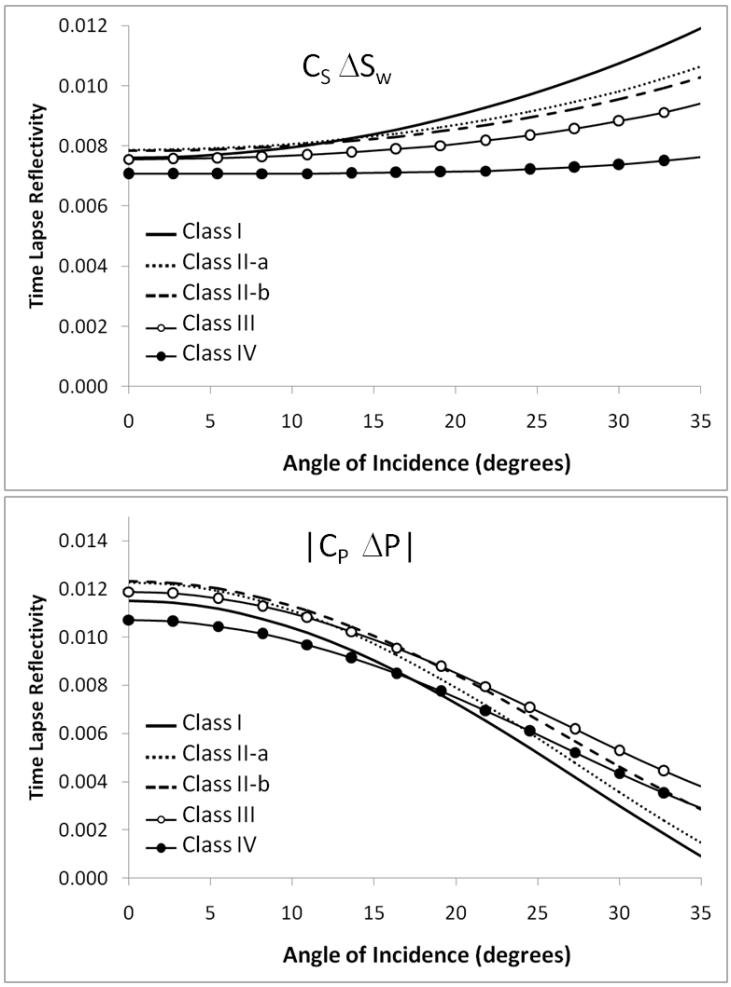

Figure 3.13: 4D AVO modelling showing the saturation (Top) and pressure (Bottom) contributions to the 4D signal for each case. The 4D AVO behaviour in all cases is very similar, regardless of the original AVO class of the base and monitor.

3.5 Shale properties and polarity of the 4D signal

In conventional 2D/3D AVO analysis (Ostrander, 1984), the change in reflectivity is directly related to the contrast between the reservoir layer and the overlying rock layer. This contrast determines the type of AVO behaviour observed as predicted by Aki and Richards approximations to Zoeppritz equations (1980). This shale/sand contrast relation was used as a basis for the classification of gas sands performed by Rutherford and Williams (1989), using the normal incidence reflectivity, and further extended by Castagna, et al. (1998), using both intercept and gradient interpretation.

The time lapse reflectivity has an additional complication, which is the fact that the polarity of the 4D signal changes, even at normal incidence. Our calculations show that this change in polarity is independent of the contrast between the sand and the overlying shale and it is only the change in pressure and saturation that determines the positive or negative polarity of the time lapse reflectivity (as pressure can be either positive or negative). To demonstrate this effect, Figure 3.14 shows the results of a simple 1D modelling, simulating an increase in acoustic impedance with time lapse (reservoir hardening) while Figure 3.15 shows the modelling for a decrease of acoustic impedance with time lapse. In both cases, comparisons are made for cases where the overlying shale impedance is higher than the reservoir impedance ($I_P^{shale} > I_P^{sand}$) and for cases where the overlying shale impedance is lower than the reservoir sand ($I_P^{shale} < I_P^{sand}$). In both cases, it can be observed that the polarity of the resultant time lapse signal taken at the top reservoir (highlighted track) is exactly the same, regardless of whether we are on a high to low or low to high impedance contrast between the shale and the sand. Another important observation is that the polarity of the 4D signal at the top reservoir has opposite polarity to that taken at the base reservoir.

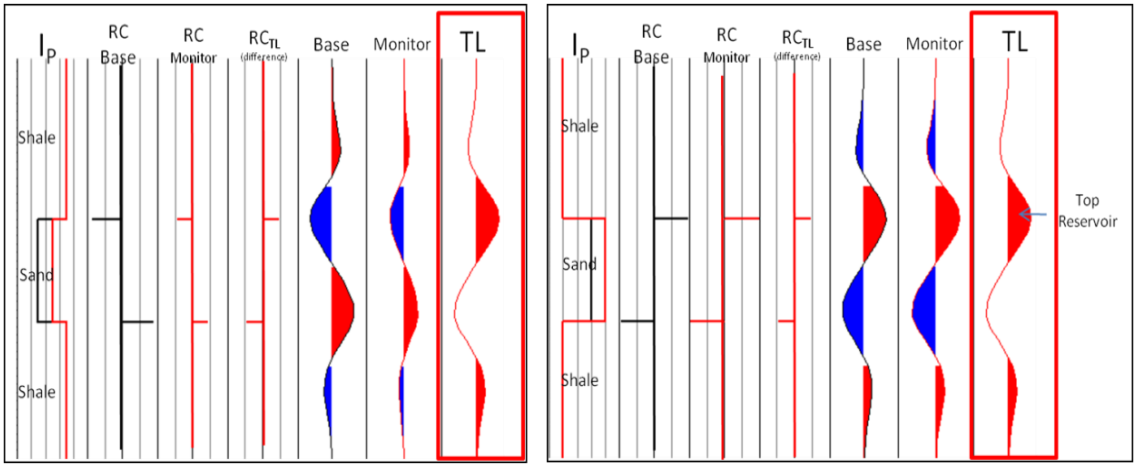

Figure 3.14: 1D modelling showing reservoir hardening (increase in impedance with time lapse). Left: $I_P^{shale} > I_P^{sand}$; Right: $I_P^{shale} < I_P^{sand}$. In both cases the polarity of the resultant 4D signal at the top reservoir is the same.

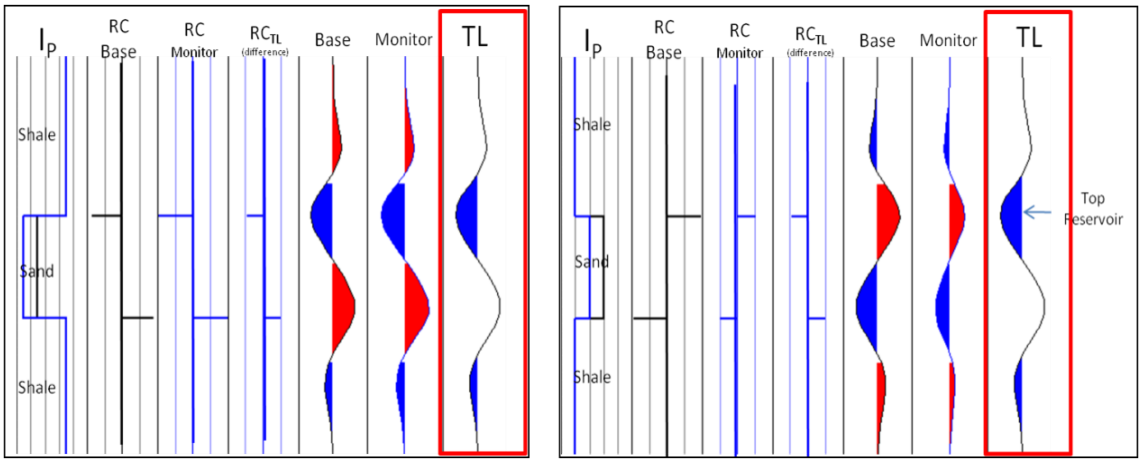

Figure 3.15: 1D modelling showing reservoir softening (decrease in impedance with time lapse). Left: $I_P^{shale} > I_P^{sand}$; Right: $I_P^{shale} < I_P^{sand}$. In both cases the polarity of the resultant 4D signal at the top reservoir is the same.

This is important, as it shows that regardless of whether we have a low to high or a high to low impedance contrast, the polarity of the 4D signal only depends on ΔP and ΔS_w, apart from their effect on separation between pressure and saturation signal, the shale properties only impact the magnitude of the time lapse amplitude (Figure 2.9).

3.6 Summary of findings in this chapter

- The dominance of the pressure or saturation signal in the final time lapse reflectivity, at near angles, depends mainly on two factors: porosity and the relative magnitude of the pressure and saturation variations.

- The contribution of the fluid pressure sensitivity in the resultant time lapse signal is very small for the case of an oil/water system.

- The main pressure dependence is related to the variations in the rock stress sensitivity, and these effects show strong angle dependence. The general behaviour observed is that the pressure signal decreases with angle of incidence.

- The pressure down signal is difficult to identify using the time lapse change, as there is a lack of variation of the combined pressure + saturation response with angle. However, the separated contributions of pressure and saturation signals show a strong variation with angle, regardless of whether pressure goes up or down. This fact opens up the opportunity to provide a way of differentiating signals related to water-flooded areas from those related to pressure decrease in 4D seismic interpretation studies

Chapter 4: Constraints on the petroelastic model

"I call our world Flatland, not because we call it so, but to make its nature clearer to you, my happy readers, who are privileged to live in Space"

Llamo a nuestro mundo Planilandia, no porque así se llame, sino para hacer su naturaleza más clara para ustedes, felices lectores, privilegiados de vivir en el espacio.

Edwin Abbot in "Flatland a romance of many dimensions"

English Scholar and writer

In this chapter, I seek to reduce the ambiguity of 4D seismic modelling by establishing constraints on the parameters of the petroelastic model. It is well known that of all the parameters involved, the rock stress sensitivity carries the highest uncertainty and, unfortunately, it is one of the most influential quantities in 4D seismic modelling. Some of the issues in calibrating the rock stress sensitivity using core based measurements are discussed and a map based methodology (flatlanders' approach) is developed to attempt to constrain this important parameter using the observed 4D amplitudes around injectors. The observations are validated using real data from datasets available in ETLP, as well as from published case studies.

4.1 The need to constrain the petroelastic model (PEM)

The theoretical development shown in the previous chapters provides a way of separating the pressure and saturation contributions into the 4D seismic signal, as well as analysing their relative interplay; this is useful in particular for 4D interpretation and feasibility studies. It was found that there are three main parameters interacting to control the pressure and saturation effects in the time lapse seismic, which seem to act as a group of parameters and cannot be separated. In equation (2.24a) we called them C_S (proportional to the fluid contrast), C_P^{rock} (rock stress sensitivity) and C_P^{fluid} (fluid pressure sensitivity. Of these, C_P^{rock} carries the highest uncertainty (MacBeth, 2004, Eiken and Tøndel, 2005), and correct numerical assignment is highly uncertain. Current prevailing opinion is that laboratory measurements over-predict the rock frame stress sensitivity. If this were true, this would reduce C_P^{rock} relative to C_S, which would reduce the impact of errors in its estimation. On the other hand, C_P^{fluid} carries less uncertainty, as comparatively more is known about the fluids in situ, particularly their behaviour with pressure (Clark, 1992, Batzle and Wang, 1992).

4.2 The elusive rock stress sensitivity

It is often questioned whether core based measurements or models based on these can be considered a reliable representation of the in situ reservoir properties. For this reason, some researchers have developed empirical relationships in an attempt to provide ways of estimating the rock stress sensitivity from, for instance, well log data (Vernik & Hamman, 2009, Avseth et al., 2009). In my derivation, however, I have selected a theoretical model (MacBeth, 2004) to incorporate the rock stress sensitivity; this increases the physical interpretability of the result and avoids relying excessively on empirical fits. Nevertheless, it is acknowledged that MacBeth's equations were derived using core measurements as a basis, and hence their parameterisation still carries high uncertainty. In the following section, we discuss the most common issues arising from the use of core data as a basis to calibrate the rock stress sensitivity.

4.2.1 *Factors that suggest an enhancement of the predicted reservoir stress sensitivity relative to that measured from a core plug*

Statistical sampling - cores taken from wells do not provide a statistically meaningful representation of the 3D heterogeneity in the reservoir because these samples are usually taken from the most competent and productive rock. Core plugs do not adequately sample the full reservoir, and thus may miss particular facies groups, or do not properly represent the nature of the geology. This may lead to stress-sensitive mesoscale pockets of unconsolidated/consolidated sands, perhaps shales, or even fractures/faults being bypassed in the analysis. Subsequent core-to-log correlations and long-wavelength seismic averages will thus underestimate stress sensitivity. This issue may be partially mitigated by the use of log-guided sampling strategies and quantitative outcrop analogue studies, but still cannot adequately represent features such as fracture zones. A counterargument to this is that we naturally bias results taken in the laboratory by focussing on those plugs which do not fall apart, and thus we do not sample the most stress sensitive parts of the subsurface, such as fractures or brecciated zones.

Time scale of production - the time scale over which production occurs (days or months) is longer than the scale over which pore pressure is cycled (minutes/hours) in the laboratory. The longer time may allow microscopic deformation and accommodation of the sample at each stress state, while the rock "creeps" into an equilibrium position. The velocity in this final condition may differ from the usual laboratory results.

4.2.2 *Factors that suggest a reduction of the predicted reservoir stress sensitivity relative to that measured from a core plug*

Core plug damage - it has been suggested that many of these defects observed in the laboratory are the consequence of internal damage in the core as a result of stress unloading during the act of coring from wells or stress release at the outcrop (Ness et

al., 2000). The degree of damage depends largely on the original stress conditions for the rock and, to a lesser extent, on the degree of consolidation. Cores loaded back to their in situ stress state do not recover their original velocities, and their stress dependence is usually larger than it was in situ. Damage resulting from core unloading needs to be estimated and subtracted from the rock-frame measurements. Another aspect is core unloading damage, which implies that we may be measuring stress sensitivities much higher than those in situ (Ness et al., 2000).

Frequency dispersion - in the saturated rock, higher velocities are generally observed at higher frequencies. This is the well-recognized problem of frequency dispersion (and attenuation) and it affects the confidence with which measurements from the laboratory can be used at seismic frequencies. This effect depends on many factors, such as rock type, clay distribution, and the presence of cracks in the core plug (Mavko et al., 1998).

Effective stress coefficient – this impacts the prediction of the true effective stress acting on the rock frame as a result of internal fluid pore pressure variations. It can be shown experimentally that effective stress, $\sigma_{eff} = \sigma_{ob} - \alpha P$, on the rock frame is a linear function of confining (overburden) stress σ_{ob} and pore pressure P, where α is the effective stress coefficient. The more unconsolidated a rock, then the closer α becomes to 1. The more consolidated rocks have α values lower than 1 (and hence this reduces the influence of pore pressure fluctuations on the elastic properties). The exact value of α is not an easy quantity to evaluate in situ, as it depends upon the property measured, the fluid flow conditions of the reservoir and consequent boundary conditions (Hoffman et al., 2005).

Geomechanical effects – the effective stress, as defined above, depends on the difference of the total stress field and the reservoir pressure, weighted by the effective stress coefficient. During deformation, the reservoir changes the surrounding stress conditions, such that the total stress has now altered. This adjustment may be written by $\gamma \Delta P$, where γ is the stress arching ratio (Sayers, 2010, MacBeth et al., 2011) which

also varies across the reservoir. As a consequence, the effective stress acting on the reservoir rocks is now given by $(\gamma - \alpha)\Delta P$. As both γ and α are defined as positive numbers but $\gamma < \alpha$ (MacBeth et al., 2011), they act to possibly reduce the pore pressure sensitivity of the reservoir rocks. A spin-off benefit is that the surrounding reservoir rocks are altered by the stress field, according to $\gamma\Delta P$, and this may be detected. In addition to the above, a secondary effect may occur in the shales – as they extend the pore volume expands and the pore pressure decreases by an amount determined by their Skempton B-coefficient (MacBeth et al., 2011).

Geomechanical effects/overburden – as the reservoir compacts, the overburden rocks extend. This effect is well documented and has been commonly used to monitor overburden stress changes and reservoir pressure (Hatchell and Bourne, 2005; Hodgson et al., 2007). This also effects the seismic response at top reservoir, and this may be significant in strongly compacting reservoirs (Corzo et al., 2011).

4.2.3 Factors that could enhance or diminish the stress sensitivity relative to that measured from a core plug

The measured 'dry' frame response – there is some doubt about the state of "dry" rock-frame saturation in the laboratory, and whether it is appropriate to use it in Gassmann's equation to represent the frame in the fully saturated rock. Some of this uncertainty relates to sample-preparation procedures prior to testing. In particular, it is the drying process that determines the small percentage of moisture adsorbed on the grains and structural water associated with clays. Differences in drying rate and temperatures can lead to a variation in measured velocities (e.g., King et al., 2000).

The role of clays and shales – the effect of clays on the stress sensitivity of sandstones is currently uncertain (MacBeth and Ribeiro, 2007). Clay-related measurements are generally not made on a routine basis, resulting in a lack of sampling of the non-

reservoir rocks, making the stress sensitive properties of the shales largely uncertain and difficult to assign (MacBeth et al., 2011).

Imperfect stress recovery - although triaxial or biaxial laboratory equipment can provide access to a range of stress pathways with variations in vertical loading and differential stress, it is not possible to reinstall the true 3D in situ stress field, because there is insufficient information on the subsurface stresses and the way they change during production (Fjaer et al., 2008).

Stress asymmetry – results from core plugs vary depending upon whether the plug is under compression or extension. This asymmetry must be taken into account in stress sensitivity calculations, and will lead to a natural hysteresis in the physical behaviour (Sayers, 2010).

4.3 Using observed 4D seismic to constrain the petroelastic model

Based on the derivations in Chapter 2, 4D seismic amplitudes are interpreted as a weighted combination of pore pressure and water saturation changes, and the results of the numerical exercise performed suggest that seismic observations can be used to back out the relative magnitudes of $\mathrm{C_S}$ and $\mathrm{C_P}$ in situ, particularly in places (such as around injectors) where pressure and saturation signals cancel each (see Chapter 3). For convenience, the initial pressure and saturations are incorporated inside C_S and C_P, so that the analysis can be performed directly in terms ΔS_w and ΔP.

Mathematically, from the approximations in Chapter 2, the influence of the petroelastic model on the time lapse seismic response can be written as:

$$\frac{C_S}{C_P} = \frac{\phi[\bar{\Gamma}_1 N_1^o + \bar{\Gamma}_2 N_2^o]}{\left[(1-\varepsilon'\phi)[\bar{\Gamma}_1 N_3^o + \bar{\Gamma}_3 N_4^o] - \phi[\bar{\Gamma}_1 N_5^o + \bar{\Gamma}_2 N_6^o]\right]} \tag{4.1}$$

or symbolically as:

$$\frac{C_S}{C_P} = \frac{FC}{[\mathrm{RSS} - FPS]} \quad , \tag{4.2}$$

where FC is the fluid contrast, RSS is the rock stress sensitivity and FPS the fluid pressure sensitivity. This equation shows that the basic observation of a 4D signature as being dominated by either saturation or pore pressure provides a simple and obvious way to determine a constraint from the seismic data. However, in order for such observations to be useful, only situations in which pore pressure and water saturation increase can be considered, as $C_S \Delta S_w$ then competes against $C_P \Delta P$ in the determination of data polarity and overall dominance of the signal. This condition, therefore, restricts our measurements to regions of the reservoir for which water is injected. Producers will not yield useful information, as pore pressure will decrease and water saturation increase, thus providing data of one polarity only and it is difficult to tell which signal is dominating. Furthermore, cases of negative ΔS_w are rare and therefore a drop in pore pressure will not yield useful information for the purposes of our study. Therefore, to obtain data points to establish the constraints on the petroelastic model, observed 4D seismic data from two different reservoirs (North Sea and West Africa) are analysed, as well as literature examples where the ΔS_w and ΔP are quoted; this allowed gathering a small database of observations that helped establishing some constraints on the petroelastic model, which can help reducing the uncertainty in the parameterisation.

4.4 Data Gathering – West of Shetlands

The first dataset used for this purpose is a Paleocene turbidite reservoir, with known high sand porosity in the range 25 to 28%, and light to medium oil (32API). The reservoir is suited to this study, as the petroelastic model is well known (Amini and MacBeth, 2011). Stacked and migrated seismic data are available for 1996 (pre-production baseline, with first production in 1998) and the 2004, 2006 and 2008 post-production monitor surveys; typical vertical sections of these data can be seen in

Figure 4.1. For convenience, the 1996 pre-production base line is labelled as 1998 to make it consistent with the simulation model.

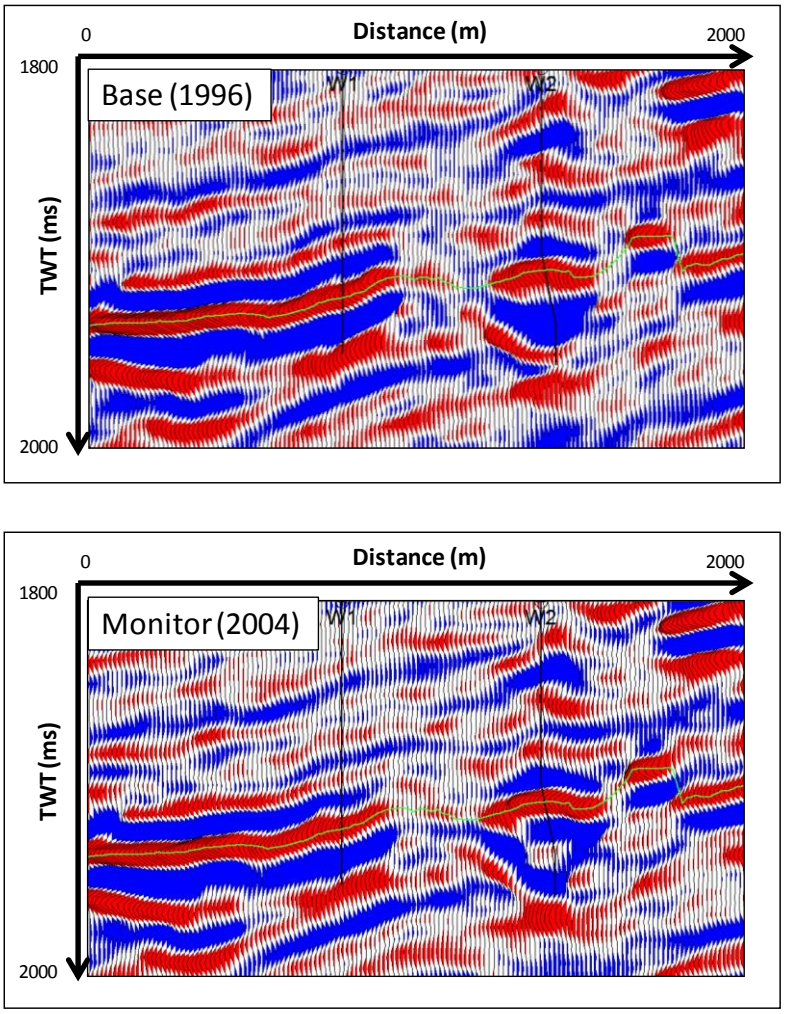

Figure 4.1: Vertical section through wells W1 and W2 for the stacked and migrated seismic from the North Sea example. The green line indicates top reservoir, from which the mapped amplitudes are evaluated.

The number of monitors available in this dataset provides an opportunity to measure the same part of the reservoir several times, but with changing ΔP and ΔS_w conditions. Three regions are identified from these data for this study, containing in total five active injectors over the 1998 to 2008 period. Figure 4.2 shows an RMS amplitude map extracted at the top of the reservoir using a 20 ms window centred on the horizon interpreted; the water injectors are shown in black and producers in white. The flow simulation model is also available and the injector wells are chosen because the

production history match in the selected areas is good, and hence the simulation predictions of pore pressure and saturation change can be trusted at the well locations. However, caution is exercised with predictions beyond the well locations, and these are therefore not used in our calculations, as they may contain model errors and cannot be reliable.

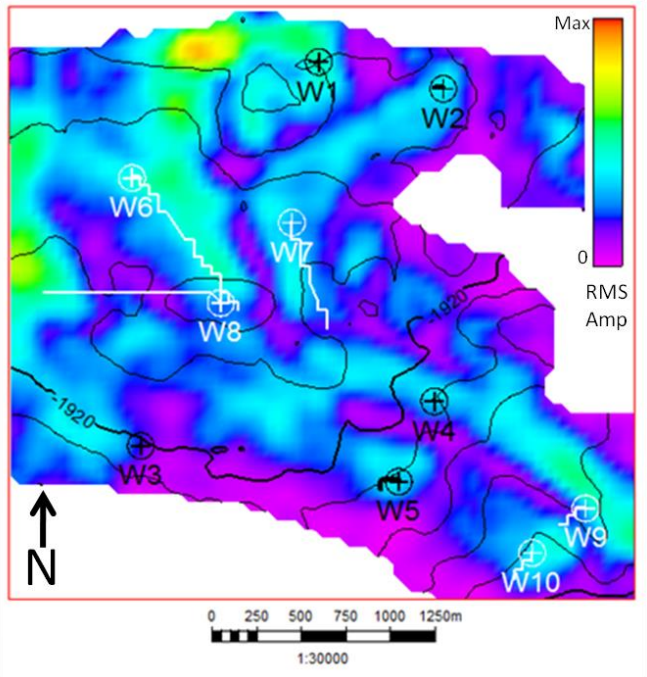

Figure 4.2: RMS amplitude map taken at the top of the reservoir using a 20 ms window around the horizon interpreted. The well symbols are shown at the base of the well, producers are shown in white and water injectors in black.

Let us consider the first example area, which contains wells W1 and W2, and shows the comparison between our predicted ΔA map compared with the observed seismic. It is important to note that the observed seismic comes from the full stack volume, which contains information for a range of angles, which is unknown, whereas our prediction comes from our equation using the near angle values for the angle dependent terms $((\overline{\Gamma_1} = 0.25, \overline{\Gamma_2} = 0.25, \overline{\Gamma_3} = 0.33)$; therefore, our comparison can only be done from visual inspection.

From the well activity plots shown in Figure 4.3, we can make the next observations. Well W1 injected water for more than three years but then stopped for one year prior

to the date of the 2004 monitor survey, restarted one year prior to the 2006 monitor, and then stopped one year before the 2008 monitor. Well W2 started injection one year before the 2004 monitor acquisition, and continued beyond 2006, decreasing the injected volume significantly prior to the 2008 monitor. Let us now look at Figure 4.4: simulation results for the period 1998 to 2004 show a pore pressure change of +3.5MPa around W2, but less than +0.5MPa around W1, due to de-pressurisation effects. Both wells have a similar saturation change during this period, this being +0.45 and +0.44 respectively. There is no gas in the area, and it is known that an increase in the observed amplitudes indicates pore pressure up in the reservoir, whilst a decrease in the amplitudes reveals an influx of water. The observed 4D seismic (2004 monitor minus 1998 baseline) shows an amplitude decrease at W1 consistent with saturation effects dominating, and probably due to the small pore pressure change, giving the relation $0.45\,C_S > 0.5\,C_P$. At W2, the observed 2004 seismic indicates a small amplitude increase signal consistent with a pore pressure increase (Figure 4.5). Thus, it looks as if the saturation and pore pressure changes partially cancel around this well, and $0.44\,C_S \approx 3.5\;C_P$. Interestingly, for this well, away from the predicted position of the waterfront, the 4D seismic indicates an amplitude increase, which can be interpreted as a cross-over to a pore pressure-up dominant regime – explained as the saturation changes are now zero.

The seismic monitor at 2006 and the 1998 baseline seismic reveal an increase in the seismic amplitudes around both W1 and W2, and hence a dominance of the pore pressure response, due to a continuation of the injection during the period 2004 to 2006. Consideration of the predicted pore pressure and saturation changes then yields two further relations: $0.45\,C_S < 6.8\,C_P$ and $0.47\,C_S < 7.5\;C_P$ (Figure 4.6 and Figure 4.7). Finally, in the period 2006 to 2008, injection diminished at both wells, and pore pressure change is negative relative to the baseline survey date (injection does not support the producers). Thus, in this case, the seismic amplitudes decrease due to both a net saturation increase and pore pressure decrease, and therefore no information can be obtained for this study.

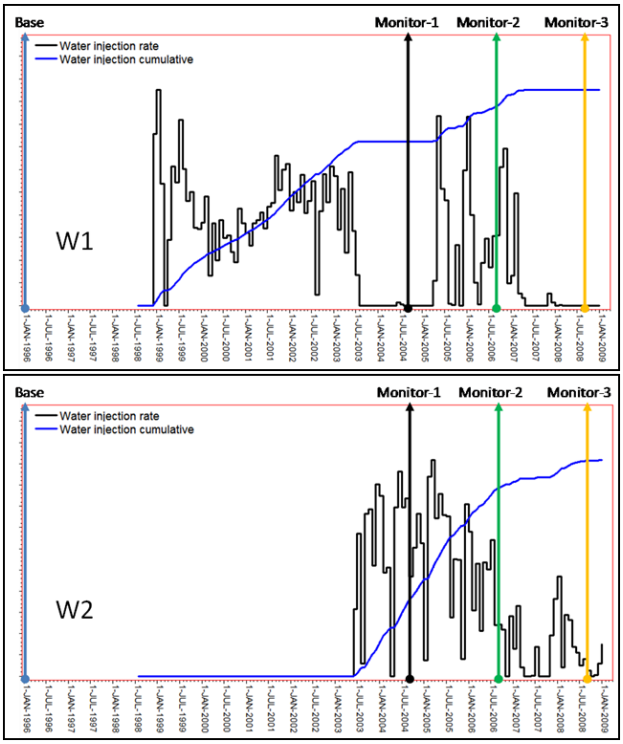

Figure 4.3: Well activity plots for wells W1 and W2, showing the water injection rate in black and the cumulative water volumes in blue.

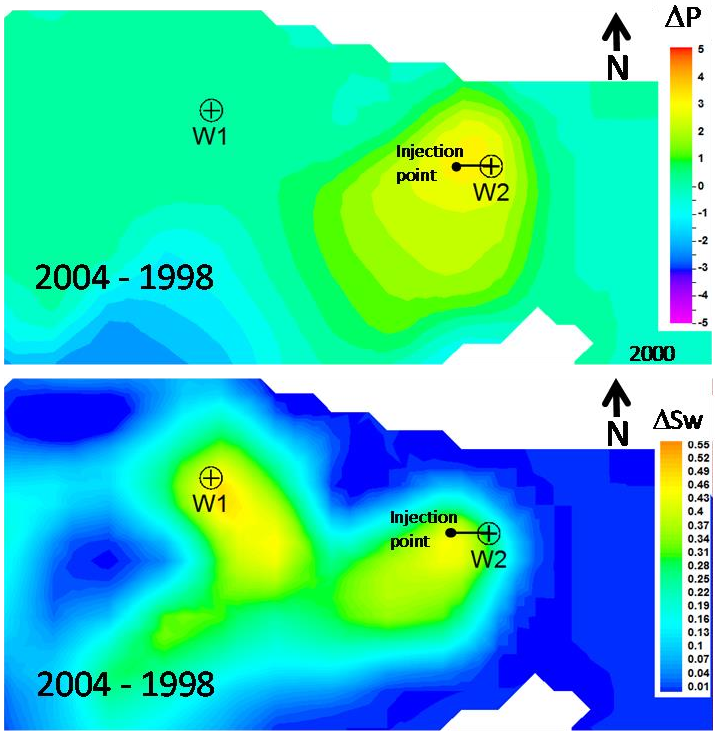

Figure 4.4: Pore pressure (top) and water saturation changes (bottom) predicted from the simulation model for selected region 1.

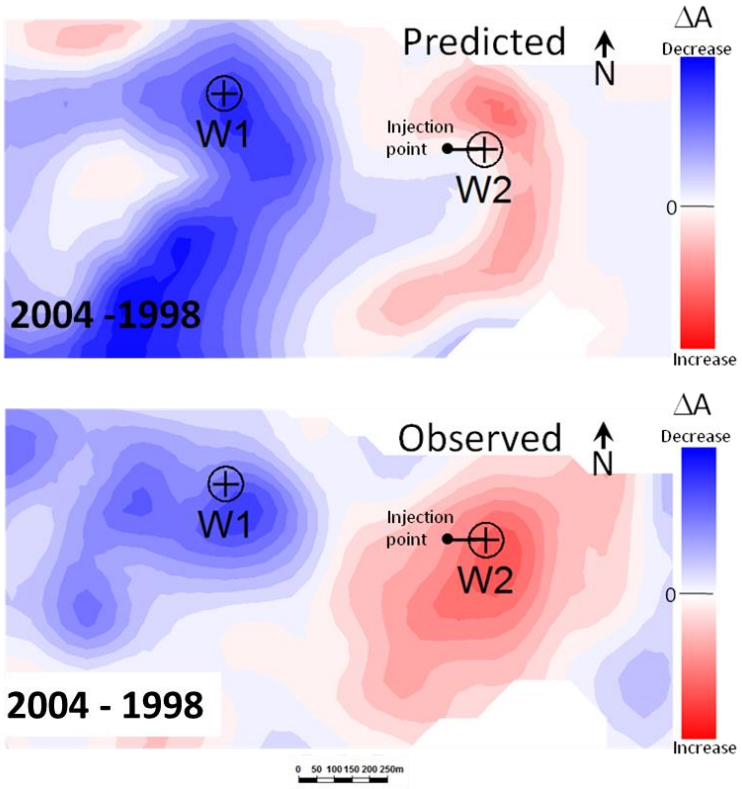

Figure 4.5: Region 1, 2004 monitor. Top: predicted time lapse amplitude change for the near angle approximation. Bottom: observed 4D seismic response from the full stack.

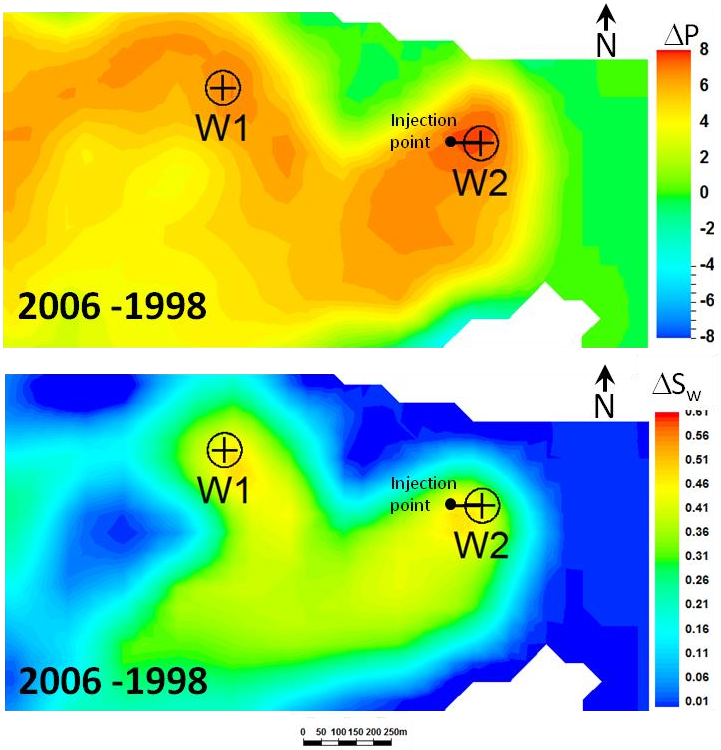

Figure 4.6: Pore pressure (top) and water saturation changes (bottom) predicted from the simulation model for selected region 1.

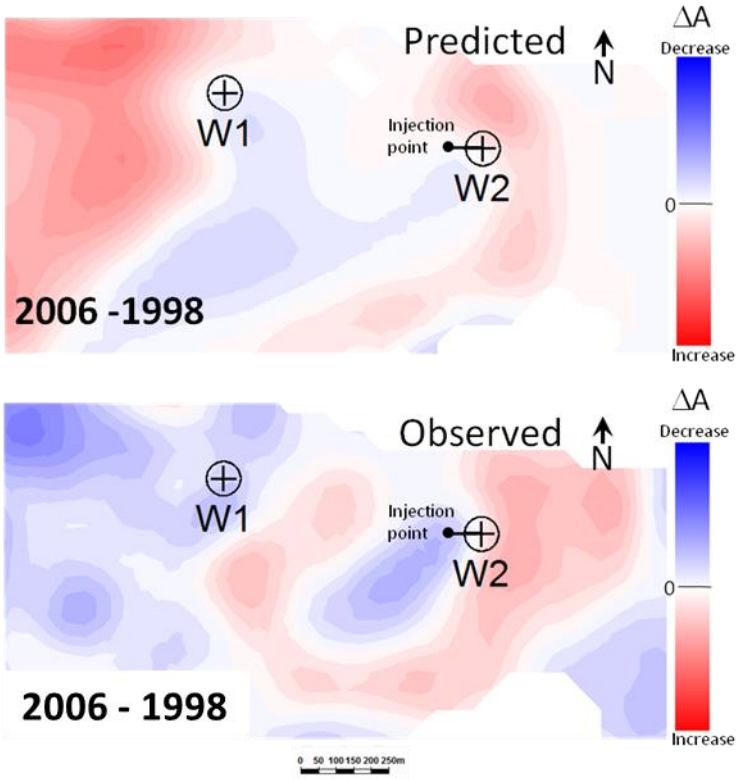

Figure 4.7: Region 1, 2006 monitor. Top: predicted time lapse amplitude change for the near angle approximation; Bottom: observed 4D seismic response from the full stack.

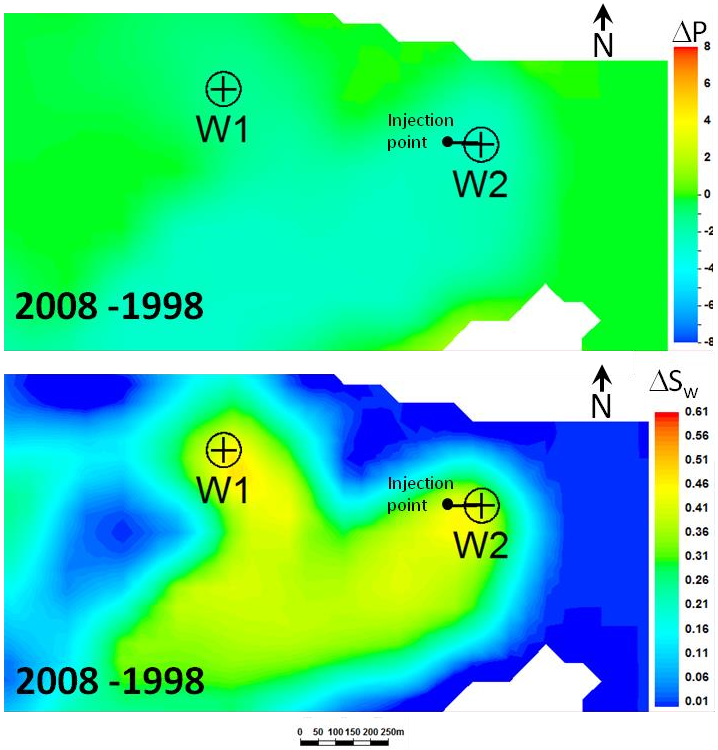

Figure 4.8: Pore pressure (top) and water saturation changes (bottom) predicted from the simulation model for selected region 1.

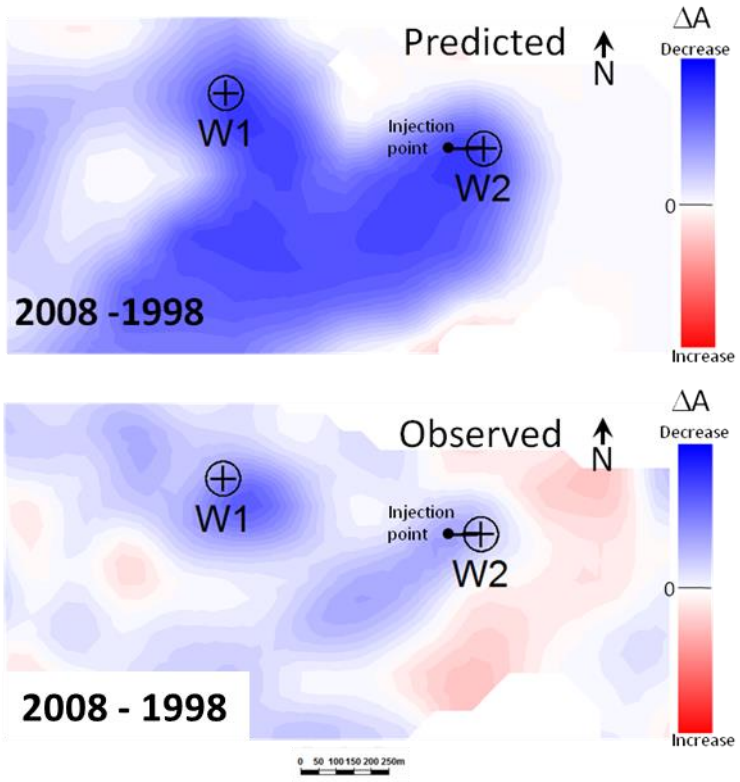

Figure 4.9: Region 1, 2008 monitor. Top: predicted time lapse amplitude change for the near angle approximation; Bottom: observed 4D seismic response from the full stack.

In the second example area, a single injector, W3, starts up a year before the date of the 2004 monitor acquisition, stops injecting one year prior to the 2006 survey and remains inactive through to the date of the 2008 survey (Figure 4.10). The predictions from the simulation for the period 1998 to 2004 reveal pore pressure changes at the well location of +2.1MPa and a saturation change of +0.38 (Figure 4.11). A decrease in 4D amplitude around W3 is associated with the waterfront, and saturation clearly dominates over pore pressure (Figure 4.12). Thus, it is concluded that $0.38\,C_S \geq 2.1\,C_P$, which establishes yet another inequality for C_S and C_P.

For the 1998 to 2006 period, the pore pressure difference is only +0.67MPa due to the reduction in injection, and there is a saturation change of 0.23, less than in the previous monitor, due to relaxation of the pore pressure at the injector (Figure 4.13). In the 4D seismic response, saturation still dominates, as the pressure change is small (Figure

4.14). This leads to the inequality 0.23 $C_S \geq 0.67\ C_P$. For the final monitor, the net pore pressure drop during this period is negative and therefore no data point can be obtained (Figure 4.15 and Figure 4.16).

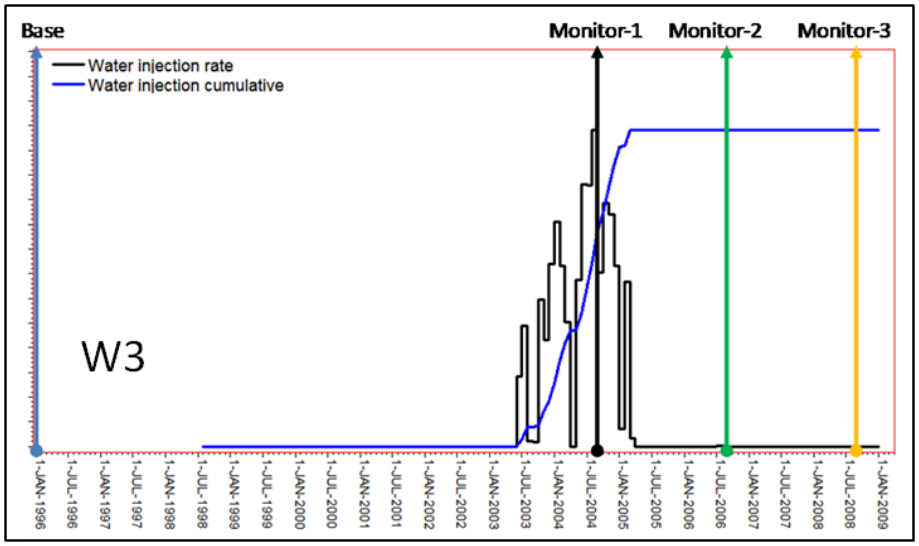

Figure 4.10: Well activity plots for well W3 in the selected region 2, showing the water injection rate in black and the cumulative water volumes in blue.

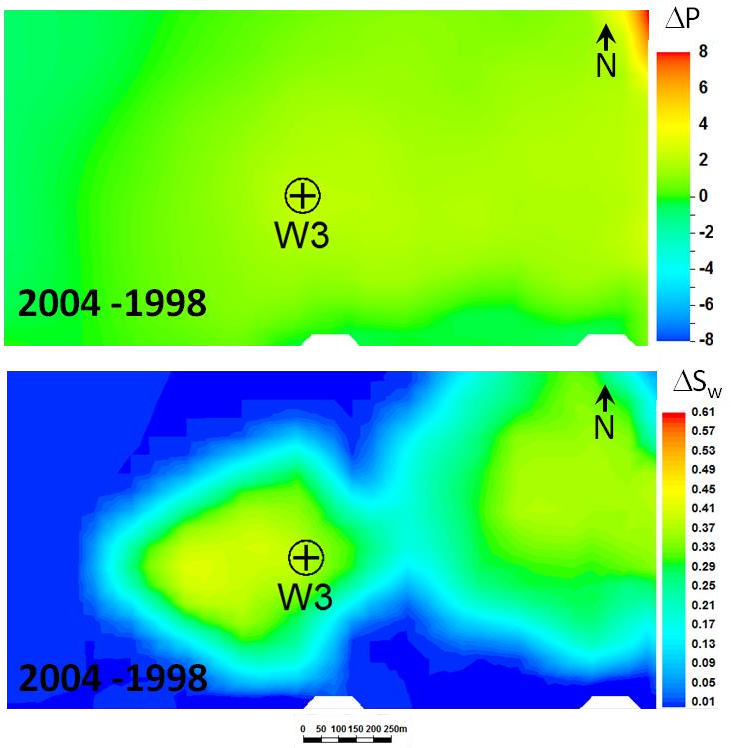

Figure 4.11: Pore pressure (top) and water saturation changes (bottom) predicted from the simulation model for selected region 2.

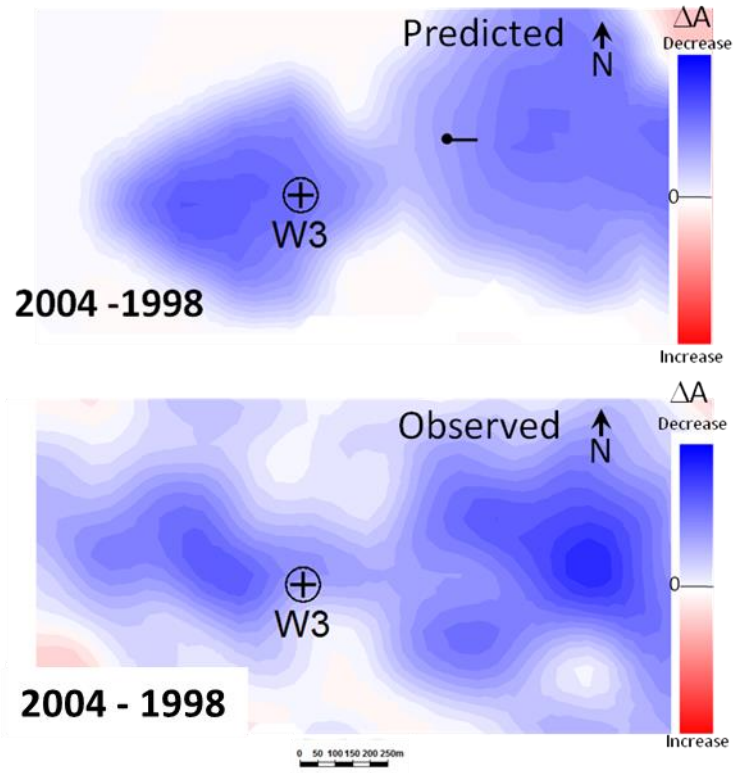

Figure 4.12: Region 2, 2004 monitor. Top: predicted time lapse amplitude change for the near angle approximation. Bottom: observed 4D seismic response from the full stack.

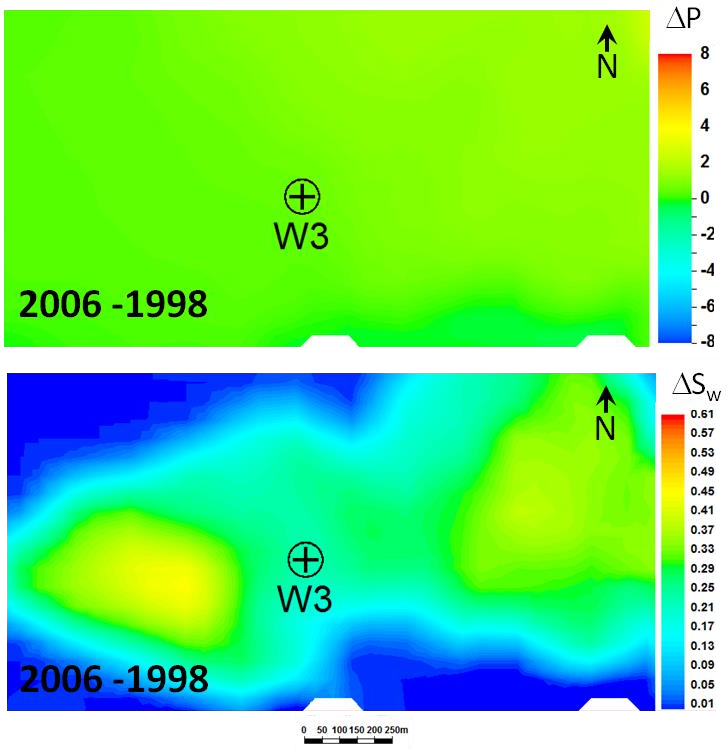

Figure 4.13: Pore pressure (top) and water saturation changes (bottom) predicted from the simulation model for selected region 2.

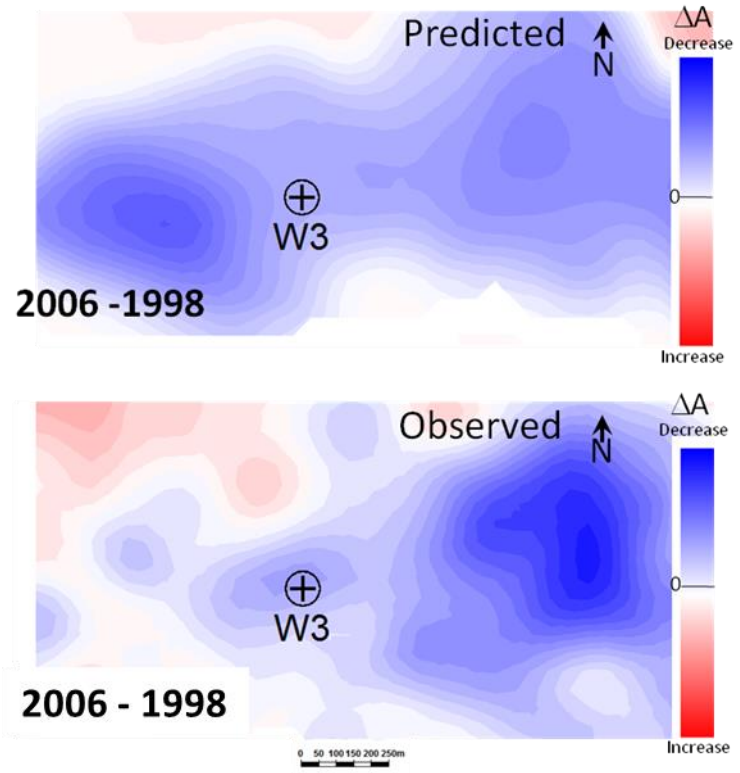

Figure 4.14: Region 2, 2006 monitor. Top: predicted time lapse amplitude change for the near angle approximation. Bottom: observed 4D seismic response from the full stack.

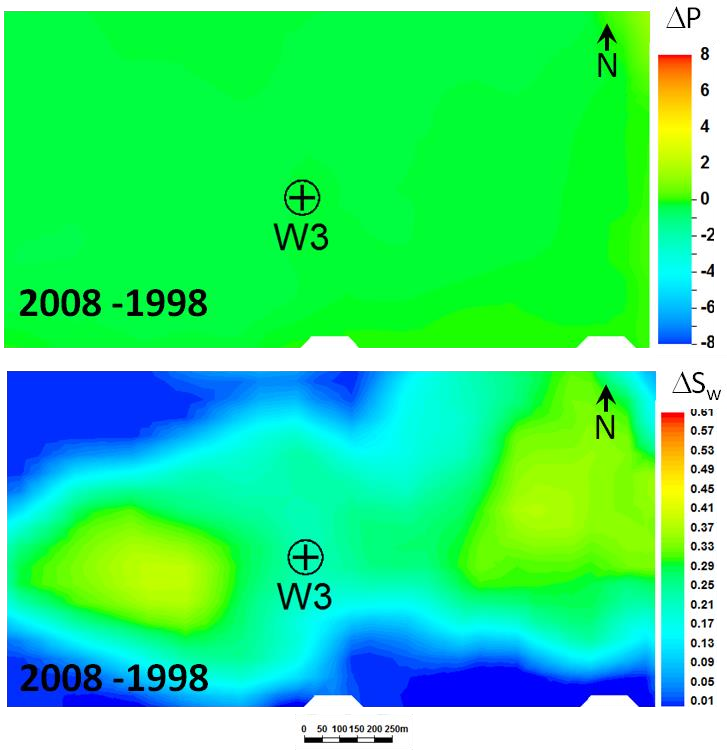

Figure 4.15: Pore pressure (top) and water saturation changes (bottom) predicted from the simulation model for selected region 2.

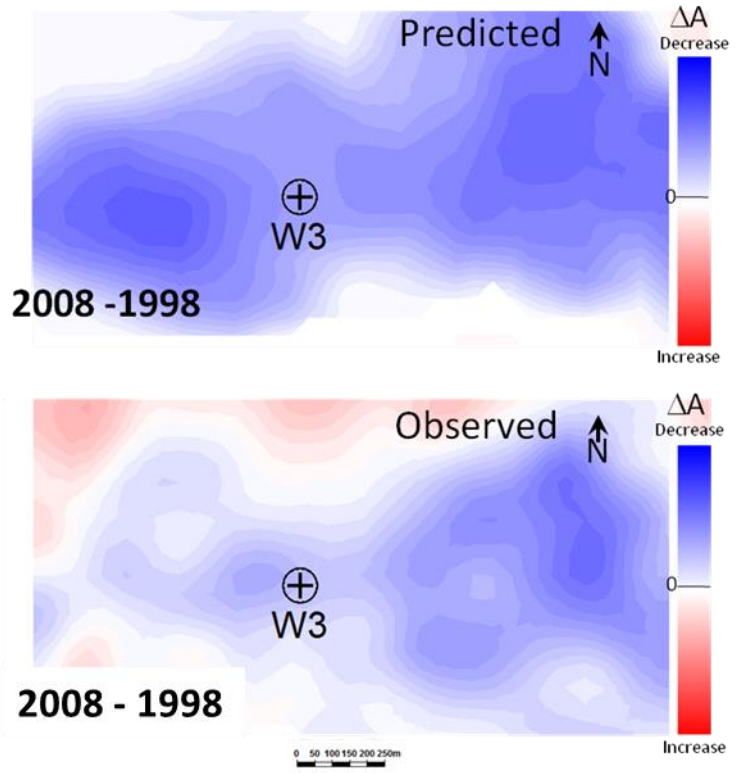

Figure 4.16: Region 2, 2008 monitor. Top: predicted time lapse amplitude change for the near angle approximation. Bottom: observed 4D seismic response from the full stack.

Finally, in the third example there are two injectors W4 and W5; Figure 4.17 shows the corresponding well activity plots. W4 started injection in 2002, initially at a high rate but reduced this rate towards the date of the 2004 monitor survey and through the subsequent monitor survey dates. W5 started injection four years prior to the 2004 monitor survey date, but stopped one year before the seismic was shot. For the 1998 to 2004 period, the simulation results show a very large pore pressure change of +12MPa around W4, due to strong compartmentalisation, but a smaller pore pressure change of +3.5MPa around W5 (Figure 4.18). Saturation changes are 0.46 and 0.45 respectively.

The observed seismic around the well shows an amplitude increase around W4 associated with the pore pressure increase; however, exactly at the location of the well there is a small, clearly visible, localised area of amplitude decrease (Figure 4.19). These observations suggest that $12\,C_P > 0.46\,C_S$ around W4, where the pore pressure-up

signal dominates. At W5 the seismic displays a strong amplitude decrease associated with the waterfront, and hence 0.45 C_S > 3.5 C_P .

For the period 1998 to 2006, at both injectors a pore pressure increase is still present, but saturation change is reduced slightly due to injector relaxation effects (Figure 4.20). The effect of water saturation change dominates at W4, leading to 0.44 C_S > 3.51 C_P ; similarly, saturation dominates at W5, which gives the inequality 0.34 C_S > 1.25 C_P (Figure 4.21).

At 2008, the pore pressures at both injectors have reduced slightly further (Figure 4.22) but the same observations hold (Figure 4.23), leading to 0.45 C_S > 2.5 C_P for W4 and 0.34 C_S > 0.75 C_P for W5.

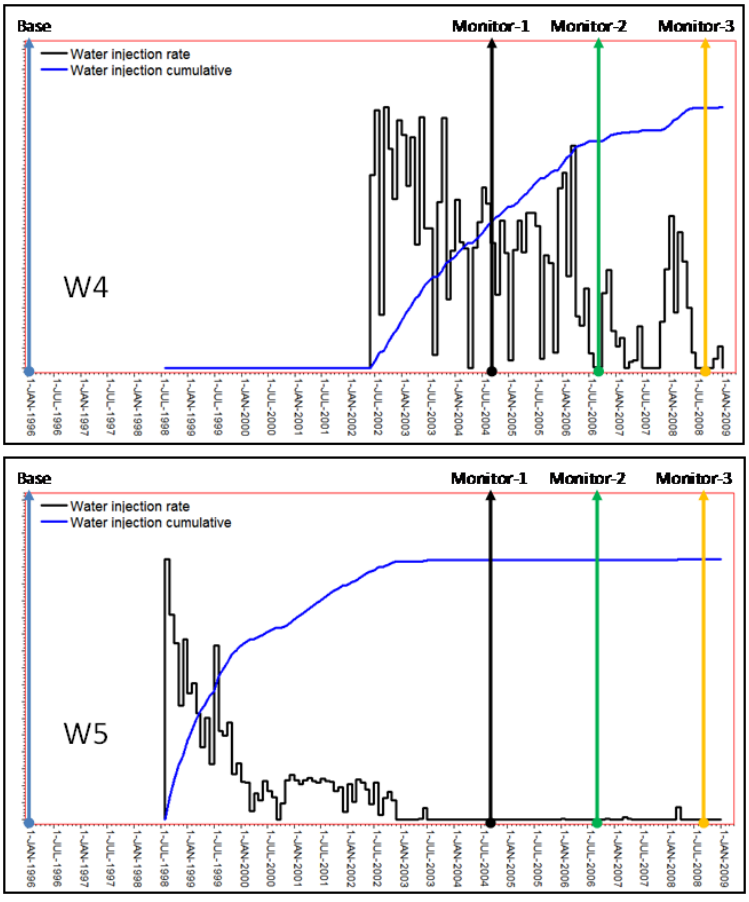

Figure 4.17: Well activity plots for wells W4 and W5 in the selected region 3, showing the water injection rate in black and the cumulative water volumes in blue.

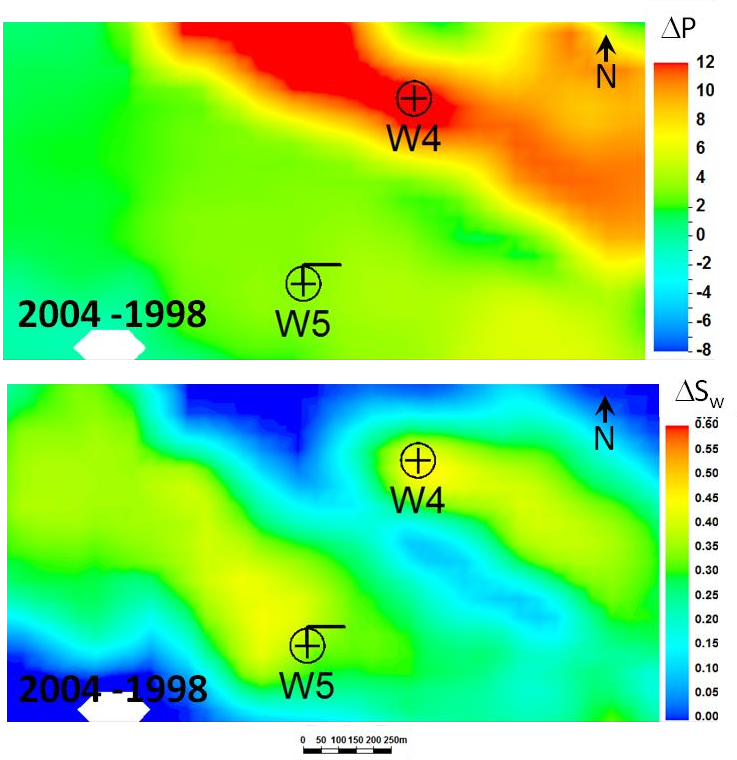

Figure 4.18: Pore pressure (top) and water saturation changes (bottom) predicted from the simulation model for selected region 3.

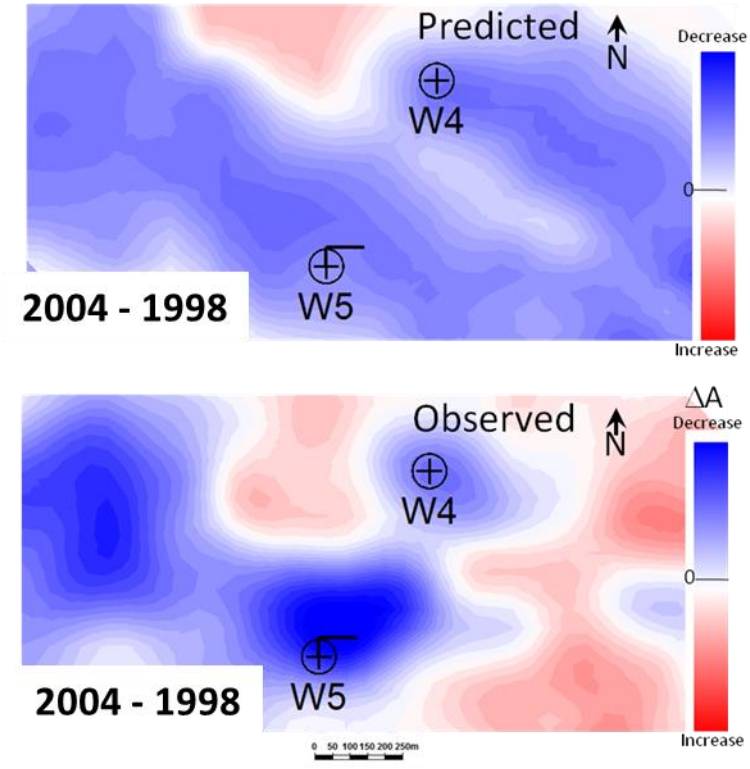

Figure 4.19: Region 3, 2004 monitor. Top: predicted time lapse amplitude change for the near angle approximation. Bottom: observed 4D seismic response from the full stack.

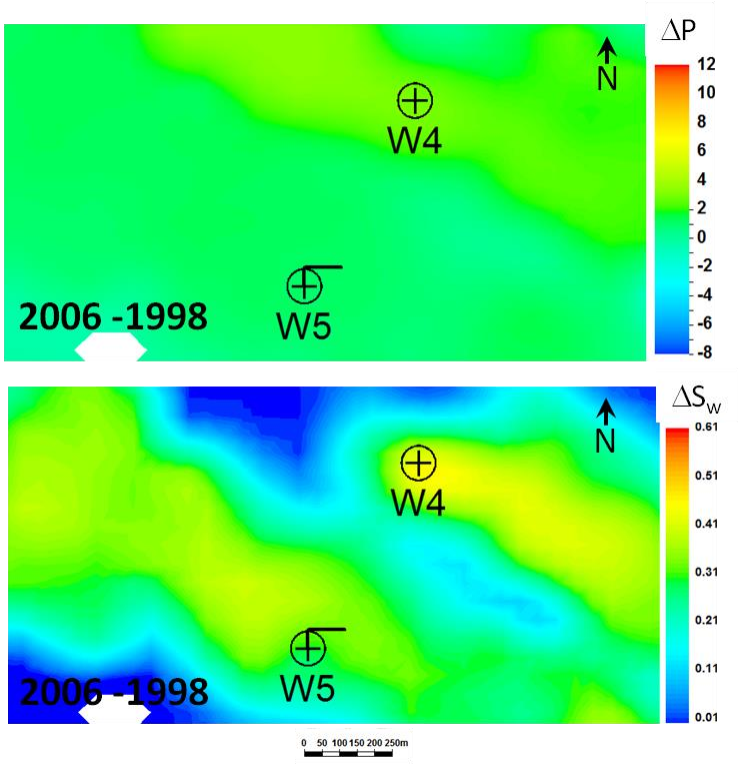

Figure 4.20: Pore pressure (top) and water saturation changes (bottom) predicted from the simulation model for selected region 3.

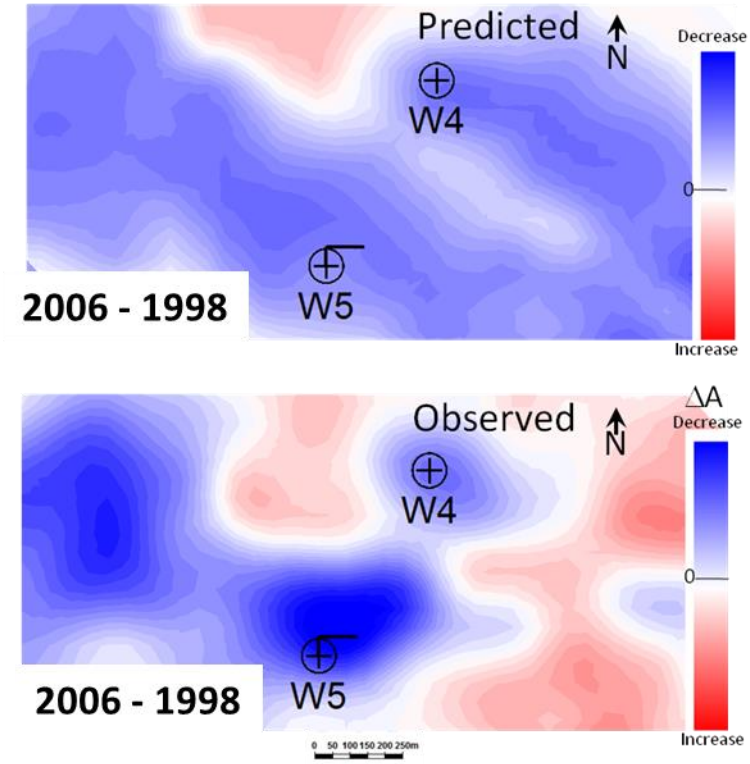

Figure 4.21: Region 3, 2006 monitor. Top: predicted time lapse amplitude change for the near angle approximation. Bottom: observed 4D seismic response from the full stack.

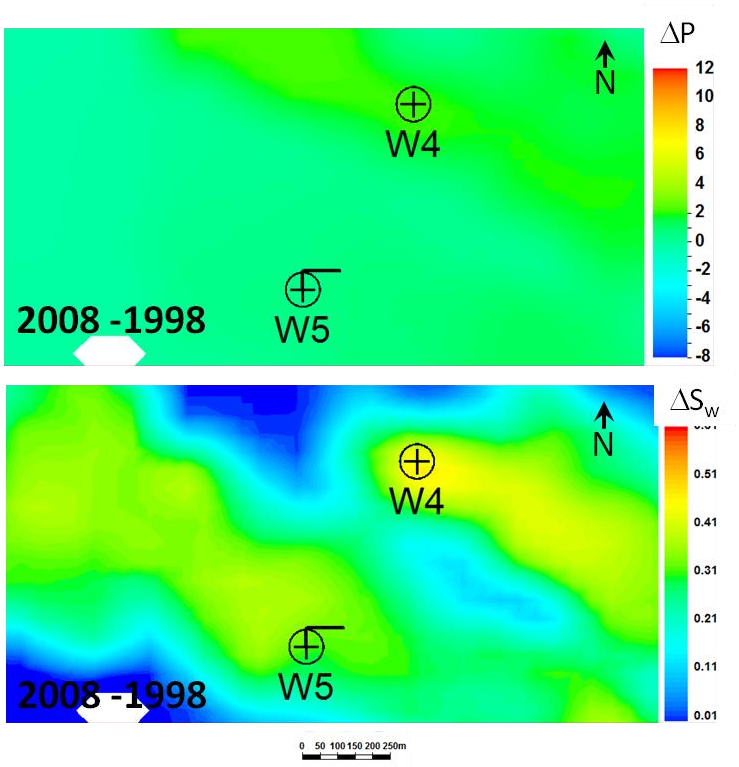

Figure 4.22: Pore pressure (top) and water saturation changes (bottom) predicted from the simulation model for selected region 3.

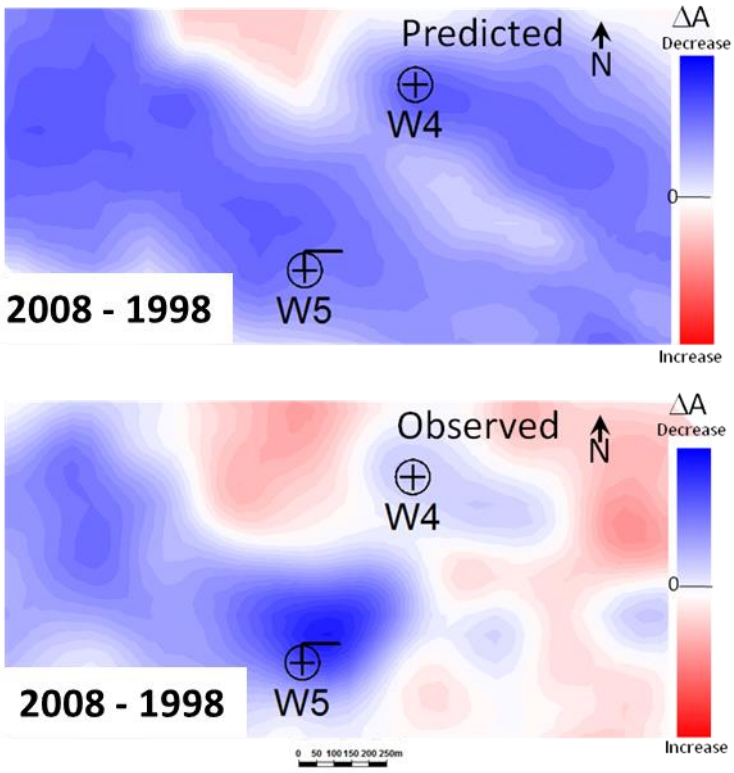

Figure 4.23: Region 3, 2008 monitor. Top: predicted time lapse amplitude change for the near angle approximation. Bottom: observed 4D seismic response from the full stack.

4.5 Data Gathering – Literature examples

A survey of 4D seismic case studies published in the open literature over the past twenty years appears to indicate that most researchers conclude that a pore pressure change signal is more difficult to detect than a saturation change signal. Also, it is often automatically assumed in many studies that saturation effects are more readily visible than pore pressure - as is the case in 3D seismic. Indeed, if field pore pressure fluctuations can be controlled, they seldom fluctuate by more than 0.5 MPa in the reservoir, and the current work supports the notion that saturation dominates most of the time. Indeed, there are many examples of detecting fluid contact movement (Kloosterman et al., 2001, McInally et al., 2001) or saturation changes due to waterflooding (Lumley et al., 1999, Johann et al., 2009).

In many instances a signal is observed despite fairly high non-repeatability levels for the 4D seismic (with an *NRMS* metric of 0.40 or above). By contrast, examples of pore pressure change are less obvious, unless there is an overpressured area or the seismic signal is assisted by compaction (for instance, the compacting chalk example of Barkved et al., 2003), or pore pressure drops below bubble point and gas is exsolved (Parr et al., 2000). The best examples are provided by pore pressure increases induced by water injection into hydraulically isolated compartments or channels (Alsos et al., 2009). The effects of pore pressure decrease due to primary depletion are less pronounced (MacBeth et al., 2006b, Staples et al., 2006).

There are, however, some clear examples of pore pressure down due to relaxation from injector shutdown (Strønen and Diagranes, 2004). The present work supports these broad statements as a natural consequence of the physics of the petroelastic model. It is somewhat surprising, however, to find that values of ΔP, ΔS_W and porosity are not readily published in many case studies in the open literature. Whilst changes of (maximum) saturation can be readily inferred from S_{wc} and S_{or} estimates, pore pressure change is less easy to assign in practice.

However, there are several examples where such measurements have been published. The first example comes from the Marlim field (Johann et al., 2009), in which injection into a compartment yields a +2.94 MPa pore pressure change, and 0.3 saturation change behind the waterfront. This provides the inequality $C_S/C_P < 9.8$, for these 24% porosity rocks.

Floricich (2006) has shown that for the Cormorant field, injection into a compartment raises the pore pressure by 6 MPa and the saturation by 0.6. This provides the inequality $C_S/C_P < 10$, for the 25% (mean) porosity rocks. Finally, the Gullfaks example of Landrø (2001) gives an identical pore pressure rise, saturation change of 0.5, and yields the inequality $C_S/C_P < 12$ for 30% porosity rocks.

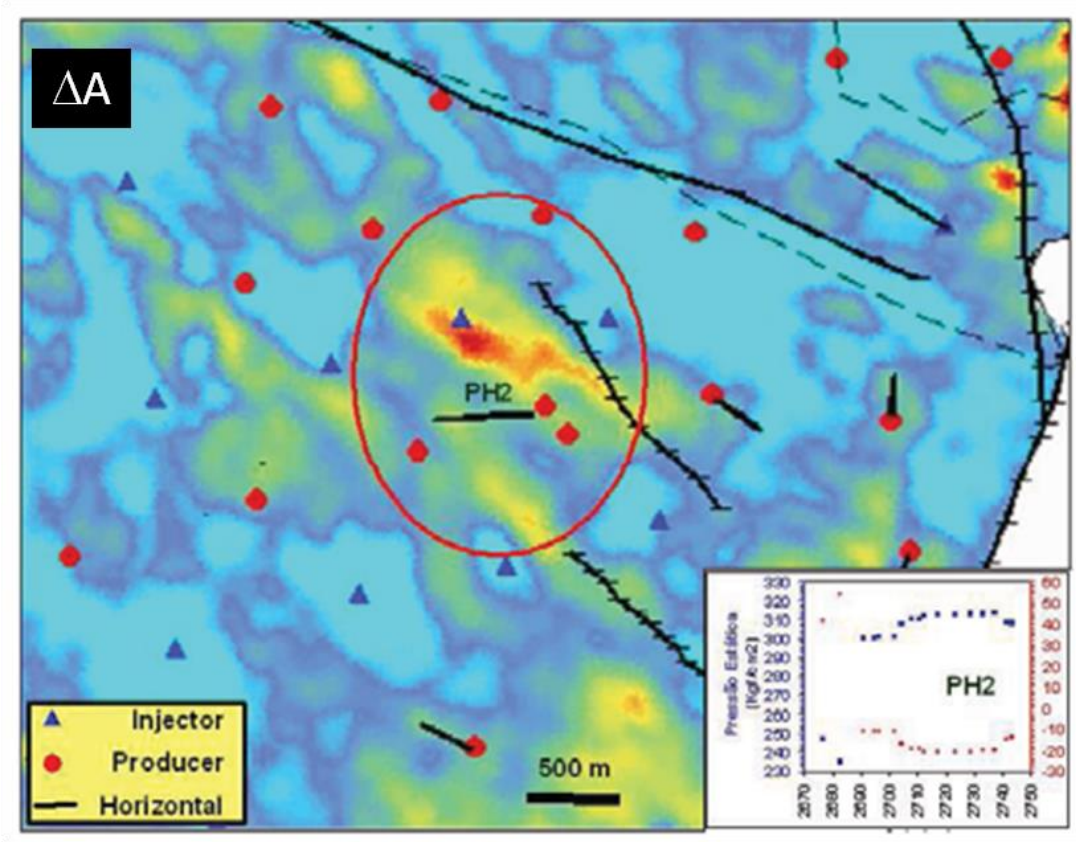

Figure 4.24: Literature example 1: 4D amplitude difference map from the Marlim field showing a pressure dominant signal around a water injector; modified from Johann et al., 2009.

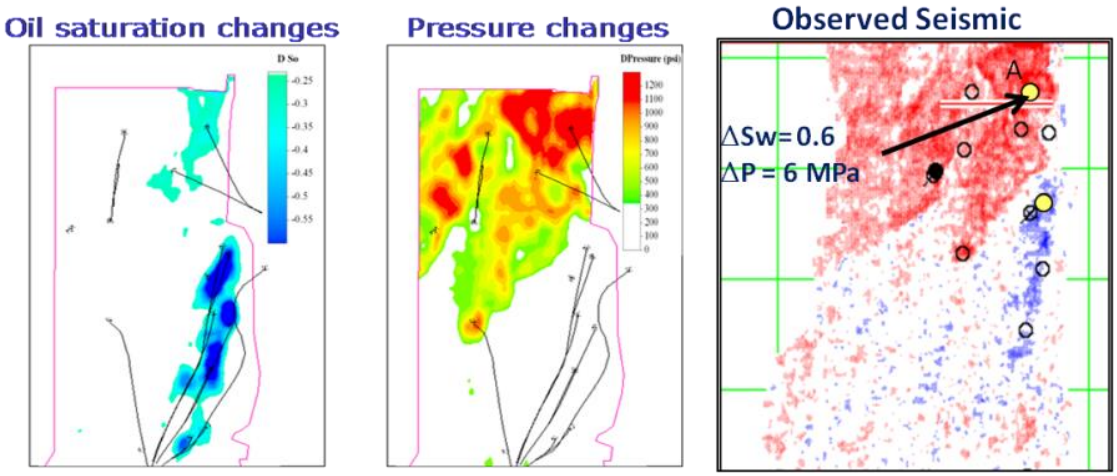

Figure 4.25: Literature example 2: 4D difference map (left) showing a pressure build-up around a water injector in the Cormorant field; modified from Floricich et al., 2006.

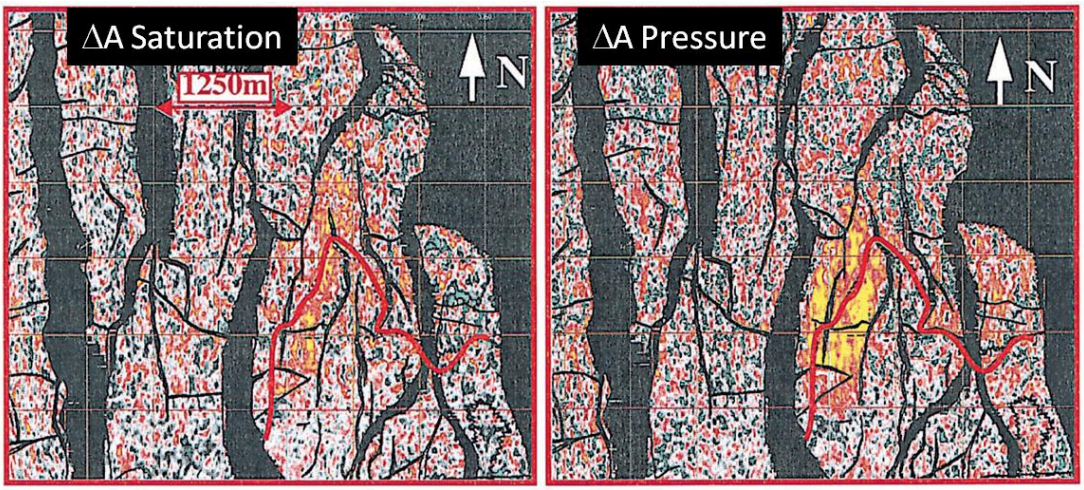

Figure 4.26: Literature example 3: 4D difference map showing the saturation (right) and pressure (right) changes in the Gullfaks field, showing pressure dominance around an injector; modified from Landrø, 2001.

4.6 Data gathering – West Africa, 4D AVO

In all of the previous examples, either full stack or near-offset data are chosen. This is appropriate for comparison in this work as the full stack amplitudes are mainly dominated by the near angle information (although they still might be affected by the far angles, it is difficult to quantify this effect). However the relative weighting of pore pressure and saturation changes on angle-dependent seismic data also carries

important information. This dependence has been discussed to some degree in the literature (for example, by Trani et al., 2011). A direct conclusion can be deduced from the data example of Landrø (2001) for Gullfaks, suggesting that the fars are dominated by saturation whilst the nears show saturation and pore pressure changes. Whilst this is a compelling result, care must be taken in generalising such a statement, as the relative magnitude of the pore pressure and saturation change signals in the 4D seismic is known to depend on the porosity. What can be concluded, however, is that C_S/C_P is expected to vary with offset. In particular, this specific study anticipates an increase in C_S/C_P with offset and the far angles being dominated by saturation, in agreement with the literature. This can be explained by equation (2.43) and by the numerical exercises in the previous chapter.

To study this effect, a dataset from a deepwater turbidite field in West Africa is analysed for which restricted offset data are accessible. Here 2001 pre-production baseline data are available, together with a 2004 monitor survey. Near angle (3 to 23°) and far angle (23 to 37°) data are available for each of the two surveys. There is an AVO effect observed in the area of study, with the amplitude on the nears being larger than that on the fars. Production start-up was in 2001, and water injection began several months after first oil. The oil is 32° API, and contrasts well with the injected water for 4D studies. There is a mean porosity of 28%, consistent with our previous example.

A simulation model is also available: the well activity on two injectors (WA1 and WA2) shows that they were injecting for a continuous period two years before the monitor survey was acquired (Figure 4.27). Two regions around the wells were selected to perform similar observations as in the previous examples. The pore pressure and water saturation differences are shown in Figure 4.28. On the seismic side, the near amplitude differences are seen to decrease at the well location, and this is interpreted as a dominance of saturation over pore pressure, leading to the inequality $0.63\,C_S > 4.74\,C_P$. However, the far amplitude differences at the injector locations are observed to show a larger magnitude difference than the near differences (Figure 4.29). Similar observations can be made on the second region selected around injector W2, (Figure

4.30 and Figure 4.31), from which the inequality $0.6\,C_S > 1.69\,C_P$ is obtained. Our theoretical predictions in both cases are consistent with the observations and can be explained by C_S/C_P increasing from around 8 on the near, to 25 on the far-amplitude differences, which means that the far angles are dominated more by the saturation effects than pressure, which is consistent with our numerical analysis in the previous chapter.

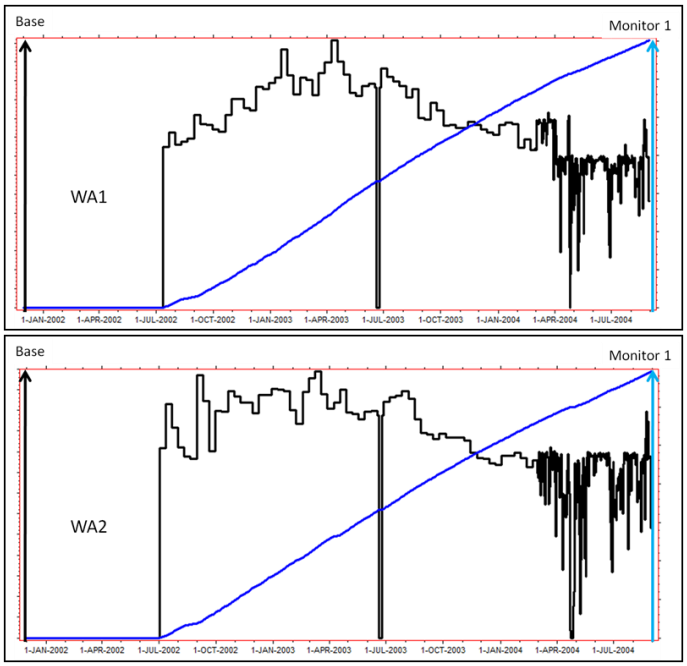

Figure 4.27: Well activity plots for wells WA1 and WA2, showing the water injection rate in black and the cumulative water volumes in blue.

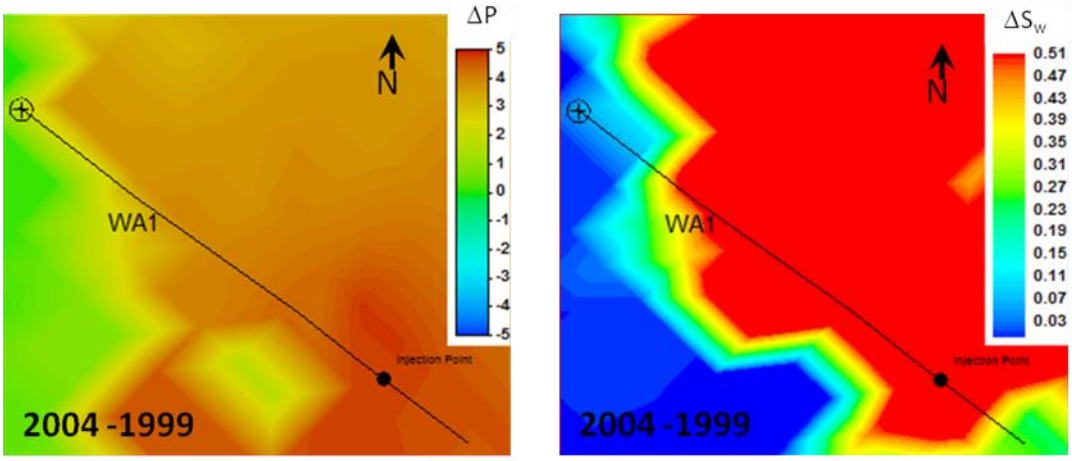

Figure 4.28: Pore pressure (left) and water saturation changes (right) predicted from the simulation model for selected region 1.

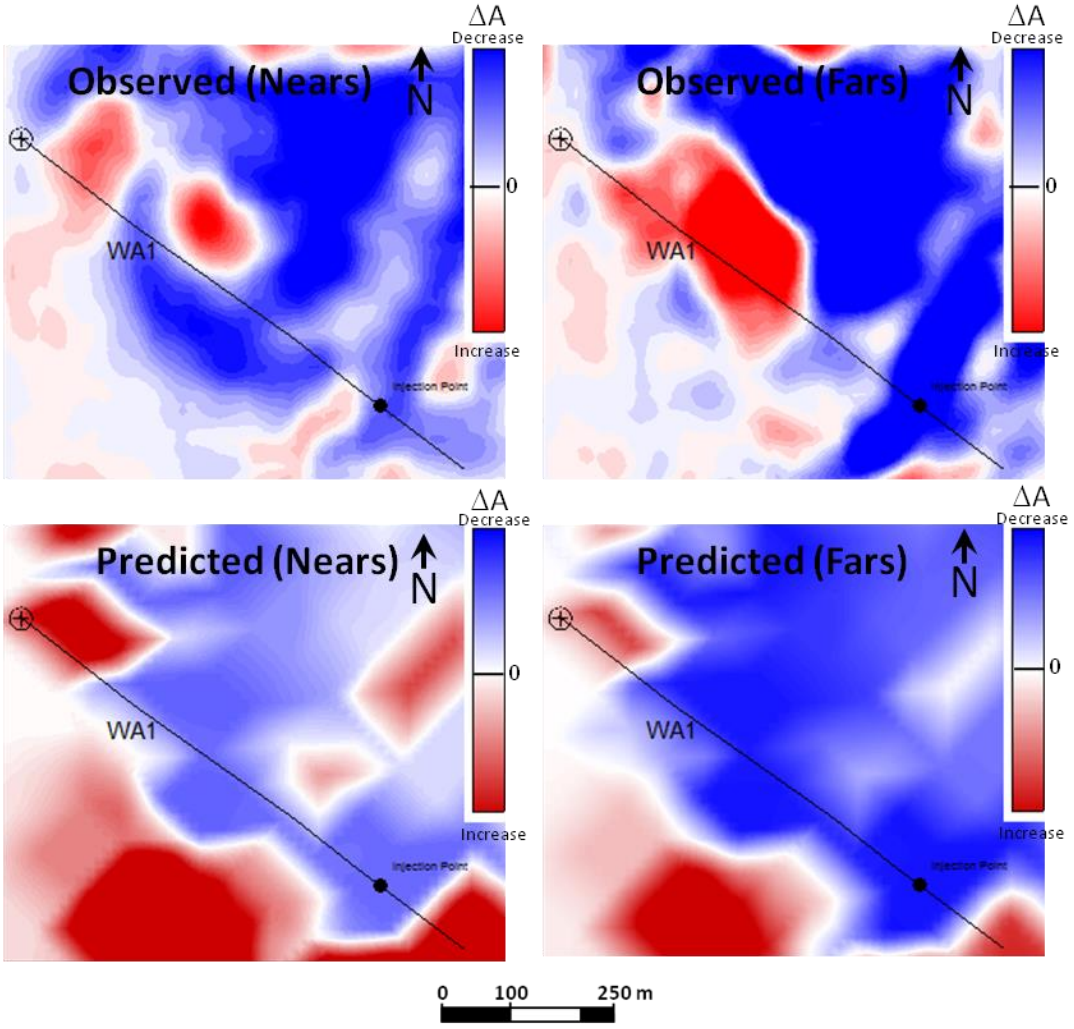

Figure 4.29: Region 1: Top: observed 4D seismic response for the near and far angles. Bottom: predictions of the 4D seismic response based on equation (2.43).

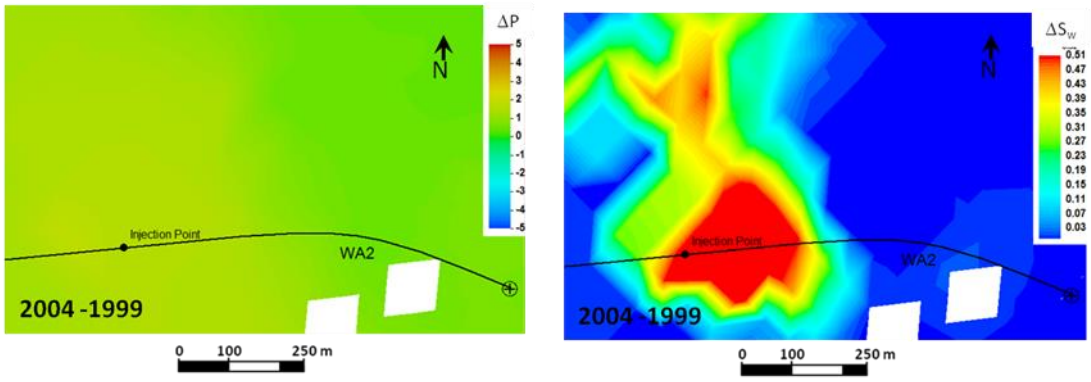

Figure 4.30: Pore pressure (top) and water saturation changes (bottom) predicted from the simulation model for selected region 2.

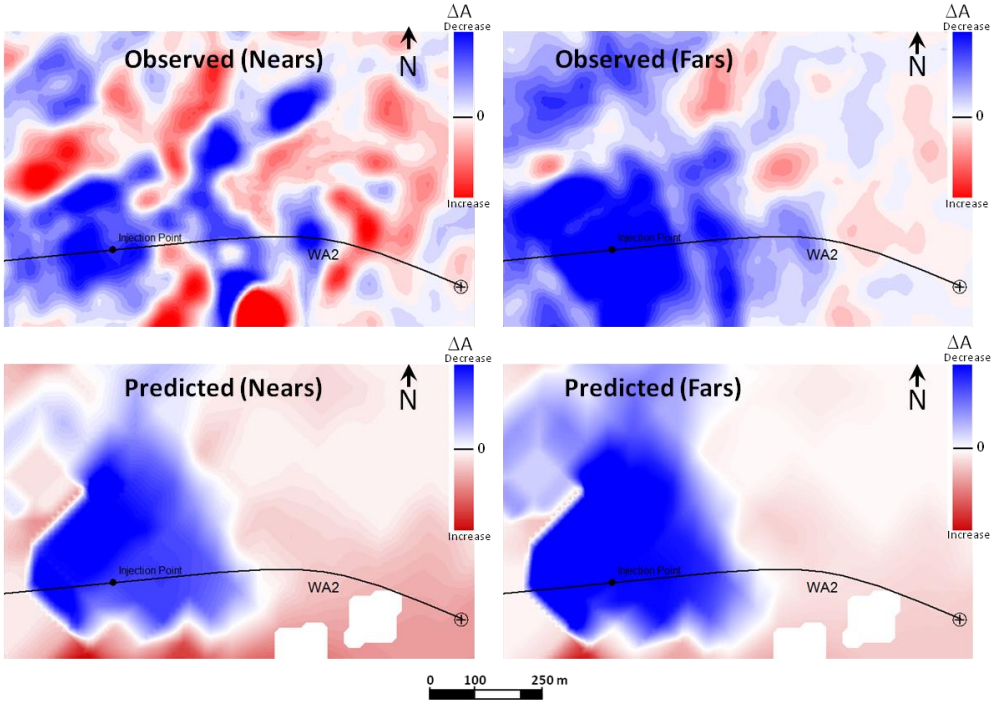

Figure 4.31: Region 2: Top: observed 4D seismic response for the near and far angles. Bottom: predictions of the 4D seismic response based on equation (2.43).

4.7 Summarising the observations

All the observations from the North Sea example are summarised in Table 4.1, and they can also be observed graphically in Figure 4.32, which plots 10 ΔS_w against ΔP to ensure the points or inequalities fall in a central location on the plot. Seismic amplitudes are assigned according to whether they are saturation or pore pressure dominated. The boundary that divides the two regimes of pore pressure and saturation dominance in this figure is a straight line with a slope C_S/C_P, and depends on the reservoir's petroelastic model parameters and mainly on porosity. It is found that the observation points for our North Sea clastic example can be divided by a line with slope $C_S/C_P \approx 8$. Calculating the value of this ratio using the known petroelastic parameters, and variable porosities for this reservoir at the individual well locations, it is observed to lie between 5 and 10, bracketing the approximate empirical trend obtained from the cross-plot.

Table 4.1: Summary of observations for the North Sea example, showing all the inequalities gathered in our exercise.

North Sea Example				
Well	**Monitor - Base**	**Point in cross-plot**	**Inequality**	**Dominance**
W1	2004 - 1998	NS1	$0.5\ C_P < 0.45\ C_S$	Saturation
W2		NS2	$3.5\ C_P \approx 0.44\ C_S$	Cancellation
W1	2006 - 1998	NS3	$6.8\ C_P > 0.45\ C_S$	Pressure
W2		NS4	$7.5\ C_P > 0.47\ C_S$	Pressure
W3	2004 - 1998	NS5	$2.1\ C_P \leq 0.38\ C_S$	Saturation
W3	2006 - 1998	NS6	$0.67\ C_P \leq 0.23\ C_S$	Saturation
W4	2004 - 1998	NS7	$12\ C_P > 0.46\ C_S$	Pressure
W5		NS8	$3.5\ C_P < 0.45\ C_S$	Saturation
W4	2006 - 1998	NS9	$3.51\ C_P < 0.44\ C_S$	Saturation
W5		NS10	$1.25\ C_P < 0.34\ C_S$	Saturation
W4	2008 - 1998	NS11	$2.5\ C_P < 0.45\ C_S$	Saturation
W5		NS12	$0.75\ C_P < 0.34\ C_S$	Saturation

Table 4.2: Summary of observations from the literature examples analysed.

Literature Examples			
Field	**Point in cross-plot**	**Inequality**	**Dominance**
Gullfaks	L1	$C_S/\ C_P < 12$	Pressure
Cormorant	L2	$C_S/\ C_P < 10$	Pressure
Marlim	L3	$C_S/\ C_P < 9.8$	Pressure

Table 4.3: Summary of observations from the West Africa examples analysed.

West Africa Examples		
Point in Cross-plot	**Inequality**	**Dominance**
WA1	$0.5\ C_P < 0.45\ C_S$	Saturation
WA2	$3.5\ C_P \approx 0.44\ C_S$	Saturation
WA3	$6.8\ C_P > 0.45\ C_S$	Saturation

Porosities in the West Africa and literature examples are fairly close to those in our North Sea examples, and thus, the points from these studies (Table 4.2 and Table 4.3) are added in Figure 4.32. These appear to support the argument of the $C_S/C_P \approx 8$ trend being consistent with most of these clastic reservoirs – probably as their porosities are

similar. Note that if the porosity increases significantly, it is anticipated that C_S/C_P would increase to a value higher than 8; however no examples of this have, as yet, been identified.

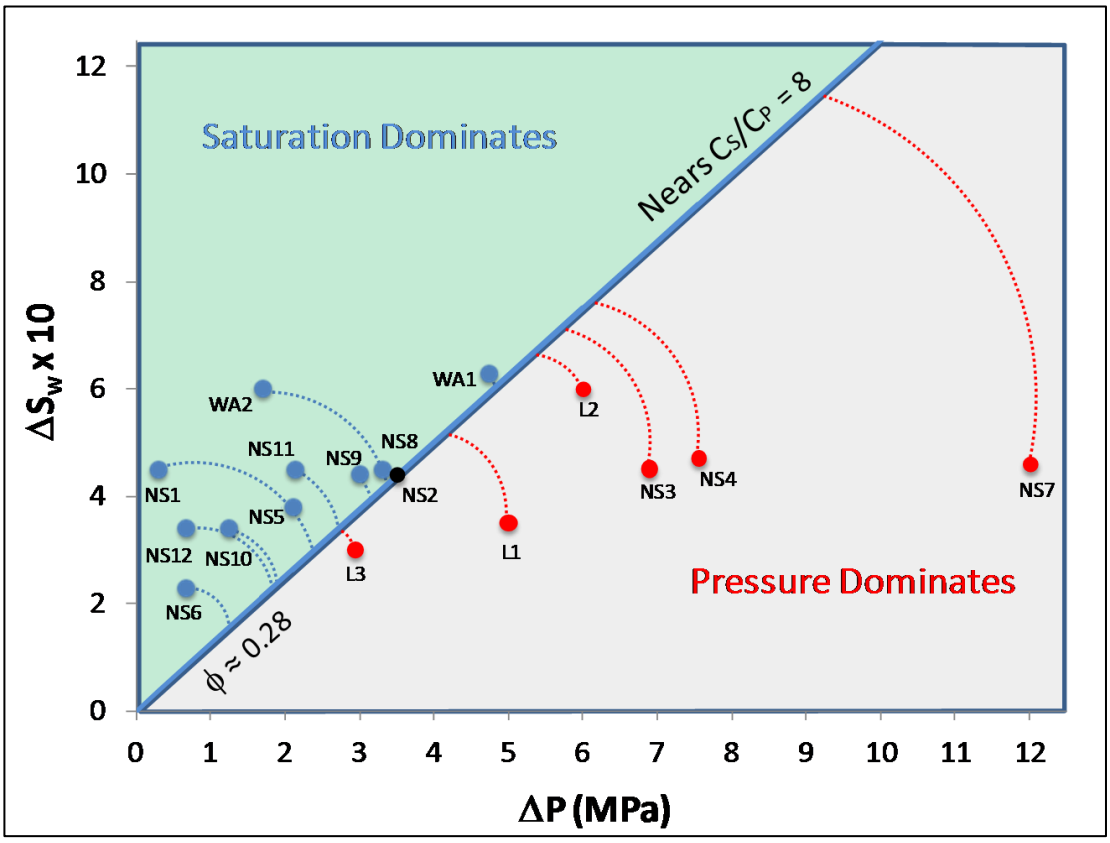

Figure 4.32: Plot of saturation change against pore pressure change, colour coded according to whether the 4D signatures are dominated by saturation (blue) or pore pressure (red). The circular arcs represent inequalities defined from our real data observations.

4.8 Using the observations to constrain the rock stress sensitivity

The results of this study suggest that C_S/C_P is a fundamental parameter that can be unambiguously extracted from the mapped 4D seismic amplitudes by observing whether saturation or pore pressure dominates the response at a select number of injector wells. Producers are generally less informative, as pore pressure and saturation effects usually act in the same direction in the seismic response for both near and far offsets. Further, according to the data collected from five different clastic reservoirs

(three from the literature and two worked examples), all with similar porosities of between 25 and 30%, it appears that $C_S/C_P \approx 8$ seems to indicate the point at which pore pressure starts to dominate over saturation, and vice-versa. Clearly, these results are for an ideal shale/sand interface, and must be adapted in future work to include variable net-to-gross variations and reservoir thickness – the latter is a parameter observed by Falahat et al. (2011) to be important in controlling the time-lapse behaviour of thin reservoirs.

Equation (4.2) shows that there is an inter-dependence between the porosity and the separate groups of parameters observed. Interestingly, for fluid pressure dependencies much smaller than the rock stress sensitivity (which in fact may be normality according to the numerical modelling), then this equation becomes

$$\frac{C_S}{C_P} \approx \frac{\phi\, FC}{(1-\varepsilon')\phi\ \mathrm{RSS}} \approx 8 \quad , \tag{4.3}$$

where the equation is now observed to link the fluid contrast between the original and displaced fluids, and the rock stress sensitivity. This equation provides a way of independently confirming the stress sensitivity. This is possible as the fluid contrast terms are relatively well-known functions of the bulk modulus and density of the oil and brine, and the initial water saturation. Thus, for a mean porosity of 28%, and oil-water displacement for the reservoirs in this North Sea example, we obtain

$$0.25\, N_3^o + 0.33\, N_4^o \approx 0.015 \quad , \tag{4.4}$$

where N_3^o and N_4^o are defined as variables dependent on the stress sensitivity functions for κ and μ, as defined in the previous chapter.

This imposes a constraint on the permissible stress sensitivity curves: an example of such a family is shown in Figure 4.33, where two plots of stress sensitivity curves for (top) bulk modulus variation, and (bottom) shear modulus variation with effective

stress/pore pressure are shown. These curves are parameterised using the relationship suggested by MacBeth (2004), and correspond to the data provided for a range of different reservoir rocks. The blue curves correspond to a selection of parameters that do not satisfy the constraint derived from the 4D seismic results. All of the other curves agree with the seismic. The red curve corresponds to the laboratory result for the field of interest in this current study.

The main conclusion from Figure 4.33 is that, it is possible for a number of stress sensitivity curves to satisfy the constraint defined in (3-4), and therefore the condition is not unique. It is concluded that, based on robust observation of mapped 4D seismic data, it may be possible to make a statement about the range of possible in situ petroelastic model (rock) parameters. This represents a way of closing the loop between the seismic-scale and the laboratory measurements, but in order to generalise these results even further, it is recognised that more seismic data would need to be added. However, there are relatively few published case studies, as yet, that quote the pore pressure and saturation changes needed to formulate these constraints.

One final, and important, conclusion from this part of the study is that the petroelastic model parameters appear to influence the mapped 4D seismic signature as collective groups of parameters, rather than individual controlling parameters. This explains the difficulties researchers have had in the past in constraining these parameters. A demonstration of this situation is the many possible scenarios for the stress sensitivity parameters that will lead to the same outcome as (3.4). The collective groups of parameters determined here are therefore the smallest predominant variables that can uniquely control the 4D signature, and it is not possible to do better than this with seismic data. Inversion for the parameters of a specific petroelastic model from seismic data is therefore uncertain, to some degree, and constraints must, instead, be placed through appropriate laboratory measurements, where possible. Interestingly, despite the non-uniqueness, equation (2.43) does, nevertheless, reveal the dependence on the main controlling reservoir parameter of porosity.

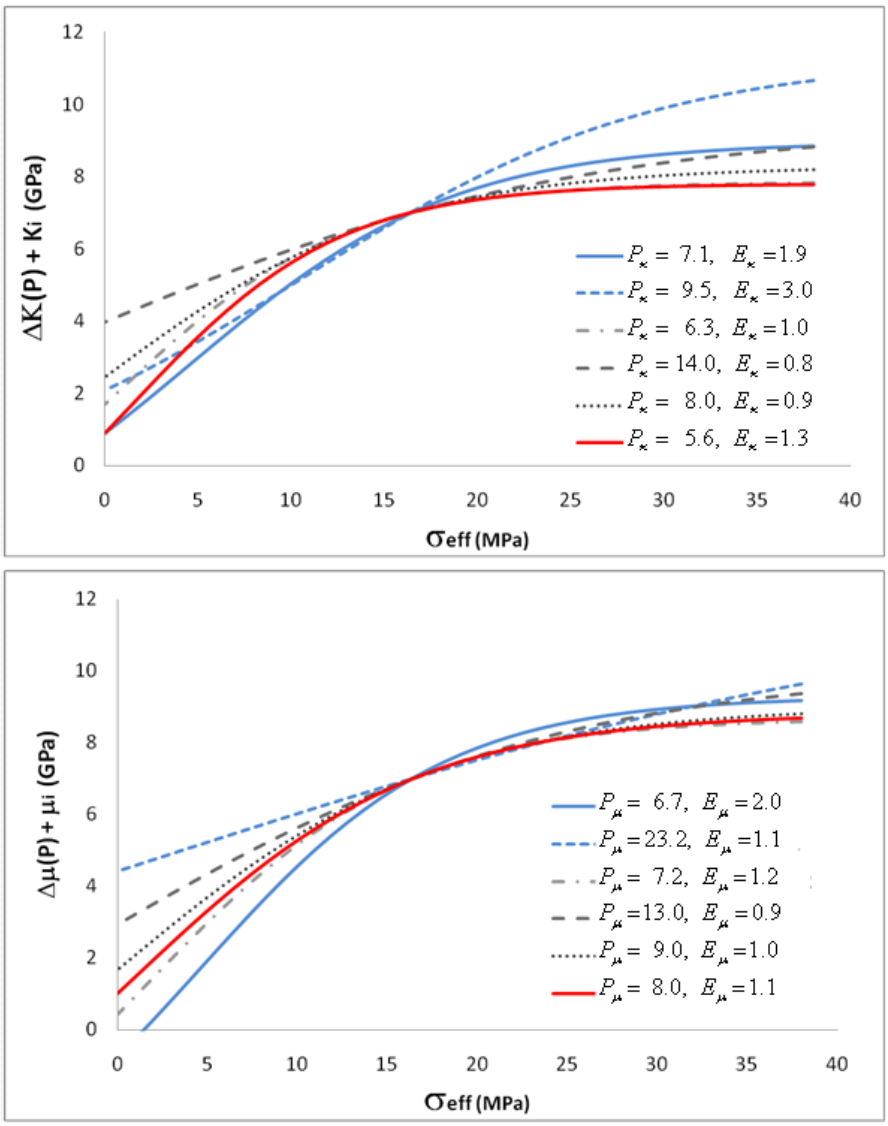

Figure 4.33: Stress sensitivity curves for (top) bulk modulus variation and (bottom) shear modulus variation with effective stress/pore pressure. The red curve corresponds to the laboratory result for the field of interest in this current study. All other curves, except those coloured in blue, satisfy the constraint imposed from the present 4D data observations.

In previous studies such as these by Landrø (2001) and MacBeth et al. (2004), it was suggested that $C_S$and C_P are functions of porosity: equation (2.24) now determines the exact nature of this dependence. Thus, the proposed formulation can be used for studies where pore pressure and saturation changes need to be separately extracted from the 4D seismic data.

4.9 Summary of conclusions of this chapter

- Of all the parameters of the petroelastic model, the rock stress sensitivity is the one which carries the highest uncertainty: the main reason for this is the difficulty of measuring this parameter using core samples. Core damage, frequency dispersion, geomechanical effects and the selection the effective stress coefficient could lead to underestimation of the rock stress sensitivity, whereas the rock drying processes, the presence of shales, imperfect stress recovery and stress asymmetry could lead to overestimating it.

- The magnitude of the rock stress sensitivity with respect to the fluid contrast determines the dominance of the pressure or saturation signal in the total 4D response. This accentuates the need to establish another way of constraining this important parameter. A method was developed, where I use the observed amplitudes in combination with the equation developed in the previous chapter to establish a constraint for the rock stress sensitivity.

- The results of this study suggest that C_S/C_P is a fundamental parameter that can be unambiguously extracted from mapped 4D seismic amplitudes by observing whether saturation or pore pressure dominates around injector wells.

- According to the data collected from five different clastic reservoirs (three from the literature and two worked examples), all with similar porosities of between 25 – 30%, it appears that C_S/C_P = 8 seems to indicate the point at which pore pressure starts to dominate over saturation and vice-versa.

- Finally, the framework and discussions outlined above are not limited by the underlying models of the rock and fluid physics, since the data comes from different fields with different geological settings; it is therefore envisaged that the formulation developed in Chapter 2 (2.24) may thus be regarded as a universal.

Chapter 5: Time lapse changes in reflectivity at fluid contacts

"Teoría es cuando piensas que lo sabes todo y nada funciona; práctica es cuando todo funciona y nadie sabe por qué. El peligro de combinar teoría y práctica es que luego nada funciona y nadie sabe por qué…"

Theory is when you think you know everything but nothing works; practice is when everything works but no one knows why. The danger of combining theory and practice is that then nothing works and no one knows why...

Popular science joke

In this chapter, I extend the derivation of the equations to reservoirs where gas is present. This includes gas reservoirs, oil reservoirs with an existing gas cap and reservoirs close to the bubble point, where a secondary gas cap is formed as a result of gas ex-solution. In this case, the derivations are based on the reflectivity changes at the fluid contacts and wavelet interference effects are incorporated, making the solution more complete (and simpler) than the single interface calculation.

5.1 Fluid contact based interpretation of the 4D signal

If the reservoir thickness is larger than the seismic tuning thickness, it is often possible to identify the seismic reflections associated with the fluid contacts, and hence associate the differences directly to changes in the hydrocarbon saturations. Commonly, this association involves the interpretation (picking) of the fluid contact reflections in the base and the monitor (Figure 5.1), or alternatively, interpretation of geobodies in the time-corrected 4D difference volumes (Figure 5.2). It has been observed in the past that even if the fluid contacts are not visible in the 3D seismic stacks, it is still possible to observe and interpret them in the 4D difference data (Osdal, et al., 2006). So far, in published case studies, the 4D interpretation process of fluid contacts relies on modelling exercises and empirical relations, which can lead to ambiguity in the results, especially in places where pressure and saturation overlap. Furthermore, these interpretations are commonly performed using the full stack and angle stacks are rarely used.

The single interface calculations derived in Chapter 2 focus on the interpretation of the top of the reservoir and assume an average saturation and pressure change across the interface, ignoring reservoir thickness or vertical differences in ΔP and ΔS_w. However, if discrete fluid contacts are visible in the 4D seismic difference, it makes sense to derive explicit equations that relate them to changes in pressure and hydrocarbon saturations; this is the objective I seek in this chapter. The reflectivity of fluid contacts has been studied previously by Wright (1986), who showed that it was possible to simplify the AVO formulae at these contacts. He concluded that the gas-water, gas-oil and oil-water contacts increase monotonically with offset. The AVO behaviour is mainly independent of V_P/V_S, and the offset behaviour is independent of the saturations. This is a useful reference and acts as a guide for the derivation, in combination with the work in Chapter 2. Using these concepts, I define equations that can be applied to gas reservoirs (gas-water system), and oil reservoirs above or below the bubble point pressure (oil-water system). Finally, I incorporate these results are into a general equation applicable to oil reservoirs with existing or newly formed gas

cap (three phase systems), where the contacts are not visible and the 4D difference is subject to tuning effects (thin reservoir approximation).

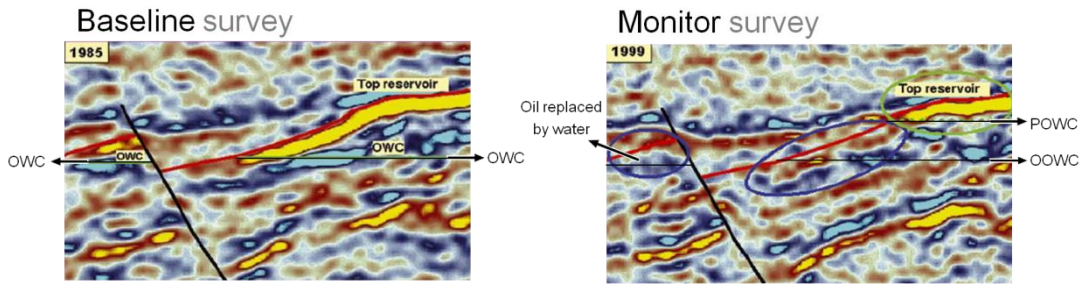

Figure 5.1: Identification and interpretation of fluid contact movements in the Gullfaks field. (Modified from Sandø, et, al., 2009).

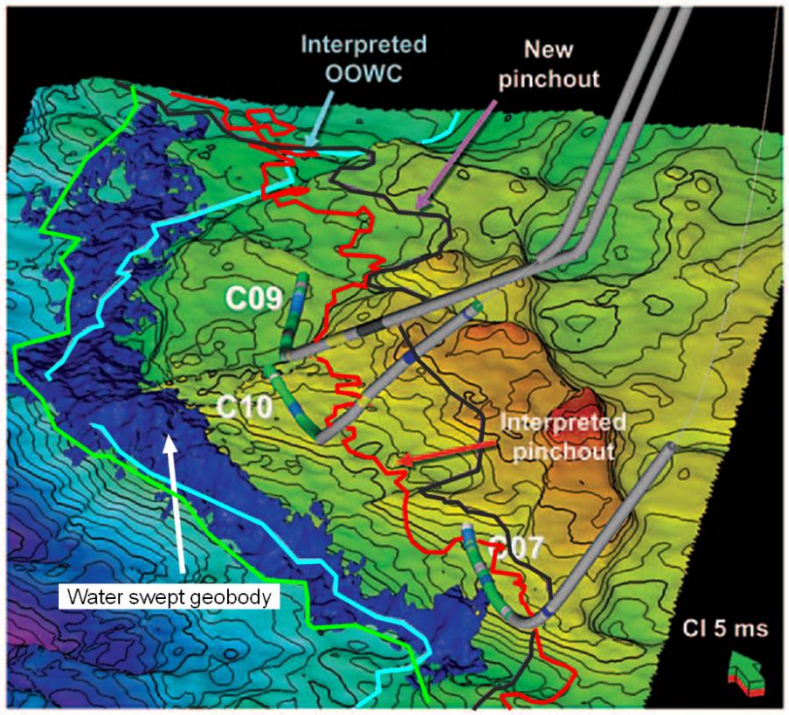

Figure 5.2: Geobody interpretation of a water swept area observed on the 4D difference. (Modified from Johnston & Laugier, 2012).

5.2 4D signature of oil-water contacts

My work starts with the conceptual model shown in Figure 5.3. The reflectivity at the oil-water contact is related to the differences in fluid saturation on each side of the

interface. Since the shear modulus is the same on both sides, $\Delta\mu^{b}_{oowc} = \mu^{b}_{Sw} - \mu^{b}_{So} = 0$. Reservoir pressure is also similar across the interface. Following Wright (1986), the reflectivity of the original oil-water contact can be defined as follows:

$$R(\theta)^{b}_{Oowc} = \Gamma_1 \frac{\Delta\kappa^{b}_{oowc}}{\overline{M^{b}}} + \Gamma_2 \frac{\Delta\rho^{b}_{oowc}}{\overline{\rho^{b}}} \quad , \tag{5.1}$$

where

$$\Delta\kappa^{b}_{oowc} = \kappa^{b}_{Sw} - \kappa^{b}_{So} \; ; \;\; \Delta\rho^{b}_{oowc} = \rho^{b}_{Sw} - \rho^{b}_{So} \; , \tag{5.1a}$$

$$\overline{M^{b}} = \frac{1}{2}\left(M^{b}_{Sw} + M^{b}_{So}\right) ; \;\; \overline{\rho^{b}} = \frac{1}{2}\left(\rho^{b}_{Sw} + \rho^{b}_{So}\right) \; . \tag{5.1b}$$

Here, the terms $\kappa^{b}_{Sw}, \rho^{b}_{Sw}, M^{b}_{Sw}, \kappa^{b}_{So}, \rho^{b}_{So}$ and M^{b}_{o} denote the bulk modulus, density and P modulus of water (sub-index S_w) and oil saturated rock (sub-index S_o) for the base line (upper-index b). For the post-production state (monitor), as observed in Figure 5.4, we have now two reflection coefficients, one for the original oil-water contact (R_{oowc}) and the one corresponding to the produced oil water contact (R_{powc}). Therefore we have

$$R(\theta)^{m}_{oowc} = \Gamma_1 \frac{\Delta\kappa^{m}_{oowc}}{\overline{M^{m}}} + \Gamma_2 \frac{\Delta\rho^{m}_{oowc}}{\overline{\rho^{m}}} \quad , \tag{5.2}$$

where

$$\Delta\kappa^{m}_{oowc} = \kappa^{m}_{Sw} - \kappa^{m}_{sp}; \;\; \Delta\rho^{m}_{oowc} = \rho^{m}_{Sw} - \rho^{m}_{sp} \; , \tag{5.2a}$$

$$\overline{M^{m}} = \frac{1}{2}\left(M^{m}_{Sw} + M^{m}_{sp}\right); \; \overline{\rho^{b}} = \frac{1}{2}\left(\rho^{m}_{Sw} + \rho^{m}_{sp}\right) \quad , \tag{5.2b}$$

Here, the terms $\kappa^{m}_{Sw}, \rho^{m}_{Sw}, M^{m}_{Sw}, \kappa^{m}_{sp}, \rho^{m}_{sp}$ and M^{m}_{sp} denote the bulk modulus, density and P modulus of the water saturated rock (sub-index S_w) and swept zone (water replacing oil, sub-index sp) at the post-production state.

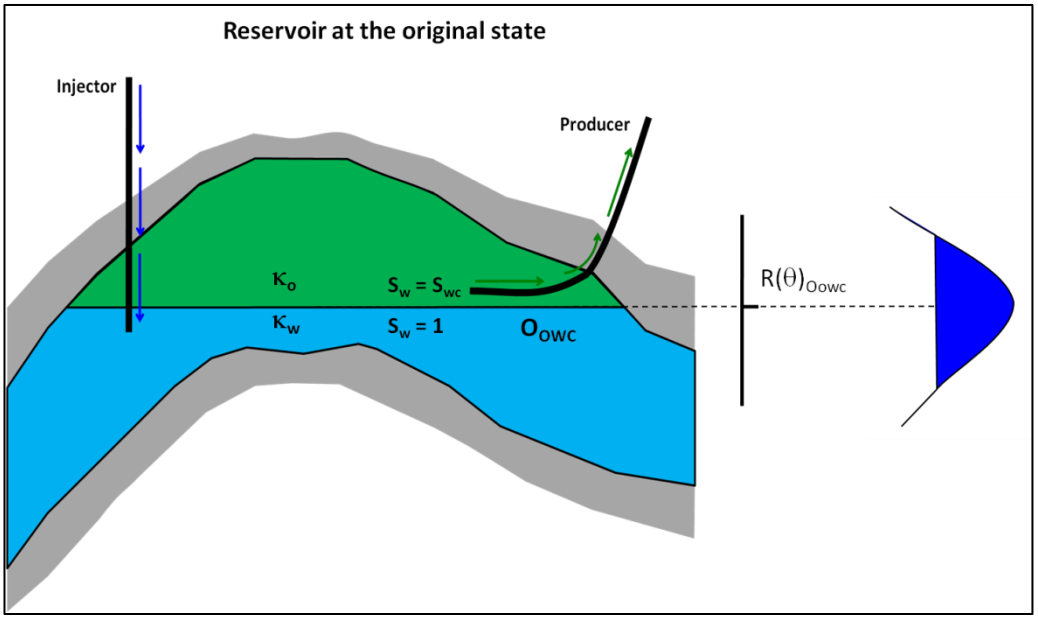

Figure 5.3: Conceptual model for a fluid contact (in this case oil-water) before production.

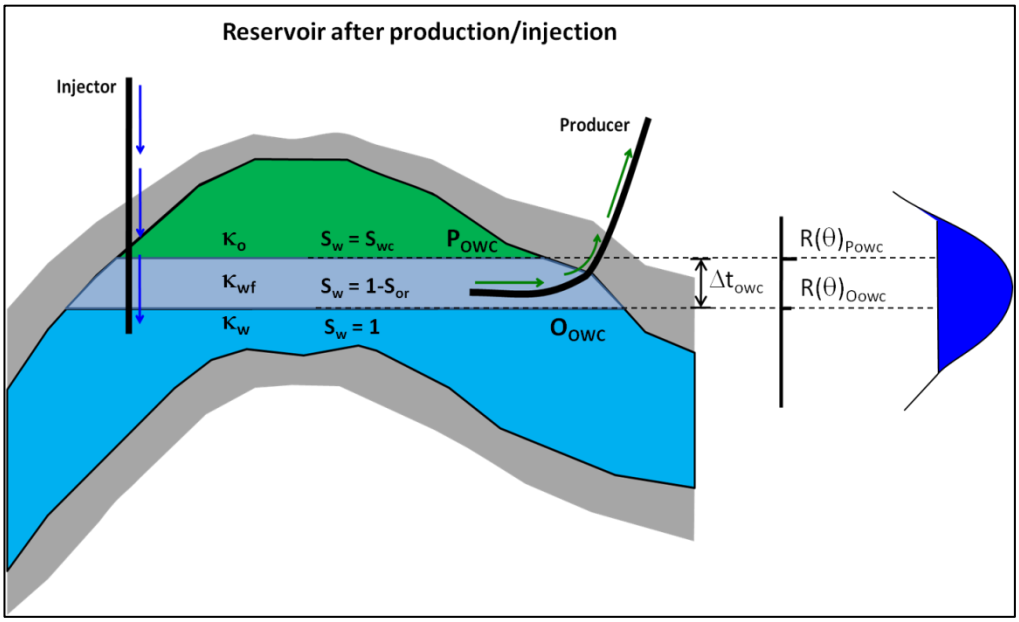

Figure 5.4: Conceptual model for a fluid contact (in this case oil-water) after production.

Based on the above, the time lapse reflectivity for the original oil-water contact will be given by

$$\Delta R(\theta)_{\mathrm{oowc}} = \Gamma_1 \left[\frac{\Delta\kappa^{\mathrm{m}}_{\mathrm{oowc}}}{\overline{M^{\mathrm{m}}}} - \frac{\Delta\kappa^{\mathrm{b}}_{\mathrm{oowc}}}{\overline{M^{\mathrm{b}}}} \right] + \Gamma_2 \left[\frac{\Delta\rho^{\mathrm{m}}_{\mathrm{oowc}}}{\overline{\rho^{\mathrm{m}}}} - \frac{\Delta\rho^{\mathrm{b}}_{\mathrm{oowc}}}{\overline{\rho^{\mathrm{b}}}} \right], \qquad (5.3)$$

which can be approximated as

$$\Delta R(\theta)_{\mathrm{oowc}} \approx \ \Gamma_1 \left[\frac{\Delta\kappa_{\mathrm{oowc}}}{\overline{M^{\mathrm{b}}}}\right] + \Gamma_2 \left[\frac{\Delta\rho_{\mathrm{oowc}}}{\overline{\rho^{\mathrm{b}}}}\right] \ , \tag{5.4}$$

where

$$\Delta\kappa_{\mathrm{oowc}} = \kappa_{\mathrm{So}}^{\mathrm{b}} - \ \kappa_{\mathrm{sp}}^{\mathrm{m}} \ \text{ and } \ \Delta\rho_{\mathrm{oowc}} = \rho_{\mathrm{So}}^{\mathrm{b}} - \rho_{\mathrm{sp}}^{\mathrm{m}} \ . \tag{5.4a}$$

For the reflection coefficient at the produced oil-water contact, since this does not exist in the base line seismic data, it can be defined as follows:

$$\Delta R(\theta)_{\mathrm{powc}} \approx \ \Gamma_1 \left[\frac{\Delta\kappa_{\mathrm{powc}}}{\overline{M^{\mathrm{b}}}}\right] + \Gamma_2 \left[\frac{\Delta\rho_{\mathrm{powc}}}{\overline{\rho^{\mathrm{b}}}}\right] \ , \tag{5.5}$$

where

$$\Delta\kappa_{\mathrm{powc}} = \kappa_{\mathrm{sp}}^{\mathrm{m}} - \ \kappa_{\mathrm{So}}^{\mathrm{m}} \approx -\Delta\kappa_{\mathrm{oowc}} \ , \tag{5.5a}$$

$$\Delta\rho_{\mathrm{powc}} = \rho_{\mathrm{sp}}^{\mathrm{m}} - \rho_{\mathrm{So}}^{\mathrm{m}} \approx -\Delta\rho_{\mathrm{oowc}}. \tag{5.5b}$$

Using the rock and fluid equations in Chapter 2, I find the time lapse reflectivity of the contacts as a function of pressure and saturation changes:

$$\Delta R(\theta)_{\mathrm{oowc}} = -\frac{(1 - S_{or} - S_{wc})}{S_{wc}} \mathrm{C_S^o} + \frac{\Delta P}{P_i} C_P^o \ , \tag{5.6}$$

$$\Delta R(\theta)_{\mathrm{oowc}} \approx -\Delta R(\theta)_{\mathrm{oowc}} \ , \tag{5.7}$$

where

$$\mathrm{C_S^o} = \phi[\Gamma_1 N_1^o + \Gamma_2 N_2^o] \ , \tag{5.8a}$$

$$C_P^o = \ [(1 - \varepsilon'\phi)\Gamma_1 N_3^o + \phi(\Gamma_1 N_5^o + \Gamma_2 N_6^o)] \ , \tag{5.8b}$$

and

$$N_1^o = \frac{\varepsilon}{\overline{M^{\mathrm{b}}}} \frac{S_{wc}\left(\kappa_w^b - \kappa_o^b\right)}{\left(\frac{\kappa_o^b}{\kappa_w^b} - 1\right) S_{wc} + \left(\frac{\kappa_w^b}{\kappa_o^b} - 1\right) S_{or} + 1} \quad , \tag{5.8c}$$

$$N_2^o = \frac{S_{wc}\left(\rho_w^b - \rho_o^b\right)}{\overline{\rho^{\mathrm{b}}}} \quad , \tag{5.8d}$$

$$N_3^o = P_i \left[\frac{\alpha \kappa_m A_\kappa}{\overline{M^{\mathrm{b}}}}\right] \quad , \tag{5.8e}$$

$$N_5^o = P_i \left[\frac{\varepsilon}{\overline{M^{\mathrm{b}}}} \frac{\kappa_w^b (1 - S_{wc}) \zeta_{BP} O_\kappa + \kappa_o^b W_\kappa S_{wc}}{S_{wc} \kappa_o^b + \kappa_w^b (1 - S_{wc})}\right], \tag{5.8f}$$

$$N_6^o = P_i \left[\frac{S_{wc} W_\rho + (1 - S_{wc}) \zeta_{BP} O_\rho}{\overline{\rho^{\mathrm{b}}}}\right] . \tag{5.8g}$$

Here the upper-index 'o' indicates that these equations are valid for an oil-water system. The constant ζ_{BP} is introduced into N_5^o and N_6^o to incorporate the effect of going above or below the bubble point pressure. ζ_{BP} becomes -1 when the system is below the bubble point pressure and 1 when is above the reservoir pressure. This is consistent with Batzle & Wang's (1992) predictions and other measurements in the NIST database, which show that local gradients of bulk modulus and density above and below reservoir pressure are similar, but with opposite sign.

$$\zeta_{BP} = \frac{P_i - P_{BP}}{|P_i - P_{BP}|} . \tag{5.9}$$

5.2.1 Incorporating wavelet interference effects

Now let us consider that we have interpreted the top ($\Delta A(\theta)_{\mathrm{Powc}}$) and base ($\Delta A(\theta)_{\mathrm{Oowc}}$) of the 4D difference (monitor-base) and that we do this for different monitors. Initially, since the position of the original and produced oil-water contacts are at similar depths, the reflection wavelet associated with each will overlap, even if those are visible in the 3D seismic above seismic resolution. This will be the case until the swept zone that develops becomes larger than the seismic tuning thickness (assuming the whole reservoir is thick enough to allow this to happen). This implies that, in some cases, to interpret the 4D differences we need to include the wavelet interference effects. Therefore, the combined time lapse response ($\Delta A(\theta)_{\mathrm{owc}}$) in the frequency domain can be expressed as

$$\Delta R(\theta)_{\mathrm{owc}}^{\mathrm{comp}} = \Delta R(\theta)_{\mathrm{powc}} + \Delta R(\theta)_{\mathrm{oowc}} \mathrm{e}^{-\mathrm{i}\omega\Delta t_o} . \tag{5.10}$$

Applying Taylor's expansion to the first order, and since $\Delta R(\theta)_{\mathrm{powc}} \approx$-$\Delta R(\theta)_{\mathrm{oowc}}$, we obtain

$$\Delta A(\theta)_{\mathrm{owc}}^{\mathrm{comp}} = \left\{ \frac{(1 - S_{or} - S_{wc})}{S_{wc}} \mathrm{C_S^o} - \frac{\Delta P}{P_i} C_P^o \right\} \Delta t_o \dot{s}(t). \tag{5.11}$$

An alternative form of equation in terms of the oil saturation changes can be given by

$$\Delta \mathrm{A}(\theta)_{\mathrm{owc}}^{\mathrm{comp}} = \left\{ -\frac{\Delta \mathrm{S_o}}{S_{wc}} \mathrm{C_S^o} - \frac{\Delta P}{P_i} C_P^o \right\} \Delta \mathrm{t_o} \dot{\mathrm{s}}(\mathrm{t}) \quad , \tag{5.12}$$

where $\dot{s}(t)$ is the time derivative of the wavelet and Δt_o represents the two way time thickness of the swept zone. An important observation from equation 5.11 is that, assuming connate water can be considered invariant with time lapse (at least in primary recovery, as it is capillary bound), at any given survey time, the only parameters changing will be S_{or} and the thickness of the swept zone (Δt_o), which can be measured from our interpretation (after eliminating pressure effects, for instance, by

interpreting the far angle stack). This means that equation 5.12 can be used to estimate sweep efficiency and therefore can help targeting areas for secondary recovery.

5.2.2 *Accuracy of the equations and applicability*

To test the above theory, 1D Seismic modelling was performed using the parameters from the North Sea dataset used in Chapter 2 with constant values for S_{or} and S_{wc} (0.18 and 0.20 respectively). The objective of this modelling is to determine when it is appropriate to use the approximations given by equations 5.6 and 5.7, and when it will be required to consider the wavelet interference effects (equation 5.12). Figure 5.5 shows the results of 1D modelling assuming maximum water replacement ($\Delta S_w = 1 - S_{or} - S_{wc}$) and a maximum pressure change of -6 MPa (depletion). The time thickness of the swept zone varies from 0 to 52 ms and the Ricker wavelet has a peak frequency of 24 Hz.

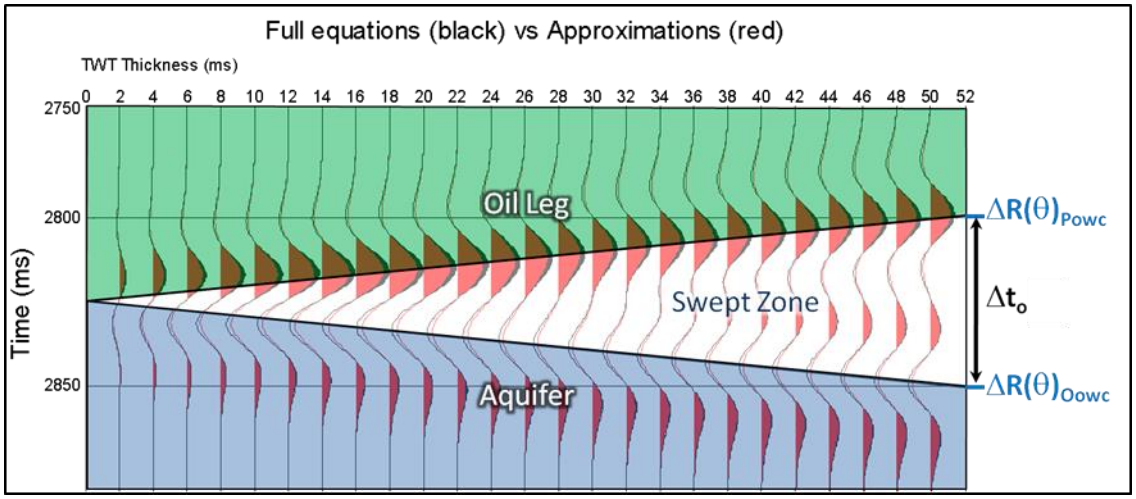

Figure 5.5: Wedge modelling results comparing the full equations (black) versus the thick reservoir equations (red) for swept zone thicknesses from 0 to 52 ms (twt). The background colours show the position of the time lapse reflection coefficients. The black seismic traces are calculated using the full rock and fluid equations and the red traces are the results of the approximations in equations 5.6 and 5.7.

By looking at the position of the seismic amplitudes in each trace, it can be observed that the peak and trough reflections only accurately represent the positions of the original and produced contacts when Δt_o> 14ms. If we were to pick the positive and negative reflections for $\Delta t_o \leq$ 14ms, we would be over-estimating the size of the swept zone, therefore in such cases a thin reservoir approximation will be more appropriate. It is important to note that this cut-off of 14 ms is data dependent and cannot be generalised, but it constitutes a useful guide for the application of the equations in real data. The thin reservoir approximation (equation 5.11) is also compared with the full equations for Δt_o< 20ms (Figure 5.6). In this case, it can be observed that the thin reservoir equation is valid for $\Delta t_o \leq$ 10 ms, whereas for $\Delta t_o >$ 10 ms it would over-predict the amplitude response. The area between $10 > \Delta t_o < 14$ ms falls within the two extremes and therefore carries the highest uncertainty.

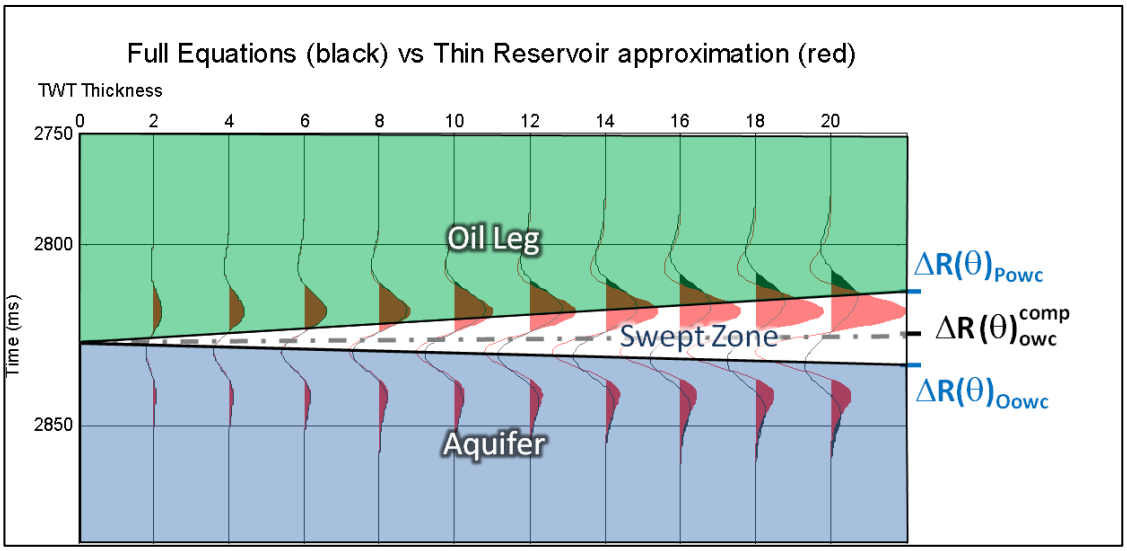

Figure 5.6: Wedge modelling results, comparing the full equations (black) versus the thin reservoir equations (black) for swept zone thicknesses from 0 to 52 ms (twt). The black traces represent the full equations and the red traces the approximation.

An additional comparison is performed in Figure 5.7, but this time to demonstrate the validity of the thin reservoir equation for pre-stack interpretation (4D AVO). As observed by Wright (1986), the reflectivity of the contact increases monotonically with offset. The fact that equation 5.11 includes the 4D AVO effects is important; this

information is rarely incorporated in conventional 4D interpretation workflows, which are commonly based on the interpretation of the full stack.

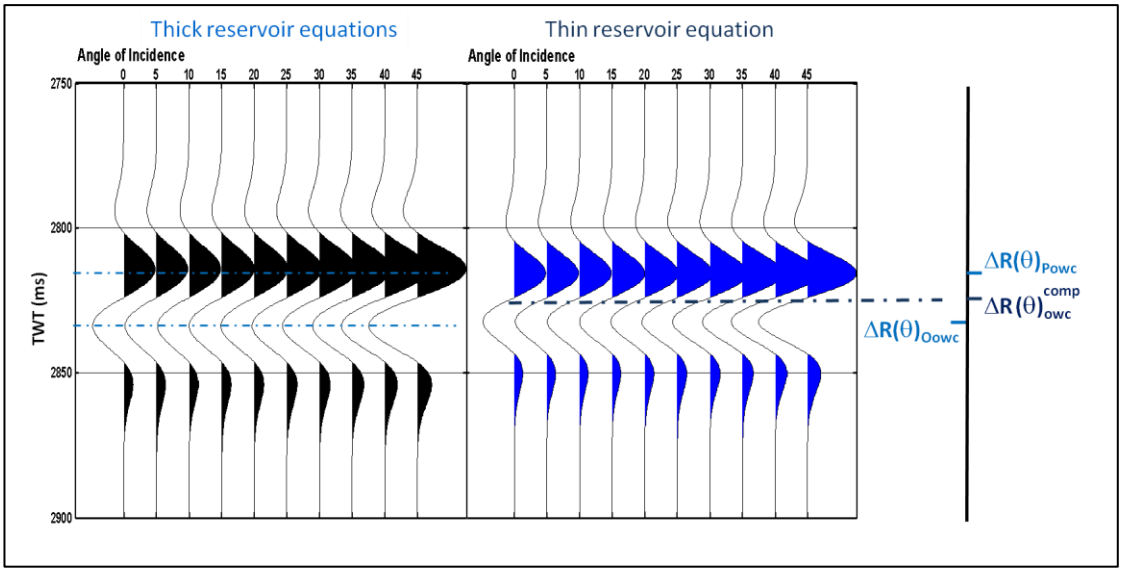

Figure 5.7: Comparison of full thick reservoir equations versus the thin reservoir approximation in the 4D AVO domain, assuming a constant Δt_{owc} of 14 ms.

Additional equations applicable to gas-water and gas-oil contacts are developed in Appendix 2. The resultant expressions are similar in form to those shown above and similar observations can be made.

5.3 Generalising the thin reservoir equations for multiple fluid phases

The previous equations in this chapter are applicable for cases where the reservoir is thick enough to allow the contacts to be visible and interpretable, at least in the 4D difference. However, there are situations where the reservoir thickness is not large enough for the fluid contacts to be interpretable or the reservoir is too complex to identify the reflections associated with the fluid contacts unambiguously. In these cases, it would be convenient to interpret the top and base of the reservoir and associate the amplitude variations with changes in the fluid contacts and reservoir pressure. Since I have already defined the time lapse responses for the different fluid

contact movements (see Appendix 2), as well as those associated with the top and base of the reservoir (Chapter 2), I can therefore combine these results into a single general equation that can be used for the situations described above.

5.3.1 Reservoirs with a pre-existing gas cap

Based on the schematic models shown in Figure 5.8 and Figure 5.9, the combined reflectivity for the pre-production case, in the frequency domain (below tuning) will be given by

$$\Delta R(\theta)_{TL}^{comp} = \Delta R(\theta)_{top} + \Delta R(\theta)_{pgoc}\, e^{-i\omega(t_g-\Delta t_g)} + \Delta R(\theta)_{ogoc}\, e^{-i\omega t_g} + \Delta R(\theta)_{oowc}\; e^{-i\omega t_o} + \Delta R(\theta)_{powc}\, e^{-i\omega(t_o-\Delta t_o)} + \Delta R(\theta)_{base} e^{-i\omega t_T}\,. \quad (5.13)$$

Assuming pressure has reached equilibrium (which means that ΔP is the same for all layers), after applying first order Taylor's expansion to the exponential terms, we can incorporate the fluid contact time lapse reflectivities derived above, obtaining

$$\Delta A(\theta)_{TL}^{comp} = \left[C_S^m \frac{(1 - S_{org} - S_{wc} - S_{gro})}{S_{wc}} \Delta t_g + C_S^o \frac{(1 - S_{or} - S_{wc})}{S_{wc}} \Delta t_o - C_P^o \frac{\Delta P}{P_i} t_T \right] \dot{s}(t), \quad (5.14)$$

or in terms of the oil and gas saturation changes,

$$\Delta A(\theta)_{TL}^{comp} = \left[C_S^m \frac{\Delta S_o}{S_{wc}} \Delta t_g + C_S^o \frac{\Delta S_w}{S_{wc}} \Delta t_o - C_P^o \frac{\Delta P}{P_i} t_T \right] \dot{s}(t), \quad (5.15)$$

$$\Delta A(\theta)_{TL}^{comp} = \left[-C_S^m \frac{\Delta S_g}{S_{wc}} \Delta t_g + C_S^o \frac{\Delta S_w}{S_{wc}} \Delta t_o - C_P^o \frac{\Delta P}{P_i} t_T \right] \dot{s}(t). \quad (5.16)$$

Additional expressions for the case of reservoirs with no pre-existing gas cap are developed in Appendix 2.

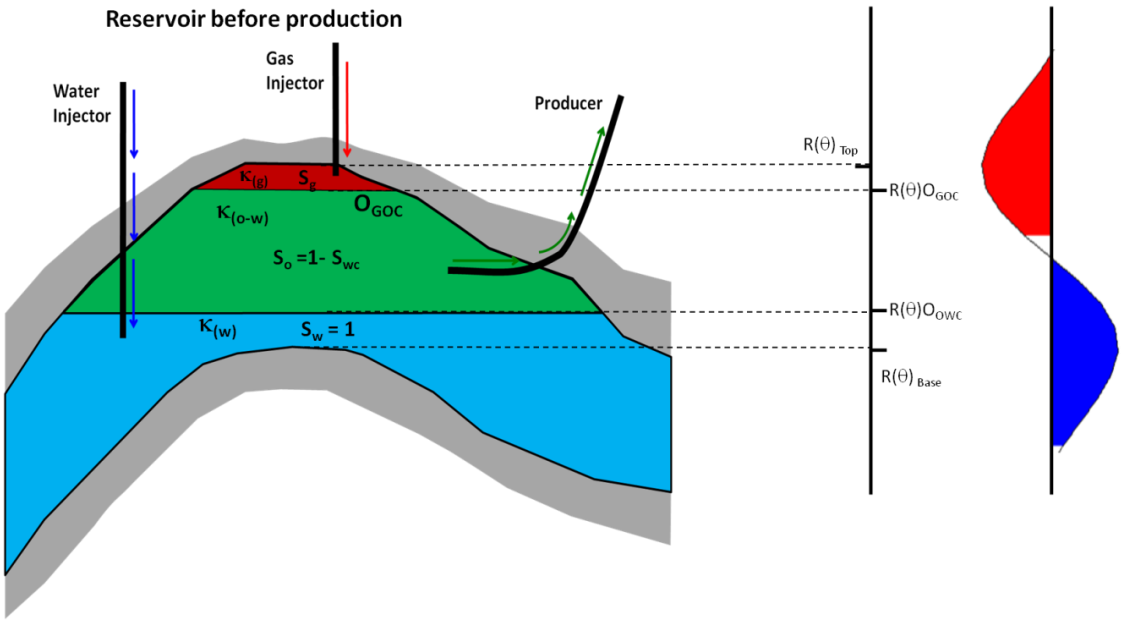

Figure 5.8: Conceptual model for an oil reservoir with an existing gas cap at the limit of seismic resolution, pre-production state.

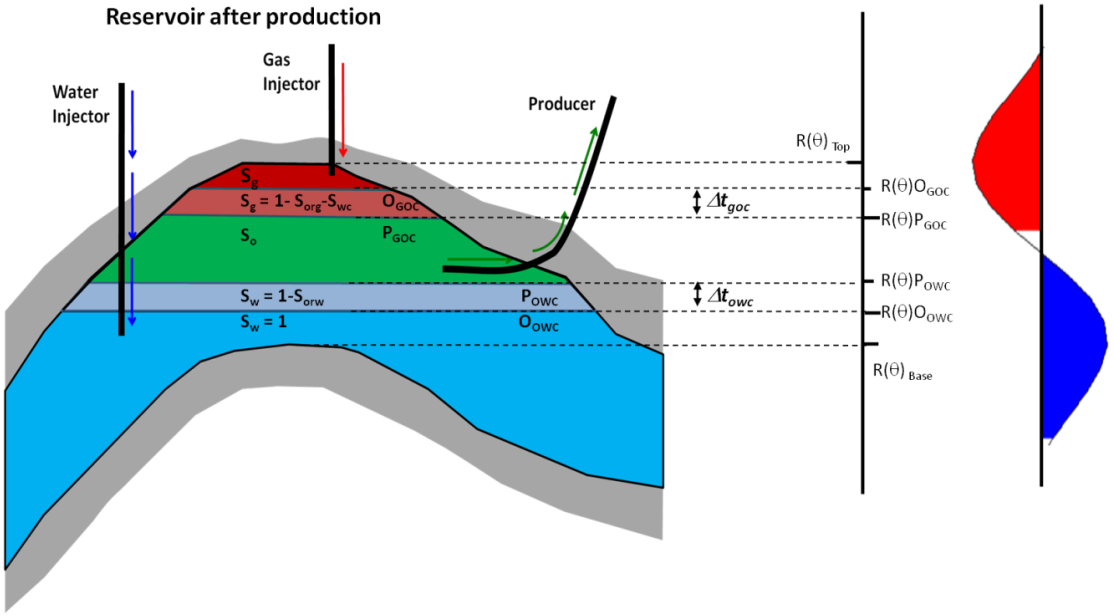

Figure 5.9: Conceptual model for an oil reservoir with an existing gas cap at the limit of seismic resolution, post-production state.

5.4 Application of the generalised equation in a real dataset

My final general equation (5.15) was tested on a North Sea dataset which is at the limits of seismic resolution and fluid contacts are not visible. For the purposes of this exercise, I concentrate on the pre-production survey (1994) and the 2004 monitor. The observed seismic is available only as full stacks and no angle stacks are available; therefore, in order to have an additional way of comparing and validating the results, simulation to seismic modelling was run (Amini and MacBeth, 2011) to generate angle stacks for the base and monitor. A sub-set of the field was selected for this part of the study, which includes 8 wells: 5 of them are injectors (W1 to W5) and 3 producers (W6, W7 and W8). Figure 5.10 shows an average porosity map from the simulation data taken between the top and base reservoir layers.

According to the well activity data available, it can be observed that the reservoir pressure is very close to the bubble point pressure and therefore gas breakout occurred in several parts of the reservoir as soon as production started. For pressure support, water has been injected into the aquifer right from the start of production. My objective is to determine if equation 5.15 is successful in combining the complex fluid interactions occurring at a sub-seismic level (and described in the simulation model) directly on the observed seismic data. A second objective is to observe the advantages of using the new equations for 4D interpretation purposes.

Figure 5.11 shows a cross-section along the trajectory of well W8, displaying the time lapse changes between 1998 and 2004. From top to bottom, I show the changes in gas saturation (ΔS_g), water saturation (ΔS_w) and reservoir pressure (ΔP), respectively. For the purposes of this exercise, I am focusing only on the upper part of the reservoir. Inside this layer, the reservoir simulator shows a number of interesting interactions between the fluids and pressure changes, for instance, we can see the areas where gas has come out of solution and moved to the local structural highs. We also observe water replacing oil in the areas around the well, due to production and effects of compartmentalisation made evident by the local pressure changes. At the base of the

layer of interest, there is a clear separation with respect to the production effects in the horizontal part of the well, which results from transmissibility barriers, represented in the model by low values in the net to gross (for this field $NTG = 1 - V_{sh}$).

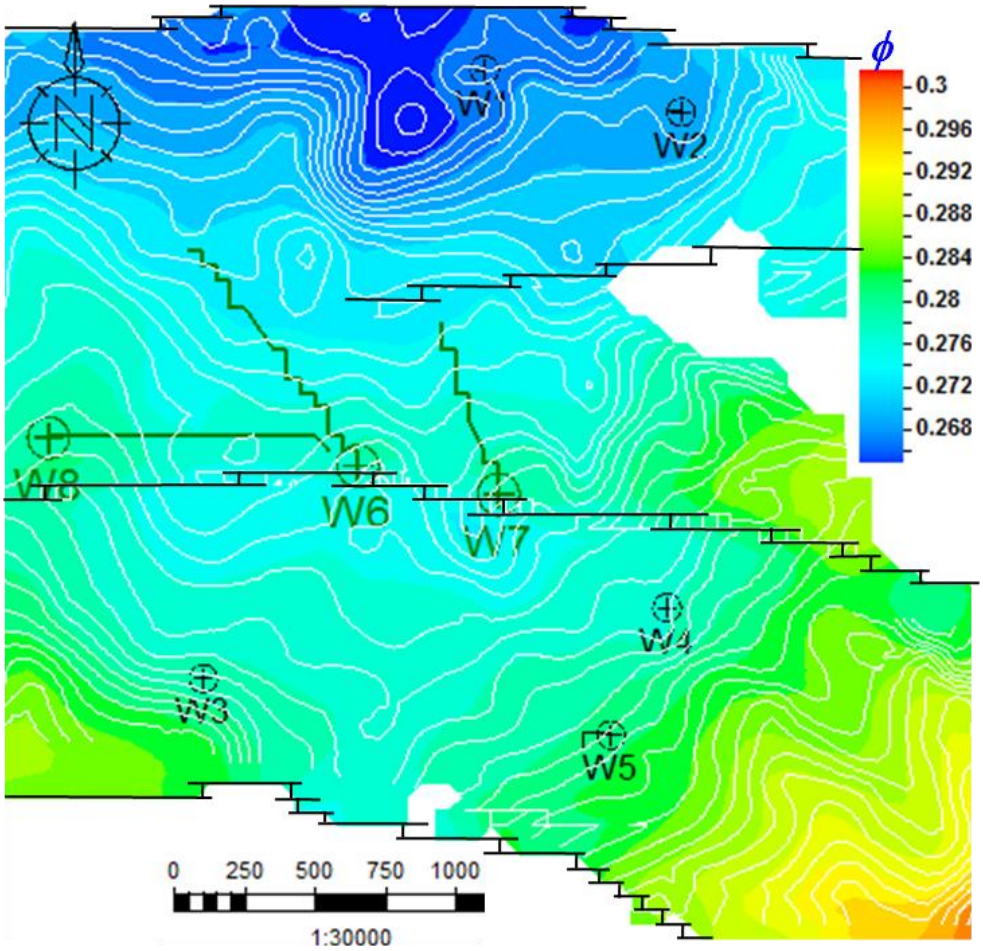

Figure 5.10: Base map showing the area of study, showing structural contours. The displayed property is porosity. The position of the well symbol is located at the intersection with the top of the reservoir; depth contours and major faults are also displayed.

The same section along W8, in the time domain, is shown in Figure 5.12. The top picture is the observed seismic and the one at the bottom is the result of the sim2seis modelling (which uses the simulation data as input) validating that the fluid changes observed in the previous figure effectively occur at a sub-seismic level.

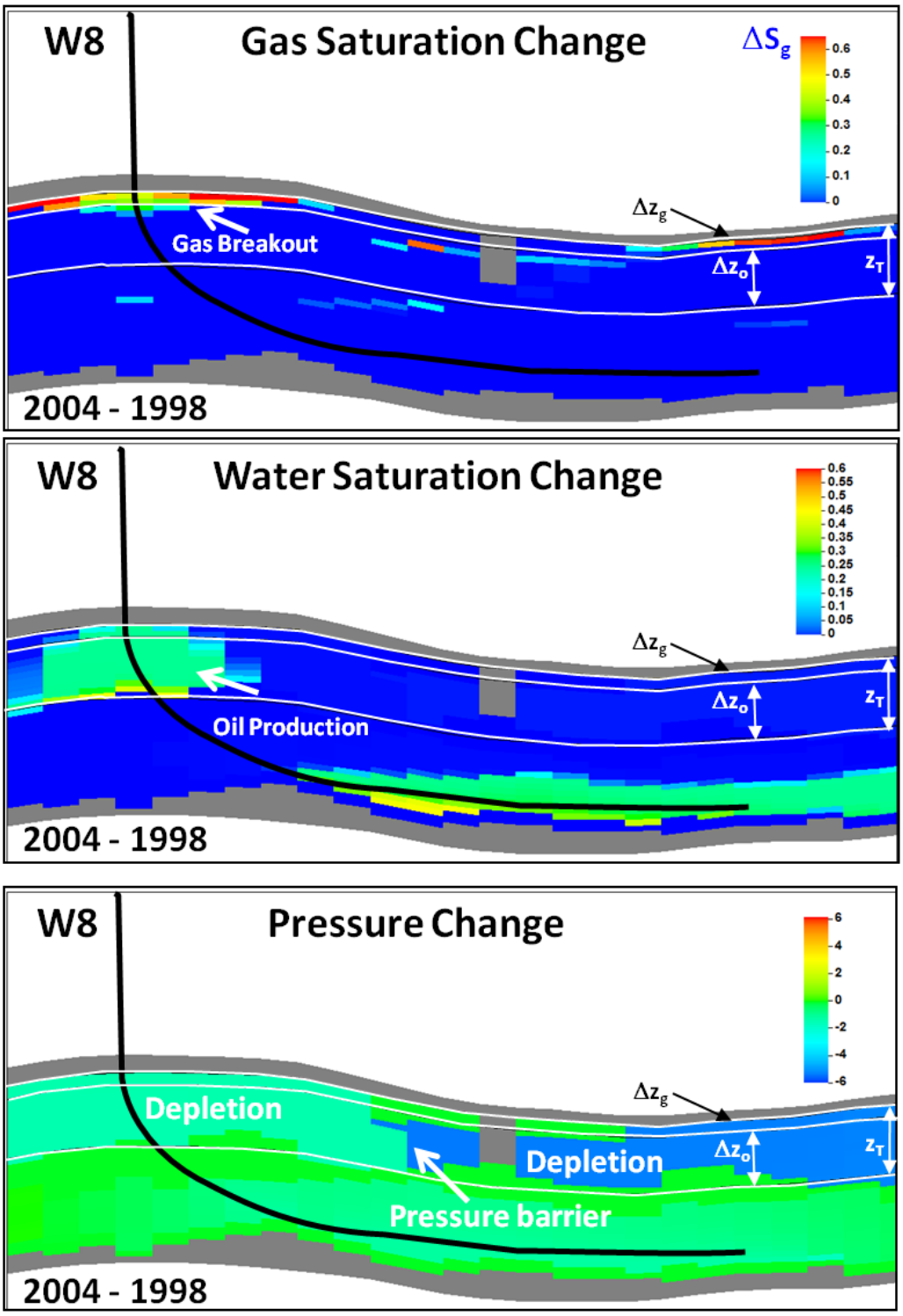

Figure 5.11: From top to bottom, changes in gas, water and reservoir pressure from the simulation model: West to East section along the trajectory of W8. The three white horizons represent the changes in the gas cap thickness (Δt_g), change in the oil column thickness (Δt_o), and the total reservoir thickness (t_T) , (they can be expressed in time or depth since the average velocity through the reservoir is known).

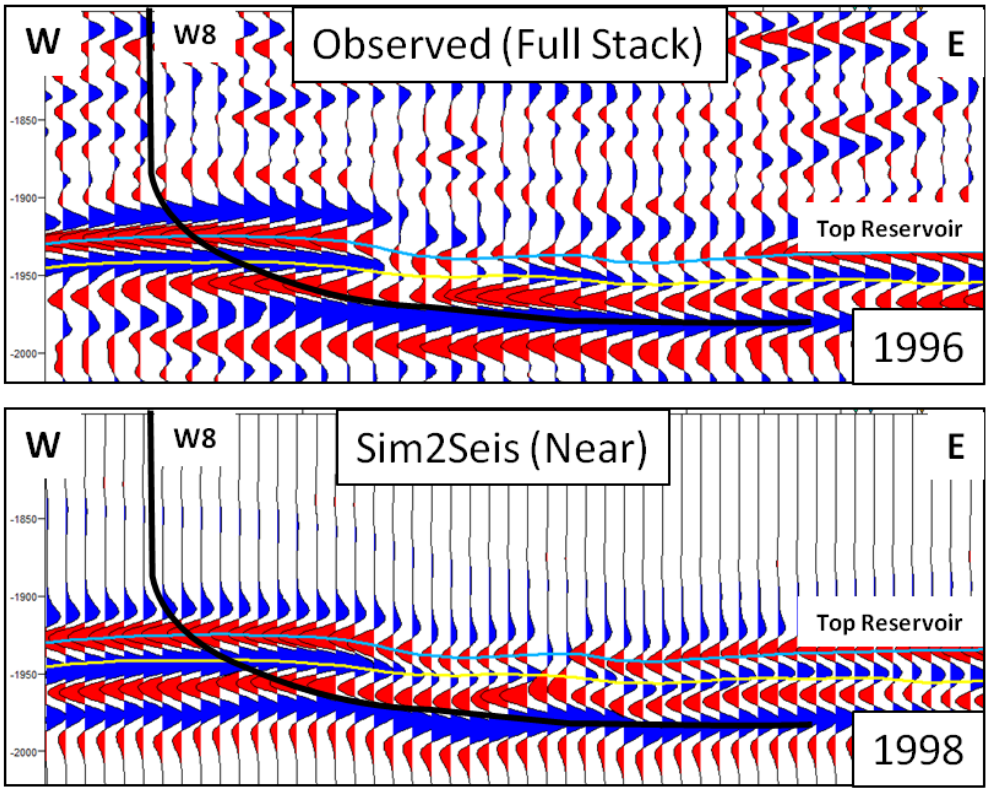

Figure 5.12: West to East seismic sections (on top), the observed seismic, and at the bottom, the result of the sim2seis modelling. The horizons in blue and yellow represent the top and base of the layer of interest.

To populate equation 5.15, average property maps were extracted from the simulation model together with the maps representing the distribution of $\Delta t_g, \Delta t_o$ and t_o respectively (white horizons in Figure 5.11). The average maps for ΔP, ΔS_w and ΔS_g are shown in Figure 5.13. RMS amplitude maps were extracted from the observed seismic (full stack) and the near angle stack coming from sim2seis modelling. For this, the available top and base horizons (Figure 5.12) were used to create an extraction window from -6 ms above top reservoir to +6 ms below the base reservoir. The observed and predicted changes in ΔA_{TL} for the near angle response are shown in Figure 5.14, Figure 5.15 and Figure 5.16. The prediction from equation 4.47 is consistent with the map from sim2seis, and is also consistent with the general distribution of the observed amplitudes map.

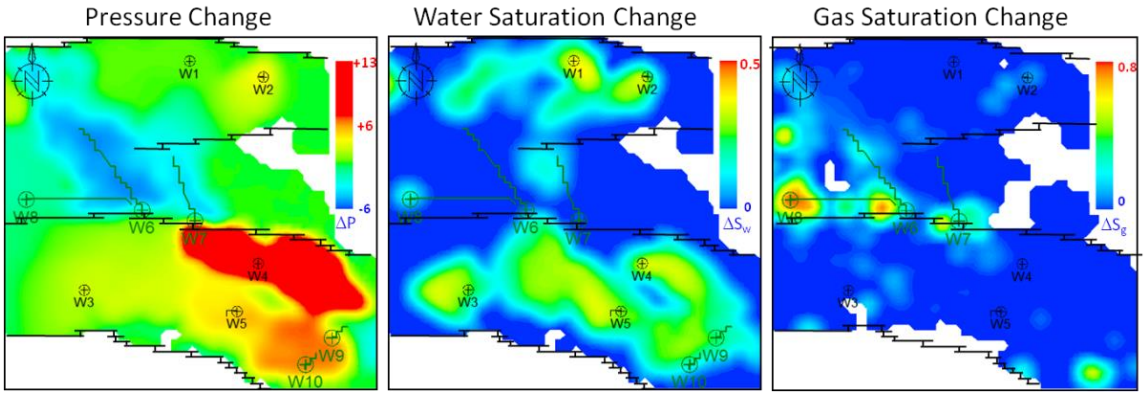

Figure 5.13: Average property maps extracted from the simulation model for the reservoir section.

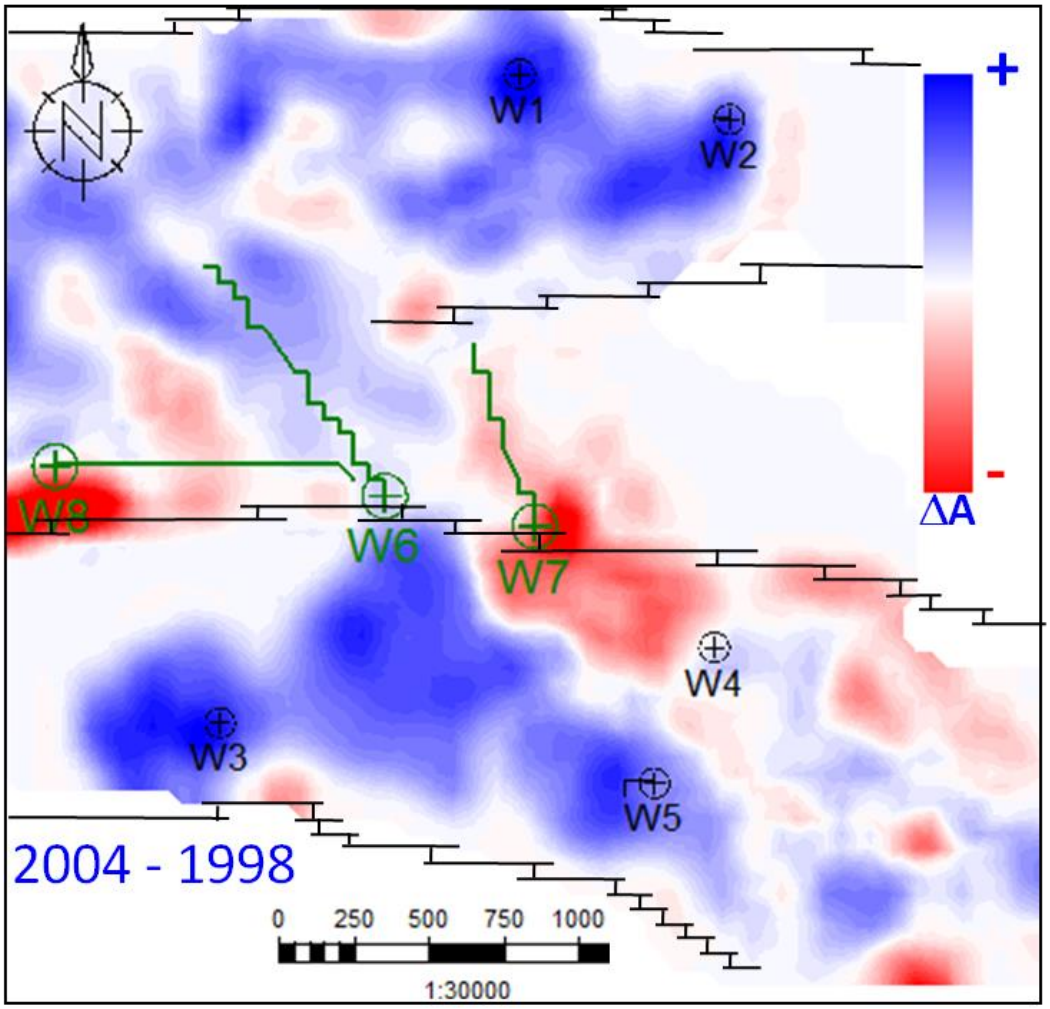

Figure 5.14: 4D amplitude map for the near angles (0 – 10), computed using the sim2seis modelling package (Amini, et al., 2012) for the 2004-1998 period. Active producer wells are shown in green and injectors in blue.

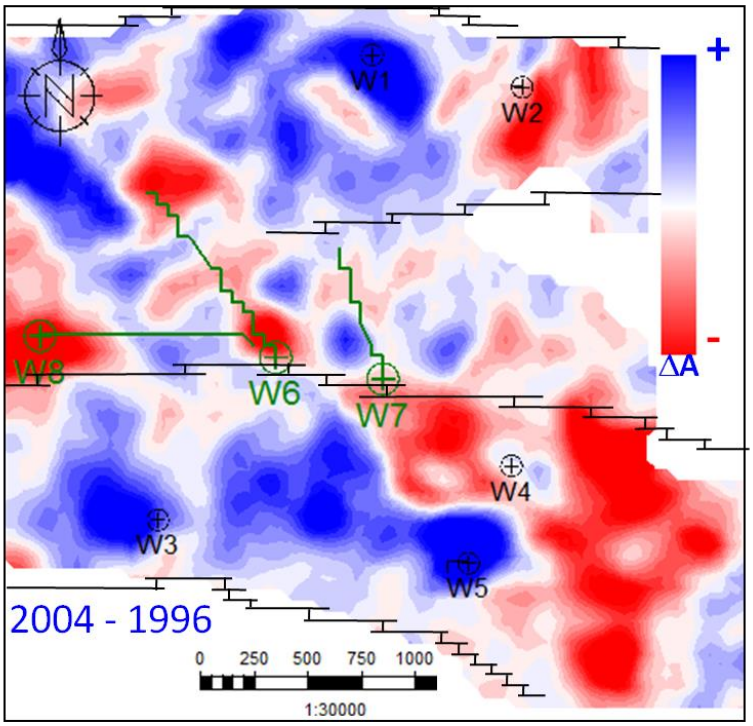

Figure 5.15: Observed 4D amplitude map from the full stack for the 1998 - 2004 period. Active producer wells are shown in green and injectors in blue.

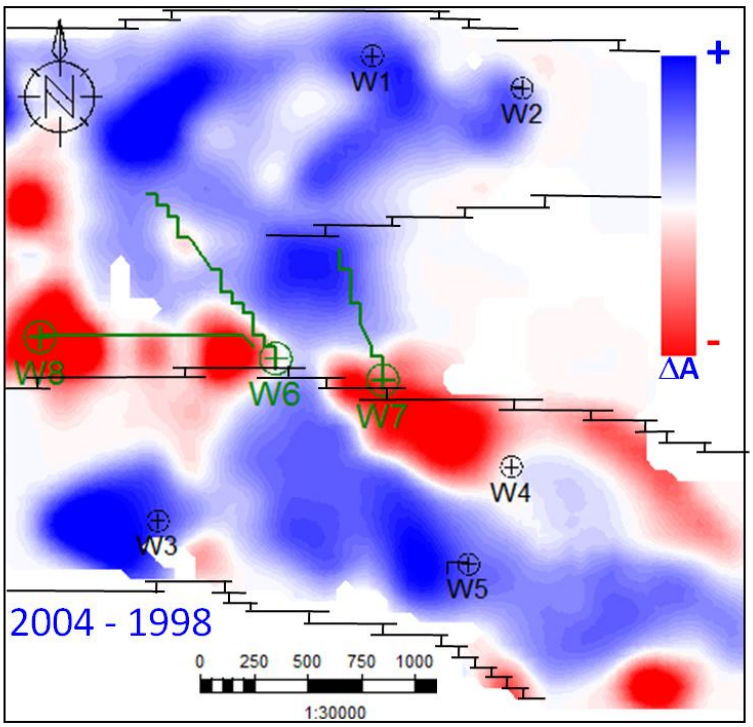

Figure 5.16: 4D amplitude map computed from equation 5.59 for the 1998 - 2004 period. Near angle stack (0-10 degrees). Active producer wells are shown in green and injectors in blue.

The comparison of modelled versus acquired 4D seismic, together with the analysis of the well activity plots, is a powerful way of interpreting the observed seismic and to obtain insights about the areas that need to be improved in the model as well as identifying bypassed oil, gas outbreaks, the presence of new compartments, and even places where the structural interpretation might be reviewed. Figure 5.17 to Figure 5.24 show the well activity plots for the wells active during the period 1998 – 2004.

W1 – Injector: This well starts injecting almost when production started and stopped injecting nearly 1 year before the 2004 monitor was acquired. Available data shows that the pressure change at this well location is +0.5 MPa and saturation change is +0.45.

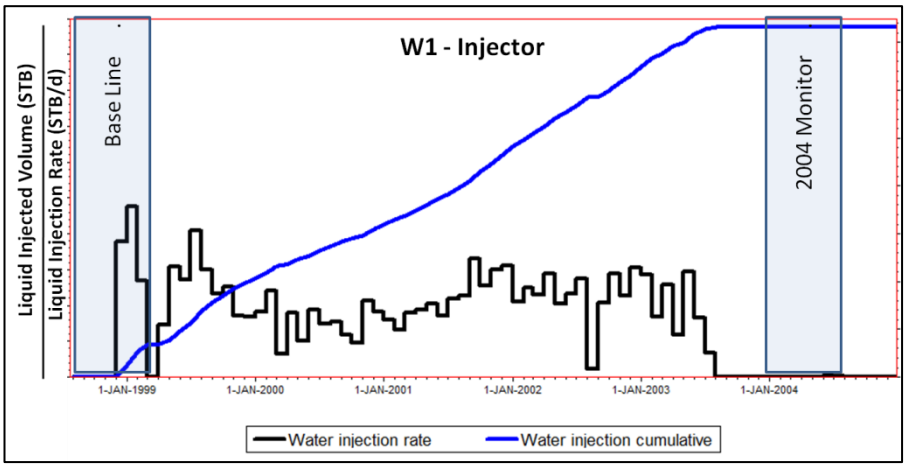

Figure 5.17: Well activity plot for W1, for the period 1998 - 2004

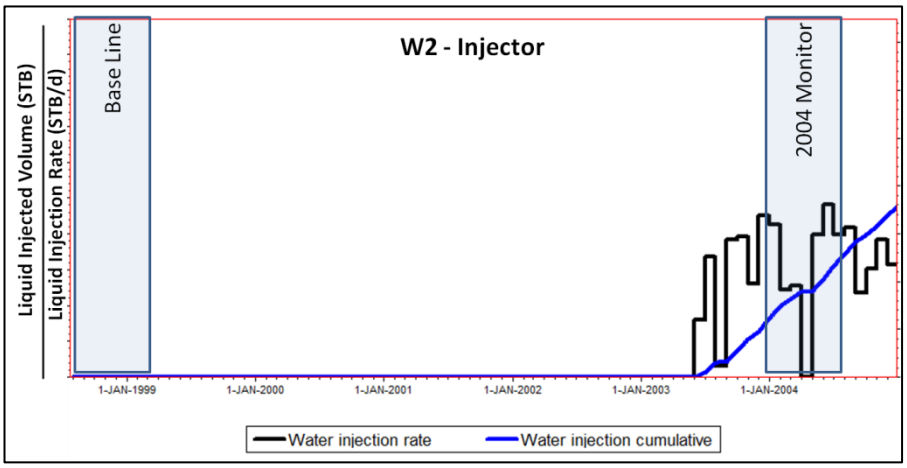

Figure 5.18: Well activity plot for W2, for the period 1998 - 2004

W2 – Injector: This well started injecting at the same time W1 stopped injecting, about 1 year before the acquisition of the 2004 monitor. Available data shows that the pressure change at this location is +3.5 M, with a water saturation change of +0.44.

W3 – Injector: This well has a similar activity as W2; it started injecting about 1 year before the acquisition of the 2004 monitor, although the injection rate decreased significantly at this time. Available data shows that the pressure change at this location is +2.1 MPa, with a water saturation change of +0.38.

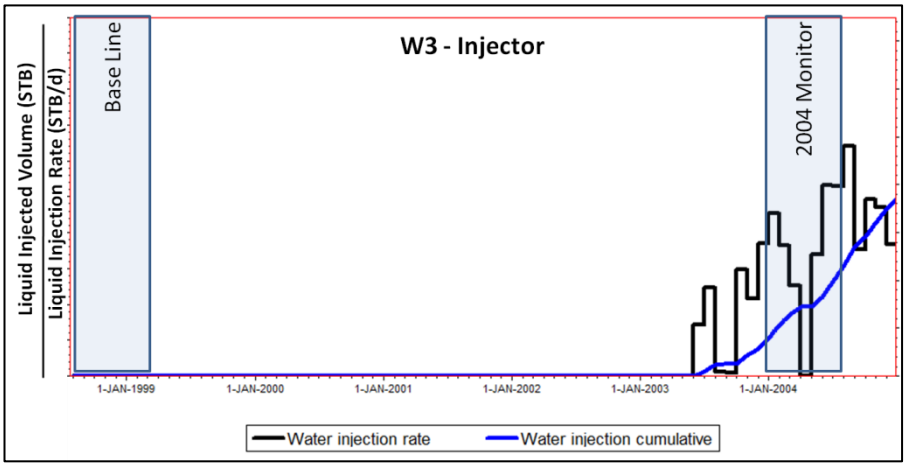

Figure 5.19: Well activity plot for W3, for the period 1998 - 2004

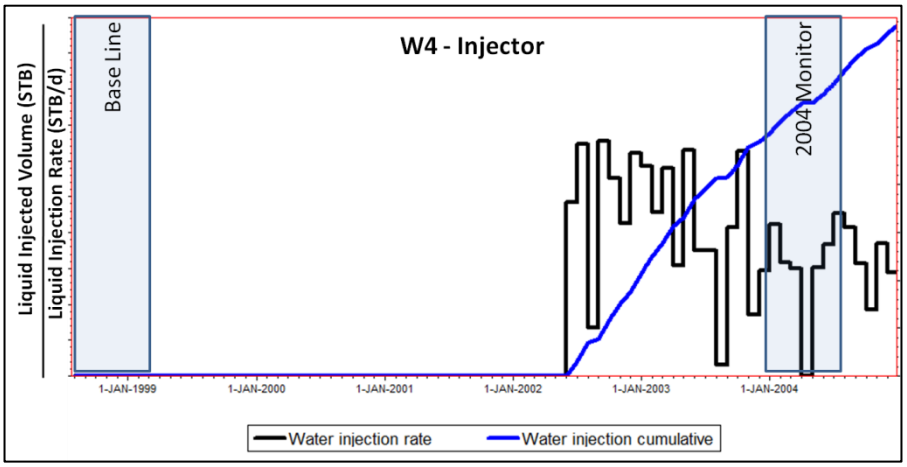

Figure 5.20: Well activity plot for W4, for the period 1998 – 2004

W4 – Injector: This well started injection by the end of 2002, initially at a high rate but reduced this rate towards the date of the 2004. Our data shows a pressure change of +12 MPa with a water saturation change of +0.45.

W5 – Injector: This well started injection right from the beginning of production but stopped one year before the 2004 monitor was shot. The simulation data shows a pore pressure change of +3.5 MPa and water saturation change of 0.34.

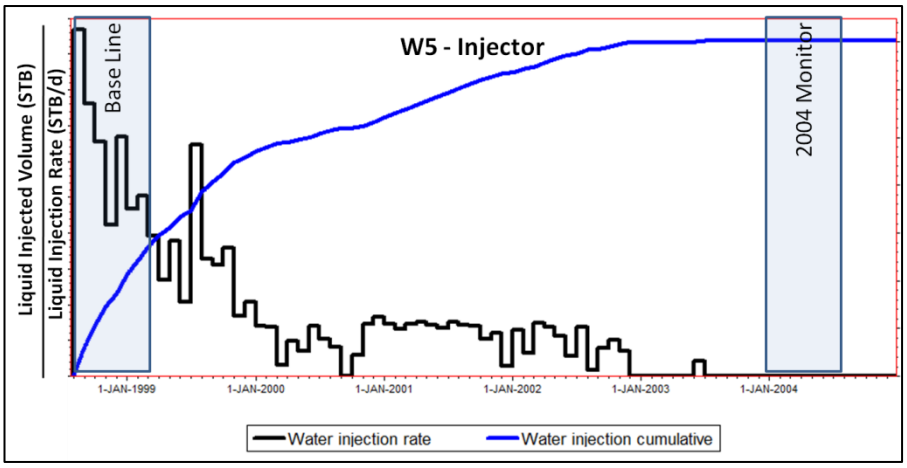

Figure 5.21: Well activity plot for W5, for the period 1998 - 2004

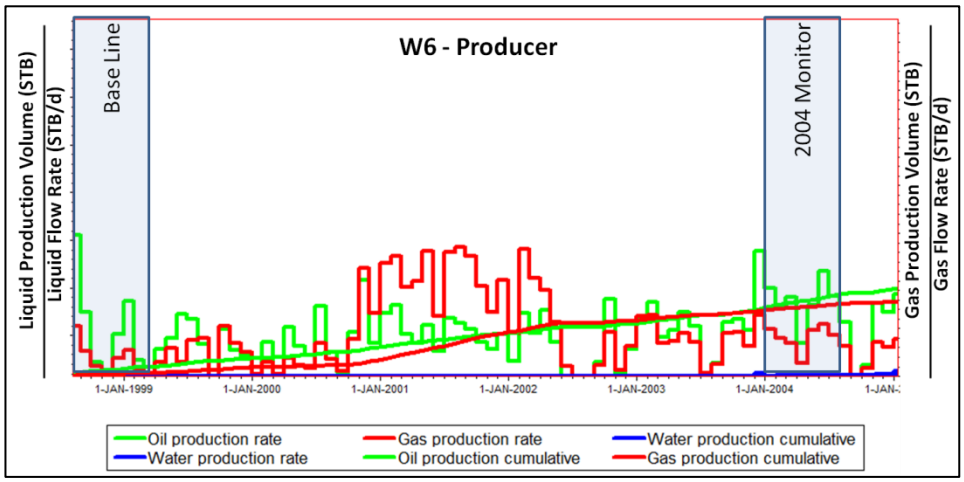

Figure 5.22: Well activity plot for W6, for the period 1998 - 2004

W6 – Producer: This well started production in 1998 and continued beyond the 2004 monitor acquisition. Large volumes of gas were produced in this well (gas coming out of solution). The cumulative gas curve shows that a strong gas response is expected at

this location; available data shows the next changes: $\Delta P = -2.1$ MPa, $\Delta S_w = 0.1$ and $\Delta S_g = +0.38$. To the west of this well, simulation data shows a massive change in gas saturation of 0.78, with a pressure change of – 4.5 MPa.

W7 – Producer: This well started production in 1999 and continued beyond the 2004 monitor acquisition. Large volumes of gas were also produced in this well (gas coming out of solution), however, the amount of gas produced had decreased by the time of the seismic acquisition. This well also shows a small water breakthrough at the end of 2003. The simulation data shows the next changes around this well: $\Delta P = -1.9$ MPa, $\Delta S_w = 0.13$ and $\Delta S_g = +0.2$, to the west of the well. Simulation data also shows a major change in gas saturation of 0.51, with a pressure change of – 2.53 MPa.

W8 – Producer: This well started production by the end of 2000 and stopped by the end of 2004, due to water breakthrough. Gas out of solution is also observed at this location, with large volumes of gas being produced. The simulation data shows the next changes around this well: $\Delta P = -1.2$ MPa, $\Delta S_w = 0.15$ and $\Delta S_g = +0.78$.

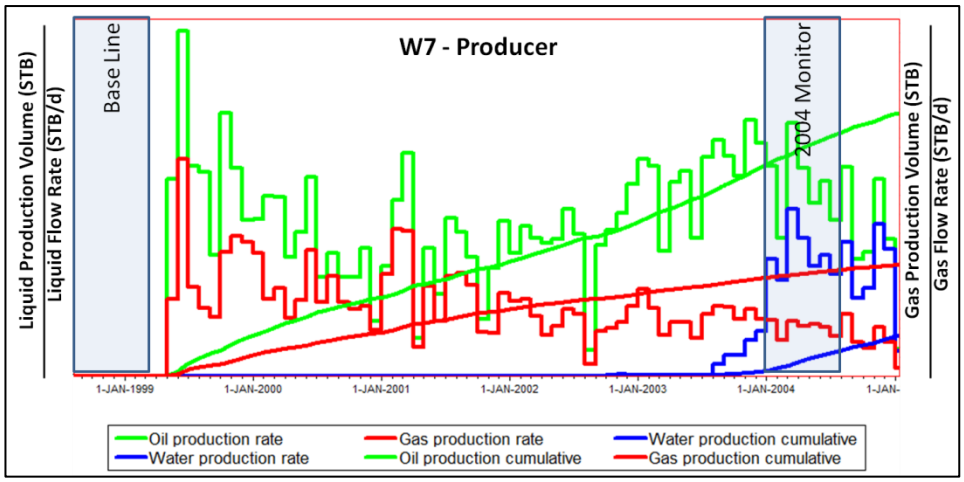

Figure 5.23: Well activity plot for W7, for the period 1998 - 2004

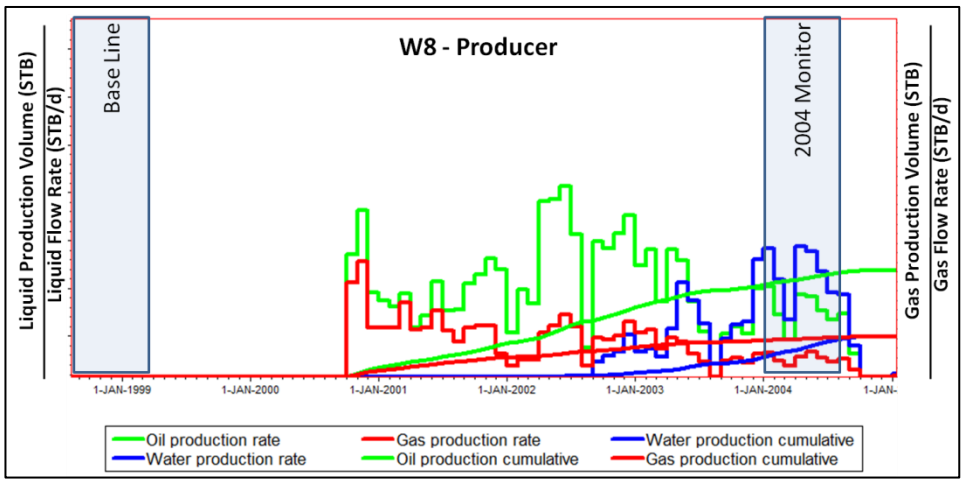

Figure 5.24: Well activity plot for W8, for the period 1998 – 2004

The results of equation 4.47 (which gives us the relative weights of the pressure, water and gas saturation responses), together with the well observations outlined above, allow us to provide a detailed interpretation of the observed 4D seismic. This interpretation is shown in **Figure 5.25**, from which the following observations can be made:

- Around W1, a water-flooding signal is observed, with a small section showing possible gas outbreak to the south-west of this well; this is currently not included in the simulation model. At W2, cancellation of the 4D signal is observed ($3.5\,C_P \approx 0.44\,C_S$), but to the east, a strong amplitude change (softening) is observed. In the previous interpretation, using the oil-water equations, this was interpreted as a potential pressure up signal. However, with the incorporation of the gas term in my equations, it is possible to determine that, given the magnitude of the seismic response and the magnitude of the pressure change at the well, the most likely interpretation is gas outbreak, which is not currently incorporated in the reservoir simulation model.

- At W3 and W5 a saturation related signal is observed and it shows the movement of the water front from these two injectors. Additionally, since water

breakthrough has been observed in well W6 and the equations developed here show that the presence of gas will dominate the water saturation signal, it is likely that the water flooding area related to W3 can be extended all the way to W6, implying that the major fault at the centre of the field is not sealing at this location. The red anomaly around W6 is consistent with the observations from the simulation and my predictions from equation 5.59.

- W8 shows strong gas breakout signals along the well trajectory and extending further to the North-West. These areas are not included in the available version of the simulation model.

- Around W7, the well activity plots show that the difference in the gas volumes between base and monitor are small. And from the modelled 4D seismic response it can be deduced that a strong gas signal is not expected at this location (despite the presence of gas outbreaks). Therefore we expect only weak gas related signals at the well location, which extend to the East, ending against the major fault at the South of the well.

- Regarding W4, this well injected at a very high rate and therefore the large signal observed beyond the well is related to pressure build up, and the observed decrease in 4D amplitude around the well is due to cancellation of pressure and water saturation signals. Since there is no visible pressure increase in W7 and the pressure up signal follows closely (although not exactly) the fault interpretation, it can be easily concluded that the fault between W7 and W4 is sealing. This analysis, however, is not so simple between W4 and W5, since the latter is an injector and therefore it has an associated pressure up signal. However, if we compare the magnitudes of the water-flooding signal around W5 with the partial cancellation of pressure up and saturation up signals at W4, it can be concluded that W4 is located in an isolated compartment.

Furthermore, the discontinuity in the softening anomaly areas to the South and South-East, give hints that additional sealing faults must be present, since the pressure build-up signal would be expected to be more uniform (as pressure diffuses rapidly into the reservoir).

As a result of these observations, it is possible to suggest an alternative interpretation of the faults in the area (**Figure 5.25**). My interpretation of the softening anomalies to the South-East is that these can be related to gas outbreak. This is supported by the fact that these areas are local structural highs and if we look at the simulation data, in 2008 two wells were drilled at these locations (W9 and W10 in the map), which only produced gas.

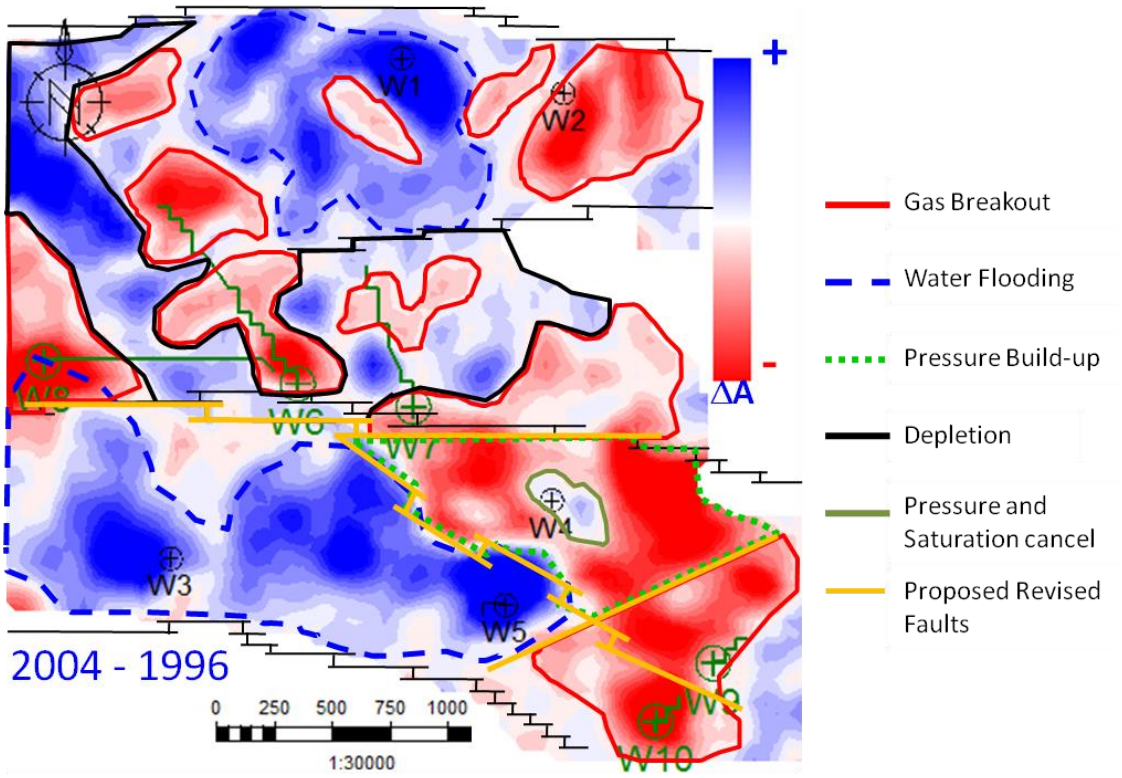

Figure 5.25: Interpretation of the observed 4D seismic signal performed using the modelled seismic response and the observations from the well activity plots. Of particular importance is to be able to differentiate pressure up signal from gas break-out signal and pressure depletion from water flooding. My suggested changes are shown in the orange lines.

5.5 Summary of findings in this chapter

- Equations applicable to fluid contact movement interpretations were found to be applicable to oil-water, gas-water and gas-oil contact movements, in reservoirs where the fluid contacts can be interpreted (picked), either in the base and monitor or directly in the 4D difference. These equations are applicable both above and below the bubble point pressure, as this is explicitly included in the fluid pressure sensitivity terms.

- The equations are expressed in such a way that parameters like S_{org}, S_{grw}, S_{wc} and S_{gro} are explicitly included and therefore directly relate to the petrophysics and engineering domains.

- An important observation resulting from my derivations is the fact that the time lapse responses ($\Delta A(\theta)_{owc}, \Delta A(\theta)_{gwc}$ and $\Delta A(\theta)_{goc}$) in the initial phases of production are subject to wavelet interferences (tuning), even if the pre- and post-production reflectivities of the contacts are above seismic resolution. As production continues and the original and produced contacts separate, the 4D response can appear above seismic resolution. The equations derived here provide a useful way of analysing this effect.

- Another important observation is that for fluid contact interpretation, the 4D AVO effects are subtle and the magnitude of the pressure response is much smaller than that related to saturation. This implies that fluid related effects can be more easily quantified by interpreting the fluid contacts in the 4D difference than by conventional interpretations based on the top of the reservoir.

- The fluid contact approximations have been incorporated into a final general equation applicable to three phase systems. This equation is applicable to

reservoirs where there is an associated tuning effect resulting from the fluid contact interactions (no individual reflections are visible for each contact). This equation is therefore applicable to map based interpretations where only top and base of the reservoir are interpreted, either for simplicity or when complex stratigraphy does not allow a more detailed interpretation

- It was found that the case of a reservoir with a pre-existing gas cap and that of a reservoir where a gas cap is formed by gas dissolution result in similar 4D responses. This happens because, below tuning, some of the terms associated with the different fluid-fluid interfaces cancel each other and therefore the resultant composite 4D difference is almost the same, with the exception of the fluid pressure sensitivity, which has a very small magnitude and is, in most cases, beyond detection.

- The general thin reservoir equation was tested in a real dataset and compared to the results of sim2seis, obtaining very similar results. This has the advantage that applying the equations takes considerably less effort and time than performing a sim2seis modelling, and most importantly, in my equations we can observe and interpret the contributions of the different fluid saturations and pressure separately. This, in sim2seis modelling, can only be done by generating multiple calculations, where pressure and saturation changes are modelled separately.

- It was shown in this chapter that the equations, combined with the well observations provide a simple and useful way of interpreting the observed 4D signal and can suggest changes to the existing models, as well as the identification of bypassed oil and pressure barriers, and also distinguish between softening signals related to gas out of solution and pressure build up, uncertainties in the fault interpretations, etc.

Chapter 6: Mapping and quantifying remaining oil saturation from 4D seismic data

"The scientist discovers a new type of material or energy and the engineer discovers a new use for it"

El científico descubre un nuevo tipo de material o energía y el ingeniero descubre una nueva forma de usarlos

Gordon Lindsay Glegg

Scottish Engineer and Writer

In this chapter, I present the development of a technique that allows the calculation of remaining oil saturation from the interpretation of the 4D amplitude differences at the original and produced contacts. The method is based on the derivations from Chapter 4 for the oil-water system and is tested in two datasets in the North Sea: first, a field with clear visible contacts and known low residual oil saturations, and second, a highly complex reservoir, where no fluid contacts are visible in the 3D seismic.

6.1 The importance of remaining oil saturation (ROS)

Accurate estimation of remaining hydrocarbon saturation is one of the main goals in reservoir monitoring and surveillance. The importance of this property is that it is used to evaluate the recovery factor, a key parameter that is used to define the strategy of production optimization in any reservoir (e.g. secondary and tertiary recovery). For reservoir management purposes, it would be useful to quantify the amount of residual oil that remains behind after oil is displaced by water due to basal or edge water drive in a reservoir. These are defined in this work as residual oil saturation (ROS) at the field scale and residual oil saturation (S_{orw}) at the pore scale. Quantitative knowledge of the spatial location of the fluids is a key input in the decision-making process and ROS can be used to define the target oil for any EOR process after waterflooding. A proper understanding of the level and distribution of ROS will lead to more appropriate plans for further recovery methods to mobilise and extract the oil (Improved oil recovery – IOR).

In Chapter 4, it was shown that the 4D difference reflectivity can be mathematically described as a combination of the different fluid contact movement interactions, and the resulting equations revealed an explicit connection with the amount of residual hydrocarbon saturation. This implies that, in principle, it should be possible to determine the residual hydrocarbon saturations from the 4D difference directly. In this chapter I focus on the application of this technique to oil reservoirs.

6.2 Definition of residual oil saturation (S_{orw}) and scale dependence.

Residual oil saturation is oil saturation that cannot be produced from an oil reservoir from the water displacement and it is usually considered the immobile oil saturation after conventional water displacement. Much effort has gone into the study of residual oil over the past 50 years in petroleum engineering research, as it is one of the key parameters for reservoir recovery and carrying out economic evaluation. At the pore

scale and in the laboratory, residual oil is described by the oil saturation, S_{orw}, representing the end-point at which the oil relative permeability to water vanishes to zero, and hence, the oil is trapped by the invading water. The other end-point is defined by the connate water saturation S_{wc} (Figure 6.1); both points are important as input into numerical flow simulation studies.

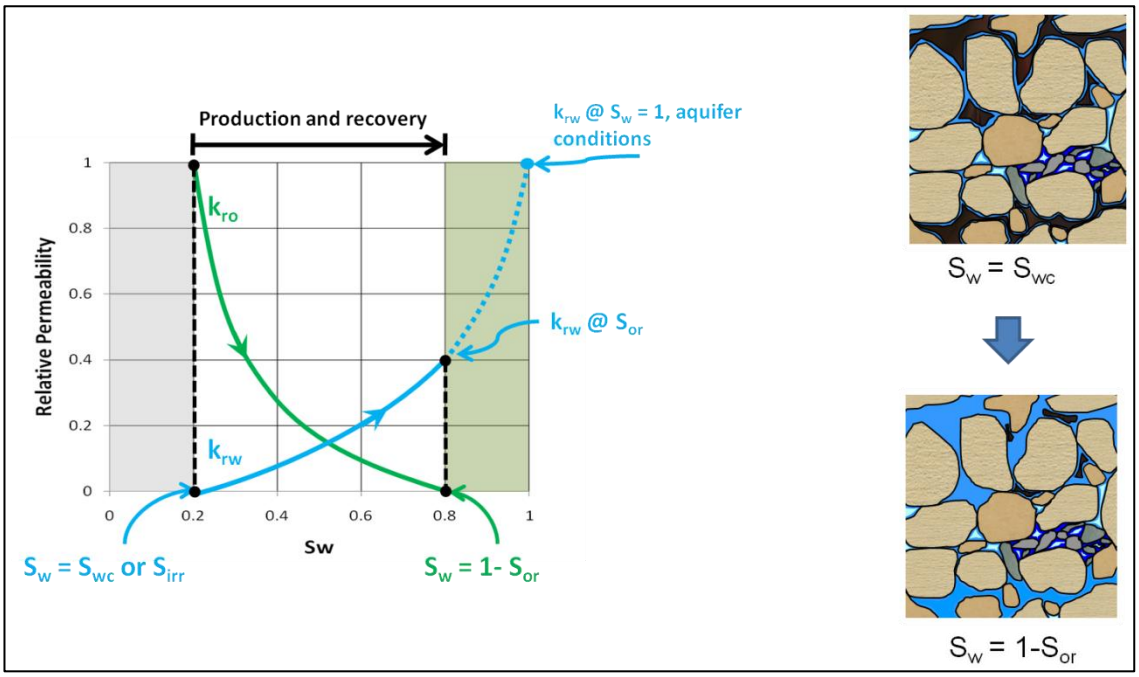

Figure 6.1: At pore scale, S_{orw} is commonly defined using the relative permeability curves (left) as the minimum oil saturation that cannot be replaced by water flooding (right).

At the core scales, however, the value of S_{orw} can change, as pore space heterogeneity can produce irregular water flow, leading to the presence of heterogeneous fluid saturations. Such patches at the pore scale can be seen as oil saturated zones, but at core scale they are immobile, and therefore can be classified as residual (Figure 6.2).

At larger reservoir scales, residual/remaining oil becomes a function of the geological environment, as trapping can occur in small-scale laminae and cross-bedding (Pickup and Hern, 2002) – affected by reservoir heterogeneity (Figure 6.3).

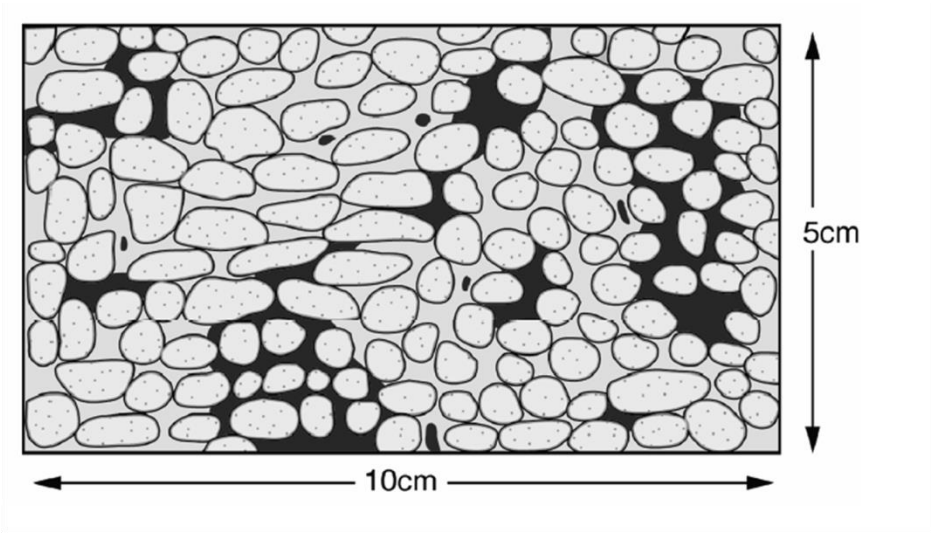

Figure 6.2: Core-scale saturation, in which there is additional residual oil due to pore space heterogeneity (MacBeth and Stephen, 2006).

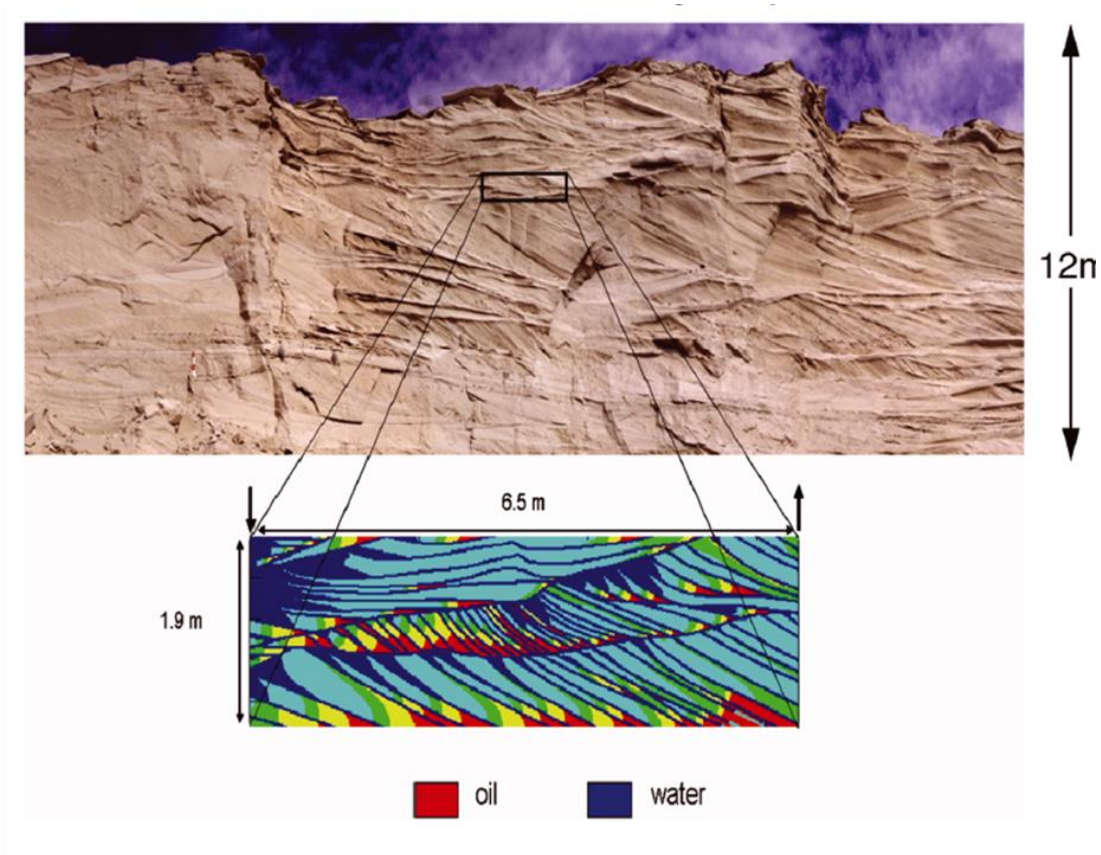

Figure 6.3: Individual bed scale where trapping of remaining oil in laminae is visible (after Pickup and Hern, 2002).

There are many factors, acting at both the macroscopic and microscopic scales that affect the magnitude of S_{orw}. At the pore scale, the most important factor is wettability and S_{orw} is found to be lower for the more strongly water-wet cases. For example, Ryazanov (2012) and others show that S_{orw} can drop from 30% to 10% when we move from an oil-wet reservoir to a water-wet reservoir. Clean rock samples for most oil reservoirs are water wet, but in real conditions, they are far from this ideal. Pore structure/pore size, texture, geometry, roughness, clay content and the fluid dynamics (gravity, viscosity, capillary forces) influence the magnitude of S_{orw} at the pore scale. At the reservoir scale, sedimentological structure-stratal forms, heterogeneities, lithologies, faults and fractures, barriers, formation/oil and water properties, gas saturation influence the magnitude of S_{orw}. At the production scale, there is a strong relationship between the speed of the water displacement, the forces in the pore volume controlling the fluid flow and distribution, and the amount of remaining oil. Important factors are well behaviour, injection and production rate, speed of waterfront, pressure gradients in general, well fluid flow dynamics and gravity.

The obvious conclusion from all these observations is that the value of S_{orw} is very different, depending on the scale at which it is measured and the efficiency of the water replacement mechanism we are dealing with. A generality can be drawn, however, in terms of their relative magnitudes:

$$S_{orw}^{pore} < S_{orw}^{core} < S_{orw}^{field} \tag{6.1}$$

6.3 Common methods to calculate S_{orw}

A common way of estimating residual hydrocarbon saturation is based on special core analysis tests (SCAL). Here, a core rock sample in the shape of a cylinder is taken from a reservoir, saturated with oil and then this is displaced (pushed out) with either water or gas. The test ends when no more oil can be produced from the core. The oil that cannot be pushed out and remains in the core is defined as the "residual oil“, which

corresponds to the lowest achievable capillary pressure during the experiment. The assumption of these measurements is that the fluid saturations are uniformly distributed with respect to reservoir thickness. However, in practice, sometimes we deal with non-uniform fluid distributions in the vertical direction, and therefore reservoir engineers must also calculate a relative permeability distribution with respect to thickness (Dake, 1998). Another issue with core based measurements is that these do not provide a reasonable sampling of the reservoir, and hence do not incorporate lateral variations in capillary pressure.

Occasionally, if a zone in a reservoir is producing only water, it may be assumed that the oil has been completely displaced. In this case, special tools are lowered into the well, and the remaining oil saturation is determined. This residual is considered a field estimate, although this again does not take into account lateral or vertical variations.

Material balance is also used as an indirect way of estimating the amount of residual hydrocarbons based on the estimate of the "stock tank" oil initially in place (STOIIP) and the production to date. However, both STOIIP and produced volumes carry high uncertainties. This information also goes into dynamic simulation, where fluid flow equations are used to come up with a series of probabilistic scenarios that show how S_{orw} is likely to be distributed. The information obtained from the relative permeability measurements is commonly used as a constraint during the dynamic simulation process.

From the above, it is generally acknowledged that there is no standard way to reliably predict residual/remaining oil saturation, particularly at the reservoir and production scale. It would therefore be useful to find alternative ways of calculating this parameter and thus provide a more realistic estimate of the volumes of hydrocarbons that are bypassed during production. In this work I suggest the use of 4D seismic data in a quantitative way to provide a lateral constraint in the estimation of residual hydrocarbon saturations. Seismic data can detect horizontal scales of 12.5m and vertical scales between 5 – 20 m, depending on the seismic frequency, processing,

acquisition, depth of the reservoir and geographical area of interest. 4D can also give us an indication of fluid contact movements, which are usually quite clear (e.g. Staples, et al., 2007) and water-floods are detected (Kloostermann, et al., 2000). However the magnitude of the changes are not typically considered and the results remain mostly qualitative and only supported by seismic modelling. The work here digs deeper and shows how we can quantify the remaining oil using the 4D seismic and provide a field-wide estimate of S_{orw} (which is commonly known as ROS).

6.4 Residual versus irreducible fluid saturations

It is important for this work to differentiate between residual and irreducible saturations. I have shown above that the value of S_{orw} is scale dependent and that the relative magnitudes of the residual oil are defined as expressed in equation 5.1. At pore scales, the value of S_{orw} refers to the minimum amount of oil possible in the rock that cannot be further reduced under present reservoir conditions, therefore,

$$S_{orw}^{pore} = S_{oir} \quad , \tag{6.2}$$

where S_{oir} is the irreducible oil saturation, and its magnitude depends mainly on these factors:

- wettability – The ability of a fluid phase to preferentially wet a solid surface in the presence of a second immiscible phase. In our case S_{oir} will change depending on whether our sample is a water wet or oil wet rock.
- pore structure – pore size, texture, geometry, roughness
- clay content
- fluid dynamics – gravity, viscosity, capillary forces

For the purposes of this work, we will refer to the pore scale residual oil saturation as the irreducible oil saturation. At larger scales, the remaining oil saturation is not necessarily equal to the irreducible saturation and hence I call it ROS. In fact, the main objective of being able to quantify S_{orw} at large scales (ROS) is to be able to identify

areas of bypassed oil or places where we can attempt to reduce the value of ROS (ideally to the value of S_{oir}), through enhanced oil recovery mechanisms; thus:

$$S_{oir} \leq ROS \quad . \tag{6.3}$$

At the reservoir scale, ROS can be larger or equal to the irreducible oil saturation, depending on the following factors:

- Geological heterogeneity: sedimentological structures, facies, faults and fractures, etc.
- Formation oil and water properties
- Gas saturation – in situ or out of solution
- Fluid flow dynamics and gravity – aquifer influx (or lack of)
- Well behaviour: injection and production rate, speed of waterfront
- Pressure gradients in general.

Similar observations apply to the connate water saturation (S_{wc}). The term connate refers to the liquids that were trapped in the pores of sedimentary rocks as they were deposited. Normally, the amount of connate water present in a conventional reservoir can be between 10 − 25% of the pore volume (Dake, 1998). As with the oil saturation, connate water (S_{wc}) is not necessarily the same as irreducible water saturation (S_{wir}), especially in the transition zone between oil and water. However, in reservoirs with high in-situ capillary pressure, connate water saturation approaches the irreducible stage (Xu, et al., 2013), hence,

$$S_{wir} \leq S_{wc} \ . \tag{6.4}$$

The magnitude of S_{wc} with respect to S_{wir} depends on the way the fluids are arranged inside the reservoir (Zhou et al., 2000); when oil migrates into a reservoir structure assumed to be water-wet, oil replaces water over thousands of years, until the fluids reach pressure equilibrium. If the reservoir is thick enough, at the top of the structure

the rock will be oil-wet, with a small amount of connate water that could not be replaced by the oil during migration ($S_{wc} = S_{wir}$). As we move deeper, the amount of connate water remains almost constant until we reach the oil-water contact (OWC). From here, connate water increases exponentially down to the free water level (FWL); this is called the transition zone, which is where the rock goes from an oil-wet to a water-wet phase. The distribution of S_{wc} is determined by the pressure difference between the oil and water phases, which is a function of capillary pressure. Oil migrating into a water-wet reservoir would display larger transition zones than a reservoir that started as an oil-wet rock (Buckley, 1997).

The size of the transition zone in the in-situ conditions can vary from a few centimetres to hundreds of metres and can be determined through a combination of the core-based capillary pressure measurements and relative permeability tests, which form the basis of saturation height functions in well log analysis. These functions define the elevation (height) of the reservoir above the free water level.

The shape of the capillary pressure and relative permeability curves also determines the way the reservoir will produce. Figure 6.4 shows a schematic representation of how the fluids are arranged inside a reservoir and their relation with capillary pressures, relative permeabilities and the production behaviour. The top graphic represents the reservoir depth, the middle graphic shows the capillary pressure curves and the bottom plot is the water cut: all three quantities are plotted versus water saturation. The point A in the top graphic represents the irreducible water saturation obtained from capillary pressure curves projected on the height function; production will be water free above this depth. Point B is obtained by the intersection of the oil and water permeability curves and, projected into the depth plot, it shows the height at which the water cut will be about 50% (hence the reservoir produces 50% oil and 50% water). Point **C** represents the irreducible oil saturation (S_{oir}), which projected onto the depth plot gives the elevation at which the reservoir will start producing only water (Crain, 1986). The implication of this plot is that, as the fluid contact rises, the transition zone grows, and therefore, depending on the factors mentioned above, the value of S_{orw} can

be found anywhere between 1- S_{wc} and S_{oir}. It is this large scale value of S_{orw} (ROS) I am interested in calculating from 4D seismic.

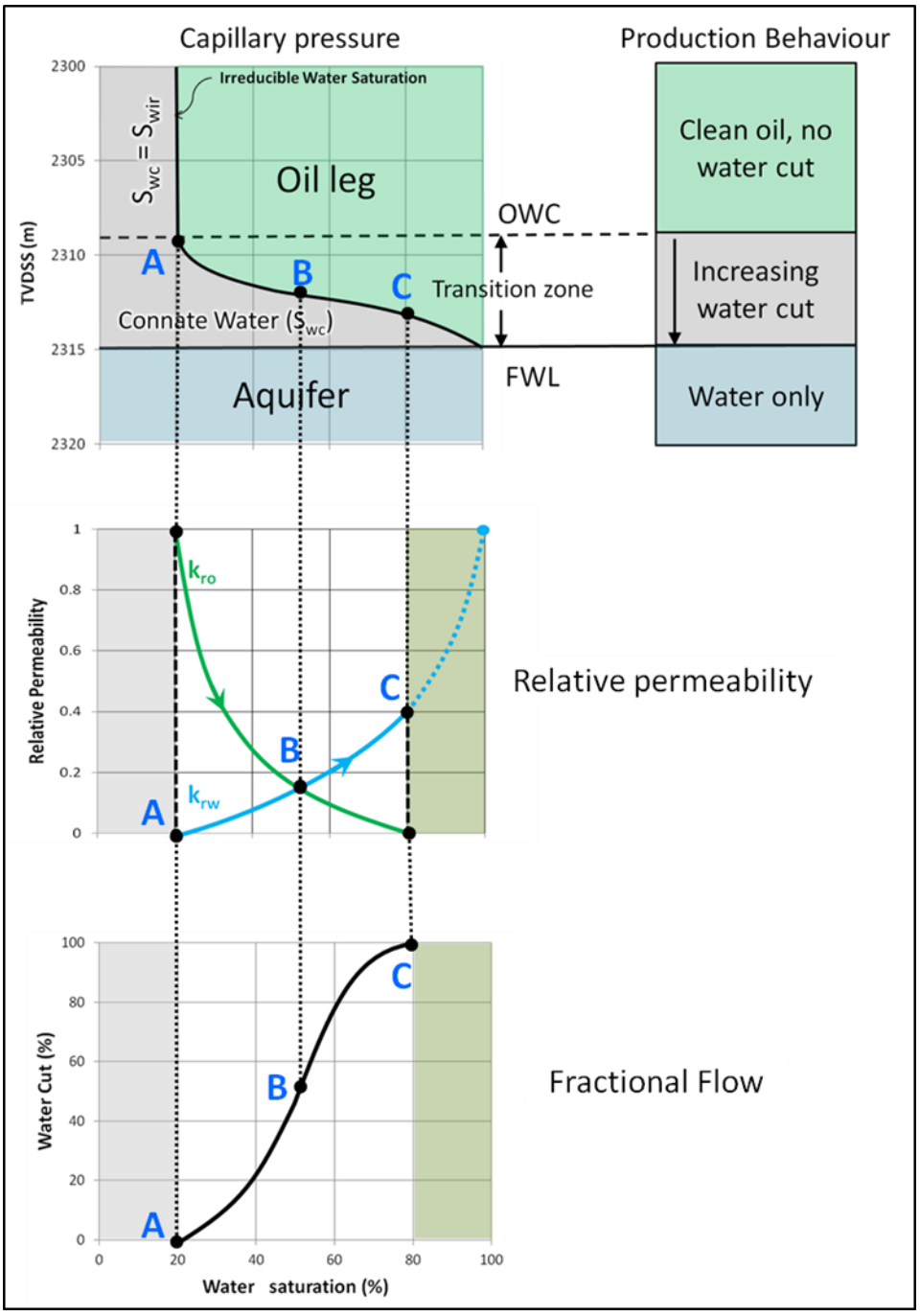

Figure 6.4: Schematic representation of the fluid arrangements in an oil-water reservoir and their relation to capillary pressure, relative permeability and production behaviour (modified from Crain, 1986; Engler, 2010).

6.5 Using 4D seismic to estimate ROS

From the results shown in Chapter 4 it can be deduced that the far angle reflection coefficients at the original OWC before and after production are given by these equations:

$$A(\theta)_{\text{oowc}}^{\text{before}} \approx \left[\frac{(1 - S_{wc}\,)}{S_{wc}}\, C_S^o\right] \text{s(t)} \quad \text{and} \quad A(\theta)_{\text{oowc}}^{\text{after}} = \left[\frac{\text{ROS}}{S_{wc}}\, C_S^o\right]\, \text{s(t)}\,. \tag{6.5}$$

Combining both results, we can find a simple relation to determine ROS:

$$\text{ROS} = (1 - S_{wc})\, \frac{A(\theta)_{\text{oowc}}^{\text{after}}}{A(\theta)_{\text{oowc}}^{\text{before}}}\ . \tag{6.6}$$

The obvious advantage of this equation is that it is independent of the rock and fluid physics and the wavelet, and depends only on the value of S_{wc}. Although in this case S_{wc} has been kept constant, in practice, changes in S_{wc} can occur in reservoirs with complex stratigraphic changes that cause changes in the pore throat size. Nevertheless, if lateral changes in S_{wc} are incorporated during geological modelling, it would be possible to include them in the calculations. However, equation 6.6 can only be used when the fluid contacts are observable and interpretable in the 3D seismic. The main drawback of equation 6.6 is that, if the amplitude of the original OWC after production goes below the noise levels and approaches zero, ROS will tend to zero, unless the result is normalised between S_{oir} and S_{wir}.

Another alternative is to define an equation that works for the 4D amplitude differences, by incorporating our definition of the time lapse reflectivity at the original oil-water contact at the far angles:

$$\Delta A_{oowc}^{far} = \left\{\frac{(1 - \text{ROS} - S_{wc})}{S_{wc}} C_S^o\right\}\, \text{s(t)}\,. \tag{6.7}$$

We know that for an oil-water system the pressure term decreases with angle of incidence (Chapter 2); therefore, if we use a mapped far angle amplitude response, we can neglect the pressure term and ROS can be calculated as follows:

$$\mathrm{ROS} = 1 - S_{wc}\left[1 - \frac{\Delta A^{far}_{oowc}}{\mathrm{C}^{o}_{S}\ \mathrm{s(t)}}\right] \quad . \tag{6.8}$$

The scaling s represents the wavelet, which, since we are working with maps, is reduced to a constant that can be determined from the well tie. The calculation of the constant $\mathrm{C_S}$ is generally straightforward, as it depends on the bulk modulus and density of the fluids, reservoir porosity and the average velocity of the reservoir at the initial conditions:

$$\mathrm{C}^{o}_{S} = \phi\left[\Gamma_1 \frac{\varepsilon}{\overline{M^{\mathrm{b}}}} \frac{S_{wc}\left(\kappa^{b}_{w} - \kappa^{b}_{o}\right)}{\left(\frac{\kappa^{b}_{o}}{\kappa^{b}_{w}} - 1\right)S_{wir} + \left(\frac{\kappa^{b}_{w}}{\kappa^{b}_{o}} - 1\right)S_{oir} + 1} + \Gamma_2 \frac{S_{wc}\left(\rho^{b}_{w} - \rho^{b}_{o}\right)}{\overline{\rho^{\mathrm{b}}}}\right] \quad . \tag{6.9}$$

It is important to note that the constants S_{wir} and S_{oir} in equation 6.9 establish the physical limits of the solution, represented by the pore scale limits of S_{orw} and S_{wc}, which can be obtained from the conventional SCAL measurements. Besides removing the need for empirical normalisation, the dependence of equation 6.8 on the rock and fluid physics gives the opportunity to perform uncertainty analysis on both S_{or} and the rock and fluid physics parameters, in particular the compressibilities of the fluids that are important parameters in reservoir engineering.

Nevertheless, the main disadvantage of equation 6.8 is that, as shown in Chapter 4, the 4D signature of fluid contacts is expected to be subject to tuning effects, at least until the fluid contact rises beyond the tuning thickness (assuming an active aquifer influx and that the reservoir is thick enough to allow this). This implies that, in the majority of cases, we have to deal with a seismic response that is subject to wavelet interferences, regardless of whether the fluid contacts are above or below tuning in the 3D seismic. I also showed in Chapter 4 that the 4D response of the original contact is the same as in

the produced contact, but with opposite sign. Based on this calculation, I found the mapped composite 4D seismic response below tuning at the far angles can be approximated as follows:

$$\Delta A(\theta)_{\text{owc}}^{\text{comp}} = \left\{ \frac{(1 - \text{ROS} - S_{wc})}{S_{wc}} C_S^o \right\} \Delta t_o \dot{s}(t) \quad . \tag{6.10}$$

Here, Δt_o is the two-way time thickness of the fluid contact movement, and $\dot{s}(t)$ is the time derivative of the wavelet (equivalent to the quadrature of the 4D difference). Using this equation we can find the remaining oil saturation through the next equation:

$$\text{ROS} = 1 - S_{wc}\left[1 - \frac{\Delta A_{comp}^{far}}{C_S^o \ \Delta t_o \ \dot{s(t)}}\right] \ . \tag{6.11}$$

The most important advantage of equation 6.11 is that it can be applied to thin reservoirs where the fluid contacts are not visible. However, it is important to note that the result will depend fully on our ability to calibrate the rock physics parameters in the field.

6.6 Application of the equations to a thick reservoir with visible contacts

To demonstrate the validity and applicability of the equations, I selected a North Sea dataset, with a reservoir thickness above tuning thickness and where the original fluid contact is clearly visible and interpretable in the pre-production base line (Figure 6.5), as confirmed by well measurements. The reservoir consists of high quality turbidite sandstones with 90% NTG and 26% porosity. The reservoir sands were deposited against a structural high associated with salt movement and the structure is dip closed and filled with oil of 37° API.

6.6.1 *Reservoir background*

The field was originally developed with one vertical well (W1); 9 years later, a horizontal infill well (W2) was drilled based on 4D seismic. A pre-production base line was shot in 1997, followed by monitors 9 and 13 years after production. Repeatability is excellent for a streamer acquisition, with NRMS in the order of 3 - 5%. Pressure support in the reservoir is weak, leading to a low recovery factor, despite the high porosity and high permeability of the rock. The total depletion after 13 years, as measured in the wells, is about -3 MPa (-450 psi) and the reservoir pressure is still above the bubble point pressure (Figure 6.6)

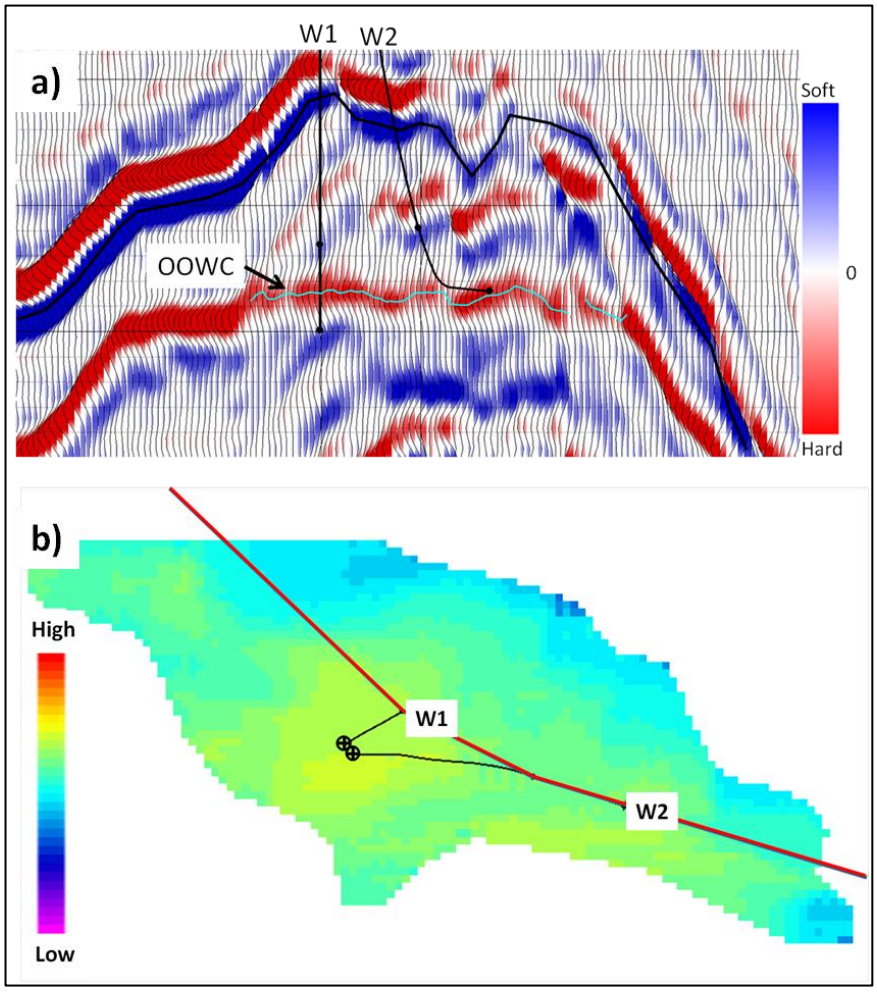

Figure 6.5: (a) cross section taken on the pre-production base line; the position of the OOWC in two-way time is represented by the light blue horizon, which is also shown in the map view (b), the red line shows the direction of the cross-section.

The field was originally developed with only one producer (W1), which produced clean oil for nearly one year and then started producing water. By the time of the first 4D acquisition, the water cut was higher than 60%, which indicates that on average, ROS is around 40% (Figure 6.7). At the time the second seismic monitor was acquired, production had decreased significantly, and ROS is expected to be near to the minimum (20-30%). Well W2 was drilled following the results of the first 4D monitor, which showed an area where oil was thought to be un-swept. W2 produced clean oil for about 3 years, much longer than W1, and by the time of the second monitor it still showed a low water cut of around 20%, suggesting a high ROS, even after four years of production (Figure 6.8).

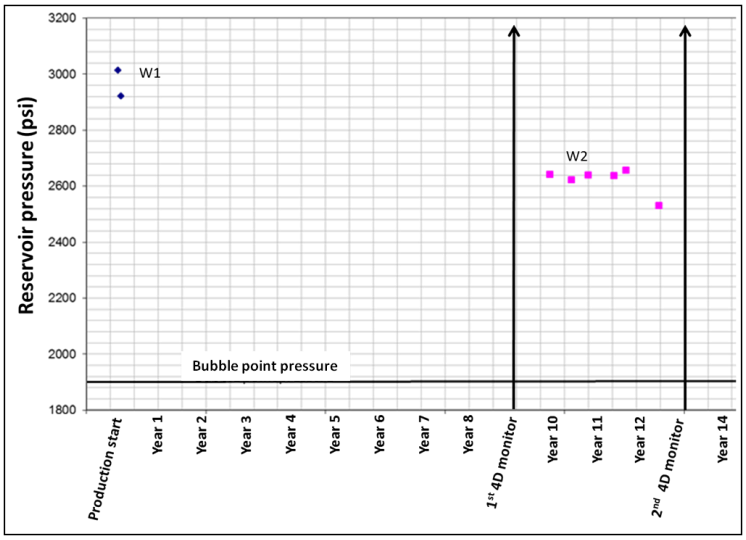

Figure 6.6: Pressure measurements taken from wells W1 and W2. The black line at the bottom shows the bubble point pressure as a reference. The arrows show the times of the monitor acquisitions.

The reservoir and petroelastic parameters available for the field are summarised in Table 6-1. Special core analysis tests were taken in W1, providing the values $S_{wc} = S_{wir} = 0.32$ and $S_{oir} = 0.22$, as illustrated in Figure 6.9. The crossover between the oil and water permeability curves is around 60%, which is consistent with the observed water cut obtained in W1. From the curves, it is also possible to determine that, depending on sweep efficiency, the value of ROS will be found between 0.22 and 0.68. Unfortunately,

no core measurements were taken in W2, but from the production obtained and the water cut observed, it is clear that the value of ROS is higher than that observed at W1.

Table 6-1: Table of reservoir and petroelastic parameters used for this exercise.

Reservoir Parameters		
Oil Gravity	37	API
Overburden Pressure	41.29	MPa
Reservoir Pressure	20.41	MPa
Bubble point pressure	12.20	MPa
Temp	90.55	C
Water salinity	72515	ppm
Porosity	0.28	fraction
NTG	0.95	fraction
Oil bulk modulus (κ_o)	0.628	GPa
Water bulk modulus (κ_w)	2.785	GPa
Oil density (ρ_o)	741	kg/m^3
Water density (ρ_w)	1080	kg/m^3
Average reservoir P-velocity	2.563	km/s
Average reservoir S-velocity	1.382	km/s
Average reservoir density	2053	kg/m^3
Pore stiffness factor (ε)	6.92	unit-less

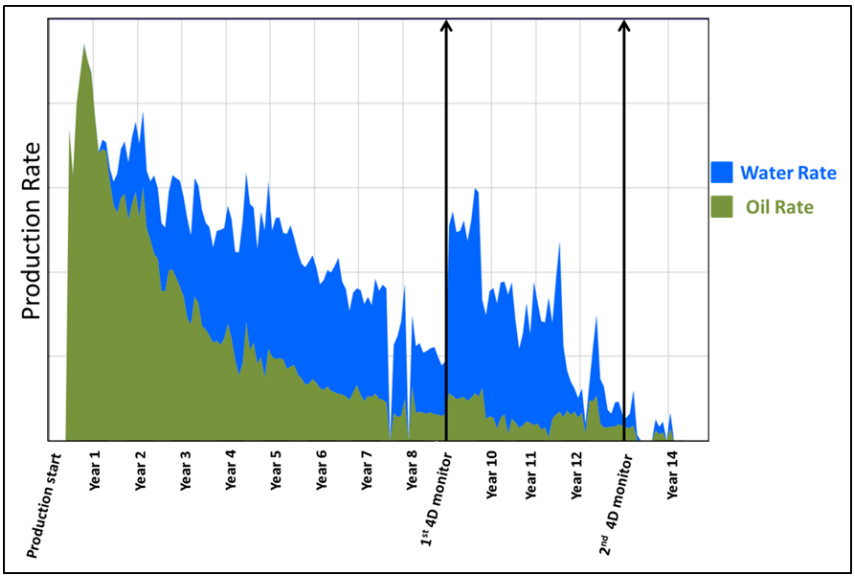

Figure 6.7: Activity plot for W1 showing the oil and water rates produced. The black arrows show the times at which the 4D seismic was acquired.

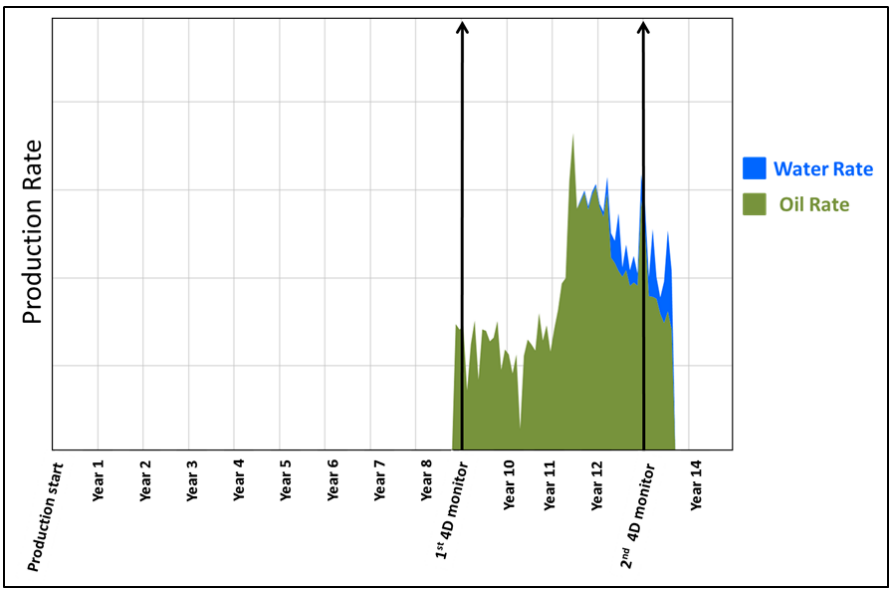

Figure 6.8: Activity plot for W2, showing the oil and water rates produced. The black arrows show the times at which 4D seismic was acquired.

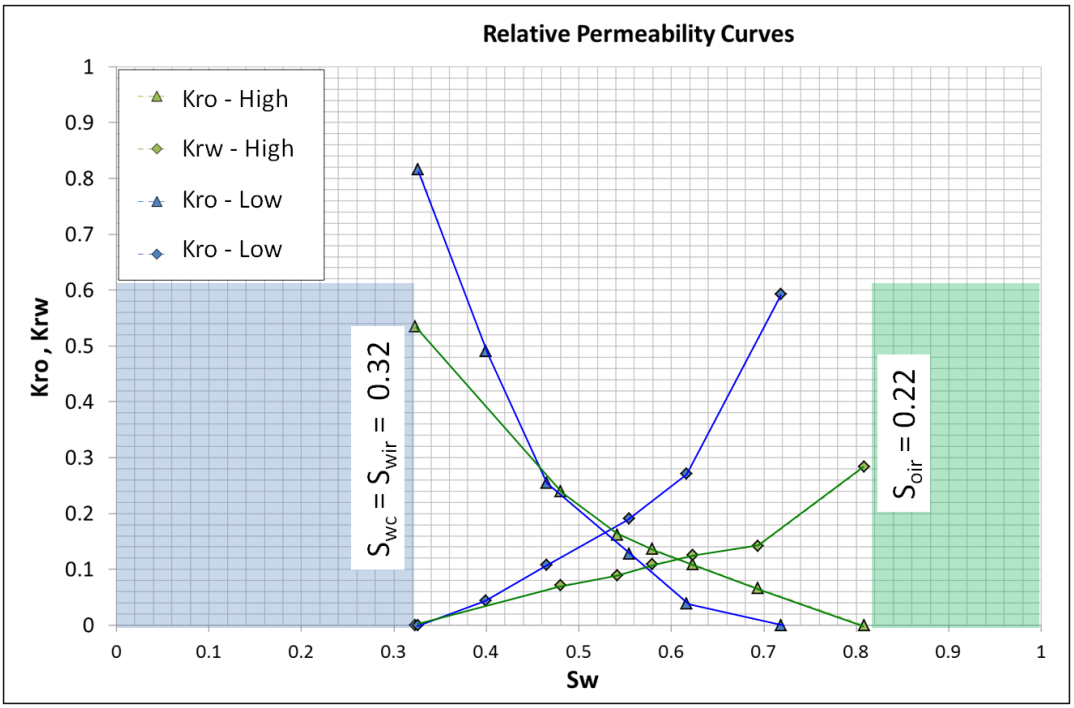

Figure 6.9: Relative permeability curves from SCAL for my field example, showing the values of the irreducible fluid saturations. Blue and green curves show measurements at different injection rates.

6.6.2 Calculation of ROS from 3D and 4D amplitude maps

Cross-sections of the 3D and 4D amplitudes showing the changes around the OOWC are displayed in Figure 6.10 and Figure 6.11. The exercise consists of extracting the mapped amplitudes and then calculating ROS, using equation 6.6 (based on 3D amplitudes of the OOWC), 6.8 (based on the 4D difference and thick reservoir equation) and 6.11 (using quadrature differences and the thin reservoir approximation). Finally I compare the results and find which method provides the most reliable results by comparison with well observations.

First, using the interpreted OOWC, amplitude maps are extracted of the base and monitor using a small window around the horizon. The extracted maps are illustrated in Figure 6.12, together with the calculation of ROS using equation 6.6, adjusted to lie between 0.22 and 0.68 (as seen in the capillary pressure curves). It is important to note that, in the monitor, the amplitude of the OOWC tends to zero in some areas. This suggests that the sweep has been efficient, and that the residual hydrocarbons are not large enough to produce a meaningful reflection in the monitor. As a consequence, the map shows areas with near-zero amplitude, which are translated into fixed values of ROS equal to 0.22 during the calculations. Different window sizes were tested to minimise this effect and it was found that the optimal way of extracting the amplitude was using a 10 ms window.

For the second case, the interpretation of the OOWC was picked using the 4D difference (reflectivity) on a trace by trace basis, and the amplitude was extracted at the intersection of the horizon. ROS was calculated using equation 6.8. Unlike in the first case, the maps obtained show higher resolution, better character and did not require a normalisation. However, any uncertainty in the rock physics parameters involved or in the calculation of the wavelet scalar will be incorporated as an error in ROS.

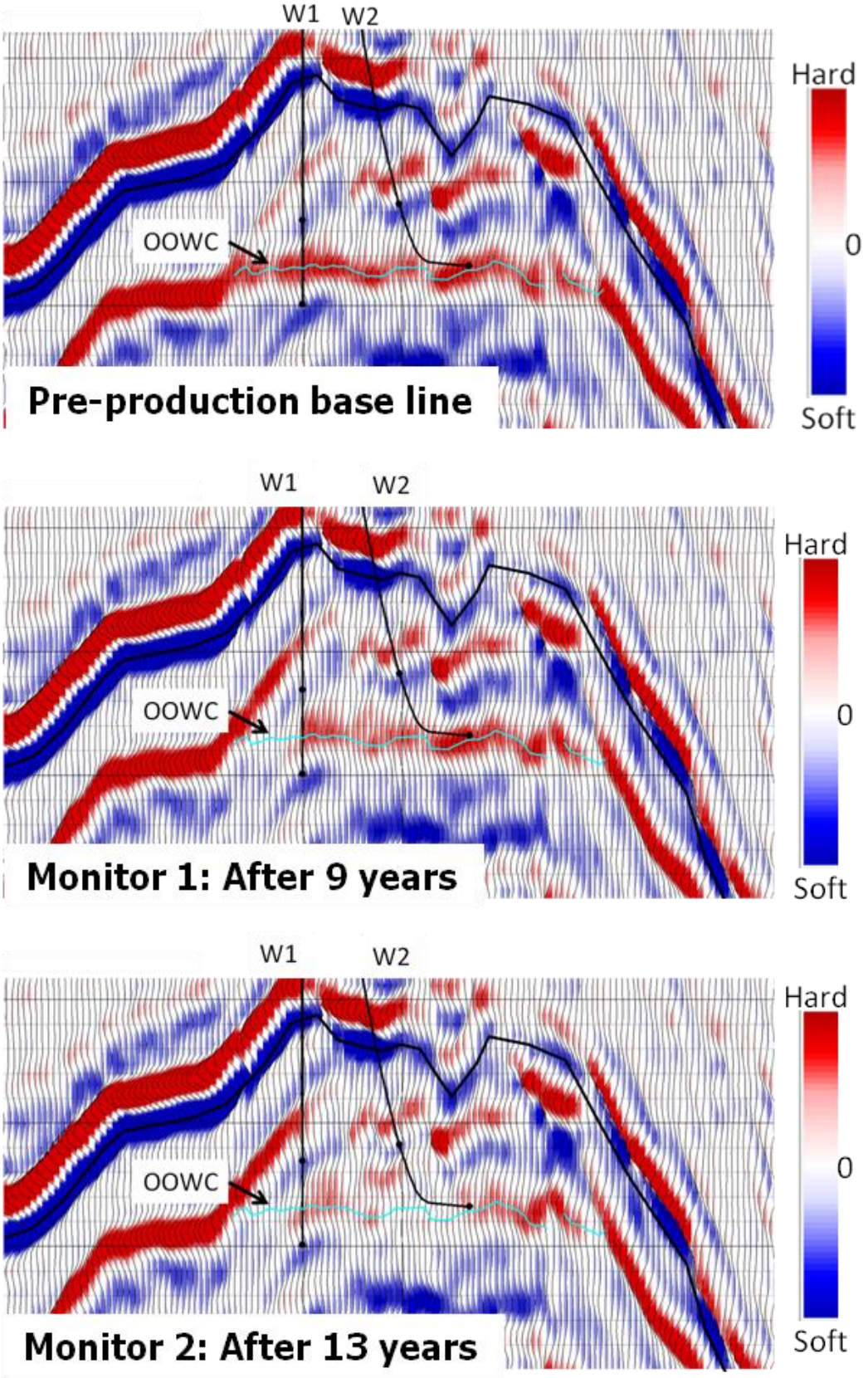

Figure 6.10: Cross-sections of the 3D amplitudes, showing the changes around the OOWC (light blue horizon). The black horizon is the top reservoir interpretation.

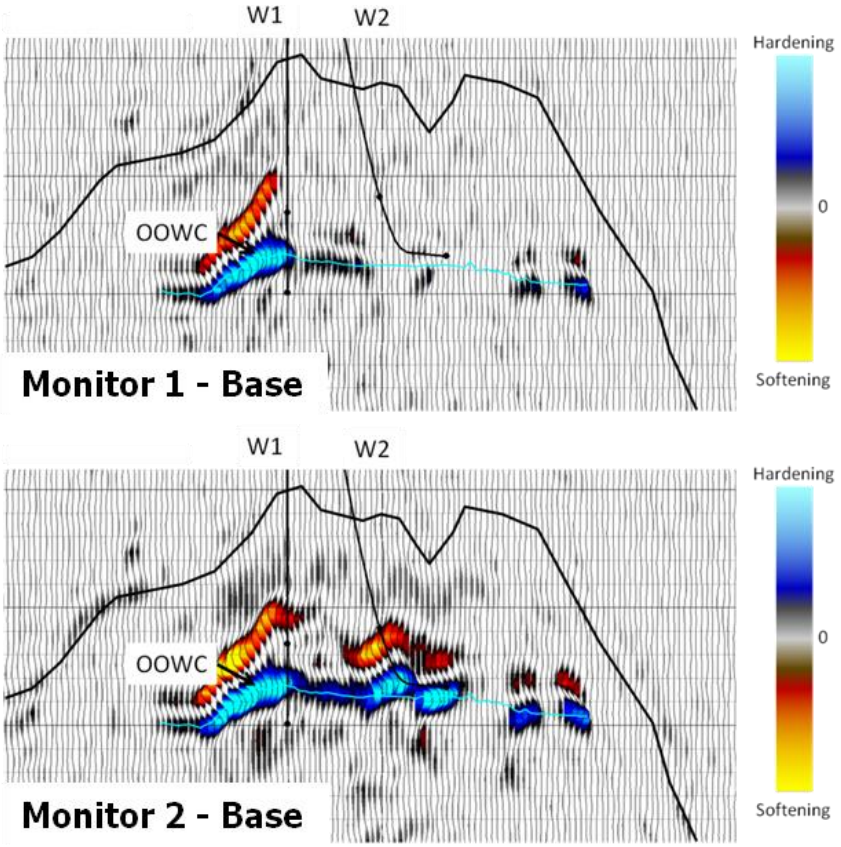

Figure 6.11: Cross-sections of the 4D amplitude differences, showing the changes around the OOWC (green horizon).

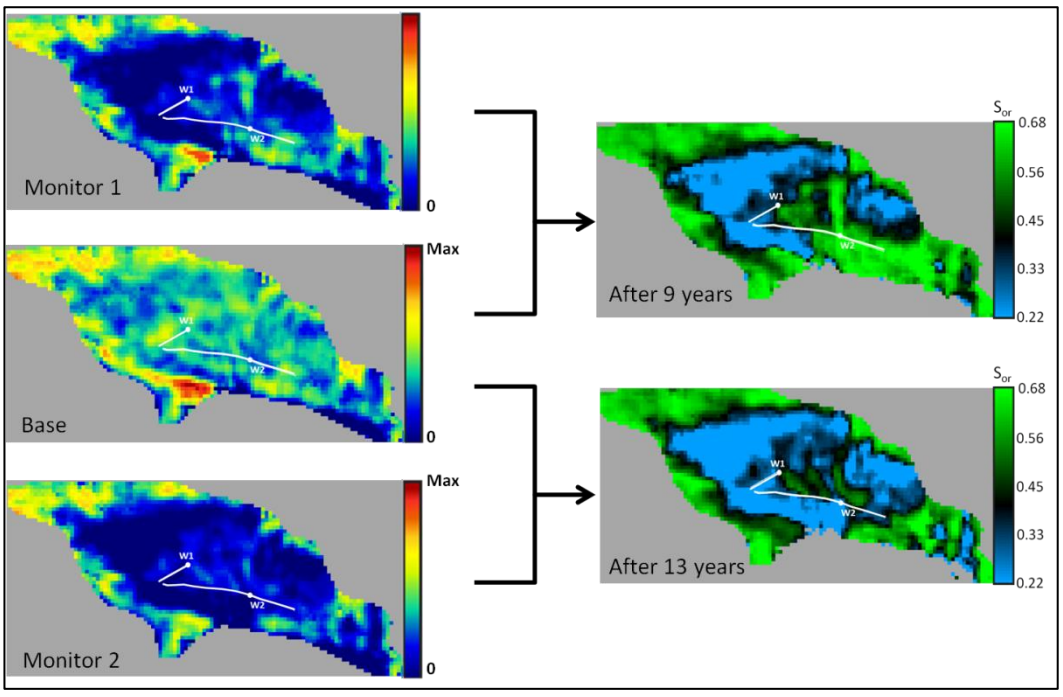

Figure 6.12: (Left) 3D amplitude maps extracted at the OOWC for the base and monitors separately, and (right) the resultant calculation of ROS.

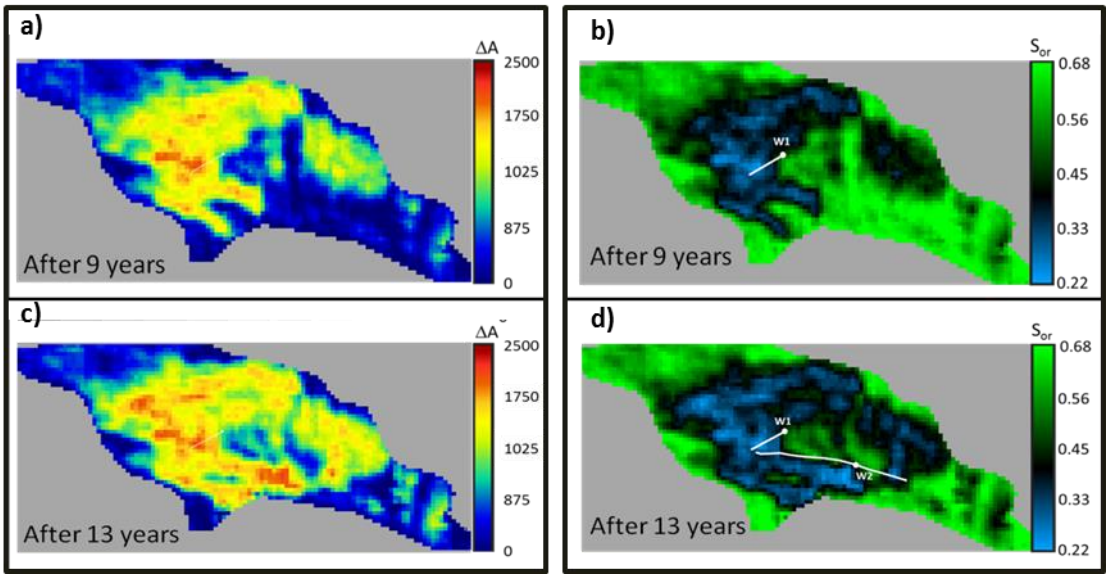

Figure 6.13: (a) 4D amplitude differences extracted at the OOWC and (b) the resultant calculation of S_{orw}.

Finally, the top and base of the swept zone were picked in the quadrature difference by interpreting the zero crossings and the amplitudes were extracted using those horizons as an extraction window. The quantity Δt_{owc} was incorporated by calculating the isopach between top and base of the anomaly. The results are shown in Figure 6.14.

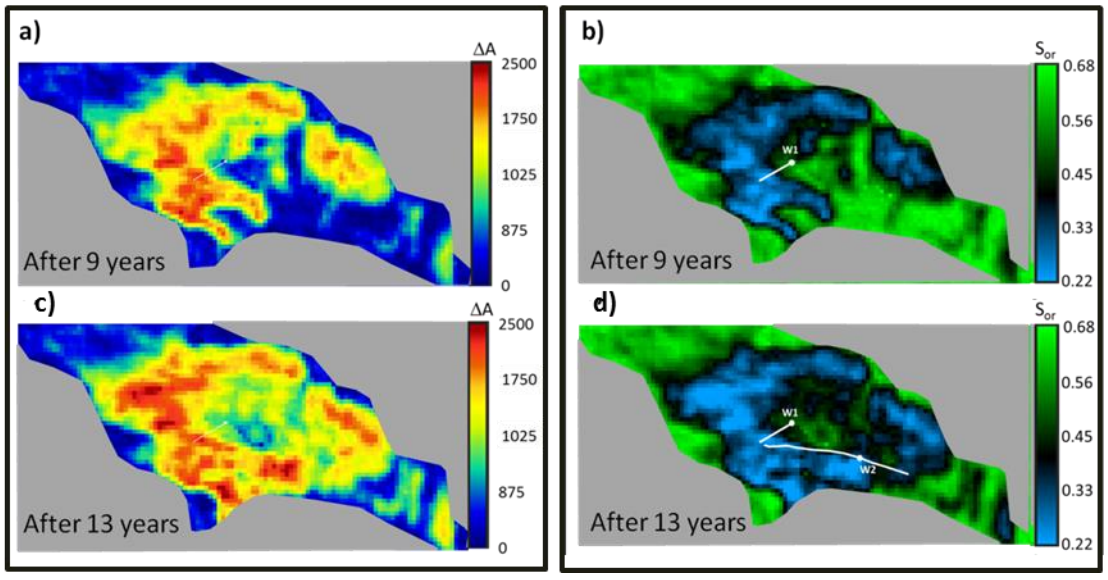

Figure 6.14: (a) 4D quadrature differences extracted at the OOWC and (b) the resultant calculation of ROS.

6.6.3 Analysis and interpretation of results

The obvious observation from these results is that the amplitude extractions based on the 4D difference provide a more reliable result, as they do not depend on a normalisation process and are not subject to clipping when the amplitude tends to zero. As a result of the clipping, the results from equation 6.6 show a lower value of ROS in most of the swept areas than those coming from equations 6.8 and 6.11. The differences between the 4D difference in reflectivity and quadrature are less obvious. However, from a qualitative point of view, all the maps obtained show some consistency. In order to better assess the results it is required to aid my comparisons with the well activity plots.

A comparison of the ROS calculations for the first monitor is shown in Figure 6.15. At this time, only W1 was active and from the production and water cut, it is estimated from material balance that the value of ROS is about 40% around this well. In this case, the map obtained from the 4D reflectivity (middle) shows consistently a 40% ROS around well W1 and also in the swept area (black colour). The map obtained from the 3D amplitudes (top) shows a lower ROS in the swept area and only a small area of ROS, of around 40%, at the location of well W1. The map obtained from the quadrature (bottom) show a lower ROS in the swept area and an unrealistic value of ROS of 60% around the well. In this case the results of equation 6.8 provide a better match with the well based observation.

For the second monitor, the results are shown in Figure 6.16. At this time, W1 had decreased production significantly and was showing a high water cut. W2 had been producing for 3 years and the water cut at the time was about 20%, still suggesting a high ROS of 55 - 65% around the well. Once more, the map obtained from the 4D differences in reflectivity (middle) shows better consistency with the well observations.

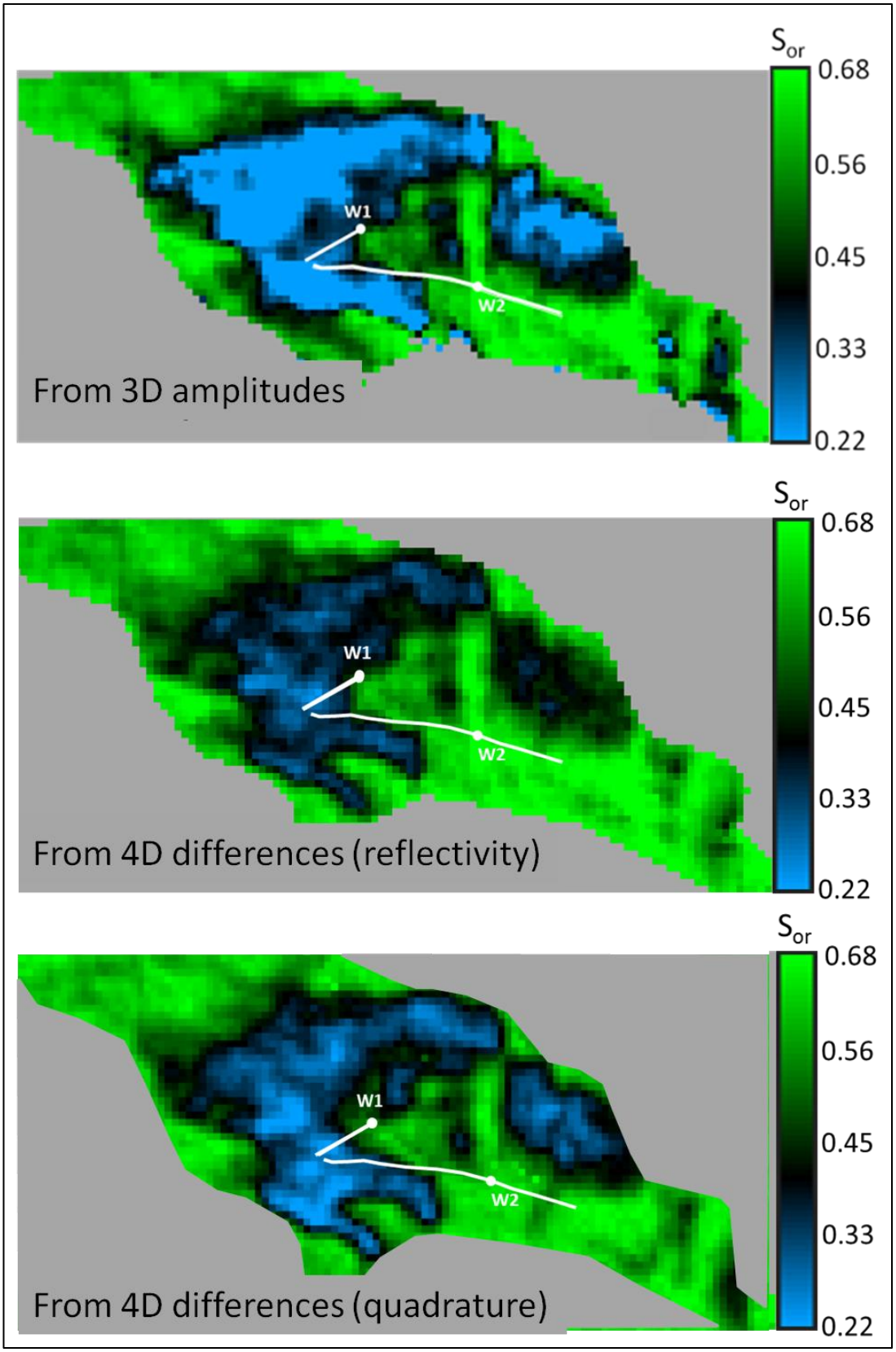

Figure 6.15: Comparison of ROS calculations obtained for the first monitor (after 9 years of production) using 3D amplitudes (top), 4D difference reflectivity (middle) and quadrature differences (bottom).

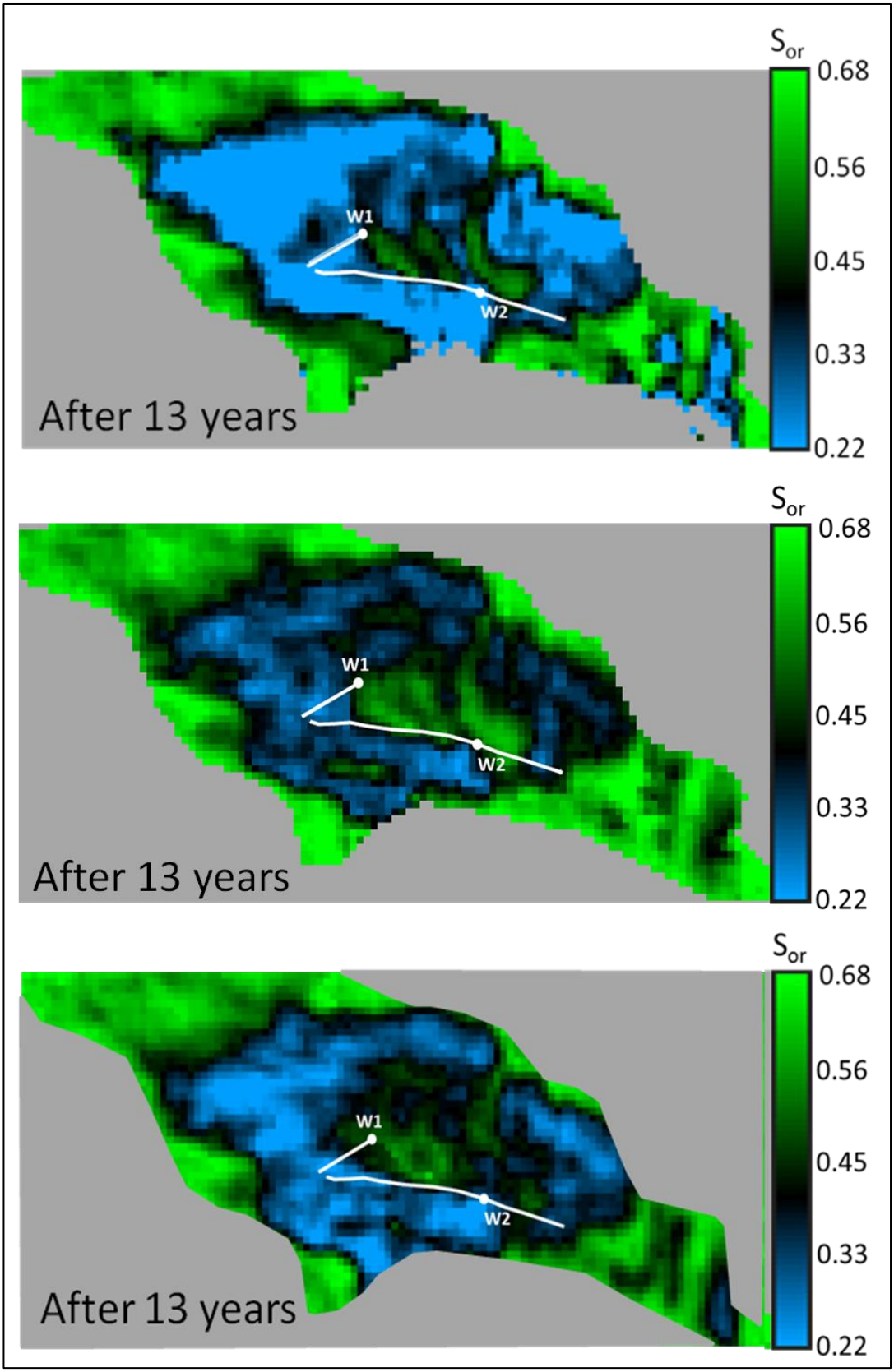

Figure 6.16: Comparison of ROS calculations obtained for the second monitor (after 9 years of production) using 3D amplitudes (top), 4D difference reflectivity (middle) and quadrature differences (bottom).

The map obtained from the 3D amplitudes shows an unrealistic ROS close to 22% around W2, suggesting the well should be producing water (which was clearly not the case), the same applies to the quadrature difference map, showing a low ROS around W2 and a high ROS around W1, which is the opposite of what the well activity suggests. The map from the 4D differences, on the other hand, shows that ROS has not changed significantly between the two monitors; this is consistent with the relatively constant water cut observed in the well over time. Around W2, the map still shows a high ROS, between 55 - 68 %, which is also consistent with the high production and low water cut observed in this well at the time.

The main reasons for the difference in the ROS calculations above may be related to the following factors: (1) effects of the averaging when extracting the 3D amplitudes using a 10 ms window, which was performed to reduce the effects of the zero amplitude in the monitor and (2) tuning effects in the quadrature differences. Since I interpreted top and base of the anomaly, if tuning is present, this interpretation will be inaccurate and will tend to over-predict the parameter Δt_{owc}, leading to over-prediction of ROS.

6.6.4 Fluid contact interpretations versus top reservoir based interpretations

A common methodology to extract 4D amplitudes when the fluid contacts are not visible is the use of amplitude extractions based on windows around the top of the reservoir. This methodology was tested in this reservoir and the results are displayed in Figure 6.17. Even though the resultant maps look clean and the fluid contact movement is visible and apparently clearer than using the 3D amplitudes mapped at the fluid contact (compare to Figure 6.2 and Figure 6.12), the resultant 4D differences are heavily affected by geological features and, therefore. using those maps for quantitative purposes could lead to bias in the interpretations. Figure 6.18 shows the comparison of the 4D differences using top reservoir based extractions (right) with those based on the fluid contact interpretations on the 4D difference (reflectivity), where the latter show greater detail and are less affected by structural and stratigraphic features.

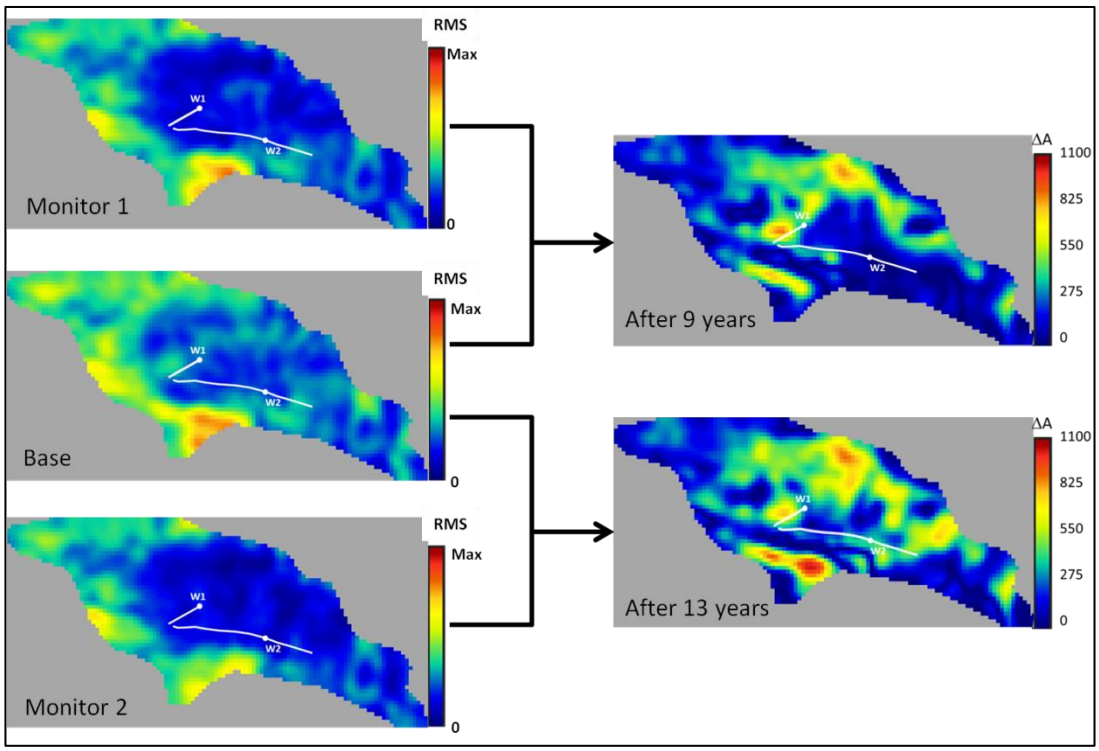

Figure 6.17: RMS based 3D amplitude extractions using top reservoir as a basis (left) and resultant 4D differences (right).

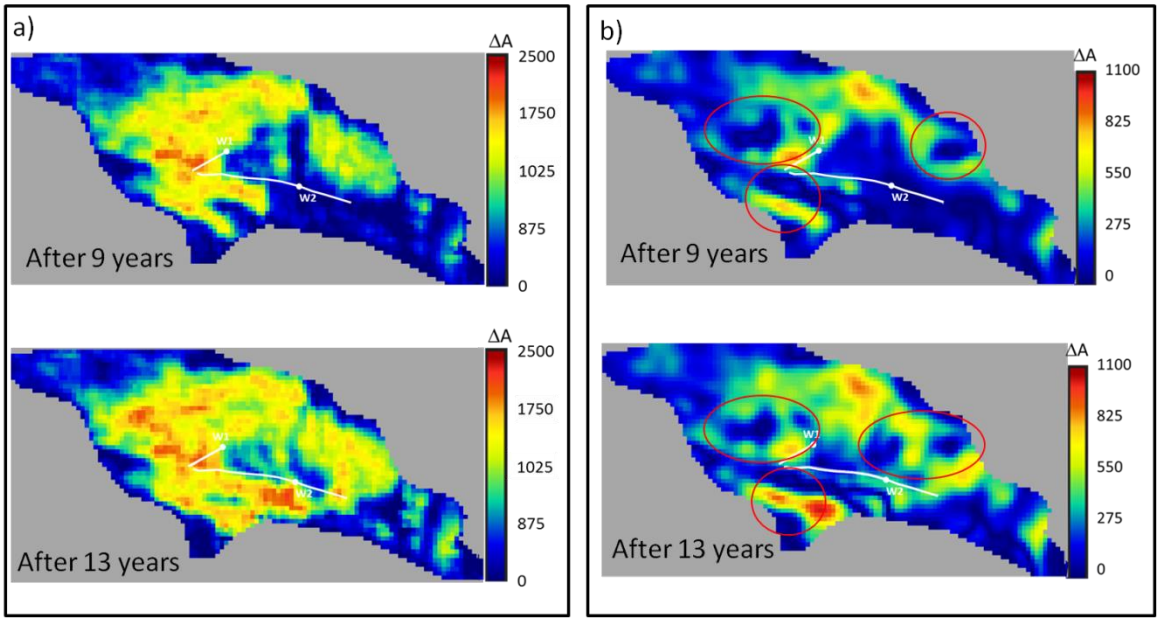

Figure 6.18: (a) 4D amplitude differences extracted at the OOWC in the 4D difference; (b) 4D amplitude maps calculated by using top reservoir to extract the average amplitude of base and monitor and then taking the difference.

6.7 ROS estimation when no fluid contacts are visible in the 3D seismic

An obvious observation from the exercise shown above is that we are dealing with a reservoir where the fluid contacts are very clear and easy to interpret. This is not the case in the majority of reservoirs. Therefore, it is worth investigating if the 4D differences can effectively be used to interpret fluid contacts, even when these are not observed in the 3D seismic. To do this, I apply my method to a large oil reservoir located in the Northern North Sea: the reservoir is highly compartmentalised and laterally complex, both structurally and stratigraphically. Production is maintained through water injection in the water leg, and although the reservoir is thick, there are no visible contacts in the 3D seismic and the reservoir pressure is close to the bubble point.

For the purposes of this exercise, I select a sub-section of the reservoir where no gas is present and the 4D differences are related only to the movement of the OOWC. A reservoir simulation model is available, which aids the analysis by allowing me to compute synthetic seismic using the sim2seis (Amini et al., 2012). Calculating S_{orw} on both the synthetic seismic and the observed seismic will help to demonstrate if, effectively, the 4D differences can be used to compute ROS when no fluid contacts are visible.

A pre-production base and two monitors are available for this analysis. Monitor 1 was shot 13 years after production started and monitor 2 was shot 3 years later (16 years from start of production). Figure 6.19 shows a cross-section of the simulation model, showing a ternary plot at the seismic base line and the results of the sim2seis (near and far angle stacks). Even in the synthetic data, the fluid contacts are not visible (even though these are included in the simulation model) and cannot be interpreted. The wavelet used for the sim2seis calculation was extracted from the observed seismic.

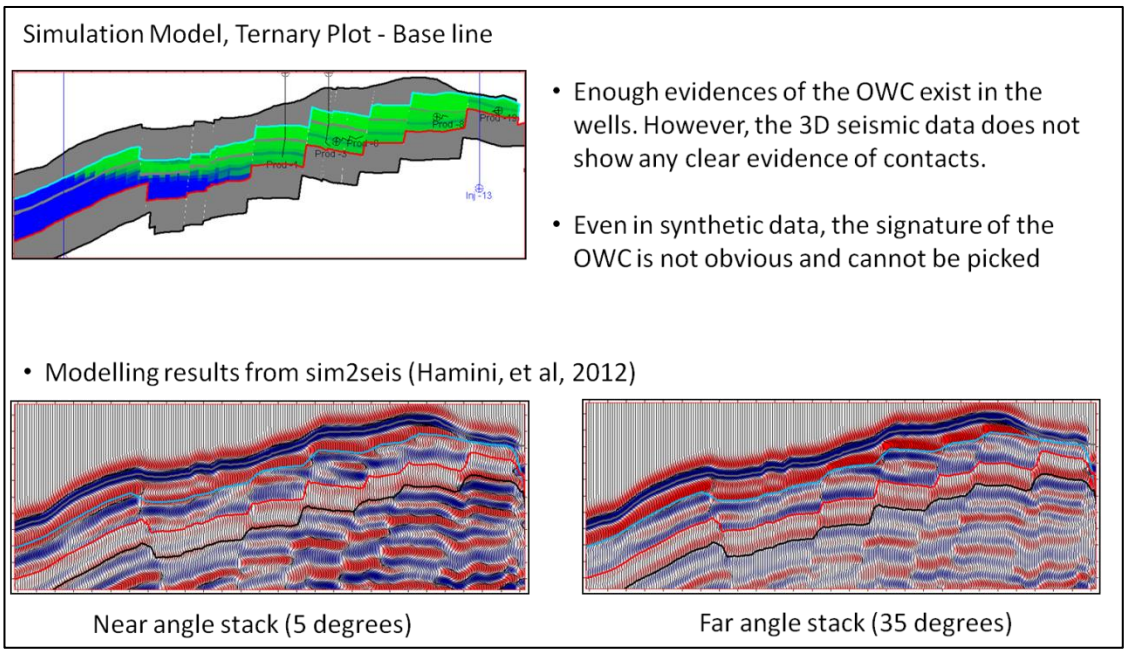

Figure 6.19: Results of the sim2seis modelling, showing that no visible fluid contacts are present.

Figure 6.20 shows a cross-section of the simulation model over the area of interest, showing the 4D changes in water saturation, pressure and gas saturation, as well as the modelled 4D differences at the far angles. Our analysis is focused on the compartment to the east of the fault marked in black, where no gas saturation is present. The 4D differences show a correspondence to the position of the OOWC in the simulation model.

A comparison between the modelled and observed 4D differences at the far angles is shown in Figure 6.21and Figure 6.22: the near-OOWC horizon was interpreted in the observed seismic and then projected onto the synthetic data as a reference. A small misalignment is observed, showing there is some uncertainty in the depth conversion. This uncertainty is minimized by working with maps instead of 3D volumes.

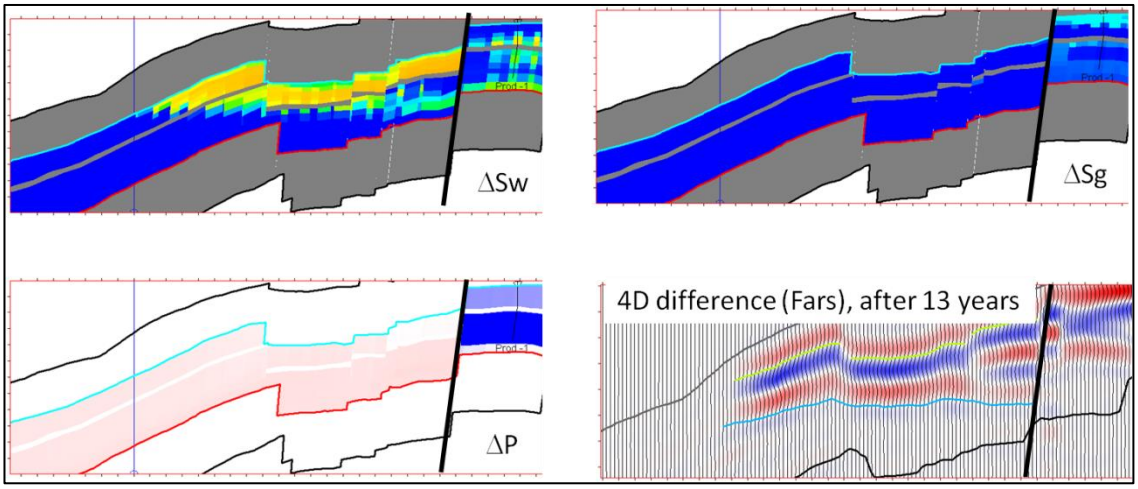

Figure 6.20: 4D changes from the simulation in water saturation ΔP (top left), gas saturation ΔSg (top right), reservoir pressure ΔP (bottom left) and the 4D differences in the far angles from sim2seis (bottom right).

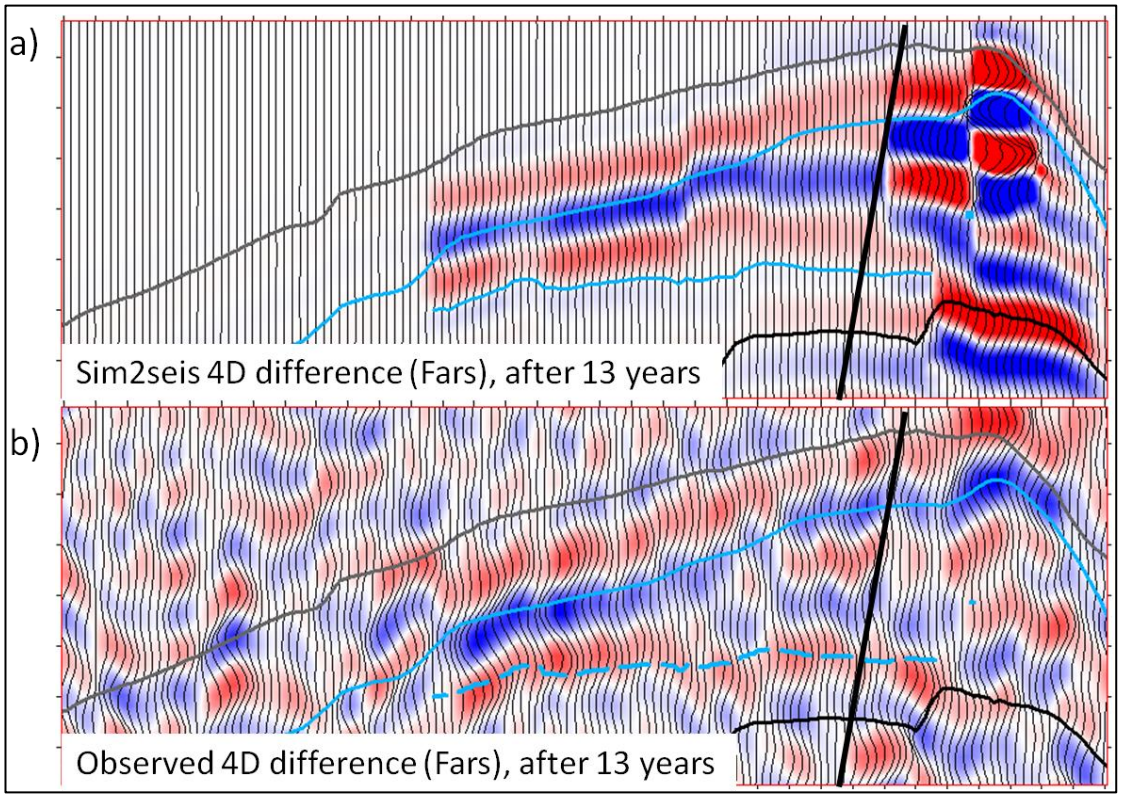

Figure 6.21: Comparison between synthetic (top) and observed 4D differences at the far angles. Monitor 1 – Base. It is possible to pick the OOWC in the far angle differences.

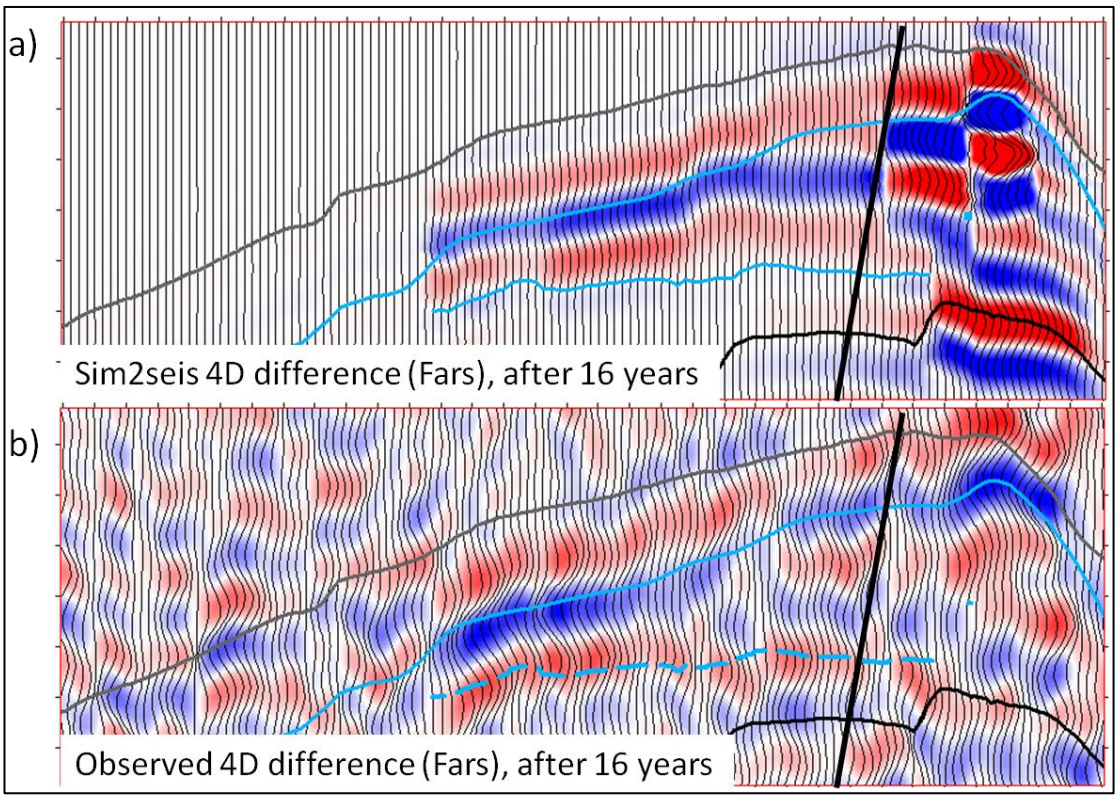

Figure 6.22: Comparison between synthetic (top) and observed 4D differences at the far angles. Monitor 2 – Base. It is possible to follow the OOWC in the far angle differences.

Despite wavelet interferences, it is possible to follow the OOWC on the far stack 4D differences with relative confidence, using trace propagation. The interpreted OOWC map is shown in Figure 6.23, and the coloured bar reveals that the response is relatively flat, as expected.

The results of the SCAL are included in the simulation and show that S_{wc} is considered to be constant and equal to 0.14, and ROS is estimated to be between 0.26 and 0.86. Figure 6.24 shows maps extracted from the simulation, showing the changes of the water saturation (left), porosity (centre) and ROS for the first monitor.

To extract the amplitude maps for the ROS calculations, the OOWC horizon was snapped to each seismic volume and the amplitude was extracted at the intersection with their respective horizon. The parameters used for the petroelastic model are described in Table 6-2.

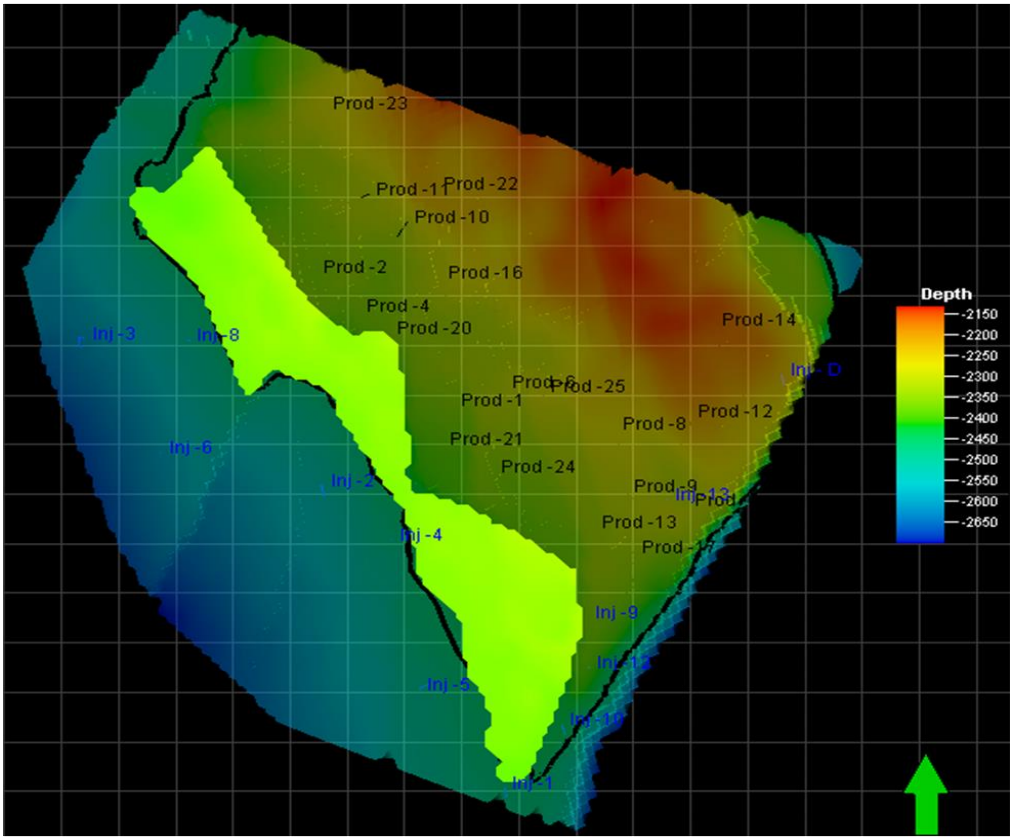

Figure 6.23: OOWC map interpreted in the observed far stack 4D differences (green). Well injectors are shown in blue and producers in black.

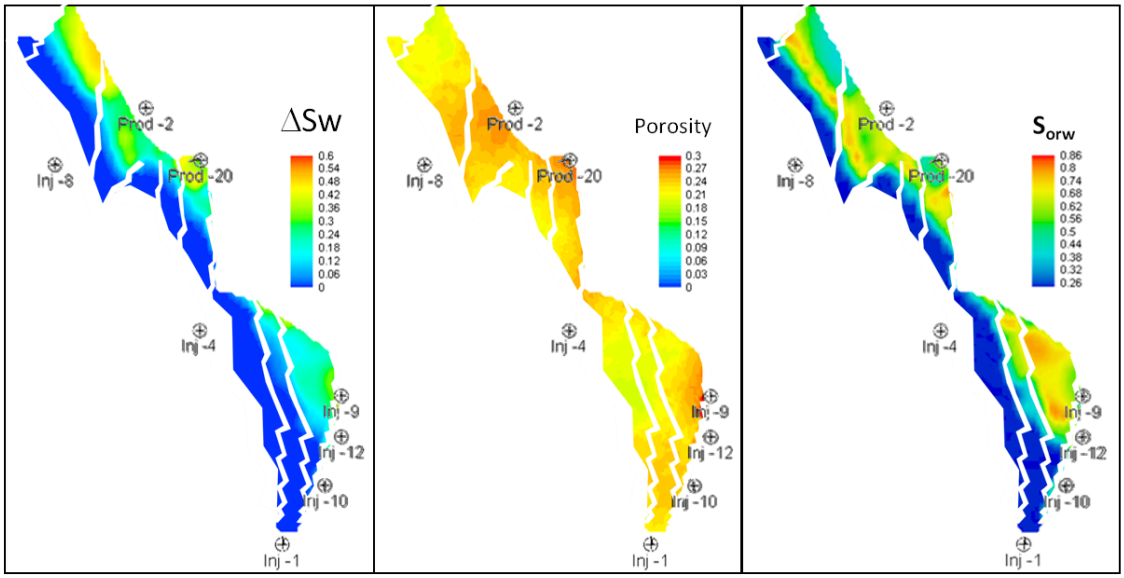

Figure 6.24: Map extractions from the simulator, showing the changes in water saturation (left), porosity (centre) and the distribution of remaining oil saturation (ROS).

Table 6-2: PEM parameters used in the calculations

Reservoir Parameters		
Oil Gravity	28	API
Overburden Pressure Gradient	0.022	MPa/m
Reservoir Pressure	20	MPa
Bubble point pressure	19	MPa
Temp	75	C
Water salinity	55000	ppm
Porosity	0.27	fraction
NTG	0.95	fraction

The results of my calculations for both monitors are shown in Figure 6.25 and Figure 6.26. Unfortunately, wavelet interference effects prevent a better match between the simulation and synthetic calculation; this is evident in the areas close to the faults. Nevertheless, the histograms (Figure 6.25 and Figure 6.26) show that there is a reasonable correspondence between my calculations and the reference simulation ROS. Interestingly, the seismic based calculations show that the area to the north (top of the map), which in the simulation-based maps shows up as a high in ROS (and hence, potentially a target), appears as flooded, and a similar situation can be observed in the compartment close to well Inj-9.

The fact that these results are heavily affected by wavelet interference effects suggests that further de-tuning is necessary in order to provide a more reliable estimation of ROS when reservoirs are heavily faulted, in the presence of complex structural or stratigraphic features.

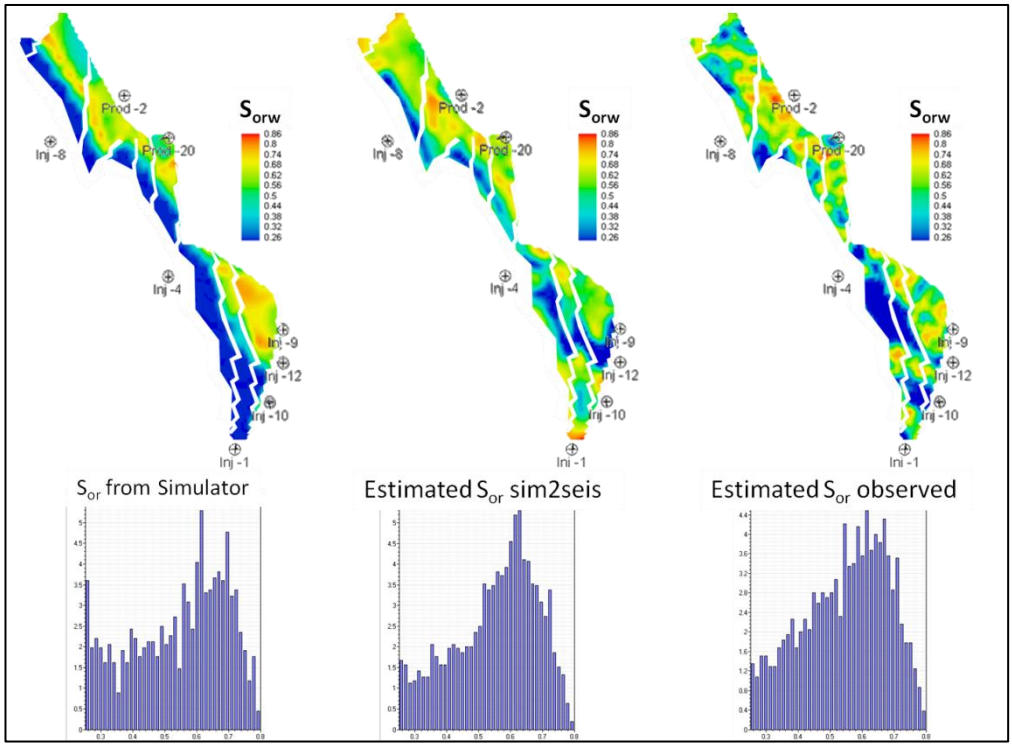

Figure 6.25: ROS calculations for monitor 1 (after 13 years): from simulation (left); from synthetic seismic (centre); from observed seismic (right).

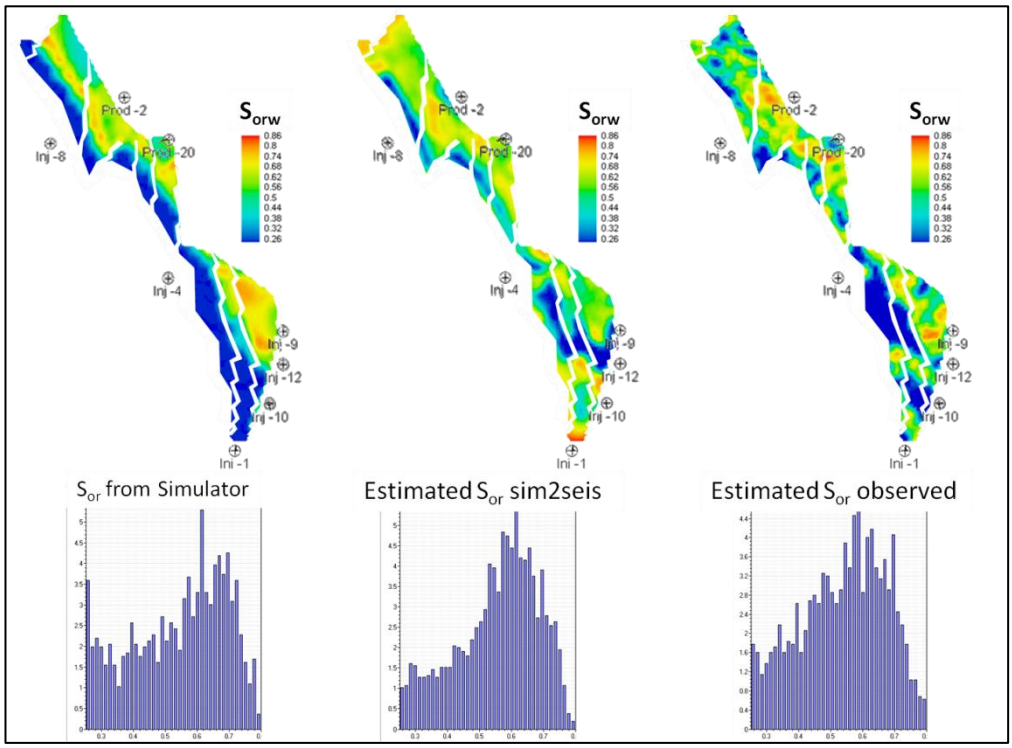

Figure 6.26: ROS calculations for monitor 2 (after 16 years): from simulation (left); from synthetic seismic (centre); from observed seismic (right).

6.8 ROS calculation in practice

Two different approaches to calculate ROS from time lapse amplitudes have been discussed and tested in this chapter. The choice to apply either method will depend on the characteristics of the field, such as:

- Visibility of fluid contacts in the base and monitor.
- Availability of measurements to calibrate the rock physics models
- Thickness of the reservoir and the presence of tuning effects
- Signal to noise ratio
- Pressure effects.

When fluid contacts are visible, it would make sense to use the mapped amplitudes at the fluid contacts, as this eliminates tuning effects and provides a result which is independent of any modelled parameters. However, if the signal to noise ratio is low or if the amplitude at the fluid contact at the monitor tends to zero (cannot be mapped), the calculations will be clipped and would need to be normalised to the appropriate scale (this is similar to the least squares solution of a straight line fit to the cross-plot of one waveform against the other, over a small time gate).

The second method uses the time-aligned amplitude differences at the fluid contacts and fully depends on the rock and fluid physics parameters. This is advantageous in the sense that uncertainty analysis could be performed on the parameters involved (such as the effect of porosity). However, it has the disadvantage of being more sensitive to tuning effects and incorporating the uncertainty of the rock and fluid parameters in the calculations. However, in cases as the second North Sea example outlined above, when fluid contacts are not visible in the seismic, this would be a useful approach to calculate ROS.

6.9 Conclusions from this chapter

- Remaining oil saturation is a scale dependent measurement; therefore, in this work, a distinction is made between the pore scale irreducible oil saturation (Soir) and the field scale remaining oil saturation (ROS).

- It has been shown that 4D seismic can be used to determine ROS reliably and a methodology has been defined, which is applicable to oil reservoirs where no gas is present. The method is based on the interpretation of fluid contacts rather than top reservoir interpretations.

- The technique only requires rock and fluid physics parameters that are commonly available in the field and it is possible to apply it even in a field where the fluid contacts are not visible in the 3D seismic. Potential applications of this method include: 4D interpretation, modelling, detection of bypassed oil and seismic history matching.

- The method requires that fluid contacts are interpretable in the 4D seismic differences (reflectivity); therefore, the use of far angle 4D differences is recommended (particularly where large pressure changes exist).

- Different ways of extracting the amplitudes were tested, including 3D amplitudes of base and monitor at the fluid contacts (where these are visible), 4D reflectivity differences and 4D quadrature differences. Each technique has its own advantages and disadvantages and their application will depend on the characteristics of the field being studied.

- The effects of the wavelet interference observed in the second exercise suggest that the use of 4D inversion could improve the results. This will be further investigated in the following chapter.

Chapter 7: 4D inversion for pressure and saturation

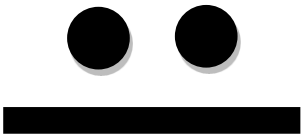

"The forecaster uses statistics as a drunken man uses lamp posts, for support rather than illumination"

El pronosticador utiliza la estadística como un borracho los postes de luz, como apoyo más que para iluminarse

Andrew Lang

Scottish poet and novelist

In this chapter I develop an inversion scheme that allows pressure and saturation changes based on 4D AVO to be computed, using the equations developed in Chapter 4 for the oil-water system as a basis. The objective is to provide a further use to the equations that goes beyond modelling and interpretation, as well as to give an alternative route to 4D inversion that simplifies the problem, reduces the amount of *a priori* information needed and also reduces computational time. The inversion is performed on a map basis but it can be extended to 3D and the method is demonstrated using a pre-stack synthetic dataset generated using the sim2seis program. The use of angle stacks versus angle gathers for the inversion is also discussed.

7.1 Seismic inversion, AVO and 4D seismic

The most common application of AVO analysis nowadays involves the use of inversion to compute attributes that can be related to changes in the rock properties. AVO inversion can be done in a relatively simple way by arranging any of the AVO equations in a matrix form to compute gradient and intercept, or similar volumes (Castagna et al., 1994). We can also use a more sophisticated scheme to invert for reflectivities, Poisson's ratio and other elastic parameters (Simmons and Backus, 1996; Wang, 1999; Lörtzer et al., 1988; Demirbag and Çoruh, 1998; de Haas and Berkhout, 1989). Or we can use a model based AVO inversion scheme (Cooke and Schneider, 1983; Hampson et al., 2005) and incorporate well-based measurements to build an initial model that then allows us to invert for elastic properties (impedances, bulk modulus, etc.).

As described in Chapter 1, AVO inversion has been extended to the analysis of 4D seismic data (Tura and Lumley, 1998; Landrø, 1999; Meadows, 2001; Cole et al., 2002; MacBeth, 2006a; Floricich et al., 2006; Andersen et al., 2009; Trani, 2013). Recently, another approach has been to extend the application of AVO inversions to 4D seismic by inverting simultaneously all vintages and then analysing the resultant differences in terms of impedance changes (Lafet et al., 2008). This process can also be performed inside the simulation grid, aided by extra constraints to reduce non-uniqueness (Thore et al., 2011; Tian et al., 2014). All these approaches have been applied with some degree of success; however, there is still room for improvement. For instance, in Landrø's (1999) method (and further modifications) it is not clear if the empirical parameters required should be laterally variable, and if so, how to account for such variations. For Tura and Lumley's (1998) approach (and further updates), the whole inversion result will depend on our ability to construct rock physics templates and the information used to build them. Since such templates are generated based on well data, the inversion solution is implicitly limited to the number and type of situations observed at the well locations. A similar issue is faced in the approach of MacBeth et al. (2006a) and Floricich et al. (2006. Finally, the simultaneous 4D AVO inversion schemes have the

disadvantage that they require extensive *a priori* information, and hence the solution will only be as good as is the initial guess and the way the initial model is perturbed.

In Chapters 2 and 5 I developed equations that explain the 4D amplitude differences as a weighted sum of pressure and saturation changes, where the weights are theoretical functions of the rock and fluid physics. These weighted functions incorporate lateral variations with porosity and vertical changes in the in-situ effective stress, as well as changes with angle of incidence. My objective in this chapter is to use these equations to develop an inversion scheme that computes ΔP and ΔS_w directly from the 4D AVO amplitude differences, trying to minimise the amount of a priori information and constraints required. The process is developed for the oil-water equations and is performed on a map basis; however, it is envisaged that it can be extended to 3D and also to incorporate the presence of gas.

7.2 Modelling versus Inversion

Modelling and inversion are intimately related: in modelling we seek to reproduce an observation (or measurement) by modifying parameters that are somehow related to such observations. Inversion, on the other hand, uses a series of observed measurements to calculate those parameters we are interested in, by calculating a series of predictions from an established model and comparing them to the observations (Menke, 1989). In both cases, the core of the process is to establish a model which relates the measurements with the parameters we wish to estimate. Modelling and inversion have different (although related) uses; Figure 7.1 shows a schematic representation of what we want to achieve in each case.

In this thesis I have developed equations (a model) dependent on the petroelastic model, which allows us to relate the 4D differences in amplitude (measurements) to pressure and fluid saturation changes (parameters). Equations for the oil-water system were defined in Chapter 2 and these were then extended for multiple-phase systems

(Chapter 5). It has been shown that the equations can be used for modelling, to aid 4D seismic interpretations, constraining the petroelastic model (Chapter 4) and to provide a quick estimate of remaining oil saturation (Chapter 6). As shown in Figure 7.1, a natural step is to develop an inversion scheme that allows inversion for pressure and fluid saturation changes directly from the 4D differences. Since the equations involve the 4D AVO changes, we can use pre-stack data either in the form of angle stacks or gathers.

As shown in Chapter 1, after some attempts to calculate pressure and saturation changes from AVO attributes, the status quo in 4D inversion is to jointly invert base and monitor for impedance changes (or changes in elastic properties) by assuming an initial 4D model and perturbing (with different types of constraints). Then rock physics equations or trends are used to back-calculate the pressure and saturation changes. The major drawbacks from these types of inversions are their dependence on the initial model (and the perturbation), the ambiguity of the results and the time involved. The idea I develop in this chapter is to attempt to simplify the 4D inversion process by using the 4D differences, and to demonstrate if inverting angle stacks will be enough, or if it is required to use pre-stack gathers.

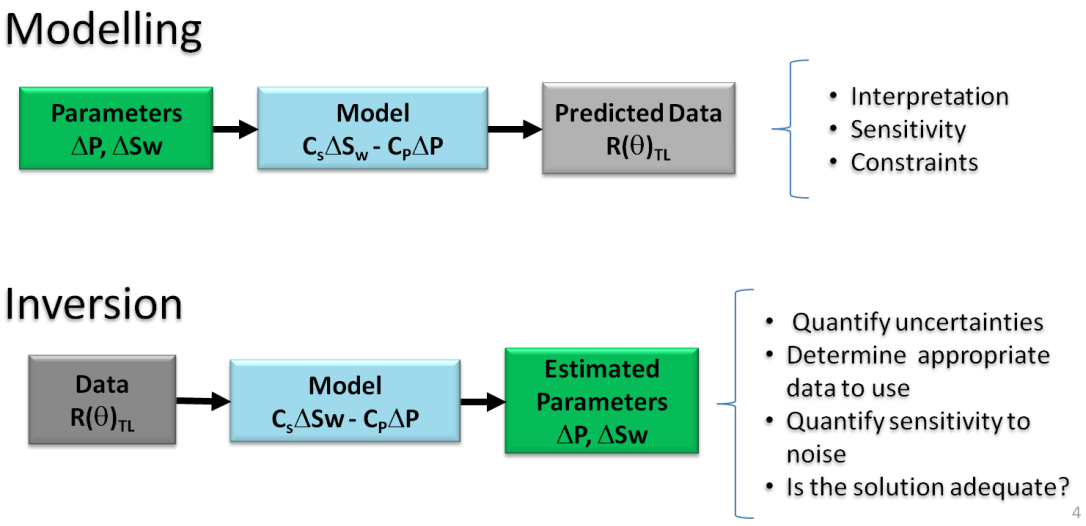

Figure 7.1: Objectives of modelling and inversion (based on Menke, 1989).

7.3 The inverse problem and the least square solution

According to Menke (1989), an inverse problem in a geophysical measurement which changes in 3 dimensions (distance in x, y and time) can be mathematically defined as an integral function that relates the measurements $d(x, y, t)$ to the parameters we wish to estimate $m(t)$ through a model $G(x, y, z)$ that relates the two, calculated over an interval in time $(t_1 - t_0)$:

$$d(x, y, t) = \int_{t_0}^{t_1} G(x, y, t) m(t)\, dt \quad . \tag{7.1}$$

$\boldsymbol{d}$ is also called the data observation matrix, m sometimes is called the parameter vector and G the data kernel matrix.

Let us consider the case where seismic measurements are available at different angles of incidence. In that case, equation 7.1 becomes:

$$\boldsymbol{d}(\boldsymbol{x}, \boldsymbol{y}, \boldsymbol{\theta}, \boldsymbol{t}) = \int_{t_0}^{t_1} \int_{\theta_i}^{\theta_n} G(x, y, \theta, t) m(\theta, t)\, d\theta dt. \tag{7.2}$$

If we perform the inversion on a sample by sample basis (or if we use maps, for instance), and since seismic data is a discrete measurement, equation 7.2 can be generalised:

$$\sum_{t=i}^{M} \sum_{\theta=j}^{N} d_{ij} = \sum_{t=i}^{M} \sum_{\theta=j}^{N} G_{ij} m_{ij} \, . \tag{7.3}$$

In this case, the vector d_{ij}represents the observed amplitudes at each given angle of incidence (amplitude differences in the present case); the parameter vector, m_{ij}, contains the pressure and saturation changes we wish to estimate and the data kernel matrix, G_{ij}, is the model relating the two (and hence, any of the equations defined in Chapter 2 and Chapter 5): for example, in the oil-water system case, equation 7.3 will be expressed as follows in a matrix form:

$$\begin{bmatrix} \Delta A_{TL}(\theta_1)_{\mathrm{t_i}} \\ \Delta A_{TL}(\theta_2)_{\mathrm{t_i}} \\ . \\ . \\ \Delta A_{TL}(\theta_N)_{\mathrm{t_i}} \end{bmatrix} = \begin{bmatrix} C_S(\theta_1)_{\mathrm{t_i}} & -C_P(\theta_1)_{\mathrm{t_i}} \\ C_S(\theta_2)_{\mathrm{t_i}} & -C_P(\theta_2)_{\mathrm{t_i}} \\ . & . \\ . & . \\ C_S(\theta_m)_{\mathrm{t_i}} & -C_P(\theta_m)_{\mathrm{t_i}} \end{bmatrix} \begin{bmatrix} \left(\frac{\Delta \mathrm{P}}{P_i}\right)_{\mathrm{t_i}} \\ \left(\frac{\Delta \mathrm{S_w}}{S_{wi}}\right)_{\mathrm{t_i}} \end{bmatrix} * \dot{s}(t). \qquad (7.4)$$

To simplify the notation, the observed (time-shift corrected) 4D amplitude at the angle $\theta_i$measured at the time $\mathrm{t_i}$ ($\Delta A_{TL}(\theta_1)_{\mathrm{t_i}}$) is replaced by $\left(\Delta A_{TL_{\mathrm{j}}}\right)$, and similarly, the $C_S(\theta_1)_{\mathrm{t_i}}$, $-C_P(\theta_1)_{\mathrm{t_i}}$ constants are replaced by C_{S_j} and C_{P_j} in the following pages, $\dot{s}(t)$ represents the time derivative of the wavelet and '*' denotes a convolution. The main idea behind an inversion scheme is that, rather than attempting to solve the inversion equation through matrix inversion, it is more convenient to parameterise the right hand side of the equation and then compare the results with the data observations and minimize the difference by finding the minimum of the prediction error ($\boldsymbol{e} = \boldsymbol{d^{obs}} - \boldsymbol{d^{pred}}$) at each sample in time.

As I observed in Chapter 3, pressure and saturation changes are expected to scatter around trends of constant C_S/C_P, and, assuming that more than two angles of incidence are available (for instance, if migrated gathers are available), the inversion problem will be over-determined (i.e. an exact solution does not exist). I select an L_2 norm as an appropriate measurement of the error length for my inversion scheme. The reason is that, whereas the L_2 norm gives similar weight to errors of different sizes, a higher order norm would put more weight on the large errors or outliers (Menke, 1989). The L_2 norm implies that the solution to this inverse problem is given by the least square solution of equation 7.3, which is given by:

$$E = \|e\|_2 = \|\boldsymbol{d} - \boldsymbol{Gm}\|_2 = \sum_{\theta=j}^{N} \left[\Delta A_{TL_{\mathrm{j}}}{}^{obs} - \Delta A_{TL_{\mathrm{j}}}{}^{pred}\right]^2. \qquad (7.4)$$

If a least square solution to this inversion problem exists, analytically, it would be given by finding the minimum of the function E, which can be found by setting to zero

the partial derivatives of E with respect to the estimated parameters $\Delta S_w/S_{wi}$ and $\Delta P/P_i$ and solving the resulting equations:

$$\frac{\partial E}{\partial \Delta S_w} = \frac{\partial}{\partial \Delta S_w} \sum_{\theta=j}^{N} \left\{ \Delta A_{TL_j}^{obs} - \left[C_{S_j} \frac{\Delta S_w}{S_{wi}} - C_{P_j} \frac{\Delta P}{P_i} \right] \right\}^2 = 0, \qquad (7.5a)$$

$$\frac{\partial E}{\partial \Delta P} = \frac{\partial}{\partial \Delta P} \sum_{\theta=j}^{N} \left\{ \Delta A_{TL_j}^{obs} - \left[C_{S_j} \frac{\Delta S_w}{S_{wi}} - C_{P_j} \frac{\Delta P}{P_i} \right] \right\}^2 = 0. \qquad (7.5b)$$

This is equivalent to applying the general least square solution (Menke, 1989) to equation 7.3:

$$\boldsymbol{m}^{LS} = [\boldsymbol{G}^{\boldsymbol{T}}\boldsymbol{G}]^{-1}\boldsymbol{G}^{\boldsymbol{T}}\boldsymbol{d}\,, \qquad (7.6)$$

where T denotes the transpose of the matrix. In this inversion scheme, the least square solution is expressed as:

$$\begin{bmatrix} \frac{\Delta S_w}{S_{wi}} \\ \frac{\Delta P}{P_i} \end{bmatrix}_{LS} = \begin{bmatrix} \sum_{\theta=j}^{N} 2C_{S_j}{}^2 & -\sum_{\theta=j}^{N} 2C_{S_j} C_{P_j} \\ -\sum_{\theta=j}^{N} 2C_{S_j} C_{P_j} & \sum_{\theta=j}^{N} 2C_{P_j}{}^2 \end{bmatrix}^{-1} \begin{bmatrix} -\sum_{\theta=j}^{N} 2C_{S_j} \Delta A_{TL_j}^{obs} \\ \sum_{\theta=j}^{N} 2C_{P_j} \Delta A_{TL_j}^{obs} \end{bmatrix}. \qquad (7.7)$$

Unfortunately, the resulting determinant of the $[\boldsymbol{G}^{\boldsymbol{T}}\boldsymbol{G}]$ matrix is equal to zero, which means that the inverse matrix does not exist and hence the least square solution fails for the case of pressure and saturation inversion. This result is somewhat expected, as it implies that data are correlated in our solution and therefore there will be several possible combinations of ΔS_w and ΔP which will produce the same change in $\Delta A_{TL_j}^{obs}$. For example, both a decrease in reservoir pressure and an increase in water saturation will generate a hardening signal. The result of 7.7 also explains the issues found by previous researchers in obtaining reliable estimations of ΔP and ΔS_w, especially the highly correlated nature of the 4D signals and the requirement for the introduction of additional constraints and *a priori* information into the inversion scheme.

The implication of this result is that the inversion problem is ill-posed and hence it is required to provide either *a priori* information or constraints in order to find a solution that falls within the expected ranges of change. In Chapter 3, it was found that the C_S/C_P ratio can be used to constrain the rock stress sensitivity, which, in essence, defines the relative weight between pressure and saturation signals. For instance, if we apply the constraint found in Chapter 4 in the North Sea dataset: $0.44\ {C_S}^{\chi} - 3.5\ {C_P}^{\chi} = 0$ (i.e. $C_S/\ C_P \approx 8$), where the upper-index χ denotes the specific angle of incidence where the constraint is satisfied. Using this constraint, if the inversion solution is represented in a 3D plot of axes ΔP, ΔS_w andΔA_{TL}, the solution must pass through the point (0.44, 3.5, 0). A simple way of introducing this constraint is through Lagrange multipliers. To calculate these, we firstly express the constraint in a similar matrix form as the inversion scheme and then we solve for both equations simultaneously (Menke, 1989):

$$\begin{bmatrix} \boldsymbol{G^T G} & \boldsymbol{H^T} \\ \boldsymbol{H} & \boldsymbol{0} \end{bmatrix} \begin{bmatrix} \boldsymbol{m} \\ \boldsymbol{\lambda} \end{bmatrix} = \begin{bmatrix} \boldsymbol{G^T d} \\ \boldsymbol{h} \end{bmatrix}, \tag{7.8}$$

where our constraint equation ($\boldsymbol{Hm = h}$) is given by

$$\begin{bmatrix} {C_S}^{\chi} & -{C_P}^{\chi} \end{bmatrix} \begin{bmatrix} 0.44 \\ 3.5 \end{bmatrix} = 0\,. \tag{7.9}$$

Incorporating this constraint to equation 7.7 we obtain

$$\begin{bmatrix} \frac{\Delta S_w}{S_{wi}} \\ \frac{\Delta P}{P_i} \\ \lambda \end{bmatrix}_{LS} = \begin{bmatrix} \sum_{\theta=j}^{N} 2{C_{S_j}}^2 & -\sum_{\theta=j}^{N} 2C_{S_j}C_{P_j} & {C_S}^{\chi} \\ -\sum_{\theta=j}^{N} 2C_{S_j}C_{P_j} & \sum_{\theta=j}^{N} 2{C_{P_j}}^2 & -{C_P}^{\chi} \\ {C_S}^{\chi} & -{C_P}^{\chi} & 0 \end{bmatrix}^{-1} \begin{bmatrix} -\sum_{\theta=j}^{N} 2C_{S_j}\Delta {A_{TL}}_{\mathrm{j}}^{obs} \\ \sum_{\theta=j}^{N} 2C_{P_j}\Delta {A_{TL}}_{\mathrm{j}}^{obs} \\ 0 \end{bmatrix}. \tag{7.10}$$

Once we apply the constraint, the determinant of the matrix $[\boldsymbol{G^T G}]^{-1}$ becomes non zero; therefore the inverse of the matrix exists and is given by

$$[G^T G]^{-1} = \frac{1}{|A|}\begin{bmatrix} \sum_{\theta=j}^{N} 2{C_S}_j{}^2 & \sum_{\theta=j}^{N} 2C_{S_j}C_{P_j} & C_S{}^{\chi} \\ -\sum_{\theta=j}^{N} 2C_{S_j}C_{P_j} & \sum_{\theta=j}^{N} 2{C_P}_j{}^2 & C_P{}^{\chi} \\ C_S{}^{\chi} & C_P{}^{\chi} & 0 \end{bmatrix}, \qquad (7.11a)$$

where |A| is the determinant of $[\boldsymbol{G^T G}]$:

$$|A| = -2(1 - j + N)\left(C_{S_j}C_P{}^{\chi} - C_S{}^{\chi}C_{P_j}\right)^2 . \qquad (7.11b)$$

The main advantage of this type of solution is that we keep the incorporation of *a priori* information to the minimum. However, we have only incorporated one constraint and we need to assume that such a constraint is valid for the whole interval of interest. Although it is possible to add as many constraints as we need in a similar fashion, in practice this makes the algebraic solution more complicated and difficult to implement. An alternative solution to this problem is to constrain the solution by setting boundaries for our parameter estimates. The boundaries can be determined from the pressure and saturation estimates at the well locations; this is reasonable, as it is expected that the maximum changes occur near the well locations. For instance, in Chapter 3, I defined the boundaries of pressure and saturation changes from the North Sea example and some other fields as follows: $0 \geq \Delta S_w \leq (1 - S_{or} - S_{wc} \approx 0.65)$ and $-4 \geq \Delta P \leq 13$ (Figure 7.2). These constraints can be incorporated in the new scheme as equations of the form $\boldsymbol{Hm} \geq \boldsymbol{h}$, leading to the linear programming problem: minimize $\|\boldsymbol{d} - \boldsymbol{Gm}\|_2 = \sum_{\theta=j}^{N}\left[\Delta A_{TL_j}{}^{obs} - \Delta A_{TL_j}{}^{pred}\right]^2$, subject to the constraints

$$\begin{bmatrix} \mathbf{1} & \mathbf{0} \\ \mathbf{-1} & \mathbf{0} \\ \mathbf{0} & \mathbf{1} \\ \mathbf{0} & \mathbf{-1} \end{bmatrix}\begin{bmatrix} \frac{\Delta S_w}{S_{wi}} \\ \frac{\Delta P}{P_i} \end{bmatrix} \geq \begin{bmatrix} \mathbf{0} \\ \mathbf{0.65} \\ \mathbf{-4} \\ \mathbf{13} \end{bmatrix}. \qquad (7.13)$$

In this North Sea example, the boundary constraints outlined above are applicable to the full area of study; however, this must be determined on a case by case basis. This

method provides a way to find a solution to this inversion problem with minimum *a priori* information. Although, analytically the solution of this problem is not straightforward, there are various algorithms in numerical methods that allow solving this type of problem (e.g. Bjorck, 1988; Coleman and Li, 1996). In this case, I select the algorithm by Coleman and Li (1996), implemented in MatLab as the function **lsqlin**.

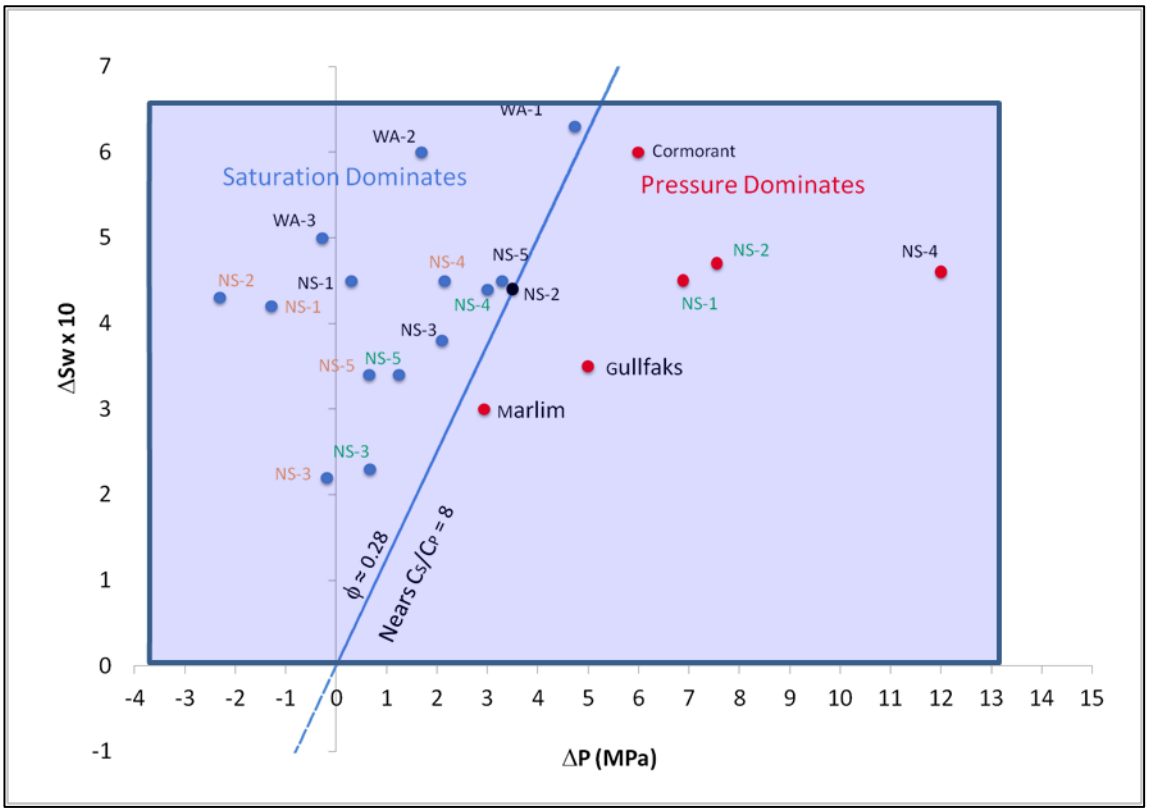

Figure 7.2: Pressure and saturation change boundaries from the analysis in Chapter 2.

7.4 Application of the inversion scheme to an oil-water system

In order to test the effectiveness of my inversion schemes (equations 7.11 and 7.13), a synthetic dataset was prepared using the North Sea example from Chapter 3. The synthetics were generated using the sim2seis tool (Amini et al., 2012), and for simplicity, a fluid substitution was included, so that no gas is present in the results and to ensure the equations derived above are fully applicable throughout the whole dataset. The Sim2Seis synthetics incorporate variations in NTG and other changes not

explicitly included in my equations, therefore the exercise is still a realistic comparison. Using the sim2seis seismic, volumes are produced for the pre-production base line (1998) and the first monitor (2004); each vintage contains a set of angle gathers from 0 to 35 degrees and 3 angle stacks within the bands, 5-15, 15-25, 25-35 (Figure 7.3).

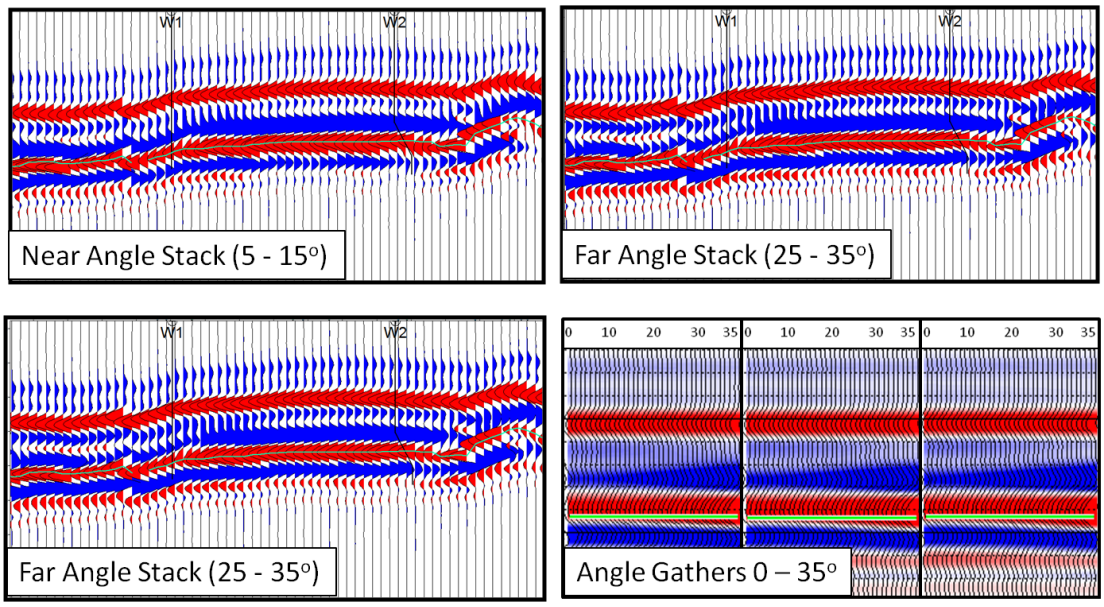

Figure 7.3: Angle stacks and angle gathers generated with sim2seis

Noise is extracted from the observed seismic data using a median filter of 7 traces and subtracting the result from the original data. Although angle stacks do not exist in this dataset, there are Intercept and Gradient volumes for each vintage. Thus, it is possible to back-calculate the reflectivity at any given angle of incidence and incorporate also angle-dependent noise into the data. The aim is to generate a seismic dataset with an NRMS between 5 and 30% (Figure 7.4) and a comparison of the 4D difference maps for near and far angles before and after adding noise (extracted from the actual data) is shown in Figure 7.5.

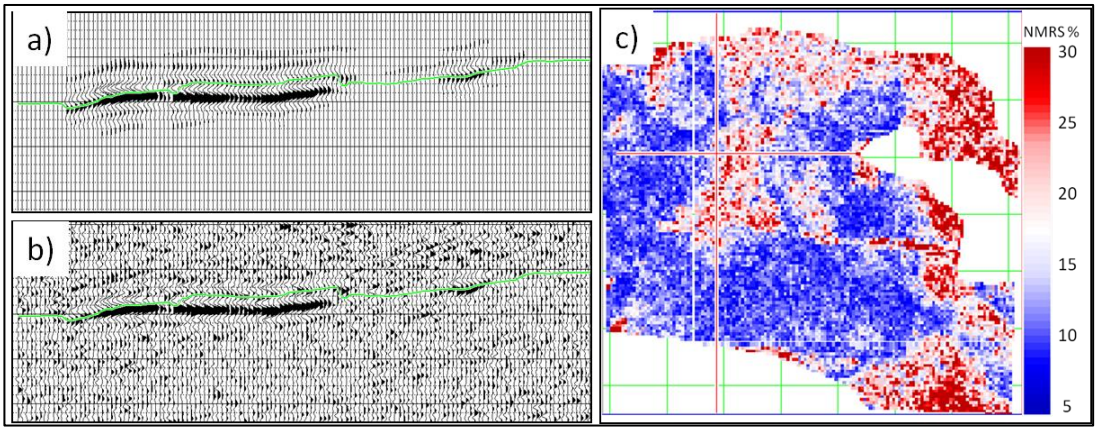

Figure 7.4: (a) Noise-free near angle stack 4D differences; (b) Near angle stack 4D difference after adding noise; (c) NRMS map taken on a 200 ms window above the reservoir showing the desired range 5 - 30%.

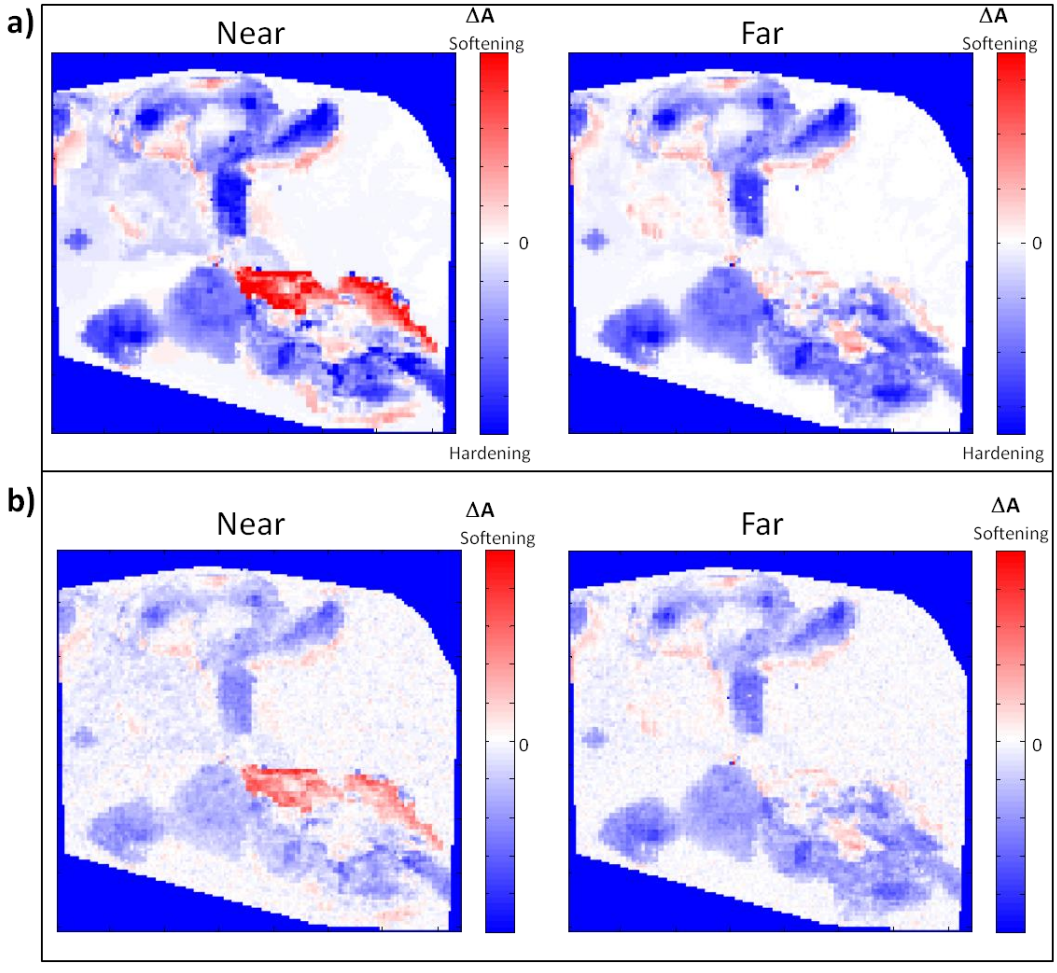

Figure 7.5: Time lapse amplitude changes obtained from sim2seis. (a) Near and far angle stack differences without noise. (b) Near and far angle stack differences after adding noise.

In this exercise I focus on 3 objectives:

- To demonstrate that the inversion schemes proposed produce realistic results
- To evaluate the effects of noise in the inversion results
- To compare the use of angle gathers versus angle stacks for the inversion.

To run the inversion, it is required to define first the parameters of the petroelastic model. Using the same parameters as defined in Chapter 3 for the North Sea example, C_S and C_P maps are calculated (Figure 7.6 and Figure 7.7). In order to incorporate the lateral variability in the maps, the porosity and overburden stress maps from the simulator are incorporated into the calculation. In practice, the porosity maps can be obtained, for instance, through post-stack inversion using impedance versus porosity transforms (e.g., Avseth, 2004, Whitcombe et al., 2002, Pedersen et al., 2008), or rock physics models (e.g. Raymer-Hunt, 1979; Krieff, 1992; Nur, 1994). The overburden stress is commonly computed as a depth trend or by integrating the density logs extrapolated to the surface and then using geo-statistics to interpolate between wells.

Using the derived C_S and C_P maps, two map based inversions were run with and without noise, using the deterministic constraint (equation 7.11) and the boundary based solution (equation 6.13). The inversions were run using 3 angle stacks and the input parameters for both processes are identical (with the exception of the constraints). Figure 7.8 and Figure 7.9 show the results of the two inversions compared with the reservoir simulation maps. Both inversion solutions are consistent and provide a reasonable match with the reservoir simulation maps. Both inversions are able to solve for pressure and saturation in areas where these effects are separated; however, as expected, both inversions struggle in areas where pressure and saturation changes overlap. The use of a deterministic constraint (inequality) can help in cases where no information is available with regard to the expected boundaries of the solution: for instance, when pressure measurements are not available at the well locations or in cases where the objective is to investigate the maximum expected changes in a reservoir. The boundary-based solution can be used in cases where the

inequality constraints are difficult to determine (for instance, if no injectors are available).

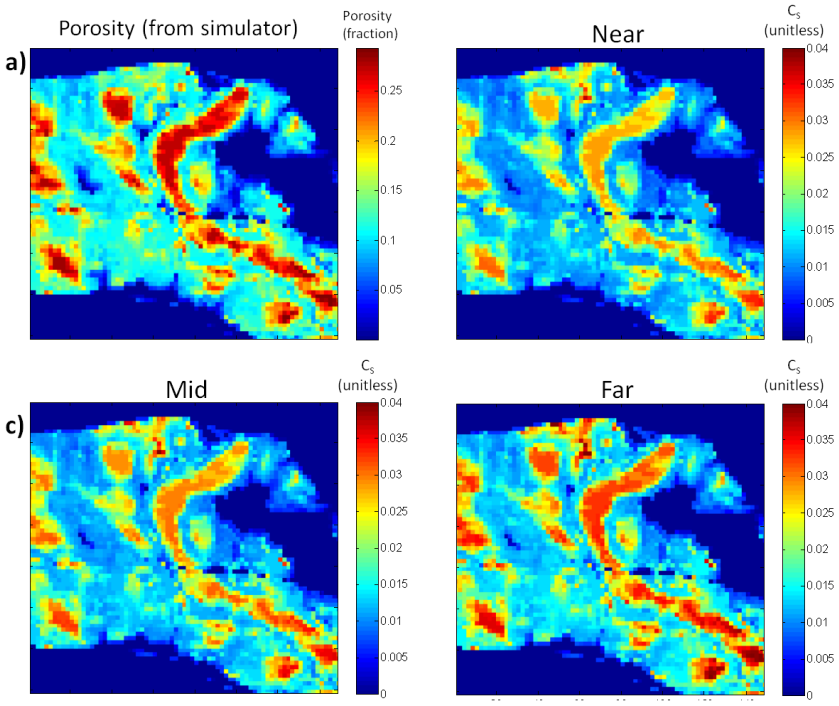

Figure 7.6: (a) Porosity map from the simulator. (b) C_S map calculated for the near angles. (c) C_S map calculated for the mid angles and (d) C_S map calculated for the far angles.

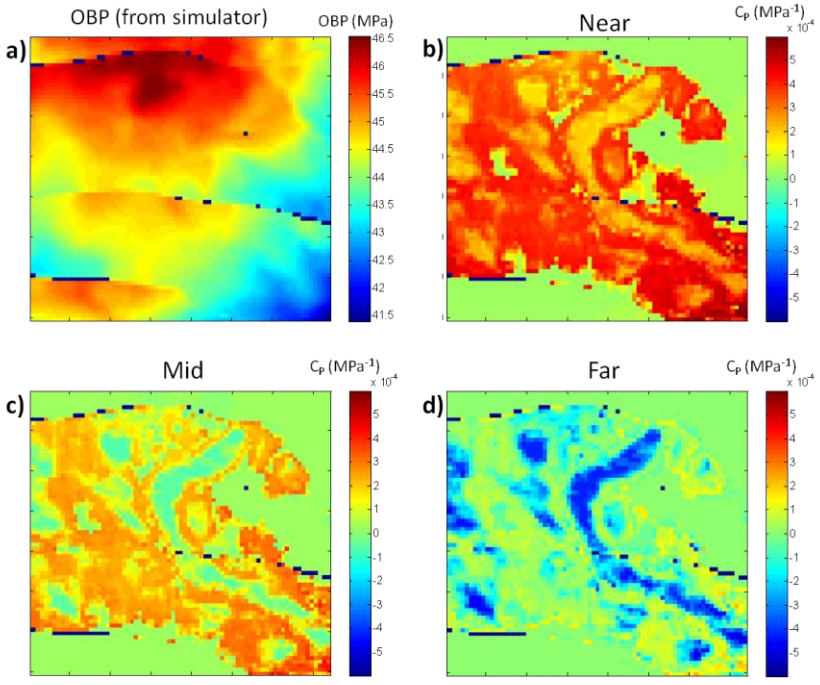

Figure 7.7: (a) Overburden stress map from the simulator. (b) C_P map calculated for the near angles. (c) C_P map calculated for the mid angles and (d) C_P map calculated for the far angles.

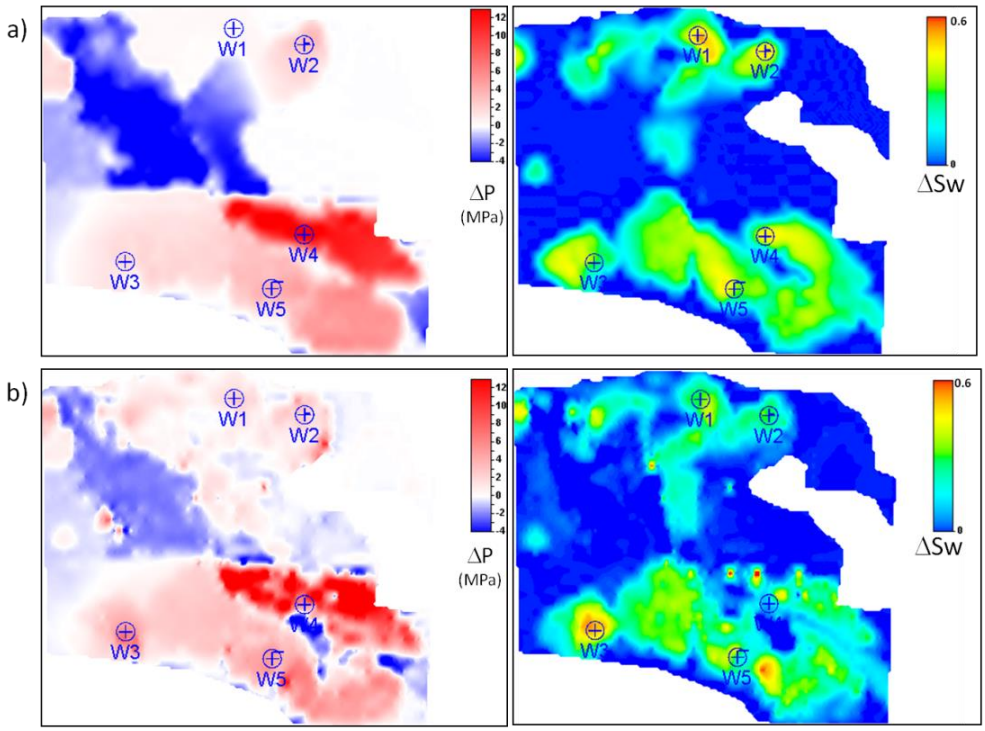

Figure 7.8. (a) Pressure and saturation change maps from the simulator. (b) Results of the inversion using a single deterministic constraint.

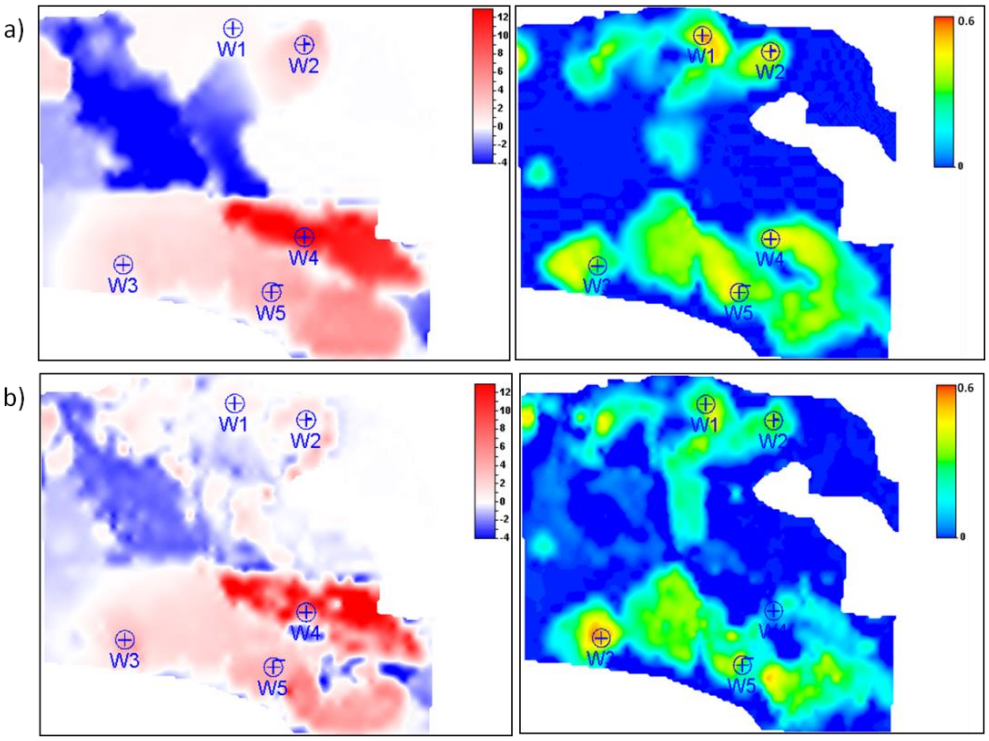

Figure 7.9. (a) Pressure and saturation change maps from the simulator. (b) Results of the inversion using bounds.

To accomplish the second and third objectives of the exercise, a numerical analysis is performed and then the results are extended to a map based inversion. Angle stacks are commonly used as inputs to AVO inversions, as they are considered to accurately represent the AVO behaviour, and therefore provide an advantage over the use of angle gathers, in terms of handling noise and computing times. It is important to determine if this is still the case for 4D inversions. It is also necessary to determine the minimum amount of data observations required to produce a reasonable outcome. Using the full rock and fluid physics equations, the 4D AVO responses are modelled at the location of well W1. The AVO curve is characterised by a monotonic increase in amplitude with angle (Figure 7.10), due to changes in water saturation and small pressure changes around this well. The process is performed using two angle stacks (5 - 15 and 25 – 35 degrees), three angle stacks (5 – 15, 15 – 25 and 25 -35 degrees), and then the full angle gathers (0 – 35 degrees). For each case, the inversion is repeated after adding noise. Surprisingly, the inversion results seem to be accurate, even with two angle stacks, and after adding noise; hence, the use of angle gathers does not seem to provide any visible benefits, although this may depend on noise and the type of AVO effect associated. However, a more in-depth analysis is required, as this situation may be different in other locations, where pressure and saturation changes overlap differently. Additionally, it is important to note that since the noise has been extracted from the observed seismic, some of our observations cannot be generalised, as the type of noise present can be data dependent (due to acquisition, geology, etc.).

Another factor to take into consideration is the fact that the 4D AVO response may be more complicated in areas where pressure and saturation changes overlap, and therefore we may need more angle stacks to describe it. In the next section I extend this comparison by running the inversion in a map and performing an uncertainty analysis on the solution at the well locations. To measure the quality of the solution I use a combination of three measurements: the spread of the data resolution matrix, the spread of the model resolution matrix and the size of the model covariance matrix (Menke, 1989), which are described below.

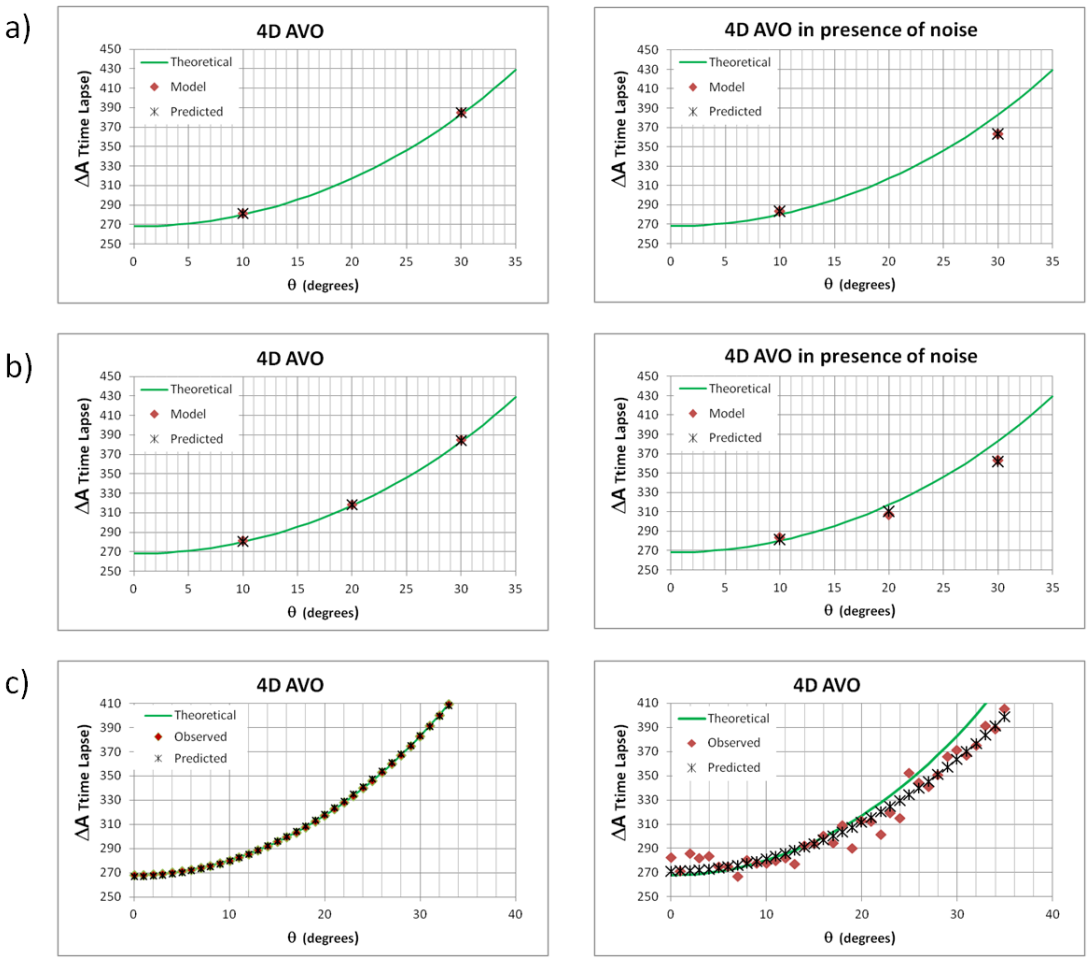

Figure 7.10: Numerical analysis performed to compare the use of (a) two angle stacks, (b) three angle stacks, (c) angle gathers. The green line is the theoretical AVO curve, the brown diamonds are the angle stacked amplitudes and the black stars are the inversion results. The left hand side panels show the results without noise and on the right are the results after adding noise.

Data resolution matrix: This provides a measure of the quality in terms of the match between the predictions and the data, and whether the data can be uniquely resolved. It is given by

$$\boldsymbol{N} = \boldsymbol{G}\boldsymbol{G}^{-\boldsymbol{g}} \ . \tag{7.14}$$

Here, $\boldsymbol{G}^{-\boldsymbol{g}}$ is the data kernel matrix that satisfies the inversion solution. When the error in the solution is zero ($\boldsymbol{d}^{\boldsymbol{obs}} = \boldsymbol{d}^{\boldsymbol{pred}}$), **N = I** (identity matrix). This type of measurement evaluates both the data and the quality of the input model **G.** As we need to calculate

this matrix on every location of the map, a more practical way of visualising this property is by calculating its spread:

$$spread(\boldsymbol{N}) = \|\boldsymbol{N} - \boldsymbol{I}\|_2^2 = \sum_{i=1}^{N}\sum_{j=1}^{N}\left[\boldsymbol{N}_{ij} - \boldsymbol{\delta}_{ij}\right]^2 \ , \tag{7.15}$$

where $\boldsymbol{\delta}_{ij}$ represents the elements of the identity matrix.

Model resolution matrix: This measurement allows us to estimate whether the inverted parameters can be uniquely resolved. It is defined as follows:

$$\boldsymbol{R} = \boldsymbol{G}^{-g}\boldsymbol{G} \, . \tag{7.16}$$

If **R** is equal to the identity matrix, it means that the inverted parameters have been uniquely estimated; otherwise these are a weighted average of the true values. As with the data resolution, for practical purposes we calculate the spread of **R** at each location as follows:

$$spread(\boldsymbol{R}) = \|\boldsymbol{R} - \boldsymbol{I}\|_2^2 = \sum_{i=1}^{M}\sum_{j=1}^{M}\left[\boldsymbol{R}_{ij} - \boldsymbol{\delta}_{ij}\right]^2 \ . \tag{7.17}$$

Unit model covariance matrix: This provides a useful way of understanding the solution's stability and sensitivity to noise, as it allows an estimation of how data errors are interpreted by the inversion as changes in the data kernel matrix. The importance of this measurement is that is independent of the data itself, and hence highlights the stability of the inversion scheme. It is defined as follows:

$$[\mathbf{cov_u}\ \mathbf{m}] = \boldsymbol{G}^{-g}[\mathbf{cov_u}\ \mathbf{d}][\boldsymbol{G}^{-g}]^{\boldsymbol{T}} \ . \tag{7.18}$$

Here, a large value in the covariance implies uncorrelated data (for instance, when noise is present) and a small covariance means that the mapped errors are small and

hence the solution is stable. Again, for visual purposes, it is preferred to calculate the size of the covariance matrix at each location, which is given by:

$$size([\mathbf{cov_u\ m}]) = \left\|[\mathrm{var_u}\mathbf{m}]^{\mathbf{1/2}}\right\|_{\mathbf{2}}^{\mathbf{2}} = \sum_{\boldsymbol{i=1}}^{\boldsymbol{M}}[\mathbf{cov_u\ m}]_{\mathbf{i}} \quad . \tag{7.19}$$

7.4.1 Inversion using two angle stacks

Figure 7.11 and Figure 7.12 show the inversion results using two angle stacks (nears and far), with and without noise. In both cases, the results are compared against the simulation maps. In general, the results of the inversion manage to reproduce the pressure and saturation changes, even in places where these overlap (for instance around wells W2 and W3). However, as expected, in the presence of noise the solution starts to break, particularly in places where the changes are small.

The quality measurements for the inversion with noise are shown in Figure 7.13. The map of spread of **R** shows values close to zero, with a nearly random distribution of high values. This shows the inherent non-uniqueness in the inversion. The map of the spread of **N** shows values close to zero everywhere except in the areas with extreme pressure and saturation changes. With two inputs and two unknowns, the inversion problem is even-determined and hence the model data are uniquely resolved. This implies that noise is treated as information and mapped as part of the inverted properties, as there is not enough information in the matrix to differentiate noise from data. The covariance map shows lower stability in the areas where pressure and saturation changes overlap. The cross-plot shows the spread of **N** versus the size of the covariance at the locations of wells W1, W2, W3 and W4. This plot provides a useful way of evaluating the quality of the solution. When pressure and saturation changes are small (W1 and W2) the solution is accurate although unstable; however, in places where higher pressure and saturation changes are present (W3 and W4), the resolution decreases, even though the stability increases.

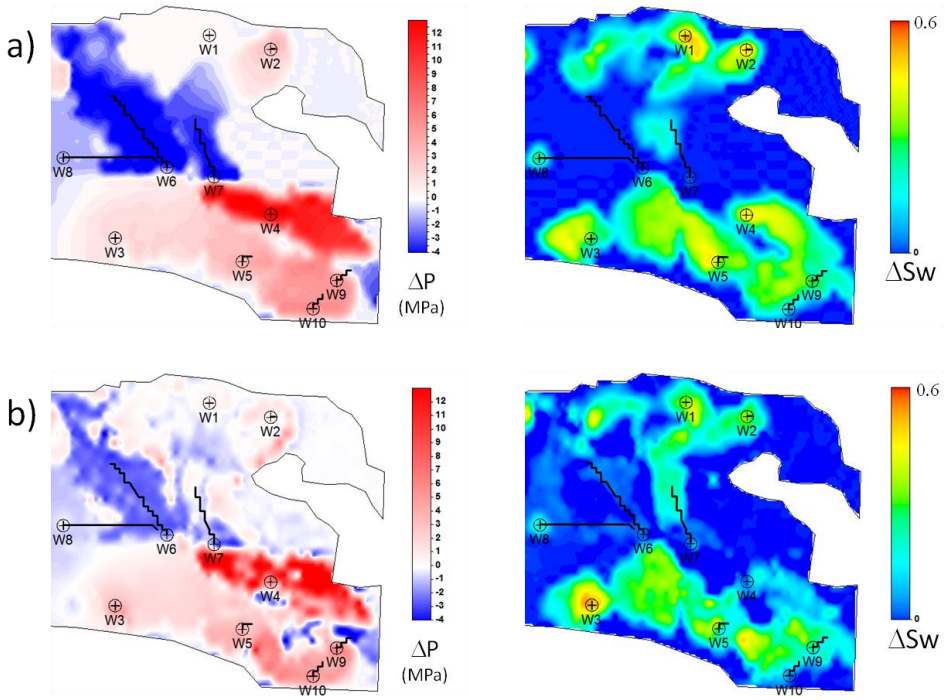

Figure 7.11: a) Reservoir simulation maps for ΔP (left) and ΔS_w (right). b) Inversion results using two angle stacks without noise.

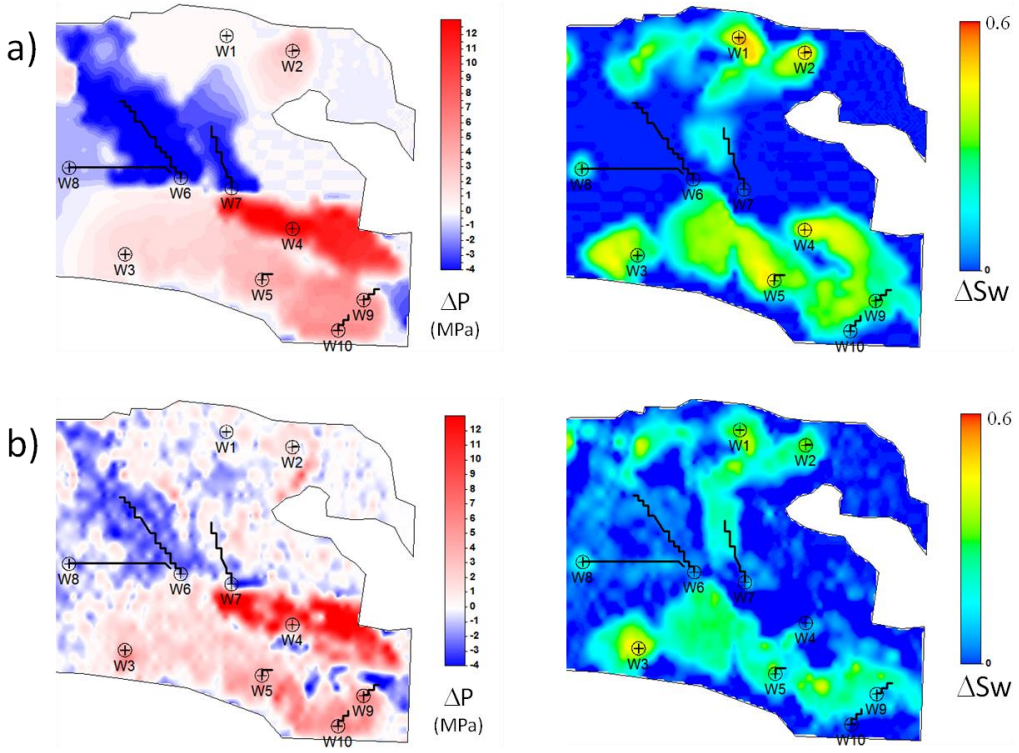

Figure 7.12: a) Reservoir simulation maps for ΔP (left) and ΔS_w (right). b) Inversion results using two angle stacks after adding noise: note that most of the noise is mapped as a property change.

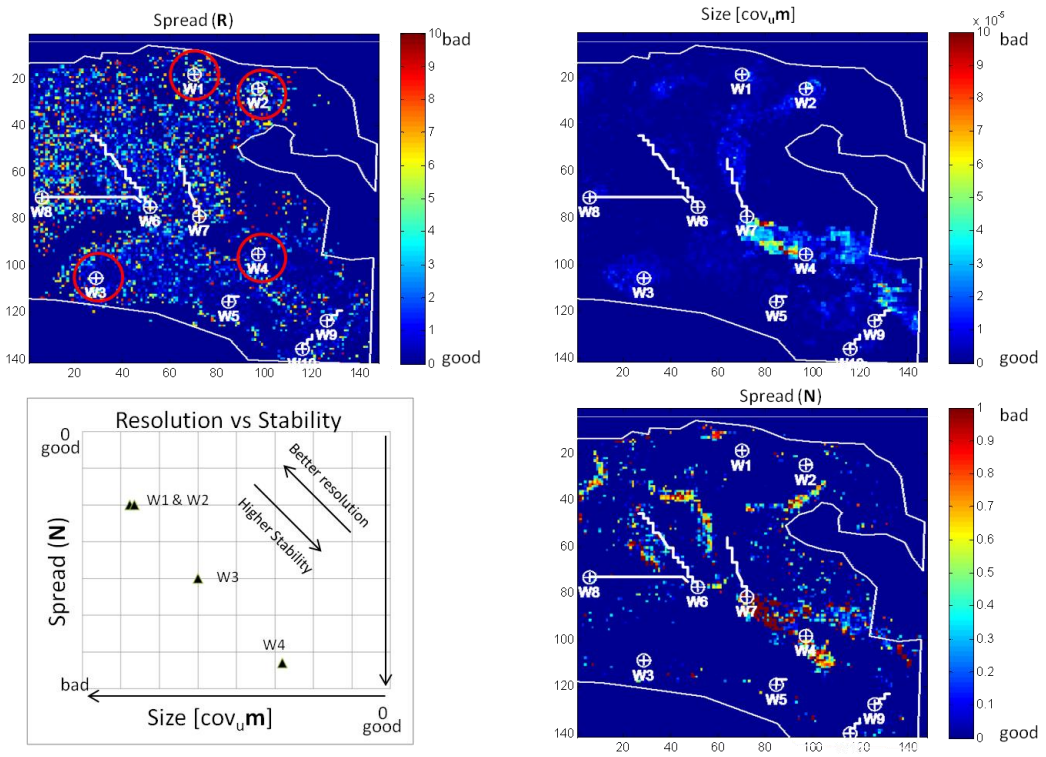

Figure 7.13: Quality plots for the inversion using two angle stacks. The spread (R) map shows a random distribution of high and low values, indicating the solution is not unique. The covariance map shows lower stability (high values) in areas where pressure and saturation changes overlap. The map of spread (N) shows low values everywhere (implying everything is used as information and inverted), except in areas with extreme pressure and saturation changes, where no solution is found. The cross-plot shows that for small pressure and saturation changes (W1 and W2) the solution is accurate although unstable, whereas, in places with extreme changes (W3 and W4), the resolution decreases.

7.4.2 Inversion using three angle stacks

The inversion results using three angle stacks are shown in Figure 7.14 and Figure 7.15 with and without noise. Compared to the inversion using two angle stacks, the new results are less sensitive to noise and closer to the simulation maps, even in the presence of noise. The only problematic area is that close to well W4, which shows an anomalously large pressure increase of > 13 MPa.

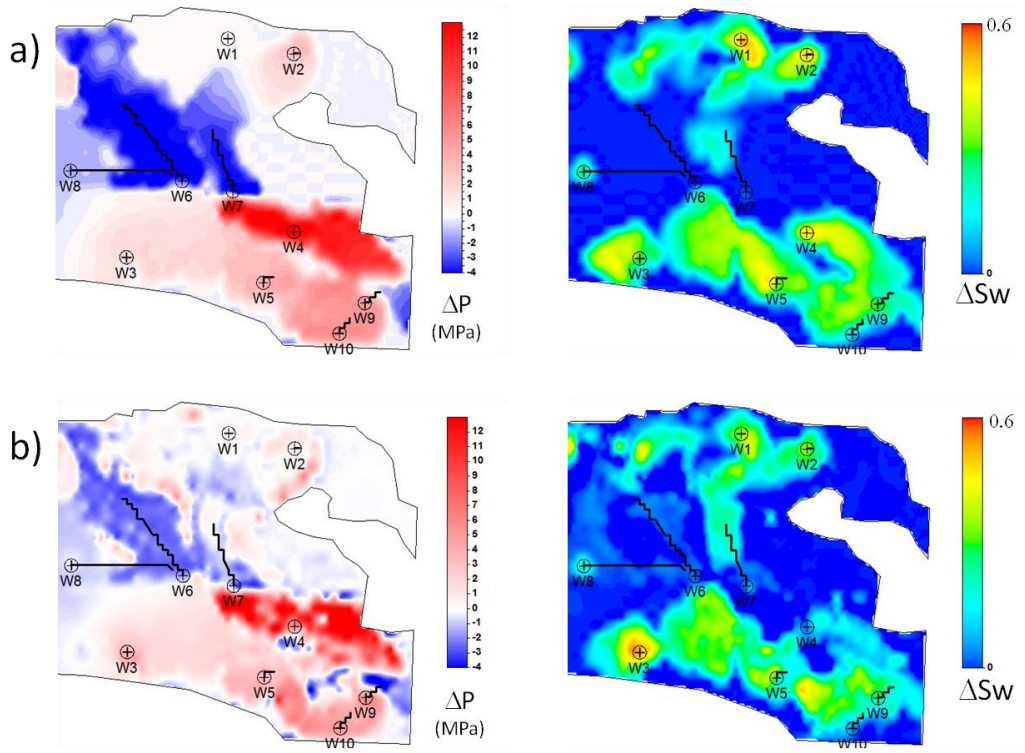

Figure 7.14: a) Reservoir simulation maps for ΔP (left) and ΔS_w (right). b) Inversion results using three angle stacks without noise.

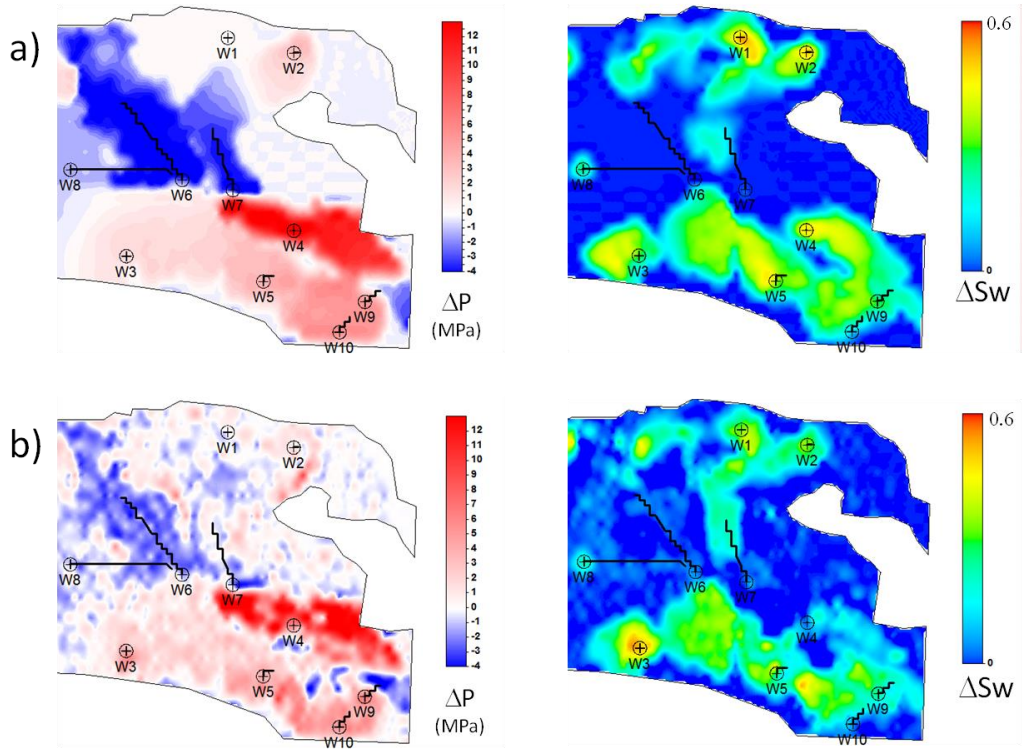

Figure 7.15: a) Reservoir simulation maps for ΔP (left) and ΔS_w (right). b) Inversion results using three angle stacks after adding noise.

The quality plots for the inversion with noise are shown in Figure 7.16. The map of spread of **R** is very similar to that of the two angle stacks; this indicates that adding an extra angle does not impact greatly the non-uniqueness of the solution. The map of spread of **N** shows values close to zero nearly everywhere. This is expected, as with three inputs, the problem becomes over-determined, and hence uncorrelated noise is no longer treated as information. This is confirmed by the covariance map, which shows higher stability in the solution, even in places where pressure and saturation changes overlap.

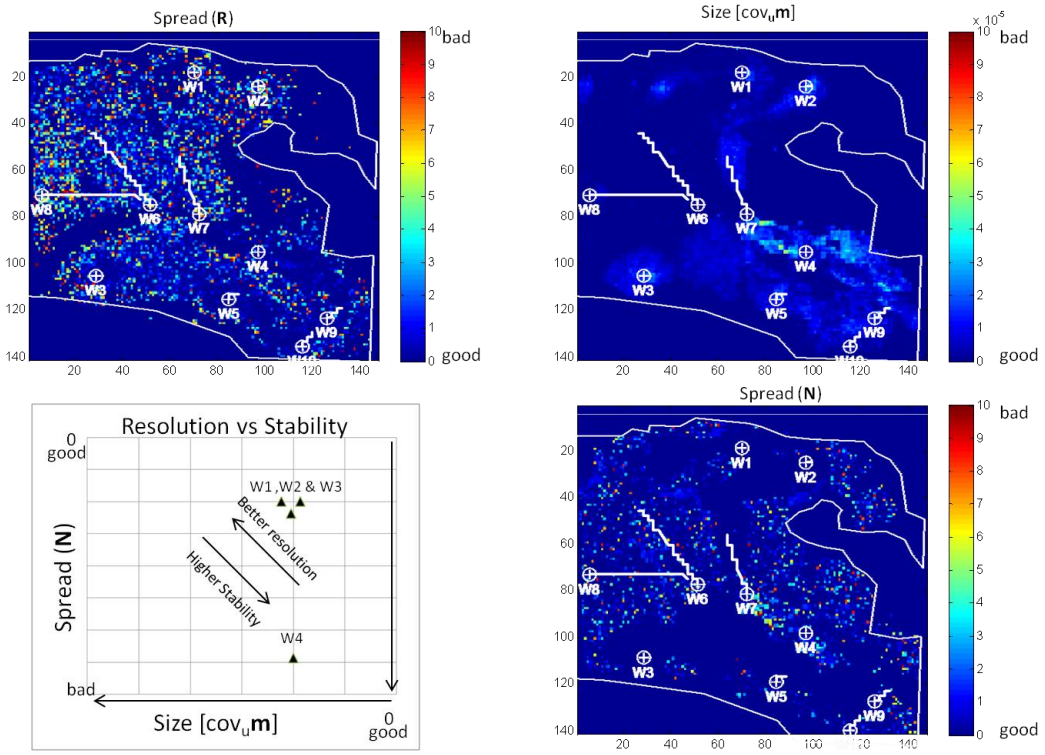

Figure 7.16: Quality plots for the inversion using three angle stacks. The map of Spread (R) is similar to that in the previous case. The covariance map shows higher stability in the solution compared to the two angle inversion. The map of Spread (N) indicates a better handle of noise in the process (random noise appears). The cross-plot shows that the solution is stable and has good resolution, except in well W4, where stability is high but resolution is poor.

The cross-plot of spread of **N** versus the size of the covariance shows that the solution is stable and has good resolution. The only anomalous point is W4, which shows high stability in the solution but poor resolution. This means that the inversion converged to

nearly the same solution every time but the error is not reduced. Nevertheless, these results are superior to those generated with only two angle stacks.

7.4.3 Inversion using angle gathers

The final test is to use the angle gathers with 35 traces to run the inversion and investigate if there is any advantage in increasing the number of traces that go into the inversion beyond the three angle stacks. The results of this inversion are shown in Figure 7.17 and Figure 7.18, again with and without noise respectively. Despite the big difference in the amounts of inputs, the resultant maps are very similar to those generated using three angle stacks.

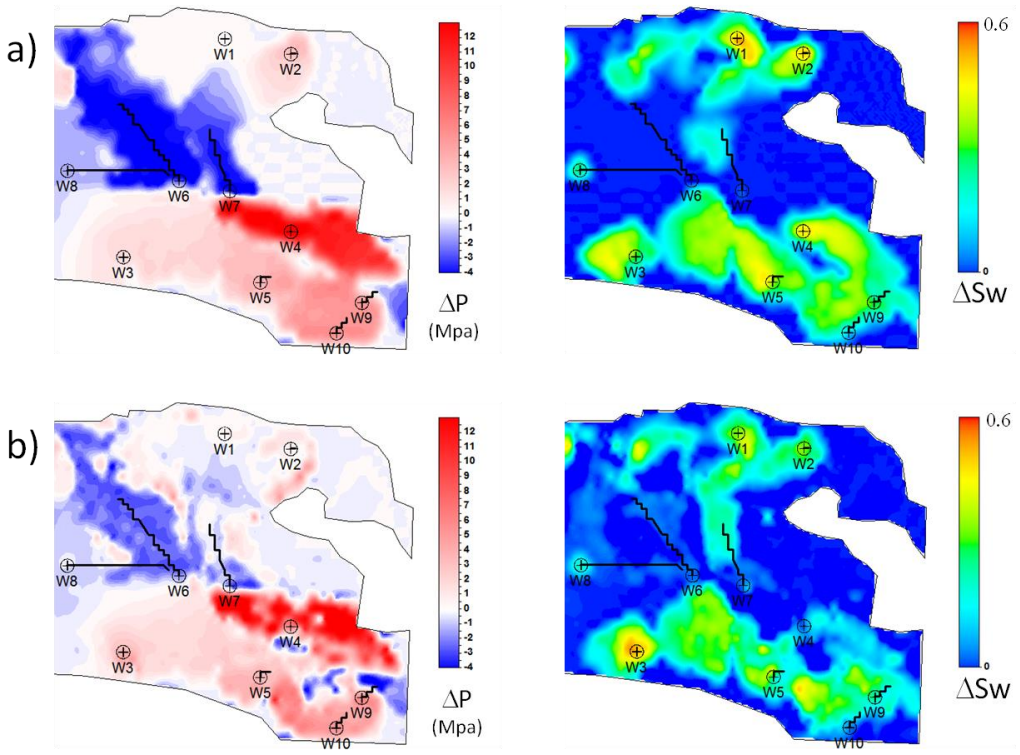

Figure 7.17: a) Reservoir simulation maps for ΔP (left) and ΔS_w (right). b) Inversion results using angle gathers (35 traces) without noise.

The inversion quality plots are shown in Figure 7.19. Interestingly, with the exception of the spread of **R** map, the quality measurements are remarkably different from the three angle stack inversion, even though the resultant maps are visually similar. The map of spread of **N** shows values near zero (**N** ≈ **I**) in the areas where pressure and saturation changes are close to the mean, and shows poor match in areas where changes are either too small or too large. The size of covariance map shows low stability in the solution in the same areas where **N** ≈ **I**; this is expected, as the inversion solution cannot solve every single input data point, as these are affected by noise. This implies that as a result of the increase of data inputs, what we gain in resolution we lose in stability of the solution. This is better illustrated in the resolution versus stability cross-plot, which shows wells W1, W2 and W3 in the high resolution but low stability area of the plot, with exception of W4, which shows a high stability but poor match.

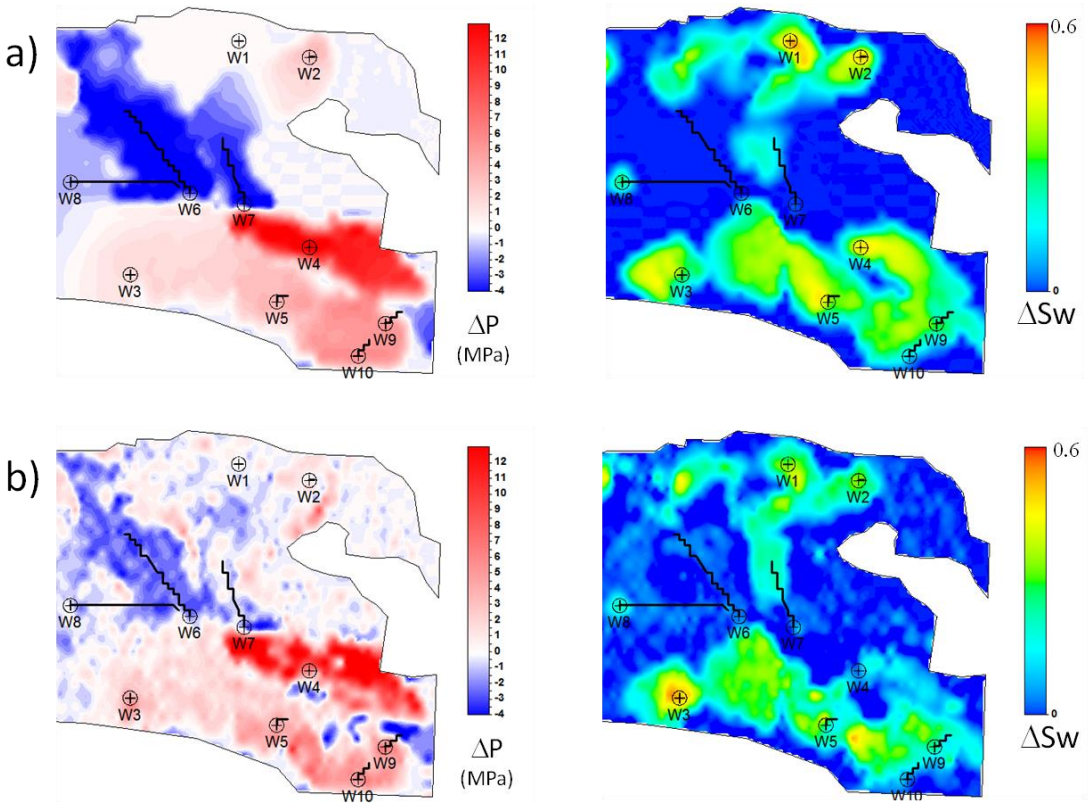

Figure 7.18: a) Reservoir simulation maps for ΔP (left) and ΔS_w (right). b) Inversion results using angle gathers (35 traces) after adding noise.

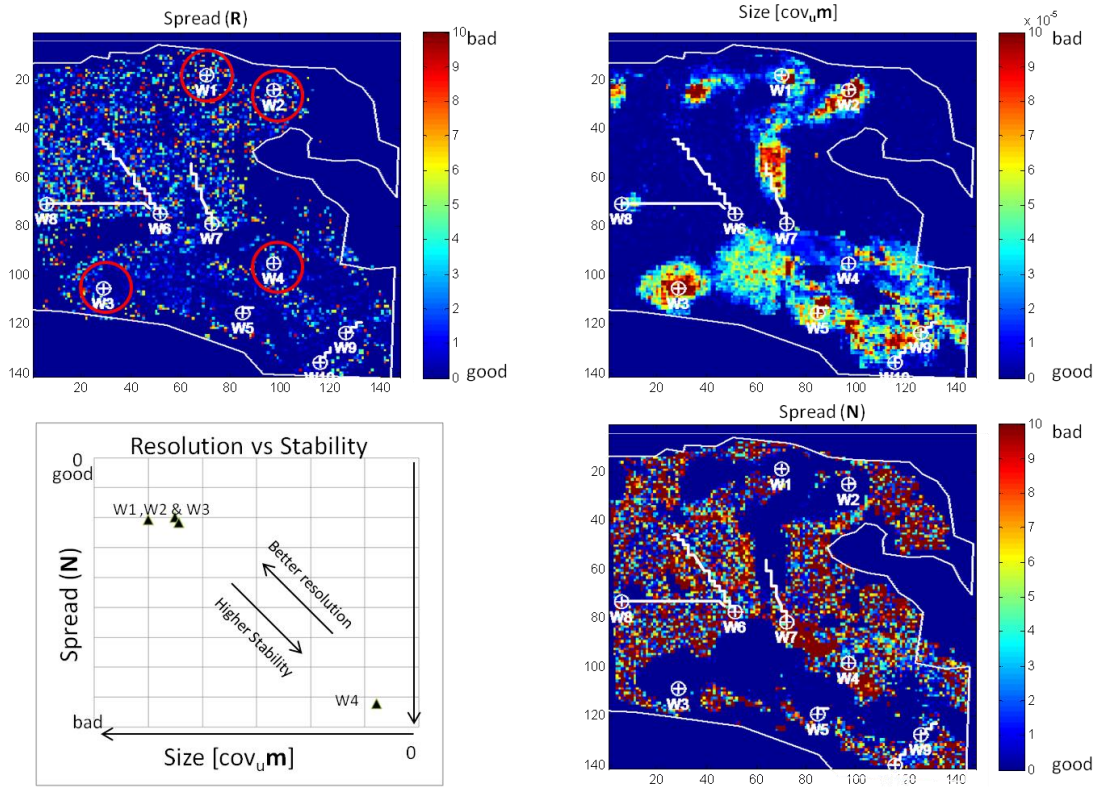

Figure 7.19: Quality plots for the inversion using angle gathers. The Spread (R) map is similar to that of the previous inversions. The map of spread (N) shows values near zero (N ≈ I) in areas where pressure and saturation changes are close to the mean, and shows poor match in areas with extreme changes. The size of covariance map shows low stability in the solution in the same areas where N ≈ I. This is expected, as the inversion solution cannot solve every single input data, as these are affected by noise. The resolution versus stability cross-plot shows wells W1, W2 and W3 in the high resolution but low stability area of the plot, with exception of W4, which shows a high stability but poor match.

7.4.4 Assessment of results

The results shown above demonstrate the effects of the trade-off between resolution and stability in the proposed inversion methodology. Although this trade-off is well known, it was still useful to investigate the minimum amount of information that is required to obtain meaningful results. Figure 7.20 shows the stability versus resolution cross-plot for all the inversion runs. Interestingly, for well W4, which has the

anomalously large pressure change, all inversion results appear in the same place, large spread(**N**) and low size[cov_u **m**] (stable solution but large residuals). This is not surprising, as the sim2seis program that generated the synthetic seismic uses an exponential form for the stress sensitivity, whereas the equations used in the inversion include a linearization of such function. Hence, it is expected to have larger errors as pressure changes increase. Nevertheless, all inversion runs are able to provide reasonable results in terms of solving for pressure and saturation changes, as shown in Figure 7.21. In all cases, the mismatch between the measured pressure and saturation changes and those obtained from the inversion is less than 2%.

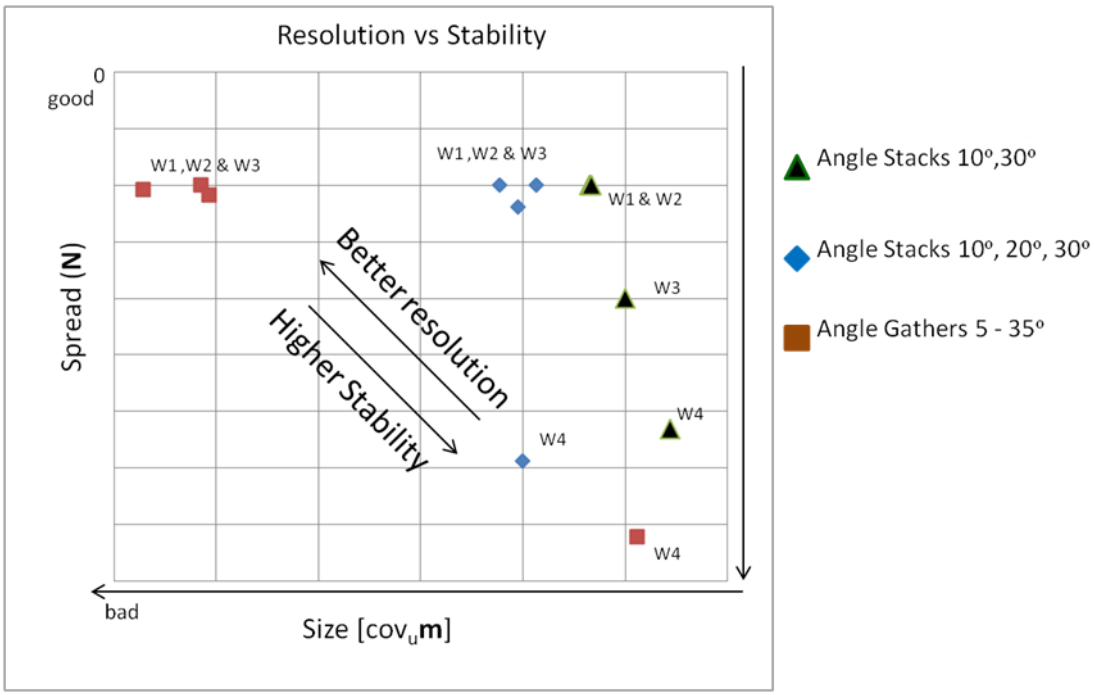

Figure 7.20: Resolution versus stability plot for all inversions

Putting all the results together helps in visualising the stability versus resolution trade-off. It seems clear that using two angle stacks is not ideal in terms of the ability of the inversion to handle noise. Three angle stacks seem to provide the best result, both in terms of stability and the ability to resolve the parameters.

It can also be concluded that, at least in this case, there is almost no added benefit in using angle gathers in the 4D inversion methodology proposed here. The reason for

this is that the angle stacks are generated from the angle gathers through stacking, which eliminates any noise that shows a random distribution across the angles. Therefore, as long as noise reduction is properly done during stacking, 3 angle stacks seem to be enough to provide a reliable inversion result in terms of overall property distribution, stability of the solution and match with the observations. However, it is recognised that the above observation depends on the levels and nature of the noise present in the data, plus there might be cases where strong non-repeatable noise is present in the data, and therefore incorporating a larger number of angle stacks may provide some benefit in terms of uncertainty analysis.

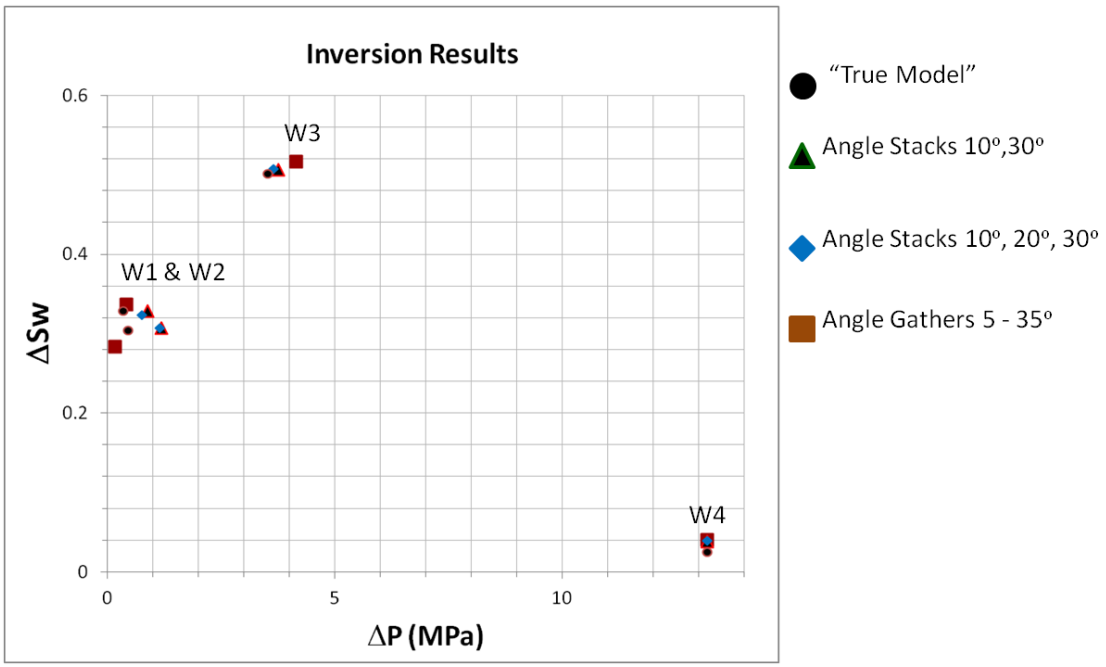

Figure 7.21: Inversion results compared with the pressure and saturation changes observed at the well locations.

7.5 Summary of findings in this chapter

- Inversion theory was applied to the equations developed in Chapter 2 for the oil-water system; it was found that the determinant of the kernel matrix is equal to zero. This implies that pre-stack 4D seismic data does not contain enough information to unambiguously solve for pressure and saturation changes. This

explains the fact that most inversions in the literature produce pressure and saturation change maps which are highly correlated; therefore, it is necessary to incorporate some sort of a priori information in order to solve the inversion matrix.

- Two types of inversion schemes have been designed, applicable to the oil-water system. The idea behind them is to provide an inversion solution that minimises the requirement of a priori information. The two schemes solve the inversion matrix by incorporating constraints; the first method uses inequality constraints, similar to those defined in Chapter 3. The second method uses boundaries, so that the resultant pressure and saturation changes fall within the ranges measured at the well locations.

- Both inversions were tested in a synthetic dataset. Both inversions gave similar results in terms of the overall distribution of the inverted properties and the match with the simulation based maps. The most important thing about these inversions is that we have kept the use of *a priori* information to the minimum and the maps obtained are not highly correlated.

- In practice, the selection of the constraints for the inversion depends largely on the inversion objectives and availability of data. In reservoirs where many wells are available with reliable measurements (core, PVT, repeated logs, pressure, etc.), there may be enough information to know a priori the minimum and maximum expected changes in pressure and saturation (boundary constraint). However, in reservoirs where only a few wells are available, or where no injectors exist, an inversion with an inequality constraint can be advantageous.

- Besides the parameters of the petroelastic model, as defined in Chapter 2, there are two key inputs to the inversion proposed here: a porosity map and an

overburden stress map. Porosity can be computed from P impedance inversion using empirical porosity versus impedance trends (e.g., Avseth, 2005, Pedersen et al., 2008, Chi and Han, 2009) or a rock physics equation (e.g. Raymer-Hunt, 1979; Krieff, 1990). The overburden stress can be computed from empirical depth trends or by integrating the density log extrapolated to the surface. Porosity provides the spatial distribution of the pressure and saturation responses and the overburden stress map incorporates the lateral variability in the rock stress sensitivity as a result of burial depth.

- The boundary based inversion was tested in a synthetic dataset from a field in the North Sea. Six different runs were performed (2 and 3 angle stacks, angle gathers, all of them with and without noise) and all the results were compared. It was found that using 3 angle stacks provides the best result in terms of resolution and stability. However, the three inversions produced reasonable match at the well location with an error of less than 2%.

Chapter 8: Conclusions and Recommendations

"We have not succeeded in answering all our problems. The answers we have found only serve to raise a whole set of new questions. In some ways we are as confused as ever, but we believe we are confused on a higher level and about more important things"

No hemos tenido éxito en resolver todos nuestros problemas. Las respuestas que tenemos solo generan una serie de preguntas nuevas. En cierta forma estamos más confundidos que nunca, pero creemos que estamos confundidos a un alto nivel y acerca de cosas más importantes

Earl C. Kelley

American Scholar and Writer

This is the final chapter of this thesis where I summarise the findings of this research and we play the adventurous game of recommending future research subjects in the context of what has been investigated in this work.

8.1 General conclusions and remarks of this thesis

The general objective of this thesis was to define equations that facilitate a quick, yet robust interpretation of the 4D seismic amplitude differences. Although some of these equations exist in the literature (as described in Chapter 1), my purpose was to minimise the use of empirical fits, maximizing the use of constants with clear physical meaning. The purpose of this is to make the result intuitive and also to be able to evaluate the influence of each parameter on the final result. All this represents an alternative to other techniques developed for this purpose, such as those by Tura and Lumley, 1998; Landrø, 2000; Meadows, 2001; Ribeiro and MacBeth, 2004; MacBeth et al., 2006a, Floricich et al., 2006; Andersen et al., 2009 and Trani et al., 2013. The development of these equations is only the first step in the process of improving our understanding of the 4D amplitude differences and their relation to reservoir changes.

In Chapter 2, I defined equations applicable to the oil-water system assuming a single interface model as a starting point and a detailed analysis on 4D AVO was performed. The resultant theoretical development shows that the time-lapse seismic amplitudes can be expressed as functions of two constants, one controlling the impact of fluid changes and the other controlling changes in the effective stress. To be consistent with previous research (MacBeth et al., 2004; Floricich et al. 2006), the constants are named C_S and C_P, but this time, instead of being empirical functions, each constant has a physical meaning. In the new equations, the role that porosity plays in the equations is now explicit. The definitions of $C_S$and C_P found in Chapter 2 form the basis of all subsequent developments in this thesis. One of the main findings in this chapter is that the parameters of the petroelastic model act as groups of parameters rather than as individual parameters, and that the 4D signal is formed of three groups of these parameters: the fluid contrast (C_S), the rock stress sensitivity (C_P^{Rock})and the fluid pressure sensitivity (C_P^{Fluid}). From a numerical exercise which was performed, it was found that the magnitude of $C_S\,\Delta S_w$ can be similar to the magnitude of $C_P^{Rock}\,\Delta P$, whereas the magnitude of $C_P^{Fluid}\Delta P$ can be as small as 1/10 of the magnitude of the previous two and hence its influence on the amplitude changes can be negligible. In

terms of polarity, for the oil-water system, the fluid change and the fluid pressure sensitivity act in the opposite way to the rock stress sensitivity, hence they have opposite signs. For this reason, 4D amplitudes are sometimes close to zero near to injectors, where a pressure up signal cancels the increase in water saturation. It was found that porosity plays a crucial role in the way pressure and saturation signals interact and the dominance of one or the other, this was intuitive for saturation but not for pressure changes.

I used all these observations in Chapter 3 to define constraints on the petroelastic model. It is well known that from all the parameters of the petroelastic model, the rock stress sensitivity is the most difficult to define and calibrate. I thus used my equations together with field data observations of amplitude changes near to injectors to define a constraint on this important parameter. My data sources include a reservoir in the North Sea available in ETLP and different published studies where pressure and water saturation changes are quoted. The results of this study suggest that C_S/C_P is a fundamental parameter that can be unambiguously extracted from the mapped 4D seismic amplitudes. For porosities of between 25 and 30%, it appears that $C_S/C_P \approx 8$ indicates the point at which pore pressure starts to dominate over saturation, and vice-versa. Defining this C_S/C_P in a reservoir can help determine a constraint and try different rock stress sensitivity curves and select only those which satisfy the constraint. Unfortunately, this type of constraint can only be found in reservoirs where pressure is supported by water injection, and there is still a great deal of non-uniqueness, even after the constraint.

The equations were extended in Chapter 4 to incorporate the effects of gas and reservoir thickness. By assuming a fluid distribution in the reservoir that is consistent with the large scale fluid distributions in reservoir engineering, equations were found applicable to (1) oil reservoirs above the bubble point, (2) gas reservoirs with active aquifers, (3) oil reservoirs below the bubble point with a pre-existing gas cap and (4) oil reservoirs below the bubble point without a pre-existing gas cap. In contrast to the equations in Chapter 2, applicable to the extraction of average (or RMS) amplitudes

based on the interpretation of the top of the reservoir, the equations in Chapter 4 are applicable to the interpretation of the fluid contacts. It has been noted in the past, that the way seismic is affected by vertical variations in the fluid distribution is frequency dependent (Sengupta, 2000). This means that any equation based on a single interface calculation requires an averaging of the fluid responses. In this case, in Chapter 2 I assumed a uniform fluid distribution (harmonic average) and after taking the 4D differences the result was linearised. This is acceptable for the oil-water system, but when gas is present this approach is no longer valid, as the contrast between the bulk moduli of gas and water is large. To avoid this problem, the equations in Chapter 4 are derived in the frequency domain, where the total response becomes a summation of the individual reflections weighted by their relative thickness (tuning). For each reservoir type, two equations were derived; one applicable to thick reservoirs, where the fluid contacts are visible and can be interpreted, either in the 3D seismic or the 4D differences, and the second one, applicable to thin reservoirs where only a map can be extracted. An important finding in this chapter is that the mathematical responses of a reservoir with a pre-existing gas cap and a reservoir with a secondary gas cap formed by gas dissolution are mathematically equivalent, the only difference being that the magnitude of the 4D signal in the first case is expected to be smaller than the magnitude of the second case. Another conclusion is that in the presence of gas and for an active aquifer, the magnitude of the pressure signal is much smaller than that of the fluid changes.

Besides incorporating the tuning function and the extension to multiple fluids, the equations are expressed in terms of the residual and irreducible fluid saturations instead of water saturation changes, as by previous researchers. This facilitates the calculation of the large scale residual hydrocarbon volumes (either gas or oil), which are key in reservoir engineering and petroleum economics. This idea is further developed and tested in Chapter 5, where a simplified version of the equations (using far angle stacks where the pressure response can be neglected) is used to determine ROS in an oil-water system. The method is applied to a synthetic dataset based on a geologically complex reservoir where no fluid contacts are visible and also to a real

dataset where fluid contacts are visible and interpretable. It was shown that there is an advantage in interpreting the fluid contact movements directly in the 4D seismic differences rather than using amplitude extractions based on an interpretation of the top of the reservoir. The results of this work show that it is possible to obtain a reasonable distribution of ROS, from the far angle 4D differences (or the full stack if the pressure change is small). This represents an alternative to the use of complex and time-consuming simulation to seismic studies to incorporate seismic data in reservoir engineering workflows, such as assisted seismic history matching. Nevertheless, it is important to mention that the results are still subject to wavelet interference effects, particularly close to the faults, and therefore using seismic inversion could help improve the results.

This last observation takes me to Chapter 6, where I apply inverse theory to the equations derived in Chapters 2 and 4 for the oil-water system, by incorporating the 4D AVO changes to separate pressure and saturation effects. By deriving the analytic expression for the least square solution of the inversion, it was possible to conclude that there is not enough information contained in the 4D AVO to unambiguously invert for pressure and saturation changes (the determinant of the inversion matrix is zero); therefore it is fundamental for the inversion to incorporate *a priori* information that allows a satisfactory inversion. Two solutions are proposed in this work to solve the inverse problem by keeping the amount of *a priori* information to the minimum; (1) by incorporating an inequality constraint similar to those established in Chapter 3, and (2) by restricting the solution to known ranges of ΔP and ΔS_w. Although both solutions provide similar results, there are situations where one may prefer to choose one over the other. For instance, if no water injectors exist, the equality constraint cannot be defined and hence the boundary-based method would be a preferred option. In the case of reservoirs with enough information available to establish reliable constraints, the first method would be the preferred choice as the amount of *a priori* information is minimal and gives higher freedom to the solution in ΔP and ΔS_w space. The inversion scheme was tested on a synthetic dataset, where it was possible to analyse the effectiveness of the pressure and saturation inversion as well as the sensitivity to noise

and the minimum requirements in terms of input data. It was found that, for an NRMS between 7 and 20%, using three angle stacks gives better results than using two angle stacks or thirty-five angle gather traces. However, in terms of matching the values at well locations, the three inversion results give less than 2% error in terms of match to the well observations. The only two pre-requisites for this inversion are an effective porosity and overburden stress maps, which can be obtained through 3D seismic inversion methods and depth trends respectively. In this work the inversion was performed on mapped amplitudes but its application can be also extended to 3D if porosity and overburden calculations are available, for instance, if the inversion is performed inside the simulation grid.

8.2 Recommendations for future research

The research presented in this thesis has only scratched the surface of our ability to understand and interpret quantitatively 4D seismic changes. There are still many more things to uncover, and hopefully this research can help define a route to improve the use of 4D seismic in reservoir monitoring and reservoir management. In the following section, potential areas of research directly related to this work are proposed.

8.2.1 Calibration of the rock stress sensitivity in the presence of gas

It was shown in Chapter 3 that the dominance between the pressure and saturation signals in the 4D differences is governed by the value of the C_S/C_P ratio, and hence depends directly on the magnitude of the rock stress sensitivity. It was also shown that measuring this parameter in the laboratory is a major challenge and many uncertainties remain on whether the values calculated are truly applicable to 4D seismic interpretations.

The calibration method proposed is based on the use of water injectors and applicable to reservoirs (or segments within the reservoirs) where no gas is present. However, it is

recognised that there are many reservoirs that fall below the bubble point after production and therefore, the presence of gas would make the applicability of the calibration technique a major challenge. Additionally, in reservoirs with a strong aquifer drive, where there is no requirement for water injection, it will not be possible to establish a constraint like those proposed in Chapter 3, and even though my finding that $C_S/C_P = 8$ seems to be a generality for porosities around 28%, the remaining level of ambiguity is still large, as shown in Figure 3.36. Amini (2014) performed a calibration of the stress sensitivity using the simulation to seismic tool by testing various rock stress sensitivity curves together with the core based stress sensitivity curves and evaluated the match to the observed seismic. It was found that the core based sensitivity curve under-predicts the amplitude changes and a higher stress sensitivity curve was required to match the observed amplitudes. However, the poor match between the simulation and the bottom-hole pressure measurements (BHP) in this dataset do not allow the results to be generalised.

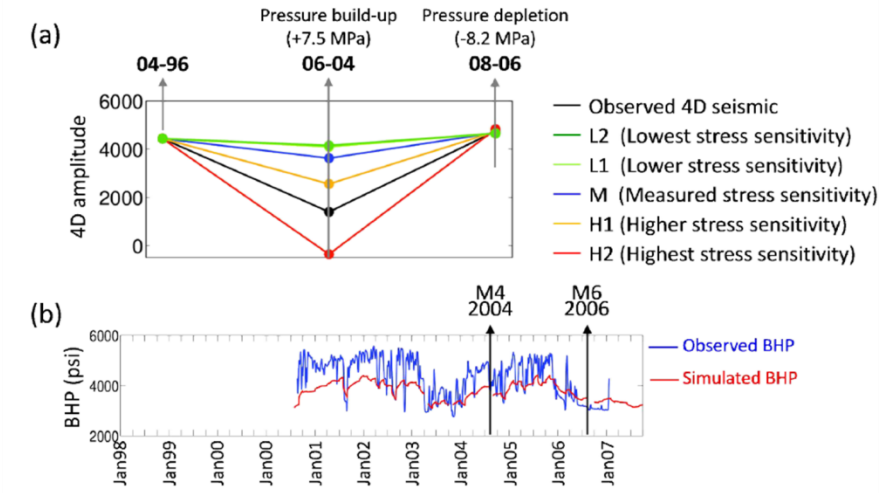

Figure 8.1: Calibration of the stress sensitivity using the sim2seis. (a) 4D amplitude variations around an injector. (b) Comparison between measured BHP and the results of the simulation.

It is recognised that more research investigation is required to properly calibrate the rock stress sensitivity; it is possible that to perform this calibration, other data sources are needed rather than just seismic (perhaps from repeated well logs, or VSP data, etc.) so that the ambiguity and uncertainty of this important parameter is reduced.

8.2.2 *4D seismic amplitude interpretation of reservoirs in HPHT environments*

According to the Department of Trade and Industry in the UK, high pressure /high temperature environments (HPHT) are defined as reservoirs with a pressure exceeding 69 MPa (10,000 psi) and a temperature above 150 °C (300 °F). In the 2013 UK economic report , HPHT environments are considered to represent the largest categories of yet-to-find reserves (YTF) in the North Sea (Figure 8.2); however, it is also acknowledged in the industry that the technology for developing such reservoirs is still under development, not to mention the ability to monitor their performance.

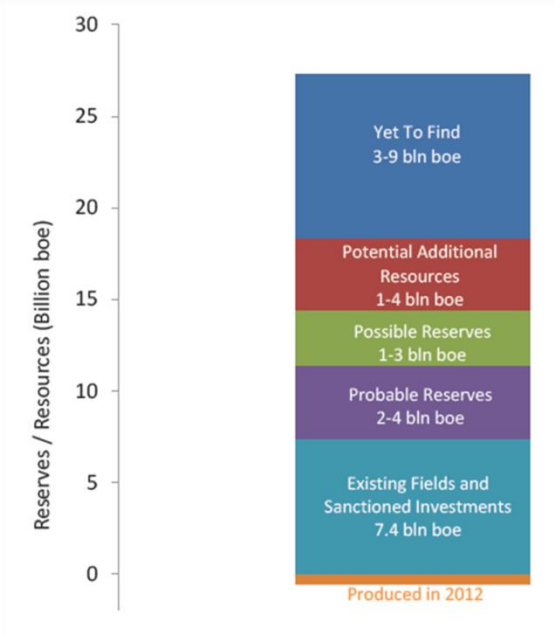

Figure 8.2: Forecast of UKCS reserves and resources by the end of 2012 (Source: 2013 economic report, Oil & Gas UK)

There are a number of challenges in developing HPHT reservoirs, particularly related to geomechanics failures of wells, not only while these are being drilled, but especially as a result of production. Well failure results in huge economic losses resulting from

the stopping of production. An additional challenge is related to field development: since the rate of depletion in an HPHT environment can be large, the ability to design a well control program becomes a huge challenge, as the margin between the controlling and loss-inducing mud gradients has disappeared or even reversed, compared to the pre-production profiles (Glass, 2005; Schutjens et al., 2009) and the exact way this occurs or their causes are still not clearly understood.

Although 4D time-shifts or time-strains have been used qualitatively or semi-quantitatively to identify partially depleted areas (Figure 8.3) and to support geo-mechanical modelling (for example: Landrø & Stammeijer, 2004; De Gennaro, 2008), there are still uncertainties in the calculation of time-shifts, as different calculation methods or window sizes can provide different results, making quantification a challenge (Staples, 2007). The use of 4D seismic amplitudes, however, has not been fully investigated in this context, and current rock physics models, including those developed and presented in this thesis, have not been validated under HPHT conditions. Additionally, one of the main assumptions made in my derivations was that reservoirs are not compacting; therefore, any time delay due to compaction is expected to be removed via cross-correlation, prior to computing the 4D differences. It would be interesting to investigate the possibility of extending the approximations to incorporate the geo-mechanical compaction: such a model could have diverse applications, starting from modelling and interpretation (to prevent well failures) to the incorporation of perturbations into the velocity model that is used to migrate the monitor and improve the calculation of time-lapse velocity changes instead of calculating them from time-shifts, which are highly dependent on noise and the window used for their calculation. This way, instead of migrating base and monitor with the same velocity (and then interpret the resulting time-shifts), it would be possible to invert for the velocity change directly. It is envisaged that this inversion process can be set up by perturbing the velocity model of the baseline according to the new equations and performing successive migrations in the monitor, conditioning the process by the seismic image from the base line.

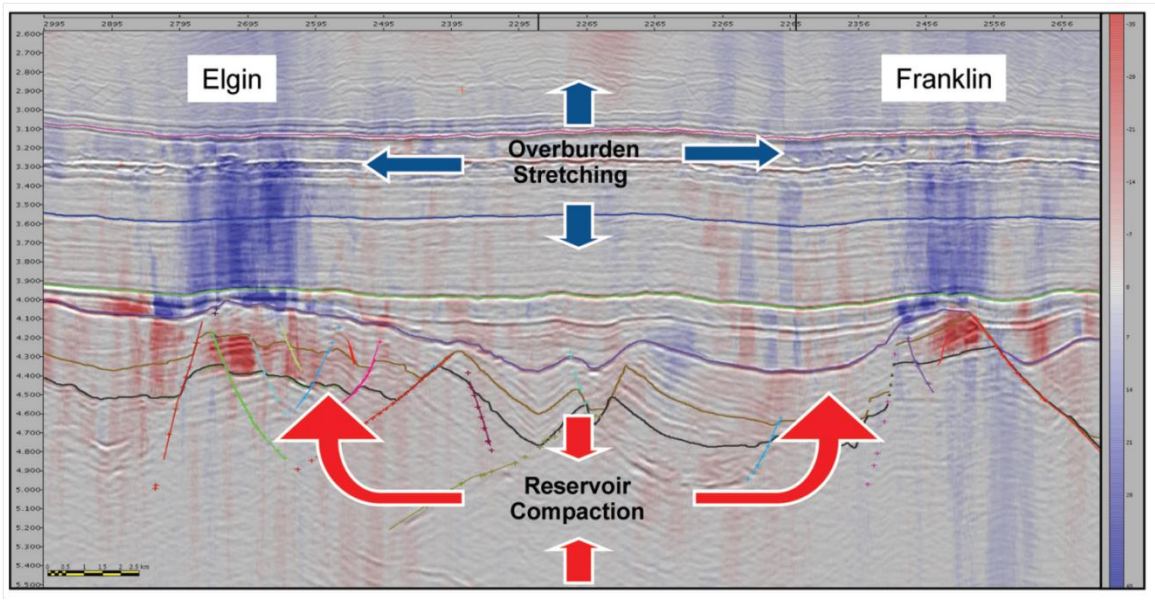

Figure 8.3: 4D interpretation in the Elgin and Franklin reservoirs to support geo-mechanical modelling (De Gennaro et al., 2008).

8.2.3 Determination of S_{gro}, S_{grw}, S_{orw} and S_{org} in multi-phase reservoirs.

In Chapter 4, equations were developed to facilitate the interpretation of fluid contacts in 4D differences. These equations formed the basis of the method defined and tested in Chapter 5 to determine S_{orw} for oil reservoirs above the bubble point pressure. Since equations have also been derived for gas reservoirs with and without aquifer influx and oil reservoirs with gas caps (either pre-production or formed via gas exsolution), it is suggested that this research can be extended to the determination of S_{gro}, S_{grw}, S_{orw} and S_{org}. This would be particularly useful in complex reservoirs where multiple fluid phases interact and changes occur below seismic resolution. As shown in Chapter 4, in the presence of multiple fluid phases, the 4D seismic response is not trivial, and in the presence of gas, the pressure and saturation signals cannot be easily separated via 4D AVO. Therefore, it is necessary to investigate if there is any additional information or measurements that can be incorporated into the analysis so that the residual hydrocarbon saturations can be calculated.

Residual gas saturation, in particular, is a challenge. Falahat et al. (2012) show that in simple reservoirs the thickness of the gas column can be more important for hydrocarbon quantification than the actual value of S_{grw} However, in reservoirs with a complex structural or stratigraphic framework, or in carbonate reservoirs, this observation may no longer be applicable.

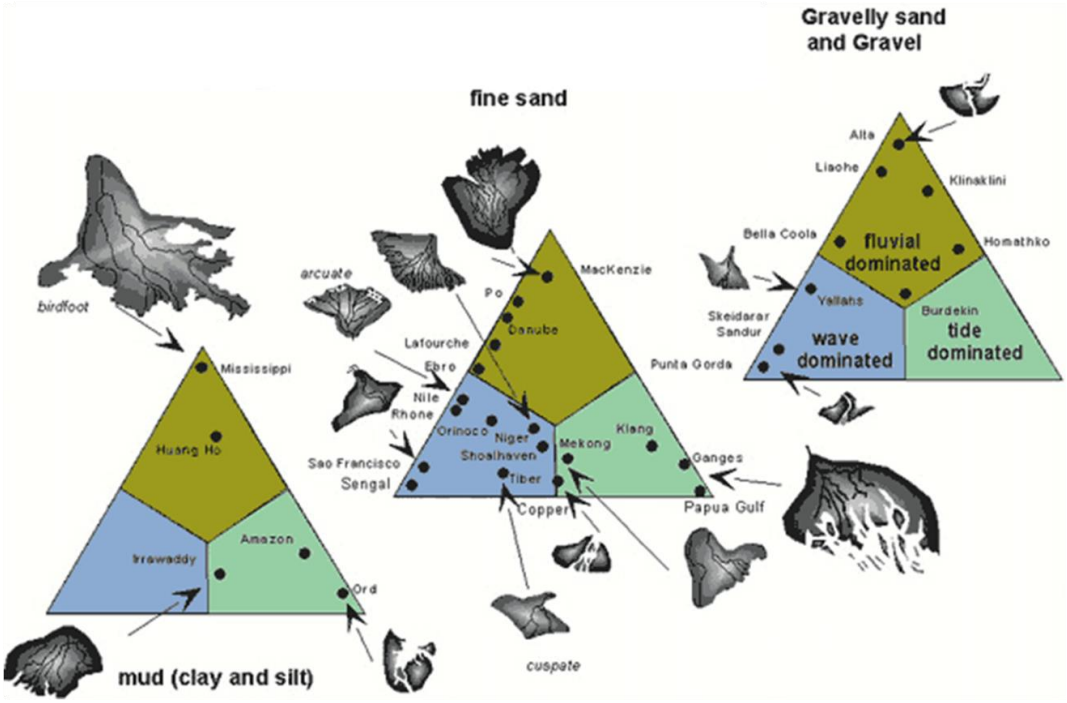

Figure 8.4: Classification of deltas by dominance of river (dark green), wave (blue) or tide (light green) dominated forces. This has an effect on the delta morphology and grain size (Orton and Reading, 1993).

Another important subject of research in this area is how to account for lateral changes in the irreducible water saturation (S_{wir}). In the methodology defined in Chapter 5, it was considered that this quantity would not change significantly for a constant porosity and NTG, and hence, it is mostly a function of height above the free water level. This assumption can be valid for clastic reservoirs with relatively clean sandstones such as North Sea or West Africa turbidite reservoirs. However, in the case of carbonates, or even in clastic reservoirs deposited in distal facies, it would be necessary to incorporate lateral variations in S_{wir} related to changes in the grain size

(Figure 8.4), which will affect the pore throat radius and hence, wettability. Variations in grain size are commonly incorporated qualitatively in reservoir modelling by interpolating well-based measurements. However, I have found in Chapter 4 that 4D seismic can be sensitive to variations in S_{wir}. At the moment, it remains unclear whether this can be used, in combination with other measurements, to condition the interpretation of geological facies related to grain size.

8.2.4 Application of S_{orw} calculations to assisted seismic history matching and production forecast

One of the key objectives in reservoir management is to be able to predict reservoir behaviour with time, so that the appropriate strategies are put in place to exploit the resources in the most efficient manner (Production Forecast). Traditionally, this process involves building a model using all available data (well logs, geological information, laboratory measurements, etc.); then production parameters are introduced, and the performance of the model and the history of the reservoir are compared and matched. When the process involves the use of 4D seismic data it is called Seismic History Matching. The general idea behind it is that if the model is able to match the history of the reservoir, then it must be able to predict the future performance. Unfortunately, the history matching process is highly ambiguous and, it is possible to match the history of the reservoir with multiple models (Figure 8.5).

Traditionally, the optimisation of the model is performed through manual modification of the model parameters; however this process can be onerous and time-consuming. Therefore, computer-based optimization techniques are increasingly common in the oil industry; this process is commonly known as assisted seismic history matching. Starting with an initial description of the reservoir, these optimization techniques automatically vary reservoir parameters until certain criteria are achieved and a history match of field performance is obtained (Figure 8.6). Although this is a great improvement over manual optimisations, the process still requires a detailed

simulation to seismic modelling or 4D inversion, which on its own it can be a very time consuming process and has many ambiguities.

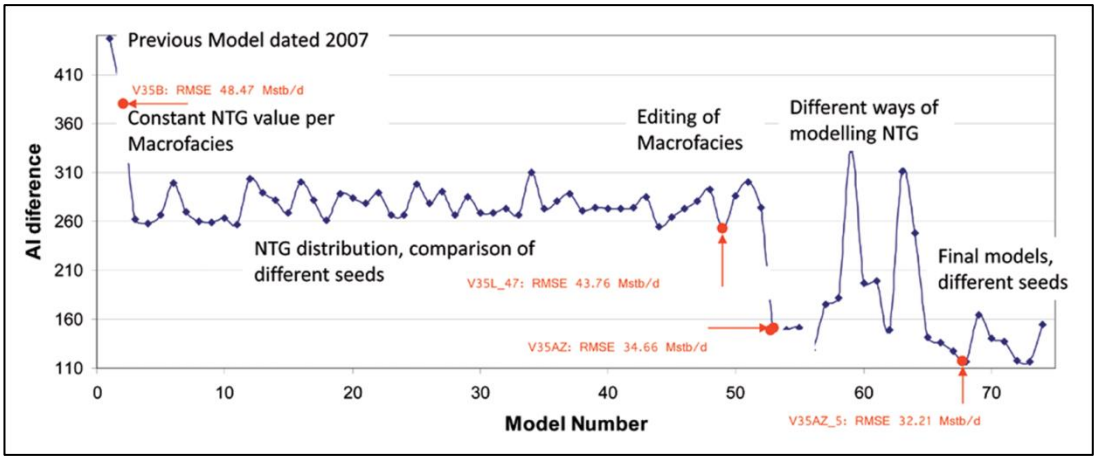

Figure 8.5: This graph shows the evolution of the assisted seismic history matching process in a North Sea reservoir and the level of ambiguity of the process. This particular case required more than 70 models to achieve an acceptable result (Gill et al., 2012).

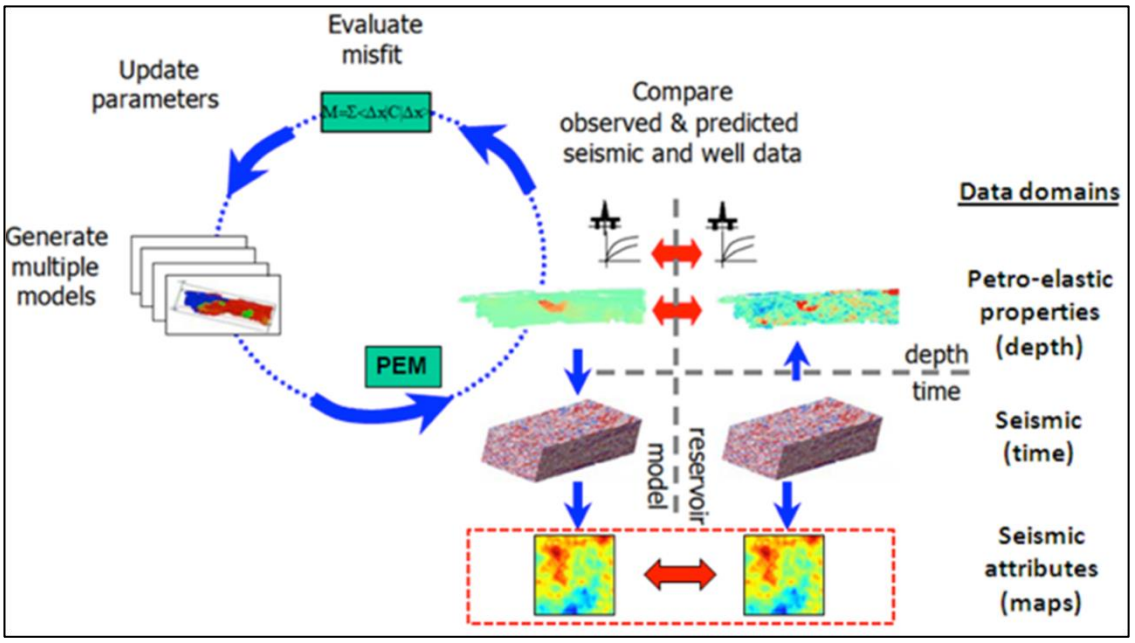

Figure 8.6: An example of an assisted seismic history matching workflow. Impedances and seismic are modelled from simulation results and compared to observed data using maps of attributes. The combined seismic and production misfit is used for parameter updating (Stephen and MacBeth, 2006).

In Chapter 5, a technique was developed to compute S_{orw} using extracted amplitude maps from 4D difference far angle stacks. This process involves the use of a single equation, which depends on two constants: C_s, which is a known function of the rock and fluid physics parameters and porosity, and S_{wir}, which depends on height above the free water level and the pore throat radius. Since the rock and fluid physics parameters and porosity are generally well established, the largest uncertainties in the equations are the thickness of the oil-water contact movement and the value of S_{wir}. Having a simple equation relating 4D amplitudes to residual hydrocarbon volumes gives the opportunity to simplify the assisted seismic history matching workflow. Instead of going through a time-consuming simulation to seismic or 4D inversion processes and ambiguous map extractions and comparison with observed amplitudes, it is envisaged that it may be possible to define an algorithm that allows selecting the S_{orw} calculations that match the production history at well locations.

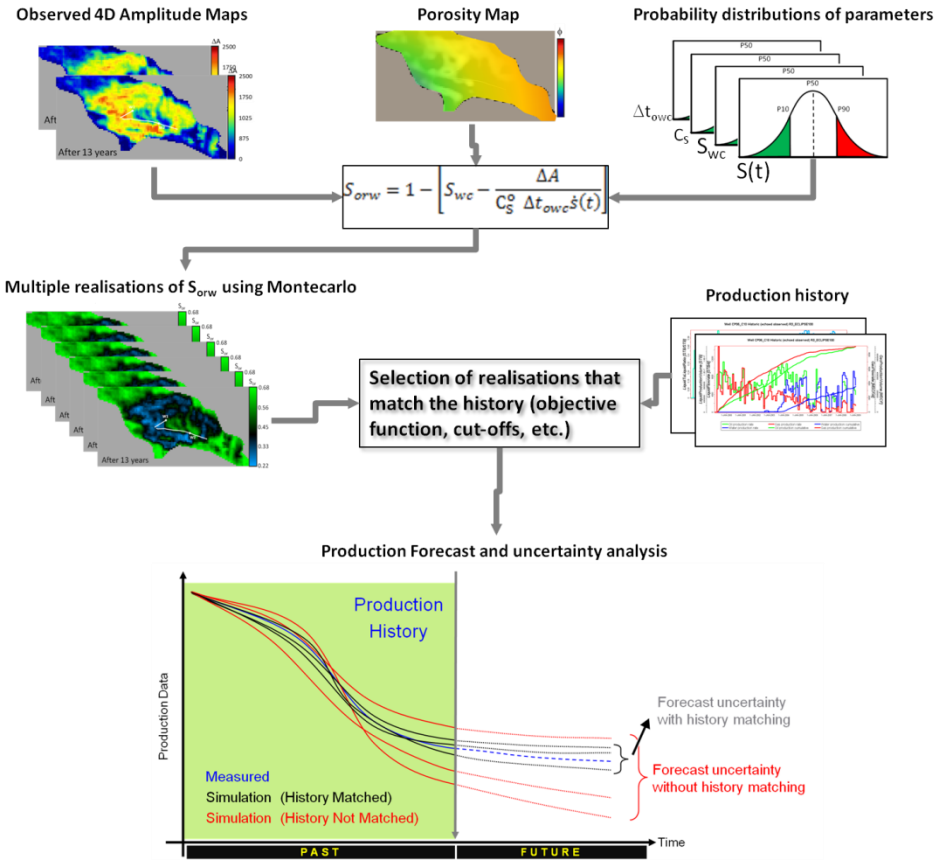

Figure 8.7: An envisaged workflow to achieve history match and production forecast, using the S_{orw} equation (Chapter 5)

One option would be to perform Montecarlo analysis on the input parameters to the equation, and then analyse their conditional probability distributions, using either Bayes theorem, or by defining an objective function that minimises S_{orw} calculated from the equations to that computed at the well locations from the simulation (Figure 8.7). This way, history matching would be achieved with an uncertainty analysis that would help production forecasting in the reservoir. Another interesting subject of research would be to extend this type of process to the use of 3D volumes and evaluate the advantages/disadvantages compared to a map-based approach.

8.2.5 Extension of the equations for applications in carbonate reservoirs

Nearly 60% of the world's petroleum reserves are found in carbonates and about 40% of the world's oil and gas production comes from carbonate reservoirs (Chopra et al., 2005). However, there are still significant challenges to develop carbonate fields; these are mostly related to their complex porosity systems, large heterogeneity and anisotropy. From a production point of view, it is recognised that variations in texture can produce complex interrelationships between porosity, permeability, S_{wir}, S_{orw}, wettability, and capillarity, which result in uneven distribution of injection, vertical communication, localized pressure sinks, compartmentalisation, water coning and complex gas migration paths (Al Hanai et al., 2000). A summary of differences between clastic and carbonate rocks is shown in Figure 8.8.

To date, the applicability of the most common rock physics models for 4D seismic monitoring to carbonate reservoirs is debatable. Some studies that suggest that shear modulus in carbonates can vary with changes in the fluid content at constant effective stress (Figure 8.9), and this would, therefore, invalidate the application of Gassmann equations (Baechele et al., 2005). However other studies suggest that, at low frequencies and when pores are connected, the application of Gassmann equations may still provide reasonable results (Adams et al., 2006).

	Carbonate rocks	Siliciclastic rocks
1.	Carbonate rocks consist mainly of two minerals: calcite and dolomite. They usually remain near their point of origin.	Siliciclastic rocks (predominantly sandstones and shales) are composed of a variety of silica-based grains. They generally have traveled hundreds of kilometers from their source.
2.	Carbonates form in special environments in shallow and deep marine settings.	Siliciclastic rocks do not require any special environment.
3.	Once formed, carbonates undergo diagenetic changes—mineral dissolution (grains dissolved to form new pore space; dissolution along fractures and bedding planes produce vugs and caves) and dolomitization (improves hydrocarbon-producing characteristics).	Siliciclastic rocks undergo minor diagenesis as specific temperature and pressure are required.
4.	Carbonate rocks are distinguished on the basis of depositional texture, grain or pore types, rock fabric and diagenesis.	Clastic rocks are distinguished on the basis of their grain composition and size.
5.	Carbonate rocks have a wide range of grains, pore types and sizes. Consequently, several types of porosities are considered.	Intergranular pores are uniformly distributed throughout the rock matrix; only intergranular porosity is generally considered.

Figure 8.8: Summary of differences between carbonate and clastic rocks (taken from Chopra et al., 2009).

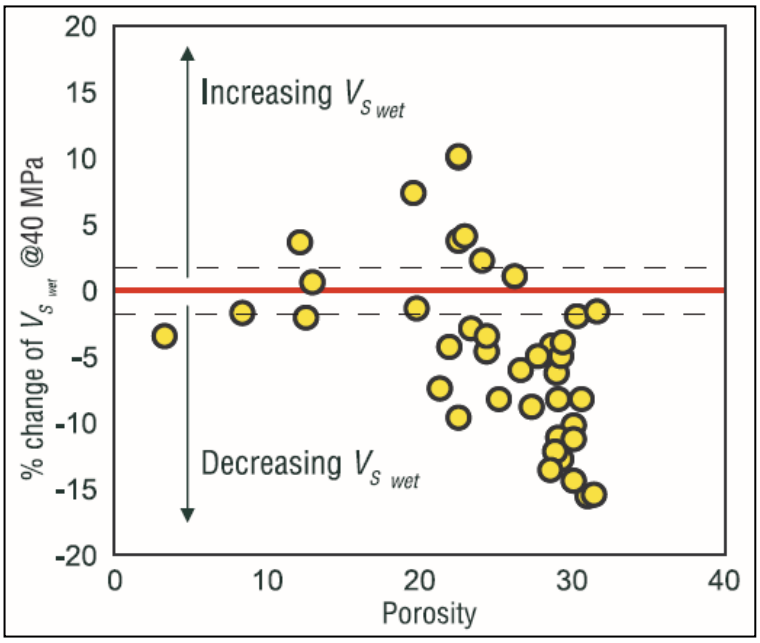

Figure 8.9. Apparent changes in shear modulus with changes in fluid saturation in a carbonate rock sample measured in the laboratory (from Baechele et al., 2009)

All the theory and applications presented in this thesis are applicable to clastic rocks with well-connected primary porosity. The applicability of the general equations to carbonate rocks has not yet been tested, therefore, it is suggested that a potential research study is to evaluate the accuracy and applicability to non-compacting carbonate reservoirs, such as those located in the Middle East, the South of Mexico or Brazil. Although carbonate rocks may require some additional considerations, both from geological (unconnected pores, fractures, diagenesis, etc.) and geophysical (anisotropy, dispersion, etc.) perspectives, perhaps some of the insights gained through this research can form the basis for the development of 4D seismic quantitative interpretation techniques applicable to carbonate reservoirs, perhaps from modified C_P and C_S functions.

8.2.6 4D inversion for multiple phase systems in 3D

Quantitative 4D seismic interpretation is concerned with the calculation of the distributions of reservoir pressure and fluid saturation variations within a reservoir. In Chapter 6, it was shown that 4D AVO variations on their own may not be enough to unambiguously invert for pressure and saturation changes, unless the model is somehow constrained by incorporating additional *a priori* information. A map-based exercise was performed for the oil-water system case, with some degree of success. There are two suggested research routes that may follow from these results: (1) to extend the map-based inversion to the use of 3D volumes and (2) to extend the inversion to reservoirs where multiple fluids interact. To do this, there are several challenges that will be faced and will require investigation, such as:

- The use of cross-correlation techniques to correct the time-delays and allow computation of the 4D differences that can cause problems, particularly in the vicinity of the faults. It is necessary to investigate how much of this would be reflected in the inversion results

- Time to depth conversion can be a major problem for 3D volumes, as the residual errors, even at well locations, can be as high as 10 m. In some reservoirs a 10 m error can implicate assigning values to the incorrect fluid flow units.
- In the proposed workflow in Chapter 6, it is required to incorporate a porosity map as an input; this means that an extension to 3D inversion will require a 3D volume of porosity. It is envisaged that a joint scheme that combines 3D inversion to calculate porosity and 4D inversion for pressure and saturation may be required.
- When multiple fluids interact, some additional constraints may be required to reduce the ambiguity of the results. For instance, it would be easy to confuse a pressure up signal with an increase in gas saturation, or depletion with water flooding. Therefore, it may be necessary to investigate what additional information can be incorporated into the inversion scheme. For instance, by inverting 4D amplitudes and time-shifts simultaneously, or by incorporating additional measurements as constraints, such as CSEM, micro-seismic, depletion measured at surface, etc.

Performing the inversion inside the simulation grid has been proposed as a solution to some of the issues mentioned above, and there are already techniques available in the literature where this process is performed (for example: Thore et al., 2011; Tian et al., 2014). At present, the common approach is by inverting separately base and monitor and then computing the 4D difference, or by artificially adding 4D perturbations to the model, using many constraints. This can make the process time consuming and computationally expensive. In this work, a relatively simple inversion scheme was presented that uses 4D amplitude differences as input; perhaps if both approaches are somehow combined it may be possible to generate a new inversion scheme that reduces computation time and the amount of *a* priori information required and improves the estimation of uncertainties.

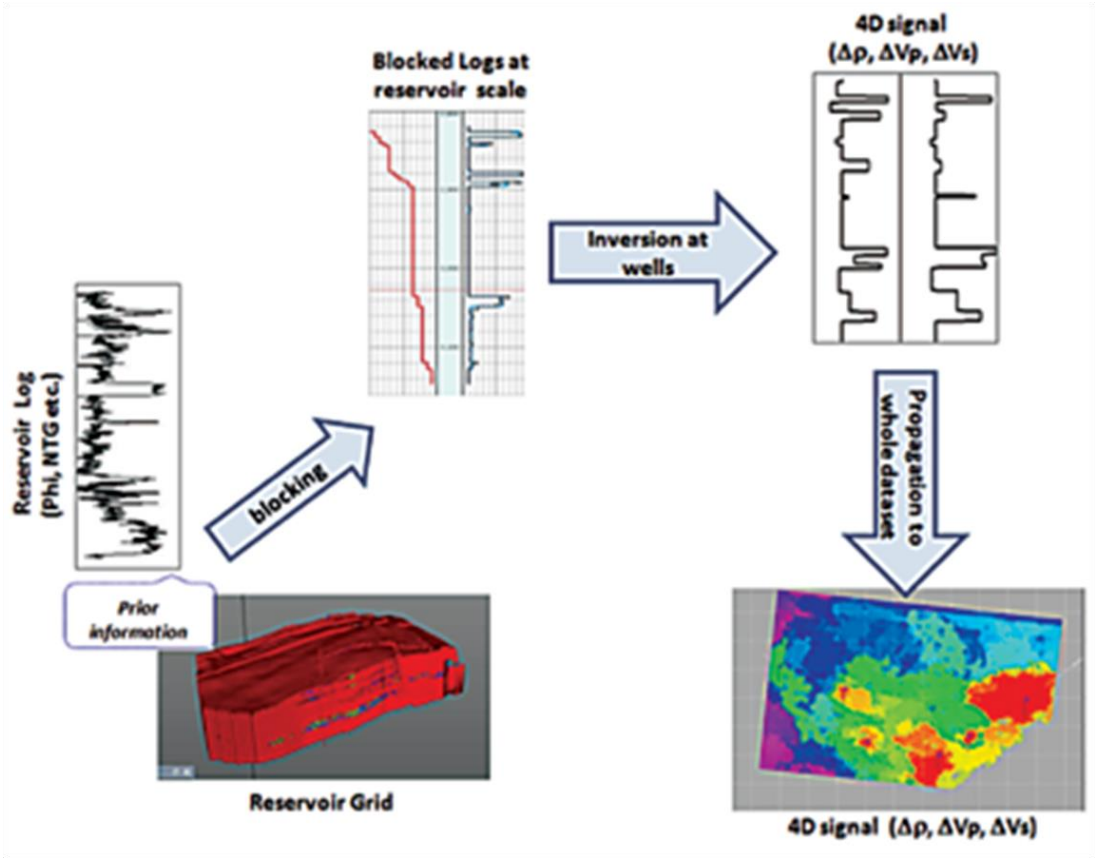

Figure 8.10: Example of a 4D inversion workflow performed inside the simulation grid (Thore et al., 2011).

8.2.7 4D seismic to aid the calculation of the recovery factor

Calculating the oil in place and recoverable oil volumes are crucial processes in any Oil & Gas Company and one of the main tasks in reservoir engineering. In each field, a great amount of resources are dedicated solely to these processes. Since oil volumes change with reservoir pressure, hydrocarbon volumes are expressed as surface conditions, at which oil and gas volumes will have separated: this is called "stock tank". When a reservoir is discovered, the stock tank oil initially in place (STOIIP) is calculated through the following formulation:

$$STOIIP = \frac{GRV\ \phi(1 - S_{wc})}{B_{oi}}\ , \tag{8.1}$$

where GRV is the gross rock volume and Boi is the formation volume factor, which has units of reservoir barrels/stock tank barrel (rb/stb). This means that one unit of Boi reservoir barrels of oil will produce one stock barrel of oil at surface, together with the gas originally dissolved in the oil (Dake, 1998). The geophysical input into equation 7.1 is generally limited to the estimation of GRV and porosity, combined with petrophysics, which also provide an estimate of S_{wc}: reservoir engineers are in charge of providing the value of B_{oi}. More importantly than oil in place is the calculation of the ultimate recovery (UR), which is computed by multiplying the STOIIP by the recovery factor:

$$UR = \left(\frac{GRV\ \phi(1 - S_{wc})}{B_{oi}}\right) RF\ , \tag{8.2}$$

where the recovery factor RF is a number between zero and one, and represents the fraction of the oil that can be ultimately extracted from the reservoir. The calculation of the recovery factor is one of the most important and difficult tasks in reservoir engineering. However, based on the results of this research, it is considered that a quantitative use of 4D seismic data has the potential to provide a way of calculating this important parameter. Let us consider the primary oil recovery of a reservoir that has an active aquifer and also a pre-production gas cap (Figure 8.11).

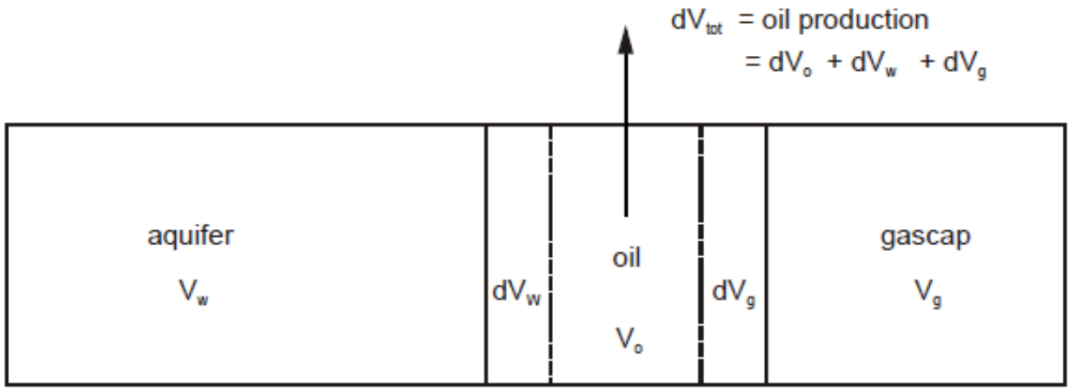

Figure 8.11: Primary oil recovery from oil-water and gas expansion (from Dake, 1998).

The total oil production is given by the arithmetic summation of the change in volume of the three fluids present in the reservoir (of course it is desired that the only volume that decreases is the volume of oil and both water and gas volumes expand). Since the amount of expansion or reduction in volume depends on the pressure drop (ΔP) and the compressibility of the fluid ($C_{fl} = 1 / \kappa_{fl}$), the total oil production (ΔV_{tot}) can be expressed in the next form:

$$\Delta V_{\mathrm{tot}} = V_{\mathrm{o}}\, C_o \Delta P + V_{\mathrm{g}}\, C_g \Delta P \; + \; V_{\mathrm{w}} C_w \Delta P \,. \tag{8.3}$$

By evaluating the a volumes of oil, water and gas extracted and comparing them with the original estimation of the oil in place and the amount of depletion, reservoir engineers are able to estimate the recovery factor.

An interesting fact about equation 7.3 is the resemblance to the multiple phase equations in Chapter 4 (equations 4.48 and 4.49), which show that the combined 4D amplitude difference is also a weighted average of the changes in the fluid volumes and reservoir pressure. It would be an important subject of research to see how much added benefit the calculation of the recovery factor would have if we incorporate the 4D amplitudes directly into the calculations. It is envisaged that this can be done in several ways, for instance:

- Analytically, by generating a new equation that expresses ΔV_{tot} as a function of 4D amplitude changes, and then using the result directly for the calculations and uncertainty analysis. The main challenge here would be to convert seismic based results into volumes.
- By inverting for ΔP, ΔS_w, ΔS_g and ΔS_o, and using the results as inputs to 8.3, performing the uncertainty analysis during the 4D inversion process.
- By using the equations as part of assisted seismic history matching; this would also provide an estimation of ΔV_{tot} via material balance.

Although the problem can sound trivial, there are many factors that need to be considered to develop the proposed methodology. The following questions would need to be addressed:

- What are the effects of the wavelet (tuning) and impact in the final calculation of ΔV_{tot} ?
- Is there really an added value compared to conventional material balance calculations or reservoir simulations?
- Can the process be performed in 3D, or is it more convenient to use maps?
- The seismic scale will be different to the reservoir scale most of the time, what are the effects of up-scaling/down-scaling? Can the whole process be done at seismic scale (including the STOIIP calculation)?
- How representative are the results of reality, is there a way to validate the results (other than history matching, which is known to be ambiguous)?

8.2.8 4D seismic to monitor carbon capture and storage (CCS)

The impact of human activities on the earth's environment is a subject of heated discussions in scientific and industry panels concerned with climate change. In particular, the impacts of CO_2 emissions in the so called "global warming" are widely investigated. One solution, proposed by the oil and gas industry, is to store the carbon dioxide emissions into depleted reservoirs, using either existing wells or by drilling low-cost side tracks (Figure 8.12). The first project of this type was the Weyburn project in Canada, where a combination of an enhanced oil recovery (EOR) project and a research CCS project were combined. At present, most developed countries are including CCS as part of their environment preservation plans for the next decades and it is expected that nearly 90% of CO_2 emissions will be reduced by these means

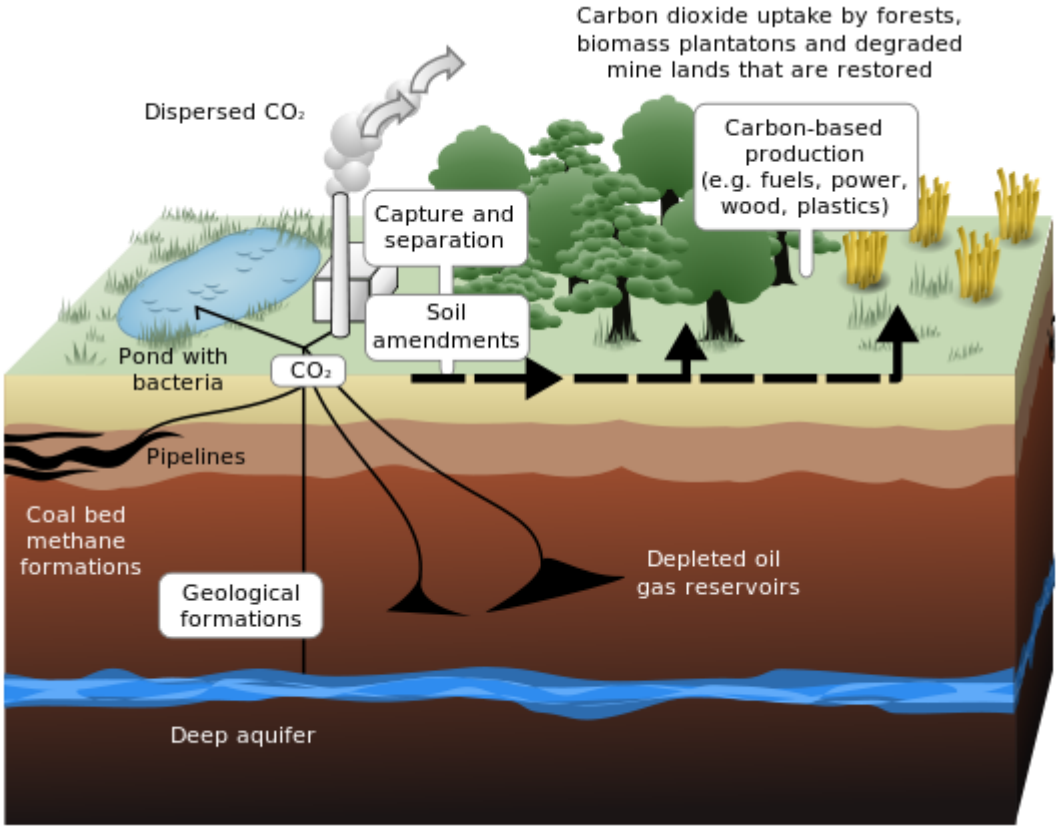

Figure 8.12: Schematic showing both terrestrial and geological sequestration of carbon dioxide emissions from a coal-fired plant (picture taken from www.wikipedia.org).

4D seismic is the obvious tool to attempt monitoring CCS; however, many challenges exist, as the geophysical properties of CO_2 are complex and still not well understood. Some researchers suggest that there might be cases where 4D seismic cannot be used to monitor CO_2 (Lumley, 2010; Vanorio et al., 2010). However, there are case studies where 4D seismic has been successfully used for this purpose (Figure 8.13). However, quantitative analysis is still a challenge.

In Chapter 4, equations for relating the 4D seismic amplitude differences in a gas-water and gas-oil system are provided. These are directly applicable to gas production and gas injection, but potentially, they could also be used for CO_2 injection, with some modifications. However, it is recognised that some research is required to incorporate the effects of miscibility of CO_2, potential chemical interactions with the rocks resulting in matrix changes, the effects of pressure and temperature in CO_2, etc. One of the main

risks of CCS is the potential leakage of the injected CO_2 to the surface; therefore, it must be ensured that the injected volumes are the same as those stored. This means that the ability to monitor CO_2 injection and quickly assess the process quantitatively would have a great impact in the success of these projects. This could be done either through a series of modelling exercises or through inversion.

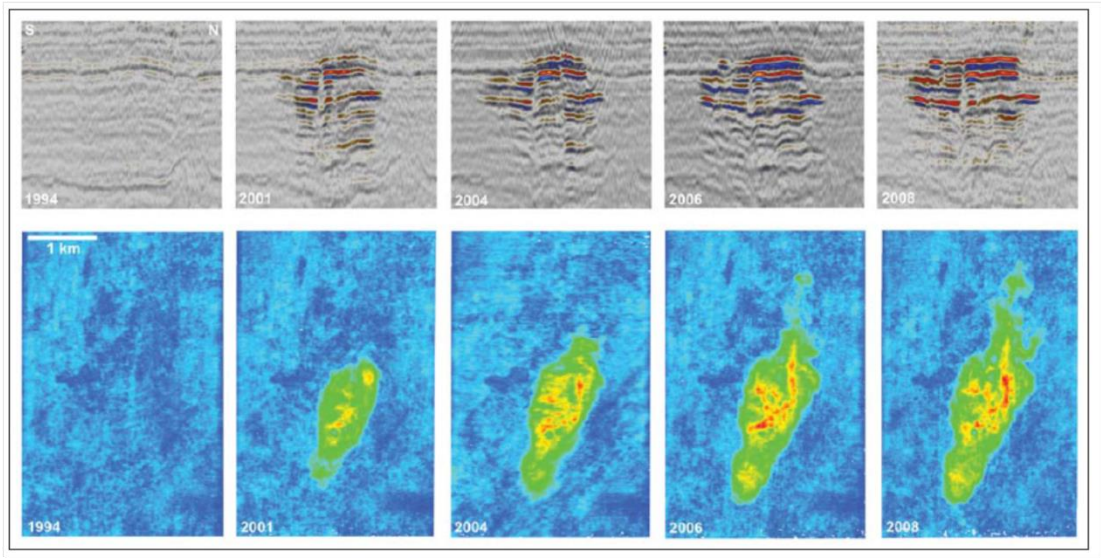

Figure 8.13: Example of CCS monitoring in Sleipner, Norway (Chadwick et al., 2010).

8.3 Final remarks

During this research work, only the very surface has been scratched of quantitative interpretation of 4D amplitudes and, although some advances have been made, it is recognized that there is still much work to be done on this subject. I hope that this research represents at least a small contribution the goal of exploiting our natural resources in a way that not just represents an economical benefit for the industry but also minimises the environmental impact of the oil and gas industry activities. But my biggest hope is that, one day, someone manages to read this work. And, as a matter of fact, if you are reading these lines without having skipped all the previous pages and without sleeping in the process that means my objective has been achieved (this of course doesn't apply to my supervisor or my examiners, as they have no choice!).

REFERENCES

Adam, L., Batzle, M. and Brevik, I. (2006). Gassmann fluid substitution and shear modulus variability in carbonates at laboratory seismic and ultrasonic frequencies: Geophysics, 71, 173-183.

Aki, K. and Richards, P.G. (1980). Quantitative seismology: theory and methods. Freeman and Co.

Al-Hanai, W., Russell, D. S. and Vissapragada, S. (2000). Carbonate Rocks: The Society of Core Analysts (SCA), pp. 1-10.

Alsos, T., Osdal, B. and Høiås, A., (2009). The many faces of pressure changes in 4D seismic at the Svale Field and its implication on reservoir management: 71st Conference & Exhibition, EAGE.

Allen, J. L., Peddy and C. P. (1993). Amplitude variation with offset: Gulf Coast case studies: Society of Exploration Geophysicists.

Allen, J. L., Peddy, C. P. and Fasnacht, T. L. (1993). Some AVO failures and what (we think) we have learned: The Leading Edge, 12, 162-167.

Amini, H. (2014). A pragmatic approach to simulator to seismic modelling for 4D seismic interpretation: PhD thesis, Heriot-Watt University.

Amini, H. and MacBeth, C. (2011). Calibration of simulator to seismic modelling for quantitative 4D seismic interpretation: 73rd EAGE Conference & Exhibition incorporating SPE EUROPEC 2011.

Andersen, C. F., Grosfeld, V., Van Wijngaarden, A-J. and Haaland, A. N. (2009). Interactive interpretation of 4D prestack inversion data using rock physics templates, dual classification, and real-time visualization: The Leading Edge 28, 898-906.

Avseth, P., Mukerji T. and Mavko, G. (2005). Quantitative Seismic Interpretation: Cambridge University Press.

Baechle, G. T., Weger, R. J. Eberli, G. P., Massaferro and J. L., Sun, Y-F. (2005). Changes of shear moduli in carbonate rocks: Implications for Gassmann applicability: The Leading Edge, 24, 507-510.

Barkved, O., Heavey, P., Kjelstadli, R., Kleppan, T. and Kristiansen, T. (2003). Valhall field - V Still on Plateau after 20 years of production: SPE 83957.

Batzle, M., Hofmann, R., Han. and D-H. (2006). Heavy oils—seismic properties: The Leading Edge, 25, 750-756.

Batzle, M. and Wang, Z. (1992). Seismic properties of pore fluids: Geophysics, 57, 1396-1408.

Bailey, B., Barclay, F., Nesbit, R. and Paxton, A. (2010). Prospect Identification using AVO Inversion and Lithology: 72th EAGE Conference & Exhibition.

Bjorck, A. (1988). A direct method for sparse least square problems with upper and lower bounds: Number Mathematics, 54, 19-32.

Bouchet, R., Levallois B., Mfonfu, G. and Authier, J-F. (2004). Girassol field optimised development: AAPG international conference, Cancun, Mexico.

Bortfeld, R. (1961). Approximations to the reflection and transmission coefficients of plane longitudinal and transverse waves: Geophysical Prospecting, 4, 485-503.

Buland, A. and Omre, H. (2003). Bayesian linearized AVO inversion: Geophysics, 68, 185-198.

Buckley, J. S., (1998). Evaluation of reservoir wettability and its effects on oil recovery, Technical Report: New Mexico Petroleum Recovery Research Center, Socorro, NM (United States)

Castagna, J. P., Batzle, M. L. and Eastwood, R. L. (1985). Relationships between compressional-wave and shear-wave velocities in clastic silicate rocks: Geophysics, 50, 571-581

Castagna, J. P. and Backus, M. (1993). Offset dependent reflectivity: Theory and practice of AVO analysis: Society of Exploration Geophysicists.

Castagna, J. P. and Smith, S. W. (1994). Comparison of AVO indicators: A modeling study: Geophysics, 59, 1849-1855.

Castagna, J. P., Swan, H. W. and Foster, D. J. (1998). Framework for AVO gradient and intercept interpretation: Geophysics, 63, 948-956.

Chadwick, A., Williams, G., Delepine, N., Clochard, V., Labat, K., Sturton, S., Buddensiek, M-L., Dillen, M., Nickel, M., Lima, A. L., Arts, R., Neele and F., Rossi, G. (2010). Quantitative analysis of time-lapse seismic monitoring data at the Sleipner CO2 storage operation: The Leading Edge, 29, 170-177.

Chi, X-G., Han and D-H. (2009). Lithology and fluid differentiation using a rock physics template: The Leading Edge, 28, 60-65.

Chopra, S., Chemingui, N. and Miller, R. D. (2005). An introduction to this special section—carbonates: The Leading Edge, 24, 488-489.

Clark, V. A. (1992). The effect of oil under in-situ conditions on the seismic properties of rocks: Geophysics 57, 894-901.

Clifford, P.J., Trythall, R., Parr, R.S., Moulds, T.P., Cook, T., Allan, P.M. and Sutcliffe, P. (2003). Integration of 4D seismic data into the management of oil reservoirs with horizontal wells between fluid contacts: SPE 8956.

Cooke, D. A. and Schneider, W. A. (1983). Generalized linear inversion of reflection seismic data: Geophysics, 48, 665-676.

Cole, S., Lumley, D., Meadows and M., Tura, A. (2002). Pressure and saturation inversion of 4D seismic data by rock physics forward modelling: SEG Technical Program Expanded Abstracts, 2475-2478.

Coleman, T. and Li, Y. (1996). A reflective Newton method for minimizing a quadratic function subject to bounds on some of the variables: Society for Industrial and Applied Mathematics, Optimization, 6, 1040-1058.

Connolly, P. (1999). Elastic impedance: The Leading Edge, 18, 438-452.

Corzo, M., MacBeth, C. and Barkbed, O. (2013). Estimation of pressure change in a compacting reservoir from time-lapse seismic data: Geophysical Prospecting, 61, 1022 – 1034.

Crain, E. R. (1986). The Log Analysis Handbook, Volume One - Quantitative Methods: Pennwell Books.

Dake, L. P. (1998). Fundamentals of reservoir engineering: Developments in Petroleum Science, 8. Elsevier Science B.V.

De Haas, J. C. and Berkhout, A. J. (1989). Practical approach to nonlinear inversion of amplitude versus offset information: SEG Technical Program Expanded Abstracts, 839-842.

De Gennaro, S., Grandi, A., Escobar, I., Onaisi, A., Ben-Brahim, L., Joffroy, G., Tindle, C. and Neillo, V. (2008). Integrating 4D Seismic, geomechanics and reservoir simulations in Elgin and Franklin. 70th EAGE Conference & Exhibition.

Demirbag⁄, E. and Çoruh, C. (1998). Inversion of Zoeppritz equations and their approximations: SEG Technical Program Expanded Abstracts, 1199-1203

Drufuca, G. and Mazzotti, A. (1995). Ambiguities in AVO inversion of reflections from a gas-sand: Geophysics, 60, 134-141.

Eiken, O. and Tøndel, R. (2005). Sensitivity of time-lapse seismic data to pore pressure changes, Is quantification possible?: The Leading Edge, 24, 1250-1254.

Eberhart-Phillips, D., Han, D-H. and Zoback, M. D. (1989). Empirical relationships among seismic velocity, effective pressure, porosity, and clay content in sandstone: Geophysics, 54, 82-89.

Engler, T. W. (2010). Fluid Flow in Porous Media: Course notes, Petroleum Engineering, New Mexico Tech.

Falahat, R., Shams, A. and MacBeth, C. (2011). Towards quantitative evaluation of gas injection using time-lapse seismic data: Geophysical Prospecting, 59, 310-322.

Fatti, J. L., Smith, G. C., Vail, P. J., Strauss, P. J. and Levitt, P. R. (1994). Detection of gas in sandstone reservoirs using AVO analysis: A 3-D seismic case history using the Geostack technique: Geophysics 59, 1362-1376.

Fjaer, E., Holt, R.M., Horsrud, P., Raaen, A.M. and Risnes, R. (2008). Petroleum related rock mechanics: Developments in Petroleum Science 53, Elsevier.

Floricich, M., MacBeth, C., Stammeijer, J., Staples, R., Evans, A. and Dijiksman, N. (2006). Determination of a seismic and engineering consistent petroelastic model for time-lapse seismic studies: Application to the Schiehallion Field: SEG Technical Program Expanded Abstracts 25, 3205-3209.

Floricich, M. (2006). An engineering-consistent approach for pressure and saturation estimation from time-lapse seismic data: PhD thesis, Heriot-Watt University.

Floricich, M., Large, S., Jones, D., Helmi, A. and Lörtzer, G. (2011). Conditioning Reservoir Model and Aiding Well Planning Using Probabilistic Seismic Inversion in a Central North Sea Field: 73rd EAGE Conference & Exhibition.

Gassmann, F. (1951). Uber die elastizitat poroser medien: Vier. der Natur Gesellschaft, 96, l-23.

Gill, C.E., Miotto, A., Floricich, M., Rogers, R., Potter, R.D., Harwijanto, J. and Townsley P. (2012). The Nelson full field model: using iterative quantitative improvements from the initial framework to the final history match: First Break, 30, 43 - 53.

Glass, A. W. (2004). High pressure, high temperature developments in the United Kingdom Continental Shelf: Research report, UK Health and Safety Executive.

Goodway, B., Chen, T. and Downton, J. (1997). Improved AVO fluid detection and lithology discrimination using Lamé petrophysical parameters; "λρ", "μρ", & "λ/μ fluid stack", from P and S inversions: SEG Technical Program Expanded Abstracts, 183-186.

Goodway, B. (2001). AVO and Lame' constants for rock parameterization and fluid detection: CSEG Recorder, 26, 39-60.

Grey, D., Goodway, B. and Chen, T. (1999). Bridging the Gap: Using AVO to detect changes in fundamental elastic constants: SEG Expanded Abstracts 18, 852-855.

Gregory, A. R. (1977). Aspects of rock physics from laboratory and log data that are important for seismic interpretation: Petroleum Geology, memoir 26.

Gurevich, B. (2004). A simple derivation of the effective stress coefficient for seismic velocities in porous rocks. Geophysics, 69, 393-397.

Haas, A. and Dubrule, O. (1994). Geostatistical inversion – a sequential method of stochastic reservoir modeling constrained by seismic data: First Break, 12, 561-569.

Hampson, D. P., Russell, B. H. and Bankhead, B. (2005). Simultaneous inversion of pre-stack seismic data: SEG Technical Program Expanded Abstracts, 1633-1637.

Harilal S. and Biswal, K. (2010). Pitfalls in seismic amplitude interpretation: Lessons from Oligocene channel sandstones: The Leading Edge, 29, 384-390.

Han, D. and Batzle, M. (2001). 'Fizz water' and low gas saturated reservoirs: SEG Technical Program Expanded Abstracts, 532-535.

Han, D. and Batzle, M. (2004). Gassmann's equation and fluid-saturation effects on seismic velocities: Geophysics, 69, 398–405

Hatchell, P. and Bourne, S. (2005). Rocks under strain: Strain-induced time-lapse time shifts are observed for depleting reservoirs: The Leading Edge, 24, 1222-1225.

Hill, R., (1952). The elastic behavior of crystalline aggregate: Proc. Phys. Soc., London A, 65,349–354.

Hodgson, N. and MacBeth, C. (2007). Inverting for reservoir pressure change using time–lapse time strain: Application to Genesis Field, Gulf of Mexico: The Leading Edge, 649–652.

Hoffman, R., Xu, X., Batzle, M. and Tshering, T. (2004). Which effective pressure coefficient do you mean?: SEG Technical Program Expanded Abstracts, 1766-1769

Hoffman, R., Xu, X., Batzle, M., Prasad, M. and Furre, Pillitteri, A. K. (2005). Effective pressure or what is the effect of pressure?: The Leading Edge, 24, 1256-1260

Huang, Y., MacBeth, C., Barkved and O., Gestel, J-P. (2011). Enhancing dynamic interpretation at the Valhall Field by correlating well activity to 4D seismic signatures: First Break, 29, 37 – 44.

Johann, P., Sansonowski, R., Oliveira, R. and Bampi, D. (2009). 4D seismic in a heavy-oil, turbidite reservoir offshore Brazil: The Leading Edge, 28, 718-729.

Johnston D. H. and Laugier, B. P. (2012). Resource assessment based on 4D seismic and inversion at Ringhorne Field, Norwegian North Sea: The Leading Edge, 31, 1042-1048.

Khatri , N.K., Sastry and Y., Mohan, S. (2013). AVO case studies in two deep-water blocks off the east coast of India: The Leading Edge, 32, 1328-1333

King, M. S., Marsden, J. R. and Dennis, J.W. (2000). Biot dispersion for P- and S-wave velocities in partially and fully saturated sandstones: Geophysical Prospecting, 48, 1075–1089.

Koefoed, O. (1955). On the effect of Poisson's ratios of rock strata on the reflection coefficients of plane waves: Geophysical Prospecting, 3, 381-387.

Kloosterman, H.J., Van Waarde, J., Kelly, R. and Stammeijer, J. (2001). A new dimension in reservoir evaluation – time lapse seismic in Shell Expro's Central North Sea Fields: SPE 71799.

Krief, M., Garat, J., Stellingwerff, J. and Ventre, J., 1990. A petrophysical interpretation using the velocities of P and S waves (full-waveform sonic). Log Analyst, 31, 355–369.

Lafet, Y., Roure, B., Doyen, P.M., Bornard, R. and Buran, H. (2008). Global 4-D Seismic Inversion and Fluid Prediction: 70th EAGE Conference & Exhibition.

Landrø, M. (2001). Discrimination between pressure and fluid saturation changes from time-lapse seismic data: Geophysics, 66, 836–844.

Landrø, M. and Stammeijer, J. (2004): Quantitative estimation of compaction and velocity changes using 4D impedance and traveltime changes: Geophysics, 69, 949–957.

Loizou, N., Liu, E. and Chapman, M., (2008). AVO Analyses and spectral decomposition of seismic data from four wells west of Shetland, UK: Petroleum Geoscience, 14, 355-368.

Leguijt, J. (2009). Seismically constrained probabilistic reservoir modelling: The Leading Edge, 28, 1478-1484.

Li, Y., Downton, J. and Xu, Y. (2007). Practical aspects of AVO modelling: The Leading Edge, 26, 295-311.

Lindseth, R. O. (1979). Synthetic sonic logs—a process for stratigraphic interpretation: Geophysics, 44, 3-26

Lörtzer, G. J. M., de Haas, J. C. and Berkhout, A. J. (1988). Evaluation of weighted stacking techniques for AVO inversion: SEG Technical Program Expanded Abstracts, 1204-1208.

Lumley, D.E., Behrens, R.A. and Wang, Z. (1997). Assessing the technical risk of a 4-D seismic project: The Leading Edge 29, 150-155.

Lumley, D.E. (2010). 4D seismic monitoring of CO2 sequestration: The Leading Edge, 29, 150-155.

Lumley, D.E., Nunns, A.G. Delorme, G., Adeogba, A.A. and Bee M.F. (1999). Meren Field, Nigeria: A 4D seismic case study: SEG Expanded Abstracts, 1628-1631.

Menke, W. (1989) Geophysical Data Analysis: Discrete Inverse Theory: Academic Press, Inc.

MacBeth, C. (2004). A classification for the pressure-sensitivity properties of a sandstone rock frame: Geophysics, 69, 497–510.

MacBeth, C., Stephen, K.D. and McInally, A. (2005). The 4D seismic signature of oil–water contact movement due to natural production in a stacked turbidite reservoir: Geophysical Prospecting, 53, 183–203.

MacBeth, C., Floricich, M. and Soldo, J. (2006a). Going quantitative with 4D seismic analysis: Geophysical Prospecting, 54, 303-318.

MacBeth, C., Stammeijer, J. and Omerod, M., (2006b). Seismic monitoring of pressure depletion evaluated for a United Kingdom continental-shelf gas reservoir: Geophysical Prospecting, 54, 29-47.

MacBeth, C. and Ribeiro, C. (2007). The stress sensitivity of shaley sandstones: Geophysical Prospecting, 55, 155–168.

MacBeth, HajNasser, Y., Stephen, K. and Gardiner, A. (2011). Exploring the effect of meso-scale shale beds on a reservoir's overall stress sensitivity to seismic waves: Geophysical Prospecting, 59, 90 – 110.

McInally, A., Kunka, J., Garnham, J., Redondo-Lopez, T. and Stenstrup-Hansen, L. (2001). Tracking production changes in a turbidite reservoir using 4D elastic inversion: 63rd Conference and Exhibition, EAGE.

Mavko, G. and Mukerji, T. (1995). Pore space compressibility and Gassmann's relation. Geophysics, 60, 1743–1749.

Mavko, G., Mukerji, T. and Dvorkin T. (1998). The rock physics handbook: Cambridge University Press.

Meadows, M. (2001). Enhancements to Landrø's method for separating time -lapse pressure and saturation changes: SEG Expanded Abstracts, 1652–1655.

Menke, W. (1987). Geophysical data analysis: discrete inverse theory: Academic press, Elsevier.

Ness, O. M., Holt, R. M. and Fjaer, M. (2000). The reliability of core data as input to seismic reservoir monitoring studies: SPE 65180.

Nur, A., Mavko, G., Dvorkin, J. and Galmundi, D. (1995). Critical porosity: the key to relating physical properties to porosity in rocks: SEG Expanded Abstracts, 878– 881.

Ødegaard, E. and Avseth, P. (2004). Well log and seismic data analysis using rock physics templates: First break, 23, 37-43.

Ojo, C. and Sindiku, I. (2006). Limitations in the use of DHI's in hydrocarbon prediction — Case histories of some dry/semi dry wells in clastic rocks in the Niger Delta of Nigeria: SEG Expanded Abstracts, 614-618.

Oldenburg, D. W., Scheuer, T. and Levy, S. (1983). Recovery of the acoustic impedance from reflection seismograms: Geophysics, 48, 1318-1337.

Orton, G.J. and Reading, H.G. (1993). Variability of deltaic processes in terms of sediment supply, with particular emphasis on grain size: Sedimentology, 40, 475–512.

Osdal, B., Husby, O., Aronsen, H. A., Chen, N. and Alsos, T. (2006). Mapping the fluid front and pressure buildup using 4D data on Norne Field: The Leading Edge, 25, 1134-1141.

Ostrander, W. J. (1984). Plane wave reflection coefficients for gas sands at non-normal angles of incidence: Geophysics 49, 1637-1648.

Parr, R., Marsh, J. and Griffin, T. (2000). Interpretation and integration of 4-D results into reservoir management, Schiehallion Field, UKCS: SEG Technical Program Expanded Abstracts 19, 1464-1467.

Pelissier, M.A., Hoeber, H., van der Coevering, N. and Jones, I.F. (2007). Classics of Elastic Wave Theory: SEG, Geophysics Reprint Series, 24.

Pedersen-Tatalovic, R., Uldall, A., Jacobsen, N.L., Hansen, T. M. and Mosegaard, K. (2008). Event-based low-frequency impedance modeling using well logs and seismic attributes: The Leading Edge, 27, 592-603.

Pickup, G. and Hern, C. (2002). The development of appropriate upscaling procedures: Transport in Porous Media, 46, 119–138.

Raymer, L.L., Hunt, E.R. and Gardner, J.S. (1980). An improved sonic transit time-to-porosity transform: Trans. Soc. Prof. Well Log Analysts, 21st Annual Logging Symposium.

Ribeiro, C. and MacBeth, C. (2004). A petroelastic-based approach to pressure and saturation estimation using 4D seismic: SEG Technical Program Expanded Abstracts, 2271-2274.

Røste, T., Moen, A.S., Kolstø, E., Brekken, M., Thrana, C., Husby, O. and Lescoffit, G. (2009). The Heidrun Field: monitoring fluid flow in the complex Åre Formation: First break, 27, 41-49.

Rauch, M. and Collins, E. (1998). The Greenshank anomaly - an AVO case history: Exploration Geophysics, 29, 565-569.

Reuss, A. (1929). Berechnung der Fliessgrenzen von Mischkristallen auf Grund der Plastizita¨tsbedingung fu¨r Einkristalle. Z. Ang. Math. Mech., 9, 49–58.

Ross, C. P. (2000). Effective AVO crossplot modeling: A tutorial: Geophysics, 65, 700-711.

Rutherford, S.R. and Williams R.H. (1989). Amplitude-versus-offset variations in gas sands: Geophysics, 54, 680 – 688.

Sagitov, I. R. and Stephen, K. D. (2012). Assisted seismic history matching in different domains: what seismic data should we compare?: SPE Europec/EAGE Annual Conference.

Sarkar, S., Gouveia, W. P. and Johnston, D. H. (2003). On the inversion of time-lapse seismic data: SEG Technical Program Expanded Abstracts, 1489-1492.

Sandø, I. A., Munkvold, O. and Elde, R. (2009). Two decades of 4D geophysical developments – experiences, value creation and future trends: 11th International Congress of the Brazilian Geophysical Society & EXPOGEF, 342-345.

Sayers, C. M. (2010). Geophysics Under Stress: Geomechanical Applications of Seismic and Borehole Acoustic Waves: SEG Distinguished Instructor Short Course, ISBN 1560802103.

Schutjens P. (2009). HPHT Overburden Mechanics: Drilling Pancakes or Arches?: HPHT Arena, SPE/Petroleum Group workshop.

Shapiro, S. A. (2003). Elastic piezosensitivity of porous and fractured rocks: Geophysics, 68, 482-486.

Sengupta, M. (2000). Integrating rock physics and flow simulation to reduce uncertainties in seismic reservoir monitoring: PhD Thesis, Stanford University.

Shuey, R.T. (1985). A simplification of the Zoeppritz equations: Geophysics, 50, 609 – 614.

Simmons, J. L. and Backus, M. M. (1996). Waveform-based AVO inversion and AVO prediction-error: Geophysics, 61, 1575-1588.

Singh, Y., Amin, K. A., Alvarez, E., Hernandez, J., Liniawati, A. and Fauzi, M., Reservoir properties prediction in the West Baram Delta through data integration constrained by rock physics: The Leading Edge, 28, 1486-1491

Smith, G. C. and Gidlow, P.M. (1987). Weighted stacking for rock property estimation and detection of gas: Geophysical Prospecting, 35, 993-1014.

Staples, R., Stammeijer, J., Jones, S., Brain, J. Smit, F. and Hatchell, P. (2006). Time-Lapse (4D) seismic monitoring - expanding applications: Presented at the Joint Convention, What's Next?: CSPG – CSEG – CWLS.

Staples, R., Brain, J., Hunt, K., Behrens, M., Charreyron, Y. and Cook, A. (2007). 4D Driving Developments at Gannet E & F: 69th EAGE Conference & Exhibition.

Strønen, L.K. and Digranes, P. (2004). Time-lapse seismic extends the lifetime of the Gullfaks Field: 66th Conference & Exhibition, EAGE.

Tarantola, A. (1987). Inverse problem theory and methods for model parameter estimation: Society for Industrial and Applied Mathematics, Philadelphia.

Thore, P. (2011). Application of a grid-consistent inversion to a 4D reservoir model: The Leading Edge 30, 1262-1269.

Tian, S., Shams, S. and MacBeth, C. (2014). Closing the loops using engineering-consistent 4D seismic inversion: The Leading Edge 33, 188-196.

Tonellot, T., Macé, D. and Richard, V. (2001). Joint stratigraphic inversion of angle-limited stacks: SEG Technical Program Expanded Abstracts, 227-230.

Trani, M., Arts, R., Leeuwenburgh and O., Brouwer, J. (2011). Estimation of changes in saturation and pressure from 4D seismic AVO and time-shift analysis: Geophysics, 76(2), C1 – C17.

Tura, A. and Lumley, D. E. (1998). Subsurface fluid flow properties from time-lapse elastic wave reflection data: Proceedings of SPIE, Mathematical Methods in Geophysical Imaging, 3453, 125-138.

Tura, A. and Lumley, D. E. (1999). Estimating pressure and saturation changes time-lapse AVO data: SEG Technical Program Expanded Abstracts, 1655-1658.

Vanorio, T., Mavko, G., Vialle, S. and Spratt, K. (2010). The rock physics basis for 4D seismic monitoring of CO2 fate: Are we there yet?: The Leading Edge, 29, 156-162.

Verm, R. and Hilterman, F. (1995). Lithology color-coded seismic sections: The calibration of AVO crossplotting to rock properties: The Leading Edge 14, 847-853.

Vernik, L. and Hamman, J. (2009). Stress sensitivity of sandstones and 4D applications: The Leading Edge, 28, 90-93.

Voigt, W. (1907). Bestimmung der Elastizita¨tskonstanten von Eisenglanz: Ann. Phys., 24, 129–140.

Walden, A.T. (1991). Making AVO sections more robust: Geophysical Prospecting, 39, 915-942.

Wood, A.W. (1955). A Textbook of Sound: McMillan Co.

Walls, J. and Dvorkin, J. (2005). Effects of pore fluid properties at high pressure and temperature on seismic response: SEG Technical Program Expanded Abstracts, 1617-1620.

Wang Y. (1999). Approximations to the Zoeppritz equations and their use in AVO analysis: Geophysics, 64, 1920-1927.

Wang, Y. (1999). Simultaneous inversion for model geometry and elastic parameters: Geophysics, 64, 182-190.

Wang, Z. (2000). Dynamic versus static properties of reservoir rocks, in seismic and acoustic velocities in reservoir rocks: SEG Geophysics Reprint Series, 19, 531–539.

Wright, J. (1986). Reflection coefficients at pore-fluid contacts as a function of offset: Geophysics 51, 1858-1860.

Yan, F. and Han, D-H. (2009). Modeling of effective pressure effect on porous reservoir rocks: SEG Technical Program Expanded Abstracts, 2025-2029.

Zhou, M., Lu, D., Dunsmuir, J. and Thomann, H. (2000). Irreducible Water Distribution in Sandstone Rock: Two Phase Flow Simulations in CT-Based Pore Network: Physics and Chemistry of the Earth, Part A: Solid Earth and Geodesy, 25, 169-174.

Zoepprtiz, K. (1919). Erdbebenwellen VIII B, Uber Reflexion and Durchgang seismischer Wellen durch Unstetigkeitsflachen: Gottinger Nachr. 1, 66-84.

APPENDIX 1: Review of AVO theory

One of the most fundamental developments in geophysics are Zoeppritz equations (Zoeppritz, 1919), which are shown in equation A1.1. These equations describe how the amplitudes of reflected and refracted P-waves are generated at non-normal incidence upon a plane interface; this interface is commonly understood as a contrast between two rock layers. Zoeppritz equations predict that, if a P-wave is induced at a non-normal trajectory, at the interface, part of its energy will reflect in the form of P-waves (and be recorded at surface) and the rest of the energy will be reflected and transmitted in the form of S-waves (and hence lost), this phenomenon is known as energy partition (Aki & Richards, 1987). The amount of energy that gets reflected, transmitted and lost depends upon the angle at which the wave is incising and the rock properties in both sides of the interface. This phenomenon implies that if we are able to induce P-waves in the same point in the sub-surface at different angles of incidence, we would observe variations in the recorded amplitude – since different amounts of energy are reflected, transmitted and lost. This variation of amplitude is known as amplitude variation with offset (AVO), where offset is the source-receiver distance (Figure A1.1).

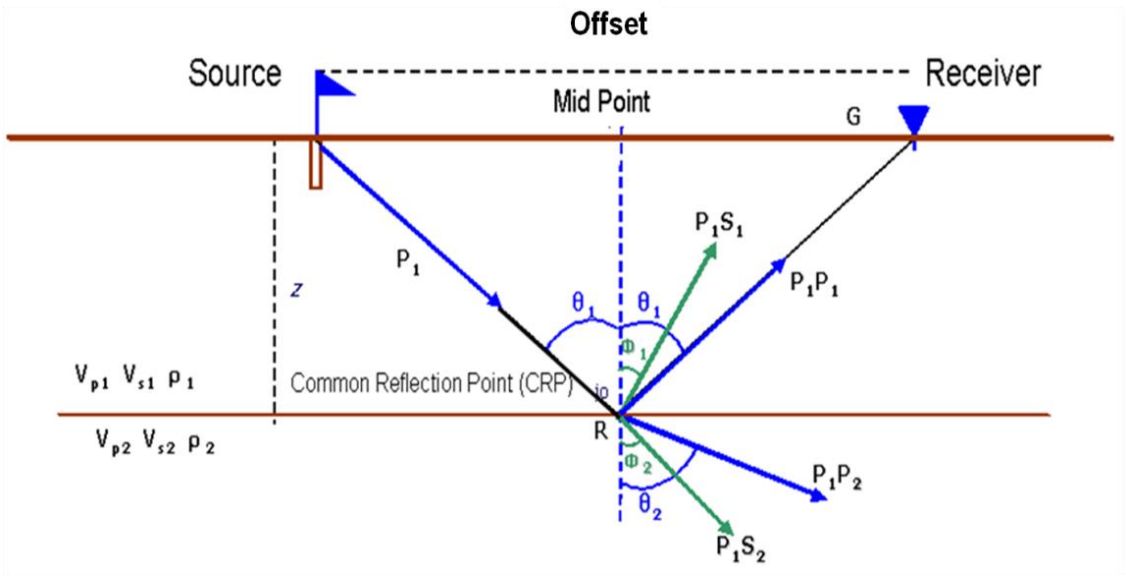

Figure A1.1:Zoeppritz equations and the partition of energy

$$\begin{bmatrix} sin\,\theta_1 & cos\,\theta_1 & -sin\,\theta_2 & cos\,\theta_2 \\ -cos\,\theta_1 & sin\,\theta_1 & -cos\,\theta_2 & -sin\,\theta_2 \\ sin\,2\theta_1 & a\,cos\,2\theta_1 & c\,sin\,2\theta_2 & -e\,cos\,2\theta_2 \\ cos\,2\theta_1 & -b\,sin\,2\theta_1 & -d\,cos\,2\theta_2 & -f cos\,2\theta_2 \end{bmatrix} \begin{bmatrix} R_{PP} \\ R_{PS} \\ T_{PP} \\ T_{PS} \end{bmatrix} = \begin{bmatrix} -sin\,\theta_1 \\ -cos\,\theta_1 \\ sin\,2\theta_1 \\ -cos\,2\theta_1 \end{bmatrix}, \qquad \text{(A1.1)}$$

where:

$$a = \frac{V_{P1}}{V_{S1}}; \quad b = \frac{V_{S1}}{V_{P1}}; \quad c = \frac{\rho_2 V_{S2}^2 V_{P1}}{\rho_1 V_{S1}^2 V_{P2}}; \quad d = \frac{\rho_2 V_{P2}}{\rho_1 V_{P1}}; \quad e = \frac{\rho_2 V_{S2} V_{P1}}{\rho_1 V_{S1}}; \quad f = \frac{\rho_2 V_{S2}}{\rho_1 V_{P1}}. \qquad \text{(A1.1a)}$$

Equations for practical AVO interpretation

Koefoed (1955) used Zoeppritz equations to establish a relation between the changes in amplitude with angle of incidence and the change in Poisson's ratio across the interface. His observations stated the basic principles used nowadays in modern AVO interpretation. Nevertheless, in practice Zoeppritz equations remained difficult to parameterise and interpret; for this reason, several attempts were made to simplify them, including the work by Bortfield (1961), Aki and Richards (1980) and Smith and Gidlow (1987). From these, given their simplicity and accuracy, Aki and Richards' approximation (equation 1.2) and the rearrangement proposed by Shuey (1985) shown in equation 1.3, are the most commonly used functional forms for AVO interpretation:

$$R(\theta) = \gamma_1 \frac{\Delta V_P}{\overline{V_P}} + \gamma_2 \frac{\Delta V_S}{\overline{V_S}} + \gamma_3 \frac{\Delta \rho}{\bar{\rho}}, \qquad \text{(A1.2)}$$

where:

$$\gamma_1 = \frac{1}{2} sec^2\theta; \quad \gamma_2 = -4 \sin^2\theta \left(\frac{\overline{V_S}}{\overline{V_P}}\right)^2; \quad \gamma_3 = \frac{1}{2} - 2 \left(\frac{\overline{V_S}}{\overline{V_P}}\right)^2 \sin^2\theta. \qquad \text{(A1.2a)}$$

Here, $\Delta\rho, \Delta V_P$ and ΔV_S denote differences across the interface and $\bar{\rho}, \overline{V_P}$ and $\overline{V_S}$ are averages across the interface. The ratios $\Delta V_P/\overline{V_P}$, $\Delta V_S/\overline{V_S}$ and $\Delta\rho/\bar{\rho}$ are called P-wave, S-wave and density reflectivities.

$$R(\theta) = A + B\sin^2\theta + C\sin^2\theta\ \tan^2\theta\ , \qquad \text{(A1.3)}$$

where:

$$A = \frac{1}{2}\left[\frac{\Delta V_P}{\overline{V_P}} + \frac{\Delta\rho}{\overline{\rho}}\right];\ \ B = \left[\frac{1}{2}\frac{\Delta V_P}{\overline{V_P}} - 4\left(\frac{\overline{V_S}}{\overline{V_P}}\right)^2\frac{\Delta V_S}{\overline{V_S}}\right];\ \ C = \frac{1}{2}\frac{\Delta V_P}{\overline{V_P}}\ . \qquad (A1.3a)$$

The terms A, B and C are commonly known as the intercept, gradient and curvature respectively.

Further rearrangements of Aki & Richards equation were later provided by Fatti et al. (1994), Verm and Hilterman (1995) and Grey et al. (1999), in terms of velocity, impedances and elastic moduli reflectivities respectively. Useful summaries of the different approximations and their assumptions and limitations are provided by Wang (1999) and Li et al. (2007).

The mathematical work by Aki and Richards allowed Ostrander (1982) to perform the first published exercise of AVO analysis applied to oil and gas exploration. Ostrander demonstrated through modelling that AVO could be used to detect gas saturated sands. The results of this work started a new era in oil and gas exploration, where new seismic surveys and processing sequences were designed with the only objective of performing AVO analysis.

AVO inversion

Conventional reflection seismic acquisitions are designed so that the same point in the subsurface (called common reflection point or CRP) is hit several times by waves coming from different sources and detected in different receivers. The main reason for this is to improve the resultant seismic image through stacking (averaging traces), which eliminates random noise and enhances the coherent signal. But this geometrical arrangement also results in P-waves hitting the CRPs at different angles of incidence, giving us the opportunity to observe amplitude changes as a function of offset, which

can be transformed to angle of incidence through the seismic velocity (Walden, 1991) as follows:

$$\sin\theta = \frac{XV_{int}}{tV_{rms}^2} \quad , \qquad (A1.4)$$

where X is the offset, V_{int} and V_{rms} are the interval and RMS P-wave velocities from processing and t is the two-way travel time. Given that we have a set of amplitudes incising at different angles, and these are related to the rock properties through relatively simple equations, it is possible define an inversion scheme to quantify such relations (Menke, 1987; Tarantola, 1987), for instance, using equation A1.2:

$$\begin{bmatrix} A(t_0,\theta_1) \\ . \\ . \\ . \\ A(t_j,\theta_i) \end{bmatrix} = \begin{bmatrix} \gamma_1(t_0,\theta_1) & \gamma_2(t_0,\theta_1) & \gamma_3(t_0,\theta_1) \\ . & . & . \\ . & . & . \\ . & . & . \\ \gamma_1(t_j,\theta_i) & \gamma_2(t_j,\theta_i) & \gamma_3(t_j,\theta_i) \end{bmatrix} \begin{bmatrix} \Delta V_P/\overline{V_P} \\ \Delta V_S/\overline{V_S} \\ \Delta\rho/\bar{\rho} \end{bmatrix} * s(t), \qquad (A1.5)$$

where $A(t_0,\theta_1)$ are our observed amplitudes at time t and angle θ, $s(t)$ is the wavelet and the symbol * denotes a convolution. The parameterisation of equation A1.4 seems relatively simple; however the terms γ_2 and γ_3 include the $(\overline{V_S}/\overline{V_P})$ ratio.

Castagna et al. (1985) gathered compressional and shear wave velocity measurements from different basins around the world and established an empirical linear equation (1.6), which allows transforming the P-wave velocity model (from processing), into a pseudo S-velocity.

$$V_P = a + b\,V_S \qquad (A1.6)$$

The local intercept and gradient in Castagna's equation (a and b respectively) are estimated empirically for the area of interest. By using equation A1.6 we can complete the parameterisation of A1.4, which means that with relatively little information, we can calculate the P-wave, S-wave and density reflectivities using standard matrix inversion methods. This type of calculation is commonly known as AVO inversion.

An alternative AVO inversion method to solve for the intercept, gradient and curvature can be defined using Shuey's approximation (Castagna, et al., 1994):

$$\begin{bmatrix} A(\theta_1) \\ . \\ . \\ . \\ A(\theta_i) \end{bmatrix} = \begin{bmatrix} 1 & (\sin^2\theta_1) & (\sin^2\theta_1 \ \tan^2\theta_1) \\ . & . & . \\ . & . & . \\ . & . & . \\ 1 & (\sin^2\theta_i) & (\sin^2\theta_i \ \tan^2\theta_i) \end{bmatrix} \begin{bmatrix} A \\ B \\ C \end{bmatrix} * \ s(t). \qquad (A1.7)$$

Both inversion schemes provide equivalent results and have been used successfully in AVO interpretation. Castagna, et al. (1998) and Ross (2000) provide useful insights for the interpretation of the gradient and intercept, using crossplots (Figure A1.2)

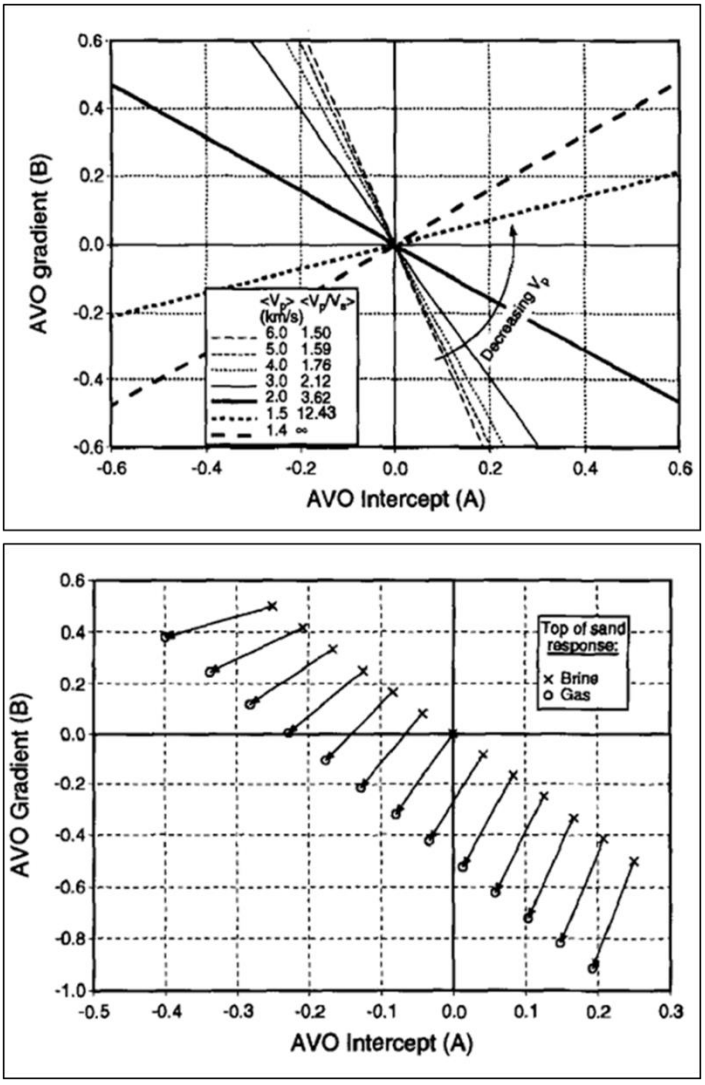

A1.2: Gradient and Intercept interpretation templates (modified from Castagna et al., 1998)

AVO Classification

A practical AVO visualisation technique was published in 1989 by Rutherford and Williams. It consists of a classification of amplitude variations with offset/angle that allows quick screening of data. Using Aki and Richards' approximations, they found that, depending on the relative magnitude of the overlying rock with respect to the reservoir, AVO behaviour in gas sands could be generalised in three classes. Later on, Castagna et al. (1998) added an extra class, using the gradient and intercept from Shuey's approximations. A graphical representation of the classes is shown in Figure A1.3 and the descriptions for positive polarity data (increase in impedance represented by a positive) are as follows:

Class I: Sands have higher impedance than the enclosing medium. The AVO behaviour shows a large positive amplitude at near angles and it decreases until it reverses polarity in the far angles.

Class IIa: The sand impedance is slightly higher than the enclosing material. The AVO displays small positive amplitude in the near angles that decreases rapidly, changes polarity and increases slightly in the far angles.

C**lass IIb**: The sand impedance is slightly lower than the enclosing material. The AVO shows a small negative amplitude in the near angles that increases slightly in the far angles.

Class III: Sands have lower impedance than the enclosing medium. The AVO behaviour is characterised by a large negative amplitude that increases with angle of incidence.

Class IV: Like Class III, sands have lower impedance than the enclosing medium. However, the AVO behaviour shows large negative amplitudes in the near angles and a decrease of amplitude with angle of incidence.

The use of AVO inversion to calculate gradient, intercept, or reflectivities allowed the screening of large volumes of data and made it possible to use this classification scheme in oil and gas exploration. Unfortunately, this type of analysis carries too much

ambiguity (Drufuca and Mazzotti, 1995), as different lithology contrasts not related to gas sands can display the exact same AVO behaviour, and many dry wells have been drilled based on false AVO anomalies.

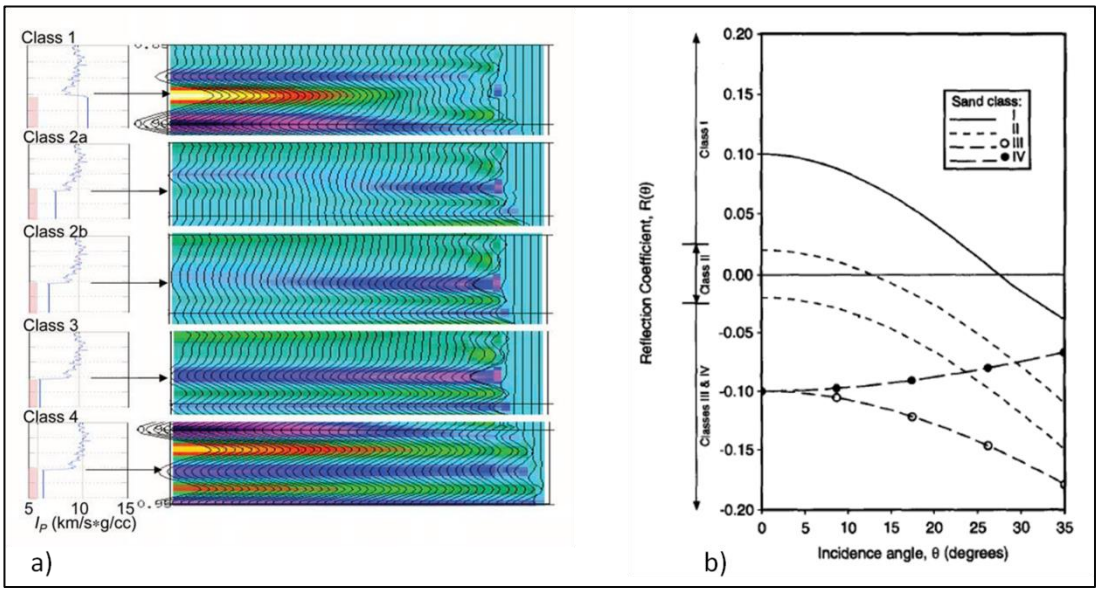

A1.3: a) Seismic modelling showing the AVO classes (Li, et al., 2007). b) AVO classes in a typical angle versus reflection coefficient plot (Castagna et al., 1998)

Constrained simultaneous AVO inversion

De-convolving seismic data through an inversion process to estimate rock properties has been an objective in the oil and gas industry for many years. And even before the development of AVO analysis, methodologies were already available for estimating rock properties from post-stack seismic data. One of the first examples is provided by Lindseth (1979), where trace inversion is achieved through the use of the next empirical relation:

$$I_{P-i+1} \approx I_{P-i} \frac{(1+R_i)}{(1-R_i)} \ , \qquad (A1.8)$$

where R_i is the reflection coefficient at time i and the initial impedance values (I_{P-i}) are assumed as a constant in order to scale the seismic to the desired output range. In practice, the application of equation A1.8 is equivalent to integrating the seismic trace,

assuming this is a fair representation of the reflection coefficients. However, since the input traces are of band-limited nature, it is necessary to artificially add the low frequency of the output by adding a low frequency trend usually generated from the seismic processing velocities. This type of inversion is commonly known as **band-limited inversion.** Another inversion method commonly known as **sparse spike** was proposed by Oldenburg et al. (1983), and consists of constructing a series of broadband reflectivity functions (in the form of spikes) that, convolved with a known wavelet, fit the data. The inherent non-uniqueness of this process is handled by assuming an equally spaced reflectivity series of the form:

$$r(t) = \sum_{j=1}^{NL} r_j \delta\left(t - \tau_j\right) , \qquad (A1.9)$$

where NL represents the number of layers, r_j the reflectivity coefficient and τ_j the two-way travel time to the j^{th} layer interface. The resultant reflectivity series is then convolved with a wavelet (usually estimated from the real seismic) and the result is compared with the observed seismic through an iterative error minimisation process (linear programming). Once the model converges, the impedance is calculated by integrating the resultant broadband reflectivity series. The main disadvantage with this approach is the lack of geological constraint in the results and non-uniqueness.

A third method, called **model based** inversion, was developed by Cooke and Schneider (1983) and consists in perturbing an initial model from which a reflectivity series is created, convolving the result with a wavelet and comparing it with the observed seismic. The difference of this recursive method with respect to the sparse-spike is that the resultant impedance is not achieved through trace integration but as a result of the perturbation of the model (commonly known as the Low Frequency Model or LFM). The main disadvantage of this method is that it requires a priori knowledge of the solution, which is commonly fulfilled by incorporating a geo-statistical interpolation of well based measurements. The problem with this approach is that the result will have a big imprint of the input LFM, and the result will depend

heavily on the number of wells used as well as the interpolation algorithm (Figure A1.4). A natural step for researchers was to extend the application of model-based inversions to include AVO effects, and therefore be able to calculate additional parameters like S impedance or Poisson's ratio. Several authors attempted to achieve this (Lörtzer et al., 1988; Demirbag⁄ and Çoruh, 1998; de Haas and Berkhout, 1989). However, due to the existing limitations in computing power, practical applications of these methods became feasible only after the mid 1990's.

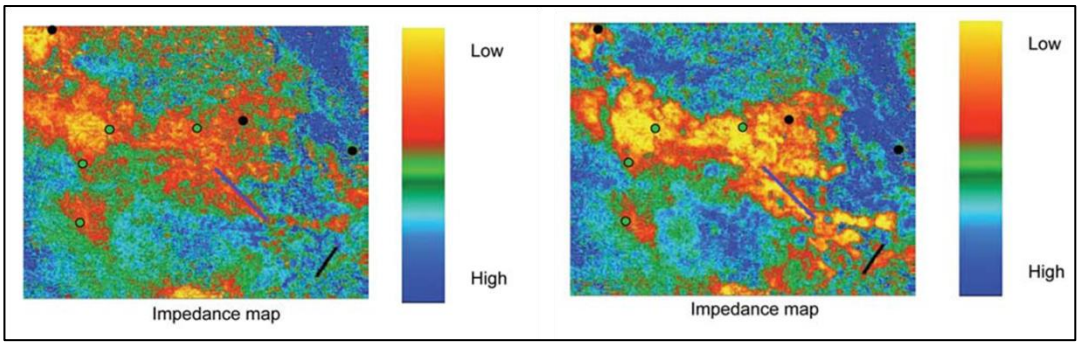

A1.4: Example of an inversion performed using different wells as inputs. The left side used only the wells in black, and the right hand side uses all the wells. (Modified from Pedersen-Tatalovic et al., 2008).

Simmons and Backus (1996) generalised inversion theory for pre-stack data and inverted successfully for reflectivities and in 1999, Wang defined an inversion scheme to invert for model geometry and elastic parameters. Their work was followed up by Buland and Omre (2003) to invert for P velocity and density by assuming a logarithmic relationship between reflectivities and velocities:

$$\frac{\Delta V_P}{V_P} \approx \Delta \, ln \, V_P \, . \qquad (A1.10)$$

In 2005, Hampson et al. developed a method to invert for P and S impedance and density, using Fatti et al.'s (1994) rearrangement of Aki and Richards' equation. To constrain the result, they used logarithmic relationships between P impedance, S impedance and density:

$$\ln I_S = k \, \ln I_P + k_c + \Delta I_S \qquad (A1.11)$$

$$\ln \rho = m \ \ln I_P + m_c + \Delta\rho \ , \qquad (A1.12)$$

where k, k_c, m, m_c are empirical constants, which can be derived from cross-plotting well data, and ΔI_S, $\Delta\rho$ are the deviations of the general trend, which is assumed to be related to the presence of hydrocarbons (Figure A1.5). The inversion matrix used is then expressed as follows:

$$\begin{bmatrix} T(\theta_1) \\ . \\ . \\ T(\theta_n) \end{bmatrix} = \begin{bmatrix} \widetilde{c_1}\, W(\theta_1) & \widetilde{c_2}\, W(\theta_1) & c_3 W(\theta_1) \\ . & . & . \\ . & . & . \\ \widetilde{c_1}\, W(\theta_n) & \widetilde{c_2}\, W(\theta_n) & c_3 W(\theta_n) \end{bmatrix} \begin{bmatrix} R_P \\ \Delta I_S \\ \Delta\rho \end{bmatrix}, \qquad (A1.13)$$

where $T(\theta)$ is the trace at the angle of incidence θ, the constants $\widetilde{c_1}, \widetilde{c_2}$ and c_3 are functions of the angle of incidence and the empirical fits from equations A1.11 and A1.12. $W(\theta)$ is the wavelet function, which it is now angle dependent, and R_P, represents the P wave reflectivity expressed as logaritmic function:

$$R_P = \frac{1}{2}[\ln I_{P\,i+1} - \ln I_P \,] \, . \qquad (A1.14)$$

The low frequency model is then introduced by initializing the solution to $[\ln I_{P0} \ \ 0 \ \ 0]^T$, where I_{P0} is perturbed at each iteration using the conjugate gradient method. Using the same principles stated above, other algorithms have been developed, incorporating different optimisation techniques and statistical methods (e.g. Haas & Dubrule, 1994; Tonellot et al., 2001). The description of such methods is beyond the objective of this thesis; however, it is important to mention that, despite their differences, the main drawback in all of them is the strong dependence of the result on the initial guess, the need of an accurate structural and stratigraphic interpretation and the dependence on the number of wells used (Pedersen-Tatalovic et al., 2008).

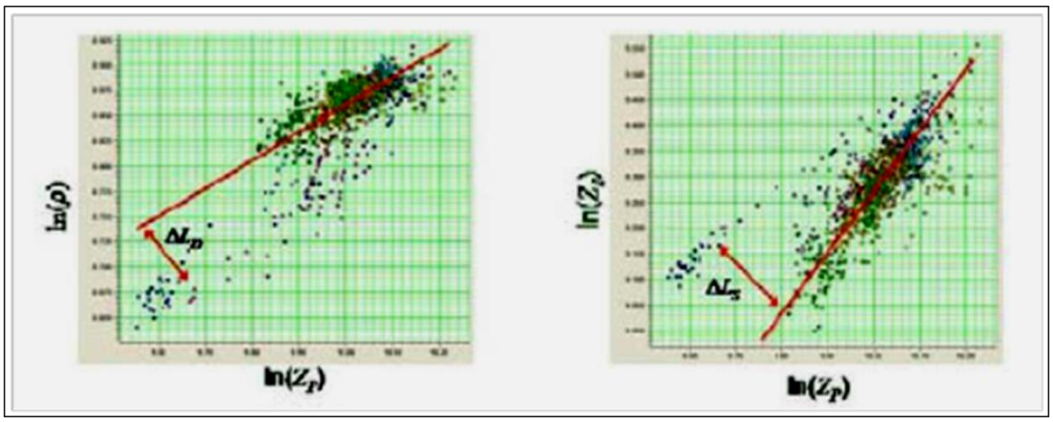

A1.5: Well based crossplots from where the logarithmic functions used to constrain the AVO simultaneous inversion are constructed (from Hampson & Russell, 2005).

The use of inverted AVO properties

The ability to use AVO simultaneous inversion to elastic parameters, which can also be obtained at well locations from P and S sonic and density logs, took AVO analysis to a new level, allowing the interpreter to measure variations in the rock properties rather than simply interpreting peaks and troughs (Figure A1.6). Furthermore, using the mathematical models that relate petrophysics variations with seismic amplitudes (called rock physics models), it is possible to generate interpretation templates that can make the analysis of AVO results more quantitative (e.g. Goodway, 1997, Oodegard and Avseth, 2004, Li et al., 2007); examples of these templates are illustrated in Figure A1.7

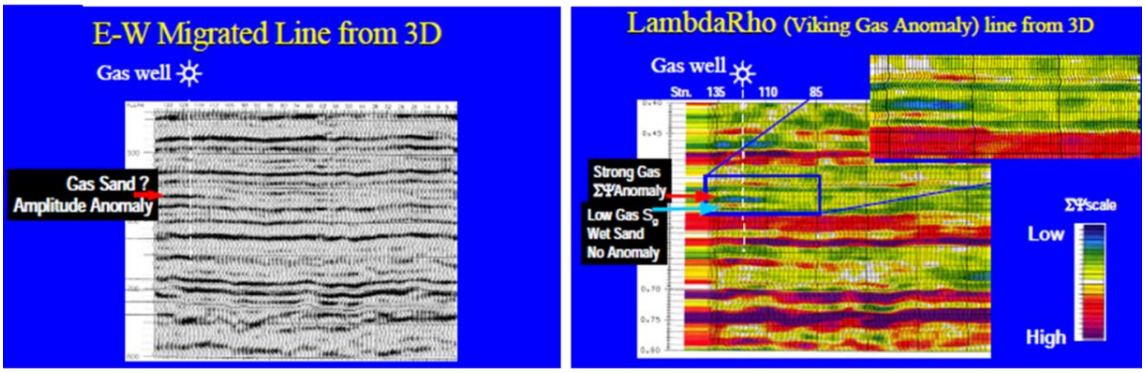

A1.7: Comparison of seismic amplitude analysis with the results of an AVO simultaneous inversion for identification of gas sands (Goodway, 2002).

Another useful application of AVO simultaneous inversion is to use the inverted properties as a lateral constrain in the construction of geological models (e.g. Leguijt, 2009; Singh et al., 2009, Floricich et al., 2011), which extended the application of geophysical analysis into the realms of geological modelling and reservoir engineering domains (Figures A1.8 to A1.10), which led to the consolidation of the discipline we now call Reservoir Geophysics.

It is important to mention that in all the applications described above, the definition of the rock physics equations and their parameterisation will determine the accuracy and confidence of the interpretations; a brief summary of the main equations used for these purposes and their extension to 4D seismic analysis will be developed below.

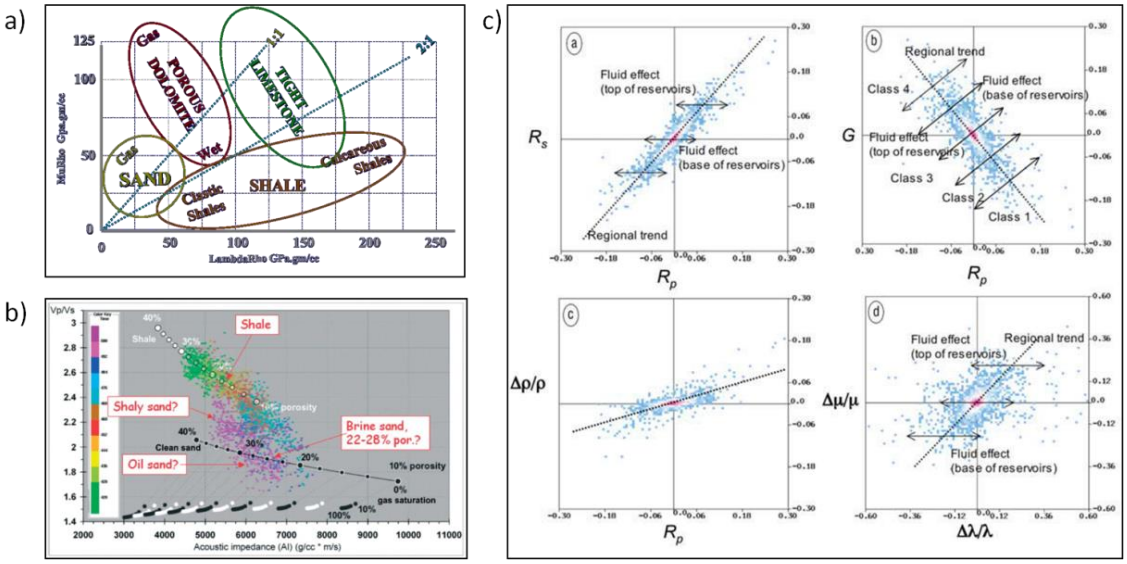

A1.9: Examples of interpretation templates for AVO inversion results using rock physics models from a) Goodway, 2002; b) Oodegard & Avseth, 2004; c) Li et al., 2007.

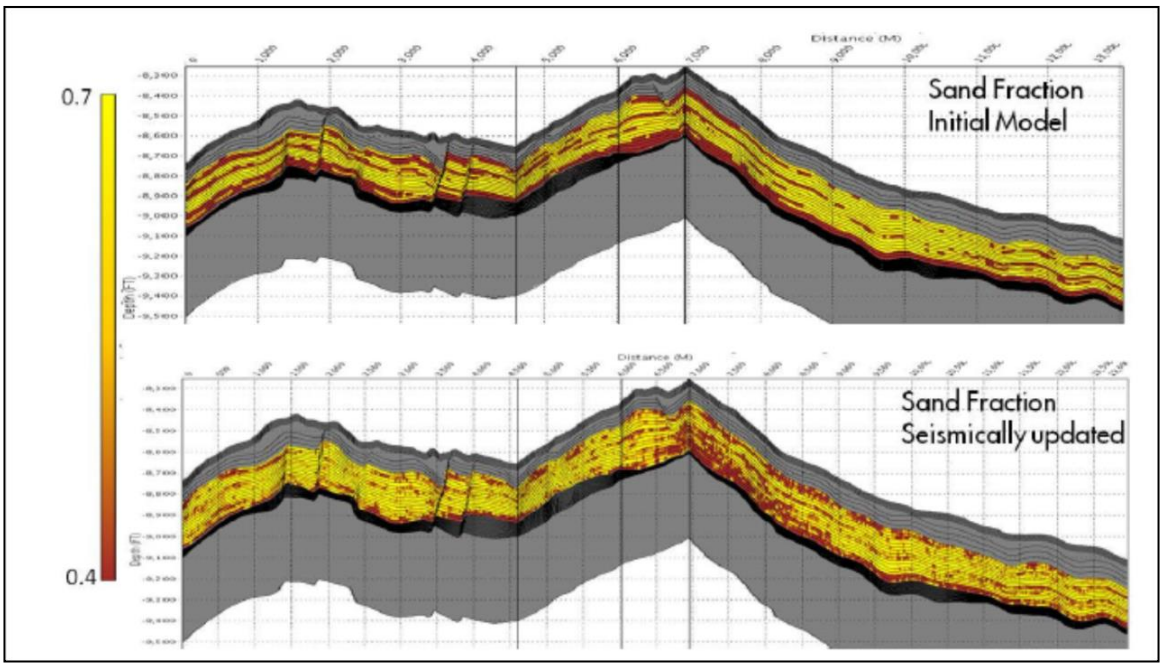

A1.10: An example of the use of inverted properties to constrain reservoir models (Floricich, et al., 2011).

APPENDIX 2: Additional equations developed for reservoirs containing free gas

4D signature of a gas-water contact movement

Using the same physical principles as before, and using the theoretical models shown in Chapter 5, we can define the effective fluid bulk modulus for the different components of the reflectivities of the original and produced gas-water contacts as follows:

$$\Delta R(\theta)_{\mathrm{Ogwc}} = -\frac{\left(1 - S_{grw} - S_{wc}\right)}{S_{wc}} \mathrm{C}_{\mathrm{S}}^{\mathrm{G}} + \frac{\Delta P}{P_i} C_P^G \qquad (A2.1)$$

$$\Delta R(\theta)_{\mathrm{Pgwc}} = -\Delta R(\theta)_{\mathrm{Ogwc}}\,, \qquad (A2.2)$$

where

$$\mathrm{C}_{\mathrm{S}}^{\mathrm{G}} = \phi\left[\bar{\Gamma}_1 N_1^G + \bar{\Gamma}_2 N_2^G\right] \qquad (A2.3a)$$

$$C_P^{G=}\left[(1 - \varepsilon'\phi)\bar{\Gamma}_1 N_3^G + \phi\left(\bar{\Gamma}_1 N_5^G + \bar{\Gamma}_2 N_6^G\right)\right] \ . \qquad (A2.3b)$$

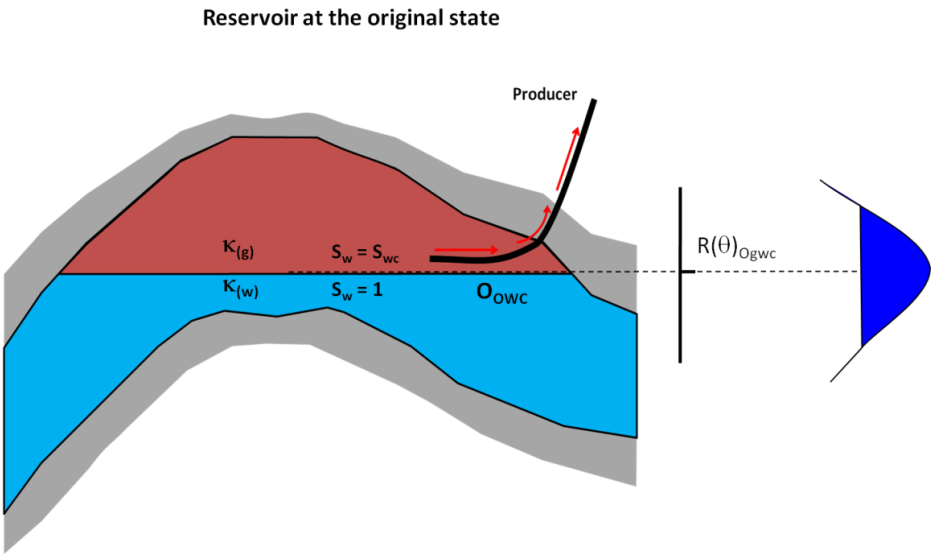

Figure A2.1: Conceptual model for a fluid contact (in this case gas-water) before production.

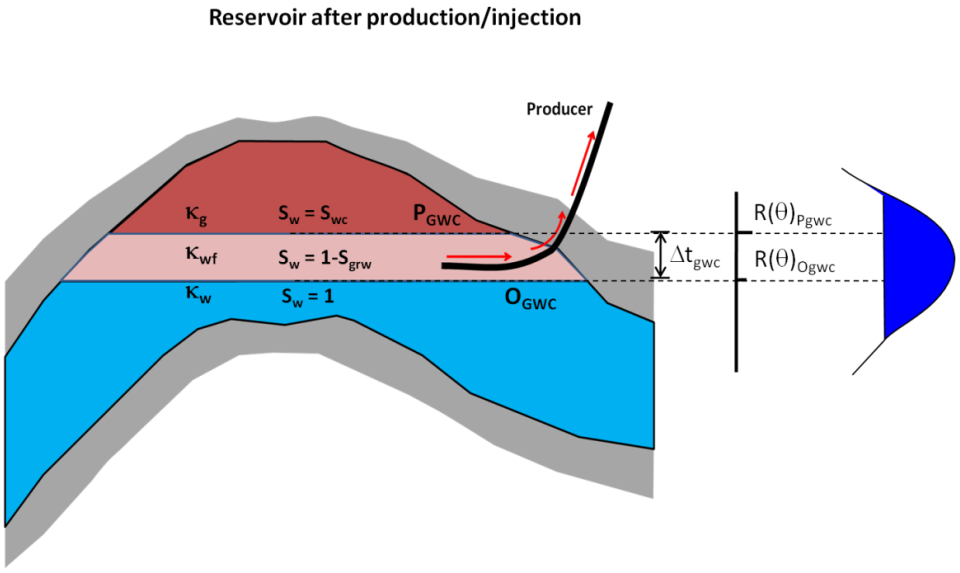

Figure A2.2: Conceptual model for a fluid contact (in this case gas-water) after production.

And:

$$N_1^G = \frac{\varepsilon}{\overline{M^b}} \frac{S_{wc}\left(\kappa_w^b - \kappa_g^b\right)}{\left(\frac{\kappa_g^b}{\kappa_w^b} - 1\right) S_{wc} + \left(\frac{\kappa_w^b}{\kappa_g^b} - 1\right) S_{grw} + 1} \quad , \tag{A2.3c}$$

$$N_2^G = \frac{S_{wc}\left(\rho_w^b - \rho_g^b\right)}{\overline{\rho^b}} \quad , \tag{A2.3d}$$

$$N_3^G = P_i \left[\frac{\alpha \kappa_m A_\kappa}{\overline{M^b}}\right] \quad , \tag{A2.3e}$$

$$N_5^G = P_i \left[\frac{\varepsilon}{\overline{M^b}} \frac{\kappa_w^b (1 - S_{wc}) G_\kappa + \kappa_g^b W_\kappa S_{wc}}{\kappa_g^b S_{wc} + \kappa_w^b (1 - S_{wc})}\right] \quad , \tag{A2.3f}$$

$$N_6^G = P_i \left[\frac{S_{wc} W_\rho + (1 - S_{wc}) G_\rho}{\overline{\rho^b}}\right] \quad . \tag{A2.3g}$$

Here, the upper-index G denotes the gas-water system and the parameters G_κ and G_ρ are the local fluid pressure gradients, which, according to my calculations, are nearly constant within the common ranges of time lapse changes (A2.3).

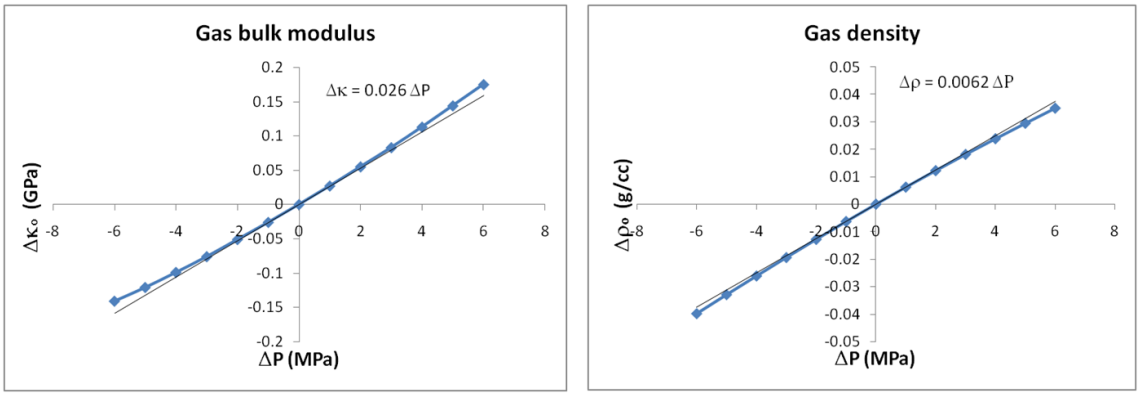

Figure A2.3: Fluid pressure sensitivity of gas computed from Batzle & Wang equations (1992). The X axis is the change in pressure and the Y axes the change in bulk modulus (left) and density (right).

Incorporating wavelet interference effects

Finally, we can calculate the composed time lapse reflectivity $(\Delta A(\theta)_{\text{gwc}}^{\text{comp}})$ for the cases where the original and produced gas-water contact reflectivities are subject to wavelet interferences, in a similar way as with the oil-water contact equations. This leads to the next result:

$$\Delta A(\theta)_{\text{gwc}}^{\text{comp}} = \left\{ \frac{\left(1 - S_{grw} - S_{wc}\right)}{S_{wc}} \mathrm{C}_{\mathrm{S}}^{\mathrm{G}} - \frac{\Delta P}{P_i} C_P^G \right\} \Delta t_g \dot{s}(t), \qquad (A2.4)$$

which can also be expressed as:

$$\Delta A(\theta)_{\text{gwc}}^{\text{comp}} = \left\{ -\frac{\Delta S_g}{S_{wc}} \mathrm{C}_{\mathrm{S}}^{\mathrm{G}} - \frac{\Delta P}{P_i} C_P^G \right\} \Delta t_g \dot{s}(t)\,. \qquad (A2.5)$$

In contrast with the oil-water equations, here both the connate water (S_{wc}) and the residual gas saturation (S_{grw}) volumes can be considered less variable with time lapse (Falahat et al., 2012). This means that ΔS_g is expected to quickly reach the maximum change $(1 - S_{grw} - S_{wc})$, and remain constant thereafter. This implies that the observed variations in the 4D signal are more sensitive to changes in the thickness of the gas

column (Δt_g) than to changes in gas saturation. This finding is important because it shows that the 4D response for gas is more linear than what is usually considered in 4D interpretation studies, which focus on the saturation changes using a highly non-linear mixing law.

Accuracy of the equations and applicability

1D modelling was performed using the same PEM as in the previous example, making Sgrw = 0.05, Swc = 0.18, maximum water flooding ($\Delta S_g = -(1 - S_{grw} - S_{wc})$ and a maximum pressure change of -6 MPa (depletion), the time thickness variation and the wavelet are the same as in the oil-water contact modelling. The results can be observed in Figure A2.4 showing the comparison against the full rock and fluid physics results, this picture also shows the start of the wavelet interferences occurring around Δt_g = 12 ms. This is consistent with the observations in Figure A2.5, where we see the comparison between the full equations and the thin reservoir equation, showing that it can be effectively used for $\Delta t_g \leq$ 12ms. The 4D AVO comparison is shown in Figure A2.6. It is important to note that, although, qualitatively, the results of the oil-water and gas-water models look similar, the magnitude of the amplitude in the gas-water system is about 75% larger than that of the oil-water system.

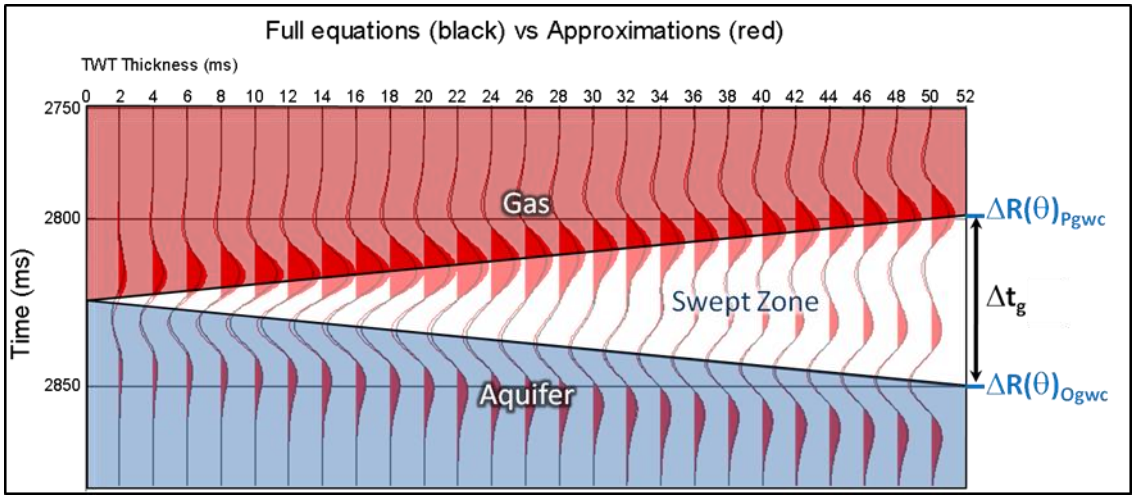

Figure A2.4: Wedge modelling results comparing the full equations (black) versus the thick reservoir equations (red) for swept zone thicknesses from 0 to 52 ms (twt).

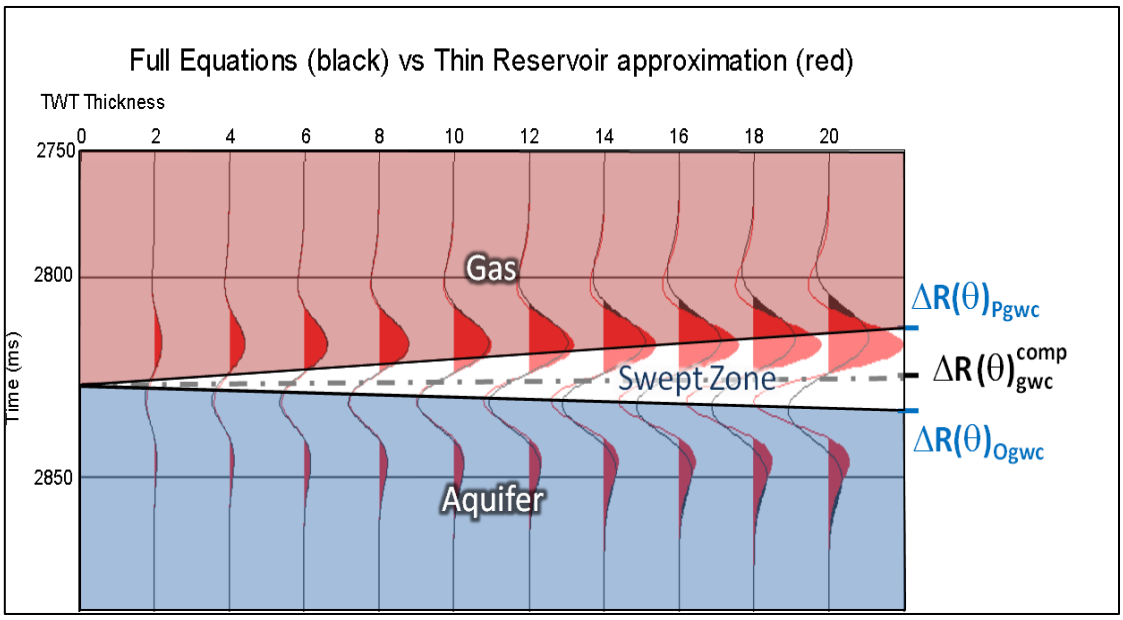

Figure A2.5: Wedge modelling results, comparing the full equations (black) versus the thin reservoir equations (black) for swept zone thicknesses from 0 to 52 ms (twt).

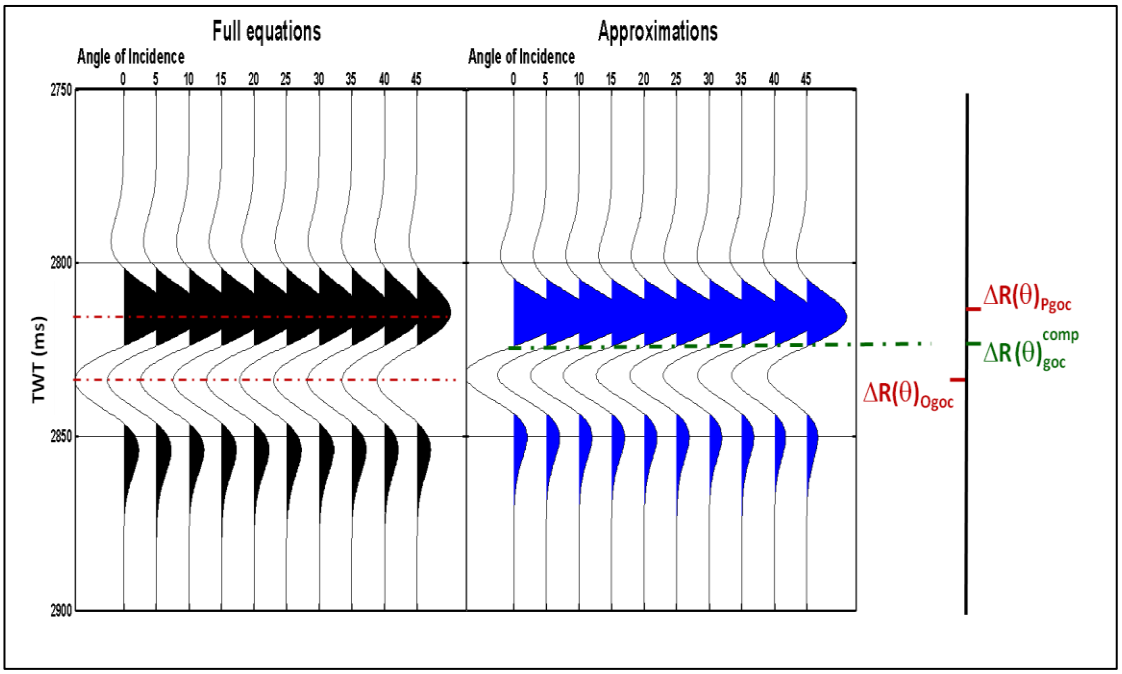

Figure A2.6: Comparison of full thick reservoir equations versus the thin reservoir approximation in the 4D AVO domain, assuming a constant Δt_g of 14 ms.

4D signature of a gas-oil contact movement

This case is slightly more complex, as there are now three fluids involved (gas, oil and connate water), and there is also a residual gas saturation (S_{gro}) in the oil leg, which comes from gas dissolution, either during production or during the formation of the gas cap in geological time. However, since the volume of connate water is small and is not expected to change significantly during production/injection, we can simplify the system finding the bulk modulus and density for the oil-water mixture in the oil leg and then introduce it to the calculations to simulate a dual fluid system as those developed before:

$$\kappa_{ow}^{b} = \frac{\kappa_{w}^{b}\kappa_{o}^{b}}{S_{wc}\kappa_{o}^{b} + (1 - S_{wc})\kappa_{w}^{b}} \tag{A2.6}$$

$$\rho_{ow}^{b} = S_{wc}\rho_{w}^{b} + (1 - S_{wc})\rho_{o}^{b} \ . \tag{A2.7}$$

Using the theoretical models shown in Figure and Figure and assuming the reservoir is sufficiently thick to allow the interpretation of the gas-oil contact and the oil-water contacts independently without any wavelet interference we obtain:

$$\Delta R(\theta)_{\mathrm{Ogoc}} \approx -\frac{\left(1 - S_{org} - S_{wc} - S_{gro}\right)}{S_{wc}} \mathrm{C_S^m} + \frac{\Delta P}{P_i} C_P^m \ , \tag{A2.8}$$

$$\Delta R(\theta)_{\mathrm{Pgoc}} \approx -\Delta R(\theta)_{\mathrm{Ogoc}} \ , \tag{A2.9}$$

where

$$\mathrm{C_S^m} = \phi[\bar{\Gamma}_1 N_1^m + \bar{\Gamma}_2 N_2^m], \tag{A2.10a}$$

$$C_P^m = [(1 - \varepsilon'\phi)\bar{\Gamma}_1 N_3^m + \phi(\bar{\Gamma}_1 N_5^m + \bar{\Gamma}_2 N_6^m)] \ , \tag{A2.10b}$$

$$N_1^m = \frac{\varepsilon}{\overline{M^b}} \frac{S_{wc}\left(\kappa_{ow}^b - \kappa_g^b\right)}{\left(\frac{\kappa_g^b}{\kappa_{ow}^b} - 1\right)\left(S_{org} + S_{wc}\right) + \left(\frac{\kappa_{ow}^b}{\kappa_g^b} - 1\right) S_{gro} + 1} \quad , \qquad A2.10c$$

$$N_2^m = \frac{S_{wc}\left(\rho_{ow}^b - \rho_g^b\right)}{\overline{\rho^b}} \quad , \qquad (A2.10d)$$

$$N_3^m = P_i \left[\frac{\alpha \kappa_m A_\kappa}{\overline{M^b}}\right] \quad , \qquad (A2.10e)$$

$$N_5^m = P_i \left[\frac{\varepsilon}{\overline{M^b}} \frac{\kappa_g^b \overline{O_\kappa} \zeta_{BP}(S_{or} + S_{wc}) + \overline{\kappa_o^b} G_\kappa S_{gr}}{\kappa_g^b (S_{or} + S_{wc}) + \overline{\kappa_o^b} S_{gr}}\right] \quad , \qquad (A2.10f)$$

$$N_6^m = P_i \left[\frac{(S_{or} + S_{wc})\overline{O_\rho} \zeta_{BP} + (1 - S_{or} - S_{wc}) G_\rho}{\bar{\rho}}\right] \quad . \qquad (A2.10g)$$

The super index ***(m)*** indicates that the constants are defined for the multi- phase system.

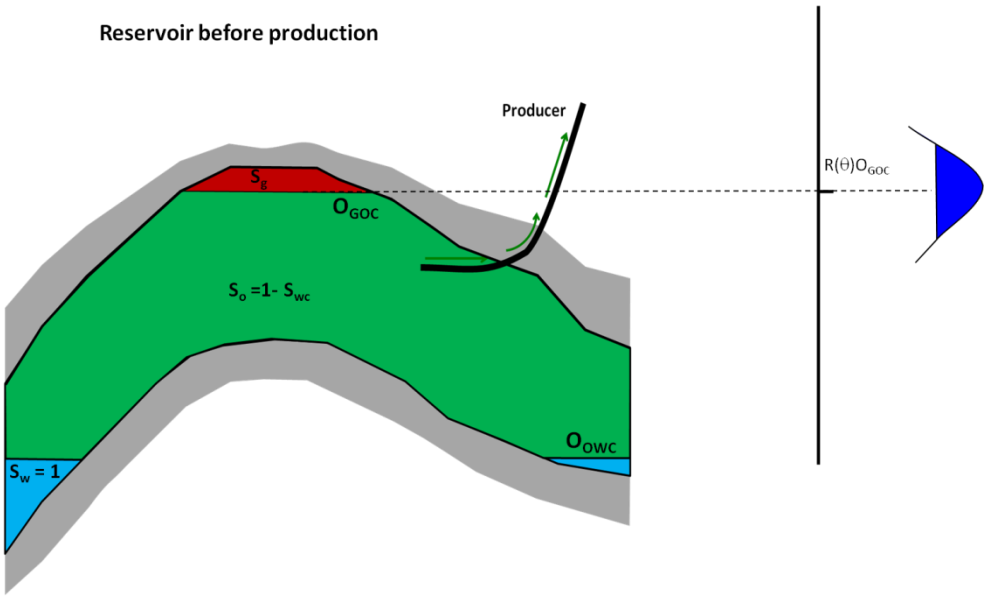

Figure A2.7: Conceptual model for a fluid contact (in this case gas-oil) pre-production

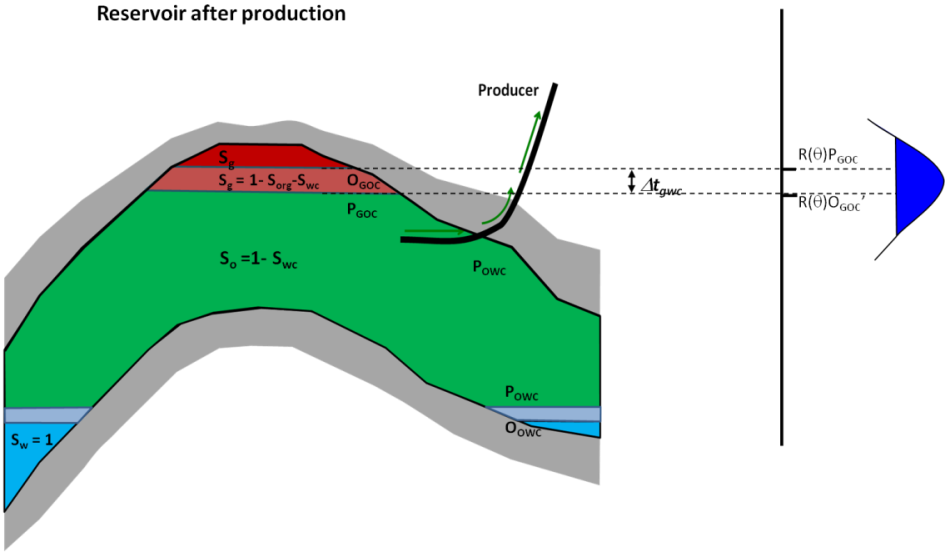

Figure A2.8: Conceptual model for a fluid contact (in this case gas-oil) post-production

Incorporating wavelet interference effects

As before, we calculate the composed time lapse reflectivity $(\Delta A(\theta)_{\text{goc}}^{\text{comp}})$ for the cases where the original and produced gas-oil contact reflectivities are subject to wavelet interferences:

$$\Delta A(\theta)_{\text{goc}}^{\text{comp}} = \left\{ \frac{\left(1 - S_{org} - S_{wc} - S_{gro}\right)}{S_{wc}} \text{C}_{\text{S}}^{\text{m}} - \frac{\Delta P}{P_i} C_P^m \right\} \Delta t_g \dot{s}(t) \qquad (A2.11)$$

or

$$\Delta A(\theta)_{\text{goc}}^{\text{comp}} = \left\{ -\frac{\Delta S_g}{S_{wc}} \text{C}_{\text{S}}^{\text{m}} - \frac{\Delta P}{P_i} C_P^g \right\} \Delta t_g \dot{s}(t) \qquad (A2.12)$$

It is important to note that these equations can be applied to both the cases where there is an existing gas cap (in which case S_{gro} would be nearly zero) and the reflectivity change will depend on the increase or decrease in S_{org}, as opposed to the case where the gas cap is formed and expands through gas dissolution (or gas injection) – in this case S_{org} will be less variable and the variability in the reflectivity will depend on the increase or decrease in S_{gro}. The fluid pressure sensitivity change is accounted for inside N_5^m and N_6^m

by the incorporation of the constant ζ_{BP}, which determines if the bulk modulus and density decreases or increases with pressure, depending on where pressure is with respect to the bubble point pressure. Batzle & Wang's equations (1992) predict that above the reservoir pressure both density and the bulk modulus of oil and gas decrease with decreasing reservoir pressure, whereas below the bubble point pressure, bulk modulus and density will increase with decreasing reservoir pressure, which makes sense considering that below the bubble point pressure the oil loses its lighter components (and hence becomes heavier) and at the same time these components are added to the gas, making it heavier.

4D AVO implications for the thick reservoir equations

A numerical exercise is conducted to analyse the 4D AVO behaviour and its relation to the fluid contact movements and pressure changes; the same North Sea example parameters from Chapter 2 were used for comparison purposes. Previously, I observed that for a single interface calculation in an oil-water system, the use of 4D AVO can help in separating pressure and saturation changes (Chapter 2), however I have also observed that when gas is present, the pressure response seems to have a much lower magnitude than the saturation changes. The objective here is to investigate if there might be any benefit from the interpretation of 4D differences at different angles of incidence (for instance, in angle stacks) in the fluid contact interpretation. Figure A2.9 shows the contributions of the pressure and saturation effects into the total 4D seismic change for the gas-oil contact case. The model was generated assuming a constant pore pressure change of -4 MPa and maximum saturation change $\left(1 - S_{org} - S_{wc} - S_{gro}\right)$. The black traces are the saturation related effects, the red traces show the contribution of the rock stress sensitivity and the blue traces show the contribution of the fluid pressure (multiplied by -1 to make it positive); Figure A2.10 shows the extracted amplitudes for each case, the black solid line is the total amplitude change for the gas-oil contact movement; the black dotted line is the contribution of the saturation change and the grey dashed line is the contribution of the rock stress sensitivity and the large

dashed line is the fluid pressure sensitivity. The main observation from these two plots is that the 4D AVO variation in the case of fluid contact interpretations is subtle (as opposed to the variations observed in the top reservoir equations in Chapter 2). This implies that the contribution of the pressure changes in the fluid contact time lapse reflectivities is weak, and therefore it is possible to associate these amplitude changes to variations in the fluid saturations. This idea is further developed in Chapter 5.

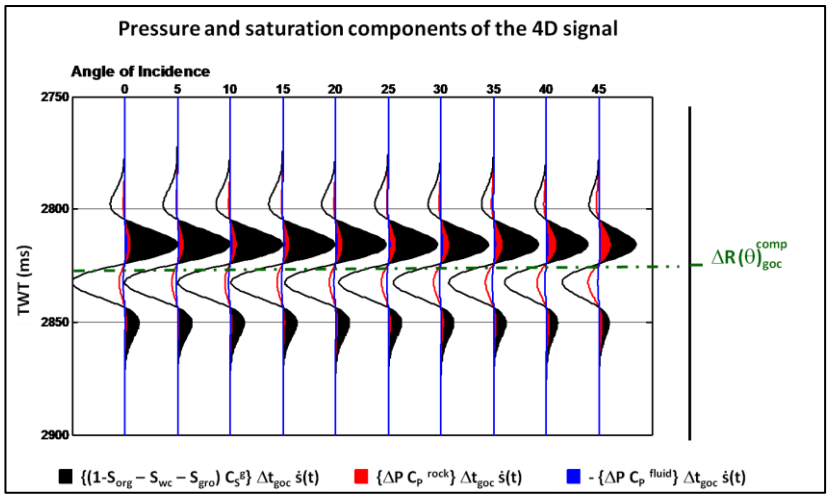

Figure A2.9 Time lapse amplitude responses from equation 4.44 showing the contributions of saturation (black), rock stress (red) and fluid pressure (blue).

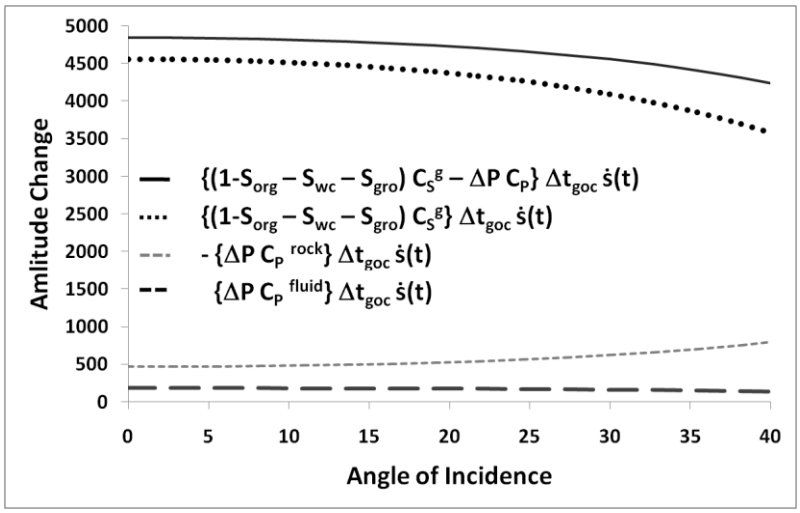

Figure A2.10: Time lapse amplitude responses from equation 4.44 showing the contributions of saturation (black dots), pressure (dashed lines) and the total response (black line).

Reservoirs with no pre-existing gas cap and below the bubble point pressure

Based on the theoretical models displayed in Figure A2.11 and Figure A2.12, the composite time lapse response can be defined as follows:

$$\Delta R(\theta)_{TL}^{comp} = \Delta R(\theta)_{top} + \Delta R(\theta)_{pgoc}\, e^{-i\omega\Delta t_g} + \Delta R(\theta)_{oowc}\, e^{-i\omega t_o} + \Delta R(\theta)_{powc}\, e^{-i\omega(t_o-\Delta t_o)} + \Delta R(\theta)_{base} e^{-i\omega t_T} \quad . \qquad (A2.13)$$

Applying first order Taylor's expansion to the exponential terms and incorporating the fluid contact time lapse reflectivities derived above we obtain:

$$\Delta A(\theta)_{TL} = \left[C_P^o \frac{\Delta P}{P_i}\right] s(t) + \left[\frac{(1-S_{org}-S_{wc}-S_{gro})}{S_{wc}} C_S^m \Delta t_g + \frac{(1-S_{or}-S_{wc})}{S_{wc}} C_S^o \Delta t_o - \frac{\Delta P}{P_i}\left[C_P^o \Delta t_o - C_P^m \Delta t_g\right] - C_P^o \frac{\Delta P}{P_i} t_T\right] \dot{s}(t). \qquad (A2.14)$$

Since the rock stress sensitivity is the same for all layers and the fluid pressure sensitivity is small in magnitude, equation A2.14 can be reduced as follows:

$$\Delta A(\theta)_{TL} \approx \left[C_S^m \frac{(1-S_{org}-S_{wc}-S_{gro})}{S_{wc}} \Delta t_g + C_S^o \frac{(1-S_{or}-S_{wc})}{S_{wc}} \Delta t_o - C_P^o \frac{\Delta P}{P_i} t_T\right] \dot{s}(t) \ . \qquad (A2.15)$$

This is exactly the same as equation 5.15 (Chapter 5), which defines the time lapse response for a pre-existing gas cap.

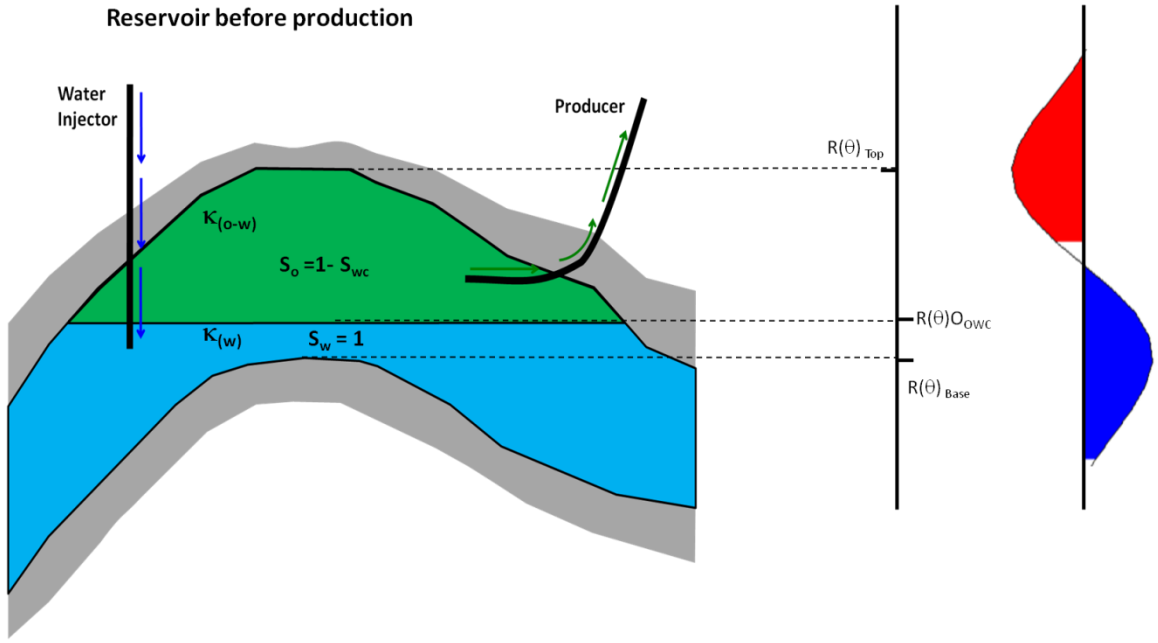

Figure A2.11: Conceptual model for an oil reservoir with no pre-existing gas cap at the limit of seismic resolution, pre-production state.

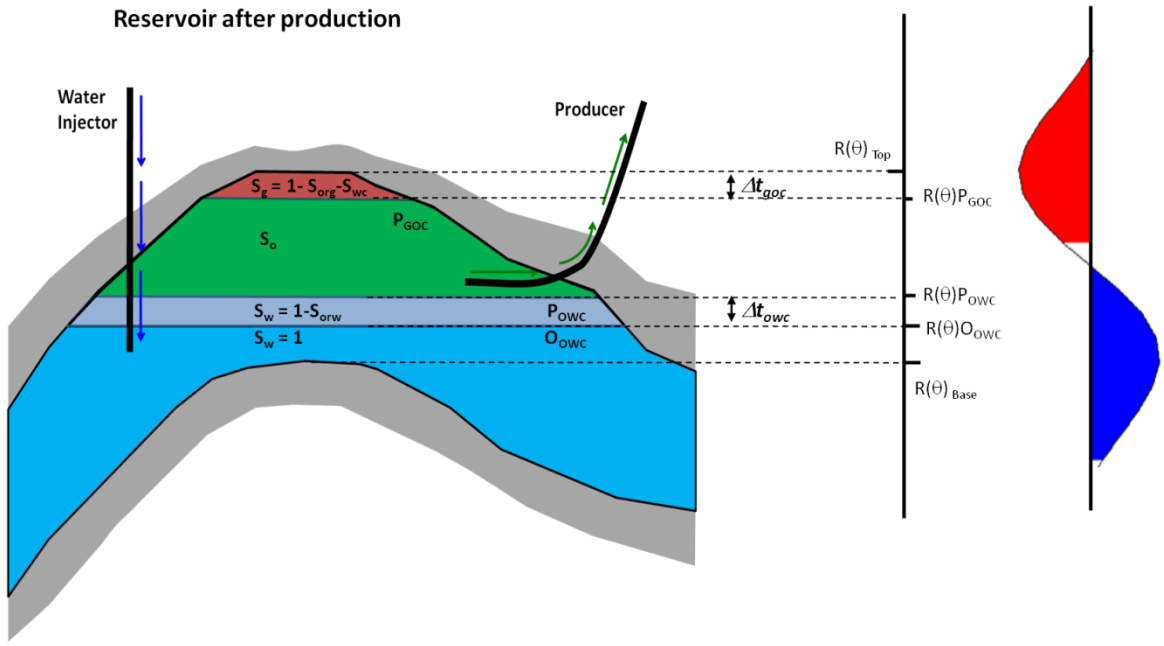

Figure A2.12: Conceptual model for an oil reservoir with no pre-existing gas cap at the limit of seismic resolution, post-production state.

APPENDIX 3: Simulation to Seismic modelling (sim2seis)

The simulation to seismic modelling technique mentioned in this thesis was developed in ETLP by Amini (2014) and it is commonly known as sim2seis. This method uses the reservoir simulation results as an input and through a series of rock and fluid equations and parameters (petroelastic model) produces a series of 3D synthetic seismic volumes at each selected simulation time (Figure A3.1). Unlike the equations derived in this work, the sim2seis approach does not model the 4D seismic directly (i.e. amplitude differences) but this is calculated by subtracting one volume from the other (generally monitor minus base). In the sim2seis approach, the rock and fluid equations related to the 4D signal are applied without any simplification or linearization; therefore it should provide a more accurate result compared to my approximations. However, still some assumptions are made regarding scaling the properties from the simulation to the seismic resolution and vice-versa, as well as the incorporation of vertical variations in rock properties, such as clay variations with depth, overburden changes, etc. These factors and the selection of the petro-elastic model are the main sources of uncertainty in the sim2seis modelling (Amini, 2014). It is also important to note that sim2seis can be computationally extensive; this increases the difficulty in parameter testing and sensitivity analysis.

Nevertheless, there are good reasons to use this technique to benchmark the results of my equations, such as:

- Sim2seis uses similar rock and fluid equations to those I used to derive my equations. Therefore this tool can provide useful information regarding the effects of the linearization and assumptions made during my derivations.
- The sim2seis uses a similar input data as the equations (i.e. property maps from the simulation model). This facilitates a one to one comparison of the results.

- The sim2seis incorporates complex wavelet interactions and vertical geological variations that are not included in the mathematical formulations. This therefore allows observing the impact of such variations in terms of the 4D seismic signal.

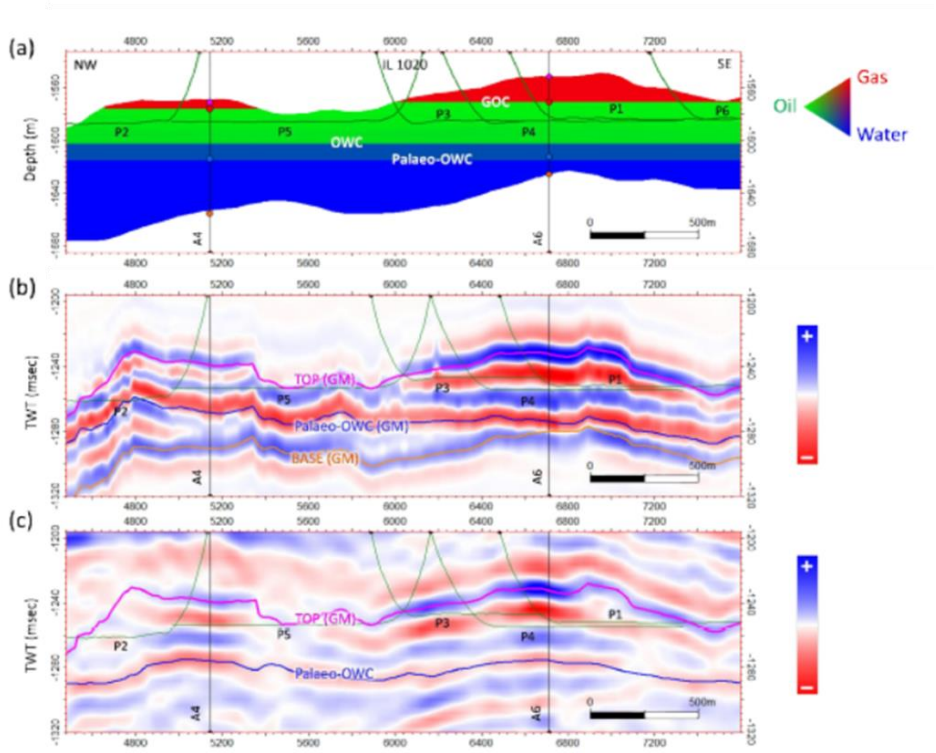

Figure A3.1: Example of the sim2seis application to the Blake field (North Sea), (a) saturation profile from the simulation model. (b) Synthetic seismic produced by the sim2seis. (c) observed seismic. The differences between modelled and observed seismic were used to suggest changes in the geological model. (Modified from Amini, 2014)

Description of the sim2seis workflow (Amini, 2014)

A detailed workflow of the sim2seis modelling technique is shown in Figure A3.2. This can be summarised as follows:

- The simulation model is run for the time steps at which seismic needs to be modelled from where static and dynamic property volumes are extracted (porosity, NTG, pressure, saturations, etc.)

- Results of the simulation are re-sampled onto the seismic grid, which is normally based on a real acquisition grid. Cells are converted to x,y trace locations. Pseudo-logs are generated from the re-sampled properties.
- Rock and fluid equations are used to convert the pseudo logs of static and dynamic properties into elastic properties (related to seismic wave propagation) that can be used to calculate the angle dependent reflectivities.
- 1D convolution of the angle dependent reflectivities with a suitable wavelet (normally extracted from the observed seismic), representing the seismic source and generation of synthetic seismograms in each grid location.
- Steps 2 to 4 are repeated for each time step and finally the 4D seismic responses are calculated by subtracting each monitor minus the seismic base line (pre-production time step)
- Finally, seismic amplitude extractions are performed at key events and seismic sections are generated to compare with the observed seismic and assess the accuracy of the simulation model.

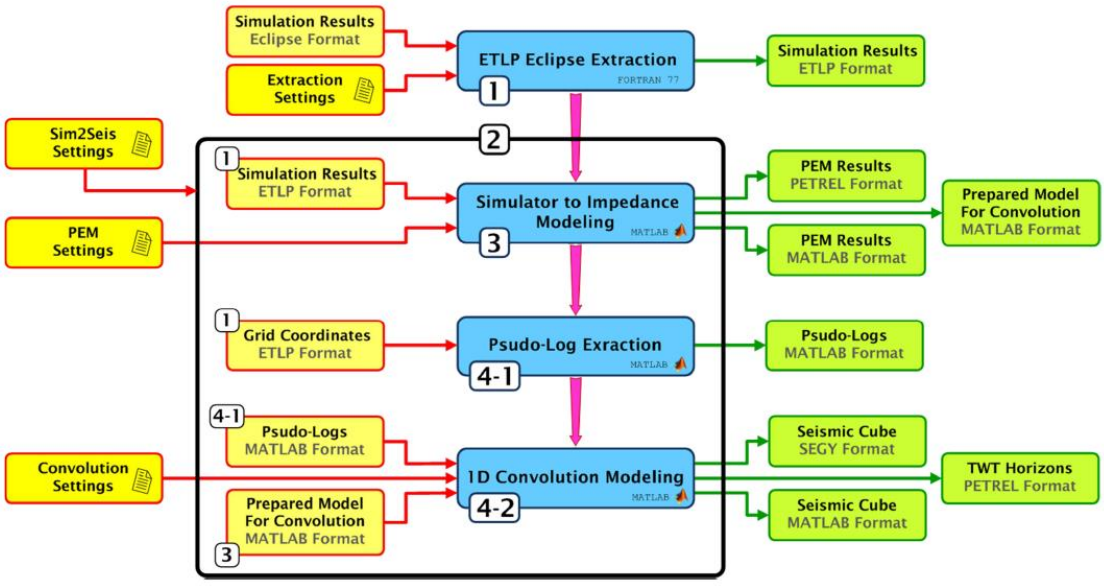

Figure A3.2: Detailed sim2seis workflow, taken from Amini (2014)

Sim2seis uses and applications

The main uses and applications of the sim2seis technique can be summarised as follows:

- *4D seismic feasibility studies:* Here the objective is to model the 4D seismic to determine whether pressure and saturation changes will be detected in a given reservoir. Depending on the rock properties and production mechanisms, it may or may not be possible to observe significant 4D seismic changes; therefore it is important to have this information prior to acquiring a 4D seismic survey. The feasibility study can also help defining the best type of survey to be acquired for the field.
- *4D seismic qualitative interpretation*: the objective is to make sense of the different 4D signals observed through a series of modelling exercises and comparisons with the observed seismic, this is particularly useful in places where saturation and pressure changes overlap and the resultant signal is ambiguous.
- *3D close the loop:* In this workflow, the objective is to test the accuracy of the geological model by generating a series of 4D modelling exercises and comparisons with the observed seismic. Any mismatches provide information about areas that require an update the geological model. After each update, the workflow is repeated until a satisfactory match is obtained. This process results in an improved geological model and understanding on the parameters that control the seismic amplitude changes.
- *4D close the loop or assisted seismic history matching:* Starting with the 3D close the loop workflow, the simulation model is run after each update and the results are tested against the production history of the field, then the simulation model can also be updated either manually or automatically (through an objective function) to match the production history. The final objective is to obtain a simulation model that can explain both the observed 4D seismic and the production history.

An example of the application of sim2seis for 3D close the loop in the Schiehallion field (North Sea) is shown in Figure A3.3.

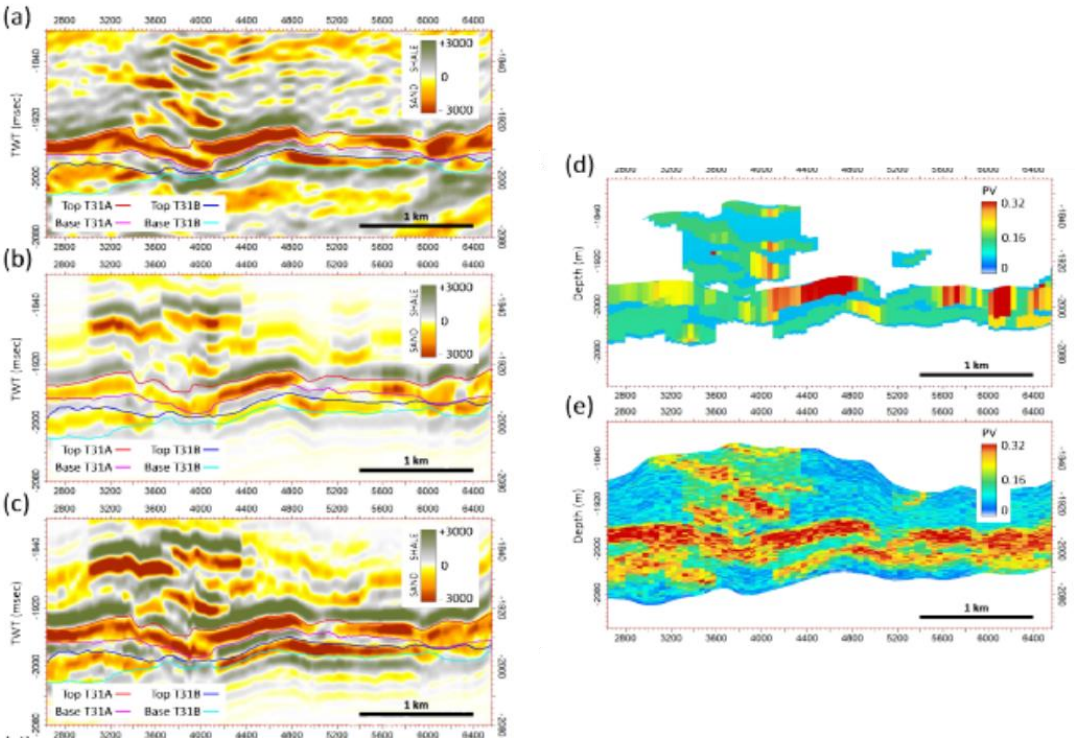

Figure A3.3: Example of the use of sim2seis in 3D close the loop. (a) Observed seismic. (b) Synthetic seismic using original model. (c) Synthetic seismic after updating the simulation model. (d) Original pore volume. (e) Updated pore volume through an automatic seismic inversion based process. Taken from Amini (2014).

APPENDIX 4: Publications related to this work

The following publications are related to this work.

Chapters 2 and 3:

Alvarez, E. and MacBeth C. (2014). An insightful parameterisation for the flatlander's interpretation of time-lapsed seismic data: Geophysical prospecting. Vol 62, No 1. 75-96.

Chapter 3:

Alvarez, E. and MacBeth C. (2012). Constraining the Petroelastic Model with a Flatlander's Interpretation of the 4D Signal: 74th EAGE Conference & Exhibition, Copenhagen. Y019

Chapter 5:

Alvarez, E. and MacBeth C. (2014). Quantification of Residual Oil Saturation Using 4D Seismic Data: 76th EAGE Conference & Exhibition, Amsterdam. We G102 15

NOTE: In this thesis, a change in the notation of the equations was incorporated so that the equations were explicitly dimensionless rather than implicitly as in the publications. This means that the equations are now expressed in terms of the ratios $\Delta S_w/S_{wi}$ and $\Delta P/P_i$ instead of ΔS_w and ΔP as before. To achieve this, the constants N_1 and N_2 in equation 2.24a are multiplied by S_{wi} and N_3 to N_6 are multiplied by P_i. Despite the difference in the notation, the equations presented here and those in the publications shown below are entirely equivalent and the results and conclusions unchanged.

Copenhagen '12

Y019

Constraining the Petro-elastic Model with a Flatlander's Interpretation of the 4D Signal

E. Alvarez* (Heriot-Watt University) & C. MacBeth (Heriot-Watt University)

SUMMARY

An analytic formulation is obtained that relates mapped time-lapsed seismic amplitudes and time-delays directly to the sum of reservoir pressure and saturation changes weighted by the principal groups of controlling parameters from the petroelastic model. Application to data from the North Sea and West Africa provides insight into how the petroelastic model controls the seismic response and the relative interplay between pressure and saturation changes for each reservoir type. These data, together with published literature examples, allow the identification of regions in the reservoir where the saturation-driven 4D signature dominates over the pressure-driven, or vice-versa. These observations are used to determine a simple constraint on the relative magnitude of the controlling groups of petroelastic model parameters. It is concluded that the evaluation of 4D seismic as saturation- or pressure-dominated is a key measurement for our understanding of the in situ petroelastic model.

74th EAGE Conference & Exhibition incorporating SPE EUROPEC 2012
Copenhagen, Denmark, 4-7 June 2012

Introduction

Past work on 4D seismic interpretation has shown how pressure and saturation changes may affect mapped time-lapse seismic amplitudes. For example, Landrø (2001) developed expressions for the AVO behaviour of the top reservoir interface. In a development suited to a generalized range of attributes and independent of the petroelastic model, MacBeth et al. (2006) suggested an expression that is linear in pressure and saturation change, with weights determined from the correlation between the 4D seismic data and the well production data. Unfortunately, neither of these techniques is immediately useful for revealing the direct impact of the petroelastic model on the 4D seismic signatures, without recourse to a full calculation. Additionally, it would be useful to be able to explicitly identify lateral variations in the 4D seismic signature with key reservoir properties such as porosity, fluid contrast, fluid compressibility or rock frame stress sensitivity. These objectives are addressed in the current work and considered for the case of clastic reservoirs for which the predominant changes are due only to fluid pressure, or oil and water movement.

Theory and method

Consider a single plane horizontal interface representing the contrast between a producing reservoir and an overlying inert shale. No variations with net-to-gross or reservoir thickness are treated in this current work, and only a single interface is considered. Our starting point is the Gray et al. (1999) first order, weak contrast approximation to the Zoeppritz equations, which gives the reflection coefficient as a function of incidence angle θ in terms of bulk modulus κ, shear modulus μ, density ρ

$$R(\theta) = \left(\frac{1}{4} - \frac{1}{3}\left(\frac{\overline{V_S}}{\overline{V_P}}\right)^2\right)\Gamma_1 \frac{\Delta\kappa}{\overline{\kappa}} + \left(\frac{\overline{V_S}}{\overline{V_P}}\right)^2 \Gamma_2 \frac{\Delta\mu}{\overline{\mu}} + \Gamma_3 \frac{\Delta\rho}{\overline{\rho}}. \quad (1)$$

Here, the operator Δ refers to a difference of that particular property across the interface and the over-score to an average of the properties either side of the interface. The equation is also controlled by the weighting of the average shear to P-wave velocity ratio at the interfaces $(\overline{V}_S / \overline{V}_P)$.The angular dependence is captured in the terms $\Gamma_1=\sec^2\theta$, $\Gamma_2=(1/3)\sec^2\theta-2\sin^2\theta$, and $\Gamma_3=(1/2)-(1/4)\sec^2\theta$.
Now consider the application of (1) to a reservoir that is imaged before, and then during, its lifetime of production and recovery. By introducing the petroelastic model and following MacBeth et al. (2006), the changes in the elastic moduli above are written in terms of first order perturbations in pressure ΔP and saturation ΔS_w and the parameters of the petroelastic model itself. The time-lapsed change in the reflection coefficient ΔR_{TL} between the monitor and the pre-production (baseline) survey time is given by

$$\overline{\Delta R}_{TL} = \phi\left[\overline{\Gamma}_1 N_1 + \overline{\Gamma}_2 N_2\right]\Delta S_w - \left\{(1-\varepsilon'\phi)\left[\overline{\Gamma}_1 N_3 + \overline{\Gamma}_3 N_4\right] - \phi\left[\overline{\Gamma}_1 N_5 + \overline{\Gamma}_2 N_6\right]\right\}\Delta P \quad (2)$$

where $\overline{\Gamma}_1$, $\overline{\Gamma}_2$, and $\overline{\Gamma}_3$ are now averages over the functions of incidence angle, ϕ the reservoir porosity and ε' a material constant. Each of the N-constants has a direct physical interpretation: N_1 relates to the contrast in bulk modulus between water (the displacing fluid) and the mobile oil, N_2 is the corresponding density contrast, N_3 and N_4 define the rock stress sensitivity (both the bulk and shear modulus parts), and finally N_5 and N_6 represent the impact of pressure changes on the fluid bulk modulus and density. Of importance to note here is that these petroelastic parameters act together as a single lumped coefficient, and thus they may be regarded as inseparable in terms of their influence on the seismic data. The accuracy of (2) is tested against full numerical computation, and for pressure changes in the range -5MPa to +5MPa, and water saturation changes in the range +20% to 80% appropriate for our reservoir of interest, with errors remaining at less than 2.5%. A comparison of (2) with full simulator to seismic modelling (Amini and MacBeth, 2011) also further validates the approach, with normalised errors in the maps of less than 3% (Figure 1).

The parameterisation in (2) captures in quantitative form much about the time-lapse seismic signature

that is already well understood intuitively. The equation provides a way of identifying how individual reservoir conditions affect the petroelastic model, and in turn how this might control and modify the resultant mapped seismic response. Interestingly, the dependence on porosity is now captured explicitly and it is seen how the time-lapse seismic signature scales with this parameter. The saturation term is controlled by a group of parameters which scale directly with the contrast between the water and oil bulk moduli and densities. On the pressure side of the equation, there are two competing parameter groups: the first relates to the magnitude of rock frame stress sensitivity and the second to the variation of the bulk modulus and density of the fluids. The equation shows that these last two terms must compete against each other.

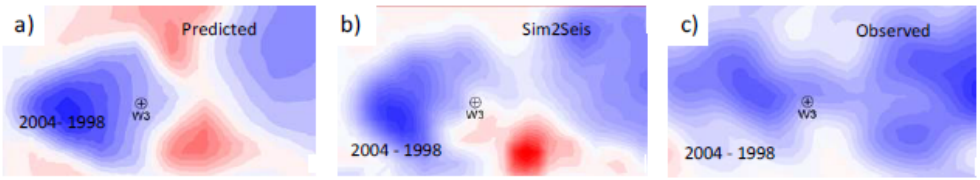

Figure 1 *Mapped seismic amplitude for a North Sea reservoir predicted from pressure and saturation changes obtained from the simulation model. (a) Predictions based on the approximate equation (2); (b) simulator to seismic calculation; (c) Observed 4D seismic response.*

4D seismic interpretation

In practice, the observed time-lapse seismic amplitude is the change in the stacked (and migrated) response for a specific range of offsets, and is estimated within a time-window defined across a particular reservoir event (usually top reservoir). The reflection coefficient ΔR_{TL} is thus scaled by a wavelet function, and should now be replaced by the amplitude ΔA_{TL}. For the purposes of the current work it is assumed that the requisite scaling factor has been absorbed into the *N*-coefficients that multiply both the pressure and saturation changes in (2). Simplifying, the seismic amplitudes can now be written in the compact form

$$\Delta A_{TL} = C_S \Delta S_w - C_P \Delta P \tag{3}$$

where the two controlling parameters C_S and C_P relate directly to the fundamental constants *N1* to *N6* and to porosity. A negative sign is preserved in (3) so that regardless of whether the impedance contrast at the event of interest is low to high, or high to low, the coefficients C_S and C_P remain positive. This also makes sense as an increase in saturation (hardening of impedance) has an opposing physical effect on the reservoir to an increase in pressure (softening of impedance).

Observed seismic data examples

Equation (3) interprets 4D seismic amplitudes as a weighted combination of pressure and saturation change, and selected seismic observations can be used to back out the relative magnitudes of C_S and C_P in situ (as defined by the ratio C_S/C_P). Here, it is observed that the basic measurement of a 4D signature as being dominated by either saturation or pressure provides a simple and obvious way to determine this constraint from the seismic data. However, only situations in which pressure and water saturation increase can be considered, as $C_S\Delta S_w$ then competes against $C_P\Delta P$ in the determination of data polarity and overall dominance of the signal. This condition restricts our measurements to regions of the reservoir for which water is injected. Observed 4D seismic data from a North Sea clastic reservoir are analysed initially (Figure 2). Stacked and migrated seismic data are available for the 1998 (pre-productionbaseline) and the 2004, 2006 and 2008 post-production monitor surveys. The flow simulation model is also available and the injector wells (W1 and W2) are chosen because the production history match in the selected areas is good. Simulation results for the period 1998 to 2004 show a pressure change of +3.5MPa around W2, but less than +0.5MPa around W1 due to de-

pressurisation effects. Both wells have a similar saturation change during this period, this being +0.45 and +0.44 respectively. There is no gas in the area and it is known that an increase in the observed amplitudes indicates pressure up in the reservoir, whilst a decrease in the amplitudes reveals an influx of water. The observed 4D seismic (2004-1998) shows a RMS mapped amplitude increase at W1, consistent with saturation effects dominating, this giving the relation $0.45C_S > 0.5C_P$. At W2, the seismic indicates only a small RMS mapped amplitude decrease signal consistent with a pressure increase. Thus, it looks like the saturation and pressure changes partially cancel around this well, and $0.44C_S \approx 3.5C_P$.

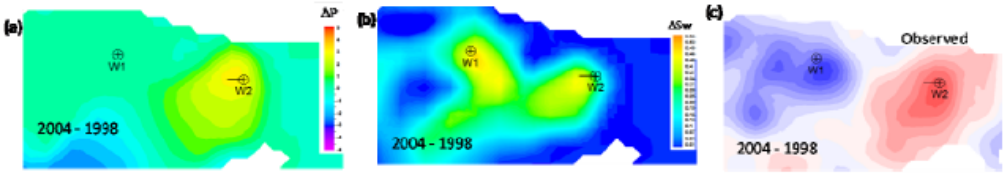

Figure 2 (a) Pressure and (b) saturation changes for our initial field example predicted from the simulation model. (c) Observed 4D seismic response (2004 to 1998 surveys only).

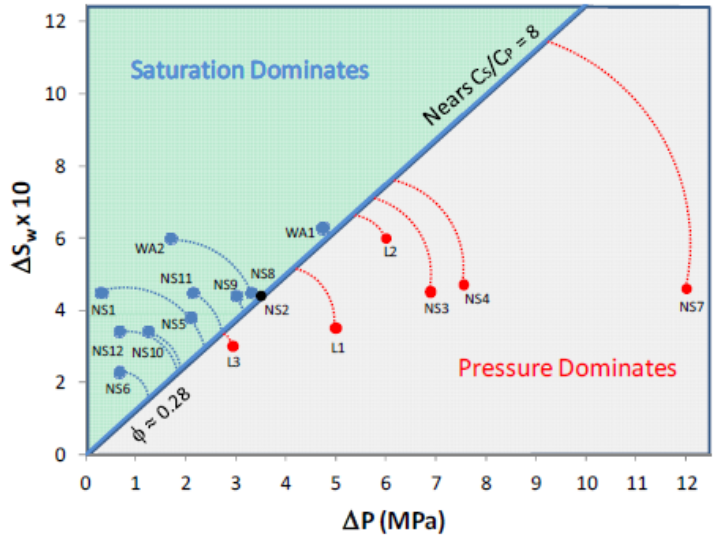

Figure 3 Colour coding according to whether the 4D signatures are dominated by saturation (blue) or pressure (red). The line $C_S/C_P=8$ is drawn as the best fit boundary between the saturation and pressure dominant domains. Points are taken from a North Sea dataset (NS1 to NS12), West Africa dataset (WA1 to WA2), and several literature examples (L1 to L3). The circular arcs represent inequalities.

The C_S-C_P data are brought together in Figure 3, which plots $10\Delta Sw$ against ΔP to ensure the points or inequalities fall in a central location on the plot. The observations above contribute points NS1 and NS2. Further points are added to this plot by the remaining monitor survey data (points NS3 to NS12), two West Africa examples (points WA1 and WA2), and gathered literature examples (Johann et al. 2009, Floricich, 2006, and Landrø, 2001) (points L1, L2 and L3).

Discussion

In Figure 3, the boundary that divides the two regimes of pressure and saturation dominance is delineated by a straight line with a slope C_S/C_P, this depending on the reservoir's petroelastic model parameters and the porosity. It is found that the observation points for our data can be divided by a line with slope $C_S/C_P = 8$. Numerical calculation of this ratio using the known petroelastic parameters, and the porosities for our North Sea reservoir conclude that it should lie between 5 and 10. Note that if reservoir porosity is low, it is anticipated that C_S/C_P will be higher than 8. However, no low porosity examples exist in the literature to date to verify this prediction. The above result has implications for the underlying petroelastic model used to characterise the rock and fluid physics. In particular, from (2) this constraint provides a way of linking the fluid contrast between the original and displaced fluids, and the largely uncertain rock stress sensitivity. This is possible, as the fluid contrast terms are relatively well known functions of the bulk modulus and density of the oil and brine, and the initial water saturation. For a mean porosity of 25%, and oil-water displacement for the reservoirs in our North Sea example, we obtain the constraint

$$0.25N_3 + 0.33N_4 \approx 0.015 \tag{4}$$

where *N3* and *N4* are defined as dependent variables of the stress sensitivity functions for κ and μ. This equation is a means of constraining possible stress sensitivity curves extracted from the laboratory or from theory. It is a useful tool for selecting those solutions acceptable to both the seismic and appropriate laboratory measurement.

Conclusions

A formulation has been obtained that predicts the relative contributions of pressure and saturation change to the time-lapsed seismic amplitudes, and brings out the explicit role of the petroelastic model parameters. It is found that porosity plays an important controlling role, and so too does the initial saturation state. It is expected for porosities larger than 20%, saturation will dominate in most reservoirs, whilst for porosities smaller than 20%, then pressure dominates. The results of this study suggest that C_S/C_P is a fundamental parameter that can be unambiguously extracted from the 4D seismic amplitudes by observing whether saturation or pressure dominates the response at a select number of injector locations. Further, according to the data collected from five clastic reservoirs, $C_S/C_P = 8$ seems to indicate the point at which pressure dominates over saturation, and vice-versa.

Acknowledgements

We thank the sponsors of the Edinburgh Time Lapse Project, Phase IV, for their support (BG, BP, Chevron, ConocoPhillips, ENI, ExxonMobil, Hess, Ikon Science, Landmark, Maersk, Marathon, Norsar, RSI, Petrobras, Shell, Statoil, and Total). Schlumberger are thanked for providing Petrel and Eclipse software. EA thanks Hamed Amini for his contribution to this work, and also acknowledges financial support from Senergy (GB).

References

Amini, H., MacBeth, C. [2011] Calibration of simulator to seismic modelling for quantitative 4D seismic interpretation. 73rd EAGE Conference & Exhibition incorporating SPE EUROPEC 2011

Floricich, M. [2006] An engineering-consistent approach for pressure and saturation estimation from time-lapse seismic data, PhD thesis, Heriot-Watt University

Gray, D., Goodway, B., Chen, T. [1999] Bridging the Gap: Using AVO to detect changes in fundamental elastic constants. SEG Expanded Abstracts 18, 852-855

Johann, P., Sansonowski, R., Oliveira, R. and Bampi, D. [2009] 4D seismic in a heavy-oil, turbidite reservoir offshore Brazil. The Leading Edge 28, 718-729

Landrø, M. [2001] Discrimination between pressure and fluid saturation changes from time-lapse seismic data. Geophysics, 66, 836–844

MacBeth, C., Floricich, M. and Soldo, J., 2006, Going quantitative with 4D seismic analysis: Geophysical Prospecting, 54, 303-318

Geophysical Prospecting

EAGE EUROPEAN ASSOCIATION OF GEOSCIENTISTS & ENGINEERS

Geophysical Prospecting, 2014, **62**, 75–96 doi: 10.1111/1365-2478.12071

An insightful parametrization for the flatlander's interpretation of time-lapsed seismic data

Erick Alvarez*,† and Colin MacBeth

Institute of Petroleum Engineering Heriot-Watt University Edinburgh, UK EH14 4AS

Received January 2012, revision accepted February 2013

ABSTRACT

An approximation is developed that allows mapped 4D seismic amplitudes and time-shifts to be related directly to the weighted linear sum of pore pressure and saturation changes. The weights in this relation are identified as key groups of parameters from a petroelastic model and include the reservoir porosity. This dependence on groups of parameters explains the inherent non-uniqueness of this problem experienced by previous researchers. The proposed relation is of use in 4D seismic data feasibility studies and inversion and interpretation of the 4D seismic response in terms of pore pressure and water saturation changes. A further result is drawn from analysis of data from the North Sea and West Africa, which reveals that the relative interplay between the effects of pore pressure and saturation changes on the seismic data can be simplified to the control of a single, spatially variant parameter C_S/C_P. Combining these results with those from published literature, we find that $C_S/C_P = 8$ appears to be a generality across a range of clastic reservoirs with a similar mean porosity. Using this C_S/C_P value, an *in situ* seismic-scale constraint for the rock stress sensitivity component of the petroelastic model is constructed considering this component carries the largest uncertainty.

Key words: Pressure change, Saturation change, Petroelastic model, AVO, 4D seismic interpretation.

INTRODUCTION

Despite some excellent examples of vertical sections from 4D seismic data (Clifford *et al.* 2003; Røste *et al.* 2009), map-based attributes remain in common use for 4D seismic interpretation as they combine the accepted visual benefits of lateral continuity with ease of use and robustness. Indeed, from maps of a suitable attribute derived at a top reservoir or perhaps a known fluid contact, it is relatively straightforward to build an understanding of the causal relationship between well production and recovery and time-lapsed seismic signatures (Huang *et al.* 2011). From past examples, it is now relatively well known that pore pressure increase due to injection into an isolated reservoir compartment or an increase in gas saturation due to a drop below a bubble point may lead to a reservoir softening (impedance reduction) and a corresponding change on the mapped seismic amplitudes (Parr, Marsh and Griffin 2000). A pore pressure decrease due to primary depletion with limited water influx or water saturation increase due to water from an injector (or aquifer) leads to a reservoir hardening (impedance increase). It is also generally understood that in some parts of a field, the 4D seismic signals of pore pressure change plus saturation change could overlap substantially making interpretation of these reservoir changes more challenging (Floricich *et al.* 2006). Of particular importance in the interpretation of the 4D signal in this situation is the relative impact of the effects of pore pressure and saturation change on the selected seismic attribute (MacBeth, Floricich and Soldo 2006a). This link between the seismic data and the reservoir changes induced by production and recovery is important and is known to strongly depend on an *in situ* seismic-scale petroelastic model. It is this connection that is investigated in this work, with the overall objective

*E-mail: erick.alvarez@pet.hw.ac.uk
†Also at Senergy Ltd, Edinburgh, UK EH3 9DN

being to devise a simple formula that can relate seismic, engineering and rock/fluid physics domains for ease of interpretation. This is of benefit as it provides a way of gaining more physical insight into the controlling components of the 4D seismic signal, aiding feasibility studies in preliminary interpretation and later offering the potential to separate pore pressure and saturation changes in a way that forward modelling cannot offer. To understand the objectives more clearly, an analogy can be made by contrasting the accuracy of forward numerical calculation using full Zoeppritz equations but the reservoir description insight gained by using the Rutherford and Williams (1989) AVO classification derived from Shuey (1985) approximations. It is this type of insightful reservoir description that we ultimately seek in our approach.

Past work has provided formulations that predict how pressure and saturation changes may affect mapped time-lapse seismic amplitudes. For example, Landrø (2001) developed expressions for the AVO behaviour of a top reservoir interface. In this work, each pressure or saturation change term is weighted by a coefficient dependent on the reservoir's elastic constants, which in turn must be numerically computed from empirical fluid equations and suitably calibrated laboratory-based measurements. This, therefore, does not fulfil our objectives, as the elastic constants need to be related to the petroelastic model. In a development in which a generalized range of seismic attributes can be input and the results obtained independently of the petroelastic model, MacBeth *et al.* (2006a) suggested an expression that is linear in pressure and saturation change, with weights determined from the correlation between 4D seismic data and well production data. This again does not reveal the role of the petroelastic model sufficiently but does highlight that for most reservoirs under production and recovery, a linear relation in pore pressure and water saturation change may suffice for inversion purposes. Both of the above approaches have been used to invert for pressure and saturation changes from time-lapsed seismic data with some degree of success (Landrø 2001; Floricich *et al.* 2006). Unfortunately, neither of the techniques can readily identify how the petroelastic model parameters manifest themselves in mapped 4D seismic signatures, this understanding would require extensive sensitivity tests using forward modelling. Additionally, it would be useful to be able to explicitly identify how lateral variations in key reservoir properties such as porosity, fluid contrast, fluid compressibility or rock frame stress sensitivity affect the pore pressure or saturation change contributions to the 4D seismic signature. This objective is addressed in the current work and considered for the case of clastic reservoirs for which the predominant changes are due only to pore pressure and oil/water movement.

THEORY AND METHOD

Consider a single plane horizontal interface representing the contrast between a producing reservoir and overlying inert shale. For the purposes of this current work we assume the reservoir can be represented by its sand properties and that elastic property changes are due to variations in pressure and water saturation only. No variations with net-to-gross or reservoir thickness are treated in this current work. Our starting point is the Gray, Goodway and Chen (1999) derivation from Aki and Richards' (1980) first-order, weak contrast approximation to the Zoeppritz equations, which gives the reflection coefficient as a function of incidence angle θ in terms of bulk modulus κ, density ρ, and shear modulus μ:

$$R(\theta)=\left(1-\frac{4}{3}\left(\frac{\overline{V_S}}{\overline{V_P}}\right)^2\right)\Gamma_1\frac{\Delta\kappa}{\overline{\kappa}}+\Gamma_2\frac{\Delta\rho}{\overline{\rho}}+\left(\frac{\overline{V_S}}{\overline{V_P}}\right)^2\Gamma_3\frac{\Delta\mu}{\overline{\mu}}. \quad (1)$$

Here, the operator Δ refers to a difference of that particular property across the interface and the over-score to an average of these properties either side of the interface. The equation is also controlled by the weighting of the average shear to compressional-wave velocity ratio at the interfaces $(\overline{V_S}/\overline{V_P})$. The angular dependence is captured in the terms $\Gamma_1=\frac{1}{4}\sec^2\theta$, $\Gamma_2=\frac{1}{2}-\frac{1}{4}\sec^2\theta$ and $\Gamma_3=\frac{1}{3}\sec^2\theta-2\sin^2\theta$. For our purposes, equation (1) can be further rewritten to involve the *P*-wave modulus *M*:

$$R(\theta)=\left(\frac{\overline{\kappa}}{\overline{M}}\right)\Gamma_1\frac{\Delta\kappa}{\overline{\kappa}}+\Gamma_2\frac{\Delta\rho}{\overline{\rho}}+\left(\frac{\overline{\mu}}{\overline{M}}\right)\Gamma_3\frac{\Delta\mu}{\overline{\mu}}. \quad (2)$$

Now consider the application of equation (2) to a reservoir that is imaged before and then during its lifetime of production and recovery. The time-lapsed change in the reflection coefficient ΔR_{TL} between the monitor and the pre-production (baseline) survey time is given approximately by:

$$\Delta R_{TL}(\theta)\approx\Gamma_1\frac{\Delta\kappa_{TL}}{\overline{M}}+\Gamma_2\frac{\Delta\rho_{TL}}{\overline{\rho}}+\Gamma_3\frac{\Delta\mu_{TL}}{\overline{M}}, \quad (3)$$

where the description of all previous terms remains as before but $\overline{M}$ and $\overline{\rho}$ are now specifically assigned to the pre-production state. This equation is valid to first order in the small time-lapse changes in the reservoir $\Delta\kappa_{\mathrm{TL}}$, $\Delta\rho_{\mathrm{TL}}$ and $\Delta\mu_{\mathrm{TL}}$. Next, the petroelastic model is introduced and following MacBeth *et al.* (2006a) the changes in the elastic moduli above are written in terms of first-order perturbations in pore pressure (ΔP) and water saturation (ΔS_w) and the parameters

of the petroelastic model itself (Appendix A):

$$\Delta K_{TL} \approx \phi \left[\frac{\varepsilon(\kappa_0/\kappa_w)(\kappa_w - \kappa_0)}{(1-S_{wi})^2 + (\kappa_0/\kappa_w)S_{wi}} \right] \Delta S_w - \left[(1-\varepsilon'\phi)(\alpha\kappa_m A_\kappa) - \phi \left(\frac{\varepsilon\,(W_\kappa \kappa_0 S_{wi} + O_\kappa \kappa_w (1-S_{wi}))}{\kappa_w(1-S_{wi}) + \kappa_0 S_{wi}} \right) \right] \Delta P, \quad (4)$$

$$\Delta\rho_{TL} \approx \phi[\rho_w - \rho_o]\Delta S_w + \phi[W_\rho S_{wi} + O_\rho(1-S_{wi})]\Delta P, \quad (5)$$

$$\Delta\mu_{TL} \approx -(1-\varepsilon'\phi)\left(\alpha\mu_m B_\mu\right)\Delta P, \quad (6)$$

where ϕ is the effective porosity and S_{wi} (defined as a fraction) represents the pre-production saturation. The remaining parameters in the square brackets of equations (4), (5) and (6) relate to the various parameters of the petroelastic model used in this work and are fully described in Appendix A and Table 1. Of importance to note here is that many of these petroelastic parameters act together as a single lumped coefficient and thus they may be regarded as inseparable in terms of their influence on the seismic data. This also means that there is a strong inherent non-uniqueness to the petroelastic parameters that define any particular seismic response. Substituting equations (4), (5) and (6) into equation (3), the limited offset, stacked reflectivity $\overline{\Delta R}_{TL}$ for the top reservoir can be finally written as:

$$\overline{\Delta R}_{TL} \approx \phi\left[\overline{\Gamma}_1 N_1 + \overline{\Gamma}_2 N_2\right]\Delta S_W - \left\{(1-\varepsilon'\phi)\left[\overline{\Gamma}_1 N_3 + \overline{\Gamma}_3 N_4\right] - \phi\left[\overline{\Gamma}_1 N_5 + \overline{\Gamma}_2 N_6\right]\right\}\Delta P, \quad (7)$$

where $\overline{\Gamma}_1$, $\overline{\Gamma}_2$ and $\overline{\Gamma}_3$ are now averages over the incidence angle range. Typical values for the near-offset data with a range of incidence from 0–10 degrees are $\overline{\Gamma}_1 = 0.25$, $\overline{\Gamma}_2 = 0.24$ and $\overline{\Gamma}_3 = 0.33$. For far offsets defined between 25–35 degrees for example, the same equation holds but $\overline{\Gamma}_1 = 0.33$, $\overline{\Gamma}_2 = 0.17$ and $\overline{\Gamma}_3 = -0.06$. The coefficients N_1, N_2, N_3, N_4, N_5 and N_6 are functions of the parameters of the petroelastic model and of the initial reservoir elastic properties (see Appendix A)

$$N_1 = \left[\frac{\varepsilon(\kappa_0/\kappa_w)(\kappa_w - \kappa_0)}{\overline{M}\left((1-S_{wi})^2 + (\kappa_0/\kappa_w)S_{wi}\right)} \right], \quad (8)$$

$$N_2 = \left[\frac{\rho_w - \rho_o}{\overline{\rho}} \right], \quad (9)$$

$$N_3 = \left[\frac{\alpha\kappa_m A_\kappa}{\overline{M}} \right], \quad (10)$$

$$N_4 = \left[\frac{\alpha\mu_m B_\mu}{\overline{M}} \right], \quad (11)$$

$$N_5 = \left[\frac{\varepsilon(W_\kappa\kappa_0 S_{wi} + O_\kappa\kappa_w(1-S_{wi}))}{\overline{M}(\kappa_w(1-S_{wi}) + \kappa_0 S_{wi})} \right], \quad (12)$$

and

$$N_6 = \left[\frac{W_\rho S_{wi} + O_\rho(1-S_{wi})}{\overline{\rho}} \right]. \quad (13)$$

Each of these N-constants has a direct physical interpretation: N_1 relates to the contrast in the bulk modulus between water (the displacing fluid) and the mobile oil, N_2 is the corresponding density contrast, N_3 and N_4 define the rock stress sensitivity (both the bulk and shear modulus parts) and finally N_5 and N_6 represent the impact of pressure changes on the fluid bulk modulus and density. The accuracy of the approximation in equation (7) is tested against numerical computation using full and exact equations. Changes in the time-lapse reflectivity are calculated for a fixed water saturation change but varying pressure change and then vice versa. The normalized root mean square error is evaluated by taking the difference of the approximate and exact solutions, dividing by the difference of the maximum and minimum time-lapse reflectivity changes for the exact solution and then multiplying by 100 to convert to a percentage. Figure 1 shows an example of the results of comparing the numerical computation (using the full equations shown in Appendix A) with the approximate equations (shown in Appendix A and the main text) and the consequent error. These comparisons are made based on the conditions of a typical North Sea clastic reservoir and time-lapse changes in reflectivity between 0–0.022 (see Table 1 for details of the conditions that lead to a mean seismic reflectivity of around 0.12). Importantly, statistics generated from the full-field flow simulation model indicate that pressure changes in this compartmentalized field are typically in the range -6 MPa to +6 MPa (although, unusually, they can be as high as 12 MPa in specific and obvious locations) and water saturation changes in the range +20% to 80% are appropriate for this reservoir. It is found that within this practical working range (which is typical of most North Sea reservoirs) the normalized root mean square errors in the approximations remain less than 2.5%. A comparison of equation (7) with full simulator to seismic modelling (Amini and MacBeth 2011) also further validates the approach (Fig. 2), with normalized errors for the maps of less than 3% despite the possibility of tuning effects and wave interferences.

Table 1 Petroelastic model parameters for the North Sea and West African clastic reservoirs used as examples in this study. The North Sea parameters are derived from the calibrated petroelastic modelling and simulator to seismic studies of Amini and MacBeth (2011). The West Africa data use similar parameters but with appropriate fluid properties and initial pore pressures (Bouchet *et al.* 2004 and operator supplied values).

Constant	Description	Units	North Sea	West Africa
κ_m	Mineral bulk modulus	GPa	36	36
μ_m	Mineral shear modulus	GPa	42	42
κ_w	Bulk modulus of water at the initial state	GPa	2.59	2.85
κ_o	Bulk modulus of oil at the initial state	GPa	1.31	0.65
R	Oil water ratio for the bulk modulus (κ_o/κ_w)	Unit-less	0.51	0.23
ρ_w	Density of water at the initial pressure state	g/cc	1.01	1.04
ρ_o	Density of oil at the initial pressure state	g/cc	0.83	0.70
A_κ	Linear fit to the MacBeth (2004) relation for $\kappa(\sigma_{eff})$	MPa^{-1}	0.003	0.009
B_μ	Linear fit to the MacBeth 2004 relation for $\mu(\sigma_{eff})$	MPa^{-1}	0.008	0.015
E_κ	Rock stress sensitivity parameters as described in MacBeth (2004)	unit-less	1.13	1.13
E_μ		unit-less	1.08	1.22
P_κ		MPa	5.62	5.62
P_μ		MPa	7.97	7.97
$\overline{M}$	Average P-wave modulus across the seal/reservoir interface	GPa	17.13	17.13
$\overline{\rho}$	Average density across the seal/reservoir interface	g/cm^3	2.44	2.44
α	Effective stress coefficient	unit-less	0.91	0.91
ϕ	Average effective porosity	Fraction	0.28	0.28
O_κ	Pore pressure sensitivity rate for the oil bulk modulus	kPa	0.013	0.011
W_κ	Pore pressure sensitivity rate for the water bulk modulus	kPa	0.006	0.007
O_ρ	Pore pressure sensitivity rate for oil density	(g/cc)/MPa	0.0005	0.0005
W_ρ	Pore pressure sensitivity rate for water density	(g/cc)/MPa	0.0004	0.0003
S_{wi}	Initial water saturation state	fraction	0.15	0.20
OBP	Overburden stress	MPa	40	34
P_i	Initial reservoir pore pressure	MPa	20	26

The parametrization in equation (7) captures in quantitative form much about the time-lapse seismic signature that is already well understood intuitively and at a qualitative level for basic feasibility studies (for example, Lumley, Behrens and Wang 1997). The equation provides a way of identifying how individual reservoir conditions affect the petroelastic model and in turn how this might control and modify the resultant mapped seismic response. Interestingly, the dependence on porosity is now captured explicitly and it is seen how the time-lapse seismic signature scales with this parameter. This is intuitive for saturation but not for pressure but is consistent with the findings of Falahat, Shams and MacBeth (2011) and previous empirical observations (MacBeth *et al.* 2006a). The saturation term is further controlled by a group of parameters that scale directly with the contrast between the water and oil bulk moduli and densities. On the pressure side of equation (7), there are two competing lumped parameter groups: the first relates to the magnitude of rock frame stress sensitivity and the second to the variation of the bulk modulus and density of the fluids. The equation shows that these last two terms must compete against each other. There are also some unexpected results. The magnitude of the N_1 and N_5 components is observed to depend on the initial saturation state of the reservoir although only the variation for N_1 is predicted to be significant. This implies that the relative magnitude of these terms might vary over time when interpreting 4D signatures derived from multiple surveys, unless each monitor is deliberately referred back to the baseline survey.

4D SEISMIC INTERPRETATION

In practice, the observed time-lapse seismic amplitude is the change in the stacked (and migrated) response for a specific range of offsets and is estimated within a time window defined across a particular reservoir event (usually the top reservoir). The reflection coefficient ΔR_{TL} is thus scaled by a wavelet function and should now be replaced by the amplitude ΔA_{TL} (we assume here that effective cross-equalization to a common wavelet has been carried out, however analysis of the process is beyond the scope of this paper). For the purposes

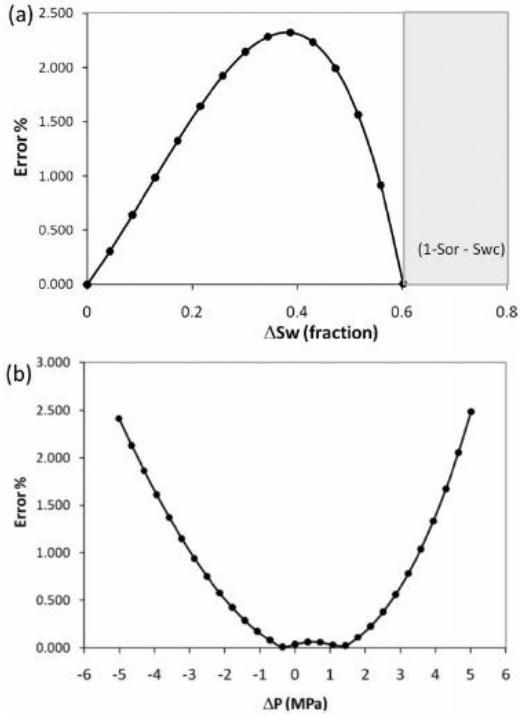

Figure 1 Normalized root mean square error (as a percentage) in the computation of the change in the time-lapse reflection coefficient when using the exact rock and fluid physics model versus the approximation of equation (7). For (a) the pore pressure change is fixed at 1 MPa whilst the saturation change is varied. For (b), the saturation change is fixed at 0.3 whilst pore pressure change is varied. The extreme limits of the pore pressure and saturation changes are guided by analysis of the field simulation results for a typical North Sea field.

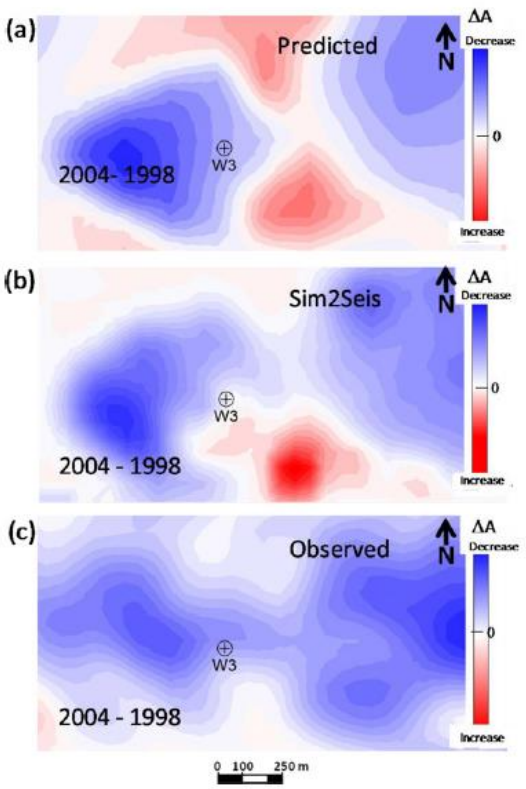

Figure 2 Mapped stacked and migrated seismic amplitudes for a North Sea reservoir predicted from pore pressure and saturation changes obtained directly from the simulation model. (a) Predictions based on the approximate equation (7) proposed in the text; (b) predictions based on convolution-based simulator to seismic modelling (Amini and MacBeth 2011); (c) observed 4D seismic response – note that the baseline pre-production seismic data was shot in 1996 but production did not begin until 1998. The horizontal and vertical scales for the map are identical.

of the current work it is assumed that the requisite scaling factor has been absorbed into the N-coefficients that multiply both the pressure and saturation changes in equation (7). However it should be noted that this scaling will need to be carefully evaluated during interpretation if a comparison is made between, for example, near- and far-offset amplitudes. Simplifying equation (7), the seismic amplitudes can be written in a compact and more general form:

$$\Delta A_{TL} = C_S \Delta S_w - C_P \Delta P, \tag{14}$$

where the two controlling parameters C_S and C_P provide the balance between the relative contribution of saturation and pore pressure change to the overall time-lapsed seismic signature. C_S and C_P relate directly to the fundamental constants N_1–N_6 and to porosity. From the previous section, these terms are known functions of the initial pressure and saturation state, the petroelastic parameters and the offset range. A negative sign is preserved in equation (14), so regardless of whether the impedance contrast at the event of interest is low to high, or high to low, the coefficients C_S and C_P remain positive. This also makes sense as an increase in water saturation (hardening of impedance) has an opposing physical effect on the reservoir to an increase in pore pressure (softening of impedance).

Numerical example

The magnitude of the coefficients C_S and C_P and in particular their relative variation (or ratio C_S/C_P) across a particular field provide insight into how pore pressure and saturation changes may combine to affect the time-lapse seismic signatures. To illustrate this, a calculation is performed for a North Sea field with specific reservoir characteristics known from previous studies (Amini and MacBeth 2011) (see Table 1). For this reservoir, numerical calculation gives a C_S value of 0.0380 and a C_P value of 0.0032 MPa^{-1}. The pressure change observed using downhole pressure gauges is matched using flow simulation model predictions. As mentioned earlier, studies of the simulation results suggest that the depth averaged pressure change could be as high as +12 MPa in specific compartmentalized regions of this field but elsewhere should be typically ±6 MPa over the time period of the surveys considered. Maximum saturation change due to a combination of edge water and basal aquifer drive yields a working maximum ΔS_w of 0.60 ($1-S_{wc}-S_{or}$, where S_{wc} is the connate water and S_{or} the residual oil saturation), although smaller changes are possible in the transition zone between the swept and unswept regions or unequal flow in different sub-layers.

To examine the relative impact of the pressure and saturation changes on the time-lapsed seismic data, C_P is split up into two components, identified in equation (7) as the fluid pressure variation $C_P^{fluid} = \{-\phi[\overline{\Gamma}_1 N_5 + \overline{\Gamma}_2 N_6]\}$ and the rock property stress sensitivity $C_P^{rock} = \{(1-\varepsilon\prime\phi)[\overline{\Gamma}_1 N_3 + \overline{\Gamma}_3 N_4]\}$, where $C_P = C_P^{fluid} + C_P^{rock}$. The relative contributions of the saturation terms and these two pressure terms are compared for both increasing and decreasing pore pressure changes in Fig. 3 and their variation with oil API shown. According to these calculations, C_P^{rock} is positive and C_P^{fluid} is negative and thus, as anticipated, the variations of the fluid properties with pressure change act in the opposite direction to the rock stress sensitivity variation. For example, as pressure decreases, the rock frame hardens due to increasing effective stress but the fluids become more compressible and hence their bulk modulus and density decrease. Interestingly, $|C_P^{rock}| >> |C_P^{fluid}|$ in the cases examined (typically $|C_P^{rock}|/|C_P^{fluid}| > 8$) and it appears that the rock stress sensitivity outweighs the fluid effect. Indeed, $|C_P^{fluid}|$ is estimated to be fairly small in magnitude when compared to the saturation term C_S for a range of oils and it is proposed that this may be valid as a generality. However, it should be acknowledged that C_P^{rock} carries a high uncertainty (MacBeth 2004; Eiken and Tøndel 2005) and correct numerical assignment of this term depends on a range of factors that may enhance or diminish the stress sensitivity relative to the calibration offered by laboratory core plug measurements (Appendix B). The current prevailing opinion is that laboratory measurements over-predict rock frame stress sensitivity. If this were true, this would reduce C_P^{rock} relative to C_P^{fluid}. C_P^{fluid} on the other hand, carries less uncertainty as comparatively more is known about the fluids *in situ*, particularly their behaviour with pressure (Clark 1992; Batzle and Wang 1992).

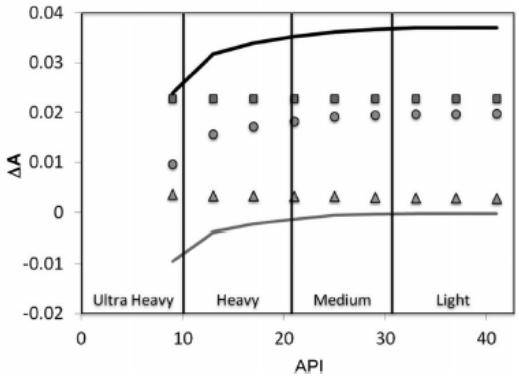

Figure 3 Change in seismic amplitude (ΔA) with oil API, showing the magnitude of contributions to saturation and pore pressure: $|C_S \Delta S_w|$ (circles), $|C_P^{rock} \Delta P|$ (squares), $|C_P^{fluid} \Delta P|$ (triangles). Solid lines are the total amplitude change for pore pressure down (black) and pore pressure up (grey). Results have been drawn for a saturation change of 0.6 and a pore pressure change of +/-6 MPa.

Finally, for the reservoir considered here, a range of conditions can be predicted for which the saturation-related 4D signature ($C_S \Delta S_w$) dominates over the corresponding pore pressure-related signature ($C_P \Delta P$), or vice-versa (Fig. 4(a,b). For small pore pressure or saturation changes the result is obvious (with the exact crossover point being a function of the petroelastic parameters). The outcome of this comparison strongly depends on the porosity and the calculations based on our North Sea reservoir suggest it is generally the case that the saturation term dominates for porosities higher than 30%, whereas when the porosities are smaller than 20% the pore pressure term dominates. The relative balance between the effects of saturation and pore pressure change also varies with offset (compare Fig. 4a with 4b, this will be discussed in more detail in the next section). It is predicted for our particular North Sea reservoir (for which C_S/C_P is estimated to be 8.24 for the nears and 38.34 for the fars from Table 2) that the pore pressure and saturation signals may mix on the nears but that the saturation signal dominates the fars. Note, however, that the relative importance of the saturation and pore pressure

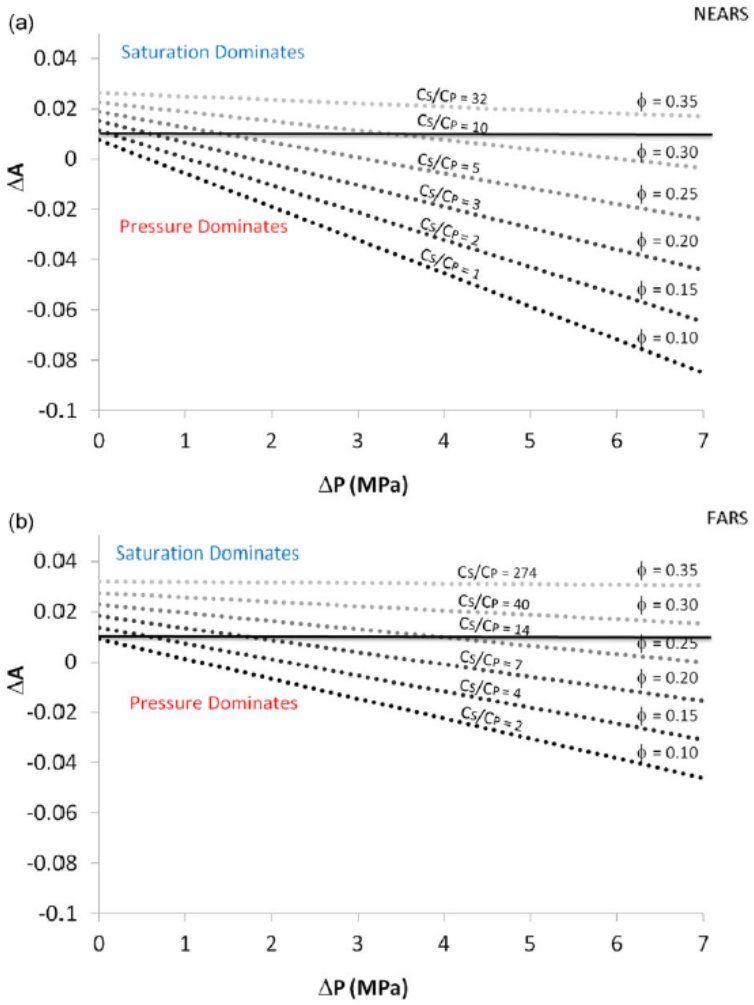

Figure 4 Change in 4D seismic signature (ΔA) with pore pressure change (ΔP) for a range of porosities ϕ and a fixed (maximum) ΔSw of 0.6. (a) Near-offset amplitudes in the angular range 0–10 degrees. (b) Far-offset amplitudes in the angular range 20– 30 degrees. Positive values represent saturation dominance, whilst negative values show that pore pressure dominates. Lines for smaller fixed saturations are simply displaced vertically downwards (hence less saturation dominance of the signal).

Table 2 Numerical values for the N coefficients used in this study, together with the resultant ratio of C_S and C_P for the North Sea and West Africa data examples calculated using Appendix and Table 1.

FIELD	N1 Fluid contrast	N2 Fluid contrast	N3 Rock stress sensitivity	N4 Rock stress sensitivity	N5 Fluid pressure sensitivity	N6 Fluid pressure sensitivity	C_S/C_P NEARS	C_S/C_P FARS
North Sea	0.3643	0.0796	0.0238	0.0252	0.0064	0.0002	8.24	38.34
West Africa	0.5984	0.2007	0.0556	0.0050	0.0071	0.0002	6.06	15.24

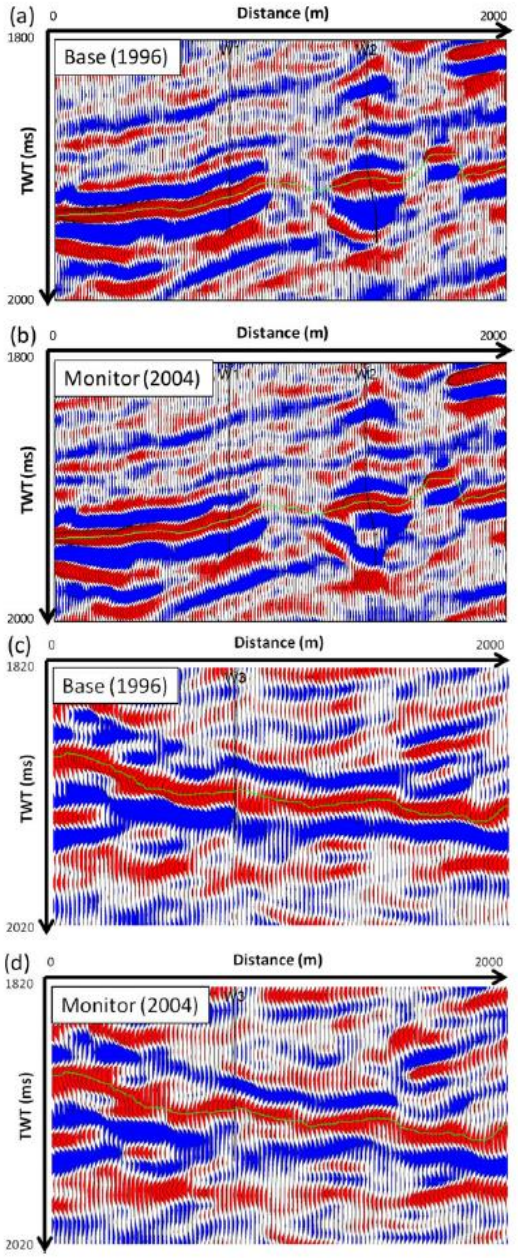

Figure 5 Vertical sections for the stacked and migrated seismic data from our North Sea example. The sections are shown for reference only and the green line indicates the top reservoir from which the mapped amplitudes are evaluated. (a) and (b) are for a section through wells W1 and W2. (c) and (d) are for sections through W3.

signals varies depending on the magnitude of these reservoir changes and the porosities involved and thus a generality for all reservoirs cannot be definitively drawn. This difference in the balance of saturation and pore pressure change signals with offset was also highlighted by Landrø (2001) who utilized this in an inversion procedure for the Gullfaks field. Finally, it appears that whilst the absolute magnitudes of C_S and C_P cannot be extracted from seismic data, from this study it can be concluded that the fundamental parameter of importance is C_S/C_P. Thus, if ΔA, ΔS_w and ΔP are known for the reservoir, then equalities or inequalities may be extracted for this ratio based on the observation of whether saturation or pore pressure changes dominate the seismic signature. This conclusion will be developed further in the sections below.

Observed seismic data examples

Equation (14) interprets 4D seismic amplitudes as a weighted combination of pore pressure and saturation change and the conclusions from the previous section suggest that selected seismic observations could be used to back out the relative magnitudes of C_S and C_P *in situ* (as defined by the ratio C_S/C_P) and hence, in turn, key groups of petroelastic model parameters. Here, it is shown that the basic observation of a 4D signature as being dominated by either saturation or pore pressure provides a simple and obvious way to determine this constraint from the seismic data. However in order for such observations to be useful, only situations in which pore pressure and water saturation increase can be considered, as $C_S \Delta S_w$ then competes against $C_P \Delta P$ in the determination of data polarity and overall dominance of the signal. This condition therefore restricts our measurements to regions of the reservoir for which water is injected. Producers will not yield useful information, as pore pressure will decrease and water saturation increase. This provides data of one polarity only and it is difficult to tell which signal is dominating. Furthermore, cases of negative ΔS_w are rare and therefore a drop in pore pressure will not yield useful information for the purposes of our study. However it should be noted that 4D seismic amplitudes at the producers is still important information as a quality control check on the general polarity of the time-lapse seismic data relative to the injectors.

To obtain data points based on the above, observed 4D seismic data from our North Sea clastic reservoir are analysed. This is a Paleocene turbidite reservoir, with known high-sand porosity in the range 25–28% and light to medium oil (32 API). The reservoir is suited to this study as the petroelastic

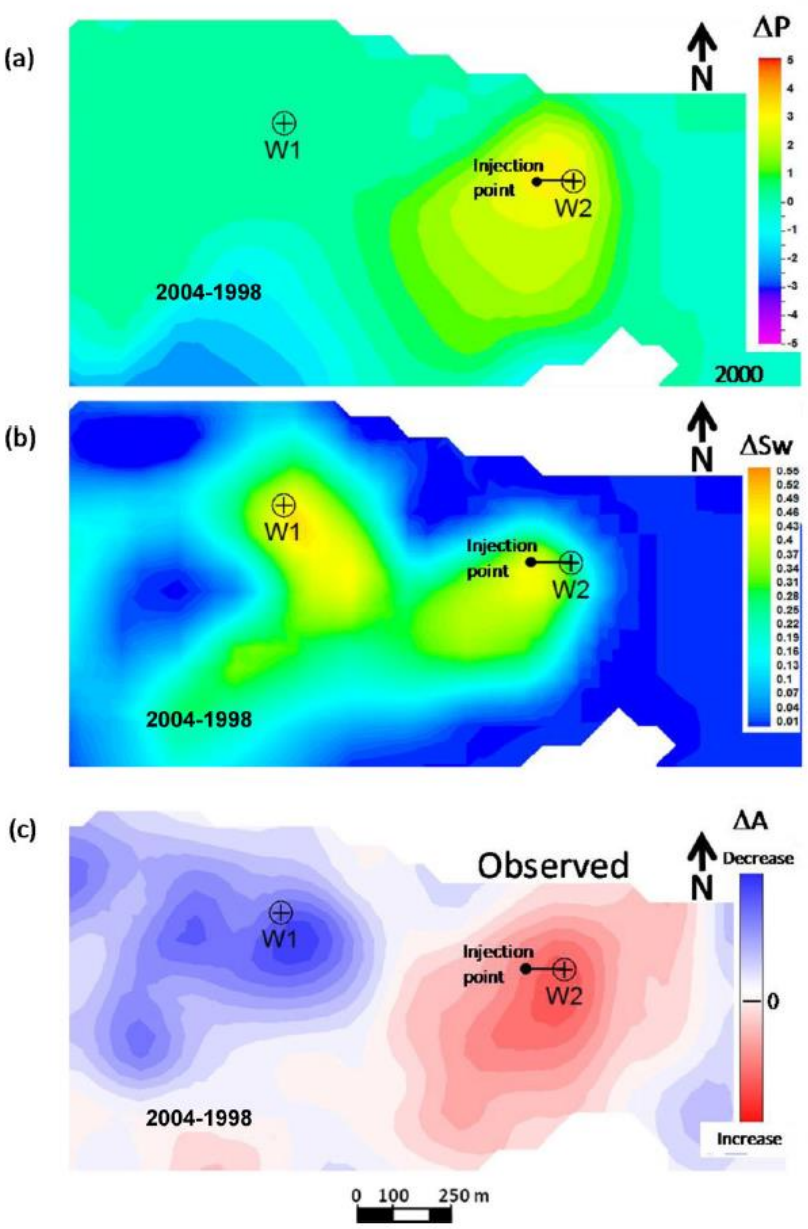

Figure 6 (a) Pore pressure and (b) saturation changes for our North Sea field example predicted from the simulation model, for selected region 1. (c) Observed 4D seismic response – note that the baseline pre-production seismic data was shot in 1996 but production did not begin until 1998. This also applies to Figs 8 and 9. The horizontal and vertical scales for the map are identical.

model is well known (Amini and MacBeth 2011). Stacked and migrated seismic data are available for 1996 (pre-production baseline, with first production in 1998) and the 2004, 2006 and 2008 post-production monitor surveys. Figure 5(a–d) shows typical vertical sections of these data. The number of monitors provides an opportunity to measure the same part of the reservoir several times but with changing ΔP and ΔS_w conditions. Three regions are identified from these data for our study, containing in total five active injectors over the 1998–2008 period. The flow simulation model is also available and the injector wells are chosen because the production history match in the selected areas is good and hence the simulation predictions of pore pressure and saturation change can be trusted at the well locations. However caution is exercised with predictions beyond the well locations and these are therefore not used in our calculations as they may contain model errors and cannot be reliable.

Consider the first example area (Fig. 6 – shown are only the 2004–1998 surveys) that contains wells W1 and W2. Well W1 injected water for more than three years but then stopped for one year prior to the date of the 2004 monitor survey, restarted one year prior to the 2006 monitor and then stopped one year before the 2008 monitor. Well W2 started injection one year before the 2004 monitor acquisition and continued beyond 2006, decreasing the injected volume significantly prior to the 2008 monitor. Simulation results for the period 1998–2004 show a pore pressure change of +3.5 MPa around W2 but less than +0.5 MPa around W1 due to de-pressurization effects. Both wells have a similar saturation change during this period, this being +0.45 and +0.44 respectively. There is no gas in the area and it is known that an increase in the observed amplitudes indicates pore pressure up in the reservoir, whilst a decrease in the amplitudes reveals an influx of water. The observed 4D seismic data (2004 monitor minus 1996 baseline) shows an amplitude decrease at W1, consistent with saturation effects dominating and probably due to the small pore pressure change, this giving the relation $0.45C_S > 0.5C_P$. At W2, the observed 2004 seismic data indicates a small amplitude increase signal consistent with a pore pressure increase. Thus, it looks like the saturation and pore pressure changes partially cancel around this well and $0.44C_S \approx 3.5C_P$. Interestingly, for this well, away from the predicted position of the waterfront, the 4D seismic data indicates an amplitude increase that can be interpreted as a crossover to a pore pressure-up dominant regime – explained as the saturation changes are now zero. The C_S/C_P data are brought together in Fig. 7, which plots $10\Delta S_w$ against ΔP to ensure the points or inequalities fall into a central location on the plot.

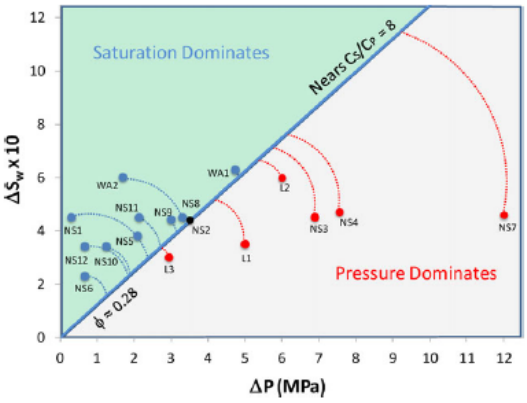

Figure 7 Plot of saturation change against pore pressure change, colour coded according to whether the 4D signatures are dominated by saturation (blue) or pore pressure (red). Points are derived from full stacks or near-offset stacks. The line $C_S/C_P = 8$ is drawn as the best fit boundary between the saturation and pore pressure dominant domains. Points are taken from a North Sea data set (NS1–NS12), West Africa data set (WA1 and WA2) and a number of literature examples (L1–L3). The circular arcs represent inequalities defined in the main text.

The observations assessed above contribute points NS1 and NS2. Seismic amplitudes are assigned according to whether they are saturation or pore pressure dominated. Further points are added to this plot by the remaining monitor survey data. The seismic monitor at 2006 and the 1996 baseline seismic data reveal an increase in the seismic amplitudes around both W1 and W2 and hence a dominance of the pore pressure response due to a continuation of the injection during the period 2004–2006. Consideration of the predicted pore pressure and saturation changes then yields two further relations $0.45C_S < 6.8C_P$ and $0.47C_S < 7.5C_P$ and the points NS3 and NS4. Finally, in the period 2006–2008, injection diminished at both wells and the pore pressure change is negative relative to the baseline survey date (injection does not support the producers). Thus, in this case the seismic amplitudes decrease due to a net saturation increase and pore pressure decrease and no information can be obtained for our study.

In the second example area from the same field, a single injector W3 started up a year before the date of the 2004 monitor acquisition (Fig. 8), stopped injecting one year prior to the 2006 survey and remained inactive through to the date of the 2008 survey. The predictions from the simulation for the period 1998–2004 reveal pore pressure changes at the well location of +2.1 MPa and a saturation change of +0.38. A decrease in 4D amplitude around W3 is associated

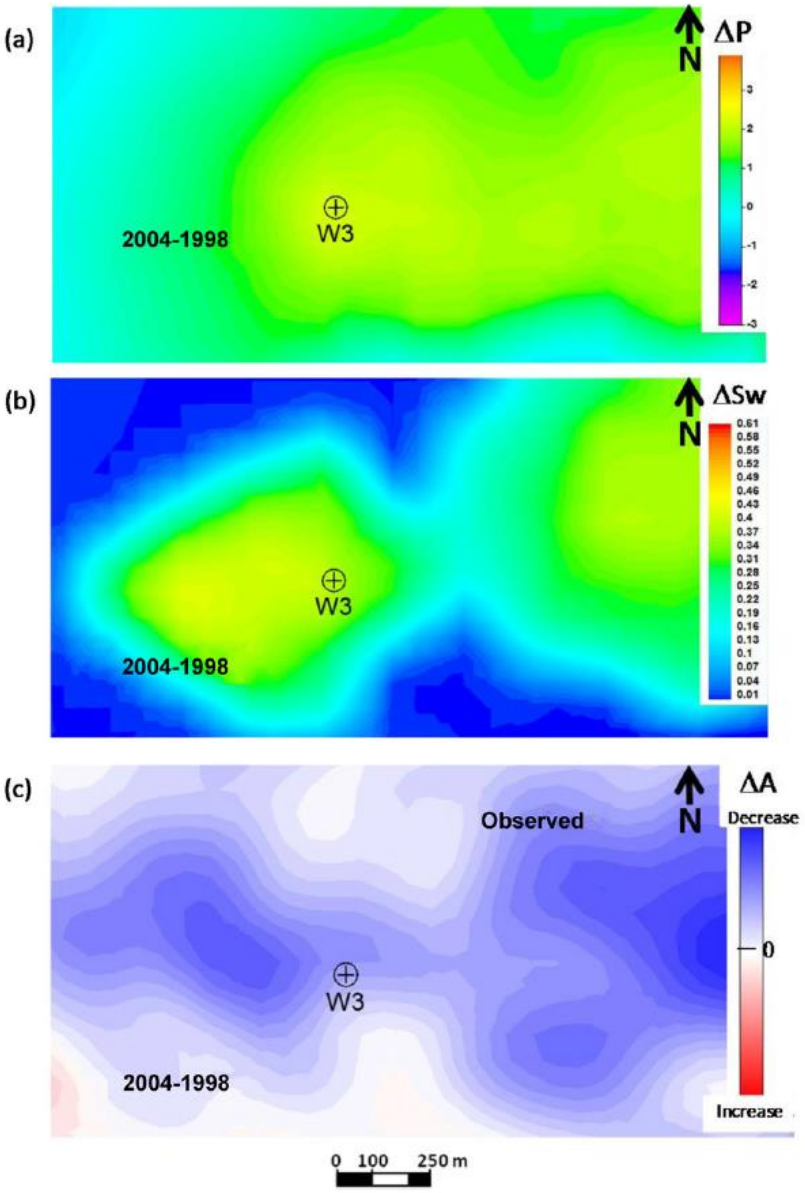

Figure 8 (a) Pore pressure and (b) saturation changes for our field example predicted from the simulation model, for selected region 2. (c) Observed 4D seismic response. The horizontal and vertical scales for the map are identical.

with the waterfront and saturation clearly dominates over pore pressure. Thus, it is concluded that $0.38C_S \geq 2.1C_P$, which establishes yet another inequality for C_S and C_P and contributes point NS5 to Fig. 7. For the 1998–2006 period, the pore pressure difference is only +0.67 MPa due to the reduction in injection and there is a saturation change of 0.23 (less, due to relaxation of the pore pressure at the injector). This leads to the inequality $0.23C_S \geq 0.67C_P$ and point NS6. For the final monitor, the net pore pressure drop during this period is negative and therefore no data point can be obtained.

Finally, in the third example (Fig. 9), there are two injectors, W4 and W5. W4 started injection in 2002, initially at a high rate but this rate reduced towards the date of the 2004 monitor survey and through the subsequent monitor survey dates. W5 started injection four years prior to the 2004 monitor survey date but stopped one year before the seismic data was shot. For the 1998–2004 period, the simulation results show a very large pore pressure change of +12 MPa around W4 due to strong compartmentalization but a smaller pore pressure change of +3.5 MPa around W5. Saturation changes are 0.46 and 0.45 respectively. The observed seismic data around the well shows an amplitude increase around W4 associated with the pore pressure increase, however exactly at the location of the well there is a small, clearly visible, localized area of amplitude decrease. These observations suggest that $12C_P > 0.46C_S$ at W4 and as before, beyond the well the pore pressure-up signal dominates – this contributes point NS7 to Fig. 7. At W5 the seismic data displays a strong amplitude decrease associated with the waterfront and hence $0.45C_S > 3.5C_P$ (point NS8). For the period 1998–2006 at both injectors, a pore pressure increase is still present but saturation change is reduced slightly due to injector relaxation effects. The effect of water saturation change dominates at W4, leading to the inequality $0.44C_S > 3.51C_P$ similarly saturation dominates at W5, implying $0.34C_S > 1.25C_P$ (giving points NS9 and NS10). At 2008, the pore pressures at both injectors have reduced slightly further but the same observations hold, leading to $0.45C_S > 2.5C_P$ and $0.34C_S > 0.75C_P$ for W4 and W5 respectively (points NS11 and NS12).

The observations above are plotted together in Fig. 7. The boundary that divides the two regimes of pore pressure and saturation dominance in this figure is a straight line with a slope C_S/C_P and depends on the reservoir's petroelastic model parameters and porosity. It is found that the observation points for our North Sea clastic example can be divided by a line with slope $C_S/C_P = 8$. Calculating the value of this ratio using the known petroelastic parameters and variable porosities for this reservoir at the individual well locations, it is observed to lie between 5–10, bracketing the approximate empirical trend obtained from the cross-plot. In the next section, more points will be added to this diagram so that the C_S/C_P can be more generally assessed.

Observations from the literature

A survey of 4D seismic case studies published in the open literature over the past twenty years appears to indicate that most researchers conclude that a pore pressure change signal is more difficult to detect than a saturation change signal. Also, it is often automatically assumed in many studies that saturation effects are more readily visible than pore pressure – as is the case in 3D seismic data. Indeed, if field pore pressure fluctuations can be controlled they seldom fluctuate by more than 0.5 MPa in the reservoir and the current work as described by Fig. 4 supports the notion that saturation dominates. Indeed, there are many examples of detecting fluid contact movement (Kloosterman *et al.* 2001; McInally *et al.* 2001) or saturation changes due to waterflooding (Lumley *et al.* 1999; Johann *et al.* 2009). In many instances a signal is observed despite fairly high non-repeatability levels for the 4D seismic data (with an *NRMS* metric of 0.40 or above). By contrast, examples of pore pressure change are less obvious, unless there is an overpressured area or the seismic signal is assisted by compaction (for instance the compacting chalk example of Barkved *et al.* 2003), or the pore pressure drops below the bubble point and gas is exsolved (Parr *et al.* 2000). The best examples are provided by pore pressure increases induced by water injection into hydraulically isolated compartments or channels (Alsos, Osdal and Høiås 2009). The effects of pore pressure decrease due to primary depletion are less pronounced (MacBeth, Stammeijer and Omerod 2006b; Staples *et al.* 2006). There are, however, some clear examples of pore pressure down due to relaxation from injector shutdown (Strønen and Diagranes 2004). Our work supports these broad statements as a natural consequence of the physics of the petroelastic model. It is somewhat surprising however to find that values of ΔP, ΔS_w and porosity are not readily published in case studies in the open literature. Whilst changes of (maximum) saturation can be readily inferred from S_{wc} and S_{or} estimates, pore pressure change is less easy to assign in practice. However, there are several examples where such measurements have been published. The first example comes from the Marlim field (Johann *et al.* 2009), in which injection into a compartment yields a +2.94 MPa pore pressure change and a 0.3

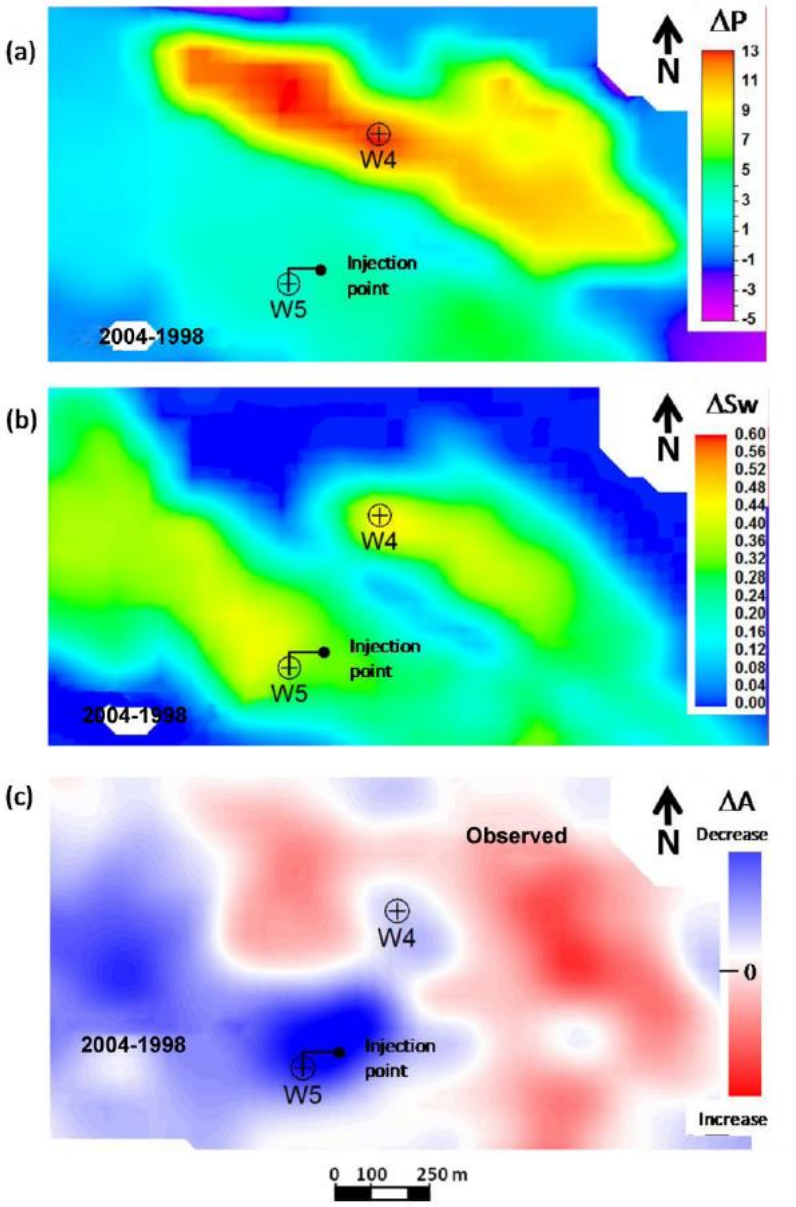

Figure 9 (a) Pore pressure and (b) saturation changes for our North Sea field example predicted from the simulation model, for selected region 3. (c) Observed 4D seismic response. The horizontal and vertical scales for the map are identical.

saturation change behind the waterfront. This provides the inequality $C_S/C_P < 9.8$, for these 24% porosity rocks. Similarly, Floricich (2006) showed that for the Cormorant field injection into a compartment raises the pore pressure by 6 MPa and the saturation by 0.6. This provides the inequality $C_S/C_P < 10$, for the 25% (mean) porosity rocks. Finally, the Gullfaks example of Landrø (2001) gives an identical pore pressure rise, saturation change of 0.5 and yields the inequality $C_S/C_P < 12$ for 30% porosity rocks. All of these porosities are fairly close to those in our North Sea data set and thus the points from these studies (labelled as L1, L2 and L3) are added to Fig. 7. These appear to support the $C_S/C_P = 8$ trend as being consistent with most of these clastic reservoirs – probably as their porosities are similar. Note that if the porosity increases significantly, it is anticipated that C_S/C_P would increase to a value higher than 8, however no examples of this have, as yet, been identified.

Observed seismic data example – near versus far offset

In the above examples displayed in Fig. 7, either full stack or near-offset data are chosen. This is appropriate for comparison in this work as the full stack amplitudes are mainly dominated by near-angle information. However the relative weighting of pore pressure and saturation changes on angle-dependent seismic data also carries important information. This dependence has been discussed to some degree in the literature (for example, Trani *et al.* 2011). A direct conclusion can be deduced from the data example of Landrø (2001) for Gullfaks, suggesting that the fars are dominated by saturation whilst the nears show saturation and pore pressure changes. Whilst this is a compelling result, care must be taken to generalize such a statement as the relative magnitude of the pore pressure and saturation change signals in the 4D seismic data is known to depend on the porosity. What can be concluded, however, is that C_S/C_P is expected to vary with offset. In particular, our specific study anticipates an increase in C_S/C_P with offset and the far angles being dominated by saturation in agreement with the literature. This can be explained by equation (7). The angular dependence of the functions of incidence angles $\overline{\Gamma}_1$, $\overline{\Gamma}_2$ and $\overline{\Gamma}_3$ (Fig. 10a) combined with the magnitude of the petroelastic parameters, predicts that $C_S \Delta S_w$ increases at far angles relative to $C_P^{rock} \Delta P$ and $C_P^{fluid} \Delta P$ (Fig. 10b). It is concluded that saturation changes dominate the far angles. However, at near angles both $C_S \Delta S_w$ and $C_P^{rock} \Delta P$ have similar magnitudes (calculated for ΔS_w as 0.60 and ΔP as 5 MPa) and the near angles will be a mixture of saturation and pore pressure changes.

To study this effect, a data set from a deepwater turbidite field in West Africa is analysed for which restricted offset data are accessible. Here 2001 pre-production baseline data are available, together with a 2004 monitor survey. Near-angle (3–23°) and far-angle (23–37°) data are available for each of the two surveys (Fig. 11). There is an AVO effect observed in the area of study, with the amplitude on the nears being larger than that on the fars. Production start-up was in 2001 and water injection began several months after first oil. The oil is 32° API and contrasts well with the injected water for 4D studies. There is a mean porosity of 28%, consistent with our previous example. A simulation model is also available, from which predictions at two injector wells (W6 and W7 injecting for a continuous period two years prior to the monitor survey) can be made as in the previous example (Fig. 11). The near amplitude differences are seen to decrease at these injectors and this is interpreted as a dominance of saturation over pore pressure, leading to the inequalities $0.63C_S > 4.74C_P$ and $0.6C_S > 1.69C_P$. These points (WA1 and WA2) are included on the cross-plot of Fig. 7 and found to remain consistent with the $C_S/C_P = 8$ trend. However, the far amplitude differences at the injector locations are observed to show a larger magnitude difference than the near differences. Theoretical predictions of the increase in the magnitude of the time-lapse difference between the nears and fars agree with our observations and can be explained by C_S/C_P increasing from around 8 on the near, to 25 on the far-amplitude differences (see Table 2). This can also be seen in the relationship $\Delta A_{nears} \propto 8\Delta S_w - \Delta P$ and $\Delta A_{fars} \propto 25\Delta S_w - \Delta P$.

DISCUSSION AND CONCLUSIONS

An approximation has been developed that relates first-order pore pressure and saturation change to mapped time-lapsed seismic amplitudes and brings out the explicit role of the petroelastic model parameters in this relation. The relation has value in 4D feasibility studies, our intuitive understanding of how to interpret 4D seismic data and at a quantitative level, inversion to pressure and saturation change. Apart from the absolute magnitude of the pore pressure or saturation change, it is found that porosity plays an important controlling role and so too does the initial saturation state. It is expected that for porosities larger than 30%, saturation will dominate the 4D seismic signatures in most reservoirs, whilst for porosities smaller than 20% then pore pressure dominates. The results of this study suggest that C_S/C_P is a fundamental parameter that can be unambiguously extracted from mapped 4D seismic amplitudes by observing whether saturation or pore

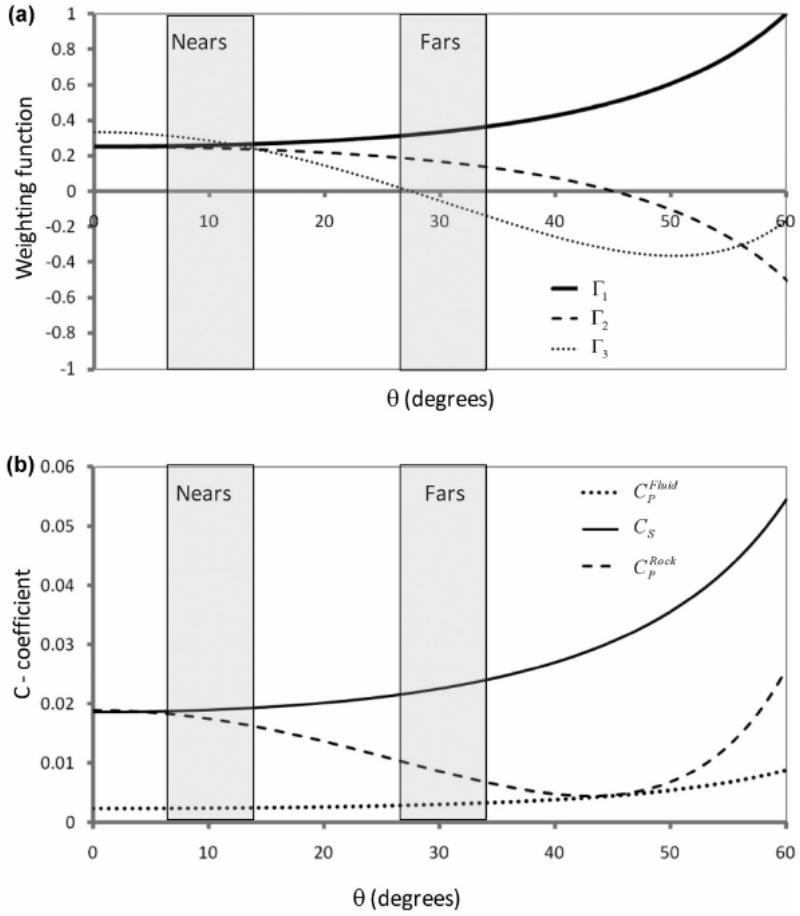

Figure 10 (a) Trigonometric functions of offset which weigh the AVO terms in our North Sea example. (b) The individual components ($C_S\Delta S_w$,$C_P^{fluid}\Delta P$and $C_P^{rock}\Delta P$) of the amplitude response, for a saturation change of 0.6 and pore pressure change of 5 MPa.

pressure dominates the response at a select number of injector wells. Producers are generally less informative, as pore pressure and saturation effects usually act in the same direction in the seismic response for both near- and far-offsets. It is predicted that these conclusions are also true of time interval differences. Further, according to the data collected from five different clastic reservoirs (three from the literature and two worked examples), all with similar porosities of between 25–30%, it appears that $C_S/C_P = 8$ seems to indicate the point at which pore pressure starts to dominates over saturation and vice-versa. Clearly, these results are for an ideal shale/sand interface and must be adapted in future work to include variable net-to-gross variations and reservoir thickness – the latter is a parameter observed by Falahat *et al.* (2011) to be important in controlling the time-lapse behaviour of thin reservoirs.

The above result has implications for the underlying petroelastic model used to characterize rock and fluid physics. In particular, from equation (7), this finding can be written symbolically as:

$$\frac{\phi.FC}{(1-\varepsilon\phi).RSS - \phi.FPS} = 8, \tag{15}$$

where *FC* refers to the fluid contrast, *RSS* the rock stress sensitivity and *FPS* the fluid pressure sensitivity terms. There is an inter-dependence between the porosity and the separate groups of parameters observed. Interestingly, for fluid

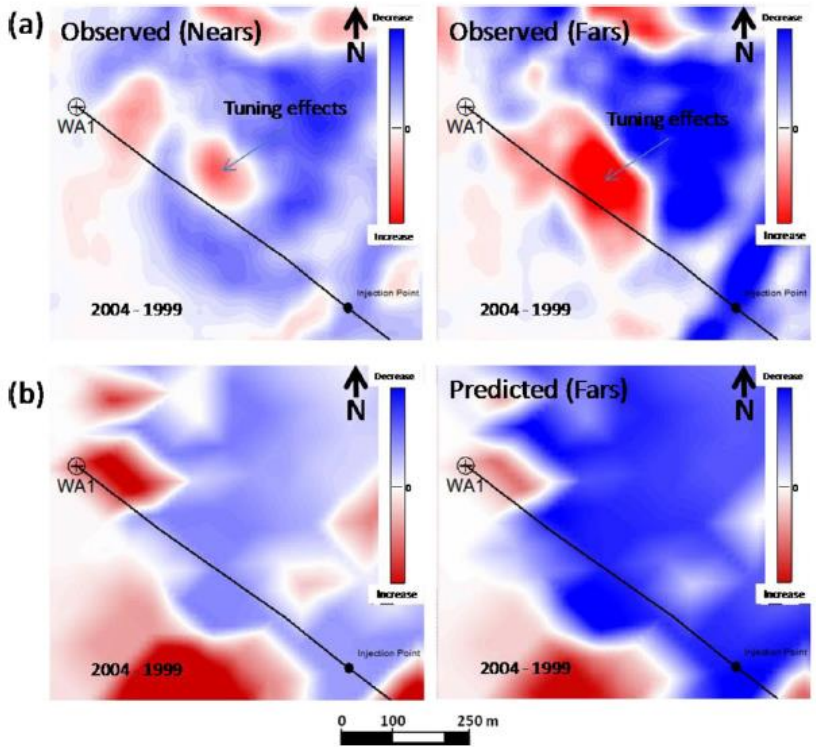

Figure 11 West Africa example: (a) observed 4D seismic response for the near and far angles; (b) predictions of the 4D seismic response based on the approximate equation (7) proposed in the text for the near- and far-angle stacked data. The horizontal and vertical scales for the map are identical.

pressure dependencies much smaller than the rock stress sensitivity (see Fig. 3 – this may in fact be normality according to our calculations), then this equation becomes:

$$\frac{\phi.FC}{(1-\varepsilon\phi).RSS} \approx 8, \tag{16}$$

where the equation is now observed to link the fluid contrast between the original and displaced fluids and the rock stress sensitivity. As it is well known that the highest uncertainty is associated with rock stress sensitivity (see Appendix B), this now provides a way of separately confirming the stress sensitivity. This is possible, as the fluid contrast terms are relatively well-known functions of the bulk modulus and density of the oil and brine and the initial water saturation. Thus, for a mean porosity of 25% and oil-water displacement for the reservoirs in our North Sea example, we obtain:

$$0.25N_3 + 0.33N_4 \approx 0.015, \tag{17}$$

where N_3 and N_4 are defined as variables dependent on the stress sensitivity functions for κ and μ in Appendix A. This imposes a constraint on the permissible stress sensitivity curves, an example of such a family is shown in Fig. 12. Here, data from MacBeth (2004) that satisfy, or do not satisfy equation (17), are highlighted. It is possible for a number of stress sensitivity curves to satisfy the constraint and therefore the condition is not unique. It is concluded that, based on robust observation of mapped 4D seismic data, it may be possible to make a statement about the range of possible *in situ* petroelastic model (rock) parameters. This represents a way of closing the loop between seismic-scale and laboratory measurements. In order to generalize these results further however, more seismic data need to be made available. However, it is our experience that there are relatively few published case studies, as yet, that quote the pore pressure and saturation changes needed to formulate our constraints.

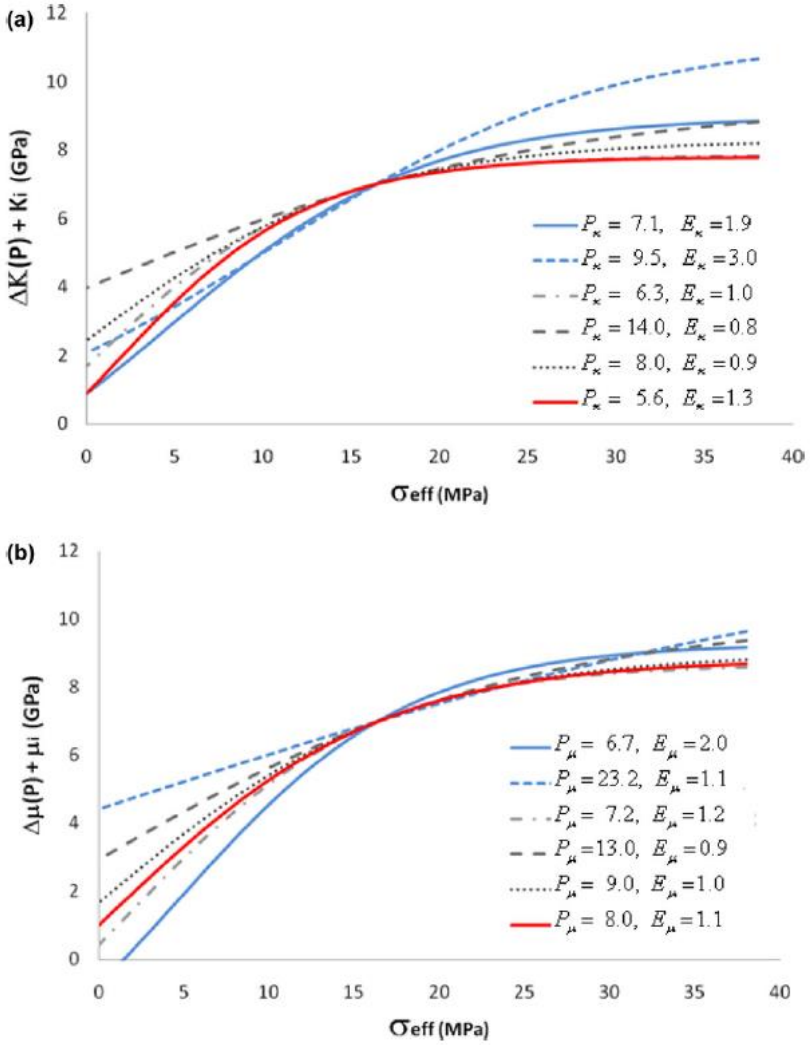

Figure 12 Stress sensitivity curves for (a) bulk modulus variation and (b) shear modulus variation with effective stress/pore pressure. These curves are parametrized using the relationship suggested by MacBeth (2004) and correspond to the data provided for a range of different reservoir rocks. The blue curves correspond to a selection of parameters that do not satisfy the constraint derived from the 4D seismic results. All of the other curves agree with the seismic data. The red curve corresponds to the laboratory result for the field of interest in this current study.

One final and important conclusion from this study is that the petroelastic model parameters appear to influence the mapped 4D seismic signature as collective groups of parameters, rather than individual controlling parameters. This explains the difficulties researchers have had in the past in constraining these parameters. A demonstration of this situation is the many possible scenarios for the stress sensitivity parameters that will lead to the same outcome as equation (17). The collective groups of parameters determined here are therefore the smallest predominant variables that can uniquely control the 4D signature and it is not possible to do better than this with seismic data. Inversion for the parameters of a specific

petroelastic model from seismic data is therefore uncertain to some degree and constraints must, instead, be placed through appropriate laboratory measurements where possible. Interestingly, despite the non-uniquenesses, equation (7) does reveal a dependence on the main controlling reservoir parameter of porosity. In previous studies such as Landrø (2001) and MacBeth *et al.* (2004), it was suggested that C_S and C_P are functions of porosity – equation (7) now determines the exact nature of this dependence. Thus, the proposed formulation in equation (7) can be used for studies where pore pressure and saturation changes need to be separately extracted from 4D seismic data. Finally, the framework and discussion above are not limited by underlying models of rock and fluid physics and the formulation of equation (14) may thus be regarded as universal.

ACKNOWLEDGEMENTS

We thank the sponsors of the Edinburgh Time Lapse Project, Phase IV, for their support (BG, BP, Chevron, ConocoPhillips, ENI, ExxonMobil, Hess, Ikon Science, Landmark, Maersk, Marathon, Norsar, RSI, Petrobras, Shell, Statoil and Total). Schlumberger are thanked for providing Petrel and Eclipse software. E. Alvarez thanks Hamed Amini for his contribution to this work and also acknowledges financial support from Senergy (GB).

REFERENCES

Aki K. and Richards P.G. 1980. *Quantitative Seismology: Theory and Methods*. Freeman and Co.

Alsos T., Osdal B. and Høiås A. 2009. The many faces of pressure changes in 4D seismic at the Svale Field and its implication on reservoir management. 71st Conference & Exhibition, EAGE.

Amini H. and MacBeth C. 2011. Calibration of simulator to seismic modelling for quantitative 4D seismic interpretation. 73rd EAGE Conference & Exhibition incorporating SPE EUROPEC 2011

Barkved O., Heavey P., Kjelstadli R., Kleppan T. and Kristiansen T. 2003. Valhall field – V Still on Plateau after 20 years of production. SPE 83957

Batzle M. and Wang Z. 1992. Seismic properties of pore fluids. *Geophysics* **57**, 1396–1408.

Bouchet R., Levallois B., Mfonfu G. and Authier J-F. 2004. *Girassol field optimised development*. AAPG international Conference, Cancun, Mexico.

Clark V.A. 1992. The effect of oil under in-situ conditions on the seismic properties of rocks. *Geophysics* **57**, 894–901.

Clifford P.J., Trythall R., Parr R.S., Moulds T.P., Cook T., Allan P.M. and Sutcliffe P. 2003. Integration of 4D seismic data into the management of oil reservoirs with horizontal wells between fluid contacts. SPE 8956.

Corzo M., MacBeth C. and Barkbed O. 2011. Estimation of pressure change in a compacting reservoir from time-lapse seismic data. Geophysical Prospecting. *In Press*.

Eiken O. and Tøndel R. 2005. Sensitivity of time-lapse seismic data to pore pressure changes. Is quantification possible? *The Leading Edge* **24**, 1250–1254.

Falahat R., Shams A. and MacBeth C. 2011. Towards quantitative evaluation of gas injection using time-lapse seismic data. *Geophysical Prospecting* **59**, 310–322.

Fjaer E., Holt R.M., Horsrud P., Raaen A.M. and Risnes R. 2008. *Petroleum Related Rock Mechanics, Developments in Petroleum Science 53*. Elsevier.

Floricich M. 2006. *An engineering-consistent approach for pressure and saturation estimation from time-lapse seismic data*, PhD thesis, Heriot-Watt University.

Floricich M., MacBeth C., Stammeijer J., Staples R., Evans A. and Dijiksman N. 2006. Determination of a seismic and engineering consistent petro-elastic model for time-lapse seismic studies: Application to the Schiehallion Field. *SEG Expanded Abstracts* **25**, 3205–3209.

Gassmann F. 1951. Über die Elastizität poröser Medien. *Vierteljahresschrift der Naturforschenden Gesellschaft in Zürich* **96**, l–23.

Gray D., Goodway B. and Chen T. 1999. Bridging the Gap: Using AVO to detect changes in fundamental elastic constants. *SEG Expanded Abstracts* **18**, 852–855.

Han D. and Batzle M. 2004. Gassmann's equation and fluid-saturation effects on seismic velocities. *Geophysics* **69**, 398–405.

Hatchell P. and Bourne S. 2005. Rocks under strain: Strain-induced time-lapse time shifts are observed for depleting reservoirs. *The Leading Edge* **24**, 1222–1225.

Hodgson N. and MacBeth C. 2007. Inverting for reservoir pressure change using time-lapse time strain: Application to Genesis Field, Gulf of Mexico. *The Leading Edge*, 649–652.

Hoffman R., Xu X., Batzle M., Prasad M., Furre A.K. and Pillitteri A. 2005. Effective pressure or what is the effect of pressure? *The Leading Edge* **24**, 1256–1260.

Huang Y., MacBeth C., Barkved O. and Gestel J-P. 2011. Enhancing dynamic interpretation at the Valhall Field by correlating well activity to 4D seismic signatures. *First Break* **29**(3).

Johann P., Sansonowski R., Oliveira R. and Bampi D. 2009. 4D seismic in a heavy-oil, turbidite reservoir offshore Brazil. *The Leading Edge* **28**, 718–729.

King M.S., Marsden J.R. and Dennis J.W. 2000. Biot dispersion for P- and S-wave velocities in partially and fully saturated sandstones. *Geophysical Prospecting* **48**, 1075–1089.

Kloosterman H.J., Van Waarde J., Kelly R. and Stammeijer J. 2001. A new dimension in reservoir evaluation –Time lapse seismic in Shell Expro's Central North Sea Fields. SPE 71799

Landrø M. 2001. Discrimination between pressure and fluid saturation changes from time-lapse seismic data. *Geophysics* **66**, 836–844.

Lumley D.E., Behrens R.A. and Wang Z. 1997. Assessing the technical risk of a 4-D seismic project. *The Leading Edge* **29**, 150–155.

Lumley D.E., Nunns A.G., Delorme G., Adeogba A.A. and Bee M.F. 1999. Meren Field, Nigeria: A 4D seismic case study. *SEG Expanded Abstracts* **18** 1628–1631.

MacBeth C. 2004. A classification for the pressure-sensitivity properties of a sandstone rock frame. *Geophysics* **69**, 497–510.
MacBeth C., Floricich M. and Soldo J. 2006a. Going quantitative with 4D seismic analysis. *Geophysical Prospecting* **54**, 303–318.
MacBeth C., HajNasser Y., Stephen K. and Gardiner A. 2011. Exploring the effect of meso-scale shale beds on a reservoir's overall stress sensitivity to seismic waves, *Geophysical Prospecting* **59**, 90–110.
MacBeth C. and Ribeiro C. 2007. The stress sensitivity of shaley sandstones. *Geophysical Prospecting* **55**, 155–168.
MacBeth C., Stammeijer J. and Omerod M. 2006b. Seismic monitoring of pressure depletion evaluated for a United Kingdom continental-shelf gas reservoir. *Geophysical Prospecting* **54**, 29–47.
MacBeth C., Stephen K.D. and McInally A. 2005. The 4D seismic signature of oil-water contact movement due to natural production in a stacked turbidite reservoir. *Geophysical Prospecting* **53**, 183–203.
Mavko G., Mukerji T. and Dvorkin J. 1998. *The Rock Physics Handbook*. Cambridge University Press
McInally A., Kunka J., Garnham J., Redondo-Lopez T. and Stenstrup-Hansen L. 2001. Tracking production changes in a turbidite reservoir using 4D elastic inversion. 63rd Conference and Exhibition, EAGE.
Meadows M. 2001. Enhancements to Landro's method for separating time-lapse pressure and saturation changes. *SEG Expanded Abstracts*, 1652–1655.
Ness O.M., Holt R.M. and Fjaer M. 2000. The reliability of core data as input to seismic reservoir monitoring studies. SPE 65180
Nur A., Mavko G., Dvorkin J. and Galmundi D. 1995. Critical porosity: The key to relating physical properties to porosity in rocks. *SEG Expanded Abstracts*, 878–881.
Parr R., Marsh J. and Griffin T. 2000. Interpretation and integration of 4-D results into reservoir management, Schiehallion Field, UKCS. *SEG Expanded Abstracts* **19**, 1464–1467.
Pelissier M.A., Hoeber H., van der Coevering N. and Jones I.F. 2007. Classics of Elastic Wave Theory. SEG, Geophysics Reprint Series, 24.
Røste T., Moen A.S., Kolstø E., Brekken M., Thrana C., Husby O. and Lescoffit G. 2009. The Heidrun Field: Monitoring fluid flow in the complex Åre Formation. *First Break* **27**(4).
Rutherford S.R. and Williams R.H. 1989. Amplitude-versus-offset variations in gas sands. *Geophysics* **54**, 680–688.
Sayers C.M. 2010. Geophysics Under Stress: Geomechanical Applications of Seismic and Borehole Acoustic Waves. SEG Distinguished Instructor Short Course, ISBN 1560802103
Shuey R.T. 1985. A simplification of the Zoeppritz equations. *Geophysics* **50**, 609–614.
Staples R., Stammeijer J., Jones S., Brain J., Smit F. and Hatchell P. 2006. Time-Lapse (4D) seismic monitoring – Expanding applications. Presented at the Joint Convention, What's Next? CSPG – CSEG – CWLS.
Strønen L.K. and Digranes P. 2004. Time-lapse seismic extends the lifetime of the Gullfaks Field. 66th Conference & Exhibition, EAGE.
Trani M., Arts R., Leeuwenburgh O. and Brouwer J. 2011. Estimation of changes in saturation and pressure from 4D seismic AVO and time-shift analysis. *Geophysics* **76**(2), C1–C17.

APPENDIX A

Derivation of Elastic Modulus Changes

Our objective is to determine the $\Delta\kappa_{TL}$, $\Delta\rho_{TL}$ and $\Delta\mu_{TL}$ terms in equation (3) as a function of the pore pressure and saturation changes ΔP and ΔS_w for an oil-water system. For this purpose, the petroelastic model used in this work is based on the standard petroelastic model implemented by MacBeth, Stephen and McInally (2005) and similar to that widely used by others. The starting point for this is the pore pressure dependent version of the saturation equation given originally by Gassmann (1951) (and subsequently translated into English by Pellisier *et al.* 2007)

$$\kappa_{sat}(P, S_w) = \kappa_{dry}(\sigma_{eff}) + \frac{(1-\kappa_{dry}(\sigma_{eff})/\kappa_m)^2}{\frac{\phi}{\kappa_{fl}(P,S_w)} + \frac{1-\kappa_{dry}(\sigma_{eff})/\kappa_m - \phi}{\kappa_m}}, \quad \text{(A1)}$$

where P and S_w are the pore pressure and saturation, κ_{sat} the saturated bulk modulus, κ_{dry} the dry frame bulk modulus, κ_m the bulk modulus of the mineral frame, κ_{sat} the effective bulk modulus of the pore fluid and ϕ the porosity. It is assumed in this current work that the porosity does not change significantly with changes in effective stress $\sigma_{eff} = \sigma_{tot} - \alpha P$ (where σ_{tot} is the unchanged overburden or external stress and α is the effective stress coefficient – Hoffman *et al.* 2005). Our next step is to utilize the linear form of Gassmann's equation given by Mavko and Mukerji (1995).

$$\Delta\kappa_{sat}(P, S_w) = \varepsilon\phi\Delta\kappa_{fl}(P, S_w), \quad \text{(A2)}$$

where ε is a rock constant and a measure of pore stiffness and is typically of around 6.25 in value.

By considering only first-order perturbations in saturation ΔS_w in the effective fluid bulk modulus:

$$\kappa_{fl} = \frac{\kappa_o\kappa_w}{S_w\kappa_o + (1-S_w)\kappa_w}, \quad \text{(A3)}$$

we arrive at the perturbation to the saturated rock bulk modulus for saturation changes ΔS_w only:

$$\Delta\kappa_{TL}(0, \Delta S_w) \approx \varepsilon\phi R \left[\frac{\kappa_w - \kappa_o}{[1-S_{wi}(1-R)]^2 - \Delta S_w(1-R)[1-S_{wi}(1-R)]}\right]\Delta S_w,$$

where $R = \kappa_o/\kappa_w$. Expansion as a Taylor's series gives the first-order term:

$$\Delta\kappa_{TL}(0, \Delta S_w) \approx \varepsilon\phi R \frac{(\kappa_w - \kappa_0)}{(1 - S_{wi})^2 + RS_{wi}} \Delta S_w. \quad \text{(A4)}$$

Despite its simplicity, this equation has been checked numerically and is found to be accurate for an ΔS_w of between 0 and 0.07.

Next, the pore pressure dependence for the dry frame bulk modulus is defined according to MacBeth (2004):

$$\kappa_{dry}(\sigma_{eff}) = \frac{\kappa_\infty}{1 + E_\kappa e^{-\sigma_{eff}/P\kappa}}, \quad \text{(A5)}$$

where κ_∞, E_κ and P_κ are parameters assigned from laboratory measurements. In his paper, MacBeth (2004) also showed that these parameters are strongly related to porosity and from a general range of laboratory data it is possible to conclude that $\kappa_\infty = \kappa_m(1 - \varepsilon\prime\phi)$, where ε' is approximately 2.8 for the sandstone samples studied. The time-lapse change $\Delta\kappa_{dry}(\Delta\sigma_{eff})$ can be linearized for small changes in $\Delta\sigma_{eff}$ (and hence ΔP) and an appropriate linear relation found by taking the first-order term in a Taylor expansion about the initial reservoir effective stress:

$$\Delta\kappa_{dry} \approx -(1 - \varepsilon'\phi)(\alpha\kappa_m A_\kappa)\Delta P. \quad \text{(A6)}$$

Here, the change in effective stress $\Delta\sigma_{eff}$ has been replaced by $\alpha\Delta P$, where α is the effective stress coefficient. A_κ is the local gradient of the stress sensitivity curve at the initial reservoir pore pressure and is a weak function of ϕ and α – the main porosity dependence is carried in the κ_∞ term. Next, for the pore pressure dependence of the fluids, the empirical relations of Batzle and Wang (1994) are used to generate a pore pressure relation numerically for guidance. These relations are linearized about the initial reservoir pore pressure, P_i. This process is found to be reasonably accurate for a number of different initial pore pressures and oils. This then yields the linear equations:

$$\kappa_w(P_i + \Delta P) = \kappa_w(P_i) + W_\kappa \Delta P, \quad \text{(A7)}$$

$$\kappa_o(P_i + \Delta P) = \kappa_o(P_i) + O_\kappa \Delta P, \quad \text{(A8)}$$

where W_κ and O_κ are positive constants that can be derived from the empirical black oil formulation of Batzle and Wang (1992) or a similar study. Finally, by also considering first-order pore pressure perturbations in the saturation equations, after some manipulation the total bulk modulus change can be written as:

$$\Delta\kappa_{TL}(\Delta P, 0) \approx -\left[\phi\left(\frac{\varepsilon(W_\kappa\kappa_0 S_{wi} + O_\kappa\kappa_w(1 - S_{wi}))}{\kappa_w(1 - S_{wi}) + \kappa_0 S_{wi}}\right) \times (1 - \varepsilon'\phi)(\alpha\kappa_m A_\kappa)\right]\Delta P. \quad \text{(A9)}$$

Finally, the first-order perturbation $\Delta\kappa_{TL}(\Delta P, \Delta S_w)$ can be obtained by summing $\Delta\kappa_{TL}(0, \Delta S_w)$ and $\Delta\kappa_{TL}(\Delta P, 0)$ as above. Note that the fluid pressure sensitivity is small compared to the rock stress sensitivity and the saturation change. For example, a 5 MPa change in pore pressure induces -0.658 GPa (-9.23%) in rock and 0.16 GPa in fluids (1.73%). In comparison, a change of 0.5 in saturation induces 1.04 GPa (11.25%) change in the bulk modulus.

The corresponding saturation equation for density is based on material balance:

$$\rho_{sat}(P, S_w) = \rho_{dry}(\sigma_{eff}) + \phi(S_w\rho_w + (1 - S_w)\rho_O), \quad \text{(A10)}$$

where ρ_{sat} and ρ_{dry} are the saturated and dry rock densities respectively and ρ_o and ρ_w the oil and water densities. From equation (A10) it is relatively straightforward to compute the result due to the change in saturation:

$$\Delta\rho_{TL}(0, \Delta S_w) = \phi(\rho_w - \rho_o)\Delta S_w. \quad \text{(A11)}$$

For pore pressure dependence, we assume that all changes in the bulk density are associated with fluids (as opposed to geomechanical effects) and following the bulk modulus calculation the density is linearized with respect to the first-order pore pressure changes. Thus:

$$\rho_w(P_i + \Delta P) = \rho_w(P_i) + W_\rho \Delta P, \quad \text{(A12)}$$

and

$$\rho_o(P_i + \Delta P) = \rho_o(P_i) + O_\rho \Delta P, \quad \text{(A13)}$$

where W_ρ and O_ρ are empirical constants associated with the fluid dependency. From this, we obtain the desired perturbation:

$$\Delta\rho_{sat}(\Delta P, 0) = \phi\left[W_\rho S_{wi} + O_\rho(1 - S_{wi})\right]\Delta P, \quad \text{(A14)}$$

and the final perturbation can be written as:

$$\Delta\rho_{TL}(\Delta P, \Delta S_w) = \phi(\rho_w - \rho_o)\Delta S_w + \phi\left[W_\rho S_{wi} + O_\rho(1 - S_{wi})\right]\Delta P. \quad \text{(A15)}$$

Finally, we consider the pore pressure dependence for shear rigidity μ following MacBeth (2004):

$$\mu(\sigma_{eff}) = \frac{\mu_\infty}{1 + E_\mu e^{-\sigma_{eff}/P_\mu}}. \quad \text{(A16)}$$

Considering only the effective stress (pore pressure) effect and treating equation (A16) in a similar fashion to the bulk modulus calculation we find that:

$$\Delta\mu_{TL} \approx -(1-\varepsilon'\phi)\left(\alpha\mu_m B_\mu\right)\Delta P, \tag{A17}$$

where the factor ε' in the linear porosity term is identical to the equivalent factor in the bulk modulus equation. The results above for the time-lapsed perturbations $\Delta\kappa_{TL}$,$\Delta\rho_{TL}$ and $\Delta\mu_{TL}$ are inserted into equation (3) in the main text to give equations (4), (5) and (6) and consequently equation (7) with the various parameters lumped to form the composite groups of terms N_1, N_2, N_3, N_4, N_5 and N_6.

APPENDIX B

Possible Factors Affecting the Stress Sensitivity of the Reservoir's Seismic Properties

The stress sensitivity of the reservoir's seismic wave properties is an important element in determining the balance between the effects of pore pressure and saturation change on the 4D seismic response. The following factors affect the determination of these properties but are not all taken into account in the standard petroelastic model. These parameters are grouped according to those that enhance and those that diminish the stress sensitivity relative to that measured from a core plug in the laboratory.

B.1 – Factors that suggest an enhancement of the predicted reservoir stress sensitivity relative to that measured from a core plug

Statistical sampling – cores taken from wells do not provide a statistically meaningful representation of the 3D heterogeneity in the reservoir because these samples are usually taken from the most competent and productive rock. Core plugs do not adequately sample the full reservoir and thus may miss particular facies groups or do not properly represent the nature of the geology. This may lead to stress-sensitive mesoscale pockets of unconsolidated/ consolidated sands, perhaps shales, or even fractures/faults being bypassed in the analysis. Subsequent core-to-log correlations and long-wavelength seismic averages will thus underestimate stress sensitivity. This issue may be partially mitigated by the use of log-guided sampling strategies and quantitative outcrop analogue studies but still cannot adequately represent features such as fracture zones. A counterargument to this is that we naturally bias results taken in the laboratory by focusing on those plugs that do not fall apart and thus we do not sample the most stress sensitive parts of the subsurface such as fractures, or brecciated zones.

Time scale of production – the time scale over which production occurs (days or months) is longer than the scale over which pore pressure is cycled (minutes/hours) in the laboratory. The longer time may allow microscopic deformation and accommodation of the sample at each stress state, while the rock 'creeps' into an equilibrium position. The velocity in this final condition may differ from the usual laboratory results.

B.2 – Factors that suggest a reduction of the predicted reservoir stress sensitivity relative to that measured from a core plug

Core plug damage – it has been suggested that many of the defects observed in the laboratory are the consequence of internal damage in the core as a result of stress unloading during the act of coring from wells or stress release at the outcrop (Ness, Holt and Fjaer 2000). The degree of damage depends largely on the original stress conditions for the rock and, to a lesser extent, on the degree of consolidation. Cores loaded back to their *in situ* stress state do not recover their original velocities and their stress dependence is usually larger than it was *in situ*. Damage resulting from core unloading needs to be estimated and subtracted from the rock-frame measurements. Another aspect is core unloading damage, which implies that we may be measuring stress sensitivities much higher than *in situ* (Ness *et al.* 2000).

Frequency dispersion – in saturated rock, higher velocities are generally observed at higher frequencies. This is the well-recognized problem of frequency dispersion (and attenuation) and it affects the confidence with which measurements from the laboratory can be used at seismic frequencies. This effect depends on many factors, such as rock type, clay distribution and the presence of cracks in the core plug (Mavko, Mukerji and Dvorkin 1998).

Effective stress coefficient – this is the prediction of the true effective stress acting on the rock frame as a result of internal fluid pore pressure variations. It can be shown experimentally that effective stress $\sigma_{eff} = \sigma_{ob} - \alpha P$ on the rock frame is a linear function of confining (overburden) stress σ_{ob} and pore pressure P, where α is the effective stress coefficient. The more unconsolidated a rock, then the closer α becomes to 1. The more consolidated rocks have α values lower than 1 (and hence this reduces the influence of pore pressure fluctuations on the elastic properties). The exact value of α is not an easy quantity to evaluate *in situ*, as it depends upon the

property measured, the fluid flow conditions of the reservoir and consequent boundary conditions (Hoffman *et al.* 2005).

Geomechanical effects – the effective stress as defined above depends on the difference of the total stress field and the reservoir pressure weighted by the effective stress coefficient. During deformation, the reservoir changes the surrounding stress conditions such that the total stress has now altered. This adjustment may be written by $\gamma \Delta P$, where γ is the stress arching ratio (Sayers 2010; MacBeth *et al.* 2011), which also varies across the reservoir. As a consequence, the effective stress acting on the reservoir rocks is now given by $(\gamma\text{-}\alpha)\Delta P$. As both γ and α are defined as positive numbers but $\gamma < \alpha$ (MacBeth *et al.* 2011), they act to possibly reduce the pore pressure sensitivity of the reservoir rocks. A spin-off benefit is that the surrounding reservoir rocks are altered by the stress field according to $\gamma \Delta P$ and this may be detected. In addition to the above, a secondary effect may occur in the shales – as they extend the pore volume expands and the pore pressure decreases by an amount determined by their Skempton B-coefficient (MacBeth *et al.* 2011).

Geomechanical effects/overburden – as the reservoir compacts, the overburden rocks extend. This effect is well documented and has been commonly used to monitor overburden stress changes and reservoir pressure (Hatchell and Bourne 2005; Hodgson *et al.* 2007). This also effects the seismic response at a top reservoir and may be significant in strongly compacting reservoirs (Corzo, MacBeth and Barkbed 2011).

B.3 The following could enhance or diminish the stress sensitivity relative to that measured from a core plug

The measured 'dry' frame response – there is some doubt about the state of 'dry' rock-frame saturation in the laboratory and whether it is appropriate to use it in Gassmann's equation to represent the frame in fully saturated rock. Some of this uncertainty relates to sample-preparation procedures prior to testing. In particular, it is the drying process that determines the small percentage of moisture adsorbed on the grains and structural water associated with clays. Differences in drying rate and temperatures can lead to a variation in measured velocities (e.g., King, Marsden and 2000).

The role of clays and shales – the effect of clays on the stress sensitivity of sandstones is currently uncertain (MacBeth and Ribeiro 2007). Clay related measurements are generally not made on a routine basis. At the larger scale this translates to a presence of shales, shales/clays but in general there is no sampling of the non-reservoir rocks. The stress sensitive properties of shales are however largely uncertain and difficult to assign due to lack of adequate data (MacBeth *et al.* 2011).

Imperfect stress recovery – although triaxial or biaxial laboratory equipment can provide access to a range of stress pathways with variations in vertical loading and differential stress, it is not possible to reinstall the true 3D *in situ* stress field, because there is insufficient information on the subsurface stresses and the way they change during production (Fjaer *et al.* 2008).

Stress asymmetry – results from core plugs vary depending upon whether the plug is under compression or extension. This asymmetry must be taken into account in stress sensitivity calculations and will lead to a natural hysteresis in physical behaviour (Sayers 2010).

APPENDIX C

Time Thickness Equation

Calculation shows that a similar equation as in equation (3) may be employed for calculation of the reservoir time-thickness at measured normal incidence. After calculation this yields:

$$\Delta T_{TL} = -T_R \left[\Delta S_w \phi \left[\overline{\Gamma_1} N_1 + \overline{\Gamma_2} N_2 \right] - \Delta P \left((1 - \varepsilon\phi) \left(\overline{\Gamma_1} N_3 + \overline{\Gamma_3} N_4 \right) - \phi \left(\overline{\Gamma_1} N_5 + \overline{\Gamma_2} N_6 \right) \right) \right], \quad \text{(C1)}$$

where $\overline{\Gamma}_1 = 0.25$, $\overline{\Gamma}_2 = 0.25$ and $\overline{\Gamma}_3 = 0.33$ and ΔT is the time-shift and T_R is the reservoir time thickness in two-way time.

Amsterdam '14

We G102 15

Quantification of Residual Oil Saturation Using 4D Seismic Data

E. Alvarez* (Heriot-Watt University) & C. MacBeth (Heriot-Watt University)

SUMMARY

A method has been developed to quantify residual oil saturation using 4D seismic differences interpreted at fluid contacts. The development is different from previous approaches in that it uses only the seismic amplitudes at the original and produced oil-water contacts instead of the top reservoir event. It requires that these contacts be visible in the 4D seismic data, although not necessarily in the 3D seismic. It is shown that the method can provide a quick semi-quantitative analysis of published field studies from visual inspection. The approach is further demonstrated by application to a field dataset from a North Sea oil reservoir. The results of this application show good agreement with the simulation model, but also some variations that suggest such residual oil estimates could be used in future history matching to update the simulation model.

Introduction

Residual oil saturation (S_{or}) can be defined as the remaining oil saturation that cannot be produced from gas or water displacement, but remains in the swept zone (Morrow, 1990). S_{or} is a key quantity in reservoir recovery and economic reservoir evaluation, as well as a fundamental parameter for studying water flooding and determining sweep efficiency. Furthermore, it is a necessary basis for planning enhanced oil recovery (EOR), Quantitative knowledge of the spatial distribution of the fluids is a key input in the decision making process. Despite numerous methods available to estimate it, such as laboratory test/core flooding, well based measurements, pore network modeling, it is generally acknowledged that there is no acceptable way to reliably measure S_{or}. Furthermore, the value of S_{or} depends upon the vertical and horizontal sweep efficiency, the heterogeneity of the geologic system, and the microscopic displacement efficiency (Adamski, et al. 2003), hence it is a scale dependent measurement. In this work we show a method to quantify S_{or} at the seismic scale using 4D seismic data by interpreting the fluid contacts in the far angle stack differences. We show through seismic modelling and a real data example that a map of 4D amplitudes at the picked original oil-water contact gives not only the regions of change and sweep, but also the magnitude of S_{or} if properly calibrated. The method requires that contacts be visible in the 4D seismic data, but not necessarily in the 3D seismic.

Reservoir engineering background

Capillary pressure tests performed in core samples are commonly used to estimate the relative permeabilities of oil and water (k_{ro} and k_{rw}) at reservoir conditions ($S_w = S_{wc}$) and after depletion ($S_w = 1- S_{or}$) as shown in Figure 1. Here, the connate water saturation (S_{wc}) and the residual oil saturation (S_{or}) represent the end points of the capillary pressure curves. This representation, however, only considers the small scale heterogeneities that affect the capillary forces; therefore S_{or} only represents the minimum amount of oil that can be taken out of the rock assuming a perfect sweep. In reality, the value of S_{or} will fall somewhere along the capillary pressure curves depending on *pore scale* factors such as wettability, pore structure, clay content or fluid dynamics. *Reservoir scale* factors like sedimentological structures, faults, fractures, barriers, formation and water properties and gas saturation are important, so too are *well behaviour* related factors such as injection/production rate, water front speed, pressure gradients, gravity and sweep efficiency. In general, the larger the scale at which S_{or} is evaluated the larger its magnitude, hence S_{or} (lab) < S_{or} (field). In this work we are concerned with the magnitude of S_{or} that can be evaluated at the field scale using seismic data.

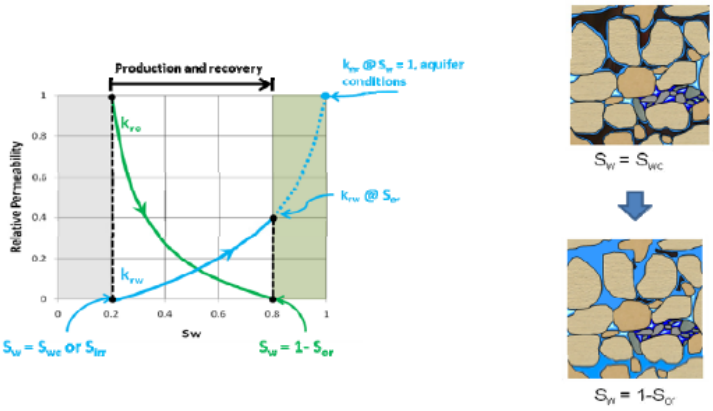

Figure 1 *End point saturations calculated from capillary pressure curves obtained from core measurements. S_{or} is oil saturation found somewhere along the green curve depending on sweep efficiency. The right hand side pictures show the different fluids that interact in the reservoir rock, oil (brown), free water (blue), connate water (light blue), clay bound water (dark blue), the latter two are not expected to change with production.*

Seismic theory and method

Literature review reveals that the majority of past work on residual oil calculation focuses on distinguishing oil from water-sands using Gassmann (1951) fluid substitution as a calibration tool for AVO or 4D seismic centered on the interpretation of the top reservoir event. However there is less attention given to the determination of S_{or} directly from the interpretation of the various fluid contacts. The main reason is that fluid contacts are not always visible in the 3D seismic, and although they are sometimes visible in 4D seismic, the interpretation is commonly performed on the full stacks by comparing the monitor and baseline vintages rather than looking at the 4D differences.

Our theoretical development starts with the conceptual model shown in Figure 2, representing an oil reservoir without a gas cap, in the pre and post-production states and showing the zone associated to the oil-water contact movement, assuming a predominantly basal aquifer drive. Following the definition of the AVO equations for fluid contacts (Wright, 1986) and equations for 4D difference interpretation (Alvarez & MacBeth, 2014) we define the changes in impedance (or amplitude) as linear functions of the changes in water saturation across each interface. Alvarez & MacBeth (2014) showed that the near angles are functions of a combination of both pressure and saturation changes, whereas the far angles, if stacked at the appropriate angle, can be nearly pressure independent. Since we are concerned only about saturation changes, we therefore concentrate on the far angles. We find that the time lapse amplitude (monitor minus base) at the original and produced oil-water contact (OOWC and POWC respectively) for the far angles is given by

$$\Delta A(\theta)^{far}_{OOWC} = -C_S^{far}(1 - S_{sor} - S_{wc}), \tag{1}$$

$$\Delta A(\theta)^{far}_{POWC} \approx -\Delta A(\theta)^{far}_{OOWC}. \tag{2}$$

Here, the constant C_S^{far} is a function of the rock and fluid physics equations as described in Alvarez & MacBeth (2014). An important observation here is that if a map of 4D amplitudes (far angles) at the OOWC is available (ΔA^{far}_{OOWC}), it indicates not only the regions of change and sweep, but also if properly calibrated can help us estimate S_{or}

$$S_{or} \approx 1 - \left[S_{wc} - \frac{\Delta A^{far}_{OOWC}}{C_S^{far}} \right]. \tag{3}$$

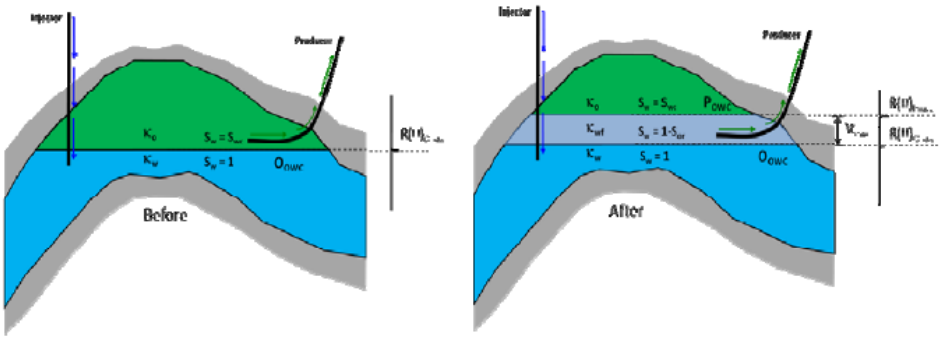

Figure 2 *Conceptual model of an oil reservoir, showing an oil-water contact movement through basal aquifer drive and the associated reflections. In the baseline we have only the reflection of the original oil-water contact ($R(\theta)_{OOWC}$), whereas in the monitor we have two reflections, the original and produced oil water contacts ($R(\theta)_{OOWC}$ and $R(\theta)_{POWC}$ respectively).*

In order to perform this calculation, knowledge of the connate water saturation, S_{wc}, is required. For our purposes, the value estimated from capillary pressure curves provides a reasonable starting point for the calculations, particularly in clastic reservoirs, since S_{wc} is not expected to change significantly with production and depends only on the pore scale factors described above. Another important finding is that, if the reservoir is sufficiently thick and clear, reflections of the original and produced contacts are visible - (2) can be used as a check during the cross-equalization process. Additionally, if the contacts are visible in the 3D seismic S_{or} can be determined from the following relation

$$\frac{A(\theta)^{after}_{oowc}}{A(\theta)^{before}_{oowc}} = \frac{S_{or}}{(1-S_{wc})} \tag{4}$$

Field data example

The equations defined above are tested on a North Sea oil reservoir with appropriate characteristics. The reservoir is between 80 and 300m thick, highly compartmentalised and geologically complex. Production is supported through water injection into the aquifer, and although the reservoir pressure is close to the bubble point and gas has been released in some areas, our study focuses on a compartment where no gas is present. The pre-production baseline and two monitors are available, all containing near (10°) and far (35°) angle stacks. Although no visible contacts are interpretable in the 3D seismic, the original oil-water contact is visible in well logs and it can be interpreted in the 4D difference for the far angle stacks. From capillary pressure curves available, S_{wc} varies between 0.15 and 0.25 and S_{or} from 0.25 to 0.85. Simulation to seismic modelling (sim2seis) is performed (Amini et al. 2011) to test our methodology and to compare the results with the observed 4D differences. Using the OOWC in the 4D difference, amplitude maps are generated and S_{or} is calculated using (3) (the parameters for C_S^{far} are known in this case). An example of the results obtained for the 2011Monitor – Baseline data is shown in Figure 3. In general a good correspondence is obtained between the simulated and predicted results, and the observed S_{or} shows some areas of potential bypassed oil. However there are areas of noise visible, possibly due to wavelet interference effects, suggesting that an inversion scheme might help to improve the results by de-tuning the data. The histograms of the mapped quantities shown in Figure 3 demonstrate that, despite the simplicity of our method, the results are a fair representation of S_{or} in the reservoir.

Conclusions

- A technique has been developed to calculate S_{or} from the far angle 4D differences of fluid contacts. The results of modelling suggest the scheme is practical, however wavelet interferences suggest that the use of a 4D inversion scheme may improve the method further
- Providing an estimate of the lateral distribution of S_{or} through a simple method can be of great support in the design of EOR plans as well as in seismic history matching, without the need to perform a full simulation to seismic modelling.
- The technique is based on the interpretation of the fluid contacts rather than an average map based on the top of the reservoir, therefore it requires that contacts be visible in the 4D seismic data, but not necessarily in the 3D seismic - although the latter is a bonus
- Fluid contacts are relatively easier to interpret than the top reservoir in 4D seismic data
- The technique has also be adapted to gas reservoirs, and can also be used for carbonate and thin, sub-tuned reservoirs

Acknowledgements

We thank the sponsors of the Edinburgh Time Lapse Project, Phase V, for their support (BG group, BP, CGG, Chevron, ConocoPhillips, ENI, ExxonMobil, Hess, Ikon Science, Landmark, Maersk, Nexen, Norsar, RSI, Petoro, Petrobras, Shell, Statoil, Suncor, Taqa, TGS, and Total). Schlumberger are thanked for providing Petrel and Eclipse software. EA thanks Hamed Amini for help and support with the sim2seis.

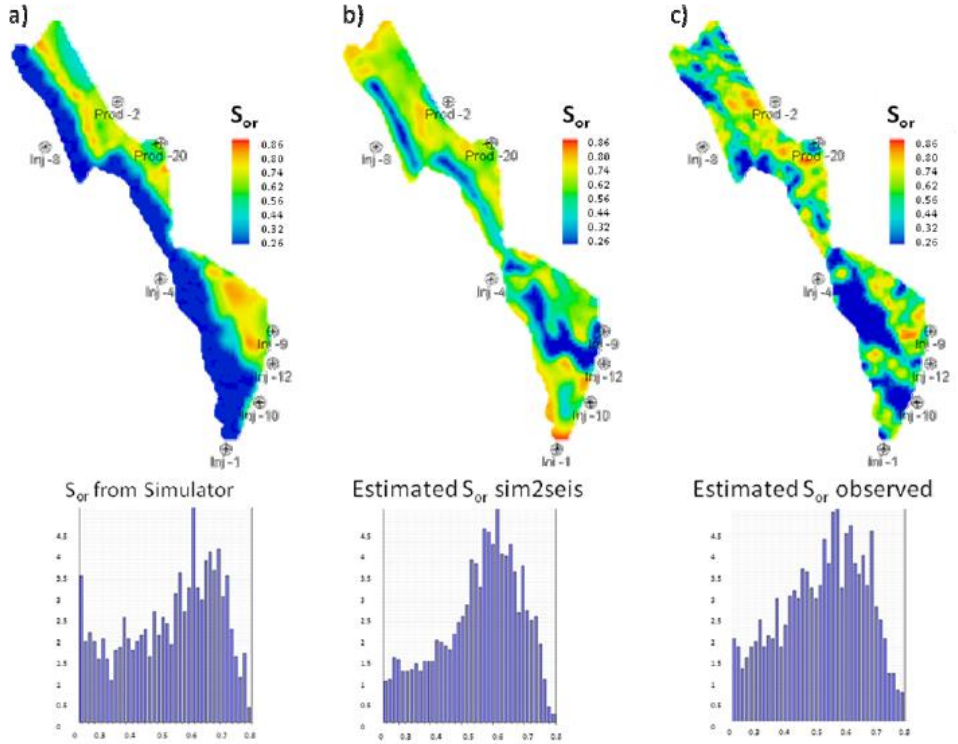

***Figure 3** Results of the S_{or} calculation: (a) from the simulator; (b) computed from the sim2seis (far angle stack); and (c) S_{or} computed from the observed far angle stack amplitudes. The histograms of each map are displayed below in each case, showing the good correspondence in the results.*

References

Adamski, M., Kremesee, V. and Charbeneau, R.J. [2003] Residual Saturation: What Is It? How Is It Measured? How Should We Use It? *Proceedings of the Petroleum Hydrocarbons and Organic Chemicals in Ground Water: 20th Conference and exposition*, Costa mesa, CA.

Alvarez, E. and MacBeth, C. [2014] An insightful parameterisation of the flatlander's interpretation of the 4D seismic signal. *Geophysical Prospecting*, **62**, 75-96.

Amini, H. and MacBeth, C. [2011] Calibration of simulator to seismic modelling for quantitative 4D seismic interpretation. *73rd EAGE Conference & Exhibition incorporating SPE EUROPEC 2011*.

Gassmann, F. [1951] Uber die elastizitat poroser medien. *Vier. der Natur Gesellschaft*, **96**, l-23.

Morrow, N.R. [1990] Wettability and its effect on oil recovery. *Journal of Petroleum Technology*, 1476-1484.

Wright, J. [1986] Reflection coefficients at pore-fluid contacts as a function of offset. *Geophysics*, **51**, 1858-1860.